Cranfield University

Andrea Cini

Scribe marks at fuselage joints:
initiation and propagation of fatigue cracks from mechanical defects in aluminium alloys

School of Applied Sciences

PhD

Cranfield University

School of Applied Sciences
Department of Materials - Damage Tolerance Group

PhD thesis

Academic Year 2011-2012

Andrea Cini

Scribe marks at fuselage joints:
initiation and propagation of fatigue cracks from mechanical defects in aluminium alloys

Supervisor: Professor Philip E. Irving

August 2012

This thesis is submitted in partial fulfilment of the requirements
for the degree of Doctor of Philosophy

Abstract

Mechanical damages, like scratches, are commonly detected on the surfaces of aircraft components and structures. They can be accidentally introduced during machining or maintenance operations or be the result of wear and impacts during aircraft service. Under the action of service loads, such mechanical damage can generate fatigue cracks reducing the component fatigue life and compromising the aircraft structural integrity. The evaluation of the effect of scratches and other small mechanical defects on the structure and component fatigue lives is therefore necessary to define an inspections programme and ensure the structural safety. Conventional fatigue life prediction methods generally consider scratches tents of microns deep too shallow to appreciably affect the fatigue performances of structural components. However the discovery of the scribe marks on fuselage joints disproved that prediction. In fact several commercial airlines discovered during inspections that aircraft which have been repainted showed multiple scratches on the fuselage skin along longitudinal and circumferential joints. Those scratches, referred to scribe marks, appear to have been caused by use of sharp tools during sealant removal process prior repainting. Scratches less than 200 μm deep were capable of severely reducing the fatigue life performance under service load rendering some aircraft beyond economical repair.

This thesis investigates the fatigue performances of 2024-T531 aluminium alloy sheets weakened by mechanically machined scratches. 2 mm thick clad and unclad samples were scribed at their gauge section using a diamond tipped tool. The scribing process produced very regular rounded V-shaped notches with an included angle of 60° across the sample width. Scratches from 25 μm to 185 μm deep, with 5 μm, 25 μm and 50 μm root radii were cut on the sample surfaces. Scribed sample were subsequently fatigue tested under constant amplitude tensile and bending load with a stress ratio of R=0.1 at a maximum stress of 200 MPa. Scribes were found to reduce the fatigue life of tension and bending samples up to 97% compared to that of smooth unscribed specimens. Both scribe shape and size affected the fatigue life of tensile and bending aluminium samples. The sharper and the larger the notch, the shorter the fatigue life.

Post failure fractography investigations were performed on sample fracture surfaces by means of optical and scanning electron microscope. Crack nucleation sites, fracture morphology and peculiar features left during crack propagation were analysed. Finally crack propagation data under different loading conditions were obtained by striation counting performed on fracture surfaces. Multiple crack initiation occurred at scribe roots usually from inclusions, defects or weak points along the root. The number and density of crack nucleation sites appeared to be determined by the scribe; increasing for notches with larger stress concentrations. Scribe geometry did not affect the fatigue growth rate but the propagation life for cracks deeper than 50-100 μm was influenced. Cracks nucleated from scribe marks showed a typical short crack behaviour growing faster than long cracks with the same linear elastic stress intensity factor.

Finite element calculations were performed on scribed samples evaluating how the presence of scribes altered the local stress and strain fields. Monotonic elastic and

elastic-plastic and cyclic elastic-plastic analyses were carried out under tensile and bending loads. Local elastic-plastic stress and strain fields in the neighbourhood of different scribes were determined by the notch shape and size. According to the occurrence of mechanical similitude conditions, scribes with the same shape but different size showed similar plastic zone and stress and strain distributions. A stabilised cyclic plastic zone was developed just at the root of scribes with a ratio between the root radius and depth $\rho/d \leq 0.2$. No correlations were observed between the occurrence of a stabilised cyclic plastic zone and the sample nucleation lives defined as the number of cycles to obtain an initial crack 50 μm deep from the notch root.

Traditional fatigue life prediction methods, based on the notch sensitivity factor, were not able to correctly characterise the effect of scratches few tens of microns deep on the fatigue life of 2024-T351 aluminium alloy components. An approach based on the critical distance theory was developed to characterise the total fatigue life reduction produced by the introduction of scribes relating the fatigue live to a critical stress range $\Delta\sigma_{lm}$. The critical stress range was capable of describing the effect of the elastic stress distribution produced by dissimilar notches on the nucleation and propagation of fatigue crack considering also the effect of the variation of the fatigue load nominal applied stress.

List of contents

List of figures

List of tables

Chapter 1
Scribe marks in aircraft structures

1.1 Scribe marks background

In 2003 several commercial airlines discovered during inspections that aircraft which have been repainted in the mid-1990s showed multiple scratches on the fuselage skin along longitudinal and circumferential joints [1-3]. The cause of these damages seemed to be maintenance-induced errors. Those scratches, referred to as scribe marks, appear to have been caused by use of sharp tools during sealant removal process prior repainting (see Fig. 1.1). Sharp metal scrapers, rather than wooden or plastic spatulas could cause damage on the aluminium skin near the joint area. Sealant is applied between aircraft panels joints to reduce air leaking from pressurised sections and to prevent corrosion damages caused by water seepages. At the external edge of the joint panels superposition area there is a pliable fillet seal of sealant (represented in green in the schematic of Fig. 1.1) that has to be removed to perform repainting procedure. If sharp non recommended tools were used for fillet removal the joint inner skin could be inevitably damaged in correspondence of the upper panel edge as shown in Fig. 1.1. To strip away the sealant fillet several passes of the tool are required and that generates multiple scratches on the inner panel (scribe marks). Moreover panels joints run along the entire aircraft surface and scribe marks can be metres long and widespread at every aircraft joint locations.

Fig. 1.1 shows how a scribe line on fuselage skin appears in a frontal view. For sake of simplicity Fig. 1.1 shows just the case of a longitudinal lap joint but circumferential butt joints and any kind of sealed joint can be potentially affected by scribe marks. Even patches installed during a previous reparation can show scribe marks. Those scratches are shallow damages, no deeper than 200-300 μm, but their location in a high stressed area of the joint, make them suitable fatigue crack nucleation spots. In addiction their extension along the joint and spreading across the entire aircraft candidate scribe marks as very probable widespread fatigue damage sites. In fact along the root of a metres long scratch, stress conditions responsible for fatigue cracks nucleation and propagation are approximately the same. That involves the presence of several weak points into the metal structure near the scratch root where multiple cracks can simultaneously nucleated, in particular in an aged aircraft that accumulated several flight hours. Those small cracks can eventually coalesce forming an instable propagating defect. On fuselage longitudinal joints, where the main stress component responsible for fatigue flaws nucleation and propagation, is the pressurisation one similar initiation conditions can be found all along the fuselage length. That is not the case of circumferential joints where stress condition are considered constant along a small portion of the scribe line.

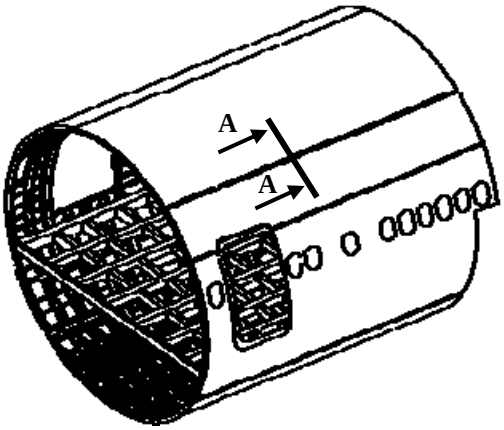

Fuselage section with longitudinal joints

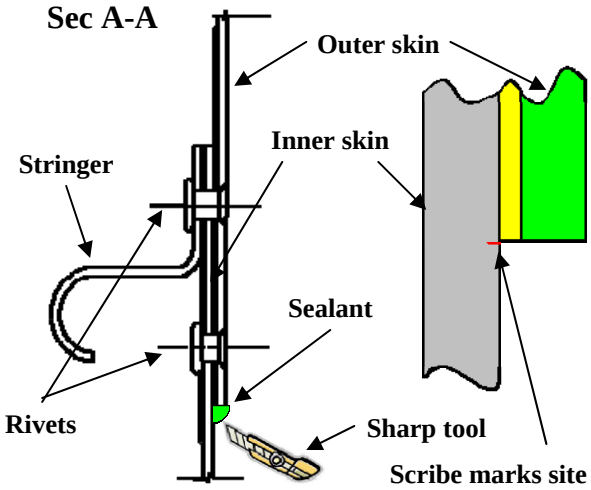

Typical longitudinal joint and sealant removal using a sharp tool

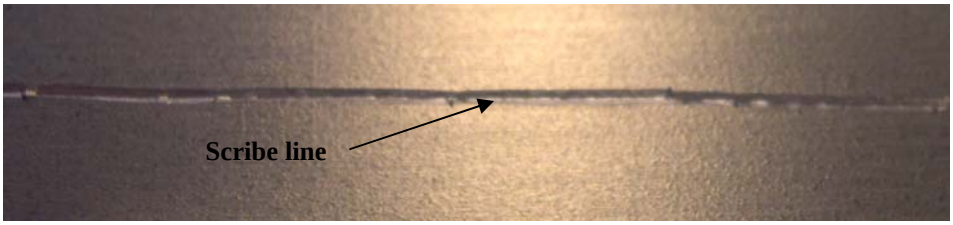

Scribe mark in inner skin

Fig. 1.1: Scribe marks origin

In themselves scratches do not constitute a threat for structural integrity, but it is their predisposition, under service loads, to generate propagating fatigue cracks which compromises the service life of structures or causes failures. In 2003 one commercial operator found six older Boeing 737-200 aircraft with damage at significant portion of the fuselage joints including critical lap joints [1]. An inspection on an aircraft revealed two cracks 120 to 250 mm long. Four other aircraft from the same fleet were affected by scribe marks at lap joints. It was immediately evident that the damage was most likely caused by the use of sharp metal tool for sealant removal during repainting at a Federal Aviation Administration (FAA) certificated repair station in the mid 1990s.

Recent research studies performed by Airbus of whole fuselage panels have demonstrated that scratches less than 200 µm deep are capable of severely reducing the fatigue life performance under service load. Furthermore ones detected during regular inspection the extent of the damage nucleated from scribe marks has rendered some aircraft beyond economical repair [2]. That means that in presence of scribe marks conventional aging Supplemental Structural Inspection Programme, even if capable of meeting damage tolerance requirements (no catastrophic failures) does not assure the achievement of the extended design service goal. A new analysis approach is required. It is the damage location and its conformation that makes conventional prediction methodologies, which inspection intervals are calculated on, inappropriate. Fig. 1.2 shows in section how in service scribe appear on a lap joint lower panel and the typical

fatigue damage propagated from them under service loads. Scribe marks look as a series of rounded V-shaped few tents microns deep notches into the cladding.

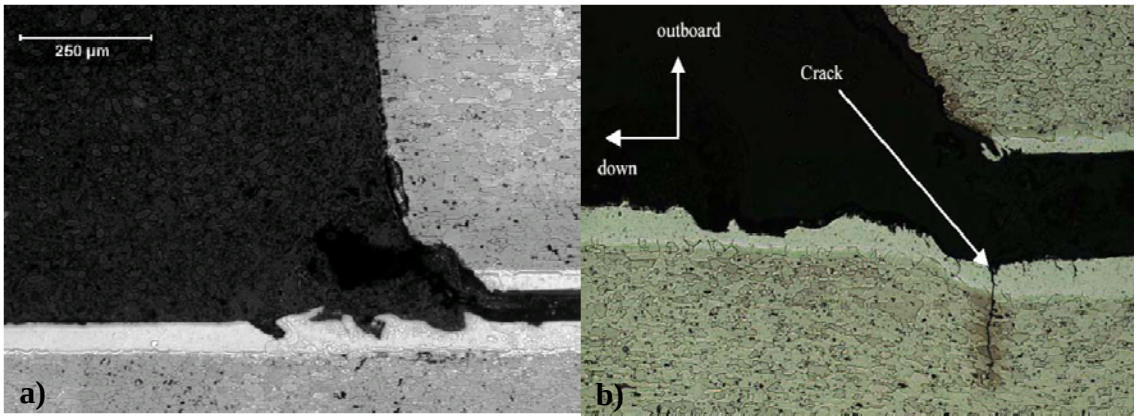

Fig. 1.2: Scribe marks at fuselage joints (from ref. [4]): a) scribes into cladding; b) crack propagated from scribe

It is surprising how such shallow defect can be so detrimental for fatigue life of fuselage joints as demonstrated by in service inspection [1,2]. Answers have to be researched, once again, in their location and conformation. Scribe mark damages are located into a region where the secondary bending, caused by the eccentric geometry of joints, reaches the maximum value (as explained in detail in paragraph 1.3). On the lower skin panel surface at the scribe site an high fatigue tensile stress, generated by the superposition of alternate joint tensile load and the resulting secondary bending component (maximum at the surface) acts (see Fig. 1.3). Locally the geometrical discontinuity introduced by the scribe line itself leads to a further stress increase due to stress concentration effect. Critical location for fatigue crack initiation at fuselage joints is therefore shifted from the outer rivet holes to the scribe location. Conventional fatigue studies showed that structure are insensitive to defect smaller that a characteristic size (see chapter 2). On the contrary aircraft joint fatigue properties appear to be very affected even by shallow scratches 50 µm deep. That seems to be inconsistent with conventional fatigue literature findings, but scribe marks cannot be catalogued as small defects. In fact while they are small along the panel thickness direction (shallow) their extension along the joint line can reach metres indeed. A long portion of material is therefore affected by high local fatigue stress and fatigue cracks are more likely to nucleate and overcome microstructural barriers even from shallow defects (see chapter 2). In other words it is more probable having several weak points inside material structure favourable for fatigue crack propagation and even if a crack can be stuck at a grain boundary another one can overcome the barrier. As explained above, scribe line length is responsible for the onset of widespread fatigue damage as well. Several small cracks nucleated almost simultaneously along the scribe root can, under service load, coalesce forming an unique elongated crack able to overcome any kind of microstructural barrier.

The tool so far used to analyse the behaviour of defects is the fracture mechanics. If the scratch is regarded as a propagating crack that tool can be used to calculate the life to failure, but this approach appears to be very conservative because it neglects fatigue cycles to create the crack. On the other side treating the component as pristine will be

non conservative at all. The use of conventional linear elastic fracture mechanics as crack growth predicting tool is complicated in the case of cracks propagating from scribe marks by the coalescence of multiple small cracks typical of widespread fatigue damage situation. The prediction of short crack propagation based on conventional linear elastic fracture mechanics can lead to non conservative results (see chapter 2 for details). That invalidates the use of conventional growth analysis for cracks originated from scribe marks as before becoming through thickness cracks they are considered short cracks being less than 2 mm in depth. Moreover few data related to crack propagation along short transversal direction (the skin thickness direction) are available in literature.

A new approach is required that takes in account the scribe mark characteristics relating them to structure fatigue life including nucleation, short and long crack propagation periods. All the aspects influencing crack development from scribe marks like material condition, fatigue load condition, joint geometry, scratch geometry, scribing procedure, have to be considered into the prediction model.

1.2 Project objectives

The objective of the present study is to investigate and rationalise the effect of small mechanical defects, such as scratches (scribe marks), on service life of aeronautical components and structures. Specific objectives are:

- To investigate the influence of different scratch geometry parameters on the nucleation and growth of fatigue cracks developing from scratches in order to establish major factors influencing the fatigue life for scratched fuselage structures.
- To rationalise the role of scratch geometry, load condition, material supplying condition (clad or unclad), scribing procedure, in determining fatigue strength.
- To develop a model for prediction of fatigue life of scribed structures and the conditions for propagation vs. non propagation of cracks from these defects.

1.3 Methodology

As mentioned earlier, geometrical discontinuity in the joint design, like rivet holes, can locally alter the stress field acting as stress concentrators. Another important effect of the joint geometry is the rising of a bending stress component called secondary bending. As Fig. 1.3 schematically shows, when a longitudinal or a circumferential joint is subjected to a tension load because of its eccentricity tends to bend generating a bending stress on the fuselage skin superimposed on the tension one. Since bending stress is caused by the load stress application is called secondary bending and it is a typical non linear geometrical effect. On the scribe marks location therefore, even if is applied just a constant amplitude tension there will be a repeated tension stress plus secondary bending acting as crack opening stress (Fig. 1.3).

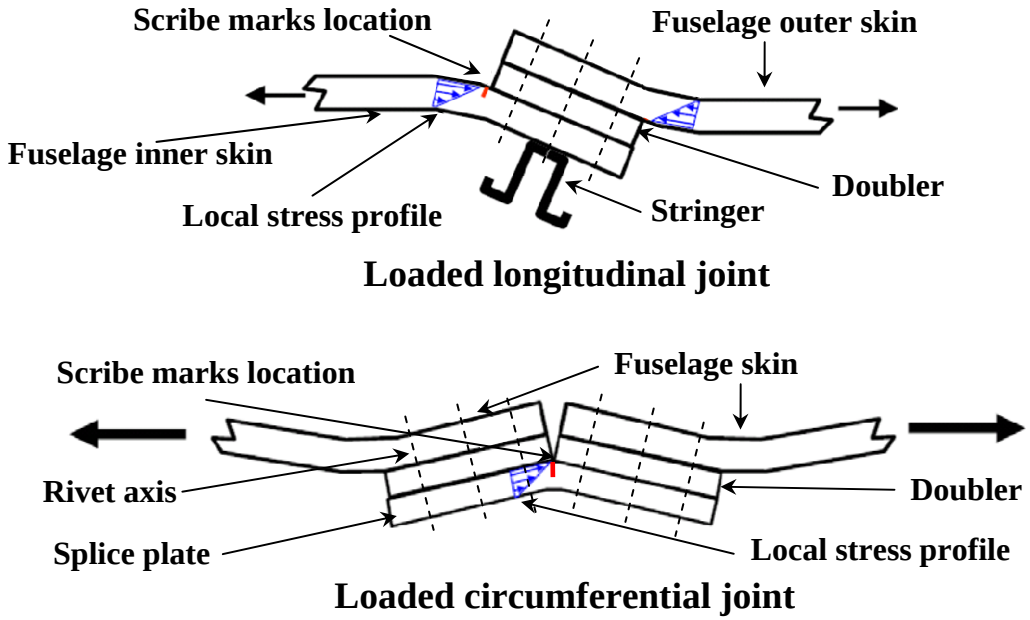

Fig. 1.3: Fuselage joints stress profile at scribe marks location effect of joint eccentricity

In order to establish major scratch parameters influencing fatigue life it was decided to analyse separately the consequences of tension and bending load on simple scribed aluminium specimens. The effect of different scratch geometries, load type and supplying condition on fatigue performance of 2024-T351 aluminium alloy samples were investigated. Tension and bending specimens were, first mechanically scribed, and then fatigue tested.

Scribes found in service on aircraft fuselage joints are damages characterised by high variability in length and depth even along the same scratch line consistently with the uncontrolled sealant scraping procedure that produces them. On the contrary the scratch cross section shape almost always resembles a rounded V shaped notch (see Fig. 1.2). To rationalise the effect of different scratch geometry on fatigue life a repeatable controlled scribing procedure is necessary. Artificial scribes of controlled geometry have to be machined on specimen surfaces before fatigue testing. To meet that particular requirement a suitable scribing procedure was developed by means of a diamond tipped cutting tool. The solution came out taking inspiration from contact lens companies where diamond tipped tool are commonly used to obtain the precision required in contact lens surface shaping. Performing several linear cutting passes with the diamond tool on aluminium surface a precise rounded V shaped notch of determined length and nearly constant depth could be machined. Fig. 1.4 shows, for instance, the cross section of a 5 µm root radius 100 µm deep diamond tool machined scribed with and open angle of 60°. It is worth noticing how the notch flanks are sharp, lacking in metal shavings. A precise shape is moreover associated with an accurate material cutting that should minimise the introduction of residual stresses. Scribing procedure is described in detail in chapter 3 together with the entire fatigue test campaign performed during this PhD project.

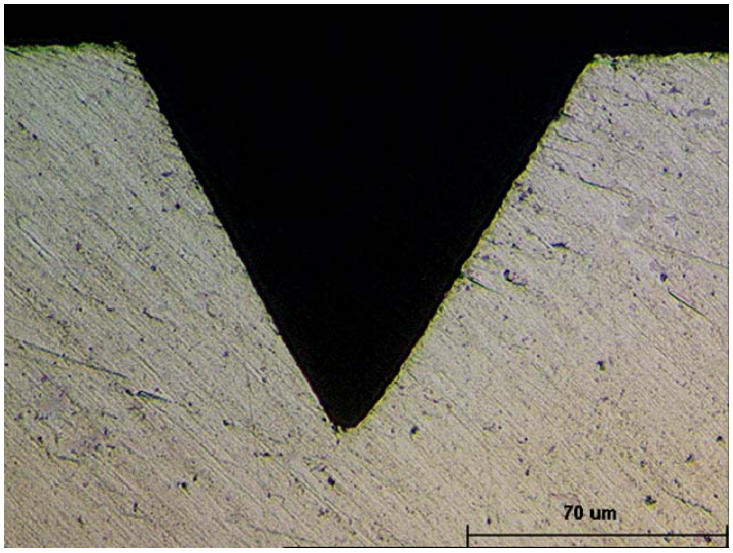

Fig. 1.4: Artificial scribe machined by diamond tipped scribing tool

After fatigue tests fracture surfaces were investigated to document the mechanisms occurring as a mechanical damage generates and transforms itself into a fatigue crack and the influence of notch geometry cladding and load condition on them. Crack growth analysis were performed as well. Continuum mechanics numerical analyses on the scratch effect under fatigue loads in term of stress concentration and plastic zone development were carried out to investigate the material properties changes caused by the scribe. On the basis of experimental and analytical evidences gathered a prediction model was developed. Nucleation of propagating cracks from scribe marks is a peculiar fatigue problem where short cracks initiate from sharp notches of depth comparable with material microstructural size. Microstructure seems likely to play an important role in crack development. On the other hand scribe lines are centimetres long and when the crack front is elongated along the scratch root the local microsctructural effect can be mitigated. A consistent fatigue life prediction approach have to be developed since conventional notch fatigue analysis and linear elastic fracture mechanics, are incapable of correct predictions in this particular contest.

Chapter 2 reports a literature review where the issue of fatigue effect of artificial scratches is investigated beside the more general state of the art of conventional notch fatigue. Notch size effect is reviewed from the early work at the beginning of the twentieth century up to more recent theory like critical distance theory. Published works concerning short fatigue crack development from notch and free surfaces are examined as well. Chapter 3 describes all the experiment studies performed during the PhD project. Fatigue test procedures for different scribed samples under different load conditions are described together with post failure fractography techniques and crack growth investigations. The new scribing procedure by means of diamond tools is accurately explained. Experimental results and achievements are listed in chapter 4. Chapter 5 is dedicated to continuum mechanics analysis of the scratch effect on the surrounding material under cyclic load. With the aid of numerical tools like finite element software monotonic and cyclic notch root stress field and plasticisation process are examined to gather information on short crack driving force. Experimental result discussion is reported in chapter 6 beside the new developed fatigue life prediction model. An attempt to rationalise crack development from micro mechanical artificial

defect mechanism is presented. Available models from literature are analysed and have their accuracy tested on scribed structure fatigue life prediction. Finally conclusions are drawn in chapter 7 together with future work suggestions.

Reference chapter 1

[1] FAA flight Standards Information Bulletin for Airworthiness-FSAW 03-10B. Fuselage Skin 'Scribe Mark' Damage on Boeing 737 Aircraft. 20/11/2003.
[2] Airworthiness Notice No. B071. Paint and sealant removal process. 3/11/2004.
[3] FAA Airworthiness Directives No. FAA-2005-20918. 31/3/2006.
[4] Das, G., Kosai, M. and Miller, M. Development of a method for damage tolerance analysis for scribe marks adjacent to fuselage longitudinal and circumferential splices. In: *International Committee on Aeronautical Fatigue (ICAF) meeting*, Napoli, Italy, 14-18 May 2007.

Chapter 2
Literature review

Crack development from scribe marks is a typical example of a fatigue problem in aircraft structures. The majority of failures in machinery and structural components can be attributed to fatigue processes. Readers can refer to dedicated books for an exhaustive analysis of fatigue phenomenon [1-3]. However an overview of major advance in fatigue research field is given in Appendix 2.1.

Crack formation at scribe marks is a fatigue problem concerning nucleation and propagation of short cracks from a stress concentrator with depth and root radius size comparable to material microstructural scale. The short crack research in aluminium and other alloys is reviewed. Experimental evidence on crack initiation and early propagation, together with interpretation and description of mechanisms are reported. Available short crack growth prediction models for different types of short crack behaviours are described and analysed. Published research on crack nucleation and propagation from notches is reviewed. Traditional S-N curve approaches together with fracture mechanics ones regarding crack propagation under local stress fields generated by stress concentrations at notches including scratches are described.

2.1 Stages of fatigue failure

The fatigue failure process can be divided into several stages, characterised by different phenomena involved as reported in reference [23]:

1) Initial cyclic damage (cyclic hardening or softening)
2) Formation of initial microscopic flaw (micro-crack initiation)
3) Coalescence of micro flaws to form a major growing defect (micro-crack growth)
4) Macroscopic propagation of such defect (macro-crack growth)
5) Final failure or crack growth instability

All those stages are of interest from a material science point of view, but in engineering terms the first three phases are grouped into the single process of macro-crack initiation responsible for the formation of an engineering-size detectable crack. Obviously the detectable crack size depends on the Non Destructive Technique (NDT) adopted and on the inspection conditions, but generally it is of the order of millimetre or tens of millimetre [32]. In engineering terms, therefore, the total fatigue life (N_{tot}) can be calculated as the sum of number of cycles to initiate a macro-crack (N_i) plus those required to propagate sub-critically the defect up to final failure (N_p).

$$N_{tot} = N_i + N_p \tag{2.1}$$

Distinctions between initiation and propagation lives can be critical for fatigue design and fatigue life prediction. Conventional fatigue design approaches are based on S-N curves reporting the total life (N_{tot}) as function of stress or strain amplitudes modified to take into account practical problem like mean stress effect, variable amplitude loading and so on. Although based on total life, that methodology essentially represents design

against crack initiation. In fact the majority of fatigue life of samples, used to experimentally obtain S-N curves, is spent to form, in particular in high cycle fatigue regime, a crack few millimetres long. With the introduction of the damage tolerance approach there was an increasing interest in fatigue propagation life [3]. That design philosophy relies on linear elastic fracture mechanics concepts and in particular on the integration of crack growth data curves to assess component fatigue lives.

2.2 Short cracks

Currently used fatigue crack growth data (characterised in term of linear elastic stress intensity factor range) are obtained experimentally testing specimens containing cracks of the order of tens of millimetres in length. However if defects encountered in service are smaller than that size their propagation behaviour could be different from that observed in laboratory. It was found, almost without exceptions, that cracks small in size, named short cracks, propagate with growth rates significantly greater that the corresponding rate of long cracks for the same linear elastic crack driving force (ΔK). Moreover small cracks can propagate under applied stress intensity factor ranges well below the crack growth threshold one (ΔK_{th}) calculated on the base of linear elastic fracture mechanics. Fig. 2.1 a) shows typical short crack growth rate trends under constant amplitude loading and load ratio, compared with the Linear Elastic Fracture Mechanics (LEFM) growth curve at the same crack driving force. The direct application of laboratory crack growth data (obtained with long crack) to design of components containing short cracks leads therefore to a non conservative approach with a dangerous fatigue life overestimation. An example of that is given in Fig. 2.1 b) for the nickel base superalloy Astroloy, used for turbine disks in aircraft engines, where the differences between fatigue life prediction up to failure obtained integrating LEFM conventional growth data and short crack kinetics ones are displayed as function of initial flaw size.

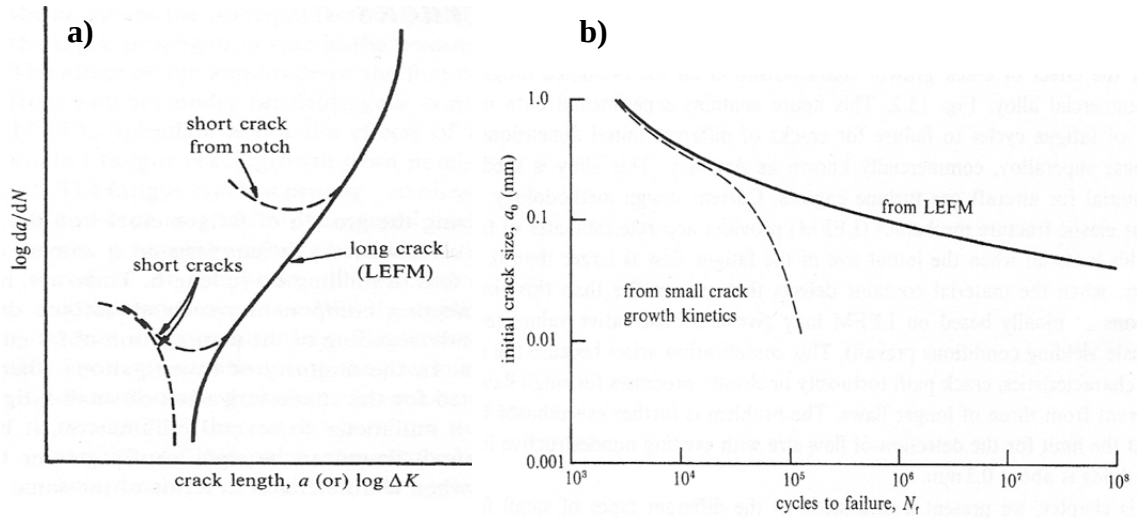

Fig. 2.1: a) Schematic of the typical short crack growth behaviour at constant amplitude loading; b) number of fatigue cycles to failure as function of initial flaws side estimated using LEFM or small crack kinetics for nickel-base superalloy (Astroloy) [3]

The first reported observations of the anomalous short crack behaviour was due to Pearson [33] in 1975 who examined fatigue crack initiation and the subsequent early

growth of very short cracks in two precipitation hardened aluminium alloys. Short crack growth data were consistent with those of long cracks when crack depth was greater than 0.127 mm. After the work of Pearson the number of publications on the anomalous behaviour of short cracks steadily increased. Complete reviews on phenomenological aspects related to short crack nucleation and propagation can be found in literature [23-29].

A practical definition of short crack is any crack, despite its size, whose growth cannot be predicted on the basis of linear elastic fracture mechanics growth rate data. In other words the fracture mechanics and its parameter, the stress intensity factor range, are not able to uniquely characterise fatigue growth when short crack behaviour occurs. Linear elastic fracture mechanics applicability assumptions are therefore violated in presence of short cracks. The characterisation by means of linear elastic fracture mechanics of the crack extension under fatigue load is based on the similitude concept [23,26,28,29]. That concept implies that for a particular material, under particular environmental conditions and subjects to a certain load history different cracks in geometrical different components will have the same near tip conditions if the magnitude of the two stress intensity factors is the same. The same near tip conditions mean the same crack driving force and therefore an equal amount of crack extension per fatigue cycle. Every mechanical, metallurgical and environmental factors invalidating the similitude between cracks of different size contribute to the short crack growth rate anomaly. Mechanisms involved in short crack growth discrepancy and the contribution of different factors to them are reviewed in section 2.1.3. Short cracks problem, in conclusion, is due more to an erroneous application of linear elastic fracture mechanics beyond its limit of validity than to an anomalous behaviour of damaged materials and structures.

Smith [30] analysed some short crack initiation and propagation models and examined their impact on engineering design method. He pointed out the substantial difference between scientific investigation, where the objective is to rationalise and predict an observed behaviour, and the engineering design where the goal is to achieve structure safety and high survive probability at low cost. Short crack propagation model could be integrated in damage tolerance design philosophy but cracks so short to be considered short cracks cannot be detected by convention inspection tools. That point was investigated by Wanhill [31] who evaluated the significance of short cracks in metal aerospace structures. Short fatigue cracks could be significant for aircraft structural safety, that is for damage tolerance approach, only if a sufficient high resolution of non destructive inspection tools is feasible. Pre-service and the in-service (less accurate) non destructive inspections must be capable of detecting short crack with high reliability.

The current situation is that the accuracy of non destructive inspection corresponds to relatively large flaws and so the biggest undetected defect, adopted as initial flaw for damage tolerance crack growth prediction, is beyond the short crack regime. All initial damage sizes are bigger than 0.5 mm which is about the limit of short crack field for most aerospace materials. Short cracks seemed to have no influence on damage tolerance and a little one on durability aircraft design in the past years [31,32]. The situation changed significantly with the introduction of the aircraft aging programmes.

In aircraft aging programme, prediction of phenomena like widespread fatigue damage become essential for structural safety. Growth of short cracks responsible for compromising residual strength and structural integrity has to be modelled to define the operative service life extension (see chapter 1).

2.2.1 Short cracks in aluminium alloys

Since the work of Pearson [33], numerous journal papers, reviews and books, documenting experimentally the anomalous short crack behaviour in different materials, have been published.

Nisitani and Takao [34] investigated the initiation, propagation and closure behaviour of microcracks on a mild steel, a α-brass and an aluminium alloy through successive observations of fatigue processes on the plain specimen surface in rotating bending tests. Substantial differences were found in crack initiation process between age-hardened aluminium alloy and annealed metals. In age-hardened aluminium alloy a slip band initiates in a small region (less than 3 μm) inside a grain and a micro crack nucleated within the slip band gradually grows towards the grain boundary [34]. In annealed metals, instead, fatigue damage is accumulated gradually at the same region with dimension closely related to the grain size and subsequently that region turns into a crack as a whole. Because of different processes involved in crack initiation it was suggested that the thickness of the surface layer affecting the crack initiation is much thinner in age-hardened aluminium alloy than in an annealed metal. That was considered the cause of the bigger notch sensitivity found in age-hardened aluminium alloy.

Lankford [35] analysed the short fatigue crack growth in 7075-T6 aluminium alloy. He discovered that short crack growth rate was up to two orders of magnitude faster than those of long cracks and that such accelerated advance occurred at stress intensity well below long crack threshold. Short crack growth was observed to decelerate and even arrested when the crack tip was approaching the grain boundaries at stress intensity factor ranges below or close to the long crack threshold. Short crack growth rate curves showed a minimum in correspondence to grain boundaries before merging with the long crack data one. Lankford observed the same qualitative behaviour for aluminium alloys with different grain sizes. Obviously the minimum growth rate was achieved at lower stress intensity factor in the finer grain material than in coarse grain one. There was a strong interaction between short crack growth and microstructural features.

Other evidences of such phenomenon are reported by Blom et al. [36]. These authors studied fatigue crack initiation and growth in two high strength aluminium alloys, Al 2024-T3 and Al 7475-T761 different in mechanical properties and microstructure. The effect of different mean stress was investigated and attempts were made to provide short and long crack growth data for identical specimens, material orientation and test conditions. Short crack propagation was monitored applying plastic replicas during the low frequency fatigue test at regular intervals. In constant amplitude tests with a stress close to the fatigue limit micro cracks initiated in Al 2024-T3 at bulky intermetallic particles (containing Fe and Si), cracked during cyclic loading, while in 7475-T761

aluminium alloy crack initiation was observed either at intermetallic particle-matrix interfaces or along slip bands present inside grains. Cracking of intermetallic particles was not observed during test for the latter alloy. The initially transcrystalline micro cracks were oriented at 45° from the stress axis and propagated along slip planes of grains, generating the typical zigzag crystallographic stage I crack growth. A clear transition from crystallographic crack growth stage I and non crystallographic crack growth stage II was observed and was found corresponding to a characteristic transition length much shorter for 7475 than for 2024 alloy [36]. Short cracks up to the characteristic length grew only at stress amplitude corresponding of or slightly above the fatigue limit. Crack retardation or halt occurred at grain boundaries. Short crack accelerated after crossing the grain boundary and decelerated again when approaching the next grain boundary. That alternating crack growth behaviour extended up to the characteristic transition length from crystallographic to non crystallographic crack propagation. Up to this characteristic length short crack growth could not be predicted by linear elastic fracture mechanics. Beyond that length short crack growth data merged the long crack growth rate curve.

In the publication of Bolingbroke and King [37] the behaviour of short cracks (20-100 μm in length) in high strength 7010 aluminium alloy was examined. Short fatigue cracks (depth < 100 μm) propagated faster than long through-thickness cracks at the same ΔK and below long crack threshold for both under and over aged alloys [37]. Short crack growth showed a discontinuous nature with acceleration and retardation associated with grain boundaries interactions. Cracks deeper than 100 μm behaved according to linear elastic fracture mechanics prediction for both the supplied conditions examined. Through-thickness long cracks and semi elliptical short cracks showed similar faced fracture surfaces in the near threshold regime indicating the same propagation mechanisms (crystallographic shear and tension growth) despite differences in propagation rate.

An example of short cracks nucleated at grain boundaries in aluminium alloys was reported by Mulvihill and Beevers [38]. They tested a peak aged Al 4.5% Cu alloy made from high purity base metals in laboratory. Short cracks propagated along the initiating grain boundaries and growth rate was primary affected by microstructural barriers like grain boundary triple points that retarded or halted cracks. 50% of the retarded short cracks resumed their propagation changing from intergranular to transgranular growth mechanism; the remaining 50% underwent to crack deflection maintain an intergranular growth. Intergranular propagation was also inhibited by inclusions, greater than 5 μm in diameter, lying at the grain boundary. The initial transgranular growth was observed to be a mode II opening crystallographic (stage I) propagation which than changed into a mode I opening stage II growth.

Plumtree and Schäfer [39] studied the initiation and early growth of short cracks in squeeze-formed aluminium 7% silicon alloy castings similar to the A356-T6 aluminium alloy. Cracks were observed to initiate at silicon particles by debonding at the interface with aluminium matrix under low cycle strain ranges, while silicon particles cracking was the initiation mode associated with high strain ranges fatigue. Short cracks, were observed to decelerate when approached microstructural barriers constitute by the first triple point after initiation in the interdendritic region. After the barrier overcoming

crack growth increased rapidly and merged with long crack data. Short crack growth behaviour was modelled using a semi-empirical model based on crack tip plasticity and taking into account microstructural barrier interaction [39]. The prediction model worked very well but empirical constants had to be determined experimentally.

Tokaji and Ogawa [40] reported a review of experimental results on the microstructurally short crack growth in seven different materials, among which 7075-T6 aluminium alloy. 7075-T6 specimens were tested in axial loading at three different stress ratios (R=0,-1,-2). Short crack growth was examined once again using replica material. It was found that cracks nucleated at inclusion particles had their growth rate decreased at the grain boundaries under a stress ratio of R=-1,-2. On the contrary short crack propagating under R=0 indicated no significant effect of microstructure. Crystallographic stage I flat and featureless facets were observed on fracture surfaces. No flat facets were found on 7075-T6 fracture surfaces obtained a R=0 showing that stage I crack growth, is strongly related to microstructural barrier effects and it is dependent on stress ratio. A transition superficial crack length, beyond which the microstructure crack growth interaction ceases, was found corresponding to 8 grain diameters for this alloy tested at R=-1.

Petit and Kosche [41] reviewed studies on the intrinsic fatigue crack growth mechanism in polycrystals aluminium alloys. Intrinsic long crack growth data were obtained without any closure effects (effective data) and without any environmental interactions (in vacuum). Compact tension specimens were tested in vacuum in threshold tests. Two different crack growth mechanism regimes could be identified. The fastest regime named as stage II was characterised by propagation of cracks which developed macroscopically along planes normal to the maximum stress direction and at microscopic scale resulted in decohesion process occurring in two or more slip planes ahead of the crack tip. The other growth regime called stage I-like, corresponded to slower crack growth rate than stage II compared at the same effective stress intensity factor range. It was similar to crystallographic stage I growth along a single slip plane at the scale of an individual grain but macroscopically the crack plane was normal to the stress direction. Stage I propagation regime was faster than the other two (stage II and stage I-like) observed in polycrystals aluminium alloys. Cracks propagated along a single slip plane where the resolved shear stress was maximum. This regime was observed in single crystal alloys at near threshold regime and in polycristals when cracks propagate in the first grain. The intrinsic behaviour of artificial two dimensional physical short cracks in 7075-T651 was the same as those of long cracks.

Another example of in vacuum fatigue short crack investigation is reported in the papers of Zhang et al. [42[42],43]. The authors performed fatigue tests in the chamber of a scanning electron microscope to examine fatigue crack growth modes in both poly and single crystal alloys. For the aluminium alloy the membrane stress was 12 MPa whereas the maximum bending stress was 252 MPa. Therefore maximum superficial stress was quite high, $0.7\sigma_{0.2}$. It was observed in 2024-T351 aluminium alloy that when crack tip approached a grain boundary new slip bands initiated in the next grain. Crack deceleration when crack tip approached grain boundaries, was observed over a crack length up to five grains. Once compared with long crack data short cracks grew faster that long ones subjected to the same ΔK. That discrepancy between short and long

cracks was possibly explained by the shear decohesion propagation mechanism observed on short cracks and by large scale yielding conditions.

The study of Xue et al. [44] attempted to rationalise the micromechanisms of fatigue damage formation and evolution in rolled 7075-T651 aluminium alloy. Systematic observation were made of the fracture surface and growth mechanism variations in three fatigue stages: crack nucleation, microstructurally/physically short cracks and long cracks. Fatigue cracks in 7075-T651 nucleated at Fe-rich intermetallic particles 4-8 μm x 8-12 μm in size located near or at the sample free surface. Most of the relatively large Fe-rich intermetallic particles fractured early in the fatigue life but only one or few fractured particles induced predominant fatigue cracks. Fractured particles at the sample free surface at points where the surface normal coincided with the short transversal direction of the rolled plate were more likely to induce final fatigue failure. The evolution of striations was demonstrated in both physically short and long crack regimes. Different fatigue crack evolution stages were not well distinguishable in low cycle fatigue regime. The misorientation of neighbouring grains altered crack propagation rates and direction as observed by the change in striation pattern direction crossing a grain boundary. Linear elastic fracture mechanics was finally implemented to predict experimental crack growth data obtained by striation counting. Initially striation distances remained almost constant as the crack increased in size. A uniform striation spacing increase took place when at crack lengths greater than 170 μm. The general growth rate trend was predicted, but striation spacing was in general greater than what estimated by linear elastic fracture mechanics.

The micro-texture and microstructure effects in short crack growth behaviour was well documented in the work of Zhai et al. [45]. With the aid of electron back scatter diffraction, the influence of grain boundary on short crack propagation in 8090 aluminium-lithium alloy and 2026-T351 aluminium alloy was investigated. In 8090 Al-Li samples short cracks were deflected at almost every grain boundaries they crossed. Crystallographic stage I crack growth was predominantly along the slip plane in the next grain forming the smallest tilt angle with the crack plane in the previous grain. 2026 aluminium alloy is a modified version of 2024 Al alloy with a crack growth predominantly crystallographic although crack initiation is often non-crystallographic with an early propagation perpendicular to the loading axis. Also in this alloy crack deflected at every grain boundaries. During crystallographic growth crack deflections contained small twist component as demonstrated by the occurrence of small fracture steps. On the contrary, where cracks propagated in a non-crystallographic mode, fracture steps were large indicating that crack driving force was big enough to overcome the resistance of large twist angles.

2.2.1.1 Short cracks from notches in aluminium alloys

Cracks develop preferentially at stress concentrations like mechanical notches, inclusions, scratches, and their early growth is affected by the local stress field due to such geometrical discontinuities. Experimental evidence of short crack nucleation and propagation from notches are reviewed in this section.

Foth et al. [46,47] investigated damage processes on notched and unnotched aluminium samples in the pre-crack and short crack stages. Fatigue behaviour of two types of double edge notch specimens, (stress concentration factor of K_t=1.22 and K_t=3.3 respectively) was compared with that of unnotched dog-bone samples. All coupons were machined from a flat 2024-T3 aluminium alloy sheet with a thickness of 4.7 mm. Cracks were observed to initiate at hard Fe and Si containing intermetallic inclusions that caused inhomogeneous plastic deformation within the surrounding material because of different mechanical properties. Usually inclusions fractured under cyclic loading and microcracks started to grow from those fractured inclusions at the gauge surface in unnotched samples or at the notch surface in notched ones. Short crack initiation and propagation at sample surfaces were divided into four different stages. Stage I was the initiation of very small cracks at inclusions particles. The number of microcracks was much larger than the number of those cracks that formed the critical main crack and stage I was considered ended as soon as intermetallic inclusions were broken and surface cracks 5-10 μm long were present. Microcracks grew on sample surface during the Stage II that terminated when short cracks began to coalesce to form a single main flaw. In the stage III cracks coalesced and propagated up to the point where the whole sample surface was cut through by one predominant crack. Finally the main crack propagated as a long through thickness crack up to the sample failure in stage IV. Cracks propagated as surface semi elliptical defects, almost semicircular, with an aspect ratio (crack depth a on crack semi-superficial length c) of a/c=0.9.

Under constant amplitude strain history of ε=0.7±0.3% the three sample types tested (notched and unnocthed) showed approximately the same crack initiation life (Stage I). However the propagation lives from stage II to stage IV became significantly different decreasing as the notch stress concentration factor decreased. Nucleation lives were equal since the same strain history was applied at the notch roots and in gauge section of unnotched samples. Once cracks propagated into the bulk material of notched specimens stress gradients generated by notches themselves and the crack driving force inevitably decreased, increasing fatigue life propagation. The total number of small cracks nucleated at the unnotched specimen surfaces was larger than those generated in notched samples as the whole cross section was subjected to the maximum strains in the former coupons. When constant amplitude strain history of ε=0.85±0.15% was applied the equivalence in fatigue initiation stage I life behaviour was lost as notched samples showed no cracks below a life of $2 \cdot 10^6$ cycles while unnothed specimens already failed before that number of cycles.

A systematic investigation on short crack growth in 2024-T3 aluminium alloy was conducted during the AGARD cooperative test programme reported by Newman, Edwards et al. [48] to assess the significance of short crack effect in aeronautical structures. Initiation and growth of short fatigue cracks (from 5 μm to 2 mm long) were monitored during over 250 fatigue tests performed by 12 laboratories from 9 countries. A 2024-T3 aluminium alloy single edge notch tensile specimen, 2.3 mm thick with a semicircular notch 3.17 mm in radius (K_t=3.17), was selected to produce naturally occurring cracks at material defects and to propagate them through a stress field representative of that encountered in riveted aircraft structures. Fatigue tests were performed under constant amplitude stress ratios, R=-2, -1, 0, 0.5, and two spectrum load sequences, FALSTAFF and GAUSSIAN.

Over 70% of the initiation sites were generally within the middle half of the specimen thickness. That could be explained by the fact that notch stress concentration factor was 5% higher in the middle of the specimen and that the occurrence of inclusions at the notch root was less probable toward the sample surfaces. High stress level fatigue histories were noted to generate more multi-crack initiation points along notch root than the low stress ones. Short cracks generally propagated as semi-elliptical surface crack, nearly semicircular (aspect ratio between crack depth, c, and crack semi superficial length, a, of c/a=1) very early in life. However cracks tented to grow more along the notch surface than away from the notch stress field and the breakthrough point c/a was about 0.7. Only about the 8% of the crack nucleated ad the notch edge ad propagated as corner quarter-elliptical cracks.

Under constant amplitude loading with negative stress ratios (R=-2, -1) short crack growth rates were faster than those of long cracks at the same stress intensity factor range above the long crack threshold. Short crack test results at R=0 showed almost the same growth rate of long cracks for identical ΔK in the region above the long crack threshold. A small stress level effect was observed under this condition. Constant amplitude fatigue tests performed at positive stress ratio (R=0.5) exhibited short crack growth rates slightly lower than long crack data at the same ΔK above the long crack threshold. No stress level effect was found for R=0.5 even though the local notch root stress was above the material yield stress. Under FALSTAFF and GAUSSIAN spectrum loadings short crack grew faster than long cracks with the same stress intensity factor ranges. Consistent stress level effect was observed in GAUSSIAN spectrum while for FALSTAFF load history, that is an high R ratio type spectrum, that effect was very small. For all the loading conditions 80% to 90% of the total fatigue life was spent to growth a crack from a length of 20 μm along the notch root. Crack growth was monitored over 90% of the total fatigue life.

Edwards, Newman et al. [49] reported further experimental investigations performed in an AGARD supplemental test programme on the short crack growth behaviour. Single edge notch tensile and centre crack tension specimens made of various aircraft sheet materials were fatigued under constant and variable amplitude loading. The basic test procedures, crack monitoring, and short crack samples were the same as defined in the AGARD cooperative test programme [48]. The aluminium alloys tested were 2024-T3, 7075-T6 and the aluminium-lithium alloy 2090-T8E41. Short crack testing was conducted under four constant amplitude stress ratio conditions (R=-2, -1, 0, 0.5) and different aircraft spectrum loading (FALSTAFF, Inverted FALSTAF, GAUSSIAN, TWIST, Felix and Fokker 100).

All the tested alloys exhibited a strong short crack effect in both constant and variable amplitude loadings. Short cracks grew at stress intensity factor levels below the long crack threshold and faster than long cracks at the same stress intensity factors. Short crack effect was more pronounced at negative stress ratios and at higher stress levels. Crack initiation occurred at inclusion clusters from defects caused by the separation of such clusters from the matrix material. Initiation sites were generally located with the middle part of the notch root. Cracks tented to growth on the notch root at 30°-35° from the loading axis in the 2090-T8E41 aluminium-lithium alloy.

Tests conducted under inverted FALSTAFF (a simple inversion of FALSTAFF spectrum) showed that short cracks grew much faster than long cracks for ΔK values below about 20 MPa·m$^{1/2}$. Inverted FALSTAFF short crack data compared well with those of FALSTAFF for a given value of ΔK. Inverted FALSTAFF is the typical load sequence experienced by the upper wing surface of a tactical aircraft but results suggested that crack driving forces acting on short cracks are nearly the same of those typical of the FALSTAFF spectrum. Short crack tests under TWIST and Fokker 100 load histories exhibited short crack growth at stress intensity factors well below the long crack threshold. Data indicated that stress level effects could exist under the TWIST spectrum and that short crack growth rates were significantly higher than long crack ones under the Fokker 100 load sequence. No long crack data were available for comparison under Felix load sequence.

Newman, Wu et al. [50-52] investigated short crack behaviour in high strength aluminium alloys. Two high strength aluminium alloy materials, 7075-T6 and LC9cs clad 2 mm thick sheet were selected. Three types of fatigue tests, that is standard S-N fatigue tests, short crack and long crack growth tests were performed. All sample types were fatigued under three constant amplitude loading conditions (R=-1, 0, 0.5) and under the aircraft wing Mini-TWIST spectrum loading. A procedure to take into account the effect of the soft clad layer, carrying a few percentage of the total section load, on the stress intensity factor was developed. In both aluminium alloys crack initiation took place early in fatigue life and occupied only a small part (about 10-20%) of the total life. Short cracks growth results under constant amplitude loadings showed the classical short crack effect in both 7075-T6 and LC9cs clad alloys, that is crack grew faster than long cracks at the same stress intensity factor and propagated below the long crack threshold. Such small crack effect was more pronounced at negative stress ratios. Under Mini-TWIST spectrum loading short cracks propagated faster and slightly slower than long cracks at the same ΔK, respectively for LC9cs and 7075-T6 samples.

Laz and Hillberry [53] studied the role of material inclusions in fatigue crack nucleation for 2024-T3 aluminium alloy. Inclusions or secondary phase particles are common sites for fatigue crack nucleation in aluminium alloy. Cracks initiated at large inclusion particles, containing iron, manganese, copper and aluminium, on the notch root surface. The inclusion size distribution was used as stochastic input for a probabilistic Monte Carlo simulation based life prediction model. The randomly selected inclusion areas were the initial defect size for the deterministic crack closure model FASTRAN II [54]. The fatigue live prediction model accurately predicted the shortest experimental lives and the overall range of data variability.

2.2.2 Short crack nucleation mechanism

To understand and predict fatigue failure it is important to know at which locations crack nucleation takes place. In fatigue experimental tests the number of nucleated cracks macroscopically observed is in general very small, if not just one, especially at applied stress close to the fatigue limit. That evidence implies that a group of favourable circumstances has to occur simultaneously at a given location inside the material to nucleate a crack. Fatigue cracks nucleate at material sites where local irreversible

inelastic deformations concentrate and accumulate. Crack formation occurs in ductile materials when the accumulated inelastic deformation, consequence of dislocations accumulation, reaches a critical value [24]. Unfortunately, while the relationship between the development of a stabilised cyclic deformation state and the kinetics of dislocations organised in slip bands has been intensively studied and rationalised, the link connecting deformation and crack nucleation still remains unexplained. Strain localisation and accumulation can be caused by material features like cyclic slip bands, inclusions and intermetallic particles, grain and twin boundaries and by mechanical elements as notches, surface roughness, residual stresses, surface damages (such as scratches, corrosion pits, fretting damage, cracked oxide layers) and macroscopic defects (like material flaws, welding and casting defects) [24].

Each of those aspects contributes to identify the most suitable locations for irreversible deformation accumulation and consequent fatigue crack nucleation. In most crack nucleation experimental investigations high quality smooth manufactured specimens with polished surfaces were adopted, eliminating therefore all the mechanical features contributing to defect generation. However those aspects are of fundamental importance in real structure applications.

The origin of fatigue cracks in pure metals and high purity alloys is characterised by the roughening of material surface due to slip bands emerging at the free surfaces [3]. Repeated cyclic straining of the material generates persistent slip bands where dislocation movement along favourably oriented slip planes is localised. The irreversibility of shear displacement along the slip bands results in microscopic hills and valleys, called extrusions and intrusions respectively, at the sample surface where slip bands emerge. Intrusions act as micro stress raisers promoting at their roots additional slip and consequent crack nucleation [3]. Crack nucleation at grain boundaries occurs in polycrystalline pure materials often in the presence of embrittling environments, which preferably attack grain boundaries, or at elevated temperature promoting creep and grain boundary sliding [3].

In engineering components made of commercial alloys, the preferential sites of crack nucleation are defects inside the material. Those defects can be metallurgical such as inclusions, voids, gas entrapments or mechanical like scratches, dents, welding flaws. Regions of microstructural and chemical inhomogeneity (triple points) as well as stress concentrators can act as nucleation site. Fatigue crack formation in commercial alloys occurs in preference at the material surfaces but in contrast with pure defect-free materials crack nucleation is possible even from near surface or internal flaws [3]. However on the material surface the restraint to cyclic slip is relatively low promoting fatigue crack development [24]. Mechanisms involved in crack nucleation from defects depend on material and inclusions strength, mechanical characteristics and susceptibility to corrosive environments. Therefore the effect of inclusions and other defects in crack nucleation is specific to different alloy systems [3]. In aluminium alloys crack nucleation is generally associated with intermetallic particle, 1-10 μm in diameter, although even slip band nucleation was reported as well [24]. However the cracking type is function of microstructure and test conditions. Cracks can form as consequence of particle inclusion cracking, debonding of the interface between matrix and inclusion or of cracking along slip band starting or terminating at inclusions [24]. Material flaws

affect the local stress distribution acting as micro notches and influence material cyclic slip. Dislocations can pile up at inclusions producing inclusion cracking or matrix-defect interface debonding. Additionally, differences in mechanical properties between inclusions and matrix produce local stress field to ensure strain congruence at the defect-matrix interface [24].

All those factors promote crack nucleation in commercial alloys. Several prediction models estimating fatigue cycles of crack nucleation at defects have been developed and can be divided in three categories [3]:

1) Analyses where voids or debonded inclusions are considered as notches and conventional nucleation life from notches is calculated
2) Models taking into consideration dislocations pile up at inclusion as crack development mechanism
3) Fracture mechanics formulations where defects are assumed as equivalent initial cracks.

Aggressive environmental agents can introduce additional crack nucleation sites on material surfaces disguised as corrosion pits. Such pits act as micro notches increasing the local stress field and moreover the local environment inside the pit can be more acid than the external surroundings enhancing the crack growth rate by corrosion fatigue mechanism.

The problem of fatigue crack nucleation from mechanical notches is a topic of considerable interest for a large variety of engineering application and it has been investigated extensively using different total life or fracture mechanics based approaches. That issue is largely discussed in the following sections. Cracks were observed to initiate at the notch surface in notched 2024-T3 aluminium alloy samples [46-48,53]. Initiation sites were generally located with the middle part of the notch root. Multiple micro cracks were found to nucleate at different sites along the notch root [46]. High stress level fatigue histories were noted to generate more multi-crack initiation points along notch root than the low stress ones [48]. Cracks nucleated from hard Fe and Si containing intermetallic inclusions that caused inhomogeneous plastic deformation within the surrounding material [46,47]. Both intermetallic particle inclusion cracking [46] and debonding of the interface between matrix and inclusions [48] were found to be the cause of crack nucleation in notched 2024-T3 samples. The largest inclusion particles on the notch root surface were the most likely crack initiation sites [53]. The effect of notches on crack nucleation is to promote the initiation at the notch root, where local deformations are increased by the stress concentration effect, without altering the mechanisms of crack formation from intermetallic particles.

Among the multitude of likely nucleation sites inside a material, just few of them become effective sources of further microcrack growth [46-53]. Apparently a number of circumstances correlated to grain orientation, size, shape, inclusion shape and stiffness should happen simultaneously in relation with the easiness of slip at the free surface [24]. Actually many evidences supported the view that crack nucleation easily occurs at several material locations; it is instead the early propagation of microscopic cracks to discriminate if a crack will propagate up to component failure or it will become non propagating [28]. Non propagating cracks were observed in various materials under different test conditions and not only at the fatigue limit [27,28].

If fatigue life is finite, crack nucleation starts very early in fatigue life [48]. Such observation entitles some researches to neglect nucleation period considering fatigue life composed entirely of crack propagation from an initial crack length close to zero [25,28]. That approach allows engineers to predict structures and components life applying a unique fracture mechanics based methodology, although modified to take into account short crack effect.

2.2.3 Short crack growth mechanism

As shown by the several experimental evidences reported in the previous sections, linear elastic fracture mechanics is not able to correctly predict short crack growth behaviour. Linear elastic fracture mechanics applicability is questioned by the breakdown of the similitude concept in presence of short cracks [3,23-29]. The similitude concept, applied to fatigue crack growth, implies that for a given material, under given environmental conditions and subjects to a given load history different cracks in geometrical different components will propagate with the same growth rate if the magnitude of the two stress intensity factors range is the same [3]. Provided that the crack tip plastic zone is small compared to all system dimensions (crack length, thickness, remaining ligament) it results small with respect to the distance in front of the crack over which the first term of the crack tip elastic stress field solution is dominant and the small scale yielding condition is fulfilled [14]. Under those circumstances both the crack tip plastic zone size and the surrounding elastic stress field are adequately characterised by the stress intensity factor K. Two cracks with the same K will show the same plastic zone and stress field regardless the geometry and there will be similitude. To have complete similitude equal conditions must exist at different crack tips. That is not guaranteed by the equality of the instantaneous values of R and ΔK since load application history can affect crack tip conditions [26]. According to crack closure argument, plastic residual deformation in the crack wake has to be equal as it is responsible for crack closure development and alters the crack tip stress field by means of closure contact stresses. More rigorously, similitude requires that the closure displacement field and the crack tip stress field are the same [26]. If all the mechanical parameters discussed above are equal for different cracks, the condition of the so called mechanical similitude exists.

Obviously the material considered should be the same with regard to microstructure, dislocation density, constituent and inclusion particle densities, orientation (in the case of anisotropic material), to respond in a unique manner to similar mechanical conditions. In other words metallurgical similitude has to take place [26]. Conventional continuum mechanics formulations, including fracture mechanics, assume materials as homogeneous where material properties are independent of the location considered inside the material itself. Real materials are well far from being homogeneous, showing microstructural complex features with different mechanical properties. However if the geometrical scale of the problem is large enough, compared with material microstructural size, local material properties can be considered as an average of the diverse properties of various grains and the material responses to mechanical conditions as it was homogeneous. The metallurgical similitude is therefore fulfilled on the average. In the case of long crack generally the crack front ranges over several grains

satisfying the metallurgical similitude conditions. However if the crack front is of the order of few grains, like in short cracks, those conditions will be easily violated [26].

Directly related to the metallurgical similitude is the similitude in crack growth mechanisms. That similitude is not a condition itself, but it is more precisely a consequence of mechanical and metallurgical similitude breakdown. Differences in crack growth mechanisms can lead to diverse crack growth rates *da/dN* [26].

If just one of aforementioned similitude conditions is not satisfied, because of the reduced crack length, the validity of linear elastic fracture mechanics in the growth prediction of short crack becomes questionable. In agreement with the explained similitude requirements a number of factors responsible for real or apparent short crack effect can be identified [23]:

1) Local plasticity effects resulting in an inappropriate short crack driving force characterisation
2) Local microstructural features perturbing growth of short cracks with size comparable with microstructural characteristic dimensions
3) Similarity in crack constrain condition
4) Interaction with other micro cracks
5) Similarity in crack growth mechanism
6) Crack closure
7) Similitude in local crack tip environmental conditions

Considering threshold condition for non propagation it appears clear that a particular crack length exists below which fracture mechanics ceases to be valid. According to linear elastic fracture mechanics crack growth threshold stress $\Delta\sigma_{th}$ can be calculated as in eq. (2.2) (function of stress intensity factor range ΔK_{th}, crack length a and crack geometrical factor β) [14]. If crack length tends to zero the threshold stress approaches infinitum but, actually for $a \rightarrow 0$, $\Delta\sigma_{th}$ should tend toward the fatigue limit ($\Delta\sigma_e$) [3]. Introducing the Irwin plastic zone correction r_p (eq. (2.3)) the problem can be overcome as for a fixed ΔK_{th} the plastic zone correction is constant [26]. However for $a=0$ the plastic zone generated by the crack is meaningless. Researchers like El Haddad et al. [55] replaced r_p with an empirical constant taking into account differences in R ratio and material but physical reasoning behind such approach remains unconvincing (see section 2.1.4.4).

$$\Delta\sigma_{th} = \frac{\Delta K_{th}}{\beta\sqrt{\pi a}} \tag{2.2}$$

$$\Delta\sigma_{th} = \frac{\Delta K_{th}}{\beta\sqrt{\pi(a+r_p)}}, \quad r_p = \frac{1}{2\pi}\left(\frac{\Delta K_{th}}{2\sigma_y}\right)^2 \tag{2.3}$$

There are different size scales below which similitude requirements are violated and linear elastic fracture mechanics is not anymore able to correctly predict crack propagation behaviour. Following those size scales corresponding to diverse main reasons for similitude breakdown and consequent linear elastic fracture mechanics framework hypotheses violation, short cracks can be broadly classified as [3]:

- *Microstructurally small cracks*. Flaws with sizes comparable to the scale of the characteristic microstructural dimension (for an Al alloy crack length ≤100-200

μm) like grain diameter, intermetallic particle spacing. At the microstructural scale the variability of mechanical and metallurgical properties leads to accelerate crack growth along favourable regions and local retardation or arrest at microstructural barriers such as grain boundaries. Fracture mechanics cannot predict microstructurally short crack growth because of breaking of continuum mechanics material homogeneity hypothesis.

- *Mechanically small cracks*. In that way are denominated flaws for which the crack tip plastic zone is comparable with the crack length (plastic zone ≥ 2 % of crack length). Plasticization effect on crack stress and strain field is not anymore negligible and the small scale yielding condition, foundation of liner elastic fracture mechanics, breaks down as linear elasticity based growth prediction.
- *Physically small cracks*. Cracks which are significantly larger than the characteristic microstructural scale and the crack tip plastic zone dimension but merely small (for an Al alloy crack length ≤ 1-2 mm). In that circumstance cracks are comparable with the length necessary to obtain a full crack tip shielding mechanism, like crack closure. The reduced cracked surface behind the crack tip decreases the wake length where shielding mechanisms take place. For instance in the case of plasticity induced crack closure, plastic wake cannot fully develop in short cracks because of the small flaw length. The decreased shielding effect causes an higher local crack driving force in small cracks compared to long ones where shielding is fully developed. Linear elastic fracture mechanics growth prediction fails because of a ΔK_{eff} similitude problem.
- *Chemically small cracks*. These are flaws nominally amenable to linear elastic fracture mechanics analyses but that experience differences in propagation rate below a given length because of diverse environmental conditions as function of crack lengths. Local concentration of corrosive species at the crack tip depends on the surface to volume ratio of the defect, on the diffusive and convective mass transport inside the crack, sites of electrochemical reaction activation; all processes sensitive to crack size. Chemically short cracks show a growth rate faster that long cracks, because the enhanced corrosion fatigue behaviour, promoted by easier corrosive species exchange and access to crack tip in case of small defects. The growth mechanism dissimilarity is the main consequence of the chemically short crack growth behaviour.

Short cracks nucleated from notches in 2024-T3 aluminium alloy samples propagated at stress intensity factors well below the long crack threshold under both constant amplitude and spectrum loadings [48]. Their growth rates were not correctly correlated by linear elastic fracture mechanics. Under constant amplitude loading short crack growth rates were faster (R=-2, -1), equal (R=0) or slower (R=0.5) than those of long cracks at the same stress intensity factor range above the long crack threshold [48]. The effect of notches in short crack growth was mainly to produce a minimum in a growth rates that was related to the different amount of closure caused by the local notch stress field and plastic zone. Moreover notches altered also the short cracks shape as cracks tented to grow more along the notch surface than away from the notch stress field [48].

Similitude conditions at notches are made more difficult to obtain because of the effect of local notch stress field. Generally local plasticity occurs at the notch root due

to stress concentration effect. Differences in deformation behaviour between notch root plastic zone and elastic surrounding material introduce residual stress field ahead of the notch. Crack tip of long cracks will be outside the notch residual stress field and plastic zone, while short cracks can be embedded in that region. If the effects of those different conditions are not considered short crack prediction on the basis of long crack data cannot be expected. However that is not a case of similitude breakdown, rather it is a consequence of the erroneous assumption of equal mechanical conditions between short and long cracks at notches [26]. Provided that effects of notch local stress field could be considered in the calculation of local ΔK and R, the short crack problem at notch would be equivalent to that of short crack at smooth surfaces where all the above considerations on mechanical and metallurgical similitude would be valid.

Stress raisers generate local multiaxial stress fields that exert control on crack nucleation location and early propagation. When cracks grow outside this region uniaxial far field begins to regulate crack growth. Such change in stress field can produce variations in crack driving force and consequently in growth rate [26]. If early propagation under multiaxial stress field is not accounted for by mixed mode and multiaxial fatigue K solutions, growth rate changes could be ascribed to short crack effect when in reality they are consequence of inappropriate crack driving force estimation. Whether the anomalous short crack behaviour at the notch root is due to the different mechanical conditions caused by plasticisation, the length at which short crack data merges with those of long cracks should be correlated to plastic zone size. Several researchers verified that such correlation indeed exists for different materials [26]. In that case short crack effect at notch root can be noticed in cracks 1-10 mm long (common length ranges of long cracks) as long as large plastic zones are developed at stress raisers. Differences in crack closure, generated by the local inelastic notch field have to be taken into account to predict short crack behaviour at least for cracks longer than material microstructural characteristic dimensions.

2.2.4 Short crack growth prediction models

Due to growth behaviour of short cracks, non conservative fatigue life overestimations are obtained when design methodologies, based on linear elastic fracture mechanics, are applied to components containing defects within the short crack range (see section 2.2). The problem is exacerbated by the lack nowadays of non-destructive inspection techniques capable of detecting defects as large as short cracks. Specific models are therefore required to predict the anomalous growth behaviour of short cracks. Those growth models become necessary tools to ensure damage tolerance properties of structural components, for all the cases, like scribed fuselage joints, where crack propagation in the short crack region cannot be neglected without compromising the structural safety. Growth prediction methods, are usually developed to describe a specific growth behaviour related to a particular type of short crack. In fact diverse kinds of short cracks are generally related to different phenomena, responsible for the violation of the similitude requirements. Consequently their propagation is determined and regulated by diverse processes that for their prediction require specific methodologies based on different mechanical behaviours.

Analytical models describing microstructurally short crack growth, take into account the variation of crack path and propagation rate caused by the local variability of mechanical and metallurgical properties inside the material microstructure and the interaction between the cracks and microstructural barriers such as grain boundaries. Prediction methods of mechanically short cracks are marked by the effect of the large scale yielding condition, describing how the big crack tip plastic zone influences the propagation of short flaws. Alternatively methods related to the growth prediction of physically short cracks are based on the characterisation of the crack tip shielding mechanisms, in particular crack closure, whose effects depend on the crack length. Finally some prediction models were explicitly developed extending concepts of linear elastic fracture mechanics to short cracks. Analytical and generally empirical corrections were applied to the definition of the linear elastic stress intensity factor to make the long crack propagation (*da/dN* vs. *ΔK*) curves able to predict the short crack growth behaviour. Those models are called fracture mechanics based models.

Crack development from scribe marks, due to the magnitude of the service stresses acting on fuselage joints at different locations, is a problem generally concerning crack propagation more than fatigue crack growth threshold. However the first investigations on short crack anomalous behaviour were focused on predicting short crack growth threshold, generally smaller than that of the corresponding long cracks. Several models were developed to describe small flaw threshold conditions [3] and they often constitute the basis for short crack growth prediction methodologies. Frequently not only the concepts behind them, but also threshold condition models themselves were extended to propagating cracks to characterise short crack growth rates. For those reasons threshold models are briefly reviewed below. Readers can refer to [3,56] for further details.

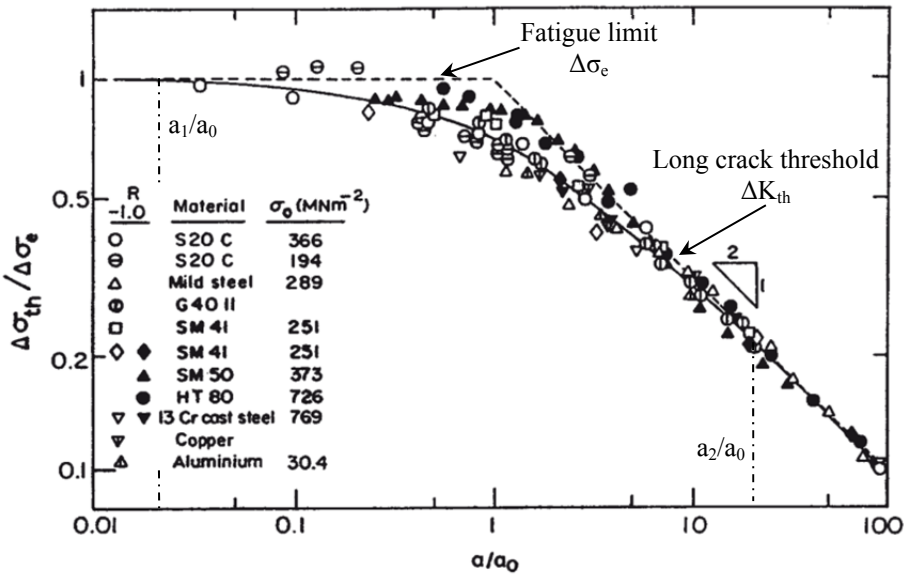

Fig. 2.2: Kitagawa-Takahashi diagram showing the effect of crack size on propagation threshold stress for several engineering alloys (from ref. [60])

Kitagawa and Takahashi [57] investigated the effect of the crack size on growth threshold of various engineering metal alloys under fully reversed load (R=-1). They plotted different threshold stress ranges, $\Delta\sigma_{th}$, against the crack length a, developing the graph that from then on is known as Kitagawa-Takahashi diagram. Fig. 2.2 shows the

Kitagawa-Takahashi diagram for the analysed engineering alloys, where the threshold stress ranges are normalised with respect to the corresponding fatigue limits $\Delta\sigma_e$ and crack lengths are normalised by the critical crack size a_0. In fact Kitagawa-Takahashi demonstrated the existence of a critical crack length a_0 below which threshold stress intensity factor range ΔK_{th} decreased according to the crack length (see Fig. 2.2). For cracks longer than a_0, $\Delta\sigma_{th}$ results an exponential function of a with an exponent of -0.5 in agreement with linear elastic fracture mechanics.

As can be observed in Fig. 2.2 critical crack size a_0 was defined as the intersection point between the lines describing the fatigue limit $\Delta\sigma_e$ and the long crack threshold stress intensity factor range ΔK_{th}. Therefore it can be calculated as follows:

$$a_0 = \frac{1}{\pi}\left(\frac{\Delta K_{th}}{\Delta\sigma_e}\right)^2 \tag{2.4}$$

The value of the critical crack length (see eq. (2.4)) is obtained from standard fatigue material properties as the fatigue limit, taken from S-N curves, and the long crack growth threshold, derived from fatigue crack growth curves. The critical crack length a_0 can be considered as the maximum defect size which the material is insensitive to. In fact a specimen containing no crack would show the same threshold stress $\Delta\sigma_{th}$, equal to the fatigue limit, as one containing a crack of length a_0. Cracks should therefore grow very easily up to that length and at the material fatigue limit only a flaw larger than a_0 could effectively cause failure. The critical length a_0 could also be considered as the boundary between propagating and non propagating cracks for stresses around $\Delta\sigma_e$. El Haddad et al. [55] suggested the following analytical expressions to predict respectively the threshold range, $\Delta\sigma_{th}$, and the threshold stress intensity factor range, ΔK_{th}^{sc} according to different crack lengths a:

$$\Delta\sigma_{th} = \frac{\Delta K_{th}}{\sqrt{\pi\left(a + a_0\right)}} \tag{2.5}$$

$$\Delta K_{th}^{sc} = \Delta\sigma_{th}\sqrt{\pi a} = \frac{\Delta K_{th}}{\sqrt{1 + \frac{a_0}{a}}} \tag{2.6}$$

According to eq. (2.5) for vanishing crack length, $\Delta\sigma_{th}$ tends to the fatigue limit $\Delta\sigma_e$ while in case of cracks longer than a_0, short crack growth threshold ΔK_{th}^{sc} approaches that of long flaws ΔK_{th} as $a_0/a \rightarrow 0$ in eq. (2.6).

Taking into account the trend of threshold stress data for short cracks, Taylor and Knott [58] defined two additional critical crack lengths a_1 and a_2 (see Fig. 2.2). Those lengths coincide respectively with the points of deviation of the $\Delta\sigma_{th}$ curve from constant stress and constant stress intensity factor straight lines (Fig. 2.2). The length a_1 is the crack size below which flaws have no effect on the component fatigue behaviour as any components containing defects smaller than a_1 show the same fatigue limit. On the other hand the length a_2 represents the crack size limit for the application of the linear elastic fracture mechanics below which the use of conventional ΔK_{th} to predict crack growth threshold becomes non conservative. Taylor and Knott [58] proved that a correlation exists between the short crack behaviour at the growth threshold and the characteristic material microstructural dimensions. They showed that a_1 was

approximately equal to the size of microstructural unit d, like the grain size, while a_2 was nearly $10d$ for various materials [58]. Several attempts were also made to correlate the critical crack lengths a_0 with characteristic microstructural dimensions of different materials [3]. A crack as long as a_2 has its front that spans many microstructural units, so that local variations in threshold conditions and growth, due to microstructure, are averaged to obtain a macroscopic behaviour.

Usami and Shida [59] suggested a different criterion for crack growth threshold, based on the crack cyclic plastic zone. Instead of considering the critical size of defects they postulated that the conditions promoting crack growth were reached when the cyclic plastic zone at the crack tip attained a critical size r_p^c. The threshold stress for different crack lengths could be therefore derived from the analytical expression defining the cyclic plastic zone size. Usami and Shida [59], using the Dugdale plastic zone estimate [14], obtained the following relation between $\Delta\sigma_{th}$ and the critical cyclic plastic zone r_p^c, valid in case of fatigue load conditions with positive load ratio ($R \geq 0$):

$$r_p^c = a\left[\sec\left(\frac{\pi\Delta\sigma_{th}}{4\sigma_y}\right)-1\right] \tag{2.7}$$

where σ_y is the cyclic yield stress of the material. Considering that r_p^c is a sort of material property independent of the crack size the variation of the threshold stress range $\Delta\sigma_{th}$ according to the crack length a, is given as follows:

$$\Delta\sigma_{th} = \frac{4\sigma_y}{\pi}\arccos\left(\frac{a}{r_p^c + a}\right) \tag{2.8}$$

The value of r_p^c could be obtained relating the Dugdale plastic zone with the threshold stress intensity factor range ΔK_{th} of long cracks which linear elastic fracture mechanics is valid for. Eq. (2.8) proved to be capable of accurately predicting the trend of the $\Delta\sigma_{th}$ curve in Fig. 2.2. Usami and Shida [59] also extended their approach to fatigue loadings with negative load ratios. However, despite the good prediction capabilities of that model physical reasons and experimental evidences proving the existence of a critical cyclic plastic zone size that regulates crack threshold conditions are still missing.

Tanaka et al. [60] assumed that the threshold conditions for short cracks were determined by the interaction between crack tip plastic zone and the grain boundaries. Short crack tip plasticity was assumed to be confined in rectilinear slip bands emanating from the crack tip and extending through the grains. Crack propagation was a consequence of the capability of slip bands to cross the barriers formed by the grain boundaries. In order to activate crack growth the local stress distribution in front of a slip band had to be large enough to exceed ΔK_c^m plus the friction stress for dislocation motion σ_{fr}. In that way slip bands could spread into the adjacent grain causing crack propagation. Tanaka et al. [60] provided the following expressions for the short crack growth threshold stress $\Delta\sigma_{th}$ and the threshold stress intensity factor range ΔK_{th}^{sc} respectively:

$$\Delta\sigma_{th} = \frac{\Delta K_c^m}{\sqrt{\pi b}} + \frac{2}{\pi}\sigma_{fr}\arccos\left(\frac{a}{b}\right) \tag{2.9}$$

$$\Delta K_{th}^{sc} = \Delta\sigma_{th}\sqrt{\pi a} = \Delta K_c^m \sqrt{\frac{a}{b}} + 2\sqrt{\frac{a}{\pi}}\sigma_{fr} \arccos\left(\frac{a}{b}\right) \tag{2.10}$$

where b is the sum of the crack length a plus the length of the persistent slip band w_0 ($b=a+w_0$). For long cracks the slip band length becomes negligible with respect to the crack length ($w_0 \ll a$) and the threshold stress intensity ΔK_{th} is given by:

$$\Delta K_{th} = \Delta K_c^m + 2\sqrt{\frac{2}{\pi}}\sigma_{fr}\sqrt{w_0} \tag{2.11}$$

Eq. (2.11) is obtained from eq. (2.10) letting $a \approx b$. On the other hand for vanishing crack, $a \to 0$, the equivalence between $\Delta\sigma_{th}$ and the fatigue limit in eq. (2.9) leads to:

$$\Delta\sigma_e = \frac{\Delta K_c^m}{\sqrt{\pi w_0}} + \sigma_{fr} \tag{2.12}$$

Assuming zero friction stress for dislocation motion ($\sigma_{fr}=0$) and substituting eq. (2.11) into eq. (2.9) the following threshold stress expression is obtained:

$$\Delta\sigma_{th} = \frac{\Delta K_{th}}{\sqrt{\pi\left(a + w_0\right)}} \tag{2.13}$$

Eq. (2.13) is nothing more than the representation of the threshold stress in term of critical crack length in eq. (2.5) where a_0 is replaced by the slip band length w_0. The critical cyclic plastic zone size threshold criterion suggested by Usami and Shida [59] turns out to be a particular case of the slip band-grain boundary interaction model. In fact eq. (2.8) can be simply obtained from (2.9) setting $\Delta K_c^m=0$. It appears evident that a sort of connection exists between diverse models developed to predict short crack threshold condition despite the different hypotheses and assumptions behind them. The influence of the grain size on short and long crack threshold conditions, namely on $\Delta\sigma_e$ and ΔK_{th}, can be rationalised by means of the slip band-grain boundary interaction model.

Other researchers explained the dependency of the threshold stress $\Delta\sigma_{th}$ on the crack length, observed in Fig. 2.2, in term of crack closure rather than of the interaction between crack and material microstructure. McEvily and Minakawa [61] considered the typical trend of the stress range required for crack propagation in the Kitagawa-Takahashi diagram, and the consequent increase of ΔK_{th}^{sc}, according to the short crack length, to be caused by the development of crack closure. Following the crack closure reasoning, flaws can propagate only if they are fully open with their flanks completely separated (see section 2.2.4.3). Therefore the crack driving force available for propagation under fatigue cycles is not the whole stress intensity factor range ΔK, but the fraction of it in which cracks are open. Such effective driving force is named effective stress intensity factor range ΔK_{eff} and is defined as follows:

$$\Delta K_{eff} = K_{\max} - K_{op} \tag{2.14}$$

where K_{max} is the stress intensity factor corresponding to the maximum stress of the fatigue cycle, while K_{op} is the stress intensity factor, related to the stress value at which the crack becomes fully open. Threshold conditions are thus defined in term of the effect driving force stating that a cracks can grow only if its ΔK_{eff} is larger than an effective threshold stress intensity factor range ΔK_{th}^{eff} (see section 2.2.4.3). The

effective threshold stress intensity factor is considered a material properties and it proved to be independent of the loading ratio R. McEvily and Minakawa [61] investigated the threshold conditions of short cracks under fully reversed fatigue loads (R=-1) in 9Cr-1Mo steel. As long as cracks are smaller than a_1 (Fig. 2.2) the endurance limit controls the crack propagation. For flaws longer than a_1 McEvily and Minakawa [61] applied linear elastic fracture mechanics defining a maximum stress intensity factor. According to eq. (2.14) K_{max} turns out to consist of the ΔK_{eff} plus the opening stress intensity factor K_{op} that was a function of the crack length:

$$K_{\max} = \Delta K_{eff} + K_{op} \tag{2.15}$$

Flaws smaller than a_1 have flanks too short to develop crack closure, as the plastic wake, responsible for the plastic induced closure, or the flank irregularities, causing the roughness induced closure, have not physical room to be effective. Therefore those cracks open as soon as the fully reversed cyclic load becomes positive showing an opening stress intensity factor, K_{op}=0. As the crack length increases, crack closure starts to develop, involving a progressive increase of the opening stress σ_{op}. The anomalous short crack behaviour is therefore rationalised in term of closure development transient, caused by the reduced size of crack flanks, before reaching a stable closure level in long crack regime. For crack longer than a_1 the opening stress intensity factor K_{op} increases, according to the crack length, from zero to a maximum value K_{op}^{max} achieved as soon as long crack regime develops. On the basis of experimental crack opening stress measurements, McEvily and Minakawa [61] suggested the following relation to predict the development of K_{op} according to the crack length:

$$K_{op} = K_{op}^{\max}\left(1 - e^{-k(a-a_1)}\right) \tag{2.16}$$

where, as explained above, K_{op}^{max} is the maximum opening stress intensity level for long cracks. The K_{op} seemed to vary from zero at a_1 to K_{op}^{max} at nominally infinite crack length following and exponential trend where the rate of variation, expressed by the parameter k in eq. (2.16), results a material constant. Substituting eq. (2.16) into eq. (2.15) and specialising it for the growth threshold conditions the maximum threshold stress intensity factor K_{th}^{max} is obtained as follows:

$$K_{th}^{\max} = \Delta K_{th}^{eff} + K_{op}^{\max}\left(1 - e^{-k(a-a_1)}\right) \tag{2.17}$$

The effective threshold stress intensity factor range ΔK_{th}^{eff} in eq. (2.17) is a material constant while K_{op}^{max} can be defined on the basis of long crack threshold ΔK_{th}. Considering that for fully reversed load $\Delta K=2K_{max}$, threshold conditions for short cracks can be expressed in term of stress intensity factor range:

$$\Delta K_{th}^{sc} = 2\Delta K_{th}^{eff} + 2K_{op}^{\max}\left(1 - e^{-k(a-a_1)}\right) = \Delta K_{th}^{*eff} + \Delta K_{op}^{\max}\left(1 - e^{-k(a-a_1)}\right) \tag{2.18}$$

where $\Delta K^{*}_{th}{}^{eff}$ is the threshold stress intensity factor range corresponding to the condition of zero crack opening stress.

Chapetti [62] proposed a method to estimate the fatigue crack propagation threshold as function of the crack length, combining both the crack-microstructural barrier interaction and the crack closure evolution. The fatigue limit is actually characterised by the resistance of the strongest microstructural barriers to crack propagation. Therefore the fatigue limit is regarded as a threshold condition for crack growth rather than for nucleation. The resistance to the flaw propagation is usually larger than the one to

initiation and thus non propagating cracks can be observed under the fatigue limit. If the strongest microstructural barrier to crack growth is located at a distance d from the crack nucleation site, flaws can grow up to a length $a=d$ under fatigue limit stress [62]. Since cracks as long as d are non-damaging with respect to fatigue limit, d corresponds to the critical length a_1 in Fig. 2.2. Chapetti [62] assumed that the effect of the material microstructure, characterised by the interaction between cracks and microstructural barriers, mainly influences crack shorter than d. The position of the strongest microstructural barrier d defines the upper limit of microstructurally short crack regime where the threshold stress is characterised by the fatigue limit. Crack closure development is considered to regulate threshold levels between microstructurally short and long crack regimes. Flaws in that region were thus thought to be physically short cracks. Chapetti [62] considered the short crack threshold stress intensity factor range ΔK_{th}^{sc} composed of an intrinsic component ΔK_{dR} defined by the resistance to microstructurally short crack propagation plus an extrinsic component ΔK_C produced by the development of closure:

$$\Delta K_{th}^{sc} = \Delta K_{dR} + \Delta K_C \tag{2.19}$$

The intrinsic threshold stress intensity factor ΔK_{dR}, being regarded as a microstructural threshold for crack growth was defined in term of the position of the strongest microstructural barrier d and of the fatigue limit $\Delta\sigma_{eR}$ as follows:

$$\Delta K_{dR} = \beta \Delta\sigma_{eR} \sqrt{\pi d} \tag{2.20}$$

The subscript R in eq. (2.20) indicates the dependence of parameters on fatigue load ratio R. Chapetti [62] used the expression suggested by McEvily and Minakawa [61] to model the development of the extrinsic threshold component mainly caused by the crack closure:

$$\Delta K_C = \Delta K_{CR} \left(1 - e^{-k(a-d)}\right) \tag{2.21}$$

where the maximum extrinsic threshold stress intensity factor range ΔK_{CR}, obtained with the fully development of closure when the long crack regime is reached at a crack length $a=a_2$ (Fig. 2.2), is given as follows:

$$\Delta K_{CR} = \Delta K_{thR} - \Delta K_{dR} \tag{2.22}$$

Analysing the experimental Kitagawa-Takahashi diagram of different material, Chapetti [62] defined the extrinsic component development rate k as function of the same microstructural and mechanical factors, ΔK_{dR} and ΔK_{CR}, characterising the threshold condition:

$$k = \frac{1}{4d} \frac{\Delta K_{dR}}{\Delta K_{CR}} \tag{2.23}$$

A good agreement was observed between the prediction of eq. (2.21) and experimental results of several materials [62]. The model proposed by Chapetti [62] is very simple and it is an attempt to rationalise by physical basis the short crack behaviour under threshold condition. However some parameter are still merely obtained by fitting of experimental results [62].

2.2.4.1 Microstructurally short cracks

Microstructurally short cracks, being comparable in size to the material characteristic microstructural dimensions, such as grain diameter and intermetallic particle spacing, are strongly influenced by the local microstructure. Their propagation usually occurs along a single crystallographic slip plane inside each grain (stage I), under shear cyclic stress (mode II). Crack tip plasticity, characterised by the dislocation motion, is generally confined inside a single grain along a unique plastic slip band. Crystallographic favourable slip systems shows various attitudes according to different grain orientations. That leads to a characteristic zigzag path of microstructurally short cracks growing through several grains in stage I. During the stage I crack growth, grain and phase boundaries act as microstructural barriers against the slip transmission into adjacent grains, reducing crack the driving force. That produces fluctuations in crack growth rate that shows the lowest values in correspondence with the microstructural barrier locations. The retardation effect of grain boundaries depends on the misorientation of the favourable slip systems inside adjacent grains. If a microstructural barrier is strong enough to block the slip transmission cracks cannot propagate into the adjacent grain becoming a non propagation flaw. Models should consider the variability of the slip plane orientations and local microstructure beside the interaction between cracks and microstructural barriers to correctly predict the growth of microstructurally short cracks.

Navarro and de los Rios [63-65] developed an analytical model describing microstructural sensitive crack growth in term of successive blocking of the crack tip plastic zone by slip barriers like grain boundaries. The crack and the respective plastic zone were modelled by a continuous distribution of dislocations [65] moving along a single plane under alternating shear stress [63]. Microstructural barriers, like grain and phase boundaries, prevented the dislocations from going to infinity. The crack growth rate was assumed to be proportional to the crack tip plastic slide displacement. Therefore propagation rate values changed in an oscillatory way every time crack tip plastic zone spread into a new grain [63]. Cracks were retarded near the barriers until the slip initiation into the adjacent grain increased the tip displacement raising the growth rate. The discrete nature of the slip has a strong effect on the short crack growth and represents the interaction between material microstructure and microstructurally short flaws.

The transition from structure-sensitive to structure-insensitive crack regime took place when the plastic zone, after crossing the first microstructural barrier, extended for more than a grain diameter [66]. The effect of different grain orientation on the microstructural barrier strength was subsequently included into the model [66]. A friction stress increase was caused by the larger repulsive force exerted by the growing number of dislocations piled up at the slip barrier as the crack approaches such obstacle. If at a given crack length the friction stress to the dislocation motion becomes smaller than the available driving force instable crack growth will occur [66-68]. The model was able to describe the higher growth rate of short cracks, their interaction with the material microstructure and the fatigue limit of components associated to the inability of a newly initiated flaw to propagate into the next grain.

Tanaka et al. [69] developed a slip band-grain boundary interaction model similar to Navarro-de los Rios one, where the theory of continuously distributed dislocations was used to calculate crack tip sliding or opening displacements and the corresponding microscopic stress intensity factors under mode I or mode II loadings. Microstructurally short cracks models based of slip band-grain boundary interaction like those suggested by Navarro and de los Rios [63] and by Tanaka et al. [69] are difficult to validate since the lack of specific experimental procedure to set material microstructural parameters. For that purpose, Marx et al. [70] developed a procedure to precisely create artificial micro cracks and to quantitatively investigate the interaction between crack tip slip bands and grain boundaries.

A substantial amount of research works concerns the use of Discrete Dislocation Technique to model microstructurally short crack propagation [71-78]. Discrete dislocation models are based on the assumption that for microstructurally short cracks it is important to consider the dynamic of discrete dislocations generated during crack propagation. That holds true in particular for growth rates of the order of few Burger vectors per cycle [74]. Short edge cracks were assumed to growth in semi-infinite components under fatigue loading due to the development local plasticity [71]. Crack tip plastic zone was generated emitting dislocations along preferred slip planes. Nucleation of dislocations occurred as soon as the resolved shear stress along a particular slip plane [74] or the local stress intensity factor [71] at the crack tip exceeded a critical value. Discrete dislocation technique were applied to model stage II transgranular growth of microstructurally short cracks, propagating perpendicularly to the external load direction [71-73], as well as crystallographic stage I growth of short flaws [74-77]. The former case refers to cracks growing from a notch under mode I by sliding along pairs of symmetrically inclined slip planes [71], the latter to microstructurally short edge cracks propagating from the component surface along a single slip plane under a combination of mode I and mode II [74]. Several aspects of microstructurally short crack growth were investigated by means of discrete dislocation technique such as the interaction between crack tip plastic zone and grain boundaries [72,73,76,77] and the formation of a zigzag crack path during crystallographic stage I growth caused by repetitive changes in the slip plane [74,75]. Grain boundaries proved to reduce, and sometimes to set at zero the growth rate of microstructurally short crack propagating under mode I [72,73]. However for short cracks growing in a crystallographic stage I way, the growth rate was found to be only affected by boundaries between grains with close orientation angles [77].

Bertolino et al. [78] modelled the tortuous fatigue crack propagation in polycrystalline materials coupling finite element and discrete dislocation approaches. The local stress computed by finite element simulations taking into account different grain orientations, was used as input for the discrete dislocation crack growth analysis [78]. Model predictions were consistent with experimental observations, reproducing the crack growth kinetics, characterised by arrest periods at the grain boundaries, and the large scatter in growth rates typical of microstructurally short cracks.

Krupp et al. [79] and Künkler et al. [80] simulated the transition from stage I to stage II crack growth, using a boundary element method based on dislocation theory. The

developed model described a propagating microstructurally short crack and its plastic zone as yields strips meshed by boundary elements consisting of dislocation dipoles.

Wilkinson [81] investigated the effect of local microstructure and texture on stage I crack growth in face centred cubic polycrystalline materials combining the Navarro-de los Rios model [63] with a Monte Carlo method. The orientation factor of every grain was determined, randomly selecting grain orientations from a probabilistic distribution. The local microstructure considerably affected the distribution of crack reaching a given length only for flaws smaller than four grain diameters [81]. Analogously Tanaka et. al [82] performed a Monte Carlo simulation of the propagation of short cracks nucleated inside the weakest grains, using the slip band model developed by the author. Microstructural effects were evaluated considering the grain size, the frictional stress and the grain boundary strength as random variables that follow two-parameter Weibull distributions [82]. The scatter and the irregularities in crack growth decreased as cracks become longer than several grain diameters. Moreover the fatigue life was found to be proportional to the friction stress and inversely proportional to the square of the applied stress [82].

Liao [83] applied the Tanaka model [69], based on continuous distribution of dislocations, to predict microstructurally short crack growth life on notched 2024-T351 aluminium samples. The stochastic variability of parameters, difficult to measure was taken into account integrating the dislocation model with a Monte Carlo program [83]. Reasonable agreement was observed between analytical and experimental results. Bataille et al. [84] developed a stochastic numerical model to predict the nucleation and propagation of superficial short cracks under the low cycle fatigue regime. Micro crack nucleation took place inside the elements of a two-dimensional mesh, composed of hexagonal grains, according to the applied plastic strain and a nucleation resistance parameter randomly assigned to each element [84]. The numerical model was able to predict the effect of micro crack density and dominant crack length on the residual fatigue life of samples, although some discrepancies were caused by influence of the crack density on the material cyclic behaviour [84].

Wilson and Taylor [85] proposed an additional probabilistic model to describe the interaction between grain structure and microstructurally short cracks. Local material microstructural properties were varied randomly defining the short crack length as a random quantity. The stochastic approach was extended to several cracks obtaining a population model capable of calculating the failure probability of a component after a given number of fatigue cycles [85]. Population model results agreed with experimental crack propagation curves and sample lives.

Potirniche et al. [86] simulated the microstructurally short crack growth behaviour in 7075 aluminium alloy using the crystal plasticity theory [87]. Contrarily to classical isotropic plasticity where plastic deformations occur equally in any material direction, crystal plasticity assumes that plastic deformations are concentrated along discrete planes of the crystallographic lattice [87]. According to the double slip crystal plasticity model applied by Potirniche et al. [86] material deformation is supposed to occurs as plastic shear strain along only two slip planes a primary and a conjugate one. Such model was implemented into finite element analyses where the anisotropic nature of

different grains was modelled considering various material properties and grain orientations. The interaction between short crack tip and grain boundaries and crack closure were also taken into account. Short crack growth rates were estimated using the numerically calculated effective stress intensity factor and long crack growth data [86]. A Good agreement was found between computational and experimental growth rates while different grain orientations seemed to explain the variability of small crack propagation data [86]. Cheong et al. [88] also proposed a crack nucleation model based on crystal plasticity theory.

2.2.4.2 Mechanically short cracks

For mechanically short cracks, as they show tip plastic zones comparable with their lengths, small scale yielding condition is not applicable. Plasticisation effects on crack stress and strain fields are not negligible and therefore linear elastic fracture mechanics fails to correctly predict mechanically short crack behaviours. Concepts developed into the framework of elastic plastic fracture mechanics, like *J*-integral, crack tip opening displacement crack tip plastic zone, have to be used to correlate mechanically short and long crack growth rates [14].

Rice and Rosengren [89] and Hutchinson [90] demonstrated that, as the stress intensity factor for linear elastic problems, *J*-integral uniquely defines the non-linear elastic stress and strain fields in the proximity of the crack tip for two dimensional geometries.

A number of researchers, like Lamba [91] and Dowling and Begley [92], extended the *J*-integral concept to cyclic loading defining the *J*-integral range ΔJ. They related the crack growth rate to the ΔJ value using the contour integral as elastic-plastic crack propagation similitude parameter [14]. Under the deformation plasticity, that is non-linear elasticity, framework, they demonstrated the path-independence of ΔJ [91]. Because the assumption of using the deformation plasticity theory to model material plastic behaviours is at the basis of the ΔJ calculation, the cyclic *J*-integral is able to correctly characterised the crack growth only in case of proportional cyclic loading and unloading. Therefor for cyclic loading, the non proportional large plastic strain region at the crack tip has to be surrounded by a larger zone of proportional loading where cyclic stress and strain are uniquely defined by ΔJ. Despite the severe limitation for its correct application, the cyclic *J*-integral proved to correlated crack growth data reasonably well in several cases. Banks-Sills and Volpert [93], for instance, used ΔJ to predict fatigue crack propagation in 2024-T351 aluminium alloy. Being related to the square of the stress intensity factor range ΔK, the cyclic *J*-integral accurately correlated crack propagation rate data for small scale yielding conditions [93]. However Lambert et al. [94] found a Paris law type correlation between crack growth rate and the cyclic *J*-integral ΔJ also under large-scale yielding conditions. The load ratio *R* seemed to modify such propagation curve [94]. Chow and Lu [95] noticed that the cyclic *J*-integral ΔJ represents only a portion of the total potential energy flowing into the crack tip during propagation. Therefore provided a new definition of the ΔJ, that under small-scale yielding conditions is equivalent to the elastic energy release rate range ΔG [95].

Inside the framework of deformation theory of plasticity (non linear elasticity) Chow and Lu [95] proved the path-independence of their new defined cyclic *J*-integral. Therefore also the application of such new ΔJ is limited to nearly proportional loading conditions. A unified fatigue crack propagation law based on the new cyclic *J*-integral ΔJ and the maximum *J*-integral J_{max} values, was derived imposing the energy balance during crack advancing [95]. Such law was able to account for the effect of different mean stress and materials as the growth rate curves of various aluminium alloys and polymeric materials, tested at several *R* ratios, coincided if plotted against ΔJ and J_{max}. Those parameters were considered to characterise better than ΔK and K_{max} the fracture process at the crack tip under fatigue loading. The crack propagation law based on the definition of ΔJ can be considered as an extension to large-scale yielding problems of the unified crack propagation formulation derived by Chow and Woo [96]. In fact they proposed a semi-empirical crack growth law in term of energy release rate range and maximum value, ΔG and G_{max} equivalent to ΔJ and J_{max} for small-scale yielding conditions. Also in this case the suggested propagation formulation was able to unified in a single curve growth rate data of 7075-T6 and 2024-T3 aluminium alloys and polymethylmethacrylate (PMMA), tested ad different *R* ratios [96].

Bruzi and McHugh [97] applied the concept of cyclic *J*-integral to model the mechanically short crack behaviour in aluminium alloys. A computational modelling methodology was developed where the cyclic *J*-integral was calculated with the aid of finite element analyses. Crack closure effects were also included into the model defining an effective cyclic *J*-integral ΔJ_{eff} [97]. The methodology was therefore suited to predict microstructurally as well as physically short cracks. Short crack growth increments per cycle were obtained from effective growth rate curves where the values of the effective stress intensity factor range ΔK_{eff} corresponding to those of ΔJ_{eff} were introduced. A good agreement between predicted and experimental fatigue life was achieved for an appropriate choice of the initial short crack length [97].

Härkegård and Wormsen [98] suggested approximate analytical formulae for estimating *J*-integral of mechanically short cracks in smooth and notched plates. *J*-integral expressions were formulated in term of equivalent nominal stress for both load and displacement control conditions. The contour integral was divided into a pure elastic term, related to the crack stress intensity factor, and an plastic one defined by a plastic geometry factor [98]. Expressions of the plastic geometry factor were obtained for small cracks in several sample configurations under bending and tensile load. The *J*-integral could be therefore estimated in the range from small-scale to large-scale yielding conditions. The accuracy of the suggested analytical solutions was assessed using finite element calculations [99]. The equations were found to be in good agreement with finite element results for both load and displacement control conditions.

Some researchers identified the size of the plastic zone at the crack tip as similitude parameter to unified the propagation behaviour of mechanically short and long cracks. Hamm and Johnson [100], for instance, proposed a generalised crack propagation model covering short crack and long crack regimes where crack growth rate were related to the cyclic plastic zone size. They noticed that short cracks generally are comparable in size with the material microstructural characteristic lengths and show a large plastic zone to crack size ratio. Thus they developed a growth predicting model for microstructurally

and mechanically short cracks. The microstructurally block slip model developed by Wang was modified to more accurately predict the transition from short to long crack regimes [100]. According to that model, short crack growth rate results an exponential function of the cyclic plastic zone. Transition functions, defining the variation of the cyclic plastic zone and of the growth law exponent according to the crack length, were determined. The whole propagation behaviour from microstructurally and mechanically short crack to linear elastic long crack regimes could be predicted by means of a unique model. A satisfactory correlation was found between model predictions and experimental crack growth rates and fatigue lives obtained under various maximum stress value at a stress ratio R=0.4 [100]. Zhang et al. [101] performed elastic plastic finite element analyses under small and large-scale yielding conditions to characterise the crack tip plastic zone size of short and long cracks under the same stress intensity factor range. Short cracks were found to have larger monotonic plastic zones compared to those of long cracks. Contrarily reverse plastic zone size seemed to be nearly insensitive to crack length [101]. If the crack growth rates were plotted against the size of the monotonic crack tip plastic zone, short and long crack data of constant amplitude loading tests fell into the same band [101]. To accurately define the boundary between small and large-scale yielding condition and to apply a more efficient plastic zone correction to linear elastic fracture mechanic crack growth data [14], Caputo et al. [102] provided a new analytical formulation of the short crack tip plastic zone size. The analytical expression was developed on the basis of finite element results with the aim of taking into account all the parameters affecting the crack tip plastic zone size such as material properties, component geometry and loading conditions [102].

Ramsamooj [103] proposed a fracture mechanics law to describe the crack growth from mechanically short to long crack regime based on the increase of the cyclic plastic zone during propagation. According to the crack extension energy balance, the growth rate was related to the size increment of the crack tip process zone, that is the cyclic plastic zone. Analytical formulae, relating the increment of the cyclic crack tip plastic zone to the stress intensity factor range, were derived, under small scale-yielding assumption, for plane strain and plane stress conditions. The effects of crack closure were included into those analytical expressions [103]. An unified crack propagation law was finally obtained considering the transition from plane strain to plane stress condition during crack propagation and considering the effect of large-scale yielding. Ramsamooj [103] validated his model using published short crack growth experimental data of various materials. Despite its empirical nature, the model proved to predict reasonably well the test data except for the growth rates of short crack strongly affected by the material microstructure (microstructurally short cracks).

Beretta et al. [104], in an attempt to find a suitable model to predict low cycle fatigue life of components containing short cracks, analysed some elastic-plastic fracture mechanics correlating parameters. The cyclic strain intensity factor and the cyclic J-integral were unable to correctly characterised experimental low cycle fatigue lives of quenched and tempered steel samples. The authors suggested a new elastic-plastic crack propagation model where growth rates were consisting of two terms: a linear elastic on based on the stress intensity factor range and a plastic one based on the Mason-Coffin law [104]. The proposed model was able to predict the experimental results but was found to be very sensitive to the crack closure value.

2.2.4.3 Physically short cracks

In case of physically short cracks the lack of similitude with the long flaws is caused by a different amount of tip shielding. In fact the reduced cracked surface behind the crack tip decreases the wake length where shielding mechanisms take place. Physically short cracks are therefore short in comparison with the length necessary to obtain a full crack tip shielding. The crack shielding is a phenomenon that causes a reduction of the effective crack driving force available for propagation, decreasing the growth rate. Cracks experience various shielding mechanisms depending on the external loadings and on materials they are propagating into [3]. For metal components, subjected to constant amplitude fatigue loadings, the most common shielding mechanism is the crack closure. The phenomenon of the crack closure was first investigated and rationalised by Elber [22,105]. He experimentally observed a variation in the elastic compliance of cracked thin aluminium sheets under tensile cyclic loading and he ascribed such change to an early closure of the crack at a far field tensile load [22]. Residual tensile strains were left on the crack flanks by the plastic behaviour at former crack tips during propagation, forming a plastic wake. The attendant reduction of the flank opening displacement caused a premature contact resulting in crack closure under tensile load. Elber [105] assumed that crack propagation can occurs only during the portion of cyclic load in which cracks are fully open as there are no substantial variations in the tip strain field of a closed crack under fatigue load. Therefore crack closure reduces the fatigue crack growth rate by decreasing the effective driving force available for crack extension. An effective stress intensity factor range ΔK_{eff} was defined as function of the crack opening stress and it was related to the crack growth rate by means of a Paris-type propagation law [105]. The effective stress intensity factor range was capable of characterising the effect of the load ratio R on the crack growth rate, as different R ratios growth rate data collapsed into a narrow band when plotted against ΔK_{eff} [105].

Since each kind of closure arises as the result of a premature contact between the crack faces, closure phenomenon involves the portion of the crack behind the advancing tip called crack wake. It is therefore not surprising that closure requires a minimum crack wake length to fully develop and to completely shield the crack tip. The short cracks, that by definition have limited wakes, will experience a less amount of closure than the corresponding long flaws. The decreased shielding effect causes an higher local crack driving force in small cracks compared to long ones where shielding is fully developed.

Several analytical and numerical models were developed to predict crack closure mechanisms, in particular plasticity-induced crack closure [3,14]. Newman [106] developed an analytical prediction model of cyclic crack growth taking into account the effects of plasticity-induced crack closure. The crack closure was analysed using a specific two dimensional model based on Dugdale crack tip plastic zone model (strip yield model) [14], but it was modified to leave plastically deformed material along the crack wake as the flaw propagates. Such model was developed for through thickness central cracks in finite width samples under uniform tensile external stress [106]. The crack tip plastic zone and the plastic wake, left on the crack surfaces, were modelled by

rigid-perfectly plastic bar elements with a flow stress that was the average between the material yield stress and the ultimate tensile strength [106]. Plane stress and plane stain conditions were considered introducing a constrain factor on the flow stress of bar elements that accounted for three dimensional effects on plasticity. The closure model was used to calculate the crack opening stress as function of different crack lengths and load histories. The effective intensity factor range, ΔK_{eff}, could be therefore calculated. A crack growth rate law was successively developed in term of effective stress intensity factor range, threshold stress intensity factor range, and fracture toughness to describe the whole sigmoidal shape generally observed for crack growth rate curves [106]. The propagation model was applied to predict crack growth behaviour under constant amplitude and aircraft spectrum loadings in aluminium alloy sheets. The predicted crack propagation lives were consistent with the experimental data [106]. On the basis of the results of his analytical plasticity-induced closure model Newman [107] derived semi empirical crack opening stress equations for two dimensional central cracks in finite width components. The opening stress σ_o turned out to be function of the stress ratio R, the maximum stress level and of the three dimensional plasticity constrain (plane stress or plane strain) [107]. The strip yield Newman's closure model was subsequently extended to problems regarding two dimensional central cracks emanating from circular holes in finite width plates, by developing stress intensity factor and crack surface displacement solutions for that specific geometrical configuration [108]. Newman [54] further applied the plasticity-induced crack closure concept to general crack growth structural analyses developing the fatigue life prediction code, FASTRAN-II.

Nowell [109] developed a different analytical model for plasticity-induced crack closure under plane stress conditions based on the boundary element method. Three different sets of dislocation dipoles were used to model the crack itself, the plastic zone at the crack tip, represented as a yield strip, and the plastic wake generated by the crack growing though the tip plastic zone. Each dipole produced, proportionally to its magnitude, a particular stress field that was added to the external stress [109]. The magnitude of the dislocation dipoles, that is the local crack face displacement or the plastic stretch in the tip plastic zone, were calculated applying boundary conditions. The crack face displacement was obtained subtracting the magnitude of the plastic wake dipoles to that of crack dipoles [109]. Doing so the local effective displacement was calculated as the elastic opening crack face displacement minus the residual stretch of the plastic wake. The dipoles, modelling the crack faces, could be either open and therefore traction free or closed, carrying compressive stress. Analogously in the crack tip plastic zone three different boundary conditions were possible: no yield, tensile yield or compressive yield. The dipoles in the plastic wake had the capability of yielding under compressive stress reducing their magnitude that is the amount of residual stretch [109]. The main difference between Nowell's model and Newman's approach was the solution technique adopted to solve the equation system, derived from the boundary condition fulfilment. Such system, typical of the boundary element method, was solved by Nowell [109] using a quadratic programming approach. Object functions which define the boundary conditions were minimised under specific constrains to obtain the magnitude of every dipoles. The quadratic programming is a very efficient method to calculate the crack opening stress since it is capable of ranging from minimum to maximum load in a single load increment step [109]. Nowell et al. [110] improved the original plane stress crack closure model and applied it to different crack configurations.

Nowell's model was further modified to predict crack closure under plane strain conditions assuming that the plastic deformation occurred at the crack tip along two slip bands inclined with respect to the propagation plane [110]. Model predictions were found to be in good agreement with other model result and data available in literature for both plane stress and plane strain conditions [110].

A number of researchers have studied plasticity-induced crack closure with the aid of finite element analyses [14,111]. Since the complexity of experimental procedure to measure the crack opening stress and the related imprecision, finite element simulations have been used as an alternative tool to evaluate closure. Finite element simulations of propagating cracks, leaving a plastic wake behind their tips, were performed mainly for two dimensional through thickness cracked configurations under plane stress or plain stress conditions. Gonzalez-Herrera et al. [112], for instance, performed two dimensional finite element simulation of crack propagation in CT specimens of 2024-T351 aluminium alloy. The cyclic behaviour of the aluminium alloy was modelled using an isotropic hardening law. Plane strain and plane stress numerical results were validated against experimental crack growth rates curves. A good correlation was found between experimental and numerical growth rate calculated using the effective stress intensity factor range [112]. Few efforts were directed toward the investigation of the closure variation along the crack front in three dimensional crack problems [111].

Solanki et al. [111] presented a comprehensive review of finite element analyses of plasticity-induced crack closure in both two and three dimensional geometries. Modeling issues and difficulties related to level of mesh refinement, crack advancement schemes, crack shape evolution, and crack opening stress measurement location and technique were underlined as well [111].

Newman [108] used his analytical plasticity-induced closure model to predict the growth of physically short cracks in order to investigate the role of crack closure in the occurrence of short crack behaviour. Crack opening stress was calculated as function of the crack length for centre-cracks in smooth plates and emanating from circular notches under constant amplitude loading. Surface crack configurations were also investigated [108]. As short cracks generally grow under high stress, a plastic zone correction was applied to the effective stress intensity factor range to account for large scale yielding conditions. Long crack growth rates were correlated to the respective plastic zone corrected effective stress intensity factor range, and the obtained law was used to predict short crack propagation under plane stress and plane strain conditions. Closure analyses were found to predict the growth short cracks in aluminium, steel and nickel alloy samples reasonably well [108]. A local minimum was observed in the growth rate curves of short cracks at particular ΔK level [108]. Such behaviour was caused by the combination between the increasing of the driving force with the crack length and the associated reduction of the effective stress range for short flaws.

Holm and Blom [113] performed a two dimensional elastic plastic finite element simulation of short crack propagation in a 2024-T3 aluminium alloy sample under constant amplitude load. Cracks growth was obtained by realising nodes at the crack tip, and a contact formulation between the crack faces was implemented to account for closure [113]. Plasticity-induced closure was found to increase according to the crack

length for short cracks. Therefore the anomalous growth rate of short cracks, higher than that of long cracks with the same nominal driving force, seemed to be caused by the larger effective stress intensity factor ranges. The same conclusions were drawn by Kendall et al. [114] analysing the behaviour of physically short cracks in structural steels. Experimental results indicated that the faster propagation of physically short cracks was mainly due to the smaller amount of closure experienced by those cracks compared to long flaws.

Nakai and Ohji [115] developed a method, to predict growth rates of physically short cracks in both smooth and notched specimens, based on crack closure. An analytical equation to calculate the opening ratio, $U=\Delta K_{eff}/\Delta K$ as function of the crack length was derived on the basis of the Kitagawa-Takahashi diagram [115]. The effective stress intensity range of physically short cracks could be calculated and related to the growth rate by means of the effective propagation law of long cracks modified to include the effective short crack threshold [115]. For short cracks in smooth specimens the propagation rates increased monotonically according to the flaw length. The difference in the short crack growth behaviour between notched and unnotched components was attributed to the different development of the crack opening stress intensity factor [115].

Newman, after the first application of its strip-yield plasticity-induced closure model to physically short crack [108] systematically reviewed and improved the capabilities of such model to predict short crack growth rate in various materials and under different fatigue loadings [116-118]. A plastic zone correction was applied to the effective stress intensity factor to take into account the large scale yielding condition that generally characterises the tip of short cracks [116]. A quarter of the cyclic plastic zone size was added to the crack length. Such plastic zone correction was obtained relating the corrected stress intensity factor to the corresponding cyclic J-integral, ΔJ. Cyclic plasticity effects and the consequent plastic zone correction, were found to be significant only for applied stress ranges larger than 0.6 times the material yielding stress [116]. Newman's analytical closure model was used to calculate short crack growth rates in notched and unnotched specimens of 2024-T3 and 7075-T6 aluminium alloys under constant amplitude and spectrum loadings.

Zhang et al. [43] analysed and measured in situ the closure of short fatigue cracks in 2024-T351 aluminium alloy samples under cyclic loading by means of a testing system inserted into the chamber of a scanning electron microscope. Surprisingly a peak value of the closure stress as high as 55% of the nominal maximum stress was observed in the short crack regime for 100-150 μm long cracks [43]. The closure stress decreased as the crack length increased to reach a constant value for cracks 1.5 mm in length. That result was in contrast with the observations of Newman [108] according to which short cracks propagated faster than long cracks with the same stress intensity factors, because they showed a smaller crack opening stress. In fact, for a given crack growth rate, Newman's analytical closure model overestimated the effective crack diving force in the whole range of analysed crack lengths [43]. Therefore for a given effective stress intensity factor range the Newman's model was found to underestimate the growth rate of short cracks. Zhang et al. [43] developed an analytical model to calculate the crack opening stress intensity factor combining the effects of both plasticity-induced and roughness-

induced closure. That model underestimated the growth rates of crack shorter than 400 μm and overpredicted, in a conservative way the propagation rate of longer flaws.

2.2.4.4 Fracture mechanics based prediction models

Taylor [119] investigating the application limits of linear elastic fracture mechanics defined a critical crack length below which crack growth behaviour could not be described by the stress intensity factor range. Such critical length coincided with the crack length a_2 defined in the Kitagawa-Takahashi diagram (see Fig. 2.2). A method to estimate a_2 was proposed and justified examining various theory on short crack behaviour. The critical length a_2 was assumed to be the larger value between 10 times the characteristic microstructural dimension d, ($10d$) and 10 times the crack tip cyclic plastic zone, r_p ($10r_p$) [119]. Experimental data showed that such assumption gave reasonably prediction of a_2.

Brown [120] analysed the various regimes of fatigue crack growth according to different external stress range and flaw length. On the basis of simple empirical short crack growth prediction models the limits of each propagation regime, characterised by a specific crack extension mechanism, were defined. An modified version of the Kitagawa-Takahashi diagram, extended to finite crack growth rates, was proposed to show which is the dominant crack propagation regime for any given stress range and crack length [120]. Six different regions characterised by distinct crack behaviours and crack tip opening modes were defined (linear elastic fracture mechanics, elastic-plastic fracture mechanics under mode I and tearing mode III, non propagating cracks, microstructurally short cracks, and crystallographic cracking). Since the difference in crack extension mechanisms inside every propagation regime, a single model cannot predict the whole crack growth process from an initial crack length to failure [120]. The extended Kitagawa-Takahashi also provided the application limits of different crack growth models.

Several researchers developed semi-empirical models to predict short crack growth using fracture mechanics parameters. Such empirical crack propagation laws were merely derived fitting experimental growth rate data without any physical or mechanical basis. For instance Hobson et al. [121] suggested an empirical model to predict the short crack behaviour in medium carbon steel specimens. Experimental tests showed that crack growth was characterised by microstructural interaction when the cracks were shorter than the material characteristic microstructural dimension and to large-scale yielding conditions for longer flaws. Therefore two empirical equations were derived to predict respectively microstructurally and mechanically short crack growth [121]. The microstructural growth rate was found to be proportional to the distance between the crack tip and the dominant microstructural barrier, defined by the material characteristic microstructural dimension, d. The proportional coefficient was function of the stress range. Cracks were predict to arrest in correspondence with the microstructural barrier. In the continuum elastic-plastic propagation law the growth rate was proportional to the crack length by a factor depending on the total strain range [121]. A threshold value corresponding to zero growth rate, was also included into the equation. Fatigue life could be predicted integrating the two propagation laws from an initial crack length to failure. In the crack length regime where the two laws overlapped both

microstructurally and elastic-plastic crack growth mechanisms were assumed to operate [121]. Crack growth rate was therefore obtained as the sum of the contributions given by the two equations. Crack growth curve showed a minimum rate in proximity of a the dominant microstructural barrier that is for a crack length approximately equal to the material characteristic microstructural dimension, d.

Angelova and Akid [122] modified the Hobson model to analyse separately the physically short crack and the long crack propagations. As, after the crack had passed the dominant microstructural barrier a further growth retardation was experimentally observed in the physically short crack regimes, an additional empirical equation was introduced to predict such behaviour [122]. A propagation law, analogous to that applied for microstructural short cracks but with a different crack length threshold, was proposed to characterised the growth rate of physically short flaws. Analogous equations were suggested to describe the crack propagation during corrosion fatigue, where the pit-to-crack transition stage was also considered. The developed empirical models proved to correctly predict the experimental fatigue life of sample in air and in aggressive environment.

Nisitani and Goto [123] developed another propagation model for short cracks in plain and notched carbon steel specimens under constant amplitude loadings. Crack growth rate in unnotched samples was found to be uniquely determined by the term $\sigma_a^n l$ where σ_a is the stress amplitude, l is the crack length and the exponent n is a constant experimentally determined. For notched specimens the short crack propagation rate was described by the same equation but, when the external stress was lower than 0.5 the yield stress the conventional Paris law was found to be valid [123]. Both those growth laws were rationalised on the basis of the same physical background assuming the crack growth rate proportional to the cyclic plastic zone size [123]. Analytical predictions were in good agreement with experimental fatigue lives.

Plumtree and Schäfer [39] proposed a microstructurally short crack growth model to predict the initial crack propagation stages in a strain cycled aluminium alloy castings. Crack growth rate was an exponential function of the stress intensity factor range and of the distance of the crack tip from the dominant microstructural barrier [39]. A parameter taking into account the effect of the relative crystallographic orientation between adjacent grains was included into the growth equation and determined experimentally according to different applied strains. The propagation law was found to be function of the applied strain amplitude as well [39].

Kujawski and Ellyin [124] suggested a short crack growth model which took into account the difference in propagation mechanisms observed between cracks in the bulk material inside the sample and superficial cracks growing in the soft layer near the free surface. Due to the less constraint of surface grains compared to interior ones, the material plastic flow stress is smaller in a superficial layer than inside the material. That variation in mechanical properties was considered one of the major cause of the short crack growth behaviour for small superficial cracks [124]. The material thickness was divided into a series of strips as thick as the crack propagation process zone size. The material yield stress was assumed linearly variable from a minimum value at the sample surface to the material macroscopic yield stress at a distance of three grain diameters

from the surface [124]. Therefore each strip showed a different amount of plasticity and cyclic strain energy at every fatigue cycles. Fatigue crack growth was modelled as local failure mechanism inside every strips caused by the plastic strain accumulated in the surface layer plus that caused by the crack stress field. The crack growth rate was derived as an exponential function of the sum of those two plastic contributions [124]. Models prediction were in good agreement with experimental short crack growth rate observed in low and intermediate strength steels specimens.

McEvily et al. [125-127] modified the linear elastic fracture mechanics approach defining a new parameter capable of correlating long and short crack growth behaviour. A new stress intensity factor range was defined introducing a material constant, which relates the crack growth threshold to the material fatigue limit, and a plastic zone correction accounting for large-scale yielding conditions. The development of crack closure was also included into the model by means of a simple analytical expression defining the opening stress intensity factor as function of the crack length [125]. The effective stress intensity factor range could be therefore calculated for every crack length. The crack growth rate was assumed to be an exponential function of the effective crack driving force that is the difference between the effective stress intensity factor range and effective crack growth threshold [126]. A unique crack growth equation, able to predict short and long crack growth rates, was developed simply modifying the conventional linear elastic fracture mechanics approach. The proposed model successfully predicted experimental short crack growth data in notched and unnotched specimens of aluminium alloys [125] and carbon steel [126]. However due to the model nature a number of material parameters have to be determined to accurately predict the crack growth rate. McEvily et al. [127] compared their single parameter crack growth prediction model [125] with the two-parameter approach of Shyam et al. [128]. If during the crack propagation process static modes of separation are not active, a single parameter approach like that proposed by McEvily et al. [125] is adequate to characterising short and long crack growth. However when static separation modes are active a two-parameter model is required [127].

Santus and Taylor [129] modified the Chapetti's model [62] to obtain a slightly different physically short crack growth law based on driving force concept. The threshold stress intensity factor as function of the crack length was evaluated by means of the El Haddad threshold equation [55] and two different crack propagation laws were used respectively for short and long cracks. For physically short cracks the Zheng and Hirt equation was proposed while for long flaws the Klesnil and Lukáš law was maintained [129]. The model was validated predicting the fatigue life of notched samples of 2024-T3, 7075-T6 aluminium alloys and Ti–6Al–4V titanium alloy. The model accurately predicted the crack propagation cycles when the initiation life was both a predominant or a negligible fraction of the total fatigue life [129].

Sadananda and Vasudevan [130,131] suggested an unified analysis frame work for short and long cracks. They assumed the long crack growth behaviour as representative of the fundamental intrinsic material behaviour. Differences in fatigue crack propagation caused by diverse stress ratios were explained using two driving force parameters the stress intensity factor range ΔK and the maximum stress intensity factor K_{max} and denying the existence of crack closure [130]. Long crack growth therefore had

its threshold defined by two different conditions ΔK_{th} and $K_{max\ th}$. The anomalous short crack behaviour was assumed not to be caused by a lack of similitude but by ignoring the two critical threshold conditions and the existence of local internal stresses increasing the crack tip driving force [131]. Such internal stresses were ascribable to the notch stress raising effect in case of short crack nucleated from notches or at material inhomogeneities as inclusions or extrusions and intrusions along persistent slip bands acting as small stress concentrators. The internal stress field has to be defined in term of continuum mechanics to correlate short and long crack growth behaviour and develop a reliable prediction model. Several example and evidences from literature were provided in [130,131] to illustrate and prove the internal stress concept that is, in a certain sense, consistent with the thermodynamic characterisation of the short crack growth proposed by Guiu and Stevens [132].

2.3 Fatigue and fracture mechanics of notched components

Engineering structures inevitably contain notches that are the principal nucleation sites of fatigue cracks. The crack initiation process at the component surface is, in fact, enhanced by the stress and strain concentration produced by the notch. The local notch stress field and the relative plastic zone also influence the early propagation stage of crack nucleated from stress raisers. For those reasons the fatigue behaviour of notched components and the growth of cracks nucleated from stress concentrators have been widely investigated since the dawning of fatigue and fracture mechanics research. Despite the large interest aroused by those investigation topics, the effect of notches on component fatigue life as well as the crack development from notches are, nowadays, not completely understood.

The influence of engineering size notches on the total fatigue life is first reviewed in the following sections. Most of the research works in literature dealt with the fatigue strength at the endurance limit conditions rather than at high and low cycle fatigue regimes. Since scribed fuselage joints have been found to develop propagating cracks in service (see chapter 1), the scribe mark problem is related to fatigue behaviour of notched components in the finite-life region. However the concepts applied to evaluate the notch sensitivity of a component at the fatigue limit can be readily extended to the finite-life region, making the review of the literature about notch effect on fatigue limit useful to rationalise the fatigue behaviour of scribed structures. The effect of different notch geometries and consequent local stress fields on the fatigue notch sensitivity is reviewed to investigate the relation between local geometrical parameters and the resistance of a component to crack nucleation and propagation. Particular emphasis is put on the notch size effect to review how component notch sensitivity changes as the notch is scaled down to microstructural dimension. Research works regarding the definition of a notch size threshold value, below which components are no longer sensitive to stress raisers are also examined. The historical background of conventional prediction methods dealing with the influence of notches in fatigue life is reviewed below. A survey of notch sensitivity models developed inside the framework of fatigue stress-life and strain-life approaches and covering fatigue limit and finite-life region is given in the following section. Notch fatigue strength prediction method based on fracture mechanics are reviewed afterwards. Such models found their application mainly for sharp notches where non propagating cracks were observed at the component

fatigue limit. Finally fracture mechanics models that assess the fatigue finite life of notched components, predicting the propagation of crack inside the notch stress and strain fields, are described.

2.3.1 Effect of notches in fatigue life

The local stress and the strain fields in the vicinity of notches strongly affect how a crack nucleates and propagates under fatigue loading. The presence of notches generally decreases the fatigue strength and the fatigue life of components with respect to that of unnotched ones under the same load conditions. The effect of stress concentrators on fatigue limit of components under constant amplitudes loads is relatively well understood and practical evaluation methods are available in literature although the mechanisms behind the formation and early propagation of cracks at notches are not completely rationalised yet [1]. The decrease of fatigue strength caused by the notch is generally characterised by a parameter called fatigue-notch factor K_f (eq. (2.24)) that is the ratio between the fatigue limit of an unnotched sample, σ_e^u, and that of a notched specimen, σ_e^n, with the same net section area [1,3].

$$K_f = \frac{\sigma_e^u}{\sigma_e^n} \tag{2.24}$$

The fatigue-notch factor definition can be extended to the finite-life regime. In that case K_f represents the ratio between the external stress amplitude of unnotched and notched samples corresponding to a given number of fatigue cycles to failure. The most direct way to obtain the fatigue-notch factor value is by experiment but the use of analytical prediction methods can reduce time and costs. Experimental evidences show that the reduction of the fatigue limit produced by notches is usually lower than the stress raising at the notch root corresponding to the stress concentration factor K_t [1,3]. In other terms notches caused less concentration effect under fatigue load than predicted by elastic analysis such that $K_f \leq K_t$. Generally K_f tends to the value of the theoretical K_t for notches showing large root radii. The degree of agreement between the values of the fatigue-notch factor end the elastic stress concentration factor is expressed by the notch sensitivity factor q defined as follows:

$$q = \frac{K_f - 1}{K_t - 1} \tag{2.25}$$

Both the fatigue-notch factor, K_f and the notch sensitivity factors q, are used to characterised the effect of notches on fatigue limit. Many empirical or semi-empirical expressions, built up on various assumptions, have been developed to correlate K_f or q to the notch geometry. Those expressions can be classified into three categories according to [133]:

1) average stress based equations
2) stress field intensity equations
3) fracture mechanics based equations

The averaged stress based models are based on the assumption that the fatigue failure occurs if the average stress over a material characteristic length at the notch root reaches a critical stress value. Stress field intensity models instead consider a damage zone at the notch root where the equivalent von Mises stress averaged by means of weight functions has to attain a critical value. Finally fracture mechanics based models assume

the fatigue limit as a threshold condition for the propagation of cracks nucleated at the notch root. Such set of notch sensitivity assessment methods is described in the following section while a survey of the most widely used equations belonging to the first two categories is given below. Comprehensive reviews of the several K_f expressions available in literature can be found in [133,134].

One of the first interpretations of the failure of the elastic stress concentration factor in predicting the notch sensitivity in fatigue was provided by Neuber [11] using the concept of elementary structural particle. Such concept was not strictly related with the nature of fatigue process but the derived semi-empirical expressions of K_f proved to predict the notch sensitivity reasonably well. Neuber [11] realised that classical theory of elasticity tended to overestimate the stress concentration factor of notches with small root radius up to predict and infinite K_t for sharp notches. The cause of the failure of the elastic theory was ascribed to the breakdown of the continuum medium assumption in case of component containing sharp notches.

Actually metals are not continua as they are formed by grains arranged in particular structures. As long as the notch root radius was large compared to the material microstructure the stress gradient at the root was so gentle to produce significant variations of the stress magnitude within distances many times longer than the average grain dimension. The size of smallest material element necessary to accurately describe the stress variation at the notch root was therefore bigger than the material microstructural length and the hypothesis of continuum medium was fulfilled [11]. On the contrary if the notch root radius was comparable is size with the material microstructural dimension the stress varied substantially within a grain diameter and the material microstructure had an effect on the stress distribution and on concentration factor. In fact in such case the assumption of the arbitrary divisibility of the material at the basis of the continuum medium hypothesis was no longer admissible [11]. Consequently for sharp notches showing steep stress gradients an elastic theory based on the concept of a material element of finite size that considered the material as composed by a multitude of small but finite particles, was suggested by Neuber [11].

It was proved, with the aid of mathematical considerations, that, to predict the stress concentration factor of sharp notches with root radius, ρ, equal to zero, the concept of finite-size particle could be just applied at the notch root where the failure of the classical elastic theory was restricted. Thus the stress field calculated by the conventional elastic theory could be still used to assess the K_t of sharp notches with the only introduction of a particle of finite size at the notch root. The particle was assumed so small that the stress acting on it could be considered constant [11]. The stress concentration factor of sharp notch with ρ=0 was obtained averaging the stress field predicted by the conventional elastic theory over the particle size. The K_t of sharp notches was therefore strictly related to the particle dimension that became a material constant. In fact half of the particle length appeared in the stress concentration factor equation of different sharp notches under various loading conditions [11]. Such quantity, named c_n in eq. (2.26), was related to the effect of material microstructure and turned out to be a new material constant which has the dimension of a length. On the basis of his results for sharp notches, Neuber [11] suggested a new equation to describe the transition of the stress concentration from the conventional elastic theory value to

those of sharp notches as function of the root radius. The stress concentration factor therefore turned out to depend, beside the notch geometry, also on the material. The new expression of the notch stress concentration was afterwards applied to define the fatigue-notch sensitivity of components. In fact, assuming that the fatigue failure on notched samples occurred when the stress at the notch root reaches the fatigue limit of unnotched specimens, Neuber [11], according to the new K_t definition, proposed the following fatigue notch factor K_f and notch sensitivity factor q expressions:

$$K_f = 1 + \frac{K_t - 1}{1 + \sqrt{\frac{c_n}{\rho}}}, \quad q = \frac{1}{1 + \sqrt{\frac{c_n}{\rho}}} \tag{2.26}$$

In eq. (2.26) K_t is the elastic stress intensity factor, ρ is the notch root radius and c_n is the material constant related to the material particle size. The notch sensitivity factor, q, depended on the ratio between the material constant c_n and the radius of curvature of the notch root. Kuhn and Hardrath [135] showed that the constant c_n depended on the material tensile strength.

On the basis of a model taking into account how inherent material flaws like cavities, inclusion, defects alter the stress field at the notch root, Heywood [136] suggested a different expression of the notch-fatigue factor:

$$K_f = \frac{K_t}{1 + 2\sqrt{\frac{c_h}{\rho}}} \tag{2.27}$$

The parameter c_h in eq. (2.27) is once again a material constant with dimension of a length which is function of both the specimen geometry and the material tensile strength. For notches commonly found in engineering components eq. (2.27) predicts nearly the same fatigue-notch factor values as eq. (2.26). Despite that the K_f expressions proposed by Neuber [11] and Heywood [136] are in principle completely different. In fact while the former considers a notch sensitivity factor depending only on the notch root radius and a material constant, in the latter q turns out to be also a function of the notch stress concentration factor [136].

Peterson [137], analysing the effect of notches on the fatigue strength, assumed that the fatigue failure of notched samples occurred when the elastic stress at a given distance δ from the notch root equated the fatigue limit value of smooth specimens. For that reason Peterson's notch fatigue prediction model, where the distance δ is regarded as a material property, is considered the first example of point stress method [133]. By means of the notch root stress gradient, the value assumed by the elastic stress at the distance δ from the notch could be related to the stress concentration factor K_t and to the root radius ρ. Equating such stress to the fatigue limit of unnotched specimens the following K_f and q expressions were obtained by Peterson [137]:

$$K_f = 1 + \frac{K_t - 1}{1 + \frac{c_p}{\rho}}, \quad q = \frac{1}{1 + \frac{c_p}{\rho}} \tag{2.28}$$

The notch sensitivity factor in eq. (2.28)) like that predicted by Neuber [11], depends on the notch root radius and a material constant c_p having the dimension of a length, but by

means of a different relation. The material constant c_p in eq. (2.28) is a function of the distance δ and of a factor considering the effect of different loading condition [137].

Appling similar assumptions to those used by Peterson for his fatigue notch factor model, Stieler and Sieber [133] derived the following expression:

$$K_f = \frac{K_t}{1+\sqrt{1+c_{ss}\chi}} \tag{2.29}$$

where c_{ss} is a material constant depending of the yield stress and χ is the stress gradient at the notch root normalised with respect to maximum stress ($1/\sigma_{max} \cdot d\sigma/dx$) [133]. Eq. (2.29) was able to accurately describe the relation between K_f and K_t for great amount of experimental data [133]. The foregoing fatigue-notch and notch sensitivity factor expressions are some of the most frequently used in engineering practice to predict the effect of notches on the fatigue limit of components. Readers can refer to [133,134] for more detailed reviews. All the examined K_f models are based on elastic stress distributions along the notch bisector, neglecting completely any probable plasticisation mechanism occurring at the notch root. Klesnil and Lucas [1] demonstrated that, in case of conventional notches with $Kt \leq 10$ in engineering materials, the effect of cyclic plasticity in decreasing the stress concentration at notch root was very weak at the fatigue limit. Therefore the influence of cyclic plasticity could be, with good approximation, neglected when the fatigue notch factor has to calculated in the fatigue limit region. However, since the analytical demonstrations of Klesnil and Lucas was based on the approximate Neuber's rule for elastic-plastic notch stress concentration factors [1], it was suggested to apply the reviewed K_f models to notches with a ratio between the notch root radius and depth larger than 0.25 ($\rho/d > 0.25$) [137]. Caution should be exercised in using the prediction models to assess the notch effect on fatigue limit of components containing deep sharp notches.

Contrary to what happens at the fatigue limit, in the fatigue finite-life region the stress reduction caused by the cyclic plasticity is not anymore negligible in comparison with the effect of stress gradient. On the other hand, due to the local high stress value, nucleated cracks leave the notch stress field relatively quickly and just a portion of their propagation is thus affect by the presence of the notch. In fact the notch stress field in the region of intermediate and low cycle fatigue mainly influences the number of cycle required for the nucleation of a crack of a specific length while its propagation up to failure will not differ from that in unnotched samples [1].

When, due to the high stress level, engineering components undergo to uniform plastic flow or localised plasticisation at stress concentrators it is generally considered more appropriate using a strain-life approach to determine the total fatigue life [3]. Such methodology consists in expressing the fatigue life of an smooth sample under constant amplitude loading as function of the total strain amplitude at the gauge section [138-140]. The total strain was written as the sum of the elastic and plastic terms that are related to the number of cyclic reversals up to the component failure. The elastic strain amplitude was linked to the total number of fatigue cycles using the Basquin equation [8] while for the plastic strain component, the relation proposed independently by Coffin [9] and Manson [10] working on thermal fatigue problems, was used. As result the total strain amplitude turned out to be the sum of two different exponential functions

of the total fatigue number of cycles [138-140]. The strain-life approach has been widely used for industrial applications, where the fatigue properties of components in the finite-life region had to be defined. In fact, such methodology not only is applied to life prediction of unnotched mechanical elements but it also constitutes the basis of the local strain approach used for notched members.

The local strain approach characterised the total or the nucleation fatigue life of notches components relating the local stress and strain fields at the notch root to the fatigue responses of smooth unnotched specimens [141-143]. A macroscopic crack was assumed to develop at the notch root after the same number of fatigue cycles as in a smooth samples under a strain amplitude equal to that obtained at the notch root. Therefore the fatigue notch-effect in the finite-life region could be assessed from the strain-life curve, derived from unnotched specimens as soon as the local stress and strain at the notch root were known [141-143]. Moreover in case of variable amplitude loading or mean stress relaxation at the notch root the whole local stress and strain histories has to be determined. The notch root deformation can be experimentally monitored with the aid of strain gages or other strain measurement techniques. Otherwise finite element elastic plastic analyses or simple analytical formulae can be applied to relate the local notch strain field to the far field nominal one.

Among those analytical methods, one of the most commonly used is undoubtedly the procedure developed by Neuber [144] and known as the Neuber's rule. According to a pure elastic assumption the stress and strain concentration factor, respectively K_σ and K_ε, have the same value equal to the elastic K_t. When plastic deformations occur however, the stress and strain concentration factors, defined as the maximum elastic-plastic stress and strain at the notch root divided by their respective nominal far field quantity, generally take different values. Neuber [144] suggested that during the plastic deformation process the geometric mean of stress and strain concentration factors, K_σ and K_ε, remained equal to the theoretical elastic stress concentration factor K_t. Therefore under cyclic loading the Neuber's role is written as follows:

$$K_t = \sqrt{K_\sigma K_\varepsilon} = \frac{\sqrt{\Delta\sigma\Delta\varepsilon E}}{\Delta\sigma_\infty} \tag{2.30}$$

where $\Delta\sigma$ and $\Delta\varepsilon$ are respectively the cyclic stress and strain range at the notch root while $\Delta\sigma_\infty$ is the nominal far field stress range and E is the Young modulus. In agreement with the majority of the engineering applications eq. (2.30) assumes the far-field stress to be inside the elastic field and thus the nominal far-field strain $\Delta\varepsilon_\infty$, is expressed as $\Delta\varepsilon_\infty=\Delta\sigma_\infty/E$. If the value of the far-filed stress range $\Delta\sigma_\infty$ is constant as in case of constant amplitude loading eq. (2.30) turns out to be the equation of a rectangular hyperbola:

$$\Delta\sigma\Delta\varepsilon = \frac{\left(K_t\Delta\sigma_\infty\right)^2}{E} = const \tag{2.31}$$

Knowing the value of the elastic K_t and the cyclic stress-strain constitutive curve of the material the local stress and strain ranges at the notch root can be obtained from solving eq. (2.31) [144]. Graphically the local stress and strain at the notch root can be considered as the intersection point at any cyclic reversal between the material cyclic stress strain curve and the Neuber's hyperbola represented by eq. (2.31) [3]. From eq.

(2.31) it appears evident that the Neuber's rule corresponds to assume the equivalence between the virtual internal work done by the elastic-plastic stress on the elastic-plastic strain at the notch root and that of the pure elastic solution. Actually if the plastic zone is localised in a small material portion and the external applied load is the same, the virtual work of the internal forces inside the whole component has to be equal between pure elastic and elastic-plastic solutions. In order to take into account that and to include the effect of the notch root stress gradient in fatigue the notch stress concentration factor in eq. (2.30) was replaced by the fatigue-notch factor K_f in the framework of the local strain approach [3]. Therefore the relation between K_f and the local stress and strain ranges at the notch root turns out to be as follows:

$$K_f = \frac{\sqrt{\Delta\sigma\Delta\varepsilon E}}{\Delta\sigma_\infty} \tag{2.32}$$

The prediction of fatigue life for notched components was found increasing using eq. (2.32) that is known as modified Neuber's rule. Other methods to correlate the fatigue-notch factor to the local stress and strain condition at the notch root were used in engineering application like, for instance, the one developed by Hardrath and Ohman [145].

Once the cyclic strain amplitude at the notch is known the finite fatigue life of a notched component can be derived from the strain-life curve of unnotched components. If the notch geometry is so large to affect the entire sample cross section, the curve relating the strain range to the total fatigue life of smooth specimens can be applied. Otherwise in case of a notch whose stress field extends over a small sample region, it is more adequate using a strain-life curve where the strain range $\Delta\varepsilon$ is plotted against the number of cycle to develop a crack of a critical length [141]. Doing so just the initiation life is determined by the local strain approach and other methods based on fracture mechanics or on strain-life curve like that described in [141], has to be applied to characterise the crack propagation.

Leis and Topper [146] analysed the causes of the decreased severity of notches in fatigue compared with that predicted by the elastic theory and defined by K_t. They suggested that the failure definition, the local biaxial stress condition at the notch root and the inaccuracy of the inelastic deformation theory like the Neuber's rule were the main factors responsible for the difference between K_f and K_t. Fatigue-notch factor is clearly very sensitive to the definition of the failure that is the critical crack length considered to assess the notch effect in fatigue. In fact the fatigue strength reduction caused by the notch can be evaluated on the basis of the total fatigue life up to the components failure or of the initiation life defined as the number of cycles required to develop cracks of an arbitrary length. It was found that the discrepancies between K_f and K_t could be reduced if the crack initiation was used as fracture criterion [146]. A definition of the fatigue-notch factor based on the equivalent von Mises stress rather than on the maximum principal stress, was able to further reduce the gap with the stress concentration factor value [146]. Leis and Topper [146] also demonstrated the inaccuracy of Neuber's rule in predicting the elastic plastic strain field at the root of sharp notches considering that one of the causes of the better accuracy of eq. (2.32) for fatigue life evaluation of notched components.

Glinka [147] presented an alternative approach to calculated the elastic plastic strain at the notch root under cyclic loading. Contrary to the Neuber's rule, the equivalence of the strain energy density between the pure elastic and the elastic plastic solutions, rather than of the virtual work, is assumed at the notch root. Moreover a plastic zone correction factor, analogous to the one suggested by Irwin for cracks [14], was introduced to take into account the stress redistribution caused by the notch root plasticisation [147]. The equivalent energy density method related the elastic plastic strain at the notch root to the theoretical elastic stress concentration factor K_t. Such approach was able to give good predictions for notches with both low and high stress concentration factors up to a nominal external stress range equal to the material yielding stress. The energy density method could be applied to notched component under both cyclic and monotonic tensile and bending loadings [147].

After the first pioneering works on the notch effect in fatigue, several other methods have been proposed to evaluate the fatigue-notch factor of components at the fatigue limit and in the finite life region. The majority of those methods rely on the definition of a specific distance or region ahead of the notch, where the stress distributions are analysed to characterise the influence of notches on fatigue life. Like for the models proposed by Neuber [11] and Peterson [137], such distances and process zone dimensions are considered material properties.

Lazzarin et al. [148] suggested two new parameters not based on the stress and strain peak values to estimate the fatigue limit of lateral rounded V-shaped notched plates under tensile loading. Two different equivalent stress factors were defined considering respectively the principal stress at a distance a_0 from the notch root multiplied by a non dimensional weight function f and the average of the principal stress integrated along the notch bisector over a distance b [148]. The distance from the notch root, where the local principal stress was evaluate was assumed to be equivalent to the effective crack length a_0, defined by El Haddad et al. [55]. Equating the equivalent stresses with the material fatigue strength for the limit cases of an unnotched (root radius $\rho=\infty$) and a cracked (root radius $\rho=0$) plates, the weight function f and the integration distance b were determined. The length b turned out to be twice the El Haddad's effective crack length a_0. The stress average concepts were also extended to finite fatigue life region [148]. The proposed methods were able to satisfactorily estimate the fatigue strength of notched components under both fatigue limit and finite life regions.

Livieri and Tovo [149] applied the average stress method suggested by Lazzarin et al. [148] to characterise the effect of notches, cracks and small defects on sample fatigue strength. The prediction approach was validated against experimental data and it proved to accurately evaluate the fatigue strength of specimens containing notches, cracks and defects.

Ostash et al. [150-153] introduced the concept of a prefracture macroscopic zone of a characteristic size d formed at the root of notches and at the surface of smooth sample under cyclic loadings. The boundary of that prefracture zone represented the major barrier for crack propagation. Its characteristic size d was assumed to be a material constant [150]. Due to the presence of the prefracture zone the notch stress

concentration effect was reduced. Ostash et al. [151] defined a new fatigue-notch factor K_f which was equivalent to that proposed by Neuber [11].

Weixing [154] suggested a different method to predict the fatigue strength of notched component called the stress field intensity approach. Fatigue failure occurred, as soon as the average over the fatigue failure region volume of a suitable equivalent stress distribution, multiplied by a weight function, reached the fatigue limit of unnotched samples [154]. The size of the fatigue failure region was assumed to be once again a material constant.

Qylafku et al. [155] modified stress field intensity approach to better consider the effect of the notch root plasticity and the stress gradient on fatigue strength of notched components. The elastic plastic maximum principal stress along the notch bisector was chosen as equivalent stress distribution and the weight function was expressed in term of the relative stress gradient [155]. The prediction accuracy of the proposed model, named volumetric approach, in characterising the fatigue notch effect was assessed against several experimental results [155-157]. The volumetric approach predictions showed a very good agreement with different test results.

Tovo and Livieri [158,159] applied another volumetric method, called implicit gradient approach, to assess the fatigue life of sharp V-notched samples and welded components under tensile and bending loads. The effective average stress range proved to correlate well the fatigue life of welded joints and sharply notched components. The implicit gradient approach was able to reduce the fatigue strength evaluation of complex component to a simple calculation of an effective stress. Moreover critical distances approaches could be seen as particular cases of the stress gradient approach where proper weight functions are taken into account [159].

Bentachfine et al. [160] analysed the effect of notches in low cycle fatigue using the so called critical volume approach. The critical volume approach is based on the consideration that the fatigue process needs a physical material volume to take place. The average of strain energy density range over that volume around the notch root, called effective volume, has to reach a critical value to generate a fatigue failure. The suggested method leaded to a reasonable prediction of the fatigue-notch factor K_f in the low cycle fatigue regime [160].

Several researches used the concept of notch stress intensity factor, introduced by Creager and Paris [161] for blunt cracks and extended by Lazzarin and Tovo [162] to rounded V-shaped notches, as predicting parameter of the fatigue strength of notched components. For instance, Boukharouba et al. [163] analysed the fatigue crack initiation of welded joints and CT specimens relating the initiation number of cycle to the stress intensity factor range calculated for rounded V-notches, $\Delta K_{\rho,\psi}$. The characteristic distance X_c, considered as a material property determined by the microstructure, was the length over which the stress distribution is approximately constant showing its maximum value. The fatigue initiation endurance limits of different notches were well correlated by the parameter $\Delta K_{\rho,\psi}/\rho^{\alpha}$ consisting of the notch stress intensity factor divided by the notch root radius raised to the degree of singularity, α, of the equivalent sharp notch with the same depth and open angle [163].

A stress field approach, based on the concept of the notch stress intensity factor, was widely applied in the fatigue strength prediction of welded joints [164-168]. Since weld ligaments were modelled as sharp V-notches neglecting the toe radii, the notch stress intensity factor was able to unambiguously characterise the elastic stress distribution close to the weld toe. The notch stress intensity factor range, ΔK_N was able to correlate the fatigue strength of different welded joint geometries in a unique curve with a scatter band considerably reduced if compared with the original S-N curves [164-168].

In the case of a weld toe or notch root radius different from zero the notch stress intensity approach was still able to describe the local stress distribution even if it slightly underestimated the component fatigue strength [166]. However, if notches with different open angles are concerned the diverse degree of singularity gives rise to notch stress intensity factors with dissimilar units of measure. Their fatigue strengths, therefore cannot be correlated in terms ΔK_N with a unique curve. Such problem was solved considering the elastic strain energy range averaged over a defined volume surrounding the sharp root of notches and weld toes [168,169]. In fact, for sharp notches the average strain energy turned out to be a function of the local notch stress intensity factor but it had the advantage of keeping the same unit of measure. The control integration volume surrounding the notch root was assumed as a circular sector with a radius depending on the material fatigue properties and the failure criterion [169]. Experimental fatigue lives of different welded joints were satisfactory correlated by the elastic average strain energy range showing a scatter band smaller than the one obtained using ΔK_N [168]. Moreover the strain energy range averaged over the control volume could be accurately calculated, even for complex three-dimensional geometries, by means of finite element models showing relatively coarse meshes [169].

Verreman and Limodin [170,171] developed an approach to predict fatigue lives of V-notched components based on the notch stress concentration and the stress intensity factor concepts. The macroscopic crack initiation life was divided into the number of cycles to initiate a crack, the size of the material microstructural dimension, and those spent to propagate such short crack to the macroscopic initiation depth. The microstructural initiation life was correlated to the maximum stress at the notch root, that is to the stress concentration factor, while the short crack propagation life was related to the notch stress intensity factor [170]. The proposed prediction method, completely neglecting the notch plasticity, required only the elastic principal stress distribution to evaluate notch fatigue lives. The material resistance to microstructural crack nucleation and to short crack propagation were defined using respectively the S-N curve of a smooth specimens, regulated by microstructural nucleation, and that of a very sharp V-notch, dominated by short crack growth [171].

On the basis of their prediction model Verreman and Limodin [170,171] rationalised the role of the notch size and geometry, material properties and fatigue life in the difference between the elastic stress concentration factor K_t and the notch-fatigue factor K_f. For blunt notches, the fatigue life was dominated by the microstructural crack nucleation and $K_f \approx K_t$. On the contrary for sharp notches the microstructural crack nucleation cycles were negligible and the most of the fatigue life was spend in short crack propagation regime. It was the short crack propagation that was responsible for

the difference between the stress concentration factor and the notch-fatigue factor, $K_f<K_t$, [171].

Atzori and Lazzarin [172-175] suggested an unified method to calculate the fatigue limit of component weakened either by V-notches or defects under mode I loadings. In that way the gap between notch sensitivity and defect sensitivity was bridged, considering these apparently different phenomena two sides of the same medal. The Kitagawa-Takahashi diagram, showing the material defect sensitivity in presence of cracks, was first extended to components. The notch size effect on the material fatigue strength was evaluated, plotting the fatigue limit against the notch depth for a given notch shape, that is for a fixed K_t, [172]. Together with the Kitagawa-Takahashi critical length a_0, related to the defect sensitivity, another length parameter, a^*, associated with the notch sensitivity, characterised the extended diagram. The critical notch depth a^* divided the sharp notch regime, where the fatigue limit is defined by a stress field criterion, like the notch stress intensity factor threshold, to the blunt notch one, where the notch sensitivity is the largest and a peak stress criterion has to be applied. If a notch was shallower than a^*, the fatigue notch sensitivity decreased and the peak stress criterion had to be replaced by the notch intensity factor one [164]. The extended Kitagawa-Takahashi diagram allowed to correlate the two critical notch depths a_0 and a^* as follows:

$$\frac{a^*}{a_0} = K_t^2 \tag{2.33}$$

linking the defect sensitivity and the notch sensitivity concepts at the fatigue limit [172]. The diagram valid for the prediction of the fatigue limit in presence of defects and notches centred in infinite plates was subsequently extended to engineering finite size component introducing the geometric correction factor used in fracture mechanics for cracks [173].

For finite size component, a critical defect length a_D equivalent to a_0 could be defined, but, in contrast to a_0, it also depended on the component not only on material properties. A relation equivalent to eq. (2.33) was obtained between the critical defect length a_D and the critical notch depth a_N of finite size elements. The diagram was validated against several experimental results available in literature, showing a good accuracy in fatigue limit prediction [172]. The effect of notch open angles different from zero was finally included into the analysis, extending the prediction approach to general rounded V-shaped notches [174,175].

Taylor [176] noticed that several methods, used for predicting the effect of stress concentration feature under fatigue and static loads, had in common the introduction of a characteristic material length parameter. He rationalised the procedures and the assumptions behind those methods, developing the prediction methodology known as the theory of critical distances. Critical distance theory is a continuum mechanics methodology for the estimation of notched component strength that groups different approaches having in common the use of linear elastic analysis and the introduction of a length scale parameter [176]. Such critical distance factor represents an attempt to include inside the frame of a continuum mechanics approach the effect of the fracture mechanisms at a microstructural level modelled by micro-mechanistic methods. The

prediction approaches forming the critical distances theory can be divided into stress-based methods, where the notch root elastic stress field averaged over a region of specific size is equated to a characteristic material strength and energy-based or stress intensity-based methods that use energetic concepts typical of linear elastic fracture mechanics to assess notch components strengths [177].

The development of the critical distance theory is a classic example of a modern rediscovery and reinterpretation of ideas and concepts well-known in the research field of material notch sensitivity. In fact even the pioneering works of Neuber [11] and Peterson [137] on notch effect in fatigue can be regarded as first applications of the theory of the critical distances [176]. More precisely Peterson [137] was the first to propose the critical distance stress-based method called point method, while Neuber [11] developed the first example of the stress-based approach known as line method. According to the point method the fatigue failure of a notched component will occur if the elastic maximum principal stress range along a focus path, generally coincident to the notch bisector, reaches the critical value, $\Delta\sigma_0$, at a characteristic distance, d_p, from the notch root [176]. The line method assumes that fatigue failure takes place when the elastic maximum principal stress distribution along the focus path, averaged over a critical distance, d_l, from the notch root, equals the critical value, $\Delta\sigma_0$. These are nothing more than the assumptions at the basis of the methods developed respectively by Peterson [137] and Neuber [11]. In those cases the lack of a methodology to determine critical distance values, beside the deficiency of accurate estimations of stress distributions in real components led to the empirical relations in eq. (2.26) and eq. (2.28) where critical distance value were empirically obtained, fitting fatigue limit data.

Taylor [178], contrary to Neuber and Peterson, stated the generality of the critical distance prediction assuming that the same methods with the same material constants could be applied to any kind of notch and stress concentrators. Using the point and line methods to predict the fatigue strength in the extreme case of a sharp crack and of an unnotched component the values of the critical distances d_p and d_l and that of the critical stress range $\Delta\sigma_0$ were determined [178]. From the case of a plain specimen under constant amplitude fatigue tensile load, the critical stress range $\Delta\sigma_0$ turned out to be equivalent to the material fatigue limit under the specific load condition $\Delta\sigma_e$. On the other hand in case of a long though crack in an infinite plate fatigue failure condition as well as the stress distribution at the crack tip are defined by the linear elastic fracture mechanics. The crack tip stress distribution at the component fatigue failure is in fact characterised only by the cyclic stress intensity factor threshold, ΔK_{th}. Appling the point and the line method respectively to a two dimensional centre crack in an infinite plate the following equations were obtained:

$$\Delta\sigma\left(d_p\right)\Big|_{crack} = \frac{\Delta K_{th}}{\sqrt{2\pi d_p}} = \Delta\sigma_e \tag{2.34}$$

$$\frac{1}{d_l}\int_0^{d_l} \Delta\sigma\left(r\right)\Big|_{crack} dr = \frac{1}{d_l}\int_0^{d_l} \frac{\Delta K_{th}}{\sqrt{2\pi r}} dr = \Delta\sigma_e \tag{2.35}$$

Solving eq. (2.34) and eq. (2.35) Taylor [178] calculated the values of the critical distances d_p and d_l:

$$d_p = \frac{L}{2}, \quad d_l = 2L \tag{2.36}$$

where:

$$L = \frac{1}{\pi}\left(\frac{\Delta K_{th}}{\Delta \sigma_e}\right)^2 \tag{2.37}$$

Both point and line methods were related to a unique length scale parameter, L function of the material fatigue limit and of the fatigue crack propagation threshold. The length L, referred as critical distance, is therefore a material property depending on the cyclic loading conditions [178]. The critical distance, L results equivalent to the material constant a_0 suggested by Haddad et al. [55] to predict short crack behaviour.

Two other stress-based approaches, the area and volumes methods, are included into the theory of the critical distances. Also these methods use the elastic stress field that is averaged over a specific region at the notch root. The area method involves the elastic stress average over a semicircular area centred on the point of maximum stress, that is on the notch root, while the volume method averages the elastic stress over an hemispherical volume with the centre at the notch root [176]. Once again notch root failure will occur when the average stresses equal the material fatigue limit, $\Delta\sigma_e$. Appling the area and volume method to the limit case of a sharp crack in an infinite plate, it was possible to demonstrate that also these approaches where related to the critical distance L, being the radius of the semicircular area $1.32L$ and that of the hemispherical volume $1.54L$ [176]. Despite their higher complexity area and volume methods do not seem to predict the experimental data more accurately that point and line methods, therefore they are not frequently used in practical problems [176]. Taylor and Wang [179] assessed the point and line method capabilities in predicting the fatigue limit of components containing stress concentrators. Stress-based critical distance approaches were validated against 47 different data sets found in literature and their prediction accuracy was compared with that of other, widely used notch sensitivity estimation models. Critical distance theory was able to successfully predict the fatigue limit of notched components of different size, geometry and material under several loading conditions [179]. Moreover the empiricism of other prediction methods can be removed using the theory of critical distances, as the critical distance L can be calculated from other material properties (eq. (2.37)).

Energy-based prediction methods, that basically are linear elastic fracture mechanics models, constitute the other branch of the critical distance theory approaches. Taylor [176] developed two energy-based models, the imaginary crack methods and the finite fracture mechanics method. According to the imaginary crack method a virtual crack is imagine to exist at the notch root. The length of that imaginary crack a_0 is assumed to be a material constant and it represents the critical distance parameter. Fatigue failure is supposed to occur, in agreement with linear elastic fracture mechanics, when the imaginary crack reaches the stress intensity factor threshold, ΔK_{th}. Some researchers suggested that a physical crack exits at the notch root but such argument leads to theoretical incongruence, as that crack will be a short crack invalidating the use of linear elastic fracture mechanics [177]. Appling the imaginary crack method to a smooth

unnotched specimen and noticing that in this case the fatigue failure occurs at the fatigue limit $\Delta\sigma_e$, the value of crack length a_0 was obtained as follows:

$$a_0 = \frac{1}{\pi}\left(\frac{\Delta K_{th}}{\beta\Delta\sigma_e}\right)^2 = \frac{L}{\beta^2} \tag{2.38}$$

The final approach of the critical distance theory is the finite fracture mechanics method. In this energy-based method the failure conditions are derived using the crack propagation energy balance proposed by Griffith [15] but assuming a finite amount of crack extension. Fatigue failure will occur if there is sufficient elastic energy to allow a crack to growth of a finite amount Δa from the notch root [180]. The finite growth length Δa is assumed to be a material constant. The energetic balance can therefore be written as follows where the integral of the energy release rate G over the finite crack extension Δa is equal to the material resistance to the crack propagation, that is the critical energy release rate G_c by Δa:

$$\int_0^{\Delta a} G da = G_c \Delta a \tag{2.39}$$

Appling the finite fracture mechanics method to the case of a central trough crack in an infinite plate it was demonstrated that the finite crack extension Δa was equal to $2L$ [180]. All the methods forming the theory of the critical distance are related to the critical distance L that is assumed to be a material constant depending on the loading condition.

Taylor and Kasiri [181] compared the fatigue limit and static failure predictions of the four methods (point method, line method, imaginary crack method and finite fracture mechanics) forming the critical distance theory. For the particular case of a centre though-thickness crack into an infinite body the line, imaginary crack and finite fracture mechanics method predictions coincide while the point method one is slightly different in the short crack regime [181]. In case of notches the predictions of the four different approaches were very similar despite the notch geometry and size, falling always within an error band of ±10%. Only for finite components with the width comparable in size with the distance L large prediction differences emerged. That was ascribed to the use of the models beyond their application limits and a combined stress and energy method was suggested to overcome this problem [181]. The similarity of the four critical distance methods allowed them to be used interchangeably. Stress-based methods are generally preferred when finite element stress solution are available, while energy based approaches allow parametric studies being expressed in form of analytical equations.

An extensive validation campaign against a multitude of experimental data showed that critical distance methods were capable of accurate prediction of the fatigue limit of components weakened by blunt, sharp and small notches [182-184]. Critical distance theory also correctly characterised phenomena like notch size effect and non-damaging notches in uniaxial and multiaxial high cycle fatigue problems [184]. Although critical distance theory proved to be a powerful engineering tool suitable for predicting real component fatigue strength, its theoretical basis are not entirely understood yet. Taylor [185] tried to give a mechanistic justifications to the line method, linking this approach to mechanisms of crack growth at the notch root.

Susmel and Taylor [186,187] extended the critical distance theory to the medium-cycle fatigue regime. Critical distance methods could be thus used to predict the finite fatigue life of notched components. The theory was reformulated introducing the idea that the material characteristic critical distance L varied according to the component number of cycles to failure. That assumption was suggested by the fact that, in general the critical distance L assumes two different values if determined at the fatigue limit or for a static failure condition [187]. According to the S-N curve relation between stress and fatigue life the critical distance was assumed to be a power function of the cycles to failure. Such law, supposed to be a material properties, could be obtained for a particular material knowing the S-N curves of a plain specimen and of a notched one under a given loading condition [187]. Obviously the link between L and the fatigue number of cycles led to a recursive procedure to predict the component life in the medium-cycle fatigue regime. The suggested prediction method was validated against experimental results for different notch geometries under several load conditions [187]. Critical distance theory could be successfully extended to the medium-cycle fatigue regime predicting notched component fatigue lives within the scatter band of the parent material data [187]. Yamashita et al. [188,189] applied the critical distance theory to estimate the fatigue strength of titanium specimens weakened by small V-shaped notches in the finite life regime. A good correlation was found between the critical distance stress and the crack initiation life at the notch root. The calculated critical distance did not substantially vary over the whole range of fatigue lives from low- to high-cycle fatigue regime [189]. Critical distance theory accurately predicted the effect of the notch geometry on the fatigue strength of the titanium specimens.

2.3.2 Fracture mechanics assessment of notch fatigue strength

Traditional methods to predict the fatigue notch factor K_f are based on the assumption that the crack initiation at the stress raiser is the critical event defining the fatigue strength on notched components. In other words the stress required to nucleate a crack at the notch root is also sufficient to propagate it up to the component failure. Frost and Dugdale [190] showed that this is indeed the case of blunt notches with a stress concentration factor K_t smaller than 4. However for sharper notches, characterised by high stress concentrations and steep stress gradients, it is the possibility of crack propagation from the notch that determines the component fatigue limit. In fact, cracks can easily nucleate at the root of sharp notches, due to the local high stress, even for loads lower than the fatigue limit, but in this case they have not enough driving force to propagating beyond the local notch stress field and cause the component failure. The component fatigue limit is defined as the minimum load allowing the growth of cracks nucleated from the notch root. Sharp notches are thus characterised by the existence of non-propagating crack at the fatigue limit [190]. Non-propagating cracks were observed also at the fatigue limit of components weakened by relatively blunt notches, like circular notches, with small size as consequence of the notch size effect and in smooth unnotched specimens [192]. The occurrence of non-propagating cracks paved the way to the use of fracture mechanics models in the fatigue strength prediction of notched components as the fatigue limit turns out to be the threshold condition for crack growth at the notch root.

Smith and Miller [191] developed a fracture mechanics based model to predict the different fatigue regimes of a wide range of notched components as function of the applied nominal stress. According to the notch geometry and size, the safe (no-failure), the non-propagating crack and the failure stress zones could be determined by means of two simple equations [191]. The crack initiation and early propagation at the notch root were assumed to be promoted by the notch plasticity while the further crack growth in the bulk of the sample was the result of the self-developed crack tip plasticity. The initiation stress was thus defined by the plain fatigue limit divided by the fatigue notch factor ($\Delta\sigma_e/K_f$) and the stress condition for crack propagation at the notch root by the threshold stress intensity factor, ΔK_{th}. Using this two approximate relations the component fatigue regimes could be characterised as function of the notch geometry [191]. Moreover the maximum and minimum possible lengths of non-propagating cracks at the root of sharp notches were also calculated [192].

Some researchers applied short crack growth models to estimate the fatigue strength of notched components and to predict the occurrence of non-propagating crack at the notch root [193-195]. El Haddad et al. [193] proposed a strain based intensity factor, including the short crack growth correction parameter l_0, to model the development of cracks at notch roots. The strain intensity factor was initially observed to decrease to a minimum value, according to the crack length, and subsequently increase up to merge the trend of equivalent long cracks. If the strain intensity factor value dropped down to the material fatigue threshold, cracks stopped growing and non-propagating cracks were formed [193]. Notched component fatigue limit stress was assumed to be the maximum value of the fatigue threshold stresses of a crack at the notch root. For blunt notches such value was reached at the initiation, that is for a crack length of zero, while in case of sharp notches the threshold stress peak value shifted to a finite crack length [193]. Both fatigue limit and non-propagating crack length predictions were in good agreement with experimental results. Meggiolaro et al. [194,195] used a slightly different approach to predict the notch sensitivity factor in fatigue from the short crack propagation behaviour at the notch root. The conventional expression of the stress intensity factor range was maintained also for short cracks while an equation was proposed to model the dependence of the threshold stress intensity factor, ΔK_{th}, on the crack length [195]. The model prediction were in good agreement with experimental K_f data.

Vallellano et al. [196-198] extended the Navarro and de los Rios micromechanical model [63] to notched components assuming that the fatigue strength was defined by the capability of short cracks, nucleated at the notch root, to overcame material microstructural barriers, such as grain boundaries. The crack initiation stress and the conventional fatigue limit of notched component, defined as the limit stress of short crack propagation were calculated by the model. The length of non-propagating cracks was also predicted. The initiation stress was considered to be the minimum applied stress required to overcome the first microstructural barrier at the notch root while the propagation limit, that is the notched component fatigue strength, was the minimum applied stress which ensured that the crack propagated across all the barriers [196]. In other words the component fatigue strength was the maximum resistance of all the barriers encountered by the crack. Applied stresses between the initiation and the fatigue limit gave rise to non-propagating cracks. The only difference with respect to the case of smooth specimens in the model application is represented by the presence of the

notch stress field affecting the driving force available for crack propagation [197]. Assuming the stress purely elastic a closed form analytical solution was derived for the stress governing the crack growth in the particular case of an elliptical notch in an infinite plate under antiplane shear [196]. Appling the concept of stress distribution similarity around different notches analytical equations were generalised to any kind of notch geometries under normal stress [197]. The proposed model was validated against experimental results showing a good prediction accuracy. Notch size effect and non damaging defects were also investigated applying the model to stress raisers the size of the material microstructure, like scratches, corrosion pits, inclusion pores [198]. Defects smaller than the material characteristic microstructural length showed not to substantially affect the component fatigue limit.

A group of prediction methods assumed the development of fatigue crack closure at the notch root to be the main cause arresting the crack propagation, and thus generating non-propagating cracks, at the fatigue limit of notched component [199-202]. By modelling the increase of crack closure with the length of short cracks at the notch root, resistance-curve could be developed to predict fatigue limit and non-propagating crack length in notched components. A crack became non-propagating when its effective stress intensity factor ΔK_{eff}, that decreases as the crack propagates from the notch root, reached the threshold effective stress intensity factor $\Delta K_{eff\ th}$ [199-202]. Different analytical relations between the crack opening stress intensity factor and the crack length at the notch root were suggested by various researchers [199-202]. All of them were based on material properties and analytical coefficients to be experimentally determined. The effect of the notch geometry was included into the opening stress intensity factor definition. Abdel-Raouf et al. [201] in addition to the geometrical strain concentration produced by the notch considered also an inherent strain concentration, caused by the easy slip of grain at the notch surface, in the stress intensity factor definition. The fatigue limit and non-propagating crack length predictions of crack closure based models proved to agree well with the respective experimental data [199-202].

The experimental evidence that the fatigue limit of engineering materials containing defects, like inclusion and voids, is not the critical condition for crack nucleation but the threshold condition where fatigue cracks initiated from defects stop propagating, allows the use of fracture mechanics based methodologies to predict the effect of small notches and defects on component fatigue strength [203-209]. The non-propagating crack occurrence at the fatigue limit implies the existence of a critical size below which notches or defects do not affect the component fatigue strength, explaining the notch size effect in fatigue [203]. In fact Murakami and Endo [203] proved that notched components containing notches or defects smaller than the non-propagating crack size found in smooth specimens at the fatigue limit showed the same fatigue strength as unnotched samples. Artificially drilled holes from 40 μm to 200 μm in diameter were machined on the surface of carbon steel fatigue specimens. Fatigue testing results showed that the critical hole diameters which did not affect the sample fatigue limit corresponded to the non-propagating size observed on plain samples [203].

A quantitative model to evaluate the fatigue strength of components containing defects was developed on the basis of the concept that fatigue limit evaluation is

essentially a crack growth threshold problems [204,205]. The definition of a stress intensity factor for crack emanating from defects or small notches is complicated due to high variability and irregularity of their size, shape, and location. A unifying approximated general method was therefore suggested by Murakami and Endo [204]. The behaviour of non-propagating cracks nucleated from defects was assumed to be regulated by the maximum stress intensity factor along the crack front, K_{max}. The maximum value of the stress intensity factor was found to be related to the fourth root of the projected area of the defect onto the plain perpendicular to the maximum principal stress ($area^{1/4}$) [204]. Actually the equivalent area should include the projected defect area plus the area of the crack nucleated from the defect itself. However the crack area is generally neglected as it is a small fraction of the entire equivalent area [205]. Semi-empirical relations, where the defect geometry was introduced using the square root of their equivalent area, were developed to predict the fatigue limit of components weakened by generic defects [204]. When √area parameter was smaller than a critical value, considered a material constant experimentally determined, the defect was non-damaging and the component fatigue strength equated that of plain specimens. The formula characterising the fatigue limit of components containing small defects was subsequently generalised to several materials including the effect of the material hardness [205]. The proposed model accurately predicted experimental fatigue limit of components weakened by different small artificial defects [205].

Lukas et al. [206-208] proposed a different fracture mechanic approach to rationalise the notch size effect and the existence of non-damaging notches in fatigue where the notch geometric characteristic, expressed in term of stress concentration factor K_t and root radius ρ, were explicitly considered. The physical interpretation of the fatigue limit as critical condition for the short crack propagation in both smooth and notched components allowed the explanation of the presence of non-damaging notches. The notch root stress concentration generally produces an increase in the driving force of crack nucleated from notches in comparison to that of crack of the same length initiated at the surface of unnotched component. This increase depends on the ratio between the length of the region affected by the local notch stress and the crack size [207]. Therefore as the local stress field extension is regulated by the notch size, there will be a critical notch dimension, for a given crack length, below which the crack driving force will be the same for notched and unnotched components.

On the basis of the fatigue notch factor expression suggested by Lukas and Klesnil [206], approximate formulae for the stress intensity factor of semi-elliptical and through-thickness cracks emanating from notches were obtained [207,208]. Assuming the critical non-propagating crack length at the fatigue limit l_0 as a material constant, an equation describing the notch effect on the material fatigue limit was derived. The notched component fatigue strength was found to be a function of the notch geometry, expressed in term of stress concentration factor an root radius, and of the material fatigue properties included into the length scale parameter l_0 [207,208]. The non-propagating crack length, l_0, could be obtained experimentally from the Kitagawa-Takashi diagram. It was related to the material fatigue limit and to the long crack growth threshold [208]. The general condition for a notch to be non-damaging was also obtained as function of the notch geometry [207]. Since the model assumed the dependence of the notched component fatigue limit on the stress concentration factor, it

is generally valid for blunt notches with $K_t \leq 4$ [208]. The derived analytical relations for the prediction of notched component fatigue strength were successfully validated against experimental results [208,209].

2.3.3 Models of crack propagation from notches

The fatigue life assessment of notched components in finite life regime requires the development of analytical models to predict crack initiation and propagation from notches. Generally crack nucleation period is very short particularly in the case of sharp notches and it can be easily neglected. Crack propagation near the notch root can be modelled, inside the framework of linear elastic fracture mechanics, as soon as the stress intensity factor of crack propagating inside the local notch stress field is known. Several linear elastic stress intensity factor solutions for cracks emanating from notches have been derived using different methodologies [210-220]. However, because of their linear elastic nature these solutions can be correctly applied only in case of long cracks under small-scale yielding conditions limiting their use for large notches with elastic local stress fields. Different approaches are required to rationalise the effect of the notch root plastic zone on the propagation of short cracks at notches.

Smith and Miller [221] derived a linear elastic stress intensity factor solution for cracks at central and edge elliptical notches. Considering that cracks at the notch roots in unnotched components had the same stress intensity factor if they showed equal growth rate for a given applied stress, the contribution of the notch local stress field to the crack driving force was determined. The notch stress field was found to affect the crack growth up to a distance, l, from the notch root being a function of the notch geometry [221]. The approximate notch stress field extent was given as follows:

$$l = 0.13\sqrt{D\rho} \tag{2.40}$$

where D and ρ are respectively the notch depth and the root radius. The stress intensity factor range of a crack emanating from an elliptical notch was approximated by the following equation:

$$\begin{aligned} \Delta K &= \left(1 + 7.69\sqrt{\frac{D}{\rho}}\right)^{\frac{1}{2}} \Delta\sigma\sqrt{\pi a} \quad if \quad a < l \\ \Delta K &= \left(1 + \frac{D}{a}\right)^{\frac{1}{2}} \Delta\sigma\sqrt{\pi a} \quad if \quad a \geq l \end{aligned} \tag{2.41}$$

Two different driving force expressions were derived whether or the crack was inside (short crack) or outside (long crack) the notch stress field [221]. For the latter case the stress intensity factor was obtained added the notch depth D to the crack length a. Crack propagation lives calculated integrating eq. (2.41) were in good correlation with experimental data [221]. Despite its linear elastic nature Smith and Miller solution proved to be able to predict short crack behaviour conservatively estimating short crack stress intensity factors [222].

Some total fatigue life and short crack growth prediction models for notched components were empirically developed on the basis of experimental data [224,225].

For instance McClung et al. [224] suggested a novel approach to assess notched component fatigue life summing crack initiation and propagation cycles. Nucleation curves to a designed small crack size were obtained by subtracting from the total life S-N curve of smooth samples the crack propagation life calculated including the short crack correction [224]. These nucleation curves were used to predict the life to initiate a crack of the designed initial length at the root of notches. The stress considered to determine the notched component initiation life was the elastic-plastic maximum principal stress achieved at a distance from the notch root equal to the crack nucleation length. Crack propagation live was then calculated integrating the relation between the growth rates and the linear elastic stress intensity factor solutions which included short crack length correction [224]. Despite its empirical nature the suggested approach proved to successfully predict fatigue life of notched components.

At stress levels producing local notch plasticity, short crack early growth takes place inside the notch plastic zone, requiring elastic-plastic solutions for its assessment. Several researchers applied linear elastic fracture mechanics concepts to predict short crack propagation from notches [46,47,226,230]. El Haddad et al. [226] used the cyclic *J*-integral to describe short crack propagation into the local plastic strain field generated by notches. The ΔJ elastic-plastic solution was modified to account for short crack behaviour introducing the effective crack length a_0 [55]. The cyclic stress and strain acting on the crack tip in the notch root region, needed to calculate the cyclic *J*-integral, were approximately derived using Neuber rule [226]. Such procedure was in agreement with notch stress fields calculated by finite element analyses. Growth rate for short cracks propagating from notches were successfully correlated with long crack data using the suggested modified *J*-integral solution [226]. Sehitoglu [227] developed a fatigue life prediction method for notched components using local strain approach and elastic-plastic fracture mechanics concepts. The cyclic *J*-integral was used to define the crack initiation length required to calculate the initiation life with the local strain approach. Short crack growth was assumed to occur inside the local notch stress field whose size defined the initial crack length [227]. Crack propagation life was obtained integrating the relation between the growth rate and ΔJ from initial to final crack length [227]. Total fatigue life predictions using the suggested method were found more accurate than those of traditional methodologies. Foth et al. [46,47] used the cyclic *J*-integral to assess short crack growth from semicircular notches in 2024-T3 aluminium alloy specimens.

Some prediction models assumed the interaction between notch plastic zone and short cracks to be the main cause of the anomalous short crack growth at the notch root [228,230]. Ahmad et al. [228] extended the Hobson short crack growth model [121] to notched components taking into account the effect of the notch root plastic zone on crack propagation. Short crack growth was considered to occur only inside the cyclic notch plastic zone. The Hobson's short crack growth equation [121] was modified substituting the microstructural barrier spacing, d, with the notch plastic zone size, Δ_n and adding the notch contribution to the crack length proposed by Smith and Miller [221]. Short crack growth rate was also an exponential function of the strain amplitude ahead of the notch [228]. A different growth rate equation was suggested for long cracks according to the Hobson's model. The proportional constants, characterising both propagation equations were experimentally determined using unnotched specimens. The

suggested model was validated against experimental data of different notched samples, showing a good accuracy [228]. Hammouda et al. [229] assumed crack initiation and propagation from notches to be regulated by the extent of the total plastic shear deformation at the crack tip. When the short crack was embedded into the notch cyclic plastic zone, the plastic shear deformation consisted of two terms, one due to the notch plasticity and the other produced by the crack tip plasticity [229]. Crack nucleation and propagation were assumed to take place when the total plastic shear deformation at the crack tip reached a critical threshold value. Crack propagation was modelled to be regulated by the difference between the available plastic shear deformation and its threshold value [229]. As long as the short crack growth from the notch the total plastic shear deformation available for propagation decreased producing eventual non propagating cracks. In a more recent paper Hammouda et al. [230] demonstrated using elastic-plastic finite element analysed that both monotonic and cyclic crack tip plastic zones showed a transition behaviour from the short crack regime affected by the local notch stress field to long crack one. A parameter that combined the extents of monotonic and cyclic crack tip plasticity, called crack tip deformation parameter, was therefore developed [230]. It was able to correlate the growth behaviour of physically short crack propagating at the root of notches

Several authors ascribed the anomalous growth behaviour of short cracks at the root of notches to the development of crack closure. Numerous short crack growth models based on the effective stress intensity factor range ΔK_{eff} were developed for notched components [48-52,231], as already described in section 2.2.4.3. Verreman et al. [231] showed that the effective stress intensity factor range ΔK_{eff} was able to correlated short crack growth rates at the toe of fillet welded joints to those of long cracks. The crack closure amount increased when the cracks grew inside the cyclic notch plastic zone to become stable for crack longer than the notch plastic zone [231]. Notch root cyclic plastic zone seemed to regulated plastic induced closure level and consequently the short crack growth behaviour. Crack closure models based on the linear elastic calculation of ΔK_{eff} can be correctly applied to notched components in case of small-scale yielding conditions. For notches showing large plastic zones, elastic plastic corrections must be introduced to define the effective stress intensity factor range [54].

Shin and Smith [232,233], analysing different methods to predict short crack growth at notches proved that elastic plastic fracture mechanics parameters, like total shear deformation, modified strain based intensity factor, cyclic *J*-integral, together with the crack closure based effective stress intensity factor were not able to correlate short and long crack growth data. Crack closure and elastic-plastic fracture mechanics seemed unable to rationalise alone the short crack propagation from notches. Inside the notch plastic zone, both the development of plasticity-induced closure and the notch plasticity affected the short crack growth, while outside the notch plastic region crack tip plasticity dominated crack propagation and ΔK_{eff} alone was able to correlate the crack growth rates [233]. Some researches, thus proposed prediction methods that combined both crack closure and plasticity concepts [234-236]. On the basis of the assumption that short crack growth inside the notch monotonic plastic zone occurred under displacement control Leis [234] defined a pseudo plastic stress intensity factor. Such parameter was nothing more than a strain intensity factor where the strain range acting on the crack tip was introduced [234]. The local stress ratio *R* variation caused by

residual stress and the plasticity-induced crack closure were also estimated as a function of the crack length. Conventional material Paris curves were used to relate crack growth rate to the pseudo plastic stress intensity factor range. The model reasonably predicted the short crack growth behaviour at the root of notches [234]. Palazotto and Mercer [235] numerically modelled the crack propagation at the notch root by means of elastic-plastic finite element analyses. A node release criterion was applied were the crack was extended one element in length at every loading cycle. The effect of the notch plastic zone on crack closure were evaluated calculation the crack opening stress [235]. The tip plastic zone of short crack was found to be 35% larger than that of long crack because of the notch stress raising effect. Such phenomenon accelerated the crack closure development in comparison with unnotched components. Chien and Coffin [236] developed a plasticity-induced crack closure model for short crack growth prediction in the vicinity of notches. A strain based effective pseudo-stress intensity fact was defined including the plastic zone correction suggested by Newman [116]. An analytical expression was proposed to describe the crack closure development according to the crack length [236]. The model was successfully validated against experimental short crack growth rate measured in 2024-T3 aluminium alloy and steel notched specimens.

2.4 Fatigue of scribe marks and scratches

Mechanical damages, like scratches, are commonly detected on components and structure surfaces. According to traditional fatigue life prediction methods based on notch sensitivity factor (see section 2.3.1), surface damages, such as scratches, were generally considered too shallow to appreciably affect the fatigue strength of mechanical components. Many materials were thus regarded as insensitive to mechanical notches the size of scratches commonly detected on components surfaces [11,137]. More recently, however experimental evidences showed that the presence of scratches had significant impact on fatigue life of components [237].

Nader [237] rationalised how scratches affected the fatigue performances of 2024-T3 clad aluminium alloy. Dog-bone unnotched and double-edge notched samples were mechanically scratched and fatigue tested under constant amplitude loads with a stress ratio of R=0.1 and a frequency of 10 Hz to obtain S-N curves for different scratch depths [237]. A special device was developed to machine by end mills rounded V-shaped scratches with a constant included angle of 90° on the specimen surfaces. Scratches, ranging from 40 μm to 225 μm in depth and with a fixed root radius, were machined with on a single sample surface across the whole gauge length. Scratches had their depths measured under optical microscope [237]. Unscratched notched and unnotched samples were also fatigue tested to obtain the S-N curves of the analysed material batch. The effect of changing stress ratio, load frequency, scratch length and position was also investigated. Rectangular specimens were used to measure fatigue crack growth rates. Crack propagation was measured along the scratch length direction. Propagation tests were performed on unscratched and scratched samples under constant amplitude loading with R=0.1 at four different maximum stress levels. Crack growth curves were drawn for scratches ranging from 40 μm to 150 μm in depth, calculating the linear elastic stress intensity factor as it was the one of an edge crack in an unscratched sample [237].

The 2024-T3 clad aluminium alloy proved to be a scratch sensitive material in regard to fatigue life and to fatigue crack propagation. For instance, 100 μm deep scratches reduced the total fatigue life as much as 98% for unnotched and 87% for notched specimens tested at R=0.1 and a maximum stress of 345 MPa [237]. As the scratch depth increased, the fatigue life at a given stress amplitude decreased for all the tested samples. The effect of increasing the scratch depth was to shift down the S-N curve of notched and unnotched specimens [237]. Scratches inside the clad layer, that is shallower than 50 μm, had a detrimental effect on the fatigue life analogous to that observed for scratches with their root embedded into the substrate. Cracks grew in scratched samples at higher growth rates than in unscratched specimens. Scratches generated short cracks that propagated faster and at lower stress intensity factor than long cracks. For a given nominal stress intensity factor range, the deeper the scratch the higher the crack growth rate [237]. Scratching just a portion of the crack growth sample gauge lengths resulted in a slower crack growth for short cracks compared to samples scratched all across their width.

Fractographic analyses showed that scratches initiated micro cracks smaller than the material grain size (30 μm) at their roots. Such micro cracks coalesced together to form a main crack able to propagate along the scratch until sample failure. The small crack formation and coalescence were responsible for the fatigue life reduction and for the faster growth rates of scratched samples [237]. The deeper the scratch the larger the number and the faster the nucleation of micro cracks.

A semi-empirical model to predict crack propagation along the scratch root in 2024-T3 clad aluminium alloy was also developed [237,238]. Two different equations based on stress intensity factor were suggested for long and short cracks growing at the scratch root. The Paris law obtained for unscratched material was assumed to be valid also in case of scratched samples. The following stress intensity factor expression was developed for long cracks growing at the scratch root:

$$\Delta K_{eff} = \beta K_t \Delta\sigma\sqrt{\pi a} \tag{2.42}$$

According to eq. (2.42), the scratch was assumed to behave as a notch, increasing the local stress range and thus the crack driving force by means of its elastic stress concentration factor, K_t [238]. However the K_t values for different scratch depths were not directly calculated using numerical or analytical models, but they were indirectly derived using the notch sensitivity factor expression suggested by Peterson (eq. (2.28)). The fatigue-notch factors value, K_f, to introduced into the Peterson's equation were empirically obtained from scratched material S-N curves [238]. A method based on the coalescence of micro cracks was developed to predict short crack growth at the root of scribes.

The Mazumdar's stress-life model [238] was applied to derive the local stress acting on propagating short cracks as a function of the density of micro cracks at the scratch root. Such stress was assumed to be the one required to initiate the micro crack population specific of a particular scratch. In fact any scratch geometry was characterised by a spacing ratio parameter, s/s_f, describing the density of micro cracks existing when a main short crack was formed [238]. The values of this parameter for different scratch depth, d, were empirically obtained by best fitting of total fatigue life

data in high cycle regime. Finally substituting the obtained local stress into eq. (2.42) short crack stress intensity factor was obtained as follows:

$$\Delta K_{scratch} = \beta K_t \left[\left(\sqrt{\frac{D}{d} \frac{s/s_f}{N_i} + 1} \right) \sigma_e (1-R) \right] \sqrt{\pi a} \tag{2.43}$$

where D is the material grain size, N_i is the number of cycles to crack initiation at the local stress, and σ_e and R are respectively the fatigue endurance limit of scratched samples and the stress ratio [238]. The developed analytical method was able to accurately characterise the short and long crack propagation in scratched samples but S-N curves of scratched materials were required to empirically derive some parameters [238].

Talia and Talia [239] investigated the effect of scratches on fatigue crack growth of 2024-T3 bare aluminium alloy. Crack propagation specimens were tested under constant amplitude loading at a stress ratio of R=0.1. Tests were performed following the procedure described by Nader [237]. Scratches were machined on the sample surface along the whole gauge length, according to the methods reported in ref. [237]. Scratches with a constant included angle of 90° and a fixed root radius were machined with three different depths (20 μm , 50 μm and 100 μm).

Crack growth rates increased as the scratch depth increases [239]. Fractographic observations revealed that micro cracks initiate from irregularities at the root of scratches. Such micro cracks growing inside the material seemed to facilitate crack propagation in scratched samples [239]. Fatigue cracks initially grew in Mode I, creating a fracture surface perpendicular to the loading direction, to then show a shear fracture mode, developing shear lips at high growth rates. The transition crack length from tensile to shear fracture mode depended on the scratch depth and the applied stress. It increased according to the scratch depth and decreased as the applied stress was increased [239]. Considering the shear lips development as a factor regulating the amount of crack closure, an analytical expression for the stress intensity factor of cracks growing at scratch root was developed. An empirical correction factor, based on the relation between transition crack length and scratch depth, was introduced into the ΔK definition [239]. The suggested model was capable of correctly predicting the crack growth rates in samples containing scratches up to 100 μm deep.

Inchekel and Talia [240] investigated the effect of surface scratches on the fatigue behaviour of 2090 F aluminium-lithium alloy. Introducing a scratch on sample surface significantly reduced the fatigue file of unnotched and notched 2090 F aluminium-lithium alloy specimens [240]. For a given applied stress fatigue live of scratched samples decreased with the increase of the scratch depth and with the decrease of the scratch root radius. Scratches of limited length seemed to be more detrimental if they were machined close to the sample edge than in the centre of the gauge section. Fractographic examinations revealed that several small cracks nucleated along the scratch root. Specimen failure seemed to be caused by the coalescence of those small cracks [240].

Everett et al. [241] performed a fatigue test campaign to assess the influence of machine-like scratches on the fatigue life of 4340 steel. Constant amplitude fully reverse (R=-1) fatigue tests were carried out on unscratched and scratched dogbone samples. 50 μm deep rounded V-shaped scratches were machined on the gauge section along the entire specimen width using an end mill [241]. Some specimens were shot peened after been scratched to verify if the compressive residual stresses produced by the shot peening would cancel the scratch detrimental effect on fatigue life [241]. Machine-like scratches were found to reduce the 4340 steel fatigue limit by 40%. A fatigue life prediction model based on small-crack theory [177,118] was suggested for scratched specimens. The model assumed the component fatigue life to be composed only by crack propagation from a small initial crack size to failure. The closure based, crack propagation computer code FASTRAN was used to calculate crack growth life from in scratched specimens [241]. Modelling the scratches as initial single-edge cracks under tensile loading, accurate fatigue life prediction were obtained by means of the small-crack theory [241].

A problem analogous to the fatigue crack development from scribe marks is the effect of surface roughness on fatigue strength of mechanical components. In fact the surfaces of machined components appear as a series of irregular micromechanical grooves similar in shape to scribe marks [243]. Such grooves, from few microns to few tens of microns deep according to the surface quality, act as stress concentrators promoting the nucleation and propagation of fatigue cracks [242,243]. Traditionally the effect of surface roughness on component fatigue strength was commonly accounted for using empirical reduction factors which modified the material fatigue limit [3]. More recently it has been widely diffused the tendency to rationalise the surface roughness effect on fatigue of materials in term of crack development from geometrical irregularities [242,243]. Fatigue and fracture mechanic approaches commonly used for predicting crack nucleation and propagation from notches have been applied to small stress concentrators few microns in size.

Such [242] investigated the influence of surface finish on fatigue limit of a low alloy steel. Samples with different surface finish were fatigued under tensile and four point bending loads [242]. A series of 50 μm deep V-shaped grooves with an included angle of 90°, similar to sharp scratches, were also machined on the surface of some fatigue samples perpendicularly to the applied stress direction. Fatigue cracks were found to initiate from the largest surface irregularities introduced by the finishing process, like surface scratches or from material inherent defects, such as inclusions or pores. Those large surface irregularities were not usually detected by conventional surface roughness scanning methods [242]. An increase in surface roughness produced a decrease in fatigue limit for both tensile and bending samples. Surface grooves, 50 μm deep, were able to reduce the fatigue limit of a fine ground surface by 50%. Regarding surface irregularities, grooves and defects as equivalent cracks the fatigue limit of samples with different surface finishes could be material accurately predicted using the material Kitagawa-Takashi diagram [242].

Suraratchai et al. [243] modelled the effect of machined surface roughness on the fatigue life of 7010 aluminium alloy, developing a fracture mechanics based model. The surface grooves, generated by the finishing process, were considered as small notches

giving rise to a local stress concentration that regulated propagation or non-propagation of surface cracks. The elastic stress concentration factor K_t, characteristic of a specific surface roughness, was calculated from finite element model of the measured surface topography [243]. As the effect of surface roughness varied according to the fatigue life regime two different approaches were proposed for predicting fatigue limit or the finite life of components. For predicting the fatigue limit, the numerically calculated stress concentration factor was included into the stress intensity factor definition of an initial crack nucleated at the bottom of a machining groove [243]. The initial crack length did not depend on the surface conditions and it was assumed to be the size of the re-crystallised grains in the material (40 μm). According to the linear elastic fracture mechanics the component fatigue limit was defined as the maximum stress range ensuring the long crack growth threshold condition [243]. For finite fatigue life prediction crack initiation and propagation lives were distinguished. Initiation life was evaluated introducing the calculated K_t into a Basquin type power law, while crack propagation cycles were obtained integrating the material Paris law [243]. Growing cracks were assumed to be semi-elliptical with the surface finish stress concentration affecting only the surface propagation. The suggested model was validated against experimental data of specimens with various surface roughness showing good fatigue live prediction capabilities.

Studying the effect of grain size on the stage I crack growth, Radhakrishnan and Mutoh [244] measured the propagation rate of cracks starting from small pre-existing notches in low carbon steel. Those notches were small rounded V-shaped edge notches, 1 mm deep with a root radius of 0.1-0.2 mm. The effect of the notch included angle on short crack growth at the notch root was examined [244]. Crack growth rates were experimentally measured and plotted against the nominal stress intensity factors calculated according to the expression suggested by Cameron and Smith [192]. In case of sharp notches with a smaller included angle crack grew shower at the notch root than for blunt notches. At the limit case of rounded tip crack, that is for an included angle of 0°, crack growth rate was zero until the stress intensity factor was higher that the crack growth threshold [192]. However when cracks become longer and they started propagating in a Stage II all the propagation curves tended to merge despite the different notch opened angle.

Zhang et al. [42] performed in situ scanning electron microscope observations of short crack growth in the 2024-T351 aluminium alloy. Rectangular samples were fatigued in vacuum directly inside the scanning electron microscope chamber and the short crack growth along the material long transversal direction was observed. The cracks initiator was a 70 μm deep rounded V-shaped notch [42]. Therefore analysing the early stage of crack propagation the effect of the stress field of a small V-notch the size of the material microstructure could be evaluated. As the crack pit approached a grain boundary new slip bands were initiated in the adjacent grain [42]. When the crack was short just a shear band was initiated in the next grain and the crack propagate across grain in a crystallographic stage I growth. Only when the crack had propagated several time the average grain size that two distinct shear bands developed at its tip. However cracks were observed to grow along a single shear band, that is in crystallographic stage I even when two shear bands were formed at the crack tip [42]. Such observation suggested that the crack propagation mechanism was shear band cohesion even for

cracks long enough to developing double slip systems at their tips, that is in the stage II growth regime.

Mezlini et al. [245] performed repeated scratch tests, to investigate the abrasive wear resistance of 5000 series aluminium alloys. Two different indenter were used for that investigation: a spherical sapphire pin one with a radius of 1.5 mm and conical indenter with an hemispherical tip diamond having an included angle of 60° and a root radius of 10 μm. Scratches were produced on sample surfaces by 1, 2, 5 and 10 repetitive passes of the indenter. Generated scratch geometry was measured using a tactile profilemeter [245]. Scratches were mainly produced by plastic deformations and material plunging as no material cutting was related to the kind of the used indenters. Increasing the number of sliding passes enhanced the scratch cross section for both hemispherical and conical indenters. However the number of sliding passes seemed not to affect the scratch depth that remained nearly constant [245]. Material pile up was observed at the scratch flanks. Scratch cross section was bigger for the conical intender, where shear-tongue formation was observed, than in case of the hemispherical one [245].

Foreign object impacts in aero-engine compressor blades result in damages generally localised at the leading edge with the shape of a V-notch [246]. Such foreign object damages significantly reduce the fatigue strength of blades generating fatigue cracks that growing under operating loads can lead to premature failure [246]. Therefore a problem of crack nucleation and propagation at the root of small rounded V-shaped notches, analogous to that of crack development from scribe marks has to be studied to assess the fatigue performances of foreign object damaged compressor blades [247]. Oakley and Nowell [247] developed an elastic short crack arrest approach to predict residual fatigue life of compressor blades after foreign object damage. Linear elastic stress intensity factor of cracks growing from foreign object damages modelled as rounded V-shaped notches were calculated using the dislocation density method [247]. The conditions for the propagation or non-propagation of cracks at the notch roots were evaluated by means of the material Kitagawa-Takashi diagram. The prediction methodology was extended to the case of combined cycle loading, considering that the blades during their operating life experience a combination of centrifugal loading and aerodynamic induced vibrations. The former was responsible for low cycle fatigue while the latter, characterised by cycles of small amplitude, gave rise to high cycle fatigue [247]. The influence of residual stresses caused by the impact was also included into the model. The analytical predictions were compared to experimental results showing a satisfactory agreement.

The discovery of scribe mark problem on fuselages of commercial aircraft (see chapter 1), kindled new interest in investigating the influence of mechanically induced scratches on component fatigue lives and the development of fatigue cracks from mechanical detects. Investigations into the effect of machined scratches on the fatigue life of different aluminium alloys used for aircraft structures were performed at Cranfield University.

Kyle [248] analysed the influence of mechanically introduced scratches on the fatigue properties of clad 7075-T6 aluminium alloy. The physical processes of fatigue cracks generation and propagation from the scratch root were also investigated.

Scratches, with nominal depths of 50 μm, 100 μm and 150 μm, were machined along the whole gauge section of dogbone fatigue samples using a milling machine with a suitably designed high speed steel tool [248]. Scratches were introduced on the sample surface by means of two scratching methods: material cutting and material plunging. Machined scribes resulted in V-Shaped notches with an included angle of 105° and a root radius of nearly 50 μm. Samples were fatigued under tensile constant amplitude load at a stress ratio of R=0.1 and a frequency of 10 Hz. The peak stress used throughout the testing was 175 MPa. Scratches with their roots inside the clad layer reduced the fatigue life by 40% compared to that of unscratched samples. Machined scratches with the roots inside the material substrate were found to reduce the sample fatigue life only if they were deeper than 190 μm [248]. In fact for scratches comparable in depth with the clad layer thickness, failure occurred away from the scratch [248]. Samples failed from the scratch root showed a slight dependency between the fatigue life and the scratch depth. The deeper the scratch the shorter the fatigue life. Despite the different amount of material piling-up characterising the two type of scratches, no substantial variation of fatigue life were observed between cut and plunged scratches [248]. Fractographic analyses showed multiple crack initiation sites along the scratch root for samples failed from the scratch. Nanoindentation measurements revealed that scratch machining produced an increase of the material hardness around the scratch in the cladding but not in the substrate [248]. Fatigue crack development seemed to be dominated by initiation for scratches terminating in the material substrate and by crack propagation for those embedded in the clad layer.

Irving et al. [249] investigated the effect of machined scratched on the fatigue life of clad 2024-T351 aluminium alloy. Dogbone 2 mm thick samples, were scribed at the gauge section using both high speed steel and diamond tipped tools. The machining process produced a single V-shaped scratch between 30 μm and 200 μm deep, across the sample width, transverse to the applied stress direction. Scribed samples were subjected to constant amplitude tensile fatigue loading with a maximum stress of 200 MPa at a stress ratio R=0.1. After testing the samples were sectioned to measure the effective scratch depth and root radius and fracture surfaces were microscopically examined [249]. Scribes made using the high speed steel tool had a root radius of 50 μm while those made using the diamond tipped tool had a root radius of 4 μm. Diamond tool scratches showed a very regular and well defined V-shaped cross section [249]. Many of the tested scribed samples failed from locations at their edges remote from the scribe. Among the samples scribed by high speed steel tool only three of them having a scratches deeper than 115 μm failed from the scribe. Two out of four samples scribed by the diamond tool failed from the scratch root. The scribes had depths of 55 μm and 87 μm. It was found that necessary but not sufficient condition for a scratch to initiate a fatigue crack at its was to have an elastic stress concentration factor K_t>4. Samples which failed from the scratches showed a 35% of fatigue life reduction in comparison with those failed away from the scribe. Linear elastic fracture mechanics modelling of fatigue crack propagation predicted that significant fatigue life reductions were produced by crack development along large length of the scribe root [249]. Therefore scratches promoting multiple crack nucleation sites at their root were generally responsible for substantial fatigue life reductions.

Morency [250] investigated how cladding and defect depth affected the development of fatigue cracks from surface scratches in 2024-T351 aluminium alloy sheets. Scratches were machined on clad and unclad fatigue sample surfaces using a diamond tipped tool. The scribing procedure produced rounded V-shaped notches along the sample gauge section with an included angle of 60° and a root radius of 5 μm. Clad and unclad dogbone samples containing 50 μm, 100 μm and 200 μm deep scribes were fatigued under constant amplitude tensile loading with a maximum stress of 200 MPa at a stress ratio R=0.1 [250]. The sample clad layer was found to be 80 μm deep. Only scratches deeper than 200 μm were able to nucleate cracks that caused failure in unclad samples. Unclad samples scribed with shallower scratches failed from locations remote from the scribe. Scratches with their roots into the cladding or deeply embedded into the substrate developed cracks leading to sample failure. 100 μm deep scribes, that terminated near the clad layer/substrate interface, did not affect the fatigue life of clad samples [250]. Scratches were found to negatively affect the fatigue life of both clad and unclad specimens up to 80% of reduction in case of 200 μm deep scribed clad samples. Fractographic investigations showed the presence of cracks at the scribe root also for samples where the failure occurred away from the scratch. Both single and multiple crack nucleation sites were observed at the scratch root. Cracks propagated therefore at the scribe root with a thumbnail shape or as flow elongated along the whole length of the scratch [250]. Prediction methods based on linear elastic fracture mechanics were applied to estimate the fatigue life of scribed samples. Such methods were not capable of accurately predicting the fatigue behaviour of scratched samples [250].

Walmsley [251] analysed the nature of real scratches that can be produced by sealant removal from fuselage joint during maintenance operations. The capability of different scraping tools, including recommended plastic scrapers, Stanley knife blades and sharpened 2024-T351 and 7075-T6 aluminium strips, in scribing the surface of clad 2024-T351 aluminium alloy sheets was evaluated. Scratches of different nominal depths were created both manually or using a milling machine [251]. In case of milling machined scratches the normal force applied to the tool during the scribing process was recorded by a suitably designed load cell. Normal forces between 5 N and 25 N, representative of the force that a maintenance technician could exert during sealant removal, were applied to generate the scratches. Fatigue tests were performed to assess the capability of the differently produced scratches in initiating fatigue cracks. Scratched samples were fatigued under constant amplitude tensile loading with a maximum stress of 200 MPa at a stress ratio R=0.1. The plastic sealant scrapers were not able to damage clad 2024-T351. Sheet aluminium scrapers were capable of generating irregular scratches that initiated fatigue cracks. However only for scratching force of 25 N such scratches penetrated into the material substrate and generated cracks [251]. In case of lower scratching forces aluminium scrapers only damaged the cladding producing a blunt scratch which terminated at the clad boundary. Stanley knife blade generated sharp V-shaped scratches able to penetrate into the material substrate also at normal forces as low as 5 N. Such scratches initiated fatigue cracks. Scribes with an elastic K_t<5.5 seemed to have low probability to initiate fatigue cracks [251].

Khan [252] investigated the residual stress field around machined scribes of different geometry in 2024-T351 aluminium alloy and the effect of fatigue loading on those

residual stresses. Rounded V-shaped scribes with different depths and root radii were machined on samples and had their residual stress fields measured by synchrotron X-ray diffraction and nanoindentation technique. Two different diamond tipped tools, producing respectively ploughed and cut scratches, were used to scribe samples. Ploughed scribes were characterised by higher level of plastic deformation, pointed out by the material piling up at the scratch flanks [252]. They also showed a severe tensile residual stress field and work hardening around their roots in comparison with cut scribes. The magnitude and the extent of residual stress field of ploughed scratches were twice those of cut scribes. An increase of root radius from 5 μm to 50 μm produced a vanishing of the residual stress field and of the material work hardening for both ploughed and cut scratches [252]. Constant amplitude fatigue tests were performed on scribed samples to investigate the effect of fatigue loading on relaxation of pre-existing residual stresses. Fatigue tests were carried out under tensile and 4 point bending loading with a maximum stress of 200 MPa at a stress ratio R=0.1. Fatigue loading were found to leave residual stresses nearly unaltered for any tested scribe [252].

Jozelich [253] studied the geometrical characteristics of real world scratches produced using tools commonly available within the aircraft maintenance environment. Such scratches, contrary to the well defined V-shaped scribes machined by diamond tipped tools, have an irregular geometry that cannot totally be defined by the notch depth, the root radius and the included angle. Scratches were produced by hand on the surface of clad 2024-T351 aluminium alloy sheet samples using manufactured tools from 7075-T6 aluminium alloy, Perspex plastic as well as Stanley knife blade [253]. The linear elastic stress fields around the produced scratches were calculated by finite element analyses after the scratch section profiles were measured. Scribed samples were also fatigue tested under constant amplitude tensile loading at a maximum stress of 200 MPa and R=0.1. The linear elastic stress concentration and stress profile ahead of a real world scratch was found to be mainly determined by the geometry of local pits and undulations rather than by global geometrical parameters [253]. For that reason the idealisation of the generic real world scratch profile as an equivalent U or V-shaped notch provided a good approximation of the local root stress field with an error of 8.5%. All the generated scratches showed sign of large plastic deformation associated to material ploughing [253]. Scratch shape measurements and fatigue tests confirmed the results obtained by Walmsley [251].

Tizard [254] examined the plasticity and residual stress fields associated to real world scribes investigating their contribution to fatigue life of scribed structures. Diamond tool machined and real world scribes were produced on 2024-T531 aluminium alloy sheet samples which were fatigue tested. Nanoindentation was performed ahead of the scribe root to assess the amount of plasticity and the residual stress field around diamond tool and real world scribes. Real world scribes showed an increased level of material hardness around their profiles caused by the ploughing nature of the scribing process. The hardness magnitude seemed to be independent of the scribe depth. The increase in material hardness was not observed for diamond tool scribes [254]. Compressive residual stresses, close to the material yield strength in magnitude, were measured at the root of real world scribes. Those residual stresses appeared to be independent of the scribe depth. The increase in material hardness and the compressive residual stress slowing crack initiation and propagation could be responsible for the

improved fatigue performances of real world scribed structures [254]. A stress concentration factor threshold of K_t=6 seemed to exist below which real world scribes did not affect the sample fatigue life.

Das et al. [255] developed a method for damage tolerance analysis of 2024-T3 longitudinal and circumferential fuselage joints containing scribe marks. The accurate stress at the scribe locations was evaluated by non linear geometric finite element analyses of longitudinal and circumferential fuselage joints. The sealant between joint outer and inner skins was also modelled as it was found to affect the stress at the scribe location transferring part of the loading [255]. Sealant stiffness was determined by strain gauge measurements on a fuselage high-blow test. The stress concentration of scribes was characterised deriving a quality parameter from service data of several airplanes [255]. Inspection threshold was defined using a widespread fatigue damage analysis with 98% of reliability and a confidence level of 95%. In fact cracks were observed to initiate at multiple site along the scribe root and coalesce during the early stage of their through skin propagation [255]. Repeat inspection intervals were calculated using a linear elastic based crack propagation analysis. A stress intensity factor based on a constant geometric modification factor for cracks growing from the scribe root though the panel skin was developed on the basis of striation counting data [255]. Stress intensity factor solutions for cracks which became through thickness flaw were also empirically determined on crack growth data. The suggested method was validated against service data of aircraft fleets. However its inaccurate description do not allow any generalisation of the methodology to different scribed structures.

Appendix 2.1: A short history of fatigue research

The first study of metal fatigue is attributed to a German mining engineer, Albert [4]. He performed, around 1829, repeated load proof tests on iron mine-hoist chain subjected to bending load. Interest on fatigue began to increase with the widespread use of ferrous structures in bridges and railway systems in the nineteenth century. Detailed researches were driven by railways failures and accidents like a famous railway disaster near Versailles which resulted in fatalities in 1842. The cause of that accident was fatigue failure of a locomotive axle. Rankine, a British railway engineer in 1843 recognised the distinctive features of fatigue fracture and understood the effect of stress concentrations in mechanical design [3]. The first systematic investigation of fatigue failure is attributed to Wöler in 1860 [5]. He observed that strength of steel, commonly used in railway axles, under cyclic loads was lower that its static strength. Wöler tested several load condition (axial, torsion and bending loading) and his rotating bending machine was conceptually the same as those used today. Wöler created the characterisation of fatigue behaviour in term of stress amplitude-fatigue life (S-N) curves and the concept of endurance limit [5]. In 1874 Geber developed methods for predicting the mean stress level effect of fatigue life while Baushinger [6] in 1886 identified the occurrence of cyclic strain softening and hardening. The interpretation of fatigue failure development is attributed to Edwing and Humfrey [7] who in 1903 showed that slip bands were responsible for fatigue cracking. Slip bands intersecting the material surface generate extrusion and inclusions that yield to fatigue propagating cracks. In 1910 Basquin demonstrated in a bilogaritmic scale the linear relation between stress amplitude and number of cycles [8]. Coffin and Manson discovered in 1954 the relation between plastic strains and fatigue damage [9,10]. It is worth mentioning among other fatigue researches in the first half of twentieth century the work of Neuber (1946) about notch effect on cyclic deformation [11].

Although fatigue damage process was documented, the mathematical framework for quantitative modelling was still missing. The situation changed with the advent of linear elastic fracture mechanics. Test books on fracture mechanics can be found in literature [12-14]. The pioneering work of Griffith in 1920 provided the first quantitative treatment of fracture in brittle solids [15]. He applied the stress analysis of Inglis [16] for an elliptical hole to unstable crack propagation. Using the first law of thermodynamics formulated a fracture criterion based on energy balance. However those ideas could not directly be applied to metallic material failure characterisation. Progress is that direction came after the second world war from the fracture mechanics research group at the US naval research laboratory led by Irwin. He firstly extended the Griffith approach to ductile metals including plastic dissipated energy into the energy balance [17]. Subsequently he showed that the elastic stress, strain and displacement near the crack tip could be characterised in term of a scalar quantity known as stress intensity factor, K [18]. Fracture criteria could be expressed in term of stress intensity factor that was related to the energy release rate introduced by Griffith [15]. In 1961 Paris and co-workers [19] suggested that fatigue crack growth increment per cycle (fatigue crack growth rate, da/dN) could be related to stress intensity factor range ($\Delta K=K_{max}-K_{min}$) during constant amplitude fatigue cycles. Even if with some initial reluctances, because of its empirical nature, Paris approach became widely used to predict fatigue crack growth life under small scale yielding (nearly linear elastic)

condition. The major appeal of linear elastic fatigue approach is the possibility of characterising fatigue crack propagation uniquely by means of the stress intensity factor range, determinate by remote load condition and component geometry without a detailed knowledge of failure mechanisms. Crack with the same stress intensity factor in the same material will behave in the same way despite geometrical differences. That concept is a milestone of linear elastic fracture mechanics and it is called similitude concept. Fracture mechanics research from 1960 to 1980 was mainly focalised to investigate the effect of significant plastic deformation when linear elastic fracture mechanics ceases to be valid. Concepts like crack tip opening displacement (Wells [20]) and J integral (Rice [21]) made possible the evolution of the elastic plastic fracture mechanics. With the application of fracture mechanics to fatigue failure, more attention was paid to subcritical crack growth mechanism under constant amplitude and more realistic spectrum loads. It was discovered that the stress intensity factor range could be dependent on the load and consequent crack advance histories making invalid the similitude concept. An important contribution in understanding that process came from the work of Elber in 1970 [22] who supplied fist evidences of fatigue crack closure mechanism. During fatigue load application crack flanks remain in contact for a fraction of the cycle even when subject to tensile load. Crack growth was postulated happening when cracks are opened and tip blunting and re-sharpening mechanism can take place. Crack closure was regulated by the amount of residual plastic deformation on the crack flank released by crack tip plasticisation caused by previous load history (see section 2.2.4.3). Further contribution to crack closure may arise from fracture surface oxidation, crack flanks roughness, presence of viscous environment. Whichever is the cause of fatigue crack closure it was evident that fatigue crack growth was not only affected by the instantaneous stress intensity factor range value but also by the prior loading history and defect size invalidating the similitude concept. The breakdown of the similitude concept was noticed by the experimental observation of the so-called short crack problem. Small fatigue cracks, even if theoretically amenable to be characterised in term of linear elastic fracture mechanics, exhibit growth rates faster than those of longer flaws subjected to the same crack driving force (ΔK). Beside the stress intensity factor crack size seems to influence fatigue crack propagation. The short crack behaviour, first documented by Pearson in 1975 [33], was the topic of a significant research fraction since the late 1970s together with crack closure phenomena with the aim of developing growth prediction methodologies. Efforts were made to characterise and predict flaw propagation in presence of large scale plasticity and in the vicinity of stress concentrators as well.

References chapter 2

[1] Klesnil, M. and Lucas P. *Fatigue of metallic materials*, 2nd ed. Amsterdam: Elsevier, 1992.

[2] Schijve, J. *Fatigue of structures and materials*, Dordrecht: Kluwer Academic Publishers, 2001.

[3] Suresh, S. *Fatigue of materials*, 2nd ed. New York: Cambridge University Press, 2004.

[4] Albert, W. A. J. Über treibseile am harz. *Archive für Mineralogie, Geognosie, Bergbau und Hüttenkunde*, Vol. 10, 1838, pp. 215-234.

[5] Wöler, A. Versuche über die festigkeit der eisenbahnwagenachsen. *Zeitshrift für Bauwesen*, Vol. 10, 1860; English summary. *Enginnering*, Vol. 4, 1867 pp. 160-161.

[6] Baushinger, J. Ueber die veränderungen der elastizitätsgrenze und der festigkeit des eisens und stahls durch strecken, quetschen, erwärmen abkühlen und durch oftmals wiederholte belastung. *Mitt: Mech-Tech Lab.*, 1886, XIII München.

[7] Edwing, J. A. and Humfrey, J. C. The fracture of metals under rapid alteration of stress. *Philosophical Transactions of the Royal Society, London*, Vol. A200, 1903, pp. 241-250.

[8] Basquin, O. H. The exponential law of endurance tests. *Proceedings of the American society for Testing and* Materials, Vol. 10, 1910, pp. 625-630.

[9] Coffin L. F. A study of the effects of cyclic thermal stresses on a ductile metal. *Transaction of the Americal Society of Mechanical Engineers*, Vol. 76, 1954, pp. 931-950.

[10] Manson, S. S. Behavior of materials under condition of thermal stress. *National Advisory commission on Aeronautics: Report 1170*, Cleveland: Lewis Flight Propulsion Laboratory, 1954.

[11] Neuber, H. *Theory of notch stresses: principle for exact stress calculation* ed. Ann Arbor, MI: Edwards, 1946.

[12] Kanninen, M. F. and Popelar, C. H. *Advanced fracture mechanics*, New York: Oxford University Press, 1985.

[13] Broek, D. *Elementary engineering fracture mechanics*, 4th ed. Dordrecht: Kluwer Academic Publishers, 1986.

[14] Anderson, T. L. *Fracture mechanics fundamentals and applications*, 3rd ed. New York: CRC Press, Taylor & Francis Group, 2005.

[15] Griffith, A. A. The phenomena of rupture and flow in solids. *Philosophical Transaction*, *Series A*, Vol. 221, 1920, pp. 163-198.

[16] Inglis, C. E. Stresses in a plate due to the presence of cracks and sharp corners. *Transaction of the Institute of Naval Architects*, Vol. 55, 1913, p. 219-241.

[17] Irwin, G. R. Fracture dynamics. *Fracture of Metals*, American Society for Metals, Cleveland OH, 1948, pp. 147-166.

[18] Irwin, G. R. Analysis of stresses and strains near the end of a crack traversing a plate. *Journal of Applied Mechanics*, Vol. 24, 1957, pp. 361-364.

[19] Paris, P. C., Gomez, M. P. and Anderson, W. P. A rational analytic theory of fatigue. *The Trend in Engineering*, Vol. 13, 1961, pp. 9-14.

[20] Wells, A. A. Application of fracture mechanics at and beyond general yielding. *British Welding Journal*, Vol. 10, 1963, pp. 563-570.

[21] Rice, J. R. A path independent integral and the approximate analysis of strain concentration by notches and cracks. *Journal of Applied Mechanics*, Vol. 35, 1968, pp. 379-386.

[22] Elber, W. Fatigue crack closure under cyclic tension. *Engineering Fracture Mechanics*, Vol. 2, 1970, pp. 37-45.

[23] Ritchie, R. O. and Suresh, S. Mechanics and physics of the growth of small cracks. AGARD Conference Proceedings 328, (1983), pp. 1.1-1.14.

[24] Schijve, J. The practical and theoretical significance of small cracks. An evaluation. In: *Fatigue 84*, University of Birmingham, UK, 1984, pp. 751-771.

[25] Miller, K. J. The initiation and growth rates of short fatigue cracks. *Fundamentals of deformation and fracture : Eshelby memorial symposium, Sheffield, 2-5 April 1984*. (edited by B.A. Bilby, K.J. Miller, and J.R. Willis) 1985, Cambridge University Press, New York, pp. 477-500.

[26] Leis, B. N., Hopper, A. T., Ahmad, J., Broek, D. and Kanninen, M. F. Critical review of the fatigue growth of short cracks. *Engineering Fracture Mechanics*, Vol. 23, No. 5, 1986, pp. 883-898.

[27] Miller, K. J. The behaviour of short fatigue cracks and their initiation Part I-a review of two recent books. *Fatigue & Fracture of Engineering Materials & Structures*, Vol. 10, No 1, 1987, pp. 75-91.

[28] Miller, K. J. The behaviour of short fatigue cracks and their initiation Part II-a general summary. *Fatigue & Fracture of Engineering Materials & Structures*, Vol. 10, No 2, 1987, pp. 93-113.

[29] Ritchie, R. O. and Peters, J. O. Small fatigue cracks: mechanics, mechanisms and engineering applications. *Material Transaction*, Vol. 42, No. 1, 2001, pp. 58-67.

[30] Smith, I. F. C. Applying fatigue research to engineering design. *The behaviour of short fatigue cracks*, EGF Pub. 1 (Edited by K. J. Miller and E. R. de los Rios) 1986, Mechanical Engineering Publications, London, pp. 15-26.

[31] Wanhill, R. J. H. Short cracks in aerospace structures. *The behaviour of short fatigue cracks*, EGF Pub. 1 (Edited by K. J. Miller and E. R. de los Rios) 1986, Mechanical Engineering Publications, London, pp. 27-36.

[32] Wanhill, R. J. H. and Schra, L. Short crack and durability analysis of the Fokker 100 wing/fuselage structure. *Short fatigue cracks*, ESIS 13 (Edited by K. J. Miller and E. R. de los Rios) 1992, Mechanical Engineering Publications, London, pp. 1-27.

[33] Pearson, S. Initiation of fatigue cracks in commercial aluminium alloys and the subsequent propagation of very short cracks. *Engineering Fracture Mechanics*, Vol. 7, 1975, pp. 235-247.

[34] Nisitani, H. and Takao, K. Significance of initiation, propagation and closure of microcracks in high cycle fatigue of ductile metals. *Engineering Fracture Mechanics*, Vol. 15, No. 3-4, 1981, pp. 445-456.

[35] Lankford, J. The growth of small fatigue cracks in 7075-T6 aluminium. *Fatigue of Engineering Materials & Structures*, Vol. 6, No 2, 1982, pp. 233-248.

[36] Blom, A. F., Hedlund, A., Zhao, W., Fathulla, A., Weiss, B. and Stickler, R. Short fatigue crack growth behaviour in Al 2024 and Al 7475. *The behaviour of short fatigue cracks*, EGF Pub. 1 (Edited by K. J. Miller and E. R. de los Rios) 1986, Mechanical Engineering Publications, London, pp. 37-66.

[37] Bolingbroke, R. K. and King, J. E. A comparison of long and short fatigue crack growth in high strength aluminium alloy. *The behaviour of short fatigue cracks*, EGF Pub. 1 (Edited by K. J. Miller and E. R. de los Rios) 1986, Mechanical Engineering Publications, London, pp. 101-114.

[38] Mulvihill, P. and Beevers, C. J. The initiation and growth of intergranularly initiated short fatigue cracks in an aluminium 4.5 per cent copper alloy. *The behaviour of short fatigue cracks*, EGF Pub. 1 (Edited by K. J. Miller and E. R. de los Rios) 1986, Mechanical Engineering Publications, London, pp. 203-213.

[39] Plumtree, A. and Schäfer, S. Initiation and short crack behaviour in aluminium alloy castings. *The behaviour of short fatigue cracks*, EGF Pub. 1 (Edited by K.

J. Miller and E. R. de los Rios) 1986, Mechanical Engineering Publications, London, pp. 215-227.

[40] Tokaji, K. and Ogawa, T. The growth behaviour of microscrucTurally small fatigue cracks in metals. *Short fatigue cracks*, ESIS 13 (Edited by K. J. Miller and E. R. de los Rios) 1992, Mechanical Engineering Publications, London, pp. 85-99.

[41] Petit, J. and Kosche, K. Stage I and stage II propagation of short and long cracks in Al-Zn-Mg alloys. *Short fatigue cracks*, ESIS 13 (Edited by K. J. Miller and E. R. de los Rios) 1992, Mechanical Engineering Publications, London, pp. 135-151.

[42] Zhang, X. P., Wang, C. H., Ye, L. and Mai, Y-W. In situ investigation of small fatigue crack growth in poly-crystal and single-crystal aluminium alloys. *Fatigue & Fracture of Engineering Materials & Structures*, Vol. 25, 2002, pp. 141-150.

[43] Zhang, X. P., Wang, C. H., Ye, L. and Mai, Y-W. A study of the crack wake closure/opening behaviour of short fatigue cracks and its influence on crack growth. *Materials Science and Engineering*, Vol. 406, Part A, 2005, pp. 195-204.

[44] Xue, Y., El Kadiri, H., Horstemeyer, M. F., Jordon, J. B. and Weiland, H. Micromechanisms of multistage fatigue crack growth in a high-strength aluminum alloy. *Acta Materialia*, Vol. 55, 2007, pp. 1975-1984.

[45] Zhai, T., Jiang, X. P., Li, J. X., Garratt, M. D. and Bray, G. H. The grain Boundary geometry for optimum resistance to growth of short fatigue cracks in high strength Al-alloys. *International Journal of Fatigue*, Vol. 27, 2005, pp. 1202-1209.

[46] Foth, J., Marissen, R., Nowach, H. and Lütjering, G. Fatigue crack initiation and microcrack propagation in notched and unnotched aluminium 2024-T3 specimens. In: *Fatigue 84*, University of Birmingham, UK, 1984, pp. 791-801.

[47] Foth, J., Marissen, R., Trautmann K.-H. and Nowach, H. Short crack phenomena in a high strength aluminium alloy and some analytical tools for their prediction. *The behaviour of short fatigue cracks*, EGF Pub. 1 (Edited by K. J. Miller and E. R. de los Rios) 1986, Mechanical Engineering Publications, London, pp. 353-368.

[48] Newman, J. C. Jr., Edwards, P. R. et al. Short-crack growth behaviour in aluminium alloy-An AGARD cooperative test programme. AGARD report 732, 1988.

[49] Edwards, P. R., Newman, J. C. Jr. et al., Short-crack growth behaviour in various aircraft materials. AGARD report 767, 1990.

[50] Newman, J. C. Jr., Wu, X. R., Venneri, S. L. and Li, C. G. Small-crack effects in high-strength aluminium alloy. NASA RP-1309, 1994.

[51] Wu, X. R., Newman, J. C. Jr., Zhao, W., Swain, M. H., Ding, C. F. and Phillips, E. P. Small-crack growth and fatigue life predictions for high-strength aluminium alloys: Part I–experimental and fracture mechanics analysis. *Fatigue & Fracture of Engineering Materials & Structures*, Vol. 21, No 11, 1998, pp. 1289-1306.

[52] Newman, J. C. Jr., Wu, X. R., Swain, M. H., Zhao, W., Phillips, E. P., and Ding, C. F. Small-crack growth and fatigue life predictions for high-strength

aluminium alloys. Part II: crack closure and fatigue analyses. *Fatigue & Fracture of Engineering Materials & Structures*, Vol. 23, No 1, 2000, pp. 59-72.

[53] Laz, P. J. and Hillberry, B. M. Fatigue life prediction from inclusion initiated cracks. *International Journal of Fatigue*, Vol. 20, No. 4, 1998, pp. 263-270.

[54] Newman, J. C. Jr. Fastran-II – A fatigue crack growth structural analysis program. NASA Technical Memorandum 104159, (1992).

[55] El Haddad, M. H., Dowling, N. E., Topper, T. H. and Smith, K. N. Fatigue crack propagation of short crack. *Journal of Engineering Materials and Technology*, Vol. 101, No. 1, 1979, pp. 42-46.

[56] Lawson, L., Chen, E. Y. and Meshii, M. Near-threshold fatigue a review. *International Journal of Fatigue*, Vol. 21, 1999, pp. S15-S34.

[57] Kitagawa, H. and Takahashi, S. Applicability of fracture mechanics to very small cracks or the cracks in the early stage. In: *Proceedings of Second International Conference on Mechanical Behavior of Materials*, pp. 627-631, Metals park: American Society for metals, 1976.

[58] Taylor, D. and Knott, J. F. Fatigue crack propagation behaviour of short cracks; the effect of microstructure. *Fatigue of Engineering Materials and Structures*, Vol. 4, No. 2, 1981, pp. 147-155.

[59] Usami, S. and Shida, S. Elastic-plastic analysis of the fatigue limit for a material with small flaws. *Fatigue of Engineering Materials and Structures*, Vol. 1, 1979, pp. 471-491.

[60] Tanaka, K., Nakai, Y. and Yamashita, M. Fatigue growth threshold of small cracks. *International Journal of Fracture*, Vol. 17, 1981, pp. 519-533.

[61] McEvily, A. J. and Minakawa, Y. On crack closure and the notch size effect in fatigue. *Engineering Fracture Mechanics*, Vol. 28, No. 5/6, 1987, pp. 519-527.

[62] Chapetti, M. D. Fatigue propagation threshold of short cracks under constant amplitude loading. *International Journal of Fatigue*, Vol. 25, 2003, pp. 1319-1326.

[63] Navarro, A. and de los Rios, E. R. Short and long fatigue crack growth: A unified model. *Philosophical Magazine A*, Vol. 57, No. 1, 1988, pp. 15-36.

[64] Navarro, A. and de los Rios, E. R. An alternative model of the blocking of dislocations at grain boundaries. *Philosophical Magazine A*, Vol. 57, No. 1, 1988, pp. 37-42.

[65] Navarro, A. and de los Rios, E. R. Compact solution for a multizone BCS crack model with bounded or unbounded end conditions. *Philosophical Magazine A*, Vol. 57, No. 1, 1988, pp. 43-50.

[66] de los Rios, E. R. and Navarro, A. Considerations of grain orientation and work hardening on short-fatigue-crack modelling. *Philosophical Magazine A*, Vol. 61, No. 3, 1988, pp. 435-449.

[67] Xin, X. J., de los Rios, E. R. and Navarro, A. Modelling strain hardening at short fatigue cracks. *Short fatigue cracks*, ESIS 13 (Edited by K. J. Miller and E. R. de los Rios) 1992, Mechanical Engineering Publications, London, pp. 369-389.

[68] Navarro, A. and de los Rios, E. R. Fatigue crack growth modelling by successive blocking of dislocations. *Proceeding of The Royal Society London A*, No. 437, 1992, pp. 375-390.

[69] Tanaka, K., Akiniwa, Y., Nakai, Y. and Wei, R.P. Modelling of small fatigue crack growth interacting with grain boundary. *Engineering Fracture Mechanics*, Vol. 24, No. 6, 1986, pp. 803-819.

[70] Marx, M., Vehoff, H., Schäf, W. and Welsch, M. The mechanisms of the interaction of microcracks with grain boundaries: in-situ investigations in the SEM by FIB, EBSD and electron channelling contrast. In: *Proceedings of FATIGUE 2006*, Atlanta, USA, 2006.

[71] Bjerkén, C. and Melin, S. A tool to model short crack fatigue growth using a discrete dislocation formulation. *International Journal of Fatigue*, Vol. 25, 2003, pp. 559-566.

[72] Bjerkén, C. and Melin, S. A study of the influence of grain boundaries on short crack growth during varying load using a dislocation technique. *Engineering Fracture Mechanics*, Vol. 71, No. 15, 2004, pp. 2215-2227.

[73] Bjerkén, C. The discrete nature of the growth and arrest of microstructurally short fatigue cracks modelled by dislocation technique. *International Journal of Fatigue*, Vol. 27, 2005, pp. 21-32.

[74] Hansson, P. and Melin, S. Dislocation-based modelling of the growth of a microstructurally short crack by single shear due to fatigue loading. *International Journal of Fatigue*, Vol. 27, 2005, pp. 347-356.

[75] Hansson, P. and Melin, S. Simulation of simplified zigzag crack paths emerging during fatigue crack growth. *Engineering Fracture Mechanics*, Vol. 75, 2008, pp. 1400-1411.

[76] Hansson, P. and Melin, S. Grain boundary influence during short fatigue crack growth using a discrete dislocation technique. *Strength of Materials*, Vol. 40, No. 1, 2008, pp. 150-153.

[77] Hansson, P. and Melin, S. Grain boundary influence on short fatigue crack growth rate. *International Journal of Fracture*, Vol. 165, No. 2, 2010, pp. 199-210.

[78] Bertolino, G., Doquet, V. and Sauzay, M. Modelling of scatter in short fatigue cracks growth kinetics in relation with the polycrystalline microstructure. *International Journal of Fatigue*, Vol. 27, 2005, pp. 471-480.

[79] Krupp, U., Düber, O., Christ, H.-J., Künkler, B., Köster, P. and Fritzen, C.-P. Propagation mechanisms of microstructurally short cracks-Factors governing the transition from short- to long- crack behaviour. *Materials Science and Engineering A*, Vol. 462, 2007, pp. 174-177.

[80] Künkler, B., Düber, O., Köster, P., Krupp, U., Fritzen, C.-P. and Christ, H.-J. Modelling of short crack propagation - Transition from stage I to stage II. *Engineering Fracture Mechanics*, Vol. 75, No. 3-4, 2008, pp. 715-725.

[81] Wilkinson, A. J. Modelling the effects of texture on the statistics of stage I fatigue crack growth. *Philosophical Magazine A*, Vol. 81, No. 4, 2001, pp. 841-855.

[82] Tanaka, K., Kinefuchi, M. and Yokomaku, T. Modelling of statistical characteristics of the propagation of small fatigue cracks. *Short fatigue cracks*, ESIS 13 (Edited by K. J. Miller and E. R. de los Rios) 1992, Mechanical Engineering Publications, London, pp. 351-368.

[83] Liao, M. Dislocation theory based short crack model and its application for aircraft aluminum alloys. *Engineering Fracture Mechanics*, Vol. 77, No. 1, 2010, pp. 22-36.

[84] Bataille, A., Magnin, T. and Miller, K. J. Numerical simulation of surface fatigue mirocracking processes. *Short fatigue cracks*, ESIS 13 (Edited by K. J.

Miller and E. R. de los Rios) 1992, Mechanical Engineering Publications, London, pp. 407-419.

[85] Wilson, S. P. and Taylor, D. Statistical analysis and reliability prediction with short fatigue crack data. *Fatigue & Fracture of Engineering Materials & Structures*, Vol. 22, 1999, pp. 67-76.

[86] Potirniche, G. P., Daniewicz, S. R. and Newman J. C. Jr. Simulating small crack growth behaviour using crystal plasticity theory and finite element analysis. *Fatigue & Fracture of Engineering Materials & Structures*, Vol. 27, No. 1, 2004, pp. 59-71.

[87] Hill, R. Generalised constitutive relations for increment deformation of metals crystals by multislip. *Journal of the Mechanics and Physics of Solids*, Vol. 14, 1966, pp. 95-102.

[88] Cheong, K. S., Smillie, M., Stevens, K. J. and Knowles, D. M. Consideration of grain interaction effects on fatigue crack initiation in metal policrystals. In: *Proceedings of FATIGUE 2006*, Atlanta, USA, 2006.

[89] Rice, J. R. and Rosengren, G. F. Plane strain deformation near a crack tip in a power-law hardening material. *Journal of the Mechanics and Physics of Solids*, Vol. 16, No. 1, 1968, pp. 1-12.

[90] Hutchinson, J. W. Singular behaviour at the end of a tensile crack in a hardening material. *Journal of the Mechanics and Physics of Solids*, Vol. 16, No. 1, 1968, pp. 13-31.

[91] Lamba, H. S. The J-integral applied to cyclic loading. *Engineering Fracture Mechanics*, Vol. 7, 1975, pp. 693-703.

[92] Dowling, N. E. and Begley, J. A. Fatigue crack growth during gross plasticity and the J-integral. ASTM STP 590, American Society for Testing and Materials, Philadelphia, PA, 1976, pp. 82-103.

[93] Banks-Sills, L. and Volpert, Y. Application of the cyclic J-integral to fatigue crack propagation of Al 2024-T351. *Engineering Fracture Mechanics*, Vol. 40, No. 2, 1991, pp. 355-370.

[94] Lambert, Y., Saillard, P. and Bathias, C. Application of the J concept to fatigue crack growth in large-scale yielding. ASTM STP 969, American Society for Testing and Materials, Philadelphia, PA, 1988, pp. 318-329.

[95] Chow, C. L. and Lu, T. J. Cyclic J-integral in relation to fatigue crack initiation and propagation. *Engineering Fracture Mechanics*, Vol. 39, No. 1 1991, pp. 1-20.

[96] Chow, C. L. and Woo, W. A unified formulation of fatigue crack propagation in aluminium alloys and PMMA. *Engineering Fracture Mechanics*, Vol. 21, No. 3, 1985, pp. 589-608.

[97] Bruzi, M. S. and McHugh, P. E. Methodology for modelling the small crack fatigue behaviour of aluminium alloys. *International Journal of Fatigue*, Vol. 24, 2002, pp. 1071-1078.

[98] Härkegård, G. and Wormsen, A. Non-linear analysis of shallow cracks in smooth and notches plates. Part 1: analytical evaluation. *Journal of Strain Analysis for Engineering Design*, Vol. 40, No. 3, 2005, pp. 237-244.

[99] Wormsen, A. and Härkegård, G. Non-linear analysis of shallow cracks in smooth and notches plates. Part 2: finite element validation. *Journal of Strain Analysis for Engineering Design*, Vol. 40, No. 3, 2005, pp. 245-254.

[100] Hamm, R. W. and Johnson, W. S. A unification of small- and large-crack growth laws. *Fatigue of Engineering Materials and Structures*, Vol. 22, 1998, pp. 711-722.

[101] Zhang, J.-Z., Zhang, J.-Z. and Yi Du, S. Elastic-plastic finite element analysis and experimental study of short and long fatigue crack growth. *Engineering Fracture Mechanics*, Vol. 68, No. 14, 2001, pp. 1591-1605.

[102] Caputo, F., Lamanna, G. and Soprano, A. An analytical formulation for the plastic deformation at the tip of short cracks. *Procedia Engineering*, Vol. 10, 2011, pp. 2988-2993.

[103] Ramsamooj, D. V. Analytical prediction of short to long fatigue crack growth rate using small- and large-scale yielding fracture mechanics. *International Journal of Fatigue*, Vol. 25, 2003, pp. 923-933.

[104] Beretta, S., Foletti, S. and Patriarca, L. Discussion of models for LCF small crack growth. *Procedia Engineering*, Vol. 10, 2011, pp. 3642-3649.

[105] Elber, W. The significance of fatigue crack closure. *Damage tolerance in aircraft structures*. ASTM STP 486 American Society for Testing and Materials, 1971, pp. 37-45.

[106] Newman, J. C. Jr. A crack-closure model for predicting fatigue crack growth under aircraft spectrum loading. NASA Technical Memorandum 81941, (1981).

[107] Newman, J. C. Jr. A crack-opening stress equation for fatigue crack growth. *International Journal of Fracture*, Vol. 24, 1984, pp. R131-R135.

[108] Newman, J. C. Jr. A Nonlinear fracture mechanics approach to the growth of small cracks. AGARD Conference Proceedings 328, (1983), pp. 6.1-6.26.

[109] Nowell, D. A boundary element model of plasticity-induced fatigue crack closure. *Fatigue and Fracture in Engineering Material Structure*, Vol. 21, No. 7, 1998, pp. 857-871.

[110] Nowell, D., de Matos, P. F. P. and Paynter, R. J. A comparison of plane stress and plane strain models of fatigue crack closure. In: *Proceedings of FATIGUE 2006*, Atlanta, USA, 2006.

[111] Solanki, K., Daniewicz, S.R. and Newman, J.C. Finite element analysis of plasticity-induced fatigue crack closure: An overview. *Engineering Fracture Mechanics*, Vol. 71, No. 2, 2004, pp. 149-171.

[112] Gonzalez-Herrera, A., Moreno, B., James, M. N. and Zapatero, J. Numerical and experimental correlation of fatigue crack closure. In: *Proceedings of FATIGUE 2006*, Atlanta, USA, 2006.

[113] Holm, D. K. and Blom, A. F. Short cracks and crack closure in Al 2024-T3. In: *Proceedings International Committee on Aeronautical Structures (ICAS)*, ICAS-84-3.7.1, 1984, pp. 783-790.

[114] Kendall, J. M., James, M. N. and Knott, J. F. The behaviour of physically short fatigue cracks in steel. *The behaviour of short fatigue cracks*, EGF Pub. 1 (Edited by K. J. Miller and E. R. de los Rios) 1986, Mechanical Engineering Publications, London, pp. 241-258.

[115] Nakai, Y. and Ohji, K. Prediction of growth rate and closure of short fatigue cracks. *Short fatigue cracks*, ESIS 13 (Edited by K. J. Miller and E. R. de los Rios) 1992, Mechanical Engineering Publications, London, pp. 169-189.

[116] Newman, J. C. Jr. A review of modelling small-crack behavior and fatigue-life predictions for aluminium alloys. *Fatigue & Fracture of Engineering Materials & Structures*, Vol. 17, No. 4, 1994, pp. 429-439.

[117] Newman, J. C. Jr., Phillips, E. P. and Swain, M. H. Fatigue-life prediction methodology using small crack theory. NASA Technical Memorandum 1103079, (1997).

[118] Newman, J. C. Jr., Phillips, E. P. and Everett, R. A. Jr. Fatigue analyses under constant- and variable-amplitude loading using small-crack theory. NASA Technical Memorandum 209329, (1999).

[119] Taylor, D. Fatigue short cracks: the limitations of fracture mechanics. *The behaviour of short fatigue cracks*, EGF Pub. 1 (Edited by K. J. Miller and E. R. de los Rios) 1986, Mechanical Engineering Publications, London, pp. 479-490.

[120] Brown, M. W. Interfaces between short, long and non-propagating cracks. *The behaviour of short fatigue cracks*, EGF Pub. 1 (Edited by K. J. Miller and E. R. de los Rios) 1986, Mechanical Engineering Publications, London, pp. 423-439.

[121] Hobson, P. D., Brown, M. W. and de los Rios, E. R. Two phases of short crack growth in a medium carbon steel. *The behaviour of short fatigue cracks*, EGF Pub. 1 (Edited by K. J. Miller and E. R. de los Rios) 1986, Mechanical Engineering Publications, London, pp. 441-459.

[122] Angelova, D. and Akid, R. A note on modelling short fatigue crack behaviour. *Fatigue & Fracture of Engineering Materials & Structures*, Vol. 21, 1998, pp. 771-779.

[123] Nisitani, H. and Goto, M. A small-crack growth law and its application to the evaluation of fatigue life. *The behaviour of short fatigue cracks*, EGF Pub. 1 (Edited by K. J. Miller and E. R. de los Rios) 1986, Mechanical Engineering Publications, London, pp. 461-478.

[124] Kujawski, D. and Ellyin, F. A microstructurally motivated model for short crack growth rate. *Short fatigue cracks*, ESIS 13 (Edited by K. J. Miller and E. R. de los Rios) 1992, Mechanical Engineering Publications, London, pp. 391-405.

[125] McEvily, A. J., Eifler, D. and Macherauch, E. An analysis of the growth of short fatigue cracks. *Engineering Fracture Mechanics*, Vol. 40, No. 3, 1991, pp. 571-584.

[126] McEvily, A. J. and Yang, Z. An analysis of the rate of growth of short fatigue cracks. *Short fatigue cracks*, ESIS 13 (Edited by K. J. Miller and E. R. de los Rios) 1992, Mechanical Engineering Publications, London, pp. 439-448.

[127] McEvily, A. J., Ishihara, S., Endo, M., Sakai, H. and Matsunaga, H. On one- and two-parameter analyses of short fatigue crack growth. *International Journal of Fatigue*, Vol. 29, 2007, pp. 2237-2245.

[128] Shyam, A., Allison, J. E., Szczepanski, C. J., Pollock, T. M. and Jones, J. W. Small fatigue crack growth in metallic materials: A model and its application to engineering alloys. *Acta Materialia*, Vol. 55, No.19, 2007, pp. 6606-6616.

[129] Santus, C. and Taylor, D. Physically short crack propagation in metals during high cycle fatigue. *International Journal of Fatigue*, Vol. 31, No. 8-9, 2009, pp. 1356-1365.

[130] Sadananda, K. and Vasudevan, A. K. Short crack growth and internal stresses. *International Journal of Fatigue*, Vol. 19, No. 1, 1997, pp. S99-S108.

[131] Vasudevan, A. K., Sadananda, K. and Glinka, G. Critical parameters for fatigue damage. *International Journal of Fatigue*, Vol. 23, 2001, pp. S39-S53.

[132] Guiu, F. and Stevens, R. N. Thermodynamic considerations of fatigue crack nucleation and propagation. *The behaviour of short fatigue cracks*, EGF Pub. 1

(Edited by K. J. Miller and E. R. de los Rios) 1986, Mechanical Engineering Publications, London, pp. 407-421.

[133] Weixing, Y., Kaiquan, X. and Yi, G. On the fatigue notch factor, K_f. *International Journal of Fatigue*, Vol. 17, No. 4, 1995, pp. 245-251.

[134] Ciavarella, M. and Meneghetti, G. On fatigue limit in the presence of notches: classical vs. Recent unified formulations. *International Journal of Fatigue*, Vol. 26, 2004, pp. 289-298.

[135] Kuhn, P. and Hardrath, H. F. An engineering method for estimating notch-size effect in fatigue test of steel. NACA Technical Note 2805, 1952.

[136] Heywood, R. E. *Designing against fatigue*. 1st ed. London: Chapman & Hall, 1962.

[137] Peterson, R. E. Notch sensitivity. In: *Meal fatigue*, edited by Sines, G. and Waisman J. L. New York: MacGraw-Hill, 1959, pp. 293-306.

[138] Smith, R. W., Hirschberg, M. H. and Manson, S. S. Fatigue behaviour of materials under strain cycling in low and intermediate life range. NASA Technical Note D-1574, 1963.

[139] Coffin, L. F. Low cycle fatigue-A thirty year perspective. In: *Fatigue 84*, University of Birmingham, UK, 1984, pp. 1213-1234.

[140] An introduction to low-cycle fatigue phenomena. ESDU report No. 04022, 2005.

[141] Manson, S. S. and Hirschberg, M. H. Low cycle fatigue of notched specimens by consideration of crack initiation and propagation. NASA Technical Note D-3146, 1967.

[142] Dowling, N. E. Combined use of strain-based fatigue methodology and notched member test data. In: *Proceedings of 2005 USAF Structural Integrity Program (ASIP) Conference*, Memphis, USA, 2005.

[143] Troshchenko, V. T. Fatigue of metals under nonuniform stressed state. Part 1. Stresses state assessment methods and results of investigation. *Strength of Materials*, Vol. 42, No. 2, 2010, pp. 129-143

[144] Neuber, H. Theory of stress concentration for shear-strained prismatic bodies with arbitrary nonlinear stress-strain law. *Journal of Applied Mechanics*, Vol. 28, 1961, pp. 544-550.

[145] Hardrath, H. F. and Ohman, L. A study of elastic and plastic stress concentration factors due to notches and fillets in plates. NACA Technical Report 1117, 1953.

[146] Leis, B. N. and Topper, T. H. Cyclic deformation and fatigue analysis for notched components. *Nuclear Engineering and Design*, Vol. 29, 1974, pp. 370-383.

[147] Glinka, G. Calculation of inelastic notch-tip strain-stress histories under cyclic loading. *Engineering Fracture Mechanics*, Vol. 22, No. 5, 1985, pp. 839-854.

[148] Lazzarin, P., Tovo, R. and Meneghetti, G. Fatigue crack initiation and propagation phases near notches in metal with low notch sensitivity. *International Journal of Fatigue*, Vol. 19, No. 8-9, 1997, pp. 647-657.

[149] Livieri, P. and Tovo, R. Fatigue limit evaluation of notches, small cracks and defects: an engineering approach. *Fatigue & Fracture of Engineering Materials & Structures*, Vol. 27, 2004, pp. 1037-1049.

[150] Ostash, O. P., Panasyuk, V. V. and Kostyk, E. M. A phenomenological model of fatigue macrocrack initiation near stress concentrators. *Fatigue & Fracture of Engineering Materials & Structures*, Vol. 22, 1998, pp. 161-172.

[151] Ostash, O. P. and Panasyuk, V. V. Fatigue process at notches. *International Journal of Fatigue*, Vol. 23, 2001, pp. 627-636.

[152] Ostash, O. P. Role of the prefracture zone in the evaluation of stress concentration in cyclically deformed materials. *Material Science*, Vol. 37, No. 3, 2001, pp. 415-430.

[153] Ostash, O. P. New approaches in fatigue fracture mechanics. *Material Science*, Vol. 42, No. 1, 2006, pp. 5-19.

[154] Weixing, Y. Stress field intensity approach for predicting fatigue life. *International Journal of Fatigue*, Vol. 15, No. 3, 1993, pp. 243-245.

[155] Qylafku, G., Azari, Z., Kadi, N., Gjonaj, M. and Pluvinage, G. Application of a new model proposal for fatigue life prediction on notches and key-seats. *International Journal of Fatigue*, Vol. 21, 1999, pp. 753-760.

[156] Adib, H. and Pluvinage, G. Theoretical and numerical aspects of the volumetric approach for fatigue life prediction in notched components. *International Journal of Fatigue*, Vol. 25, 2003, pp. 67-76.

[157] Adib, H., Gilgert, J. and Pluvinage, G. Fatigue life duration prediction for welded spots by volumetric method. *International Journal of Fatigue*, Vol. 26, 2004, pp. 81-94.

[158] Tovo, R. and Livieri, P. An implicit gradient application to fatigue of sharp notches and weldments. *Engineering Fracture Mechanics*, Vol. 74, 2007, pp. 515-526.

[159] Tovo, R. and Livieri, P. An implicit gradient application to fatigue of complex structures. *Engineering Fracture Mechanics*, Vol. 75, 2008, pp. 1804-1814.

[160] Bentachfine, S., Pluvinage, G., Gilgert, J., Azari, Z. and Bouami, D. Notch effect in low cycle fatigue. *International Journal of Fatigue*, Vol. 21, 1999, pp. 421-430.

[161] Creager, M. and Paris, P. C. Elastic field equations for blunt cracks with reference to stress corrosion cracking. *International Journal of Fracture*, Vol. 3, No 2, 1967, pp. 247-252.

[162] Lazzarin, P. and Tovo, R. A unified approach to the evaluation of lineal elastic stress fields in the neighbourhood of cracks and notches. *International Journal of Fracture*, Vol. 78, 1996, pp. 3-19.

[163] Boukharouba, T., Tamine, T., Niu, L., Chehimi, C. and Pluvinage, G. The use of notch stress intensity factor as a fatigue crack initiation parameter. *Engineering Fracture Mechanics*, Vol. 50, No. 3, 1995, pp. 503-512.

[164] Lazzarin, P. and Tovo, R. A notch intensity factor approach to the stress analysis of welds. *Fatigue & Fracture of Engineering Materials & Structures*, Vol. 21, 1998, pp. 1089-1103.

[165] Atzori, B., Lazzarin, P. and Tovo, R. From a local stress approach to fracture mechanics: a comprehensive evaluation of the fatigue strength of welded joints. *Engineering Fracture Mechanics*, Vol. 22, No. 5, 1999, pp. 369-382.

[166] Atzori, B., Lazzarin, P. and Tovo, R. Stress field parameters to predict the fatigue strength of notched components. *Journal of Strain Analysis for Engineering Design*, Vol. 34, No. 6, 1999, pp. 437-453.

[167] Lazzarin, P. and Livieri, P. Notch stress intensity factors and fatigue strength of aluminium and steel welded joints. *International Journal of Fatigue*, Vol. 23, 2001, pp. 225-232.

[168] Lazzarin, P., Lassen, T. and Livieri, P. A notch stress intensity approach applied to fatigue life predictions of welded joints with different local toe geometry. *Fatigue & Fracture of Engineering Materials & Structures*, Vol. 26, 2003, pp. 49-58.

[169] Lazzarin, P., Berto, F., Gomez, F. J. and Zappalorto, M. Some advantages derived from the use of strain energy density over a control volume in fatigue strength assessment of welded joints. *International Journal of Fatigue*, Vol. 30, 2008, pp. 1345-1357.

[170] Verreman, Y. and Limodin, N. Fatigue life prediction of V-notched components. In: *Proceedings of FATIGUE 2006*, Atlanta, USA, 2006.

[171] Verreman, Y. and Limodin, N. Fatigue notch factor and short crack propagation. *Engineering Fracture Mechanics*, Vol. 75, 2008, pp. 1320-1335.

[172] Atzori, B. and Lazzarin, P. Notch sensitivity and defect sensitivity under fatigue loading: two sides of the same medal. *International Journal of Fracture*, Vol. 107, 2000, pp. L3-L8.

[173] Atzori, B., Lazzarin, P. and Meneghetti, G. Fracture mechanics and notch sensitivity. *Fatigue & Fracture of Engineering Materials & Structures*, Vol. 26, 2003, pp. 257-267.

[174] Atzori, B., Lazzarin, P. and Meneghetti, G. A unified treatment of the mode I fatigue limit of components containing notches or defects. *International Journal of Fracture*, Vol. 133, 2005, pp. 61-87.

[175] Atzori, B., Lazzarin, P. and Meneghetti, G. Estimation of fatigue limits of sharply notched components. In: *Proceedings of FATIGUE 2006*, Atlanta, USA, 2006.

[176] Taylor, D. The theory of critical distances. *A new perspective in fracture mechanics* ed. Amsterdam: Elsevier, 2007.

[177] Taylor, D. The theory of critical distances. *Engineering Fracture Mechanics*, Vol. 75, 2008, pp. 1696-1705.

[178] Taylor, D. Geometrical effects in fatigue: a unifying theoretical model. *International Journal of Fatigue*, Vol. 21, 1999, pp. 413-420.

[179] Taylor, D. and Wang, G. The validation of some methods of notch fatigue analysis. *Fatigue & Fracture of Engineering Materials & Structures*, Vol. 23, 2000, pp. 387-394.

[180] Carpinteri, A., Cornetti, P., Pugno, N., Sapora, A. and Taylor, D. A finite fracture mechanics approach to structures with sharp V-notches. *Engineering Fracture Mechanics*, Vol. 75, 2008, pp. 1736-1752.

[181] Taylor, D. and Kasiri, S. A comparison of critical distance methods for fracture prediction. *Engineering Fracture Mechanics*, Vol. 75, 2008, pp. 1696-1705.

[182] Susmel, L and Taylor, D. Fatigue design in the presence of stress concentrations. *Journal of Strain Analysis for Engineering Design*, Vol. 38, No. 5, 2003, pp. 443-452.

[183] Taylor, D. Analysis of fatigue failures in components using the theory of critical distances. *Engineering Failure Analysis*, Vol. 12, 2005 pp. 906-914.

[184] Susmel, L. The theory of critical distances: a review of its applications in fatigue. *Engineering Fracture Mechanics*, Vol. 75, 2008, pp. 1706-1724.

[185] Taylor, D. A mechanistic approach to critical-distance method in notch fatigue. *Fatigue and Fracture in Engineering Material Structure*, Vol. 24, 2001, pp. 215-224.

[186] Susmel, L and Taylor, D. On the use of the theory of critical distances to estimate fatigue strength of notched components in the medium-cycle fatigue regime. In: *Proceedings of FATIGUE 2006*, Atlanta, USA, 2006.

[187] Susmel, L and Taylor, D. A novel formulation of the theory of critical distances to estimate lifetime of notched components in the medium-cycle fatigue regime. *Fatigue & Fracture of Engineering Materials & Structures*, Vol. 30, 2007, pp. 567-581.

[188] Yamashita, Y., Ueda, Y., Kuroki, H., and Shinozaki, M. Fatigue life prediction of small notched Ti-6Al-4V specimens using critical distance. *International Committee on Aeronautical Fatigue (ICAF) symposium*, Rotterdam, Netherland, 27-29 May 2009.

[189] Yamashita, Y., Ueda, Y., Kuroki, H., and Shinozaki, M. Fatigue life prediction of small notched Ti-6Al-4V specimens using critical distance. *Engineering Fracture Mechanics*, Vol. 77, 2010, pp. 1439-1453.

[190] Frost, N. E. and Dugdale, D. S. Fatigue tests on notched mild steel plates with measurement of fatigue cracks. *Journal of Mechanics and Physics of Solids*, Vol. 5, 1957, pp. 182-192.

[191] Smith, R. A. and Miller, K. J. Prediction of fatigue regimes in notched components. *International Journal of Mechanical Science*, Vol. 20, 1978, pp. 201-206.

[192] Cameron, A. D. and Smith, R. A. Upper and lower bounds for the lengths of non-propagating cracks. *International Journal of Fatigue*, Vol. 9, No. 1, 1981, pp. 9-15.

[193] El Haddad, M. H., Topper, T. H. and Smith, K. N. Prediction of non propagating cracks. *Engineering Fracture Mechanics*, Vol. 22, No 2, 1985, pp. 279-293.

[194] Meggiolaro, M. A., Miranda, A. C. O., Castro, J. T. P. and Freire, J. L. F. Notch sensitivity factor predictions based on short crack threshold estimates. In: *Proceedings of FATIGUE 2006*, Atlanta, USA, 2006.

[195] Meggiolaro, M. A., Miranda, A. C. O., Castro, J. T. P. and Freire, J. L. F. Short crack threshold estimates to predict notch sensitivity factors in fatigue. *International Journal of Fatigue*, Vol. 29, 2007, pp. 2022-2031.

[196] Vallellano, C., Navarro, A. and Domínguez, J. Fatigue crack growth threshold conditions at notches. Part I: theory. *Fatigue & Fracture of Engineering Materials & Structures*, Vol. 23, 2000, pp. 113-121.

[197] Vallellano, C., Navarro, A and Domínguez, J. Fatigue crack growth threshold conditions at notches. Part II: generalization and application to experimental results. *Fatigue & Fracture of Engineering Materials & Structures*, Vol. 23, 2000, pp. 123-128.

[198] Vallellano, C., Mariscal, M. R., Navarro, A. and Domínguez, J. A Micromechanical approach to fatigue in small notches. *Fatigue & Fracture of Engineering Materials & Structures*, Vol. 28, 2005, pp. 1035-1045.

[199] Tanaka, K. and Nakai, Y. Propagation and non-propagation of short fatigue cracks at a sharp notch. *Fatigue & Fracture of Engineering Materials & Structures*, Vol. 6, No. 4, 1983, pp. 315-327.

[200] Tanaka, K. and Akiniwa, Y. Resistance-curve method for predicting propagation threshold of short fatigue cracks at notches. *Engineering Fracture Mechanics*, Vol. 30, No. 6, 1988, pp. 863-876.

[201] Abdel-Raouf, H., DuQuesnay, D. L., Topper, T. H. and Plumtree, A. Notch-size effects in fatigue based on surface strain redistribution and crack closure. *International Journal of Fatigue*, Vol. 14, No. 1, 1992, pp. 57-62.

[202] McEvily, A. J., Endo, M., Yamashita, K., Ishihara, S. and Matsunaga, H. Fatigue notch sensitivity and the notch size effect. *International Journal of Fatigue*, Vol. 30, 2008, pp. 2087-2093.

[203] Murakami, Y. and Endo, M. Quantitative evaluation of fatigue strength of metal containing various small defects or cracks. *Engineering Fracture Mechanics*, Vol. 17, No. 1, 1983, pp. 1-15.

[204] Murakami, Y. and Endo, M. Effect of small defects on fatigue strength of metals. *International Journal of Fatigue*, Vol. 2, No. 1, 1980, pp. 23-30.

[205] Murakami, Y. and Endo, M. Effects of hardness and crack geometries on ΔK_{th} of small cracks emanating from small defects. *The behaviour of short fatigue cracks*, EGF Pub. 1 (Edited by K. J. Miller and E. R. de los Rios) 1986, Mechanical Engineering Publications, London, pp. 275-293.

[206] Lukas, P. and Klesnil, M. Fatigue limit of notched bodies. *Material Science & Engineering*, Vol. 34, 1978, pp. 61-66.

[207] Lukas, P., Kunz, L., Weiss, B. and Stickler, R. Notch size effects in fatigue. *Fatigue & Fracture of Engineering Materials & Structures*, Vol. 12, 1989, pp. 175-186.

[208] Lukas, P., Kunz, L., Weiss, B. and Stickler, R. Non-Damaging notches in fatigue. *Fatigue & Fracture of Engineering Materials & Structures*, Vol. 9, No. 3, 1986, pp. 195-204.

[209] DuQuesnay, D. L., Topper, T. H. and Yu, M. T. The effect of notch radius on the fatigue notch factor and the propagation of short cracks. *The behaviour of short fatigue cracks*, EGF Pub. 1 (Edited by K. J. Miller and E. R. de los Rios) 1986, Mechanical Engineering Publications, London, pp. 323-335.

[210] Newman, J. C. Jr. and Raju, I. S. Stress-intensity factor equations for cracks in three-dimensional finite bodies subjected to tension and bending loads. NASA Technical Memorandum 85793, Apr 1984.

[211] Niu, X. and Glinka, G. Weight functions for edge and surface semi-elliptical cracks in flat plates and plates with corners. *Engineering Fracture Mechanics*, Vol. 36, No. 3, 1990, pp. 459-475.

[212] Fett, T. and Munz, D. Local stress intensity factors for small semi-elliptical cracks under exponentially distributed stresses. *Engineering Fracture Mechanics*, Vol. 64, 1999, pp. 105-116.

[213] Fett, T. Estimated stress intensity factor for semi-elliptical cracks in front of narrow circular notches. *Engineering Fracture Mechanics*, Vol. 64, 1999, pp. 357-362.

[214] Xu, R. X., Topper, T. H. and Thompson, J. C. Mode I stress intensity factor equations for cracks at notches and cavities. *Fatigue & Fracture of Engineering Materials & Structures*, Vol. 20, No. 9, 1997, pp. 1351-1361.

[215] Brennan, F. P. and Teh, L. S. Determination of crack-tip stress intensity factors in complex geometries by the composition of constituent weight function solutions. *Fatigue & Fracture of Engineering Materials & Structures*, Vol. 27, 2004, pp. 1-7.

[216] Teh, L. S. and Brennan, F. P. Stress intensity factors for cracks emanating from two-dimensional semicircular notches using the composition of SIF weight

functions. *Fatigue & Fracture of Engineering Materials & Structures*, Vol. 28, 2004, pp. 423-435.

[217] Teh, L. S., Love, A. J. and Brennan, F. P. Mode I stress intensity factors for edge cracks from 2-D U-notches using composition of constituent SIF weight functions. *International Journal of Fatigue*, Vol. 28, 2006, pp. 355-365.

[218] Teh, L. S. and Brennan, F. P. Evaluation of mode I stress intensity factors for edge cracks from 2-D V-notches using composition of constituent SIF weight functions. *International Journal of Fatigue*, Vol. 29, 2007, pp. 1253-1268.

[219] Wormsen, A. Fjeldstad, A. and Härkegård, G. The application of asymptotic solutions to a semi-elliptical crack at the root of a notch. *Engineering Fracture Mechanics*, Vol. 73, 2006, pp. 1899-1912.

[220] Fjeldstad, A., Wormsen, A. and Härkegård, G. Approximate stress intensity factors for cracked V-notched specimens based on asymptotic solutions with application to T-joints. *Engineering Fracture Mechanics*, Vol. 75, 2008, pp. 1083-1098.

[221] Smith, R. A. and Miller, K. J. Fatigue cracks at notches. *International Journal of Mechanical Science* , Vol. 19, 1977, pp. 11-22.

[222] Hussey, I. W., Byrne, J. and Duggan, T. V. Behaviour of small fatigue cracks at blunt notches in aero-engine alloys. *The behaviour of short fatigue cracks*, EGF Pub. 1 (Edited by K. J. Miller and E. R. de los Rios) 1986, Mechanical Engineering Publications, London, pp. 337-351.

[223] Evans, W. J. and Spence, S. H. Small crack growth at notches in IMI 829. *Short fatigue cracks*, ESIS 13 (Edited by K. J. Miller and E. R. de los Rios) 1992, Mechanical Engineering Publications, London, pp. 293-304.

[224] McClung, R. C., Francis, W. L. and Hudak, S. J. Jr. A new approach to fatigue life prediction based on nucleation and growth. In: *Proceedings of FATIGUE 2006*, Atlanta, USA, 2006.

[225] Pasha, R. A. and Hammounda, H. A Model for notch fatigue life. *Material Science & Engineering A*, Vol. 483-484, 2008, pp. 319-321.

[226] El Haddad, M. H., Dowling, N. E., Topper, T. H. and Smith, K. N. J integral application for short fatigue crack at notches. *International Journal of Fracture*, Vol. 16, No. 1, 1980, pp. 15-30.

[227] Sehitoglu, H. Fatigue life prediction of notched members based on local and elastic-plastic fracture mechanics concepts. *Engineering Fracture Mechanics*, Vol. 18, No. 3, 1983, pp. 609-621.

[228] Ahmad, H. Y., Clode, M. P. and Yates, J. R. Prediction of fatigue crack growth in notched members. *International Journal of Fatigue*, Vol. 19, No 10, 1997, pp. 703-712.

[229] Hammouda, M. M., Smith, R. A. and Miller, K. J. Elastic-plastic fracture mechanics for initiation ad propagation of notch fatigue cracks. *Fatigue & Fracture of Engineering Materials & Structures*, Vol. 2, 1979, pp. 139-154.

[230] Hammouda, M. M. I., Sallam, H. E. M. and Osman, H. G. Significance of crack tip plasticity to early notch fatigue crack growth. *International Journal of Fatigue*, Vol. 26, 2004, pp. 173-182.

[231] Verreman, Y., Bailon, J. P. and Masounave, J. Fatigue short crack propagation and plasticity-induced crack closure at the toe of a fillet welded joint. *The behaviour of short fatigue cracks*, EGF Pub. 1 (Edited by K. J. Miller and E. R. de los Rios) 1986, Mechanical Engineering Publications, London, pp. 387-404.

[232] Shin, C. S. and Smith, R. A. Fatigue crack growth from sharp notches. *International Journal of Fatigue*, Vol. 7, No. 2, 1985, pp. 87-93.

[233] Shin, C. S. and Smith, R. A. Fatigue crack growth at stress concentrations-the role of notch plasticity and crack closure. *Engineering Fracture Mechanics*, Vol. 29, No. 3, 1988, pp. 301-315.

[234] Leis, B. N. Displacement controlled fatigue crack growth in inelastic notch field: Implication for short cracks. *Engineering Fracture Mechanics*, Vol. 22, No 2, 1985, pp. 279-293.

[235] Palazotto, A. N. and Mercer, J. G. A finite element comparison between short and long cracks within a plastic zone due to a notch. *Engineering Fracture Mechanics*, Vol. 35, No. 6, 1990, pp. 967-986.

[236] Chien, C.-H. and Coffin, L. F. A new method for predicting fatigue life in notched geometris. *Fatigue & Fracture of Engineering Materials & Structures*, Vol. 21, 1998, pp. 1-15.

[237] Nader, N. A. *The effect of scratches on fatigue life and fatigue crack growth of Al 2024-T3 clad*. PhD thesis, Wichita State University, 1993.

[238] Talia, M. and Talia, J. E. Crack propagation modeling for surface generated scratches in Al 2024-T3 clad alloy. *Journal of the Mechanical Behavior of Materials*, Vol. 8, No. 2, 1997, pp. 117-139.

[239] Talia, M. and Talia, J. E. The effects of scratches and shot peening on the high cycle fatigue crack growth of aluminium alloy 2024-T3. In: *High Cycle Fatigue of Structural Materials*, Indianapolis Indiana USA, 14-18 Sept 1997, pp. 409-426.

[240] Inchekel, A. and Talia, J. E. Effect of scratches on the fatigue behaviour of an Al-Li alloy. *Fatigue & Fracture of Engineering Materials & Structures*, Vol. 17, No. 5, 1994, pp. 501-507.

[241] Everett, R. A. Jr., Newman J. C. Jr. and Phillips, E. P. The effect of Machining-like scratch on the fatigue life of 4340 steel. *Journal of the American Helicopter Society*, Vol. 47, No. 3, 2002, pp. 151-155.

[242] Suhr, R. W. The effect of surface finish on high cycle fatigue of a low alloy steel. *The behaviour of short fatigue cracks*, EGF Pub. 1 (Edited by K. J. Miller and E. R. de los Rios) 1986, Mechanical Engineering Publications, London, pp.68-86.

[243] Suraratchai, M., Limido, J., Mabru, C. and Chieregatti, R. Modelling the influence of machined surface roughness on the fatigue life of aluminium alloy. *International Journal of Fatigue*, Vol. 30, 2008, pp. 2119-2126.

[244] Radhakrishnan, V. M. and Mutoh, Y. On fatigue crack growth in stage I. *The behaviour of short fatigue cracks*, EGF Pub. 1 (Edited by K. J. Miller and E. R. de los Rios) 1986, Mechanical Engineering Publications, London, pp. 87-99.

[245] Mezlini, S., Kapsa, Ph., Abry, J. C., Henon, C. and Guillemenet, J. Effect of indenter geometry and relationship between abrasive wear and hardness in early stage of repetitive sliding. *Wear*, Vol. 260, 2006, pp. 412-421.

[246] Nowell, D., Dini, D. and Duò, P. Stress analysis of V-notches with and without cracks with application to foreign object damage. *Journal of Strain Analysis for Engineering Design*, Vol. 38, No. 5, 2003, pp. 429-441.

[247] Oakley, S. Y. and Nowell, D. Prediction of the combined high- and low-cycle fatigue performance of gas turbine blades after foreign object damage. *International Journal of Fatigue*, Vol. 29, 2007, pp. 69-80.

[248] Kyle, C. *Investigation of the transformation of defects in aircraft structures into cracks*. M Sc thesis, Cranfield University, 2005.

[249] Irving, P. E., Hopper, B. and Scott, A. J. Investigation of the effect of machined scratches on fatigue life of clad 2024-T351. Canfield University Report for Airbus ABH1, Dec 2005.

[250] Morency, R. *Fatigue crack initiation and growth from scratches in 2024 T-351 aluminium*. M Sc thesis, Cranfield University, 2006.

[251] Walmsley, S. W. *Fatigue potential of tool scratches on clad 2024-T351 aluminium alloy*. M Sc thesis, Cranfield University, 2007.

[252] Khan, M. K. *Scribe marks at fuselage joins-Determination of residual stress and effect of fatigue loading using nanoindentation and synchrotron X-ray diffraction*. PhD thesis, Open University, UK, 2009.

[253] Jozelich, A. M. *Investigation of the transformation of defects into fatigue cracks*. M Sc thesis, Cranfield University, 2009.

[254] Tizard, D. G. I *The influence of plasticity and residual stress in the fatigue performance of real world scribes in fuselage materials*. M Sc thesis, Cranfield University, 2010.

[255] Das, G., Kosai, M. and Miller, M. Development of a method for damage tolerance analysis for scribe marks adjacent to fuselage longitudinal and circumferential splices. In: *International Committee on Aeronautical Fatigue (ICAF) meeting*, Napoli, Italy, 14-18 May 2007.

Chapter 3
Experimentation

Scratch geometrical parameters (in particular scratch depth and root radius) as well as residual stress fields and material plasticisation, induced by the scribing procedure were considered the main factors influencing fatigue crack nucleation and early propagation from scribe marks. It was decided to start two PhD projects to investigate the effects of scratch geometry and scribing procedure respectively at Cranfield University and at the Open University [1].

The effect of different scratch geometries, load type and supplying condition (clad and unclad) on fatigue performance of 2024 aluminium alloy samples were investigated during this PhD project. In order to analyse the major scratch geometric parameters influencing fatigue life it was decided to examine separately the consequences of pure tension and bending load on simple scribed aluminium specimens. A new scribing procedure, adopting a diamond tipped cutting tool, able to machine very regular and reproducible artificial scratches, was developed. The process was capable of cutting the material by swarf generation, minimising therefore the material plastic deformation and the induced residual stresses. Rounded V shaped cross section notches could be machined within an acceptable tolerance. That made scribe geometry controllable supporting a systematic investigation on the role of scratch geometric parameters on component fatigue life.

After fatigue testing, a fractography investigation was carried out for all samples in order to gather information about fracture morphology and characteristic of cracks nucleated from scribe marks. Fracture surface inspections were performed using optical and scanning electron microscopes to compare the effect of different notch geometries on crack morphology. To obtain data on crack growth and so separate nucleation life by propagation one, striation counting was performed on tension and bending specimens.

3.1 Fatigue test sample preparation

The first part of this investigation was directed to the fatigue behaviour of aluminium sheet samples scribed and tested under constant amplitude load in pure tension and pure bending. Specimens were machined from two 2 mm thick rectangular panels (1200x5000 mm) of aluminium alloy 2024-T351 supplied in clad condition. A clad panel consists of a substrate of aluminium alloy protected by two, one per side, external layers of pure aluminium. Pure aluminium, although it has poor mechanical properties, possesses better corrosion resistance than alloyed aluminium and shields the panel from the aggressive external environment. Cladding however is very soft and can be easily scratched; moreover it is less resistant to crack nucleation and early propagation, so cracks can nucleate from scratches and propagate through the substrate reducing the component fatigue life. It is evident that that clad layer plays a substantial role on crack development from scribe marks and that was studied. Clad and unclad samples were tested and compared. Unfortunately the material supplier did not manufacture 2 mm

thick bare 2024-T351 panels and it was decided to produce unclad material stripping the cladding from a 2 mm thick clad panel by chemical milling. That procedure inevitably changes the surface finish and reduces the thickness of the unclad stripped specimens, adding more variables into the problem. The thickness of 2 mm was selected to be comparable with the average thickness of a civil aircraft fuselage. Since a mechanical controlled scratch with the depth of the order of 10-100 μm has to be machined into the sample surfaces any other accidental scratch or mechanical damage can make the specimen useless for the research purpose. A plastic protecting film, used as anti-corrosion film during chemical milling, was therefore applied on the samples surface to prevent damage during transport.

Fig. 3.1 shows the fatigue sample geometry used for pure tension testing. This is a rectangular cross section dogbone specimen with continuous radius between ends. A precise machined rounded V-shaped notch, representative of a scribe mark, was introduced on a sample face across the entire gauge section width perpendicular to the load application direction (Fig. 3.1). The scribing procedure is described in detail in the following section. The need for a mechanical notch representative of meter long scribe marks found in service fuselage, made the gauge section 80 mm width. That implied a design non consistent with the guidelines given by the ASTM standard [2]. In fact for a standardised samples a radius of curvature no less than eight times the gauge section width is required to minimise the stress concentration factor. To avoid machining a very long sample, a radius of roughly four times the gauge width was adopted. Finite element analysis were developed to check the stress concentration factor of the adopted configuration that had an acceptable value of K_t=1.01 [3].

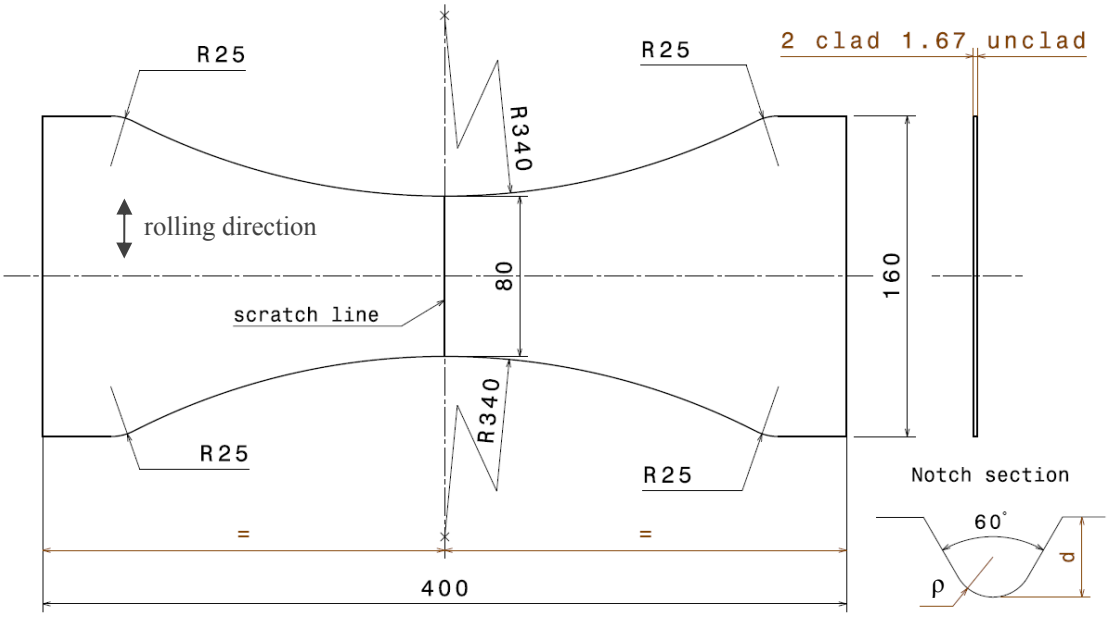

Fig. 3.1: Fatigue tension sample geometry and notch section (drawing not in scale)

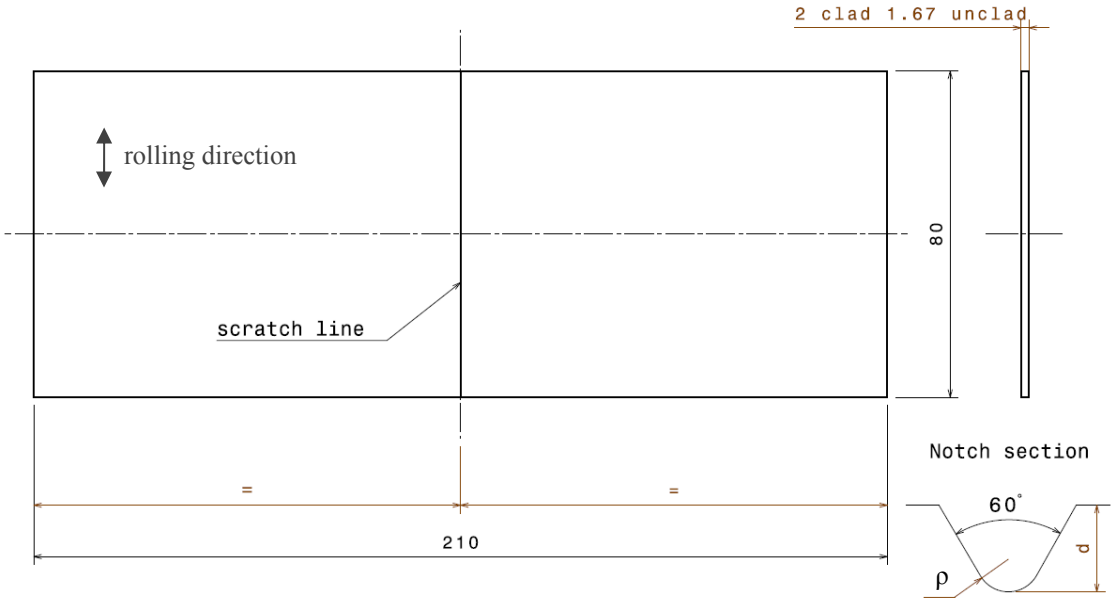

Fig. 3.2: Fatigue 4 point bend sample geometry and notch section (drawing not in scale)

Fig. 3.2 shows the sample geometry for pure bending fatigue tests. Pure bending loadings were obtained at the gauge section performing 4 point bend tests. A simple rectangular shape with an artificial scratch machined in the middle was considered suitable for the 4 point bend test. There was no ASTM standard regarding 4 point bend test guidelines, therefore the sample length was selected on the basis of 4 point bend grip design (Fig. 3.14). The width was 80 mm as tension specimen gauge section in order to hold scribes with the same length and facilitate result comparison between different loads. Bending load was applied by means of rollers (Fig. 3.14) that bent the sample along its longitudinal axis so that the scribe line was perpendicular to the bending stress. Samples were machined with the rolling direction perpendicular to the specimen longitudinal axis, that is parallel to the scribe line (see Fig. 3.1 and Fig. 3.2), to correspond with the material texture conditions found in longitudinal fuselage joints. In fact in aircraft fuselage the panel rolling direction, along with the rolled pancake shape grains, are elongated and aligned with the plane longitudinal axis and thus with the scribe lines cut on longitudinal joints.

As explained above, unclad samples had smaller thickness than clad ones due to chemical milling clad removing during manufacturing. Chemical milling did not ensure very precise manufacturing tolerances and different unclad specimens could have different thicknesses. Unclad thickness mean value was around 1.67 mm but for every tested samples gauge section thickness was measured to determine the right external load required to have the desired nominal stress at the gauge section.

3.1.1 Material characterisation

The material investigated was the aluminium-copper aluminium alloy 2024-T351. This alloy is widely used in aircraft structures, where fatigue crack growth resistance is the main requirement, for its good combination of specific mechanical properties and fracture toughness. Fuselage panels and joints of the majority of civil aircraft in service

are made of this alloy. The Al 2024 chemical composition is reported in Table 3.1 [4,5]. Limits of impurities are expressed as a maximum while limits of alloying elements are shown as a range. No information was available for the pure aluminium composition constituting the clad layer. Material was supplied in T351 temper condition. That corresponds to an heat treatment consisting in solution treatment at 490°C<T<500°C, quenching down to T≤40°C followed by stress releasing by stretching and naturally aging at room temperature for more than 5 days after solution heat treatment [4,6,7]. After stretching, that yields 0.5% to 3% of permanent strain for sheet, the product receives no further strengthening.

Material characterisation of this particular batch was performed before fatigue testing: crystallographic examination was carried out at Cranfield and mechanical properties were tested at Open University, partner of this research project. Small pieces of clad and unclad material were cut out from the panels for a grain structure analysis. The aluminium was put under epoxy resin. The samples obtained were mechanically polished and chemically etched using a solution of 5% HF in saturated molybdic acid to make grain boundaries visible. Specimens were observed under optical microscope and grain size measured by the line counting method.

Table 3.1: Al 2024 chemical composition [4,5]

Element	Si	Fe	Cu	Mn	Mg	Cr	Zn	Ti	Others		Al
									Each	Total	
Mass %	0.50	0.50	3.8-4.9	0.3-0.9	1.2-1.8	0.10	0.25	0.15	0.05	0.15	Base

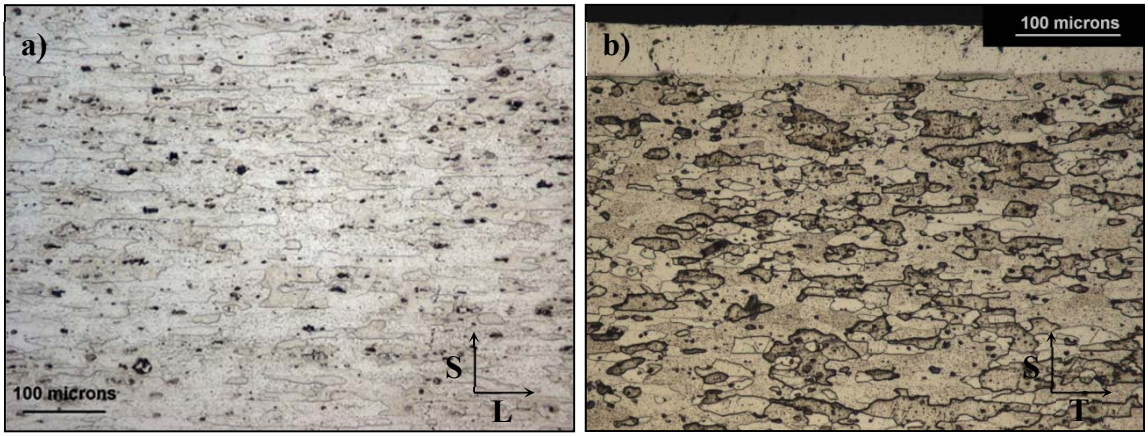

Fig. 3.3: Al 2024-T351 grain texture, section by LS plane (a), section by ST plane (b)

Fig. 3.3 shows the grain structure of Al 2024-T351 on two perpendicular section planes containing the through thickness (direction S): the first one including the rolling direction L (Fig. 3.3 (a)) and the second the scribe line direction T (Fig. 3.3 (b)). Grains were elongated along the rolling direction L having the typical pancake shape that can be found in rolled sheets. Grain were approximately 150-200 μm long along rolling direction L, 80-100 μm along T and 20 μm along thickness direction S. In Fig. 3.3 (b) cladding can be observed on the top of the pictures as a brighter layer but unfortunately no grain structure was visible. Clad layer depth has to be a defined percentage of the whole thickness, variable for different sheet or plate thicknesses. For a 2 mm thick sheet

it is around 3.5% of the whole thickness [4], that means a 70 µm deep cladding. Clad depth was measured using optical microscope and consistent values from 70 to 80 µm were found (see Fig. 3.4). Anyway a real sharp boundary should not be expected, since some diffusions of alloying element from the substrate to the cladding occur during hot rolling and solution heat treatment.

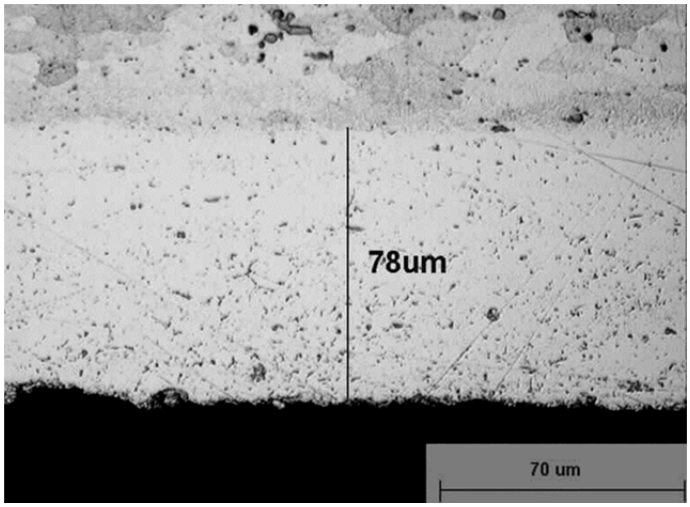

Fig. 3.4: Clad layer depth

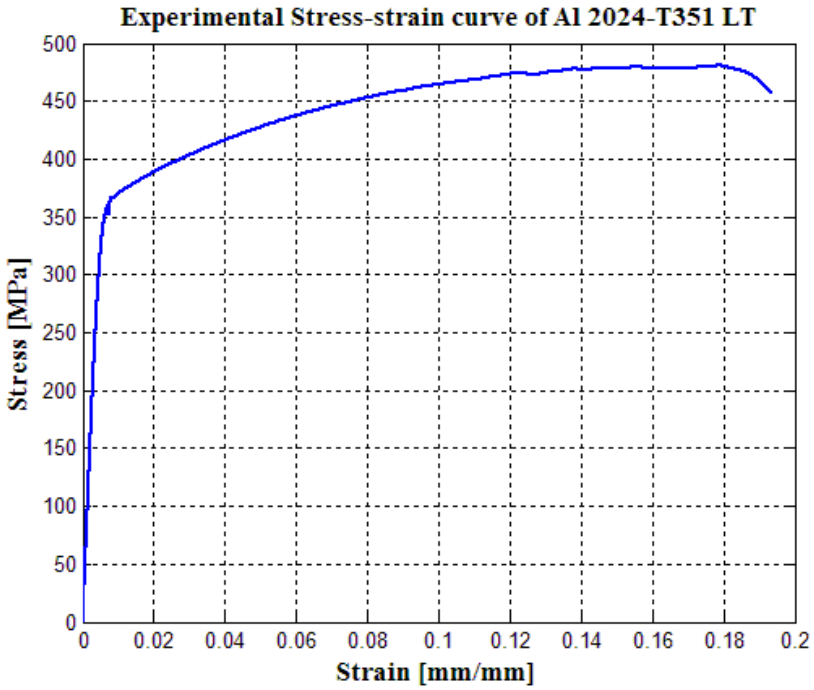

Fig. 3.5: Experimental Al 2024-T351 unclad stress-strain curve obtained by applying traction along long transverse direction [1]

Tensile test was carried out by Open University to characterise the mechanical properties of this batch of Al 2024-T351. A rectangular section dogbone standard tensile test specimen was machined from an unclad (stripped) spare 4 point bend sample with the longitudinal axis aligned whit that of the bend sample. The test was performed

therefore along the long transverse LT direction of the material. Displacement was applied by a servohydraulic test machine at a rate of 0.01 mm/s and load and axial strain, measured by an extensiomenter, were recorded [1]. The axial stress was calculated and the stress-strain curve for unclad Al 2024-T351 obtained in the LT direction (see Fig. 3.5). Clad material was not tested.

Table 3.2: Al 2024-T351 mechanical properties (E=Young modulus, ν=Poisson ratio, $\sigma_{0.2}$=Yield stress, σ_{UTS}=Ultimate tensile stress, ε_f=Elongation at fracture)

Al 2024-T351		E [MPa]	ν	$\sigma_{0.2}$ [MPa]	σ_{UTS} [MPa]	ε_f [%]
Stripped LT (tensile test [1])		72000	0.33	360	481	19
Unclad [8]	L	72398	0.33	324	441	15
	LT			290	434	15
Clad [4]	L	$65500 \leq E \leq 70500$	0.33	310	420	-
	LT			280	425	15

Measured mechanical properties are listed in Table 3.2. Properties found in literature for clad and unclad Al 2024-T351 in different direction are also reported for comparison (see [4] and [8]). Experimental yield stress ($\sigma_{0.2}$) and tensile strength (σ_{UTS}) resulted respectively 24% and 10% higher that literature value for unclad material tested along LT [8]. Table 3.2 also shows how cladding can reduces sample global mechanical properties and even the Young's modulus, having very low yield and tensile strength compared to the substrate. In fact its load capacity is reduced and that affects negatively the whole sample properties. Moreover cladding yields at smaller stress than the substrate causing a reduction of stiffness and so of the Young's modulus. This effects are discussed in detail below.

3.1.2 Scribing procedure

Scribe marks found on aircraft fuselage joints during service inspections are scratches with irregular cross section geometry and length (see chapter 1). Since one of the aims of this research was to investigate the effect of different scribe geometry on fatigue performances of aluminium samples, the tested scratch geometry had to be regular with controllable geometrical parameters. Therefore more than a scratch on the sample surface had to be introduced, that is machined, a micro mechanical controlled notch. Notch section size had to be representative of a real scribe mark geometry and so it was of the order of microns. As explained in chapter 1, the majority of scribe marks found in service can be comparable with a micro V-shaped notch with rounded root. This notch shape was adopted and kept constant for all the tests while geometrical parameters, like notch depth (d) and root radius (ρ), were varied (see Fig. 3.1 and Fig. 3.2) to study the fatigue effect of different scratch geometry. Geometrical parameters that can be varied in a V notch are notch depth (d), root radius (ρ) and the included angle (θ).

In order to save time it was decided to analyse just the effect of different root radii and notch depths, keeping constant the included angle, since it has less effect on stress concentration for notches with $\theta \leq 104°$ [9]. The cutting procedure had to create a scribe introducing the least possible amount of plasticity and associated residual stresses. In

other words the scribe had to be precisely cut, removing material and not plunging and plasticising it. Investigation of the effect on fatigue strength of different types of scribing procedure was out of the scope of this work. Analyses of this type can be found in [10]. A comprehensive study of residual stresses associated with scribe marks and their effect in fatigue was performed at the Open University within a parallel research project [1].

A very small, precise and sharp tool was hence required to scribe fatigue test specimen. The solution came from contact lens industries where small diamond tipped tools are used to shape contact lens. Three different sintered diamond tipped tools were bought. The small prismatic diamond rounded V-shape tip ensured a well defined regular cut notch without any sign of material piling up typical of a plunging procedure (see Fig. 3.7). Different tools were required in order to create scratches with different cross section area. The diamond tips had a cylindrical shape to make easier tool repair by simply re-polishing. Diamond damages were frequent. It was decided to buy initially two diamond tools producing V-shape scratches with an included angle of 60° (Fig. 3.1 and Fig. 3.2) and two different root radii (5 µm and 50 µm). After a Scanning Electron Microscope (SEM) inspection, the 5 µm tip radius tool, used in the preliminary campaign by Morency [11], seemed damaged and it was replaced. The new undamaged tool was used to scribe the 5 µm root radius sample tested in this campaign. Afterwards a further tool to machine 25 µm root radius scribes was bought.

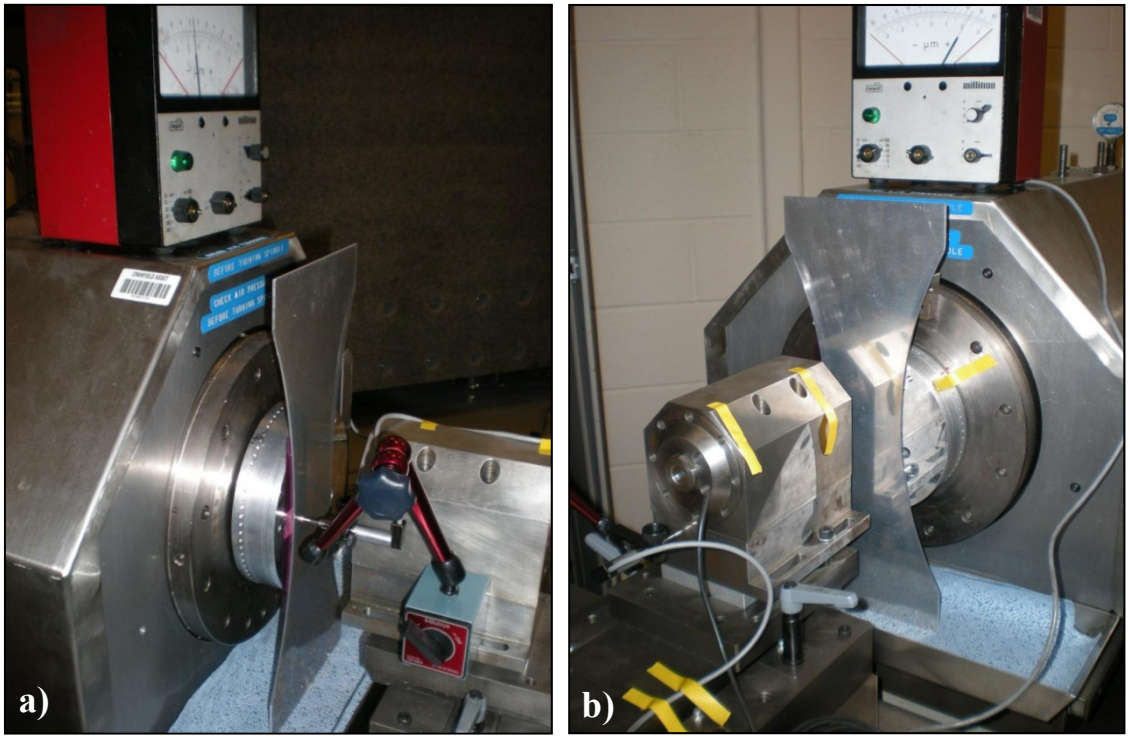

Fig. 3.6: Precision scribing flatness measurement configuration (a), cutting configuration (b)

Regular notches with three root radii (5 µm, 25 µm and 50 µm) were cut on one side of the tension an bending specimens using a precision planing machine with a vertical head (Fig. 3.6 (b)). The sample was held in place on a vertical lapped support surface by a vacuum jig. Machine head and or samples were lifted up, when needed, by machined aluminium spacer and support to cut scribes always in the middle of the specimen

despite different geometry. Coupons were scribed across the entire gauge section from one edge to the other with approximately constant depth. In that configuration the notch starts and terminates on the free edge where local grain plastic deformation is facilitate by the reduced constraint exerted by the absence of surrounding grains. Moreover at the free edge a condition of plane stress is experienced contrarily to the sample centre where plane strain is present. All these phenomena can affect sample fatigue behaviour that can differ from the one of a scribe on a fuselage panel where are no free edges. Nevertheless this scratch configuration was adopted because producing a scribe with the ends inside the specimen could damage the diamond tool during its extraction.

One of the major tasks of scribing was to maintain a constant depth along the entire notch length. In fact the machine head was aligned with the lapped vertical support plane where the sample was fixed (see Fig. 3.6 (a)), therefore the scribe would have had every point of its root at the same distance from the reference support. In that way, since notch depth is conventionally measured from the external surface, scratch depth would have been affected by the sample flatness and positioning errors on the vacuum jig. To have a constant depth, sample surface had to be used as scribing reference surface instead. That was not possible on the machine so the only way to obtain a fairly constant depth scribe was making sample external surface parallel to the machine head. The goal was achieved by means of a tedious procedure. Samples were fixed on the lapped support after having their edges deburred (Fig. 3.6 (a)). First sample flatness was measured by an electronic micrometer equipped with a finger probe with a nylon tip to avoid damage during contact with sample surface (Fig. 3.6 (a)). The probe was firmly fixed on the machine head and put in contact with the sample surface. Than after setting to zero the measurement scale, the head linear motion was activated and the flatness measured at the position where the scribe would be machined. Flatness was defined as the difference between the maximum and minimum value recorded and the sensitivity of measurement was ± 1 μm. If the flatness was less than 10% of the future scribe depth the sample could be scribed otherwise it had to be made flat by shimming. Sample was removed from the support and, following the indication obtained by the previous measurement, suitable plastic stripes of shimming paper with different controlled thickness (from 5 to 50 μm), were applied between the support and the sample in appropriate positions. Afterwards flatness was further measured and if again it was not less than 10% of scribe depth, the shimming procedure was repeated with a different shims configuration until the requirement was respected. Once the samples were made flat the scribing could take place.

The diamond tool was positioned at 20 μm from a point on the sample surface and the linear motion machine activated. The tool was progressively brought closer to the sample by step of few microns (generally no more than 5 μm) until approximately half of the gauge width was scribed. That was considered the zero condition from which start cutting a notch of the desired depth. Doing so, a scratch with an average depth closer to the nominal value could be obtained despite of the flatness inaccuracy. Scribes were machined at a low speed of 100 mm/min by several progressive cutting steps, 10 μm deep apart from the last two that were 5 μm deep, down to the desired depth. That reduced residual stresses associated to swarf removal and assured a well defined notch cross section shape (see Fig. 3.7). V notch with 60° included angle, three different root radii (5 μm, 25 μm and 50 μm) and five different depths (25 μm, 50 μm, 100 μm, 150

µm and 185 µm) were introduced into tension and bending samples in clad and unclad condition. The notch depth was limited to the maximum value of 185 µm since the diamond tip was 200 µm long and the cutting deeper than the tip length could damage the tool. Two examples of notch cross section shape are shown in Fig. 3.7.

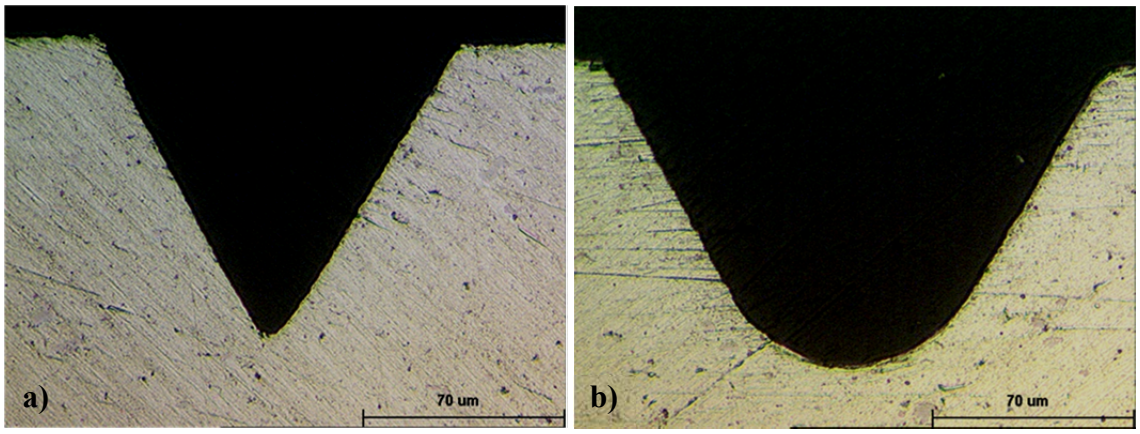

Fig. 3.7: Cross section shape of diamond tool machined notches: 100 µm deep 5 µm root radius notch (a), 100 µm deep 50 µm root radius notch (b)

The scribing procedure, developed using diamond tipped tools, was capable of producing rounded V-shaped notches tens of microns deep with very regular and controllable cross sections (Fig. 3.7). Scribe marks had to be introduced on the sample surface cutting the material to minimise the amount of plasticity and residual stresses induced by the scribing process. Those induced changes in the local mechanical conditions of the material, as they influence the crack development at the notch root, have to be avoided to investigate the relation between the scribe geometry and the fatigue life of scratched samples. The swarfs coming off the sample surface during the scribe machining and the absence of material piling up at the notch flanks (see Fig. 3.7) seemed to prove the cutting nature of the developed scribing procedure. Moreover the residual stress fields around machined scribes of different geometry were measured by Khan [1] using synchrotron X-ray diffraction and nanoindentation technique. Scribes machined by diamond tipped tool showed negligible level of tensile residual stresses and work hardening at their roots [1]. However damaged diamond tools, like the one used by Morency for his fatigue test campaign [11], could produce scratches ploughing the material on the sample surface. Ploughed scribes, showing material piling up at notch flanks, were characterised by severe tensile residual stresses and work hardening around their roots in comparison with cut scribes [1].

3.1.2.1 Scribe depth measurement

The accuracy of the scribing procedure developed was examined afterwards, controlling the geometry of scratches already machined on samples. All samples had their scratch depth checked using a standard optical microscope and selected specimens had the whole scribed profile examined by a scanning confocal microscope. The entire scratch cross section geometry could be measured by the scanning confocal device along the entire scribe length. Since that procedure was very time consuming, just a selection of samples was analysed mainly to check root radius and open angle. Scratch depth measurement was performed using a standard optical microscope with a

calibrated focus. After positioning the sample on the microscope, the bottom of the notch was brought into focus, and the distance, on the graduated scale, recorded. The focus was adjusted to bring the sample surface into focus, the distance recorded again and the depth determined by simple subtraction. Notch depth was measured at three points along the scratch length: 5 mm from the left edge (denominated left point), on the sample centre line (centre point) and 5 mm from the right edge (right point). The microscope graduated scale had a sensitivity of ±1 µm but bigger measurement errors were expected because of difficulties associated with bringing into focus notch root and sample surface. In fact in particular with the deepest and sharpest notches it was not an easy task to determine when the scratch bottom line was in focus due to light reflection of the notch flanks.

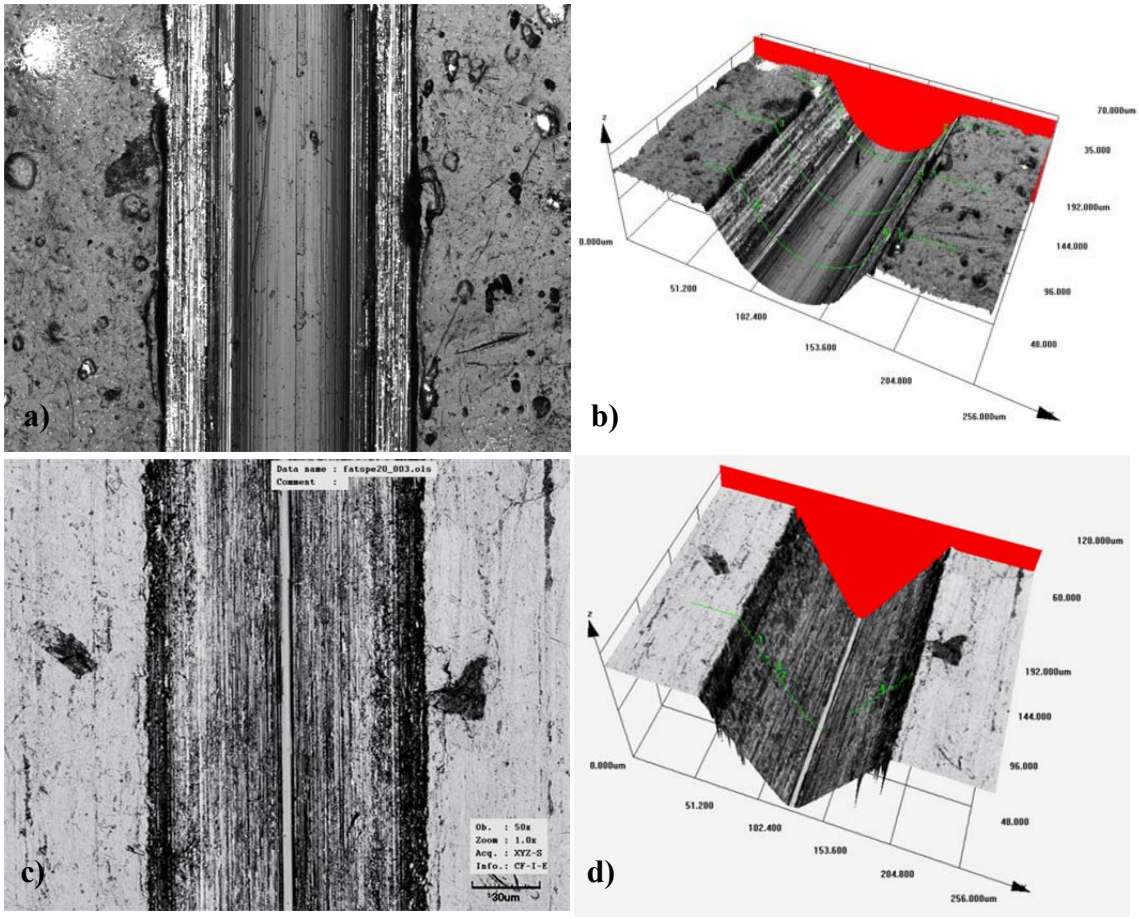

Fig. 3.8: Unclad 100 µm deep 50 µm root radius optical picture (a), scanning confocal profile (b); clad 50 µm deep 5 µm root radius optical picture (c), scanning confocal profile (d)

On the other hand surface roughness, made arbitrary the definition of focus depth, in particular in unclad samples where corrosion pits were present due to chemical milling (Fig. 3.8 (a)). To increase accuracy several measurements were performed on every point and the mean value recorded. Moreover notch depth measurements were carried out during post-fracture fractography by SEM as well. Optical calibrated microscope measurements taken on every sample together with the maximum absolute and relative errors from nominal values are reported in Table A.3.1 of appendix 3.1. As can be seen the relative error was always less than 10% and worst case values are obtained for shallower notches (50 µm deep with 5 µm of maximum error).

Using the scanning confocal microscope it was possible to obtain a detailed 3D map of the notch. Examples are displayed in Fig. 3.8 together with top views of the analysed areas for a 100 µm deep 50 µm root radius scribed unclad sample and a 50 µm deep 5 µm root radius scribed clad sample respectively. Difference in surface roughness between clad and unclad (stripped by chemical milling) are visible comparing Fig. 3.8 (a) and (c). Clad specimens had a better surface finish than unclad ones, where corrosion pits from chemical milling were present. The accurate and well defined shape of the diamond tool notch is pointed out by in Fig. 3.8 (b) and (d) where the strange sharp fissures are just noise effects created by light reflection. Example of scribe profile measurements taken at a specified section along the scratch length are shown in Fig. 3.9 for a 50 µm deep 50 µm root radius scribed unclad specimen and a 100 µm deep 5 µm root radius scribed clad one.

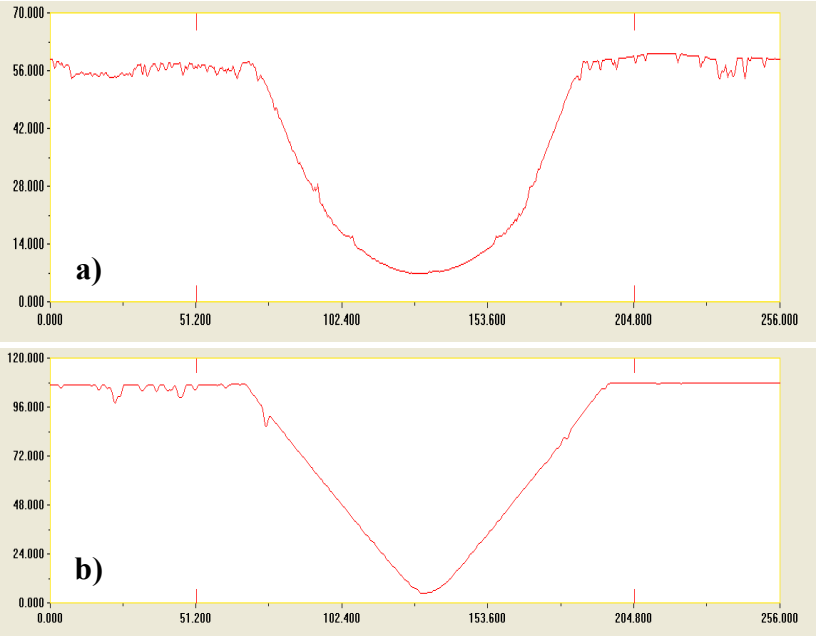

Fig. 3.9: Scanning confocal unclad 50 µm deep 50 µm root radius scratch profile (a), clad 100 µm deep 5 µm root radius scratch profile (b)

3.2 Fatigue testing

All tests were performed under the same nominal loading conditions. That is the same nominal cyclic stress was applied at the gauge section despite the load type, sample and geometry. Pure bending load is resolved into a zero mean stress distribution linearly variable across the thickness with maximum absolute values at the sample surface. In this case the nominal stress condition was referred to the surface stress and for comparison it had to have the same value of an uniform tensile stress. Tension and bending samples were tested under constant amplitude cyclic load with nominal stress ratio R ($R=\sigma_{min}/\sigma_{max}$) of 0.1 and maximum stress of 200 MPa at the gauge section. The cyclic load had to be representative of the constant amplitude fatigue load imposed on a civil aircraft fuselage by the pressurisation at every flight. The cyclic stress level was chosen because it generated, on unscribed samples under tensile load, fatigue lives

comparable to the average medium-range aircraft service life, extended by the aging programme (10^5 flights) [12]. A stress ratio of 0.1 instead of R=0 of the pressurisation cycle was used to avoid problems of zero load application on a four point bending jig. In fact machine load control can be difficult at zero stress. Four additional tension samples containing the same notch geometry were fatigued under different nominal maximum stress (σ_{max}=100 MPa and 160 MPa) but equal R ratio to gather some preliminary information on stress effect in scribed coupon fatigue life.

Difficulties arose in the clad sample gauge stress definition. The sample section is constituted of two materials pure aluminium cladding and the 2024-T351 substrate with different mechanical properties. Fig. 3.10 shows the uniaxial stress-strain curves of Al 2024-T351, that forms the substrate, and of cladding that was assumed to be aluminium with a purity of 80% (Al 1080) at the suggestion of the project sponsor. The substrate stress-strain data were measured as described in section 3.1.1, while cladding ones were supplied by Alcoa. Two curves are displayed for cladding: one without pre-stretching (ε_0=0%) and the other for a pre-stretching of a permanent strain of 2% (ε_0=2%), representing stretching procedure of T351 heat treatment. Due to material hardening, pre-stretched cladding shows a yield stress of 132 MPa in contrast with the lower value of non pre-stretched (10 MPa). As consequence the elongation at failure is reduced for the hardened material. Even if it has been increased by the heat treatment, the cladding yield stress is still nearly three times smaller than the substrate one (Fig. 3.10). This implies that once tension or bending test load is applied on clad samples the substrate remains elastic and clad layer undergoes to plasticity. Therefore cladding stiffness is reduced and the maximum stress that it can withstand is limited by its post-yielding behaviour (see stress-strain curve in Fig. 3.10). To equilibrate the external load applied by the machine the stiffer substrate has to carry additional elastic stress compensating for the limited stress acting on the clad layer.

In fact the test machine applies by means of its grips a displacement that corresponds to a continuum strain field across the gauge section, uniform for tension load and linearly varying for bending. At the same uniform strain value applied in tension, if both material are in elastic field the corresponding stresses will be identical in clad and substrate, but if the strain is large enough to plasticise cladding, different stresses arise, as can be seen from Fig. 3.10. At the strain that corresponds to the applied load, the stress in the clad sample gauge section will be discontinuous, resulting in larger stresses in the substrate and reduced ones in the cladding compared with the elastic case. That complicates the gauge stress definition. It was decided to consider a nominal equivalent stress that is the stress that the gauge section would withstand if the cladding was purely elastic and it is equivalent to the gauge stress of an unclad sample of the same size, if the substrate remains in the elastic field. This is equivalent to neglecting the clad layer and consider the sample just made of Al 2024-T351 and it is the general procedure adopted during component design.

Nominal equivalent stress definitions for tension (σ^{tens}_{nom}) and bending ($\sigma^{bend}_{nom\ max}$) loads are shown respectively in eq. (3.1) and eq. (3.2), where F_{ext} and M_{ext} are the externally applied tensile force and bending moment; A and I are the whole gauge section (including cladding) area and moment of inertia respectively and t is the section thickness. For comparison the nominal equivalent maximum stress in clad samples had

to be equal to the unclad samples one (that is 200 MPa) and the discontinuous and higher stress in the substrate was included into the cladding effect on fatigue life.

$$\sigma_{nom}^{tens} = \frac{F_{ext}}{A} \tag{3.1}$$

$$\sigma_{nom\ \max}^{bend} = \frac{M_{ext}}{I}\frac{t}{2} \tag{3.2}$$

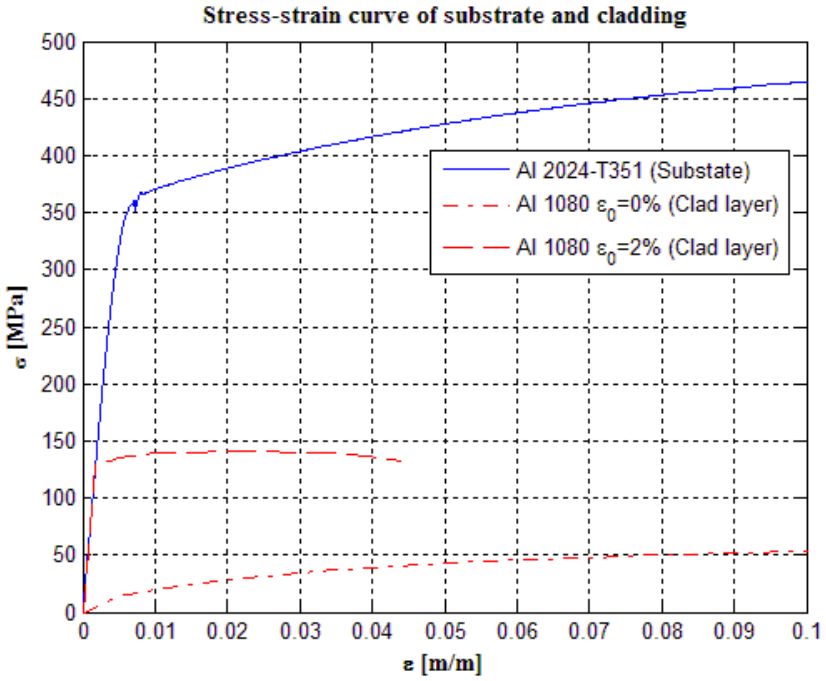

Fig. 3.10: Tensile behaviour of substrate and cladding material

Before testing strain measurements were taken to check the accuracy of fatigue test machines and to control the stress at sample gauge section. Strain gauges were bonded on the gauge section of four unscribed specimens (one for each condition clad, unclad, tension and bending) and the strains recorded during a static ramp load application from zero up to the load corresponding to the maximum load of fatigue cycle. A strain gauge, one each surface, was positioned in the middle of the gauge section of tension and bending samples, as shown in Fig. 3.11 and Fig. 3.12.

Strain as a function of applied load for clad and unclad tension samples are displayed in Fig. 3.11, while Fig. 3.12 shows the corresponding results for bending samples. Elastic and elastic-plastic prediction models based on San Venant beam theory are reported as well. Substrate and cladding mechanical behaviour were modelled using the material curves displayed in Fig. 3.10 for Al 2024-T351 and for Al 1080 with ε_0=2% respectively. A strain field (constant for tension and linearly variable across the thickness for bend loading) was assumed to act on the gauge section. For each cross section point the stress value corresponding to the local strain was obtained using the uniaxial stress-strain curves of clad and substrate materials (Fig. 3.10). Finally, once the stress field (discontinuous in clad samples for material unhomogeneity) acting on the gauge section was obtained, the section load, equal to the applied one for equilibrium

condition, was calculated by stress integration. Tension (F_{ext}^{tens}) and bending (F_{ext}^{bend}) applied loads were calculated using the formulae shown in eq. (3.3) and eq. (3.4) respectively. Section integrations were performed along sample thickness direction (y) in an inertial reference frame, that is with frame origin coincident with the section centre of gravity. W is the rectangular cross section width while t is the section thickness. In the case of pure tension load on clad samples, as the strain is constant across the section, integration turns into a simple addition of the load contribution given by the constant elastic stress ($E\varepsilon$) bore by the substrate section area (A_{sub}) plus that elastic-plastic given by cladding (σ_{clad}) on the two clad layer areas (A_{clad}). Cross section moment in bend loading condition is generated by the contact forces of the external loads introduced by rollers (see Fig. 3.14) multiplied by the spacing between upper and lower rollers (b). The bending moment consists of two terms in clad sampels: that caused by clad layer and the substrate elastic one. The latter turns into nothing more than the flexural stiffness of the substrate section, where I_{sub} is the substrate section moment of inertia, E the Young's modulus, and y_{bound} is the coordinate of the cladding-substrate boundary multiplied by the strain at the cladding-substrate boundary ($\varepsilon(y_{bound})$). The multiplying factor 2 in eq. (3.4) turns out because the force applied by the test machine, actuating two rollers (see Fig. 3.14), is twice the one introduced by a single roller. While stress integration is trivial for cladding tension sample, in the case of pure bending load, since strains are linearly variable across section thickness, numerical integration is required for the clad layer contribution (eq. (3.4)). That was performed with the aid of Matlab software. When unclad samples are considered eq. (3.3) and eq. (3.4) are still valid as long as the cladding terms are neglected.

$$F_{ext}^{tens} = \int_{-t/2}^{t/2} \sigma(\varepsilon) W dy = 2A_{clad}\sigma_{clad}(\varepsilon) + A_{sub}E\varepsilon \tag{3.3}$$

$$F_{ext}^{bend} = \frac{2}{b}\int_{-t/2}^{t/2} \sigma\left(\varepsilon(y)\right) W y dy = \frac{2}{b}\left(2W\int_{y_{bound}}^{t/2} \sigma_{clad}\left(\varepsilon(y)\right) y dy + \frac{I_{sub}E}{y_{bound}}\varepsilon(y_{bound}) \right) \tag{3.4}$$

As can be seen from Fig. 3.11 for the unclad tension sample the elastic model agrees perfectly with experimental measurements; moreover the agreement between the strain measured on opposite surfaces (strain gauge 1 and 2 respectively) shows the absence of bending due to grips misalignment. Two lines are displayed for clad sample: one elastic-plastic taking in account cladding plasticity and the other purely elastic representative of the assumptions made considering the nominal equivalent stress for clad samples (eq. (3.1)). The models are coincident when cladding is in elastic field and diverge nearly at 21 kN when clad plasticity begins. Due to the smaller global stiffness, samples with plasticised clad layer, have a gauge section strain 5% larger than the elastic case, when the same external load is applied. The substrate equilibrium stress is hence 5% higher in clad samples compared with unclad.

Both calculated curves over predict the experimental strain gauge measurements in clad sample (see Fig. 3.11). This error was thought to arise from bonding the strain gauges directly on the clad surface. Since the cladding shear stiffness is low and comparable with the tensile stiffness of the gauge, local measurement is affected by the gauge itself. Local surface strain is therefore reduced, compared to the internal one, by the gauge which resists to deformation and tends to compress the clad material that is easily deformed having low stiffness. So for the same external load applied strain values result smaller than predicted. The different thickness involves the application of higher

load on clad sample to obtain the same strain of an unclad one. The external fatigue tension load, the test machine had to applied to achieve the desired nominal gauge section stress, was calculated using the elastic model, or in other terms eq. (3.1), for clad and unclad samples.

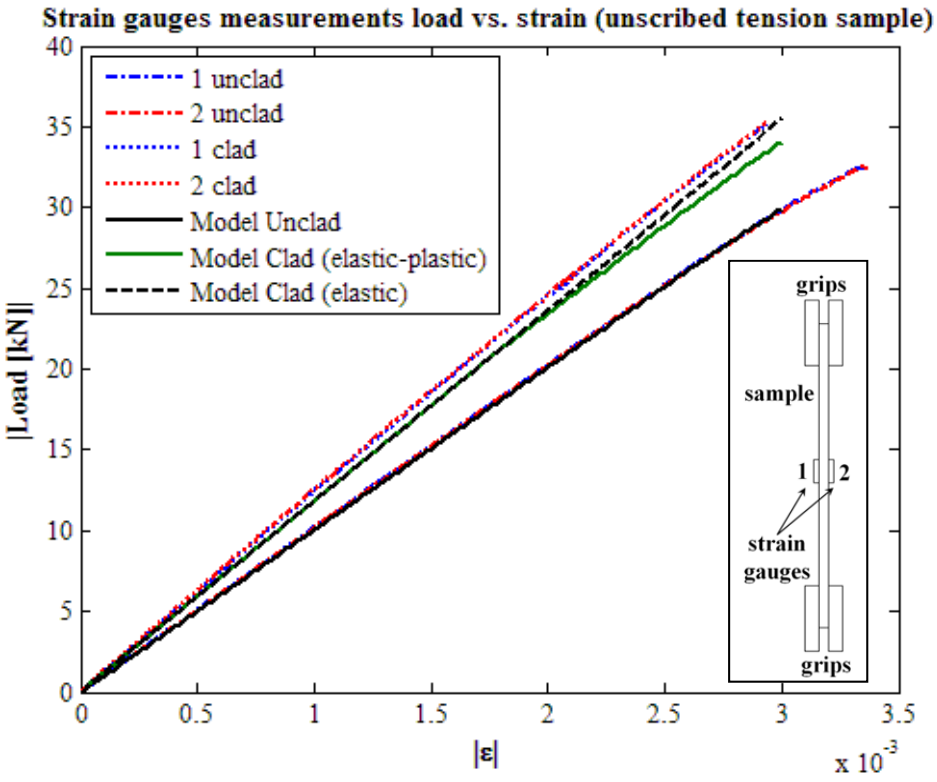

Fig. 3.11: Strain gauges measurements on unscribed tension sample

Fig. 3.12 shows strain gauge measurements for clad and unclad four point bending samples. As in the case of tension load measurements, the strains measured on opposite surfaces by strain gauge 1 and 2 are consistent, implying the existence of pure bending load at the gauge section of both unclad and clad samples. Elastic-plastic geometrical linear (indicated simply as model in Fig. 3.12) and elastic-plastic geometrical non linear model results for clad and unclad specimens are displayed in Fig. 3.12 as well. Elastic plastic models based on slender beam theory [13,14] (eq. (3.3) and eq. (3.4)) underestimate the experimental applied force for a given strain value, even for unclad samples. This error was thought to be due to non linear effects caused by the large displacement underwent by the rollers during loading (10 times the sample thickness). The roller displacements and the consequent sample deformations make the contact points between the specimen and the rollers change locations on the roller circumference reducing the effective couple arm (*b*). The effective bending moment introduced at a given external force value is therefore decreased causing a fictitious enhancement of sample stiffness (Fig. 3.12).

For that reason the measured gauge section strain is smaller than that calculated by the geometrical linear model. Because of the large displacements, the change of the roller force application point during loading was not negligible, and the assumption of small structure displacement became invalid. Following such assumption, if the

structure displacement is small compared with the problem geometrical characteristic size, external loads can be considered applied on the non deformed configuration during the whole loading event. Changes in force application point locations were included into a beam theory model developing a geometrical non linear prediction. The applied force corresponding to a given bending strain field was calculated again by means of eq. (3.4) but the couple arm (b) was considered function of the roller displacement (d) recorded throughout the loading procedure. Neglecting in first approximation the effect of the sample deformation, consistently with the small deformation hypothesis, the couple arm can be expressed by eq. (3.5) where b_0 and $2r$ are respectively the horizontal and vertical distances between the roller centres in the zero load configuration when roller are in contact with the sample surface.

$$b(d) = b_0 - 2r\frac{d}{b_0} \tag{3.5}$$

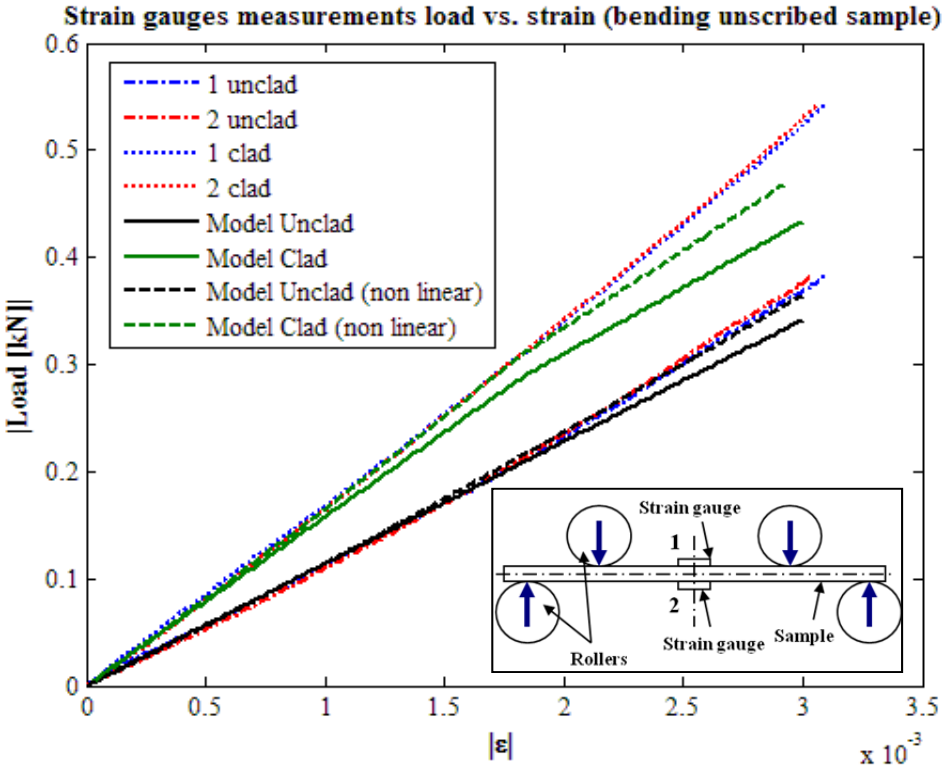

Fig. 3.12: Strain gauges measurements on unscribed bending sample

The geometrical non linear model accurately predicts the mechanical response of unclad sample in bending as can be seen from Fig. 3.12. In the case of clad samples both geometrical linear and non linear models, that take into account the clad layer local plasticity, underestimate strain gauge values. As under tension loading, the error was imputed to strain gauges bounded directly on the clad surface. Cladding plasticity produces a loss of sample stiffness as confirmed by a slope reduction in the external force-strain curves of prediction models. Cladding plasticity effects do not seem so evident on strain gauge measurements. The elastic models including the non linear effects of force application point changes were used to calculate the fatigue load to achieve the desired nominal gauge section stress for clad and unclad samples.

All samples had their gauge section thicknesses measured by a calliper before testing. Sample edges were rounded with emery to remove burrs and reduce corner stress concentration to prevent crack initiation at those sites. Emery with grit size of 240 was used to give the rounded shape and the finer 1200 to give a suitable surface finish.

3.2.1 Tensile fatigue testing

Tension fatigue tests were performed on a 100 kN servohydraulic test machine. Fig. 3.13 shows a dogbone tension sample set on the machine during fatigue test. Samples were gripped by hydraulic jigs after they were correctly aligned with the load axis. A total of 49 tensile specimens were tested following the text matrix reported in Table 3.3. All tests were carried out at room temperature in lab air, at a frequency of 10 Hz, under constant amplitude cycles with R=0.1 and resulting in σ_{max}=200 MPa at the gauge section. Fatigue effect of scribes with a combination of five different depths (25 µm, 50 µm, 100 µm, 150 µm, 185 µm) and three root radii (5 µm, 25 µm, 50 µm) was investigated in clad and unclad samples. Unscribed specimens (0 µm scribe depth in Table 3.3) were fatigued as well to have reference lives for comparison. Two samples were tested under each test condition apart from specimens with scribes 25 µm deep, 25 µm root radius.

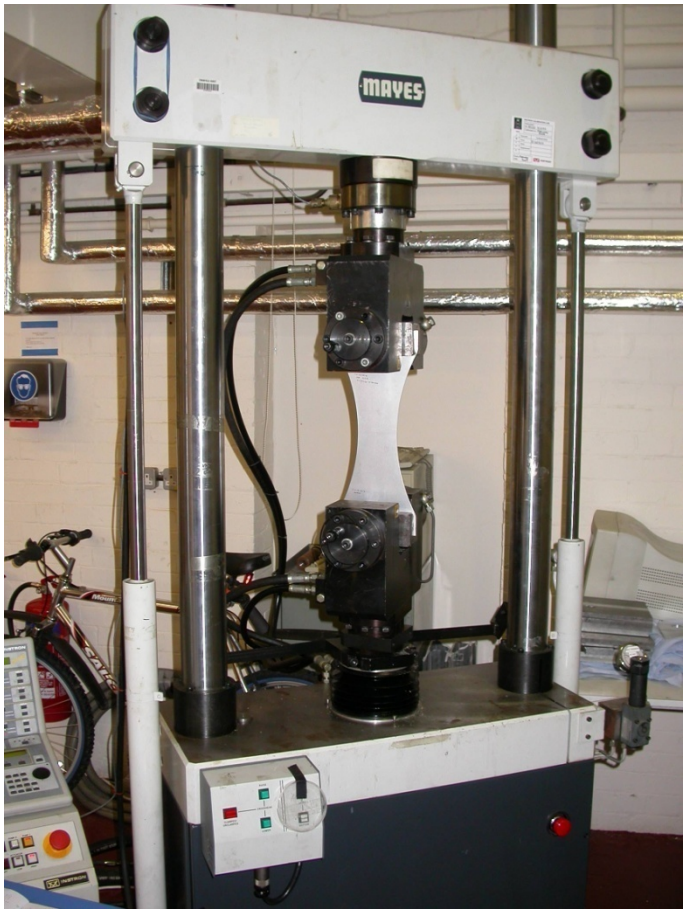

Fig. 3.13: Fatigue tension test machine setup

Table 3.3: Fatigue tension test matrix

Tension		Scratch depth [µm]					
Material supplying	**Scratch root radius [µm]**	0	25	50	100	150	185
Clad	5	2	1	2	2	2	2
	25		1	2	1	1	2
	50		2	2	2	2	2
Unclad	5	2	1	2	2	2	2
	25		1	-	-	-	-
	50		1	2	2	2	2

In order to throw light upon the effect of different maximum gauge stress on scribed sample fatigue life an additional small preliminary test campaign was carried out under tension load (see Table 3.4). Two clad and two unclad 185 µm deep and 5 µm root radius scribed samples were tested under constant amplitude tension load with a stress ratio R=0.1 and a resolved maximum gauge stress of respectively σ_{max}=100 MPa and σ_{max}=160 MPa following the text matrix showed in Table 3.4.

Table 3.4: Fatigue tension with different maximum stress test matrix

Different max stress in tension			Max nominal gauge stress [MPa]	
Material supplying	**Scratch root radius [µm]**	**Scratch depth [µm]**	100	160
Clad	5	185	1	1
Unclad			1	1

3.2.2 Bending fatigue testing

A suitable four point bend jig was designed and it is schematically illustrated in Fig. 3.14. The gauge section between the upper rollers, where the constant bending moment acts, was a 80x80 mm square and the arm of the force couple generating bending, that is the axial space between upper and lower rollers, was 50 mm. Lower rollers were properly profiled with external shoulder (see Fig. 3.14) to accommodate samples and prevent lateral movement during load application. Fig. 3.15 shows the four point bend sample set on the fatigue machine. Tests were performed on a servohydraulic test machine with maximum load capacity of 20 kN at room temperature in lab air. The upper rollers were free to rotate on two supports and kept in place by rubber bands while the lower ones were fixed and firmly connect to a support bar. Samples were accommodated on the lower jig where the roller shoulders and metal supports at their extremity prevented lateral and axial movements (Fig. 3.15).

Anti-fretting graphite grease was smeared on the rollers and sample surfaces in contact contact to reduce friction preventing wear and ensuring a smooth load transfer. Due to the large vertical displacements involved in this kind of test, load was applied at a frequency of 1 Hz increasing the testing time. 26 bending clad and unclad specimens in total were fatigued with R=0.1 and a maximum gauge stress on the sample surface of σ_{max}=200 MPa following the text matrix of

Table 3.5. In contrast to tension tests, scratches with just two different root radii (5 µm and 50 µm) and three depth values (50 µm 100 µm and 185 µm) were tested.

Unscribed specimens (0 µm scratch depth) reference fatigue lives were obtained, testing just one sample each in the clad and unclad conditions.

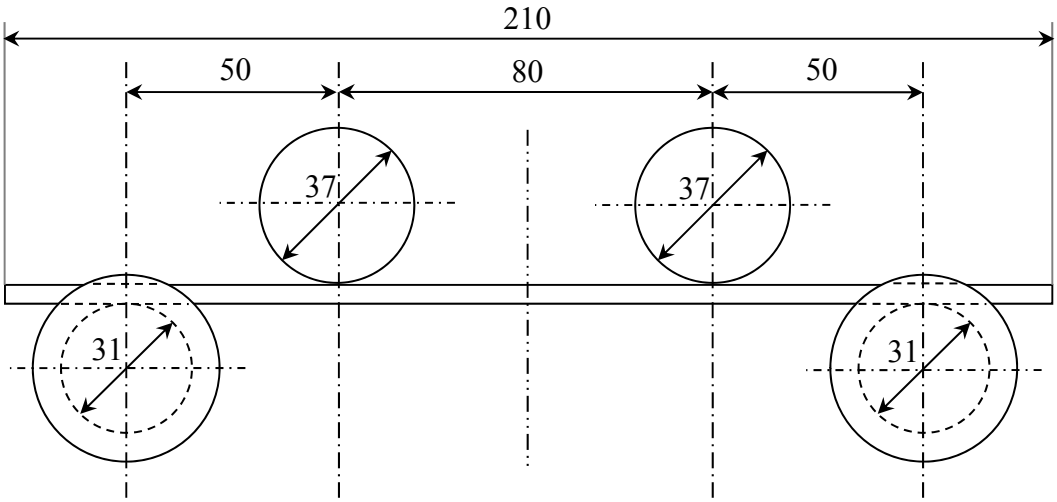

Fig. 3.14: 4 point bend jig configuration sketch (dimensions in mm)

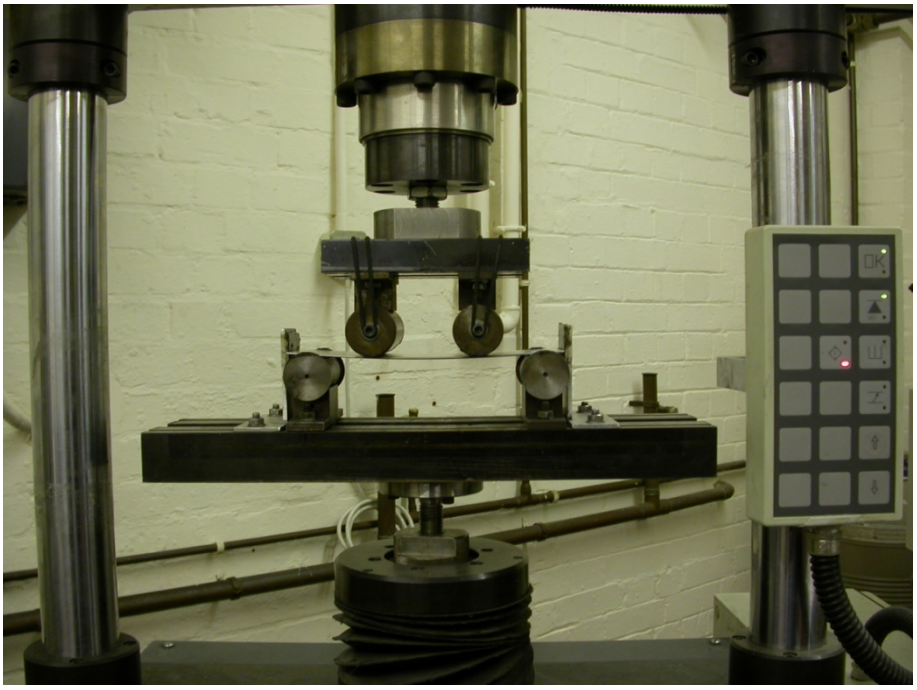

Fig. 3.15: 4 point bend fatigue test machine setup

Table 3.5: Fatigue 4 points bend test matrix

Bending		**Scratch depth [µm]**			
Material supplying	**Scratch root radius [µm]**	0	50	100	185
Clad	5	1	2	2	2
	50		2	2	2
Unclad	5	1	2	2	2
	50		2	2	2

3.3 Microscope analysis

Microscope investigations were performed on tested and untested samples in order to gather information about machined scratch geometry and rationalise the fatigue crack nucleation and propagation process from scribe marks. The analyses were carried out by means of both optical and scanning electron microscope on all samples.

Firstly notch section geometries produced by diamond tool were characterised on specimens cut out from untested samples. Afterwards scratches, introduced on tested tension and joint samples during Airbus internal investigations on the effect of scribe marks on component fatigue lives, had their cross sections analysed as well. Airbus tested both reproducible scribes with regular geometry produced by Electrical Discharge Machining (EDM) and irregular scratches, generated by a cutting knife, similar to the scribe marks found on in-service aircraft. The cross section geometry of Airbus EDM and cutting knife scribes were investigated on specimens cut out from tested samples, but not failed from the scratch.

Fracture morphology and crack characteristics were recorded by fracture surface inspections on fatigued specimens and the effects of different notch geometries on crack evolution compared. The size and shape of final fatigue cracks were recorded as well. Quantitative crack growth analysis was performed. Since the difficulty in monitoring fatigue crack growth rate during the fatigue tests, crack growth measurement was carried out after failure by striation counting on specimen fracture surface. After failure the entire fracture surface was cut out from the samples and, once cleaned in alcohol bath with ultrasound for about two minutes, observed under the high resolution FEG SEM.

3.3.1 Scribe section measurement

Different diamond tool scribe sections on clad and unclad aluminium were measured to verify if the machined notch geometry shape was consistent with the nominal desired one. Four diamond scribes were introduced respectively on the gauge section of one clad and one unclad four point bend rectangular specimen. The four scribes were 50 and 100 μm deep with 5 and 50 μm root radii and were cut across the entire gauge section width. Small samples containing each scribe type were extracted and mounted in epoxy resin for scribe section observation under optical microscopy. The samples obtained were ground using emery with progressively finer grit: 240, 1200 and 8000. Final polishing was done using 6 μm diamond polder suspension.

Optical microscopy using a magnification of 200X was employed to measure notch depth, root radius and included angle with an image processor software. Fig. 3.7 shows examples of diamond tool notch section shapes. Geometry was very well defined and very close to the nominal rounded V notch one with an included angle of 60°.

EDM notch section characterisation was also performed on joint and dogbone samples scribed by Airbus. Airbus chose the electrical discharge machining to produce regular scribes by material removal, minimising the amount of residual stresses induced by the scribing procedure. EDM scribing procedure was performed, by a particular knife

like tool, controlling just the notch depth. No information about scribe section geometry was available. It was decided therefore to carry out some investigations using lap joint and tension samples fatigue tested internally in Airbus but not failed from the scribe mark. Measurements on scribe marks produced by hand with a cutting knife on fatigued samples were performed too. They were introduced on samples and fatigue tested internally in Airbus to investigate the effect of scratches similar to the ones found in service, produced during sealant removal procedure. Such scratches, unlike diamond tool and EDM scribes, were characterised by local material plasticity and consequent residual stresses pointed out by the presence of piled up metal at their flanks (chapter 4). Scribe segments were cut out from tested samples and the specimens for cross section observation were prepared and polished following the same procedure described above for diamond tool scribes. Section analysis was performed under optical microscope (magnification 200X) and measurements with the image processor software.

Table 3.6: Scribe marks section characterisation specimens cut from Airbus fatigue tested samples

Specimen		**Scribe mark**	**Crack nucleation point**
Fatigue specimen	Microscope specimen		
Lap joint 1 mm thick	J9	EDM 60 µm	rivet row
	J12	EDM 80 µm	rivet row
Lap joint 1.2 mm thick	J13	EDM 30 µm	rivet row
	J16	EDM 30 µm	rivet row
	J19	razor knife	rivet row
Tension clad (Dogbone)	D3	EDM 39 µm	edge
	D14	knife, 90°, 60 µm	edge
	D16	knife, 90°, 160 µm	edge
	D17	knife, 45°, 60 µm	edge
	D20	knife, 45°, 120 µm	edge

Table 3.6 shows the list of all the scribe mark section geometries, cut from Airbus fatigued samples and measured under the optical microscope. Microscope observed specimens nomenclature, joint and tension fatigue specimens they were cut from, scribe mark type and failure crack nucleation point are reported in Table 3.6 as well. For EDM scribes the nominal notch depth is indicated in µm while for knife cuts together with notch depth the cutting angle is reported. The cutting angle was defined as the angle included between the knife blade and the scribed surface. It was demonstrated that diamond tool machining and EDM can produce scribes with well defined section shape and controlled dimensions (chapter 4). Also the hand made knife cuts showed a rounded V notch shape but it was quite irregular with substantial piled up material at the scratch flanks (chapter 4). The piled up material seemed to point out the presence of considerable plasticity involved in the cutting procedure.

3.3.2 Fracture surface investigation

Fracture surface observation was carried out on fatigued tension and bending samples by means of scanning electron microscope. After failure the entire fracture surface was cut out from the samples and, once cleaned in alcohol bath with ultrasound for about two minutes, observed under the high resolution FEG SEM. All fatigued samples had their fracture surfaces observed and data from at least one surface for each

kind of fatigue tested specimen were recorded. Failure surface morphology, was investigated in order to gather information on crack development and evaluate the effect of different scribe geometry, load condition and cladding on crack evolution from nucleation sites to final fracture. Fracture surface features were correlated with the corresponding crack growth stage.

Unfailed samples were sectioned and examined under microscope for non propagating cracks. Scribe internal surface was examined under the SEM for evidences of non propagating cracks. Portions containing the entire scribe length were cut out from fatigue samples, polished in ultrasounds alcohol bath and observed under SEM. Possible non propagating cracks had their length measured by image processor software. During SEM fracture surfaces observation, quantitative measurements of final cracks size and shape were carried out evaluating how notch severity affects the crack shape.

3.3.3 Crack growth rate measurements

A trial explorative test campaign was carried out to verify if the replica technique was able to replicate the entire front of a crack nucleated by a scratch and propagating inside the sample thickness. Fatigue crack growth tests were performed on aluminium 2024-T351 clad and bare samples from an old batch of material. Samples were scribed following the test matrix of Table 3.7.

Table 3.7: Crack growth test matrix

Crack growth		**Scratch depth [μm]**
Sample type	**Scratch root radius [μm]**	200
Clad	5	4
Unclad	5	4

Small rectangular specimens 300 mm X 10 mm (see Fig. 3.16) were fatigued under tension load with R=0.1 and σ_{max}=200 MPa. These reduced size samples were obtained by scribing two 300 mm X 80 mm rectangular samples, one clad and one unclad using the above procedure and subsequently cutting them into 4 strips, 10 mm wide. The reduced sample width allowed replication of crack shape with a moderate quantity of material. All the scribes were 200 μm deep with a 5 μm root radius. Fatigue tests were performed on a servohydraulic Instrion test machine with maximum load capacity of 20 kN. Fig. 3.16 shows the crack growth test set up during replica material application. Tests were repeatedly stopped at maximum load, and the black rubbery replica material was spread into the notch (as displayed in Fig. 3.16). Replicas were examined to measure crack depth under the SEM. Optical fracture surface observation was performed as well.

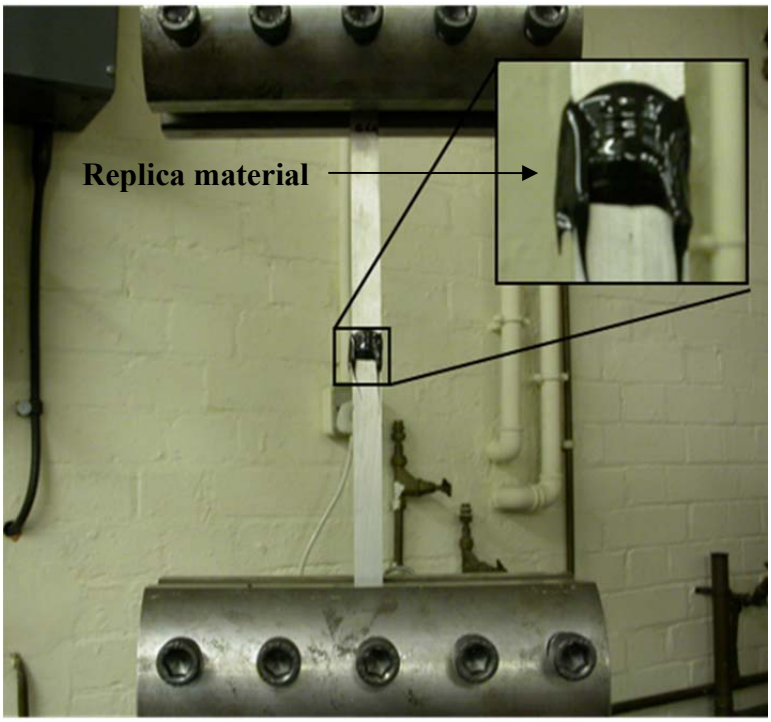

Fig. 3.16: Crack growth test set up and replica material

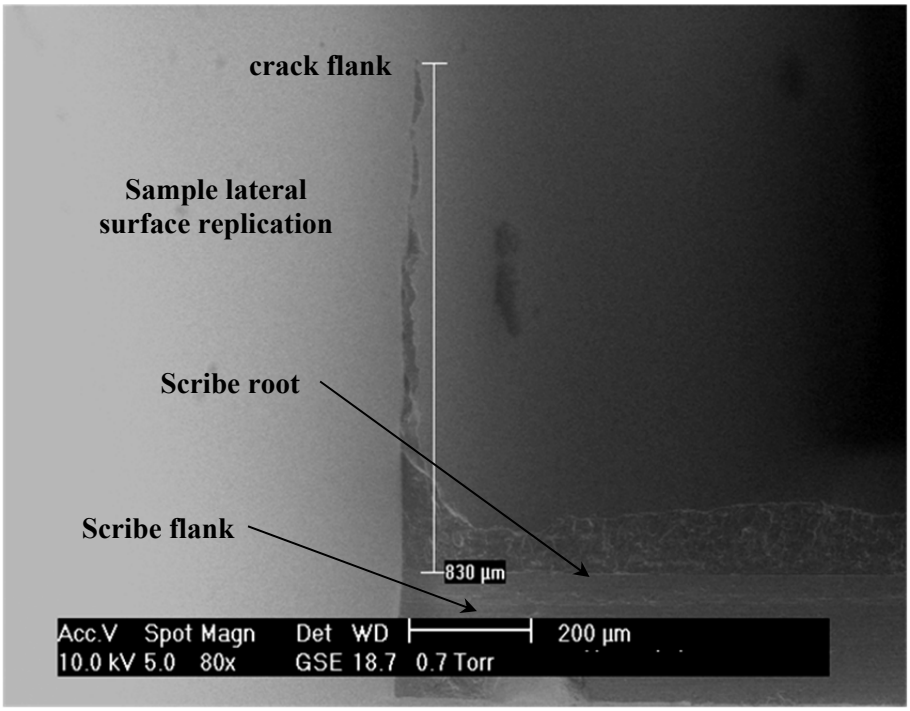

Fig. 3.17 : Unclad sample edge notch replication under max load at 97% of fatigue life (SEM picture)

Fig. 3.17 shows an SEM picture of crack replica taken from an unclad sample at 97% of its fatigue life. It can be seen that replica material can reproduce the crack flank features but it is not capable of seeping into the full depth of the crack. Optical fracture observations showed a final crack deeper and different in shape compared with the

replicated one in Fig. 3.17. It is very unlikely that the crack shape and size change considerably from 97% to 100% of fatigue life. Moreover the L shape the crack shows close to the sample lateral edge is very unusual for a corner crack having generally a quarter elliptical front (Fig. 3.17). The rationale explanation is that replica material is not able to penetrate deep into the flaw but can replicate just few microns from the notch or sample surface.

It was decided to obtain crack growth rate data by means of post failure striation counting. Striation spacing was measured directly after fatigue testing on fatigue fracture surfaces using a high resolution FEG SEM. Measuring the gap between striations, crack growth rate estimation in term of crack length increment per number of cycles can be obtained. That method is based on the assumption, verified experimentally [15,16], that striations are marks left every fatigue cycle.

Striation counting was performed on fracture surface of selected tension and bending samples. The entire fracture surface of bending and tension specimens after cutting out from the sample and cleaning in alcohol bath with ultrasound was introduced in the SEM chamber. A particular sample width coordinate was selected as gauge section for the SEM measurement. Striation spacing was measured where the final crack front was deeper into the sample thickness.

Crack depth, that is the crack size along the thickness, measured from the notch root, was divided into at least 10-15 intervals for tension samples and 15-20 for the deeper cracks in bending specimens. Three different spots, where striations were identified, were selected for every crack depth interval. Pictures were taken at each spot, with magnification up to 130000X, and a total of 3 striation spacing measurements performed for each crack depth. The distance between 11 striation peaks was measured in the SEM and the local crack growth rate, expressed in μm/cycle, was readily obtained dividing by ten (the striation number). A total of 8 tension samples, 4 clad and 4 unclad, containing respectively 185 μm and 50 μm deep scratches with 50 μm and 5 μm root radius were analysed. Crack growth rate was measured on just 4 bending samples: a clad and an unclad 185 μm deep 5 μm root radius scribed specimen, a 185 μm deep 50 μm root radius and a 50 μm deep 5 μm root radius scribed unclad sample. In order to confirm results obtained for tension samples and assess the effect of different parameters, analyses were performed changing one parameter per time among cladding notch depth, and root radius.

Appendix 3.1

Table A.3.1: Diamond tool scribe depth measurements by optical microscope

Tension samples	Left [µm]	Centre [µm]	Right [µm]	Mean [µm]	Nominal [µm]	Error [µm]	Error [%]
T-U-185-5-1	185	177	190	184.00	185	8	4.32
T-U-185-5-2	178	185	183	182.00	185	7	3.78
T-U-150-5-1	150	155	156	153.67	150	6	4.00
T-U-150-5-2	152	150	155	152.33	150	5	3.33
T-U-100-5-1	101	98	99	99.33	100	2	2.00
T-U-100-5-2	101	97	100	99.33	100	3	3.00
T-U-50-5-1	54	48	48	50.00	50	4	8.00
T-U-50-5-2	54	46	48	49.33	50	4	8.00
T-U-25-5-1	25	25	24	24.67	25	1	4.00
T-U-25-25-1	24	26	26	25.33	25	1	4.00
T-U-185-50-1	182	187	187	185.33	185	3	1.62
T-U-185-50-2	189	187	188	188.00	185	4	2.16
T-U-150-50-1	150	153	148	150.33	150	3	2.00
T-U-150-50-2	153	148	151	150.67	150	3	2.00
T-U-100-50-1	101	105	105	103.67	100	5	5.00
T-U-100-50-2	96	99	102	99.00	100	4	4.00
T-U-50-50-1	49	55	51	51.67	50	5	10.00
T-U-50-50-2	51	47	49	49.00	50	3	6.00
T-U-25-50-1	26	25	26	25.67	25	1	4.00
T-C-185-5-1	180	178	182	180.00	185	7	3.78
T-C-185-5-2	182	177	189	182.67	185	8	4.32
T-C-150-5-1	143	146	145	144.67	150	7	4.67
T-C-150-5-2	146	146	148	146.67	150	4	2.67
T-C-100-5-1	96	97	103	98.67	100	4	4.00
T-C-100-5-2	95	98	103	98.67	100	5	5.00
T-C-50-5-1	50	49	52	50.33	50	2	4.00
T-C-50-5-2	51	52	48	50.33	50	2	4.00
T-C-25-5-1	25	24	23	24.00	25	2	8.00
T-C-185-50-1	185	184	189	186.00	185	4	2.16
T-C-185-50-2	187	190	188	188.33	185	5	2.70
T-C-150-50-1	151	154	147	150.67	150	4	2.67
T-C-150-50-2	144	148	152	148.00	150	6	4.00
T-C-100-50-1	102	107	104	104.33	100	7	7.00
T-C-100-50-1	99	104	104	102.33	100	4	4.00
T-C-50-50-1	55	52	54	53.67	50	5	10.00
T-C-50-50-2	54	53	48	51.67	50	4	8.00
T-C-25-50-1	26	24	24	24.67	25	1	4.00
T-C-25-50-2	24	26	25	25.00	25	1	4.00
T-C-185-25-1	184	181	188	184.33	185	4	2.16
T-C-185-25-2	185	183	189	185.67	185	4	2.16
T-C-150-25-1	153	155	152	153.33	150	5	3.33
T-C-100-25-1	98	98	97	97.67	100	3	3.00
T-C-50-25-1	52	53	52	52.33	50	3	6.00
T-C-50-25-2	51	52	48	50.33	50	2	4.00
T-C-25-25-1	26	24	26	25.33	25	1	4.00

Different max stress tension samples							
T-U-185-5-1-(160MPa)	183	184	182	183.00	185	3	1.62
T-U-185-5-1-(100MPa)	184	186	183	184.33	185	2	1.08
T-C-185-5-1-(160MPa)	186	182	183	183.67	185	3	1.62
T-C-185-5-1-(100MPa)	184	185	184	184.33	185	1	0.54
Bending samples							
B-U-185-5-1	187	182	183	184.00	185	3	1.62
B-U-185-5-2	188	190	186	188.00	185	5	2.70
B-U-100-5-1	99	103	100	100.67	100	3	3.00
B-U-100-5-2	101	97	98	98.67	100	3	3.00
B-U-50-5-1	48	47	49	48.00	50	3	6.00
B-U-50-5-2	48	50	49	49.00	50	2	4.00
B-U-185-50-1	188	189	183	186.67	185	4	2.16
B-U-185-50-2	184	185	190	186.33	185	5	2.70
B-U-100-50-1	103	104	102	103.00	100	4	4.00
B-U-100-50-2	103	99	102	101.33	100	3	3.00
B-U-50-50-1	55	51	49	51.67	50	5	10.00
B-U-50-50-2	53	54	52	53.00	50	4	8.00
B-C-185-5-1	186	183	182	183.67	185	3	1.62
B-C-185-5-2	183	188	188	186.33	185	3	1.62
B-C-100-5-1	102	104	101	102.33	100	4	4.00
B-C-100-5-2	104	100	104	102.67	100	4	4.00
B-C-50-5-1	51	52	47	50.00	50	3	6.00
B-C-50-5-2	48	54	49	50.33	50	4	8.00
B-C-185-50-1	185	188	189	187.33	185	4	2.16
B-C-185-50-2	183	185	187	185.00	185	2	1.08
B-C-100-50-1	103	101	97	100.33	100	3	3.00
B-C-100-50-2	98	103	103	101.33	100	3	3.00
B-C-50-50-1	50	53	49	50.67	50	3	6.00
B-C-50-50-2	53	55	51	53.00	50	5	10.00

References chapter 3

[1] Khan, M. K. *Scribe marks at fuselage joins-Determination of residual stress and effect of fatigue loading using nanoindentation and synchrotron X-ray diffraction*. PhD thesis, Open University, UK, 2009.

[2] ASTM International 2005, E 466-96 (Reapproved 2002). Standard practice for conducting force controlled constant amplitude axial fatigue tests of metallic materials.

[3] Furfari, D. Scribe Marks – A300 – IMA Dresden Tests. Airbus Technical Report, 2007.

[4] Airbus Material Specification AIMS 03-04-022, issue 4, October 2003.

[5] British Standard BS EN 573-3:2007. Aluminium and aluminium alloy - Chemical composition and form of wrought products - Part 3: Chemical composition and form of products, 2007.

[6] British Standard BS EN 2032-2:1994. Metallic materials - Part 2: Coding of metallurgical condition in delivery condition, 1994.
[7] British Standard BS EN 515:1993. Aluminium and aluminium alloy - Wrought products - Temper designations, 1993.
[8] Military Handbook, MIL-HDBK-5H. Metallic materials and elements for aerospace vehicle structures, Vol. 5H, Department of Defence, USA, 1998.
[9] Nowell, D. Dini, D. Duò, P. Stress analysis of V-notches with and without cracks with application to foreign object damage. *Journal of Strain Analysis for Engineering Design*, Vol. 38, No. 5, 2003, pp. 429-441.
[10] Walmsley, S. W. *Fatigue potential of tool scratches on clad 2024-T351 aluminium alloy*. M Sc thesis, Cranfield University, 2007.
[11] Morency, R. Fatigue crack initiation and growth from scratches in 2024 T-351 aluminium. M Sc Thesis Cranfield University, 2006.
[12] Bristow, J. W. The age of the plane. *Presented at Aerospace industries division institute of mechanical engineers*, April 1993 London, UK.
[13] I. S. Sokolnikoff. *Mathematical theory of elasticity*, 2nd ed. New York: McGraw-Hill, 1956.
[14] S. P. Timoshenko and J. N. Goodier. *Theory of elasticity*, 3rd ed. Singapore: McGraw-Hill, 1970.
[15] Schijve, J. *Fatigue of structures and materials*, Dordrecht: Kluwer Academic Publishers, 2001.
[16] Suresh, S. *Fatigue of materials*, 2nd ed. New York: Cambridge University Press, 2004.

Chapter 4
Experimental results

In the first part of the chapter fatigue test results are shown and explained for the two different load conditions: pure tension and pure bending. In the second part post failure quantitative and qualitative fractography analysis findings are pointed out. Fracture surface morphology and typical features were investigated as well as notch geometry and the occurrence of non-propagating cracks. Finally crack growth data obtained by striation counting are shown for different scribed samples. Results are just explained and described in the following sections.

4.1 Fatigue testing results

Scribed samples were positioned on fatigue machine and fatigued, under pure tension and 4 point bend loading, in load control condition. Tests were carried out up to complete failure. Sample complete failure was, therefore, selected as failure criterion and any fatigue life, obtained in this test campaign, has to be considered as the number of cycles required to completely break a given scribed sample. Hydraulic machines were set to interrupt the test as soon as the sample failed and the applied load dropped down to zero. Limitations on the maximum rollers stroke were adopted, in the case of bending tests where, because of the jig design (see Fig. 3.15), compressive load can be withstood by the structure even in presence of a broken sample. Once the maximum roller stroke was exceeded the machine stopped and returned into the standby position. Only the number of cycles to failure was recorded during fatigue testing. In fact attempts to monitor crack propagation during testing were made without satisfactory results since the three dimensionality of crack development from a long scribe marks rendered ineffective any in situ growth measurement techniques (see chapter 3). While tension specimens were found completely separated in two halves when the machine stopped, some bending samples remained integral connected by a small uncracked ligament of plasticised material. That configuration was considered the end of the test, that is the sample fatigue failure, and specimen were statically separated to allow fracture observation. If fatigue failure did not occur within a defined amount of cycles, tests were interrupted anyway and considered runout.

The effect of scribe geometry on fatigue behaviour of bending and tension samples under the predetermined loading condition, equivalent to a nominal maximum stress at the gauge section of σ_{max}=200 MPa and a stress ratio of R=0.1, can be evaluated comparing total fatigue lives of different scribed specimens. Cladding and loading influences can be assessed in term of fatigue number of cycles confronting respectively clad with unclad and tension with bending samples that contain scribes with the same geometry. To facilitate results comparison total fatigue number of cycles required to completely fracture a sample were reported in tables and graphs of the following section as function of notch depth and root radius for different supplying and load conditions. The results of the preliminary test campaign on the effect of different maximum gauge stress on scribed sample fatigue life were reported as well.

A sample code nomenclature was adopted to make easier specimen definition. Nomenclature, which with a combination of numbers and letters defines sample load condition, material supplying, introduced scribe geometry and different maximum nominal stress applied, is described in Table 4.1.

Table 4.1: Fatigue sample nomenclature decoding

Sample name:	**A-B-C-C1-D-(E)**	
	A	indicates the load condition (T=tension load, B=bending load)
	B	indicates the material supplying condition (C=clad, U=unclad)
	C	indicates the scratch depth in μm (e.g. 185 for a scratch 185μm deep; 0 for unscribed coupons)
	C1	indicates the scratch root radius in μm (e.g. 50 for a scratch with a root radius of 50μm)
	D	indicates the number of the sample with the same characteristics
	(E)	where present indicates a different load condition from the usual: σ_{max}=200 MPa and R=0.1 (e.g. (100 MPa) for a load corresponding σ_{max}=100 MPa and R=0.1)
Example: T-C-150-25-2	is the second of tension dogbone clad sample scribed with a 150 μm deep and 25 μm rood radius notch and tested at the conventional σ_{max}=200 MPa and the stress ratio R=0.1	

4.1.1 Tensile tests

Fatigue tension tests were performed up to sample complete failure apart from specimens that, after having achieved a life of about $7 \cdot 10^5$ cycles without failure, were considered runout and had their tests interrupted. Tension fatigue test results are reported in Table 4.2. There information on sample code and thickness (t), notch nominal geometry and failure site are shown together with the fatigue life defined as the number of cycles required to completely fracture the sample. Scribe rounded V shaped section geometry is defined in term of nominal notch depth (d), root radius (ρ) and open angle (θ). Life, expressed as percentage of the reference life (L_{ref}) that is the mean life of unscribed samples (clad and unclad respectively), and the corresponding percentage of life reduction from L_{ref} are displayed as well. Percentage life reduction was defined as the percentage difference between the life of the scribed sample and the reference one divided by the latter, $(L-L_{ref})/L_{ref} \cdot 100$. In the calculation of the unscribed samples mean life the life of specimens insensitive to scratches, that is those samples that even if scribed and failed at the scratch site showed fatigue life comparable to the unscribed ones, was included. Those specimens have their failure site indicated as "scratch site (minimum section)" in Table 4.2.

Table 4.2: Fatigue tension test results (σ_{max}=200 MPa and R=0.1)

Sample	t [mm]	d [μm]	ρ [μm]	θ [deg]	Failure site	Fatigue life [cycles]	Life as % of L_{ref}	Life reduction [%]
T-C-0-0-1	2	-	-	-	gauge section	411221	96.60	3.40
T-C-0-0-2	2	-	-	-	gauge section	377831	88.76	11.24
T-C-25-5-1	2	25	5	60	scratch site	278176	65.35	34.65
T-C-50-5-1	2	50	5	60	scratch site	60296	14.16	85.84
T-C-50-5-2	2	50	5	60	scratch site	64360	15.12	84.88

T-C-100-5-1	2	100	5	60	scratch site	33570	7.89	92.11
T-C-100-5-2	2	100	5	60	scratch site	34694	8.15	91.85
T-C-150-5-1	2	150	5	60	scratch site	18732	4.40	95.60
T-C-150-5-2	2	150	5	60	scratch site	18600	4.37	95.63
T-C-185-5-1	2	185	5	60	scratch site	12438	2.92	97.08
T-C-185-5-2	2	185	5	60	scratch site	15057	3.54	96.46
T-U-0-0-1	1.7	-	-	-	gauge section	251649	84.66	15.34
T-U-0-0-2	1.7	-	-	-	gauge section	393595	132.42	-32.42
T-U-25-5-1	1.67	25	5	60	scratch site	81914	27.56	72.44
T-U-50-5-1	1.65	50	5	60	scratch site	36359	12.23	87.77
T-U-50-5-2	1.65	50	5	60	scratch site	35189	11.84	88.16
T-U-100-5-1	1.65	100	5	60	scratch site	23665	7.96	92.04
T-U-100-5-2	1.65	100	5	60	scratch site	24679	8.30	91.70
T-U-150-5-1	1.65	150	5	60	scratch site	13391	4.51	95.49
T-U-150-5-2	1.65	150	5	60	scratch site	13407	4.51	95.49
T-U-185-5-1	1.7	185	5	60	scratch site	6849	2.30	97.70
T-U-185-5-2	1.7	185	5	60	scratch site	7611	2.56	97.44
T-C-25-25-1	2	25	25	60	scratch site	286563	67.32	32.68
T-C-50-25-1	2	50	25	60	scratch site	129424	30.40	69.60
T-C-50-25-2	2	50	25	60	scratch site	131186	30.82	69.18
T-C-100-25-1	2	100	25	60	scratch site	52529	12.34	87.66
T-C-150-25-1	2	150	25	60	scratch site	25344	5.95	94.05
T-C-185-25-1	2	185	25	60	scratch site	15322	3.60	96.40
T-C-185-25-2	2	185	25	60	scratch site	13772	3.24	96.76
T-U-25-25-1	1.67	25	25	60	scratch site (minimum section)	246478	82.92	17.08
T-C-25-50-1	2	25	50	60	scratch site (minimum section)	476920	112.03	-12.03
T-C-25-50-2	2	25	50	60	scratch site (minimum section)	436796	102.61	-2.61
T-C-50-50-1	2	50	50	60	scratch site	188345	44.24	55.76
T-C-50-50-2	2	50	50	60	scratch site	169514	39.82	60.18
T-C-100-50-1	2	100	50	60	scratch site	55347	13.00	87.00
T-C-100-50-2	2	100	50	60	scratch site	62389	14.66	85.34
T-C-150-50-1	2	150	50	60	scratch site	29899	7.02	92.98
T-C-150-50-2	2	150	50	60	scratch site	31940	7.50	92.50
T-C-185-50-1	2	185	50	60	scratch site	21278	5.00	95.00
T-C-185-50-2	2	185	50	60	scratch site	21070	4.95	95.05
T-U-25-50-1	1.74	25	50	60	runout	797159	-	-
T-U-50-50-1	1.65	50	50	60	scratch site	124177	41.78	58.22
T-U-50-50-2	1.65	50	50	60	scratch site	92764	31.21	68.79
T-U-100-50-1	1.65	100	50	60	scratch site	36589	12.31	87.69
T-U-100-50-2	1.65	100	50	60	scratch site	39816	13.40	86.60
T-U-150-50-1	1.65	150	50	60	scratch site	22345	7.52	92.48
T-U-150-50-2	1.65	150	50	60	scratch site	21761	7.32	92.68
T-U-185-50-1	1.65	185	50	60	scratch site	13874	4.67	95.33
T-U-185-50-2	1.65	185	50	60	scratch site	13966	4.70	95.30

Tension fatigue tests results are displayed in Fig. 4.1 where the effect of different notch geometry on fatigue life can be evaluated. Number of cycles required to completely fracture the samples are plotted in a semi-logarithmic scale as function of

scratch depth and root radius for clad and unclad specimens. Runout samples are indicated by arrows.

All samples failed at the gauge section apart from a tension unclad sample with a 25 µm deep, 50 µm root radius scratch (T-U-25-50-1) that after nearly $8 \cdot 10^5$ cycles had its test stopped. Every introduced scratch, despite different geometry, was the nucleation site for the crack that fractured the specimen. Scratched samples, failed from the notch root that have a life comparable to the unscribed ones, were considered scribes insensitive. As can be seen in Table 4.2 and Fig. 4.1 the introduction of mechanical machined scribes caused a very reduced fatigue scatter. Scatter increased for shallower and blunter notches but remained small for a fatigue investigation. Scribes had a severe detrimental effect on fatigue performance reducing life up to 97.7% for the deepest and sharpest notch (T-U-185-5).

Even shallow scratches like the 25 µm deep and 25 µm root radius in T-C-25-25-1 resulted in a 30% life reduction. Fatigue life decreased with increasing scribe depth for a given root radius notch. Reducing the root radius with a fixed notch depth had the same effect (see Fig. 4.1). In other words the notch sensitivity increased as the scribe became deeper and sharper. The effect of cladding was to shift the curve to longer lives compared to unclad samples, even for unscribed specimens.

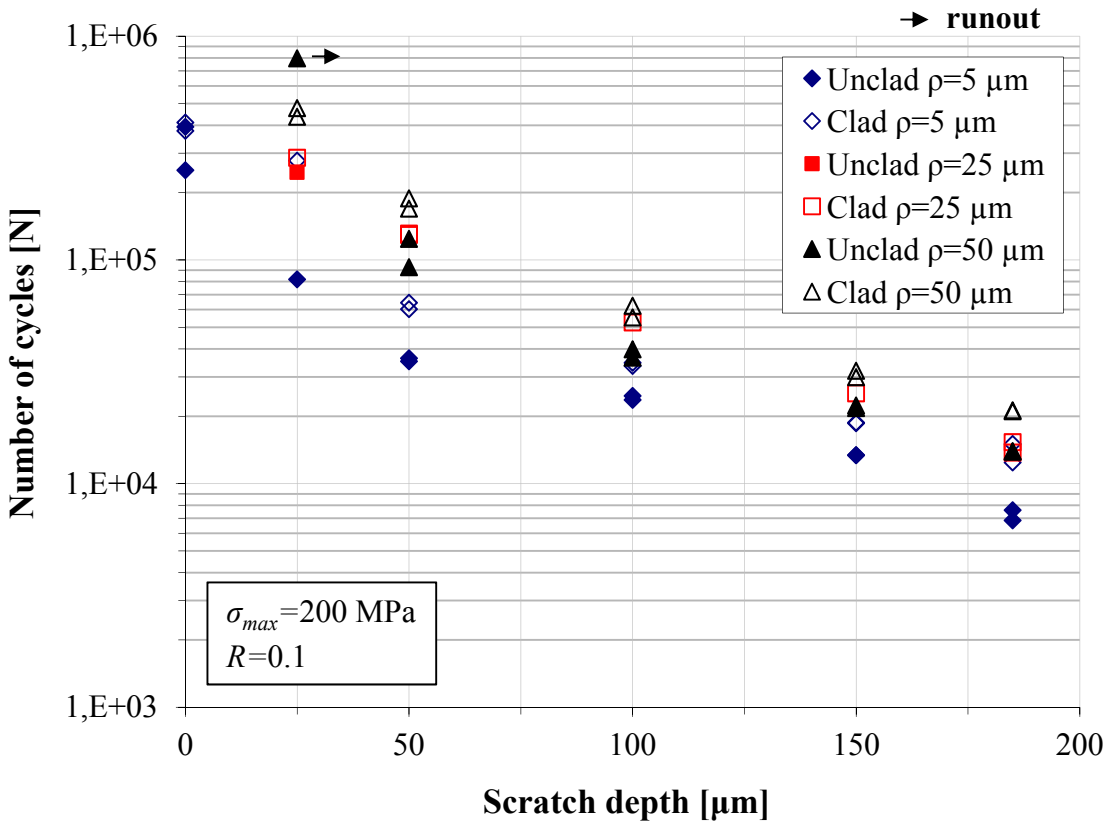

Fig. 4.1: Sample fatigue life under tension load as function of notch depth and root radius

Life reduction from the unscribed reference (L_{ref}) was similar in clad and unclad samples with scratches having same geometry (Table 4.2). The only exception was 25 μm deep scribes which showed different life reductions for clad and unclad samples. Cladding appeared to alter only the fatigue life of 25 μm deep scribes sufficiently embedded within the 80 μm thick pure aluminium layer, making clad samples less sensitive to sharp 5 μm root radius scribes. Blunter notches had the opposite effect. Unclad and clad samples seemed insensitive to scratches as small as 25 μm deep with root radius equal or bigger than 25 μm (T-U-25-25) for unclad specimens and 50 μm for clad ones (T-C-25-50). Cladding therefore appeared to increase the notch sensitivity in presence of 25 μm and 25 μm root radius scratches since unclad samples were insensitive to those scribes. It is worth noticing that fatigue life of clad 25 μm deep 25 μm root radius scribed sample (T-C-25-25) could just lie inside the scatter band of undamaged specimen life making clad and unclad samples insensitive to the same scribe types.

Table 4.3: Results of fatigue tension test with different maximum nominal stress

Sample	t [mm]	d [μm]	ρ [μm]	θ [deg]	σ_{max} [MPa]	Failure site	Fatigue life [cycles]	L/L_{200}
T-C-185-1-(160 MPa)	2	185	5	60	160	scratch site	36736	2.67
T-C-185-1-(100 MPa)	2	185	5	60	100	scratch site	178758	13.00
T-U-185-1-(160 MPa)	1.67	185	5	60	160	scratch site	27652	3.82
T-U-185-1-(100 MPa)	1.67	185	5	60	100	scratch site	124479	17.22

Table 4.3 reports tests results from the preliminary fatigue campaign on the effect of different maximum tension stress. Fatigue life ratio with lives of corresponding scribed samples, tested with the reference maximum gauge stress of 200 MPa (L_{200}), is displayed too. A 20% stress reduction (at 160 MPa) resulted in lives 2.5-4 times longer, while a halved stress of 100 MPa produces 13-17 times the lives of corresponding scribed samples tested at a maximum gauge stress of 200 MPa. Using those preliminary results segments of S-N curve can be drawn for scribed clad and unclad 2024-T351 with R=0.1.

4.1.2 Four point bend tests

As for tension case, tests were performed up to sample complete failure but the runout threshold was set at nearly $2 \cdot 10^6$ cycles. Fatigue test results are reported in Table 4.4 and graphically plotted in Fig. 4.2 as number of cycles required to completely break the sample according to the different notch geometry. Like in the previous section, sample thickness (t), scratch depth (d), root radius (ρ), open angle (θ) and failure site, are listed in Table 4.4 for bending samples together with fatigue lives reported as number of cycles and as percentage of the reference life (L_{ref}). Percentage life reductions from reference life are listed as well. Reference life for clad and unclad samples was the mean fatigue life under bending load of corresponding unscribed specimens, calculated including, in case, lives of scratched coupons not failed from scribe marks.

There was just one runout sample (B-U-0-0-1) with its test stopped after over 2 millions of cycles but unfortunately was the only unscribed unclad sample tested and no undamaged fatigue reference for unclad condition was obtained. Anyway it was decided not to repeat the test saving time since test conditions were close to unclad endurance limit in bending [1]. The missing fatigue life datum was provided by the project sponsor and it is displayed in both Table 4.4 (between brackets) and Fig. 4.2. That value was used as reference life for unclad samples. All the other samples failed at the scratch site or at other locations in the gauge section far from the scribe in case of scratch insensitive specimens. A failure, which started under an upper roller, was observed in one scratch insensitive specimen (B-C-50-50-1). Even under pure bending scratch introduction produced a reduced scatter although bigger compared to tension tests.

Table 4.4: Fatigue 4 point bending test results (σ_{max}=200 MPa and R=0.1)

Sample	t [mm]	d [µm]	ρ [µm]	θ [deg]	Failure site	Fatigue life [cycles]	Life as % of L_{ref}	Life reduction [%]
B-C-0-0-1	2	-	-	-	gauge section (no under the roller)	972070	90.14	9.86
B-C-50-5-1	2	50	5	-	scratch site	137000	12.70	87.30
B-C-50-5-2	2	50	5	60	scratch site	150548	13.96	86.04
B-C-100-5-1	2	100	5	60	scratch site	97408	9.03	90.97
B-C-100-5-2	2	100	5	60	scratch site	92048	8.54	91.46
B-C-185-5-1	2	185	5	60	scratch site	42636	3.95	96.05
B-C-185-5-2	2	185	5	60	scratch site	54510	5.05	94.95
B-U-0-0-1	1.67	-	-	-	runout	2243584 (794906)	100.00	0.00
B-U-50-5-1	1.67	50	5	60	scratch site	112140	14.11	85.89
B-U-50-5-2	1.67	50	5	60	scratch site	101608	12.78	87.22
B-U-100-5-1	1.67	100	5	60	scratch site	56140	7.06	92.94
B-U-100-5-2	1.67	100	5	60	scratch site	55970	7.04	92.96
B-U-185-5-1	1.67	185	5	60	scratch site	34424	4.33	95.67
B-U-185-5-2	1.67	185	5	60	scratch site	29236	3.68	96.32
B-C-50-50-1	2	50	50	60	gauge section (no under the roller)	1184640	109.86	-9.86
B-C-50-50-2	2	50	50	60	under the roller	879424	81.55	18.45
B-C-100-50-1	2	100	50	60	scratch site	198792	18.43	81.57
B-C-100-50-2	2	100	50	60	scratch site	172280	15.98	84.02
B-C-185-50-1	2	185	50	60	scratch site	66728	6.19	93.81
B-C-185-50-2	2	185	50	60	scratch site	66760	6.19	93.81
B-U-50-50-1	1.67	50	50	60	scratch site	273108	34.36	65.64
B-U-50-50-2	1.67	50	50	60	scratch site	244224	30.72	69.28
B-U-100-50-1	1.67	100	50	60	scratch site	95312	11.99	88.01
B-U-100-50-2	1.67	100	50	60	scratch site	101044	12.71	87.29
B-U-185-50-1	1.67	185	50	60	scratch site	50050	6.30	93.70
B-U-185-50-2	1.67	185	50	60	scratch site	44282	5.57	94.43

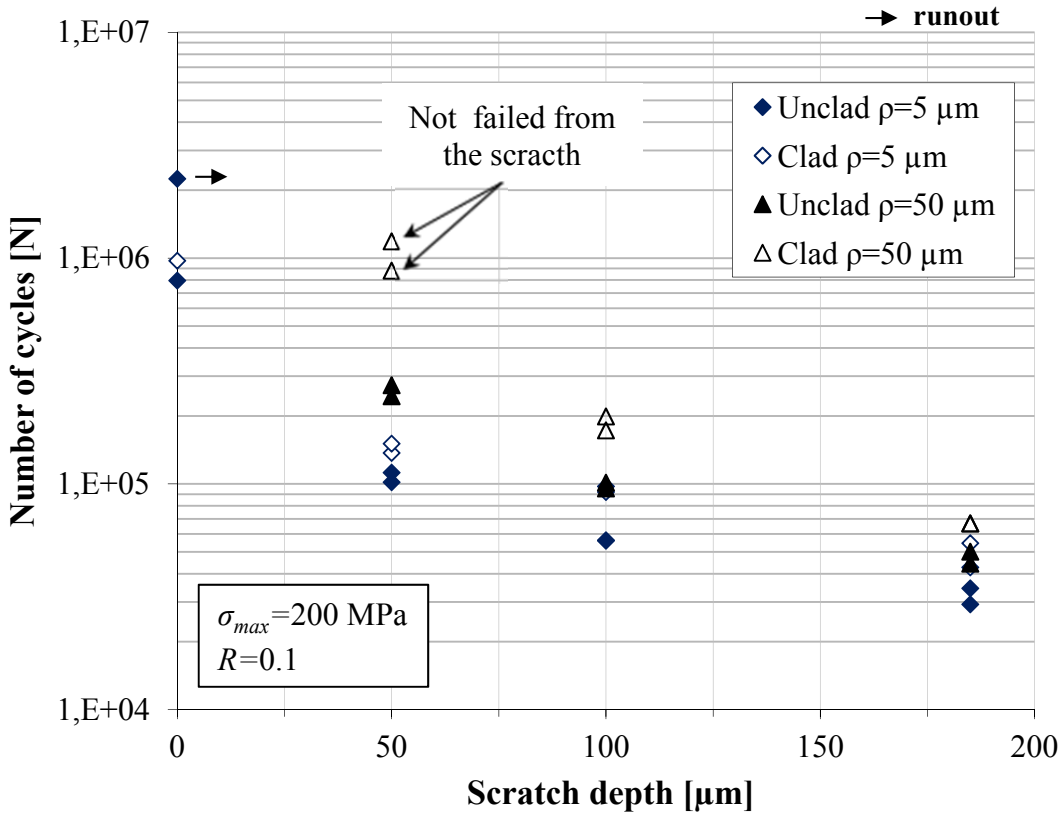

Fig. 4.2: Sample fatigue life under 4 point bending load as function of notch depth and root radius

Because of the stress gradient acting on the gauge section, bending fatigue lives were longer than those in tension at the same surface stress. However the life reduction caused by scratches was of the same order as under pure tension (Table 4.4). Reduction of fatigue life up to 96% were observed for the deepest and sharpest notch (B-C-185-5). As for the tension case, bending fatigue life decreased as notch depth increased and root radius was reduced (see Fig. 4.2). Scribed clad samples showed longer life compared with unclad ones having the same scratch geometry. Clad and unclad samples containing the same scribe geometry showed the similar life reduction apart from 50 µm deep scratches with 50 µm root radius. Unclad samples with these scribes failed from notch root while clad ones failed from other locations. Cladding appeared to reduce 2024-T351 scratch sensitivity under bending load when scribes are entirely contained in it. Clad samples were insensitive to notches less than 50 µm deep and with root radius equal or bigger than 50 µm (B-C-50-50) failing at other locations than the scratch site. These fatigue lives were included in the calculation of undamaged samples mean life. Unclad specimens were sensitive to all scribes tested under pure bending and nothing could be said regarding precise notch depth and root radius values, they are insensitive to. Obviously those scribes will be shallower than 50 µm and or with a root radius lager than 50 µm.

4.2 Microscope analysis results

During this research project, fractography and scribe geometry investigations were performed by means of optical microscope and mainly of scanning electron microscope.

Geometrical features were measured on pictures using an image processing software. A given length on a picture was measured in term of number of pixels, then converted into units of length multiplying by a conversion factor. Such factor was obtained measuring the length scale printed on the picture by the microscope software. In that way scribe sections and crack shapes were readily measured, making quantitative analyses feasible.

Section geometries of mechanical machined and as in service scribes were measured and the results are reported in the following section. Fracture surfaces of tension, and bending samples were analysed to assess crack nucleation sites, fracture morphology and peculiar features left during crack propagation. Measurements on fatigue fracture final shape and size were carried out. Finally crack propagation data, obtained under different loading conditions by striation counting performed on fracture surfaces, are described.

4.2.1 Scribe geometry measurements

Scribe cross section geometry was measured to verify the accuracy of diamond tool scribing procedure. Electrical discharge machined scribes, produced by Airbus, had their cross sections measured and characterised as well, since the adopted scribing procedure allowed only the notch depth to be controlled. Moreover, cross sections of scratches manually introduced by knives were investigated to gather information on as in service scribe geometries.

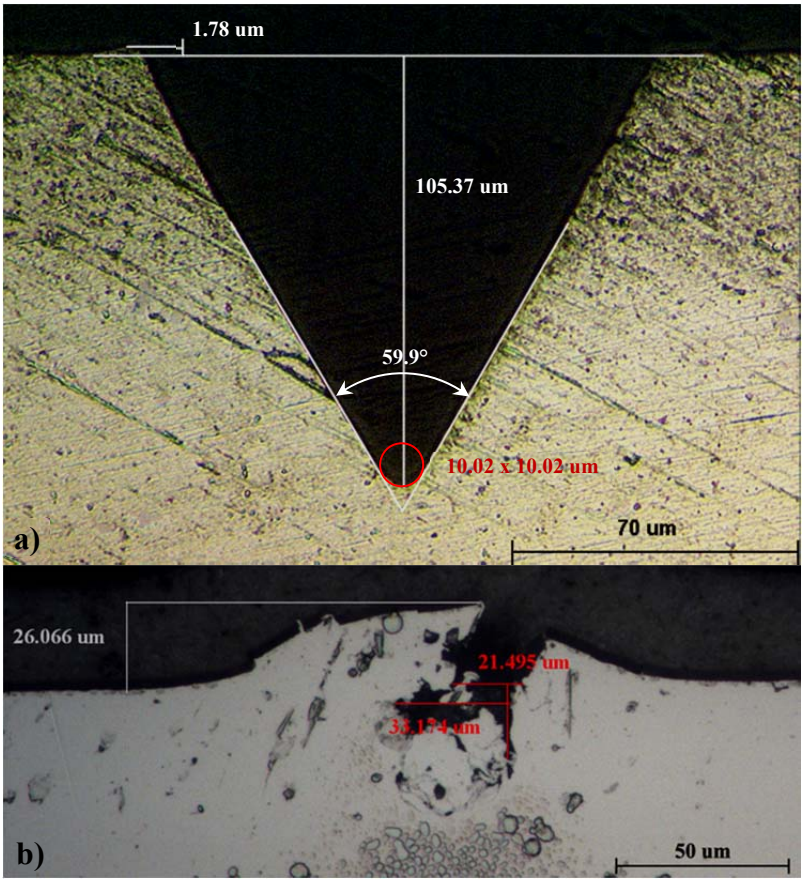

Fig. 4.3: Scribe section geometry measurements: DT 100 µm, ρ=5 µm (C-100-5) (a), razor knife (J19) (b)

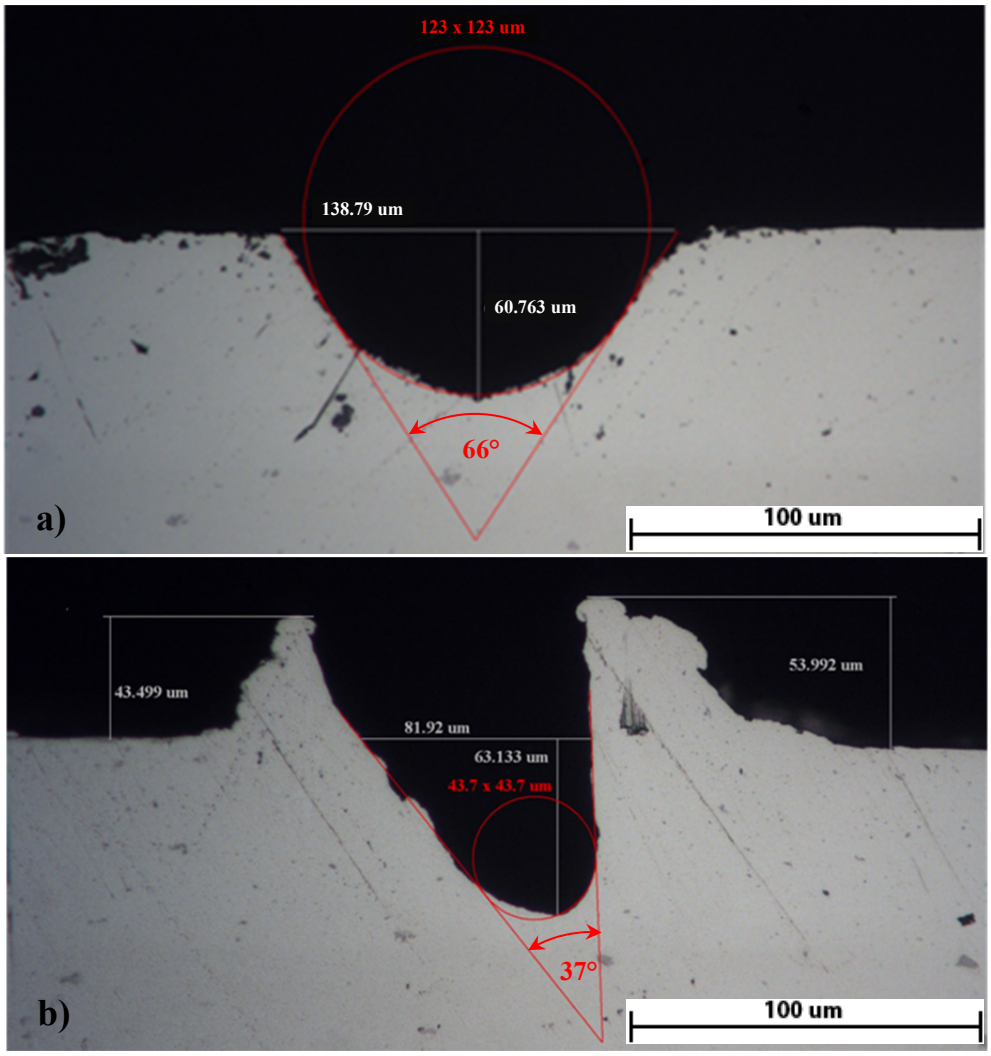

Fig. 4.4: Scribe section geometry: EDM 80 µm (J12) (a), knife, 45°, 60 µm (D17) (b)

Samples were prepared and observed under optical microscope following the procedure described in chapter 3. Fig. 4.3 shows examples of section measurements on diamond tool and razor knife scribes, while those performed on EDM and knife scribes are reported in Fig. 4.4.

Since the majority of the scribes examined showed a rounded V shaped section, their geometry was characterised just measuring the scribe depth (d), the root radius (ρ) and the angle included between notch flanks (θ). The height of the material piled up from the sample surface at the scribe edges was measured too (see Fig. 4.3 and Fig. 4.4). In fact, because such extrusions were produced by the plunging action, exerted by the scribing tool, they can be an indication of the plasticisation involved in scribe formation. If scribes were machined just cutting away material shavings no piling up should be present. Notch root radii were measured with the aid of a visual procedure. A circle was drawn on the notch root, then scaled and deformed to be coincident with the root edge. Once precise superposition was achieved, the axes of the obtained ellipse were measured and the root radius calculated as mean value of the two axes lengths (see Fig. 4.3).

Table 4.5: Scribe section measurements

Sample type	Sample name	Nominal scribe	d [µm]	ρ [µm]	θ [deg]	piling up [µm]	
						left	right
Untested diamond tool scribed coupon	U-50-5	DT 50 µm, ρ=5 µm	50.83	4.85	60.0	1.65	1.34
	U-100-5	DT 100 µm, ρ=5 µm	100.81	5.41	60.6	0.00	0.00
	U-50-50	DT 50 µm, ρ=50 µm	53.22	49.65	62.5	0.00	0.00
	U-100-50	DT 100 µm, ρ=50 µm	105.53	49.93	59.3	0.00	0.00
	C-50-5	DT 50 µm, ρ=5 µm	51.01	5.15	60.1	4.97	2.38
	C-100-5	DT 100 µm, ρ=5 µm	105.37	5.01	59.0	1.78	0.00
	C-50-50	DT 50 µm, ρ=50 µm	49.36	49.82	59.9	0.00	0.00
	C-100-50	DT 100 µm, ρ=50 µm	100.54	49.75	59.8	0.00	1.82
Tested joint sample not failed from scribe marks	J9	EDM 60 µm	55.69	69.00	76.60	0.00	0.00
	J12	EDM 80 µm	60.76	61.50	66.30	0.00	0.00
	J13	EDM wire tool	27.42	-	-	-	-
	J16	EDM 30µm	34.36	31.55	59.90	0.00	0.00
	J19	razor knife	21.50	-	-	26.07	-
Tested Airbus dogbone sample not failed from scribe marks	D3	EDM 39 µm	29.94	33.35	65.30	0.00	0.00
	D14	knife, 90°, 60 µm	74.13	35.68	54.70	54.33	54.67
	D16	knife, 90°, 160 µm	116.21	42.95	38.70	62.03	88.61
	D17	knife, 45°, 60 µm	63.13	21.85	36.60	43.50	53.99
	D20	knife, 45°, 120 µm	111.10	57.50	28.00	51.46	54.53

Table 4.5 lists measured notch depth (d), root radius (ρ), open angle (θ) and piling up height at the two scribe edges together with designating nomenclature of the specimen and the sample type it was cut from. Notch type (DT for diamond tool) beside nominal depth and root radius, when known, were specified into nominal scribe column (Table 4.5). For knife scratches the cutting angle (see chapter 3) is reported.

Notches cut using diamond tools showed very consistent geometrical parameters (Table 4.5). The percentage error from nominal notch depth was 6.4% maximum, well below the 10% threshold defined during scribing. Maximum percentage errors from nominal root radius and open angle were respectively 8.2% and 1.6%. Piling up phenomenon was very restrained in diamond tool scribes, confirming the lack of plasticity, and consequent residual stress introduced, during scribing procedure. Piled up material was nearly absent in unclad samples, with the exception of 50 µm deep scribe with 5 µm root radius (U-50-5), showing trivial pile ups of about 1 µm. Clad samples showed slightly bigger pile ups (see Table 4.5), possibly because of the cladding low yield strength of 100 MPa. Diamond tool scribing procedure proved to be a precise and controllable process to machine scribe marks on aluminium samples.

The EDM scribing process, where the only cutting depth was controlled, was more inaccurate, showing deviation from nominal depth up to 21.1% in the case of 80 µm deep scribed sample (J12). EDM scribes exhibited a rounded V shaped section with root radii varying with the notch depth, but the notch root radius to depth ratio (ρ/d) was maintained nearly constant ranging from ρ/d=0.88 to ρ/d=1.24. The mean value of ρ/d=1.02 was adopted to characterise the constant shape aspect ratio of EDM scribes. As regards the open angle it was almost constant fluctuating around a mean value of

θ=63.4°. A constant value of θ=60° was assumed for EDM scribes as this deviation had negligible effect on the local notch stress field (see chapter 5). It is worth mentioning that the cross section shape and its aspect ratio are highly dependent on machining speed, as the removed material by electrical discharge is function of the time a portion on material is exposed to the tool sparks for. No piling up was observed in EDM scribed samples because EDM does not introduce any plasticity; no physical contact takes place between the tool and the machined material.

Scratches introduced by knife showed, as expected, irregular geometries but comparable to a rounded V shaped cross section (see Fig. 4.4). As those scratches were introduced by hand, controllable scribe depth was difficult to obtain. Errors up to 27.4% from nominal notch depth were found in a 160 μm deep scribed sample (D16) with a cutting angle of 90° (Table 4.4). Root radius values were variable giving rise to an aspect ratio from ρ/d=0.35 to ρ/d=0.52 (mean ρ/d=0.43). The open angle was sharper than that of diamond tool and EDM scribes showing a mean value of θ=39.5°. Pile up heights were of the same order of magnitude as scribe depths (see Fig. 4.4 and Table 4.4) indicating large plasticity. The cutting angle seemed not to modify significantly the scribe section geometry. Scribe introduced by razor knife showed an irregular section and the geometry parameters were difficult to measure (see Fig. 4.3 b)) while the EDM wire tool appeared to produce a wide depression on the sample surface more than a scratch.

4.2.2 Fracture surface morphology

Since duplicate specimens, containing scribes with the same geometry, showed very similar fractures, observation were performed only on one fracture surface per each kind of fatigued specimen. Results of the morphological fractography examination are listed in Table 4.6. For each sample, identified by the usual nomenclature, information on fatigue fracture front type and the number of observed cracks is reported beside main cracks size measurements. Table 4.6 also reports the main crack shape types used to calculate the stress intensity factor (see chapter 6).

Three different shapes were identified: 2D through-width crack, semi-elliptical surface crack and quarter-elliptical corner crack. Fracture surface was ideally divided along its width into three equal areas (1, 2, 3) numbered from left to right. The main final crack depth was measured starting from the scribe root at each fracture surface region. In case of a unique elongated through-width crack front, depths were measured at the sample left edge (a_1), at the centre line (a_2) and at the right edge (a_3). If surface or corner cracks were found, the main flaw depth was measured separately and recorded with a different subscript, according to the fracture area it belonged to (see Table 4.6). The main crack length along the sample width (c) and the aspect ratio (a/c) were measured as well for corner and surface flaws (see Fig. 4.5). Fig. 4.5 shows elliptical cracks and fracture surface size nomenclature. Percentages of the total fracture surface (S_f) occupied by fatigue cracks (S_c) including projected scribe area (S_d) are listed in the last column of Table 4.6.

Table 4.6: Final crack front morphological characteristics

Sample	Fracture front	Cracks number	Main crack measurements						
			Crack shape	a_1 [µm]	a_2 [µm]	a_3 [µm]	c [mm]	a/c	$(S_c+S_d)/S_f$ [%]
T-U-0-0	1 elliptical	1	surface	-	-	1560	2.89	0.54	5.2
T-U-25-5	multiple cracks	13	corner	1440	-	-	9.12	0.16	17.1
T-U-50-5	elongated	1	through	671	151	354			22.3
T-U-100-5	elongated	1	through	210	144	674			23.0
T-U-150-5	elongated	1	through	680	127	553			31.2
T-U-185-5	elongated	1	through	311	118	587			27.8
T-U-25-25	multiple cracks	13	corner	1350	-	-	11.10	0.12	19.1
T-U-25-50	no failure	-	-	-	-	-			
T-U-50-50	multiple cracks	15	corner	1320	-	-	11.50	0.11	21.1
T-U-100-50	coalesced	1	through	266	111	598			22.0
T-U-150-50	coalesced	1	through	554	106	672			30.7
T-U-185-50	coalesced	1	through	610	114	297			27.9
T-C-0-0	1 elliptical	1	corner	-	-	1840	6.20	0.30	5.6
T-C-25-5	multiple cracks	10	surface	1760	-	-	6.00	0.29	22.0
T-C-50-5	coalesced	1	through	865	119	327			20.1
T-C-100-5	elongated	1	through	835	142	263			21.7
T-C-150-5	elongated	1	through	865	150	261			24.7
T-C-185-5	elongated	1	through	819	144	389			27.5
T-C-25-25	multiple cracks	8	surface	1840	-	-	4.50	0.41	17.5
T-C-50-25	multiple cracks	7	corner	1800	-	-	11.50	0.16	22.8
T-C-100-25	coalesced	1	through	524	153	779			24.6
T-C-150-25	coalesced	1	through	761	176	540			27.5
T-C-185-25	coalesced	1	through	815	131	668			30.8
T-C-25-50	multiple cracks	5	surface	1910	-	-	4.50	0.42	18.1
T-C-50-50	multiple cracks	15	corner	-	-	1020	9.00	0.11	17.2
T-C-100-50	coalesced	1	through	903	162	356			24.2
T-C-150-50	coalesced	1	through	787	133	373			24.9
T-C-185-50	coalesced	1	through	721	122	314			24.8
B-U-0-0	no failure	-	-	-	-	-			
B-U-50-5	multiple cracks	7	corner	1540	185	1470	10.50	0.14	53.9
B-U-100-5	elongated	1	corner	1420	292	1420	11.00	0.13	56.3
B-U-185-5	elongated	1	corner	1240	264	1400	11.00	0.12	57.7
B-U-50-50	2 elliptical	2	corner	1500	-	1530	10.75	0.14	22.1
B-U-100-50	multiple cracks	4	corner	1430	224	1390	11.25	0.13	54.7
B-U-185-50	elongated	1	corner	1350	275	1360	11.25	0.12	59.1
B-C-0-0	1 elliptical	1	surface	1920	-	-	18.50	0.10	34.9
B-C-50-5	multiple cracks	6	corner	1850	376	1730	11.60	0.15	55.6
B-C-100-5	elongated	1	corner	1790	165	1840	14.00	0.13	55.3
B-C-185-5	elongated	1	corner	1720	275	1770	14.00	0.12	59.5
B-C-50-50	no scribe failure	1	corner	1910	-	-	20.00	0.10	21.3
B-C-100-50	multiple cracks	5	corner	1780	-	1820	13.75	0.13	34.2
B-C-185-50	coalesced	1	corner	1740	242	1750	14.35	0.12	59.0

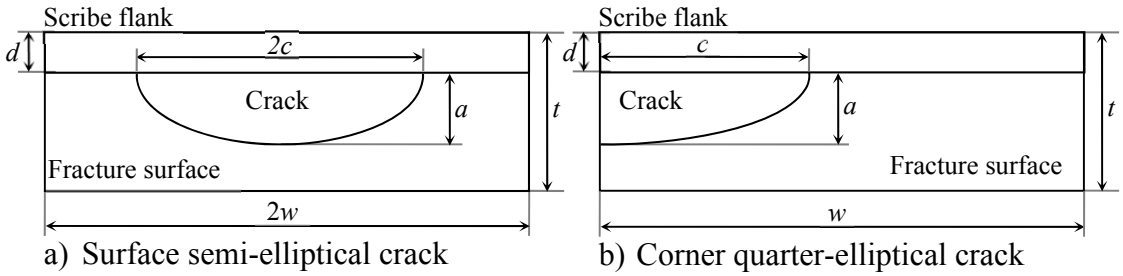

Fig. 4.5: Surface (a) and corner (b) crack dimensions

The boundary between the fracture produced by the stable fatigue crack propagation and the void coalescence, characterising the unstable final failure, was identified in each sample analysed (see Fig. 4.6). This designated the size and shape of fatigue cracks. Different crack front shapes were found depending on the geometry of the machined scribe. Fig. 4.7 shows schematically the various fatigue crack front kinds, found during the fractography investigation.

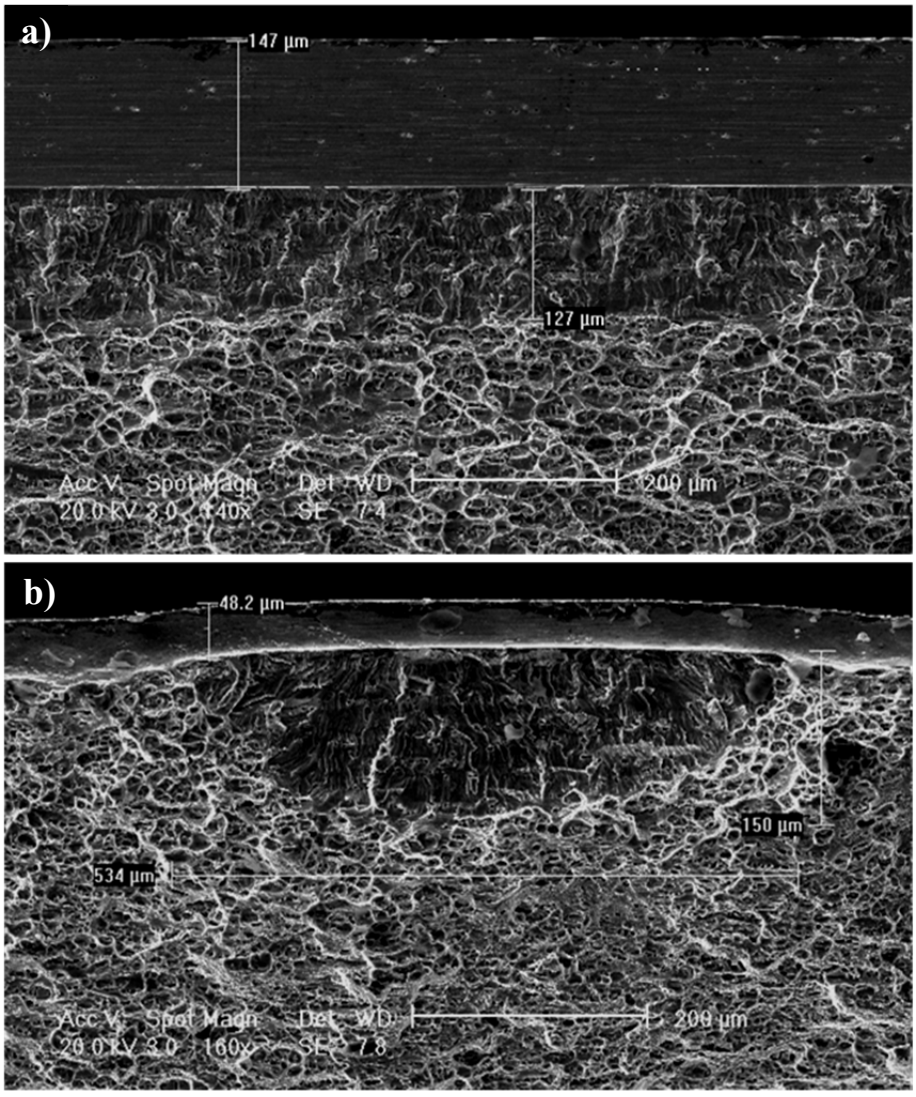

Fig. 4.6: Crack and notch depth measurement using SEM for T-U-150-5 (a) and T-C-50-50 (b)

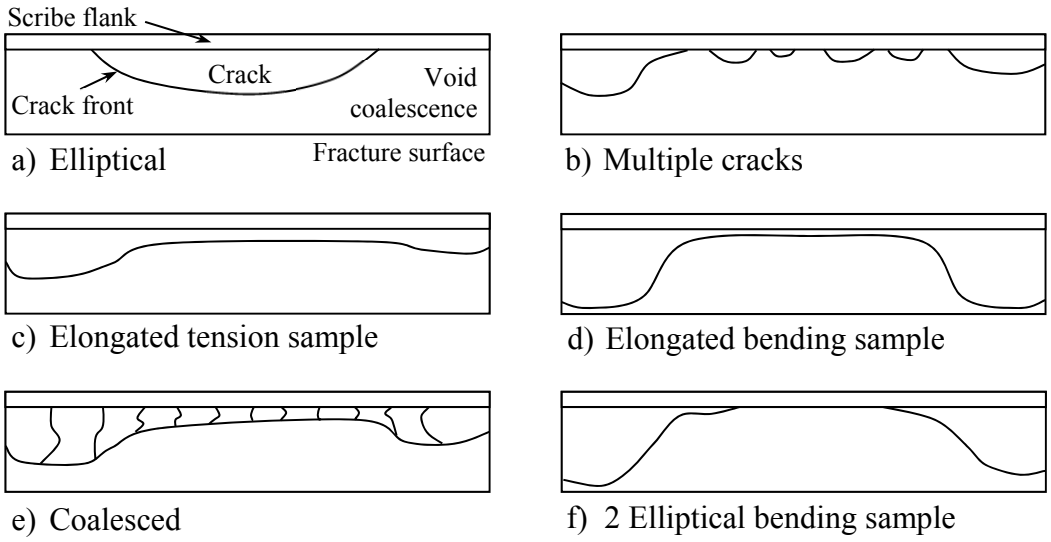

Fig. 4.7: Fatigue crack front shape schematics

4.2.2.1 Unscribed samples

All the unscribed tension samples failed via a unique fatigue elliptical fatigue crack (see Fig. 4.7 a) and Fig. 4.8 a)) nucleated from a material inclusion at the sample surface. The nucleation point was far away from the sample edge in the unclad specimen and the crack grew as a semi-elliptical surface crack (Fig. 4.8 a)). On the other hand in the clad one, since the initiation site was close to the sample corner, the crack was modelled mainly as a quarter-elliptical corner crack (Fig. 4.5 b)). Crack aspect ratio (a/c) in unscribed samples was ≤1, (Table 4.6). Crack depths reached almost the sample thickness, 92% of t in unscribed clad and unclad samples before developing shear lips (Table 4.6). Fig. 4.8 a) shows an example of a thumbnail crack found on the unscribed unclad sample (T-U-0-0). The crack nucleation site is also visible in the picture.

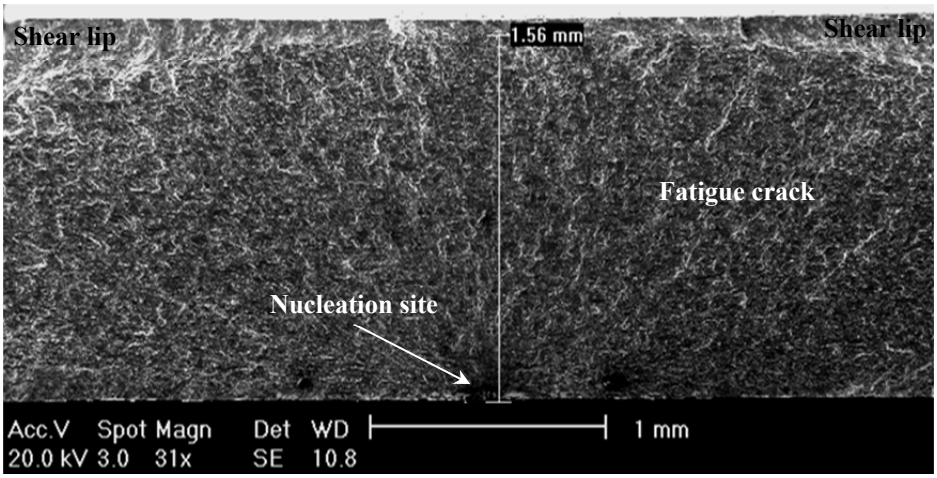

Fig. 4.8: Semi-elliptical crack front in T-U-0-0 fracture surface

Regarding bending unscribed samples, fractogaphy information was available only for clad specimens. Fracture data for cracks not nucleated from the scribe root (see Table 4.6) were considered unscribed data. As for pure tension loading, fracture

surfaces of unscibed bending clad samples showed a unique surface (B-C-0-0) or corner crack (B-C-50-50) nucleated from cladding at the sample surface. Those cracks grew more in the sample width direction than happened under tensile load, showing an aspect ratio of a/c=0.1.

Once cracks reached bending sample thickness they became through thickness and propagated along specimen width. The fracture surface remained perpendicular to the loading direction, no shear lips were observed, but the through thickness crack was markedly deeper at the sample surface under tensile loading, showing a slanting crack front. Thumbnail and corner crack developments occupied respectively 35% and 21% of the entire fracture surface, reaching a crack depth nearly 96% of the sample thickness (Table 4.6).

4.2.2.2 Scribed tensile samples

Fatigue cracks nucleated from the scribe root and grew through the sample thickness in clad and unclad tension scribed samples. Three different fatigue fracture front types were found according to the scratch geometry. If the scribe had a root radius of 5 μm and was 50 μm deep or deeper, unclad samples exhibited a single elongated crack front parallel to the notch root and going across the entire specimen width (see Fig. 4.7 c) and Fig. 4.9 a)). Clad layer seemed to prevent scribes totally embedded inside the cladding, from exhibiting elongated fronts, shifting its occurrence towards deeper scratches. In fact in clad samples such front was found only for 5 μm root radius scribes as deep as or deeper than 100 μm, that is with their root inside the substrate (Table 4.6). Elongated crack depth was not uniform along the scribe root (see Table 4.6) and the front showed two lobes at the sample edges as sketched in Fig. 4.7 c). Cracks were deeper close to sample edges.

Fig. 4.9 a) shows the central portion of the elongated crack front found in the 185 μm deep scribed unclad sample with 5 μm root radius (T-U-185-5). If the 5 μm root radius scribes were shallower than 50 μm a fracture front consisted of multiple thumbnail cracks, developed along the notch root, was found in unclad samples. Fig. 4.7 b) shows the sketch of such type of fatigue fracture front. It was constituted by a number of cracks ranging from 4 to 15 according to scribe geometry and loading conditions (Table 4.6). Two larger cracks always grew close to the sample edges. Fig. 4.9 c) shows multiple thumbnail cracks at the 50 μm root radius of a 50 μm deep scribe in clad sample (T-C-50-50).

Tension clad samples, containing 50 μm deep sharp scribes with 5 μm root radius showed instead a particular fracture front named coalesced in Table 4.6. In fact that crack front that was an elongate front, running parallel to the notch root from one sample edge to the other, on the whole, made up of several cracks coalesced together. Crack nucleated independently at the notch root and after growing on different planes coalesced to form an unique front before the sample failure. A sketch of that fracture front type is displayed in Fig. 4.7 e). As can be observed from the picture free edge effect was responsible for the formation of a lobed fracture front deeper at the sample edges.

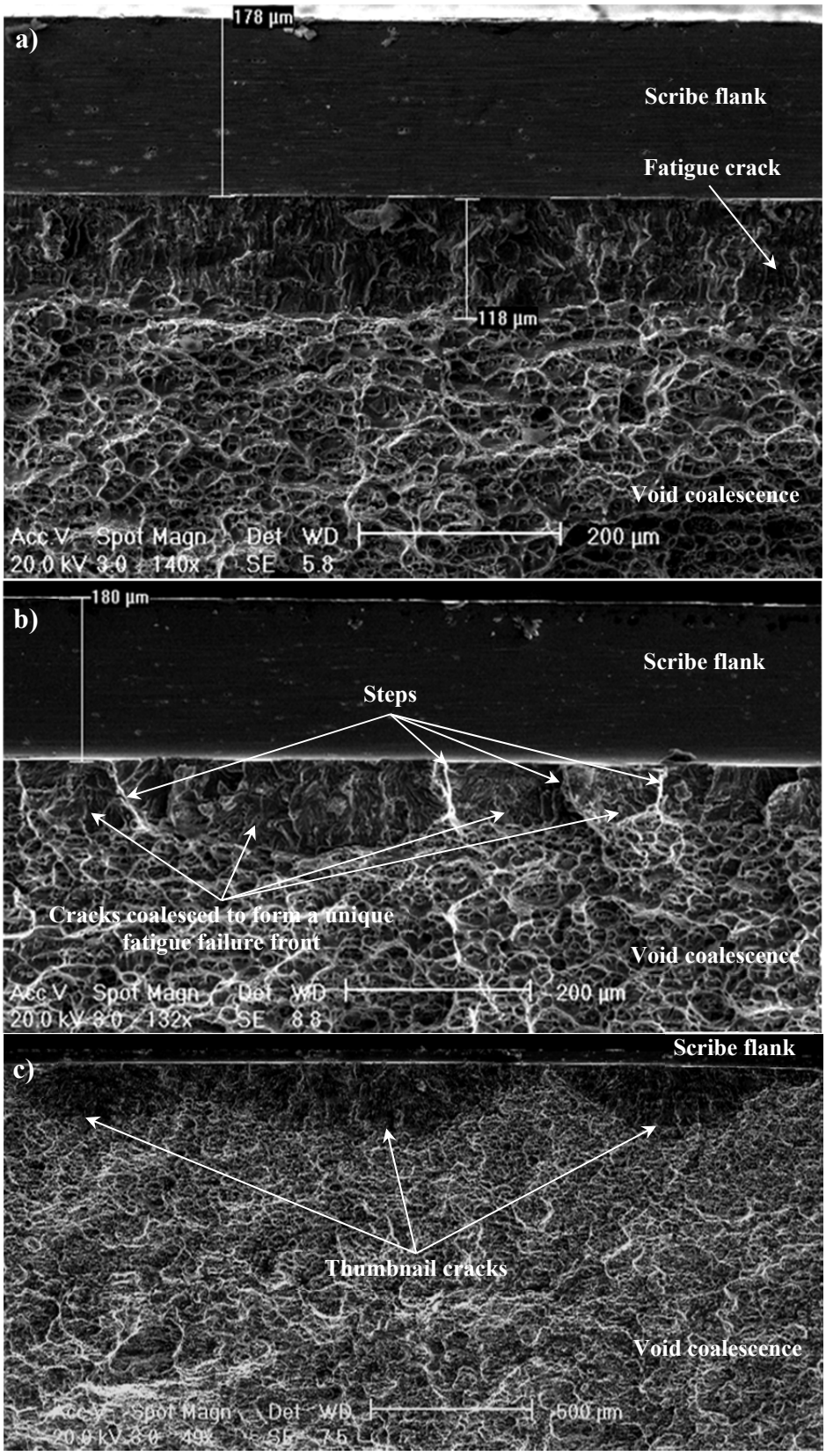

Fig. 4.9: Unique elongated crack front in T-U-185-5 fracture surface (a), elongated fatigue failure front formed by the coalescence of several cracks in T-C-185-50 fracture surface (b) several thumbnail cracks in T-C-50-50 fracture surface (c)

Fig. 4.9 b) shows the coalesced crack front found at the 50 μm root radius of the 185 μm deep scribed clad sample (T-C-185-50). Steps, produced by static shear failure of material between thumbnail are visible in Fig. 4.9 b). Such steps could be found all across the fatigue fracture front.

In presence of scribes with 25 μm and 50 μm root radii elongated crack fronts were not observed in either clad or unclad tension samples. If scribes were deep enough ($d \geq 100$ μm) clad sample fracture surfaces showed the coalesced crack front for both 25 μm and 50 μm root radii (see Table 4.6). Otherwise for notches shallower than 100 μm multiple thumbnail cracks were found. The same behaviour occurred in 50 μm root radius unclad samples. The unclad tested sample containing a 25 μm root radius scribe (25 μm deep) exhibited a multiple cracking as the corresponding clad scribed specimen.

Fatigue fractures showing elongated and coalesced crack fronts were modelled as produced by 2D through-width cracks propagating from the notch root up to a critical crack depth (see chapter 6). Critical crack depth value was the one ensuring that the fracture surface area covered by the through-width crack before the final failure was the same as that occupied by the fatigue crack on the measured sample. Fracture front constituted by multiple thumbnail cracks were modelled, neglecting all the secondary cracks, and considering the failure caused only by the main crack propagation. Main cracks were regarded as thumbnail surface or quarter-elliptical corner cracks nucleated at the notch root and propagated with a fixed aspect ratio up to the size measured during fractography analysis and reported in Table 4.6.

Despite differences in scribe geometry and clad state main corner cracks on tension sample fracture surface exhibited an aspect ratio from a/c=0.11 to a/c=0.16. Main surface cracks, observed only on scribed clad samples, instead were less lengthened along the notch root showing aspect ratios of a/c=0.29 and slightly above a/c=0.40 (see Table 4.6). No correlation was found between notch geometry changes and aspect ratio of main cracks in multiple cracks fronts. Although at the root of notches with various sharpness and, therefore subjected to different stress conditions, cracks showed similar shapes anyway. Clad layer seemed to produce multiple crack fronts on tension samples, where main cracks grew as surface flaws, when 25 μm deep scribes were entirely contained in it (see Table 4.6). The soft cladding made easier the development of main cracks even if they were not affected by the free edge effect. That did not happen for 50 μm deep scribes that, although had their roots embedded inside the clad layer, showed corner cracks as main flaws.

Stable propagation of all the multiple cracks forming the fracture fronts occupied on average nearly 19.4% of the entire fracture surface, including the surface part removed during scribing. Surface and corner main cracks reached maximum depths from 83% to 97% of the sample thickness apart from the 50 μm deep 50 μm root radius scribed clad tension samples (T-C-50-50) where the main flaw depth was just the 54% of t. Despite that anomalous depth value the fracture surface portion occupied by fatigue cracks was consistent with the other measurements. Unique elongated and coalesced cracks occupied on average 25.6% of the fracture surface. They showed, as mentioned above, a continuous failure front with two lobes at the sample edges connected by a shallower central strip of stable crack growth. Fatigue fracture was 3-5 times deeper at the edges

than inside the sample (Table 4.6). However the crack front was deeper at one edge reaching in some cases a depth 3 times the one measured at the other sample edge. Crack front was generally deeper at the edge where the unstable final crack propagation was believed to start from (see section 4.2.3.2). The shallower inner crack front running parallel to the scribe root was generally 100-160 μm deep despite different scratches and the presence of cladding (see Fig. 4.9 a) and b)). On the other hand the deepest point of the crack front reached nearly the 50% of the sample thickness in both clad and unclad specimens.

4.2.2.3 Scribed bend samples

Bend scribed samples showed the same fracture front types as tension ones but with some differences in shape. These were attributed to the presence of nominal stress gradient. As in the tension samples, fatigue cracks initiated at scribes and grew through the sample thickness with the exception of 50 μm deep, 50 μm root radius scribed clad specimens which failed away from the scribe. Both unclad and clad samples scribed with 5 μm root radius scribes deeper than 50 μm exhibited a unique elongate crack front, crossing the entire fracture surface. Fig. 4.7 d) shows the sketch of the elongated crack front found in case of bending loading. Once again the free edge effect promoted the formation of two lobes making the crack front deeper at the sample edges. However, in contrast to tension samples, cracks at the edges were so deep to reach almost the opposite sample surface (see Table 4.6). Fracture fronts were symmetric having nearly the same depth at the two sample edges.

For 5 μm root radius 50 μm deep scribes multiple cracks were found at the notch root in both clad and unclad samples. The number of multiple cracks per fracture surface was smaller than in case of tension samples, ranging from 6 to 7. The two main cracks at the sample edges were considered as quarter-elliptical corner flaws. Crack length along the notch root (c) and the aspect ratio values were obtained as the average of the measurements performed on the two main flaws. On the scribe root central part, thumbnail cracks 185 μm and 376 μm deep were observed in both unclad and clad samples (Table 4.6). Main corner cracks were lengthened along the scribe root with a constant aspect ratio (a/c=0.14-0.15) even if the notch was machined in the cladding.

In the case of 50 μm root radius scribes crack fronts transition was shifted toward deeper scratches. In fact a unique crack was observed only for 185 μm deep scribed as an elongated front in unclad and as a coalesced front in clad samples (Table 4.6). Coalesced fatigue fractures under bending load had the same shape of a common bending lobed elongated front but contained steps, characteristic of cracks coalescence (Fig. 4.9 b)). 4-5 multiple cracks developed at the 50 μm root radius of clad and unclad 100 μm deep, while only 2 corner cracks grew at root of unclad 50 μm deep scribed sample (see Fig. 4.7 f)). Main corners cracks, one per fracture surface edge, exhibited an aspect ratio of 0.12-0.14 when nucleated from 50 μm root radius bending scribed samples. Corner cracks reached on average a maximum depth 94% of the sample thickness before their growth become unstable leading to fracture. Multiple cracks occupied in all, together with the scribe, on average 44.1% of the entire fracture surface. A fatigue fracture area of 22.1% comparable with the one of unscribed samples was found for the fracture front composed only by two elliptical corner cracks (Table 4.6).

Since elongated and coalesced fronts were from 7 to 12 times deeper at the edges than in the middle of the sample they were modelled as two corner cracks neglecting the central part. In fact those fatigue fractures resemble more the one produced by two symmetrical quarter-elliptical corner cracks than an uniform trough-width flaw. All the fatigue failure of scribed bending samples were modelled as produced by two corner cracks with equal size and shape growing simultaneously up to the critical depths listed in Table 4.6 (see chapter 6). In case of elongated and coalesced fracture fronts, corner cracks depth was considered equal to the average of the front depths measured at the two sample edges. Superficial corner crack length (c) and the consequent aspect ratio (a/c) were calculated measuring the extent of fracture front lobes along the scribe root. Lobe dimensions were measured at each fracture surface edge and then averaged out to obtain the lengths c and the aspect ratios of the modelled pairs of corner cracks, reported in Table 4.6. Modelled corner cracks showed a shape, slightly more elongated than that of main flaws in multiple cracks fronts, with an aspect ratio of a/c=0.12-0.13 (Table 4.6). Elongated and coalesced fracture fronts reached a maximum depth 95% of the sample thickness covering, including the removed surface by the notch, the 57.8% of the fracture surface on average. The part of the fracture in the middle of the scribe was generally two times deep than in the corresponding scribed tension sample, confirming the tendency to produce deeper cracks under bending load even without the free edge effect.

To conclude fatigue crack development from scribe marks and subsequent fracture surface morphology seemed to be regulated by the scribe geometry and by different loading conditions. Crack development is analysed and reconstructed in the following sections.

4.2.3 Fatigue fracture development

Fatigue failure process in test samples was investigated a posteriori to gather information on how fuselage joints develop cracks from scribe marks under repetitive service loads. The whole fracture evolution, from nucleation to final failure was deducted, analysing the characteristic marks left by growing cracks on fracture surfaces. Peculiar features were identified and associated to corresponding crack development stages and behaviours.

In the first place crack nucleation and propagation processes were examined in unscribed samples to rationalise how scribe mark introduction alters the fatigue fracture evolution. The effects of load conditions and cladding were considered as well. Afterwards the crack development from machined scribes was analysed pointing out the consequences of different notch sharpness. Shapes of small cracks nucleated at the scribe root were measured to investigate the effect of material microstructure and notch stress field on local crack driving force. Finally the observation of non propagating flaws at the scribe root threw a light upon early propagation stage of fatigue cracks subject to the notch stress gradient.

4.2.3.1 Crack development in unscribed samples

Unscribed tension and bending samples failed as a consequence of single surface or corner crack development (see Table 4.6). Fig. 4.10 shows the surface of the fatigue crack, developed at the gauge section of unscribed unclad tension samples. Crack surface overall SEM picture and the magnification of the nucleation site and early propagation region are displayed respectively in Fig. 4.10 a) and b). The crack seemed to nucleated from a quite large inclusion cluster located close to the sample surface (Fig. 4.10 b)). The cluster, that remained attached to the fracture surface, showed a nearly ellipsoidal shape (10.3 x 10.1 x 23.6 μm). For unscribed unclad tension samples the nucleation mechanism involved seemed to be the debonding of the interface between inclusion and matrix, as the cluster of Fig. 4.10 did not show any apparent sings of fracture. Nucleation site identification was made easier by the presence of sunrises (Fig. 4.10 a)). Those radial marks in fact, being parallel to the local propagation direction, diverge from the nucleation point and make it recognisable. Sunrises generally are produced by crack propagation on offset planes or by the coalescence of different growing cracks providing information even on crack propagation.

Cracks propagated as a semi-elliptical flaw and the early crack growth was characterised by a strong effect of the material grain structure. A microstructure sensitive crack growth region, showing a faceted surface was identified around the nucleation site (Fig. 4.10 b)). No striations were observed in that region. Early propagation phase sensitive to microstructure, which is generally called stage I, is characterised by cracks propagation by dislocation motion on crystallographic planes where the resolved shear stress is maximum. The crack tends to follow crystallographic planes, but changes direction at discontinuities, such as grain boundaries. The variation of primary slip system direction in different grains makes the crack deflect, producing a facetted fracture surface (Fig. 4.10 b)). The typical stage I surface made by a mixture of large nearly planar facets and ‘feathery’ corrugated facets could be observed at the side regions of Fig. 4.10 b). In the central part, where crack grew through the short transverse direction, an array of lamellar features were found. Those lamellae seemed to change orientation in different grain making recognisable the grain boundaries (see Fig. 4.10 b)). Similar features were observed during short crack crystallographic growth of 7010 aluminium alloy reported in [2]. Voids left by inclusion particles can be observed on the fracture surface of Fig. 4.10 b).

After the first microstructure sensitive growth the crack propagated perpendicular to the loading direction and striations were visible. In other words crack began to develop transgranular stage II growth propagating in mode I. It is conventionally assumed in literature that transition to stage II takes place when the crack tip plastic zone reaches the size of a grain. The boundary between microstructure sensitive growth (stage I) and the stage II region, sketched in Fig. 4.10 a) was defined as in [3]. Transition to stage II crack propagation was assumed to occur when facets occupied less than 10% of an imaginary crack front and striations appeared on the fracture surface. The microstructure sensitive stage I growth was in a nearly semicircular zone about 250 μm of radius with the nucleation inclusion in the centre (Fig. 4.10 a)). Its shape suggested that the crack initially grew as a semicircular flaw taking later on during further propagation a thumbnail shape with an aspect ratio a/c=0.54. Even the first part of stage

II short crack propagation appeared to be characterised by the growth of a semicircular defect as pointed out by sunrises direction in Fig. 4.10 a). Afterwards the growth along sample width, that is in the rolling direction became easier and the crack assumed a semi-elliptical shape (see Fig. 4.8 a)). Once, close to the sample opposite surface, the crack became a through flaw, and began to grow in the sample width direction. From that moment shear lips developed at the sample surface, crack growth rate increased considerably and after few thousands of cycles the flaw became unstable braking the sample.

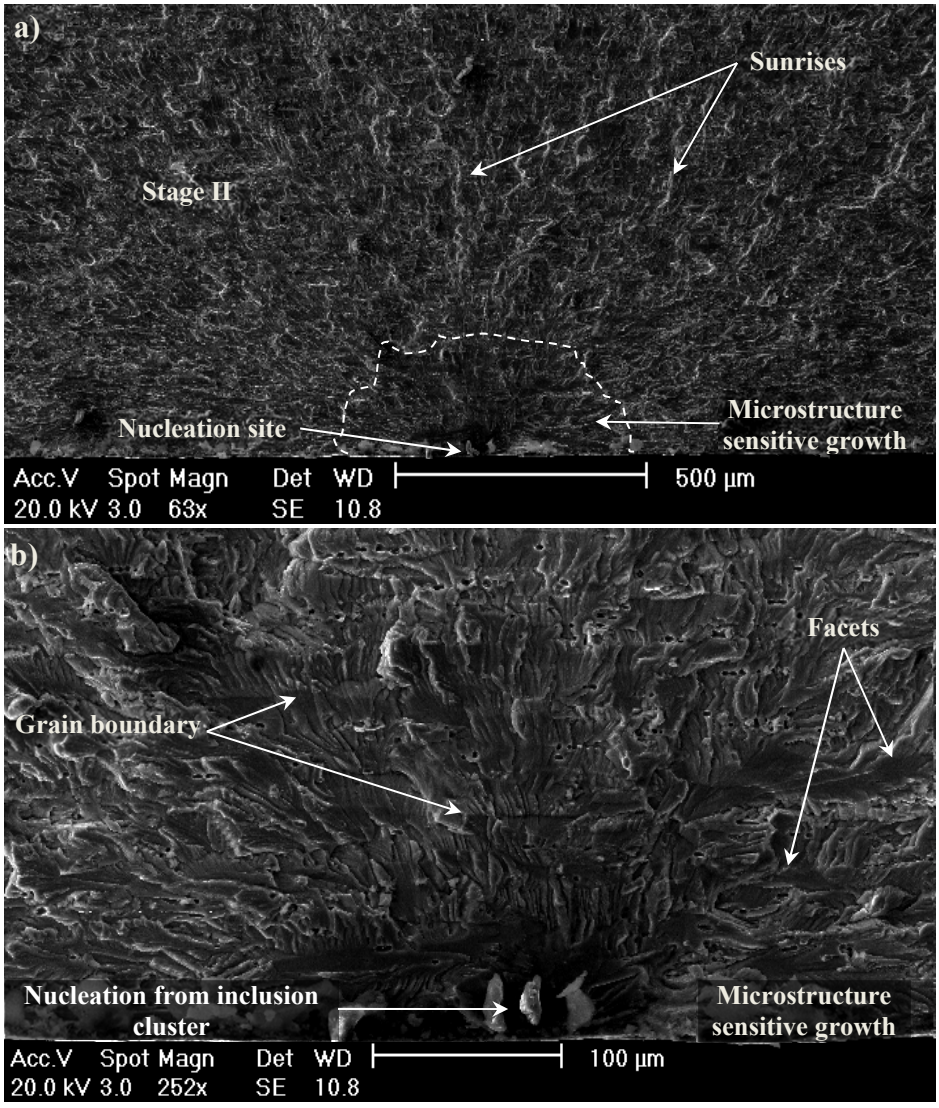

Fig. 4.10: SEM picture of fatigue crack development from inclusion in T-U-0-0 (a), early propagation stage (b)

Unscribed tension unclad samples showed the typical 45° slanted ductile final fracture, caused by voids coalescence under plane stress condition. It was located at both sides of the flat fracture surface, produced by stable crack growth under plane strain condition. That was the evidence proving that the crack became a through flaw before the sample failure. In fact if the unstable growth, leading to the final failure, had occurred along the sample thickness, as in the case of a surface crack, it would have been mainly flat experiencing plane strain conditions.

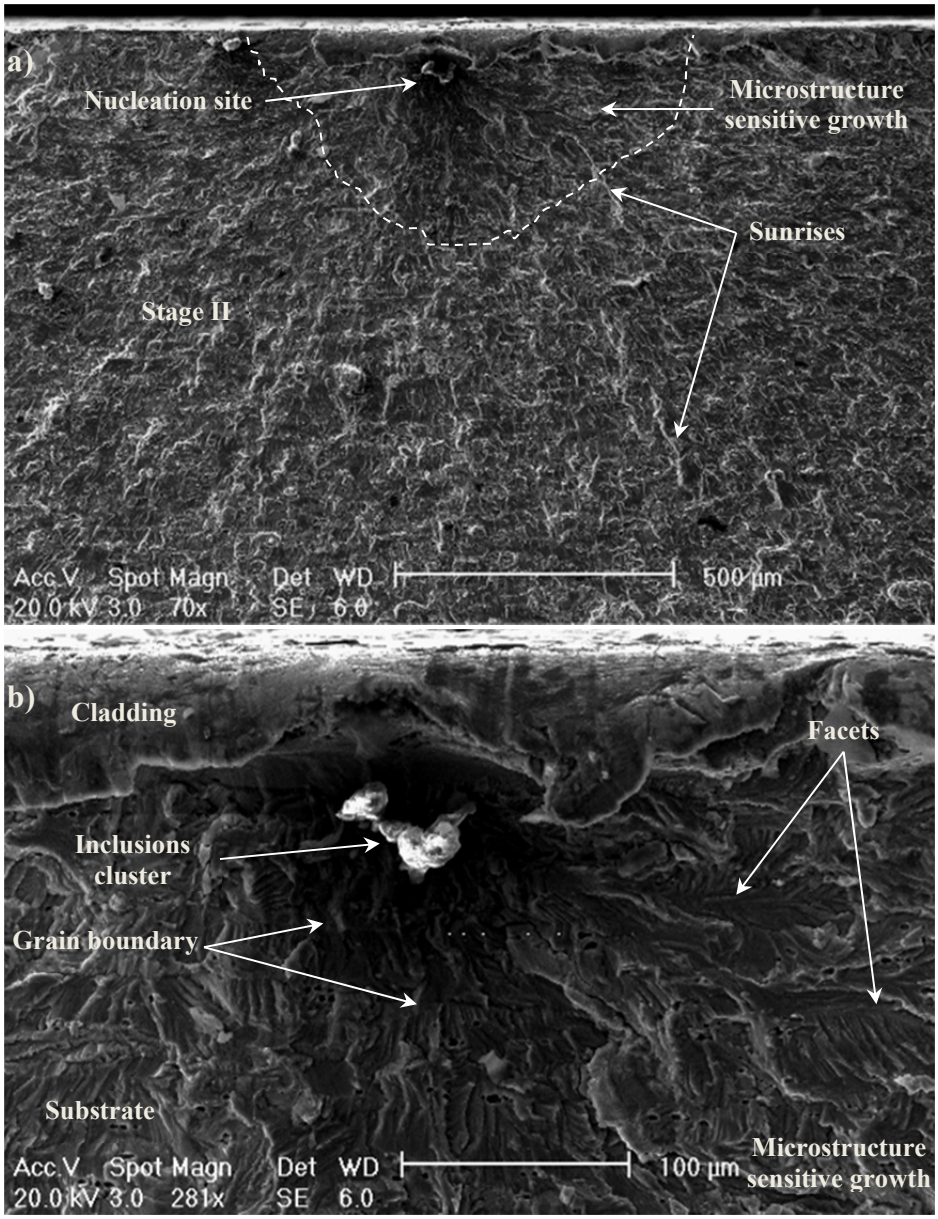

Fig. 4.11: Fatigue crack nucleation from inclusions in T-C-0-0 (a), early propagation stage (b)

Unscribed tension clad samples exhibited a fracture surface similar to that observed in corresponding unclad specimens. Fig. 4.11 shows the fatigue crack surface around the nucleation site (Fig. 4.11 a)) with a magnification of the microstructure sensitive growth region (Fig. 4.11 b)). Sample failure was caused by the development of a single main crack nucleated from an inclusion cluster in the material substrate located near the cladding-substrate interface (Fig. 4.11 b)). Such inclusion resembled the one initiating crack in unclad specimens but it was bigger in size (59.3 x 37.0 x 13.6 µm), showing an irregular shape. An early microstructure sensitive (stage I) growth region followed by a transgranular stage II propagation one characterised by fatigue striation and sunrises were observed also in clad samples (see Fig. 4.11 a)). Characteristic nearly planar and 'feathery' corrugated facets beside arrays of lamellae, changing orientation at grain boundaries, could be observed on stage I growth surface in the aluminium substrate

(Fig. 4.11 b)). Cladding appeared to fold inside the sample as a consequence of plasticisation caused by repetitive fracture surface contacts during fatigue.

After a subsurface nucleation the crack began to propagate through cladding in the crystallographic stage I way, reaching soon the free surface. From that moment it kept growing in stage I as a semicircular surface crack up to reaching a radius of nearly 400 μm (see Fig. 4.11 b)) it developed stage II and the crack path became perpendicular to the loading direction. During stage II growth the crack took gradually an elliptical shape lengthening along the sample width direction. The nucleation point was 1 mm far from the sample edge thus the growing crack became first a corner and subsequently a through flaw reaching respectively the close sample edge and the opposite surface. Once the crack become a 2D flaw growing through the sample width, shear lips appeared at the sample surfaces. The crack quickly propagated few millimetres farther, up to a critical length, where the sample failed. The final failure showed a 45° slanted ductile void coalescence running through the sample width.

Non propagating cracks were observed also on the clad layer of unscribed tension samples as shown in Fig. 4.12 a). They were recognised on the fracture surface thanks to fatigue striations on the cladding in a zone where the substrate exhibited void coalescence final failure (Fig. 4.12 a)). Fatigue striations covered the whole cladding thickness proving that cracks become non propagating once the substrate was reached. Clad layer initiated many cracks but samples failed by cracks nucleated at big subsurface inclusion clusters. Evidence of a secondary crack nucleated from the cladding and propagated into the substrate was found as shown in Fig. 4.12 b). Such defect was able to penetrate into the material substrate, but the main crack development process from inclusions was easier and broke the sample arresting its growth. The secondary crack nucleated at the cladding surface and propagated as a semicircular surface flaw (Fig. 4.12 b)). Substrate fracture showed the typical crystallographic stage I growth surface containing facets and ‘feathery’ corrugated features. On the contrary the clad layer exhibited more marked facets with a 45° slanted smooth planar region at the nucleation point. No particles were found at the nucleation site. Fig. 4.12 b) supplies a further evidence of the early crack propagation as a semicircular surface flaw.

Unscribed bending clad samples showed fracture surfaces with features similar to those found on clad tension samples. Nucleation occurred always at the clad layer subjected to tensile stress and crack propagated as corner or surface cracks. Due to stress gradient cracks were forced to propagated more through the sample width assuming an elliptical shape with a small aspect ratio (see Table 4.6). Cracks grow in crystallographic stage I way with a nearly semicircular shape. Microstructure sensitive growth region had the same extent as the one of tension sample. Cracks during propagation reached the opposite sample surface and kept growing as described in section 4.2.2.

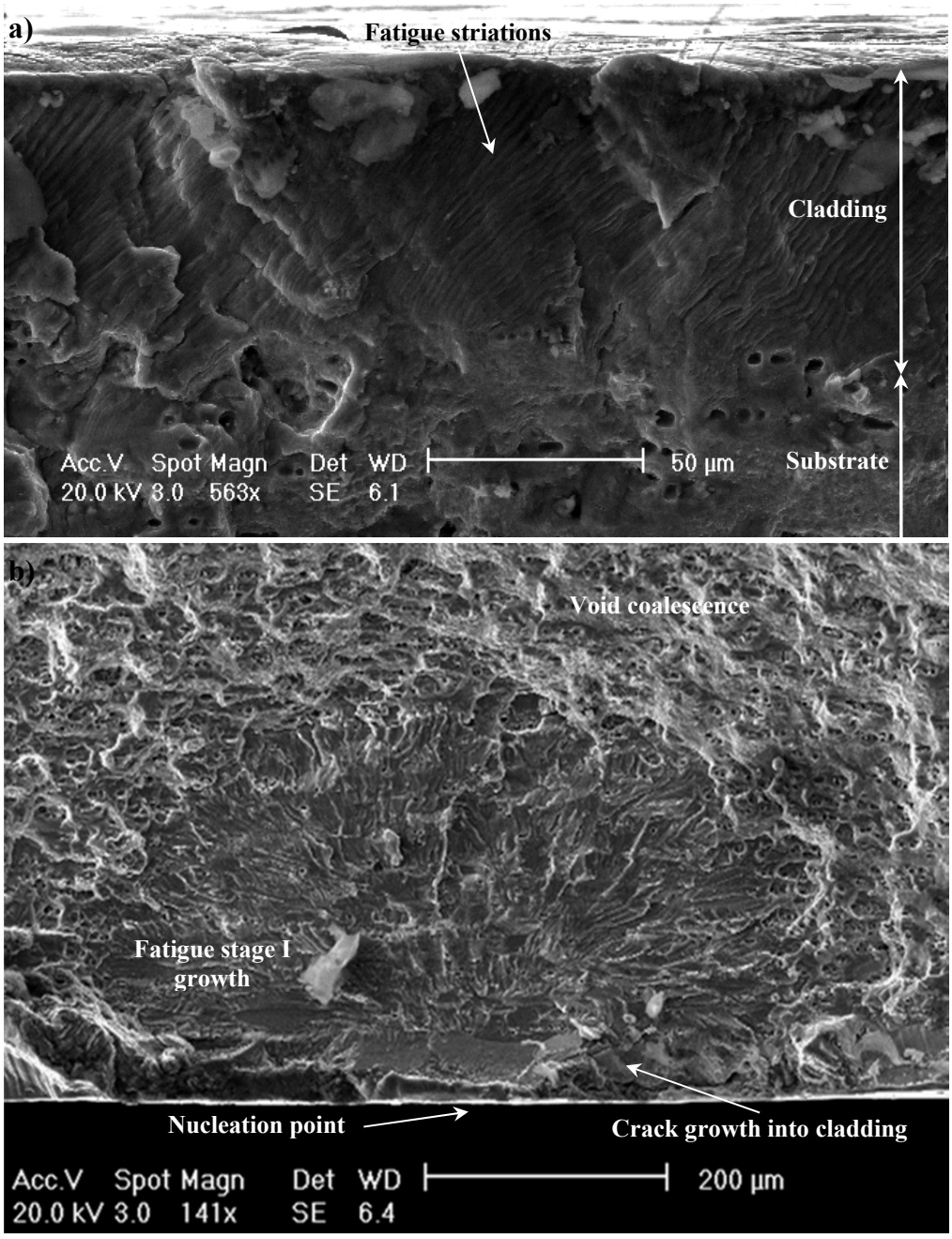

Fig. 4.12: Clad layer cracking (a), secondary crack nucleated into the cladding (b) in T-C-0-0

4.2.3.2 Early development crack from scribe marks

Scribed samples showed different fracture surface morphology, with a variable number of fatigue cracks, depending on the scribe geometry (see section 4.2.2). Crack nucleation occurred at the scribe root in every scribed samples, since it was the zone of higher stress where more energy is available for crack initiation. Stress conditions were nominally the same along the notch root but the microstructure variability implied that crack nucleation took place just at favourable locations along the notch root where microstructure conditions (grain size, orientation and or inclusion size) were such to promote crack formation.

In tension samples, showing a fracture surface composed by several cracks (Table 4.6), multiple nucleation points were observed at the scribe root. The number of nucleation sites per sample was generally no bigger than 20. Cracks nucleated mainly at the scribe root from defects like inclusion particles and superficial damages, even though nucleation from slip bands in favourably oriented grains was observed as well. Fig. 4.13 a) shows a small surface crack nucleated from inclusion particles at the 50 μm root radius of a 50 μm deep scribe in tension unclad sample (T-U-50-50). Cracks initiated from every nucleation location and grew as independent surface flaws under fatigue loading until the main crack developed unstable growth, breaking the sample. If the nucleation points were close enough, cracks could coalesce during propagation to form a bigger surface flaw. No information was available on when cracks developed at different nucleation sites. It is not known if all the multiple cracks nucleated at the same time and the main crack became larger during its growth, or if secondary cracks initiated after the main flaw initiation as consequence of the stress increase produced by the net gauge section reduction.

Nucleated cracks began to growth as a small surface flaws in the region affected by the notch stress field. Even if the characteristic facets of stage I growth were absent on the fracture surfaces (see Fig. 4.13 a)), the early growth stage of multiple cracks, seemed to occur along crystallographic planes. In fact fracture surfaces, produced by early crack growth, showed arrays of parallel lamellar features that formed micro cliffs perpendicular to the local growth direction. Such lamellae converged toward the nucleation point facilitating its identification and showed smooth surfaces without any sign of striations on them (Fig. 4.13 a)). They appeared be sensitive to the material microstructure changing orientation and planar slope at grain boundaries (Fig. 4.13 a)). Therefore a kind of stage I like growth with different orientation in every grain should have taken place. The planar faces of the lamellae showed different tilt angles at the grain boundaries (Fig. 4.13 a)).

Therefore also the early propagation stage of small semi-elliptical surface cracks under the scribe stress field was locally controlled by the material microstructure being crystallographic. On the whole cracks remained perpendicular to the loading direction but locally grew along crystallographic planes. After the microstructural growth stage cracks continued to propagate as a superficial flaws in transgranular stage II as described below. The effect of scribe geometry on crack shape evolution is analysed in the following section.

Single coalesced crack fronts were produced by the coalescence of several cracks separately nucleated at notch roots (section 4.2.2). Scribed samples, failed developing single coalesced crack fronts on their fracture surfaces exhibited, therefore, a multitude of nucleation points all along the scribe root. Fig. 4.13 b) shows some of the nucleation sites identified at the 50 μm root radius of 185 μm deep scribe machined in an unclad tension sample. Preferential nucleation sites were voids and defects produced at the notch root, during the scribing procedure, and weak points consisting of grains with slip systems favourably oriented for dislocation motion (Fig. 4.13 b)). Due to the large number of active sites along the scribe root, some nucleation points resulted inevitably few tens of microns far from each other. Depending on nucleation points distance cracks

could coalesce during their early microstructure sensitive growth or when stage II propagation was already developed. Fig. 4.13 b), for instance, shows steps produced by a small cracks coalescence occurred during the very early stage of growth.

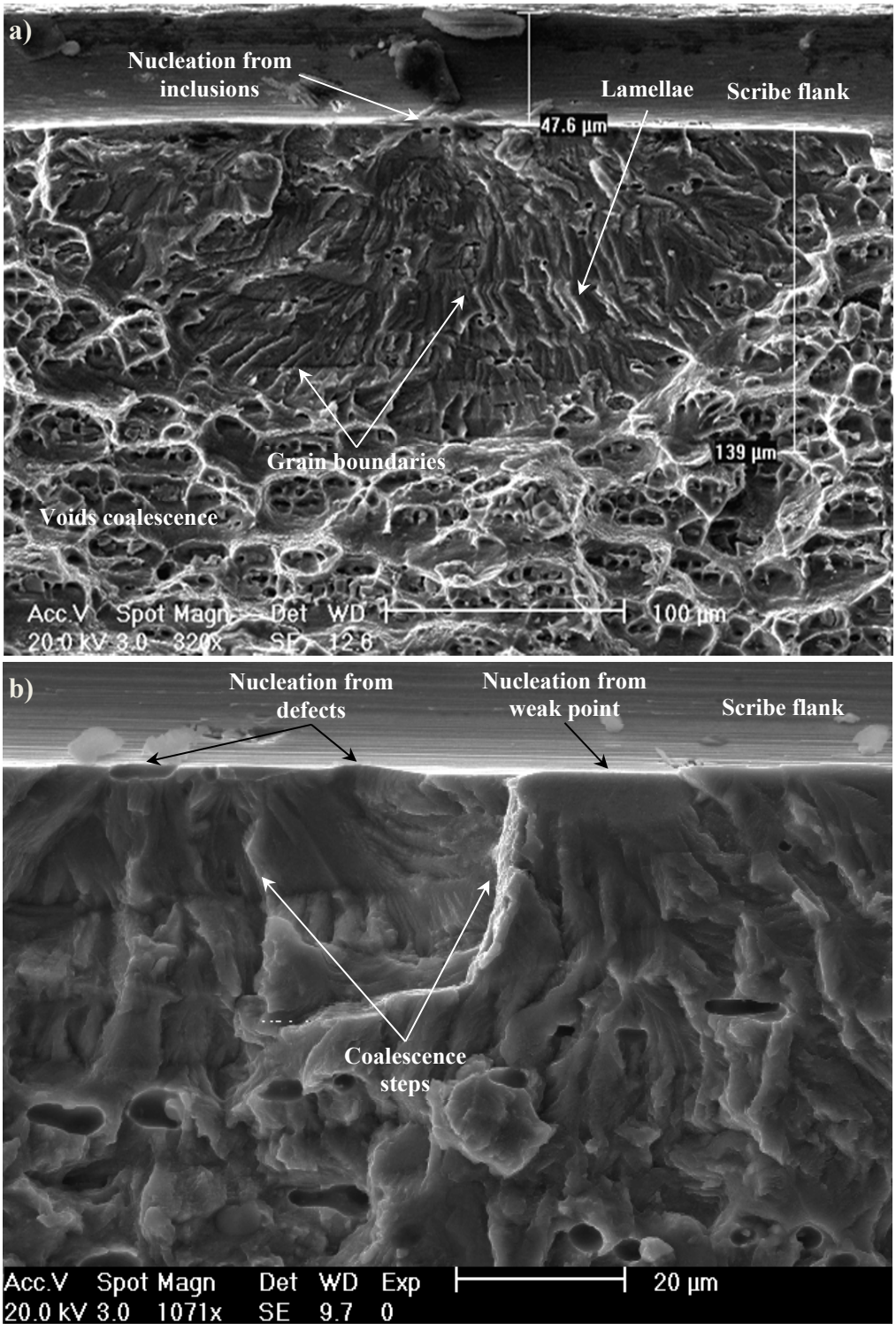

Fig. 4.13: Crack nucleation at the scribe root: from inclusions in T-U-50-50 (a), from defect in T-U-185-50 (b)

Cracks propagated from nucleation sites at the scribe root as semi-elliptical surface flaws and in the first propagation stage they were subjected to a strong microstructure influence. Lamellae arrays, like those found on multiple cracks fracture surfaces, were observed in coalesced fracture fronts near the notch root (Fig. 4.13 b)). The fracture surface morphology suggested that nucleation of different cracks took place almost simultaneously in various notch root locations. In fact coalescence steps were almost evenly spaced, indicating the simultaneous growth of multiple cracks. However an easier nucleation was expected to occur close to the sample edge, where plane stress conditions existed, producing a deeper crack front at those locations (see section 4.2.2). Multiple cracks coalesced during their propagation to form a single front. It was the further growth of such unique fatigue fracture front, made by cracks propagating on parallel plane, that leaded to samples failure.

Tension samples failed by means of single elongated fronts did not show any evidence of multiple crack nucleation or coalescence along the scribe root. Nucleation was likely to occur slightly before at the scribe root portions close to sample edges, where a deeper crack front was observed. Fig. 4.14 shows a portion of the 2D elongate crack nucleated from the root of a 50 µm deep, 5 µm root radius clad tension sample. Even if inclusions particles and machining introduced defects were observed at the scribe root they appeared not to be favourite sites for crack nucleation, but to be situated on the crack growth plane instead. The fatigue crack seemed to be initiated by dislocations motion on primary slip systems activated in every grains at the scribe root. Therefore a single crack, few microns deep, but running all along the notch root length was produced during nucleation stage. Such newly formed crack began to propagated across the sample thickness up to the sample failures.

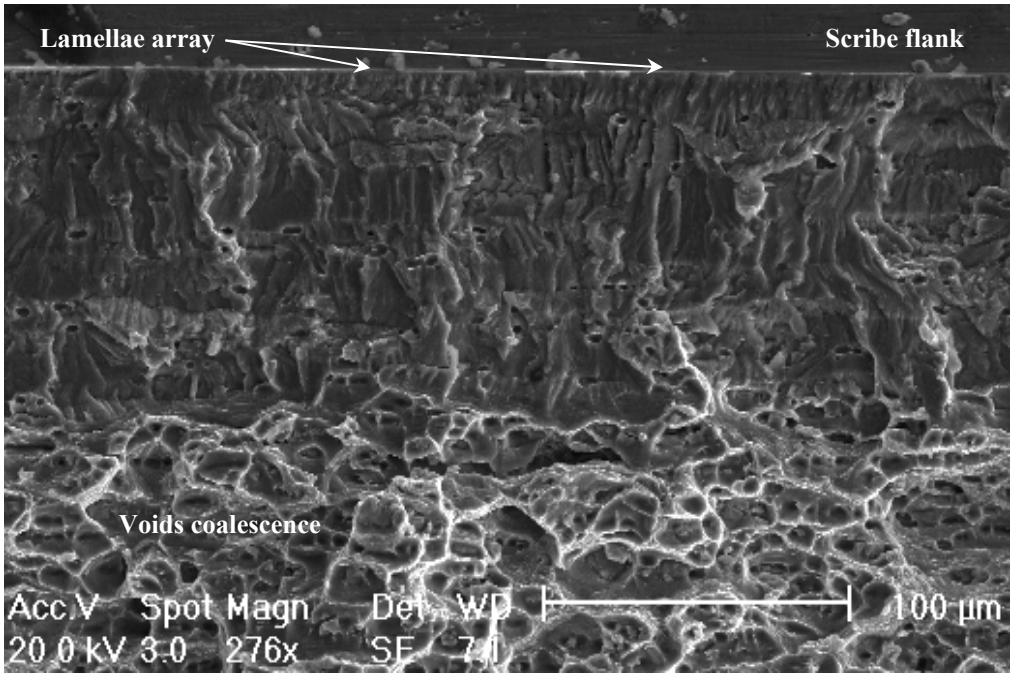

Fig. 4.14: Crack nucleation in T-C-50-5

Once again the early growth stage of elongated short cracks was influenced by the local microstructure taking place in a crystallographic way. That was proved by the

characteristic arrays of crystallographic lamellae and steps found at the notch root (see Fig. 4.14). They were oriented perpendicularly to the scribe root indicating an homogeneous growth of the entire crack front through the sample thickness. In fact, if multiple surface cracks had developed and grown, the lamellar steps, being parallel to the local crack propagation direction, would have assumed a radial disposition pointing to the nucleation point as in Fig. 4.13 a).

If scribe roots were completely embedded into the clad layer, as in the case of 25 and 50 μm deep scribed clad tension samples, no substantial changes of the various nucleation mechanisms, described above for unclad specimens, were observed. The number of multiple nucleation sites along notch roots were approximately the same (see Table 4.6) despite the cladding and depended only on scribe geometry. The only difference for clad samples with scribe roots contained into cladding was that no nucleation from inclusions or machining defects were observed. That was a consequence of the absence of inclusion intermetallic particles inside the superficial clad layer.

Cracks, showed the same nucleation process from scribe roots of both bending and tension clad and unclad scribed samples. Bending samples showing elongated fronts, were discovered to nucleate single through width short cracks either, while the number of multiple nucleation points and relative initiation mechanisms involved in multiple cracks and coalesced bending fracture fronts were similar to those found on tension samples. Once again regions close to the sample edges seemed to experience a slightly quicker nucleation causing a deeper fatigue fracture front (section 4.2.2). Fractographic features analogous to those shown in Fig. 4.13 and Fig. 4.14 were observed at the scribe root of bending clad and unclad specimens. Cracks, nucleated at the scribe root under pure bending load, experienced the usual crystallographic microstructural sensitive early growth. However it extend through a larger portion of the surface in comparison with tension samples. Crack grew in their early stage of propagation as superficial or through-width flaws and eventually coalesced following the same mechanism observed under tensile loading. The only difference was the tendency of superficial cracks to grow more along the scribe root assuming a more elongated shape. That mechanism, consequence of the bending stress gradient, was mainly observed for cracks propagating away from the zone influenced by the notch stress field.

4.2.3.3 Crack propagation from scribe marks

Typical fracture surface features, common to different kinds of tested samples, were identified and correlated to particular crack growth behaviours. At the notch root of every scribed sample, where crack nucleation takes place, a peculiar irregular fracture surface was observed. Fig. 4.15 shows, for instance, the fracture surface, left by a crack growing from the 5 μm root radius of a 50 μm deep scribe in unclad tension sample. An uneven region, few microns deep, extended along the whole notch root. It was characterised by micro-cliffs separated by regions with irregular appearance (Fig. 4.15 a)). These were actually fracture surface portions composed of a multitude of rectangular scales (Fig. 4.15 b)). Micro-cliffs showed a flat top surface containing repetitive linear marks similar to striations although with a more uneven aspect. The whole fracture surface was tilted from the notch symmetry plane and appeared to

change orientation in correspondence of grain boundaries (see Fig. 4.15 a)). That was a further evidence of the microstructure sensitive growth experienced by the crack in its early propagation stage. The same surface features were found at the scribe root no matter it was located into the clad layer or into the aluminium substrate. The depth of the irregular notch root region seemed to be regulated by the scribe geometry and by the different loading conditions, being deeper for deeper and sharper notches.

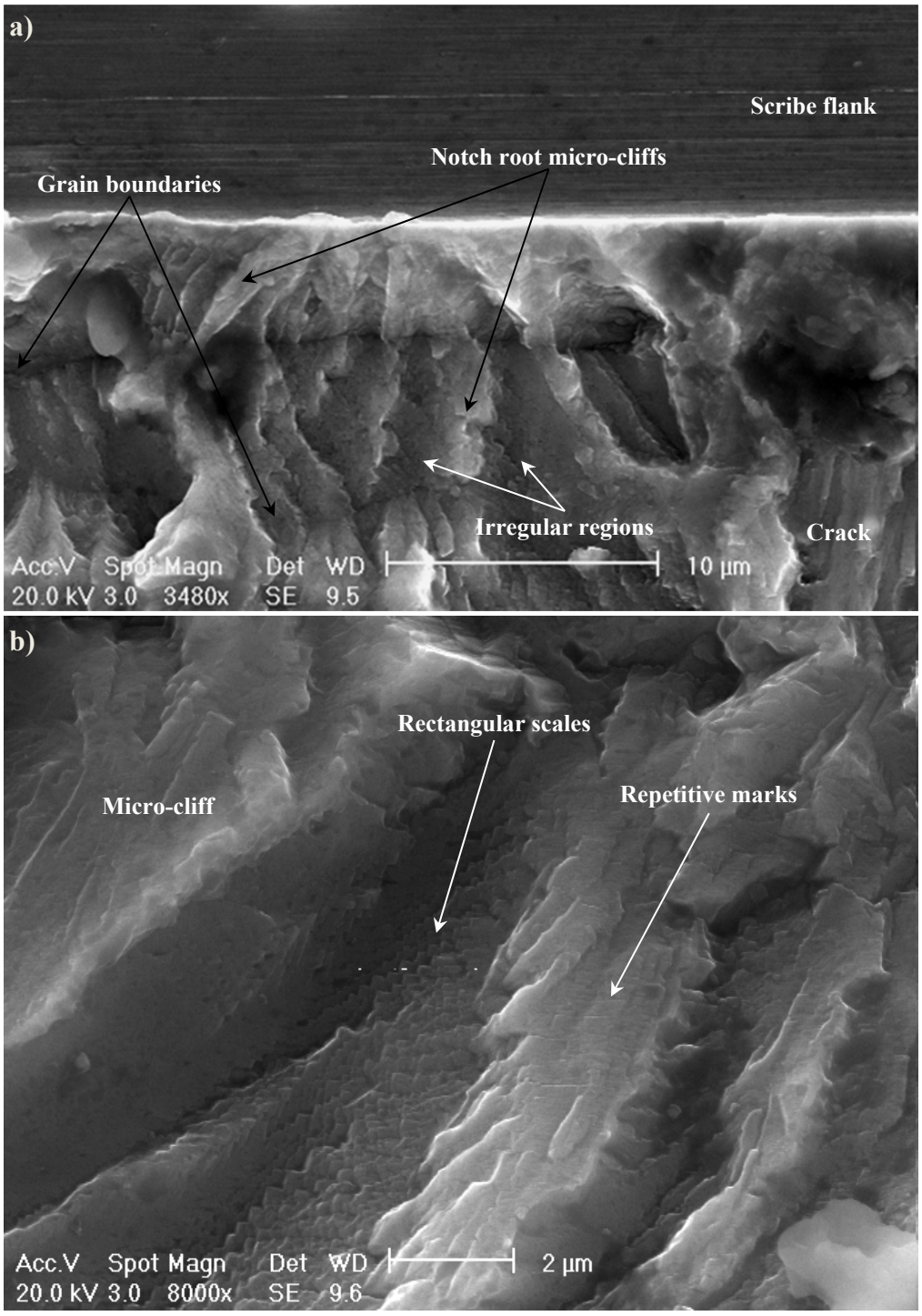

Fig. 4.15: Fatigue crack surface at the notch root in T-U-50-5 (a), notch root features magnification (b)

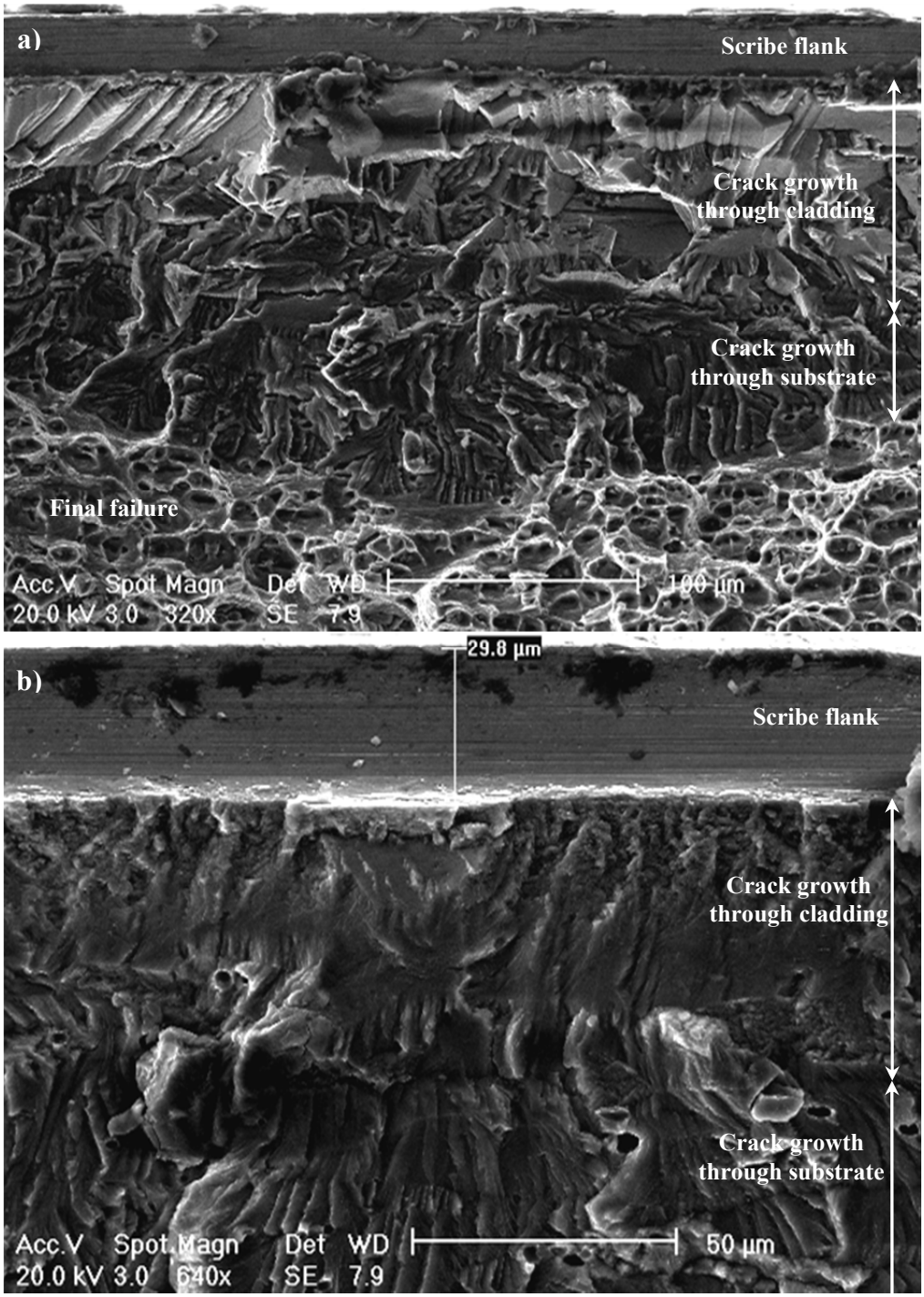

Fig. 4.16: Crack growth through cladding: structure sensitive propagation of a thumbnail crack in T-C-25-5 (a), propagation in T-C-25-25 (b)

Once the crack crossed the few microns deep uneven region in front of the notch, its fracture surface assumed different appearance depending on whether the propagation occurred inside the clad layer or the substrate. If scribes were completely embedded into cladding as in the case of 25 µm and 50 µm deep scribes machined on tension and bending clad samples part of crack growth was spent into the pure aluminium, forming the soft cladding. Beside, different mechanical properties, responsible of different plastic deformation behaviour, cladding showed diverse microstructure compared with

the hard substrate. It is therefore obvious that propagation into the clad layer was characterised by different features in particular because it coincided with the early microstructure sensitive growth stage.

Fig. 4.16 a) and b) show the crack growth through cladding from 25 μm deep scribes with respectively 5 μm and 25 μm root radii in clad tension samples. Generally on the surface of small thumbnail cracks growth through cladding was characterised by a geometric structure composed by regular facets (see Fig. 4.16 a)). Such features, typical of crystallographic stage I crack growth were very similar to those distinguishing the structure sensitive crack growth through the clad layer found in [4]. It was evident that crack propagated in cleavage-like stage I along parallel crystallographic planes, joined by cleavage steps, inside the same grain [5]. Growth plane orientation changed at grain boundaries. As soon as the crack get closer to the substrate the geometric structure was replaced by the 'feathery' corrugated features typical of crystallographic stage I growth in 2024-T351 aluminium alloy.

Crack growth in the substrate was recognisable (Fig. 4.16 a)) by development of lamellar features arrays like those found in Fig. 4.13 a). It is worth noticing that the entire propagation stage of the thumbnail crack, being crystallographic, was affected by the material microstructure (stage I like growth). In case of large thumbnail or through sample width cracks, growth into cladding generally resulted in a different fracture surface morphology (Fig. 4.13 b)). It was more amorphous than the growth through the substrate, which showed a more regular surface with crystallographic lamellae and steps. Crack propagation into cladding seemed to be structure insensitive, being perpendicular to the loading direction. No sighs of crystallographic facets, as in the case of the growth surfaces of small thumbnail cracks, were found. Propagation returned microstructure sensitive once the crack grew into the substrate. A similar clad layer fracture surface was found in [4]. The same clad fracture surface appearance was observed in both bending and tensile samples.

If scribes were machined in unclad samples or deeper than the clad layer thickness in clad specimens cracks grew into 2024-T351 aluminium alloy. No differences were observed in the morphology of fracture surfaces produced by cracks growing in unclad samples or in the material substrate of clad specimens. Fig. 4.17 shows an example of substrate fracture appearance close to the 5 μm root radius of a 50 μm deep scribe in unclad tension samples. Fracture surface showed a facetted aspect with arrays of lamellae and steps parallel to the local crack growth direction. Such lamellar features were formed by crack growth along different planes of the same slip system inside a grain. Lamellar steps changed their plane orientation at grain boundaries because of the tilt angle between favoured slip systems in adjacent grains. Different crack propagation plane orientations in diverse grains are pointed out by variations of surface brightness in Fig. 4.17. Such variations make grain boundaries clearly recognisable. Lamellar step surfaces were smooth with no signs of striations. Crack growth from micromechanical notch root inside 2024-T351 aluminium alloy was therefore crystallographic (stage I-like), showing a strong microstructure sensitivity. Crack nucleated from scribe marks exhibited microstructure sensitive early propagation as in the case of naturally initiated cracks in unscribed samples. The only difference seemed to be the absence of 'feathery'

corrugated features observed only in unscribed sample fracture surfaces. Stage I like growth was observed in every region along the notch root, where cracks developed.

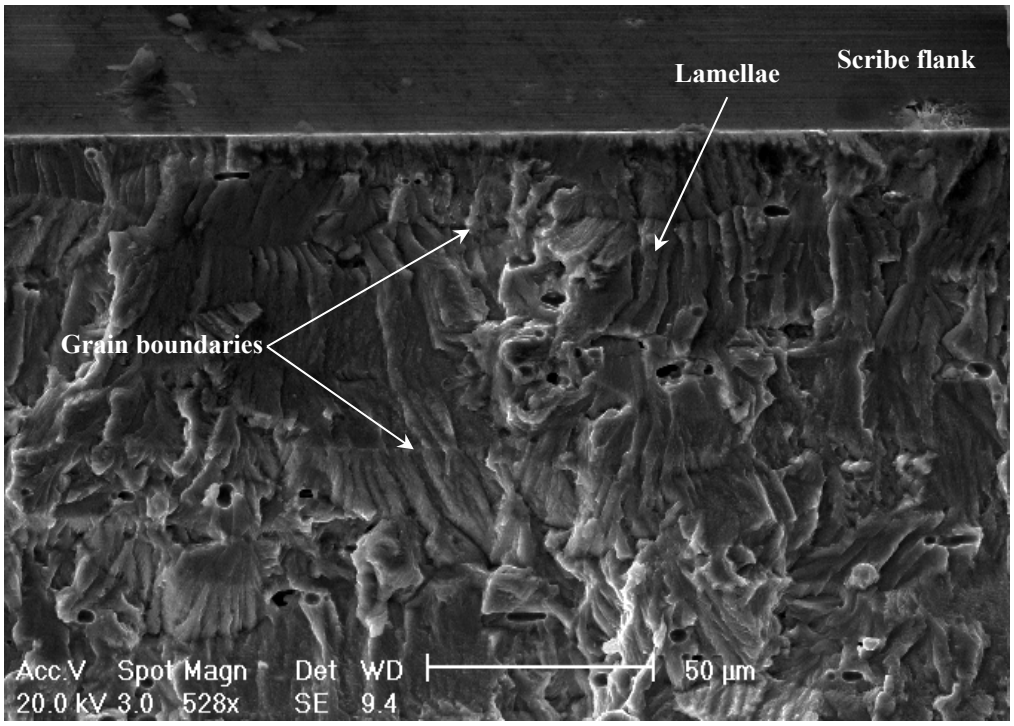

Fig. 4.17: Crack growth through substrate features in T-U-50-5

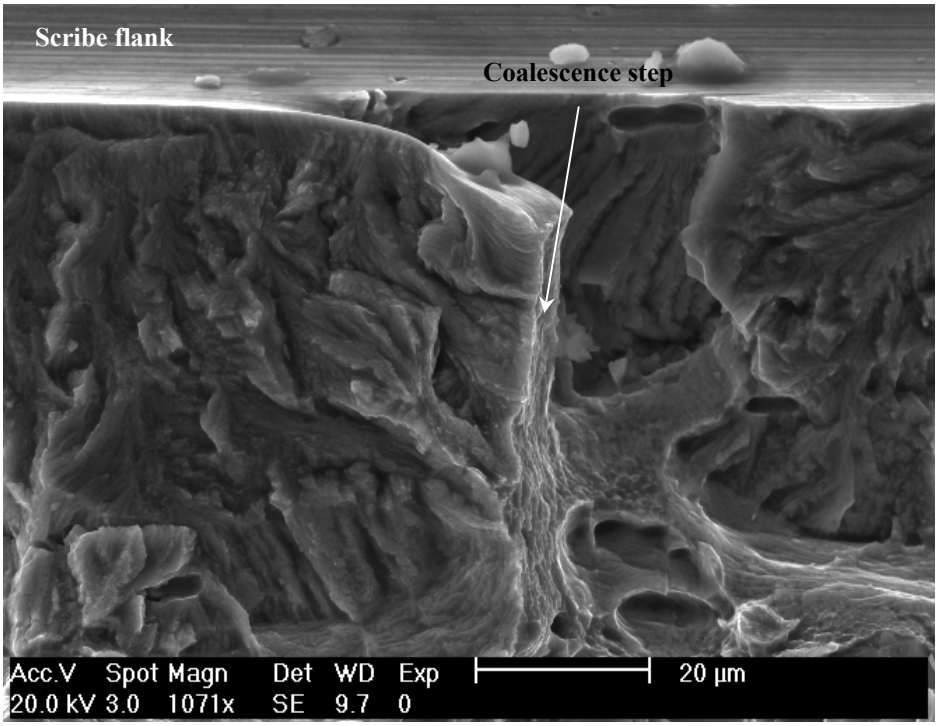

Fig. 4.18: Coalescence step in T-U-185-50

Cracks showed similar fracture surface features independently of fracture front shape. In case of multiple nucleation sites along the scribe root, cracks could

coalescence during their growth. Distinct cracks commonly propagated on offset parallel planes and coalescence occurred by the formation of steps. Fig. 4.18 shows a coalescence step on the fracture surface of a 185 μm deep, 50 μm root radius scribed unclad tension sample. The coalescence step was produced by unstable shear fracture of the material ligament linking two offset crack growth planes. Sometimes cracks can overlap before the step is fully developed and coalescence occurs (see Fig. 4.18). The step surface was characterised by irregular longitudinal marks produced by the shear failure.

Microstructure sensitive stage I-like crack growth was observed close to the notch root in all the scribed samples fracture surfaces analysed. Early crack growth seemed to be strongly influenced by material microstructure despite different notch geometry, cladding and load conditions. The scribe geometry, loading condition, and cladding regulated the depth of the fracture surface region at the notch root occupied by the microstructure sensitivity growth (microstructural short crack region). Fig. 4.19 a) and b) show respectively the crack growth through different propagation stages from the notch root in the 185 μm deep, 5 μm root radius scribed tension clad sample and in the 100 μm deep, 5 μm root radius scribed bend unclad specimen. As can be clearly seen from Fig. 4.19 microstructure sensitive growth region was nearly four times deeper in bend samples than in tension ones.

Cracks nucleated from the same scribe geometry respectively in clad and unclad samples, and propagated under equal load conditions, developed stage II growth at similar distances from the notch root. Cladding seemed not to affect the transition from crystallographic stage I-like to stage II growth. If scribe root was contained into the clad layer, and clad amorphous non-crystallographic growth developed, crack began to propagated in crystallographic manner as soon as it reached the substrate. Even in that case transition to stage II growth in clad samples took place at the same distance from the scribe root as in the corresponding unclad specimens.

Obviously cracks with different shapes (thumbnail or 2D through sample width) exhibited transitions at diverse depth but the differences were of few microns and therefore negligible. Scribe root radius did not play any roles in determining microstructure sensitive growth region depth on fracture surfaces, as specimens tested under the same loading and containing equally deep scribes, with different notch root radius, showed crack growth stage transition at comparable distance from the notch root. Only scribe depth and loading condition were discovered to affect considerably the crack depth where stage II growth developed. The deeper was the scratch the shallower was the region influenced by crystallographic propagation. 185 μm deep scribed tension samples showed transition to transgranular growth nearly 50 μm far from the notch root (Fig. 4.19 a)), while in those 50 μm deep, transition took place, when cracks had grown about 100-130 μm through the sample thickness. The equivalent scribed samples, tested under bending load, nucleated cracks from scribe roots growing in crystallographic stage I-like respectively for 100 μm and 190 μm.

Actually if the scribe depth (d) was added to the transition crack depth, that is if the transition depth was measured starting from the sample free surface, growth shift to transgranular stage II seemed to occur, under the same load conditions, at similar

distances from the sample surface. In fact microstructure sensitive crack propagation appeared to develop on tension samples in a zone 180-235 µm deep from the sample surface despite different scribe geometries. Bending test samples load had an increased depth of stage I-like growth reaching up to 240-285 µm from the sample surface.

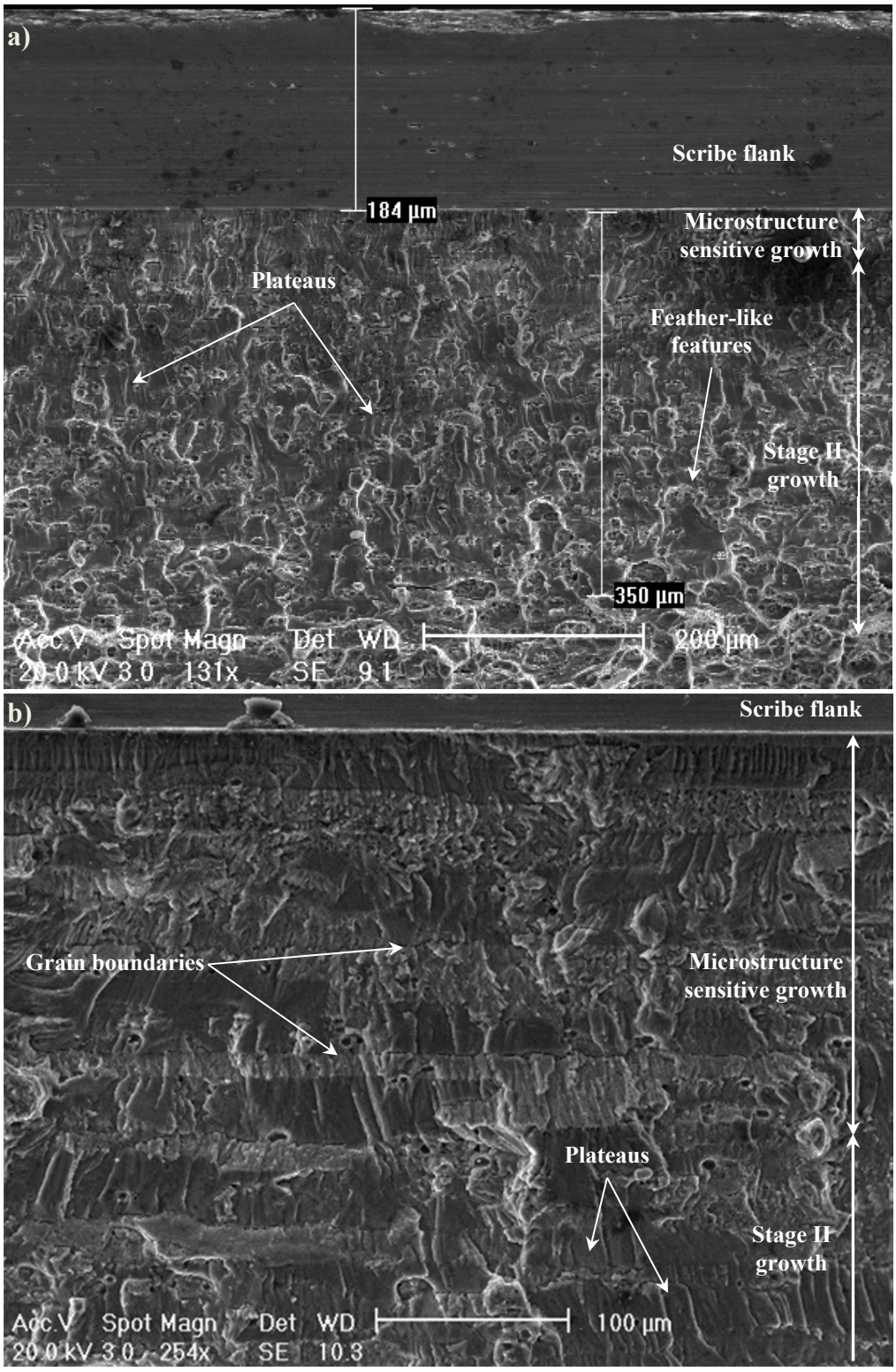

Fig. 4.19: Crack growth through different stages in T-C-185-5 (a) and in B-U-100-5 (b)

No striations were found in the microstructure sensitive growth region. Fracture surface changed orientation at grain boundaries, pointing out the characteristic pancake grain structure, typical of rolled sheets, with grains elongated along the rolling direction (Fig. 4.19 b)). Crack surface in microstructure sensitive growth region was facetted showing single planar facets inside every grain. When transgranular crack growth developed, the effect of local microstructure ceased and the crack path became globally perpendicular to the loading direction. Cracks often propagated on multiple plateaus that were at different elevations with respect to one another (Fig. 4.19). On the surface of such plateaus, joined either by tear ridges or walls, fatigue striations were detected [5]. In the final regime of crack propagation feather-like features were observed as well (see Fig. 4.19 a)) [6].

While crack nucleation and early growth were affected mainly by notch stress field, different remote load conditions altered the further crack development. Diverse fracture fronts types (see section 4.2.3) were mainly a consequence of different nucleation processes at the scribe root, however loading conditions played a role on defining crack front shapes. Analogous fracture fronts exhibited different shapes whether they developed under tension or bending load (see Fig. 4.7). In fact the stress gradient, characterising pure bending load, promoted the formation of thumbnail cracks more elongated through the sample width than under tension load. The favoured crack growth along the notch root direction facilitate cracks coalescence, as proved by the smaller number of surface cracks, forming multiple cracks fronts in bending samples than in tension ones (Table 4.6). Elongated and coalesced fracture fronts, developed from scribe marks under bending load, were deeper at the sample edges than the corresponding ones observed in tension samples. They showed a bi-lobed shape with large lobes close to the sample edges. That was surprising since bending stress gradient should had promoted the formation of a front uniformly deep along the scribe root rather than a bi-lobed one. The phenomenon is not entirely understood. Sunrises and fatigue striation directions on fracture surfaces confirmed the radial crack growth from the sample edge inward. During further crack propagation lobes settled down to a quarter-elliptical shape with an aspect ratio a/c=0.10-0.16 (Table 4.6). When crack fronts at sample edges get close to the opposite surface, specimens failed.

All tested samples failed showing a final ductile fracture characterised by void coalescence. It is possible to observe in Fig. 4.9 the clean separation between the nearly smooth surface, distinctive of stable crack growth, and the dimples generated by void coalescence during unstable final ductile fracture. Such clean boundary was indicative of the fact that the unstable crack propagation, leading to failure, did not originate from the central part of the fracture fronts, shown in the pictures. In fact there, the crack was completely motionless when final failure took place, producing a sort of fatigue fracture snapshot with the peculiar clean boundary.

Actually it was the fatigue crack itself that, once reached a critical size, started to growth unstably, by void coalescence, and quickly fractured the sample. Transition between stable and unstable crack growth however did not happen suddenly and fracture surface regions, containing evidences of that transition, were expected to be found where final failure initiated. Fig. 4.20 shows the crack growth transition region

close to the edge of the 50 μm deep, 5 μm root radius tension clad sample (T-C-50-5). The transition region was observed in tension and bending samples to coincide with the deepest region of elongated and coalesced crack fronts located at the sample edge. In fracture fronts, formed by single or multiple surface and corner cracks the transition was found around the main flaw. Transition region was constituted by alternation of voids and fatigue striations (see Fig. 4.20). The void density increased, for bigger distances from the notch root, up to the point where striations disappear an final failure occurred. From that point void coalescence almost instantly spread over the entire net ligament surface and the sample failed.

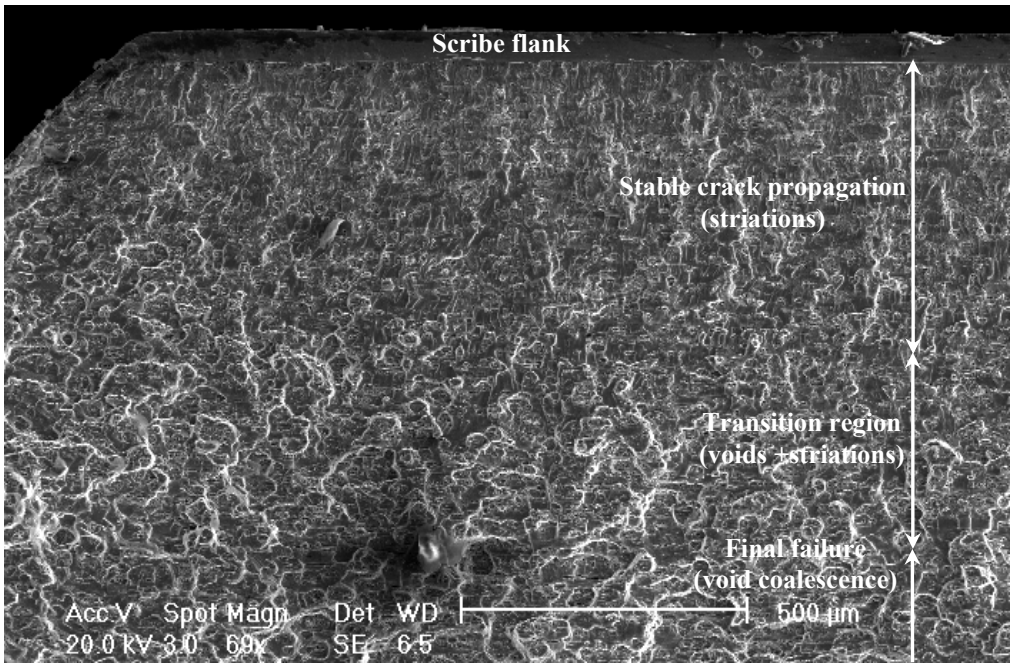

Fig. 4.20: Crack propagation features close to the edge of T-C-50-5 fracture surface

4.2.3.4 Crack shape

The shape of semi-elliptical surface cracks nucleated from the scribe root was measured. Secondary surface cracks, forming multiple crack fronts on scribed sample fracture surfaces, had their final depth (a) and half length, on the scribe root surface (c) measured. Crack aspect ratio (a/c) was then calculated and, as multiple secondary cracks on the same fracture surface reached different depths, information on crack shape evolution could be obtained. Post failure measurements were performed only on cracks showing a single nucleation point at the scribe root. However cracks, grown on the same fracture surface, could mutually interact, if they were close enough, modifying their shapes one another. Fig. 4.21 shows surface crack aspect ratios a/c as function of crack depth (a) in microns measured on multiple crack fracture fronts of tension and bending samples.

All the aspect ratios measured on fracture surface of different scribed samples ranged between a/c=0.24 and a/c=0.75 (Fig. 4.21). It means that all the measured cracks, despite different notch geometry and loading conditions, showed a semi-elliptical shape with the major axis along the scribe root. That should not be surprising, as crack

propagation along scribe roots took place under the raised stress field generated by notches. However also naturally nucleated cracks from material inclusions in unscribed samples, after an early growth stage as semicircular flaws turned into a semi-elliptical shape elongated through the sample width (see section 4.2.3.1). The entire body of data as a whole showed a large scatter for cracks shallower than 200-250 µm (Fig. 4.21). Such scatter was gradually reduced, as the crack depth increased, up to nearly 500 µm deep flaws where the aspect ratio stabilised around a value of a/c=0.5, despite different scribed samples.

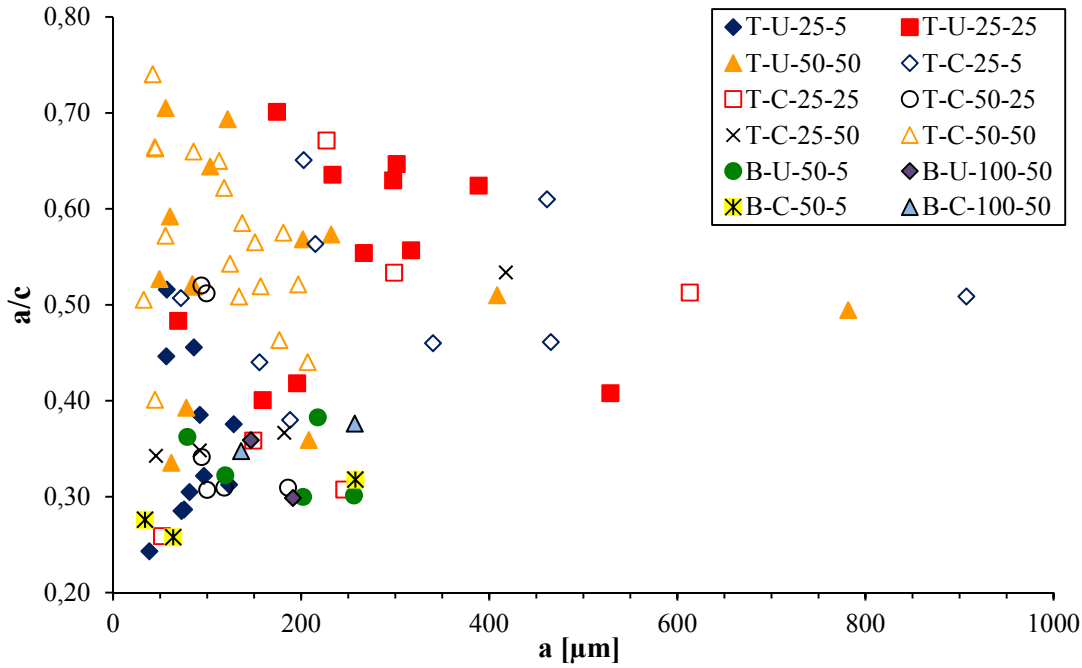

Fig. 4.21: Surface crack aspect ratio evolution at notch root of different scribed samples

Crack aspect ratio settled down to a value similar to that found for cracks fracturing unscribed clad and unclad tension samples. No secondary cracks deeper than 260 µm were measured in bending samples (Fig. 4.21). Most cracks did not growth beyond the microstructure and notch affected zone, being shallower than 200-300 µm. A large scatter was observed also for cracks belonging to the same fracture surfaces. Sharp notches like 25 µm deep 5 µm root radius scribes seemed to promote the formation of thumbnail cracks with an aspect ratio between a/c=0.52 and a/c=0.26 in unclad tension samples (Fig. 4.21). The mean aspect ratio (a/c=0.36) bore evidence of the crack inclination to grow more under the notch stress field. Different behaviour was observed when the same notch was embedded into cladding. In fact 25 µm deep scribe with 5 µm root radius in clad tension samples showed cracks with a larger mean aspect ratio of a/c=0.51.

Clad tension samples containing 50 µm deep, 25 µm root radius (T-C-50-25) and 25 µm deep, 50 µm root radius (T-C-25-50) scribes showed cracks with an average aspect ratio respectively of a/c=0.38 and a/c=0.40. In the former samples the small aspect ratio was produced by the higher notch stress field. On the contrary in the latter specimens containing blunt notches an aspect ratio, smaller than the typical value of

a/c=0.50 observed with other 50 μm and 25 μm root radius scribes, could be caused by interaction and coalescence of small cracks during their early growth stage.

Crack shape data showed smaller scatter in bending samples than under tensile load. Bending load stress gradient appeared to reduce the crack aspect ratio down to average values of *a/c*=0.28-0.36 (Fig. 4.21). Fracture surface main crack aspect ratios were generally smaller than those showed by secondary cracks (see Table 4.6). In conclusion scribe geometry appeared to affect crack shapes and relative aspect ratios more by regulating the number of nucleation points along their root than by the effect of their increase stress fields. The shape of main cracks was therefore modified by the occurrence or not of the coalescence of small cracks nucleated close each other rather than by the different notch stress fields.

4.2.3.5 Non propagating cracks

Fractography observations revealed that non propagating cracks developed at the scribe root of 50 μm deep, 50 μm root radius scribed clad bending samples. Those specimens failed at the gauge section by cracks nucleated from other locations than the scribe root. Main cracks nucleated in the clad layer on the sample surface subjected to tensile stress [7] and grew like those found in unscribed bending samples. A second crack developed from the scribe root, although it never reached the critical size necessary to trigger the unstable final failure fracturing the sample. Such flaw was considered as a non propagating crack even if it was not verified whether the crack really stopped growing during fatigue life or if its growth was interrupted by the sample failure. A picture of the non propagating crack is shown in Fig. 4.22. Non propagating crack occurrence seemed related to the presence of cladding since unclad bending samples containing a 50 μm deep, 50 μm root radius scribes, failed from the notch root.

The non propagating crack was 6.22 mm long on the notch root surface with its external tip located 0.82 mm from the sample edge. No information was available on crack depth, as only a SEM microscope inspection of the notch surface was performed. Fig. 4.22 a) and b) show respectively a portion of the non propagating crack profile along the scribe root and a detail of the crack path. The crack grew mainly on the scribe root symmetry plane where the stress was maximum but deviations, like those shown in Fig. 4.22 a), were frequent. However crack path remained confined into a circular sector of ±30°. Crack branching were observed as well (Fig. 4.22 a)). Some parts of the path were composed by very regular straight segments. The majority of such segments developed along parallel offset planes, perpendicular to the loading direction and connected by shear steps (Fig. 4.22 b)). Other path portions were much more irregular (Fig. 4.22 a)).

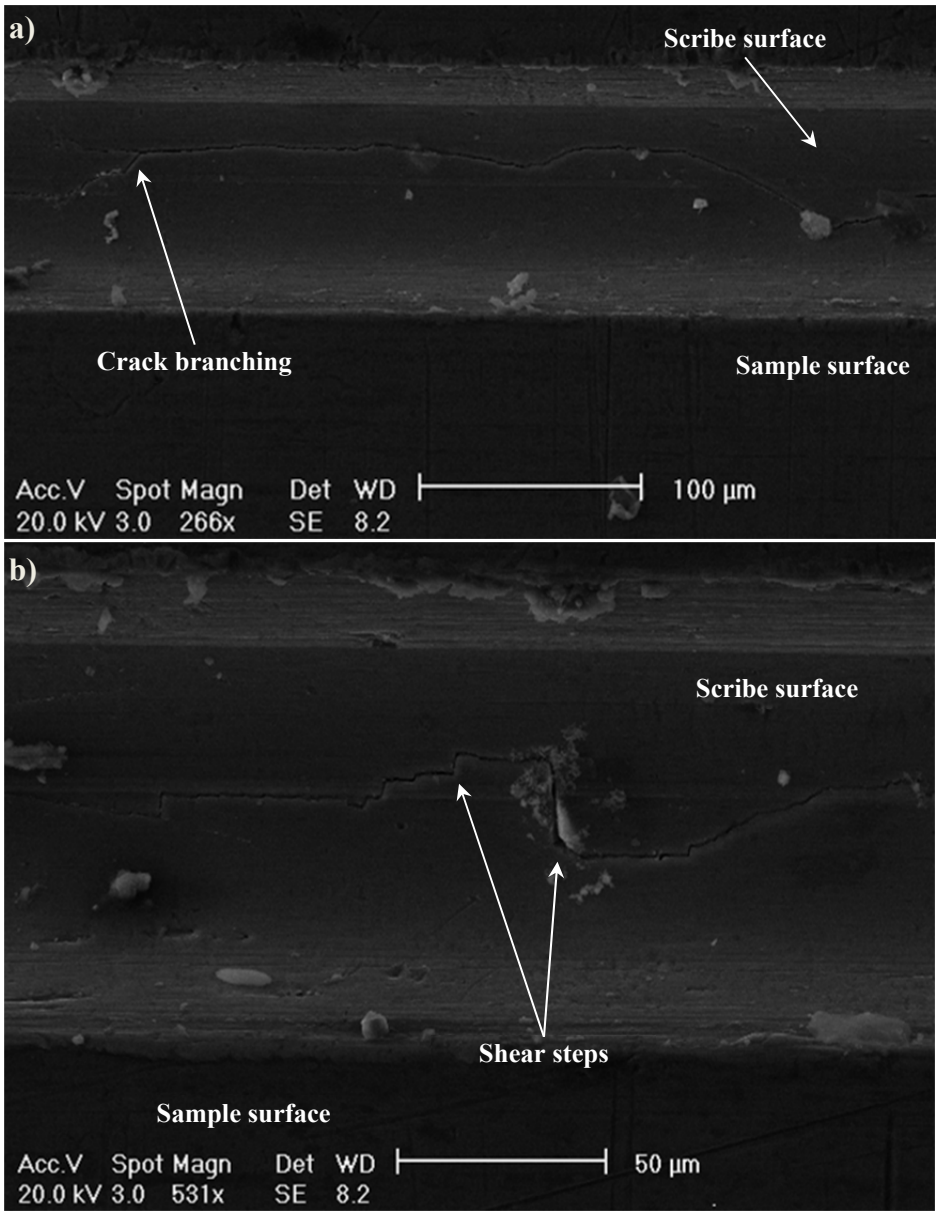

Fig. 4.22: Non-propagating crack in B-C-50-50 (a), crack path magnification (b)

4.2.4 Crack growth rate

Crack growth rate was measured on selected tension and bending samples by striation counting, performed following the procedure described in chapter 3. Crack growth rate data, were recorded for different crack depths. No striations were found in the region of microstructure sensitive propagation. Fracture surfaces produced by crack growth through cladding whether crystallographic or amorphous did not show striations (see section 4.2.3.3). It was decided to perform striation counting only at the sample width coordinate where the front was the deepest and void coalescence started. Those were locations along the fracture front where the fastest crack growth took place. In case of thumbnail main cracks just the growth rate through the sample thickness was analysed and no information on superficial propagation along the scribe root was obtained. Striation spacing measurements were carried out up the crack depth where

voids occupied nearly 50% of the transition region from stable to unstable crack propagation (see Fig. 4.20). Further stable crack growth was expected to occur beyond such depth but at so high rates to be negligible in term of propagation life. Striation counting data were used to predict crack propagation lives from scribe marks as described in chapter 6.

4.2.4.1 Crack propagation under tensile load

Striation counting was firstly carried out on fracture surfaces of 185 µm deep, scribed clad and unclad samples with 5 µm and 50 µm root radii. Fig. 4.23 shows growth data measured on 185 µm deep scribed tension samples plotted in semi-logarithmic scale against crack depth measured from the scribe root. Growth rates in every sample seemed to be an exponential function of the crack depth, showing a linear trend in a semi-logarithmic plot. Trend lines are shown in Fig. 4.23. Crack growth rate increased with crack depth. No growth data were obtained for cracks shallower than 30-50 µm since below such depth flaws experienced microstructure sensitive growth (section 4.2.3.3). Measured growth rates ranged from a minimum value of 0.035 µm/cycle up to a maximum of 0.680 µm/cycle. All data showed a quite moderate scatter around trend lines (Fig. 4.23). Scribe root radius seemed not to influence crack growth rates as 5 µm and 50 µm root radius scribed samples exhibited similar values (see Fig. 4.23). Propagation of cracks was slower in clad samples than in unclad ones at the same depth.

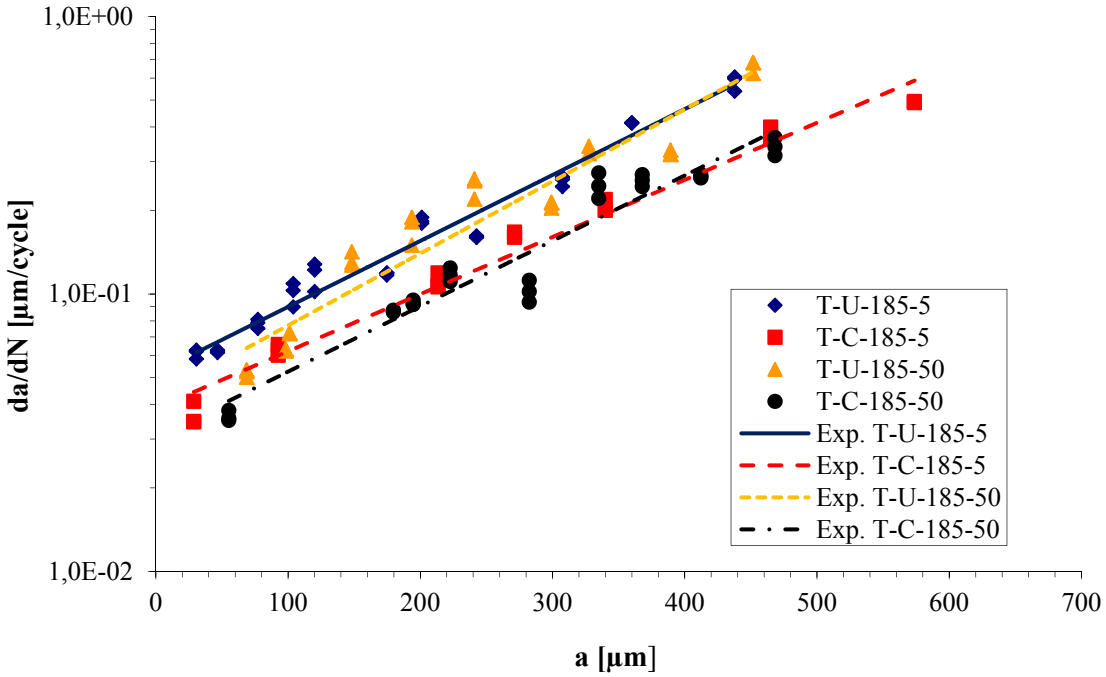

Fig. 4.23: Experimental crack growth rate in 185 µm deep scribed tension samples

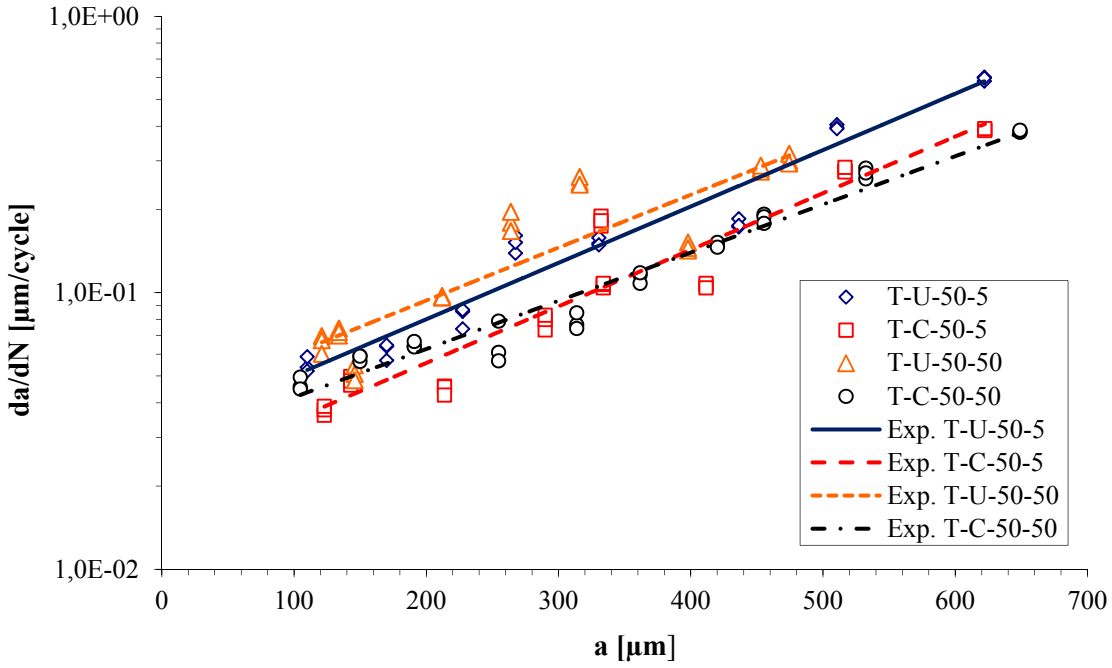

Fig. 4.24: Experimental crack growth rate in 50 µm deep scribed tension samples

Fig. 4.24 shows growth rate data obtained on 50 µm deep scribed clad and unclad samples with different root radii (5 µm and 50 µm). Once again growth rate was an exponential function of the crack depth, scatter being slightly bigger than in 185 µm samples. No growth rate data were obtained for cracks shallower than 100-120 µm. Scribed clad and unclad samples with 5 µm root radii showed an elongated or coalesced crack fronts while 50 µm root radius scribes produced multiple crack fracture front. However despite the different shape between thumbnail and elongated main cracks, 50 µm and 5 µm root radius scribed specimens exhibited nearly the same growth rate for fixed crack depth.

The effect of different notch depth on crack growth rate can be evaluated in Fig. 4.25 where experimental measurements of all tension samples investigated are reported. Trend lines accurately predicted experimental data showing R^2 from 0.88 to 0.94. Cracks nucleated from scribes as deep as 50 µm grew slower than the ones from 185 µm deep notches at a given distance from the scribe root (a). The deeper the scribe the faster the crack propagation.

In order to take into account the sample finite thickness effect, the crack growth rates measured in all tension samples were plotted against the thickness fraction reached by different crack tips. Crack depth (a) was added to the notch depth (d) and divided by the sample thickness (t), obtaining $(a+d)/t$. Fig. 4.26 shows growth rate data of all the measured scribed tension samples plotted versus this parameter. As can be seen, once the finite thickness effect was considered, growth rates of different scribed clad and unclad tension samples lay on the same trend line. All the experimental data, despite different scribe geometry and cladding, followed, scatter apart, the same exponential function of the sample thickness fraction parameter. The equation of the line is displayed in Fig. 4.26 together with the goodness of the fit (R^2). The R^2 value of 0.89

indicated the effectives of the thickness fraction parameter in predicting growth rates of crack nucleated from different scribes.

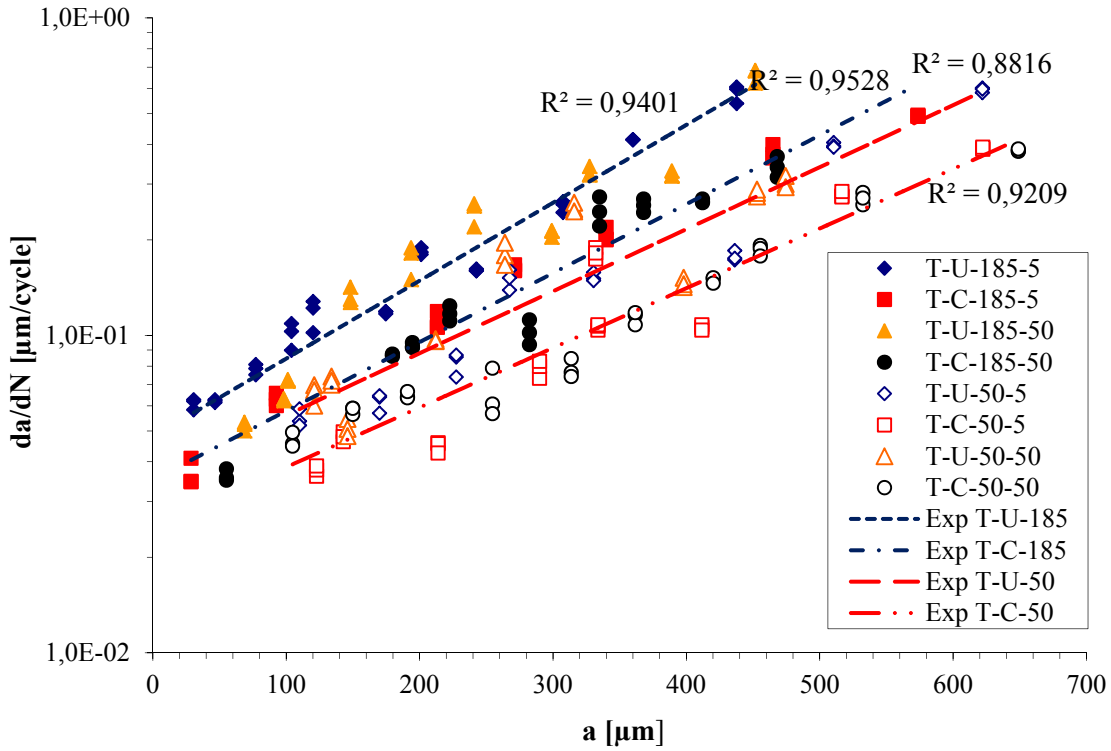

Fig. 4.25: Experimental crack growth rate in clad and unclad tension samples

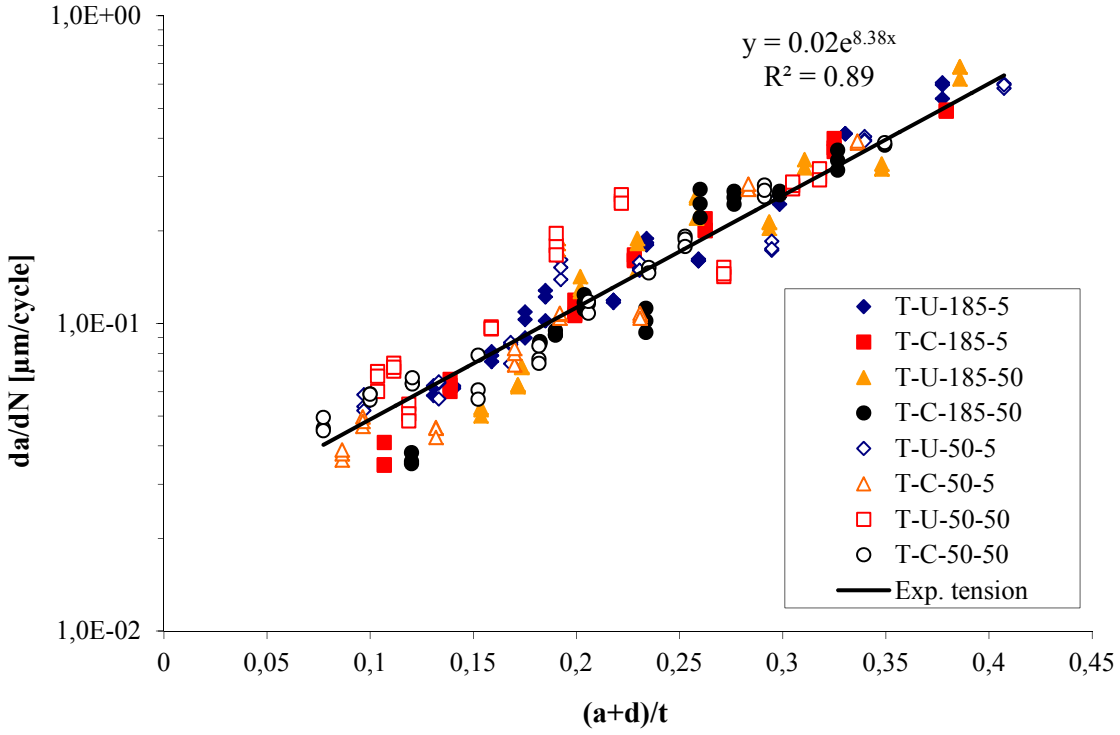

Fig. 4.26: Experimental crack growth rate in tension samples versus non dimensional parameter including finite thickness effect

4.2.4.2 Crack propagation under bending load

Striation spacing under bending loads was measured on 4 selected samples in the same way as for tension loaded samples. Clad and unclad 185 µm deep, 5 µm root radius, unclad 185 µm deep, 50 µm root radius and 50 µm deep, 5 µm root radius scribed bending samples were selected. Fig. 4.27 shows crack growth rates in µm/cycle plotted against the crack depth, measured from the notch root, together with best fit trend lines. Under bending load data seemed to be approximated by a third degree polynomial function of crack depth. Crack growth rate increased slowly or were nearly constant in the first stage of propagation. Then it raised with almost a constant slope in a semi-logarithmic scale to settle down again around higher constant values in the final growth phase. Growth rates followed an S shaped trend in all the samples (see Fig. 4.27). In some case, as for 50 µm deep, 5 µm root radius unclad scribed sample, propagation rate was observed to decrease at remote distances from the notch root.

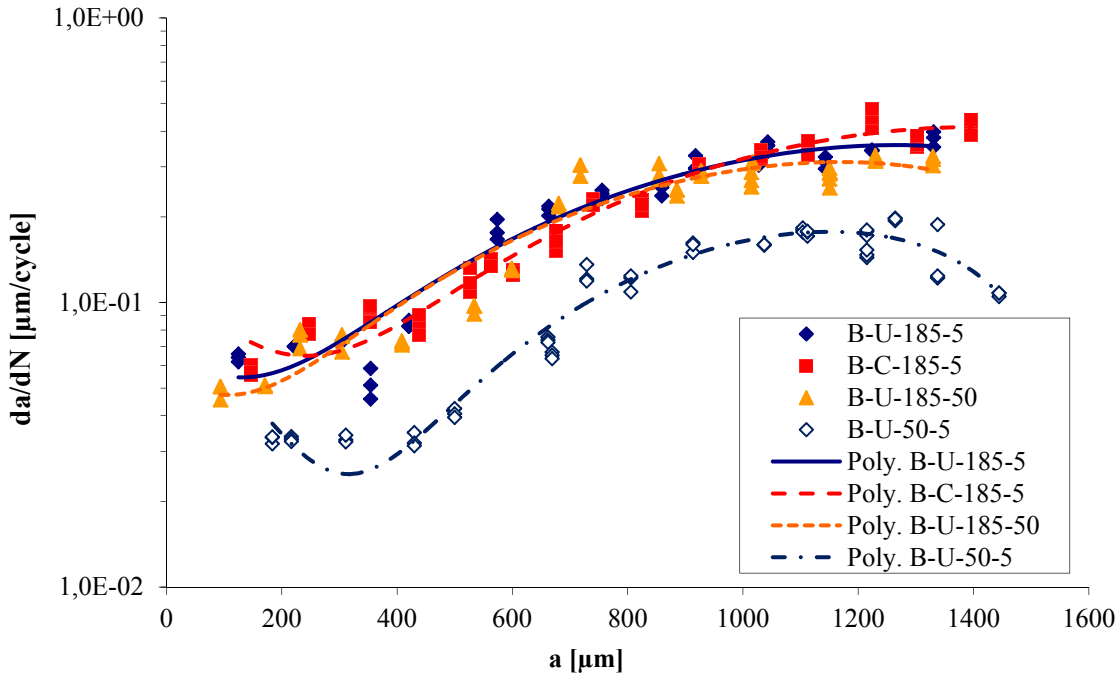

Fig. 4.27: Experimental crack growth rate in bending samples

Measured growth rates ranged from a minimum of 0.032 µm/cycle up to a maximum of 0.440 µm/cycle. No growth data were available for cracks shallower than 100-140 µm and 190 µm respectively in 185 µm deep and 50 µm deep scribed samples (Fig. 4.27). As in the case of tension samples, scribe root radius did not affect measured growth rate. There was no effect of clad layer on measured growth rates (Fig. 4.27). Crack propagation from shallow scribes as deep as 50 µm, with 5 µm root radius was slower than from deeper notches for a given crack length as observed under pure tensile load (Fig. 4.27).

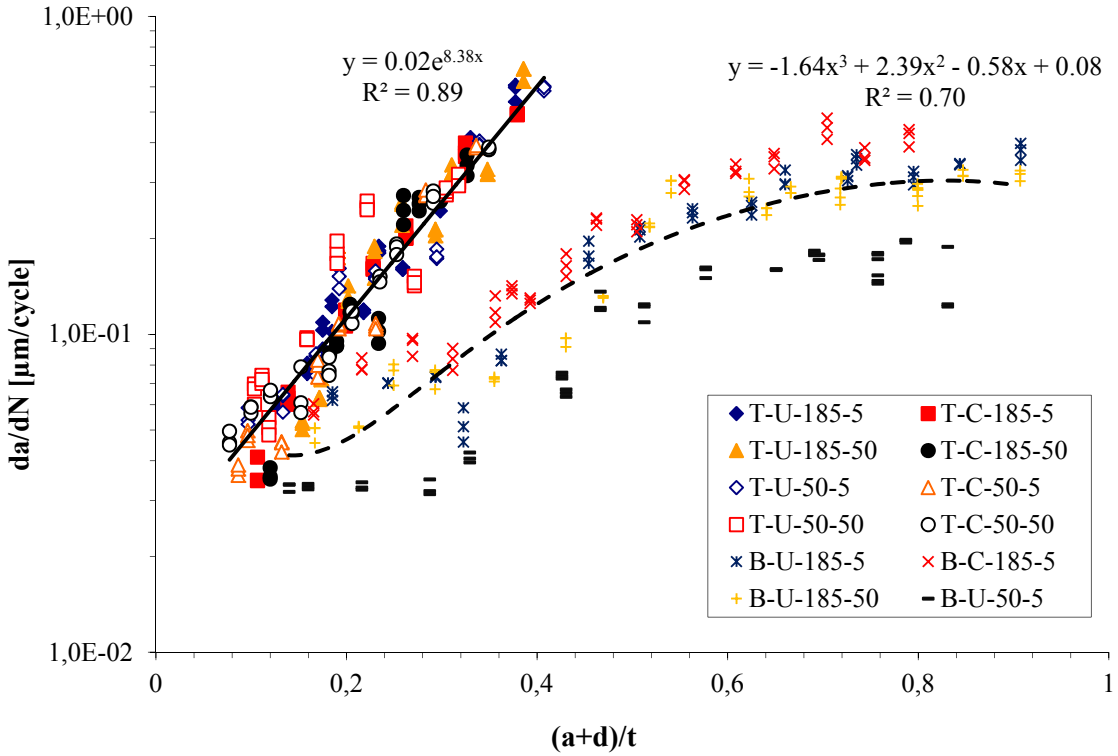

Fig. 4.28: Experimental crack growth rate in bending samples versus non dimensional parameter including finite thickness effect

Fig. 4.28 shows growth rate data of all the scribed bending samples plotted against the sample thickness fraction parameter *(a+d)/t* taking into account finite thickness effect. For comparison tension data are displayed as well. Trend lines of the whole bending and tension experimental data and their equations are reported in Fig. 4.28 together with goodness of fit parameters (R^2). In case of bending load the sample thickness fraction parameter was not able to unify growth rates in different scribed samples as accurately as for tensile loading. In fact growth rate correlation under bending load exhibited a larger scatter than in tension samples (R^2=0.7).

In particular propagation rates from 50 µm deep, 5 µm root radius scribed sample were still smaller than those from other bending data even after considering the finite thickness effect (see Fig. 4.28). The different crack front composed by multiple cracks rather than the elongated one showed by the other measured bending samples (Table 4.6) it was believed to be the main cause of growth rate reduction. In fact crack front morphology produced main cracks with a bigger aspect ratio (a/c=0.15) and consequent reduction of the driving force at the crack deepest point where growth rate was measured. For small values of sample thickness fraction, scatter apart, crack propagated at comparable rates under tensile and bending loads (Fig. 4.28). As soon as cracks became bigger, they experienced more and more the bending stress gradient effect, reducing the driving force, and the bending growth rate turned out to be slower than the tension one at a given *(a+d)/t* value. Also under bending load the notch stress field and cladding seemed not to considerably influence crack propagation under bending load and every crack nucleated from scribe marks is expected to follow the same growth behaviour.

4.3 Summary of experimental results

Constant amplitude fatigue tension and four point bending tests (σ_{max}=200 MPa, R=0.1) of clad and unclad 2024-T351 sheet samples, containing diamond cut scribes, were performed considering the sample complete failure as failure criterion. Notch depths ranged from 25 to 185 μm and root radii from 5 to 50 μm. Scribes on clad and unclad samples negatively affect the fatigue life under tensile and bending loads causing up to 97.8% of life reduction. The notch sensitivity increased as the scribe became deeper and sharper. The effect of cladding was to shift the curve to longer lives compared to unclad samples, although the life reduction from the unscribed reference was similar in both clad and unclad specimens. Unclad and clad samples seemed insensitive to scratches as small as 25 μm deep with root radius equal or bigger than respectively 25 μm and 50 μm. Bending scribed specimens showed fatigue lives longer than the corresponding tension ones, but the life reduction caused by scratches was of the same order as under pure tension. Clad bending samples were insensitive to 50 μm deep notches with 50 μm root radius.

Notches cut produced by diamond tools showed very precise and reproducible cross sections with the absence of material piling ups. That confirmed the cutting nature of scribing procedure related to the lack of machining-induced plasticity and residual stresses. As in service scratches, introduced by knife, showed irregular geometries but comparable to the rounded V shaped cross section of diamond tool scribes. However, in opposition to diamond tool notches, they were characterised by large scribing-induced material plasticity and consequent residual stresses, as pointed out by pile ups heights of the same order of magnitude as scribe depths.

Fatigue cracks nucleated at the scribe root and grew through the sample thickness in clad and unclad tension and bending scribed samples. Multiple crack initiation occurred at scribe roots usually from inclusions, defects or weak points along the scribe root under tensile and bending loads. The number and density of crack nucleation sites appeared to be determined by the scribe sharpness, increasing for deeper notches with smaller root radii. According to the number of nucleation points, multiple cracks could coalesced during their propagation, forming fracture surfaces with different shapes. For scribes deeper than 50 μm in clad and unclad tension sample, the large number of active nucleation sites made short cracks coalesced during their early propagation, forming a unique fracture front elongated along the whole sample width. Scribes shallower than 50 μm in tension samples showed fracture surfaces made of multiple thumbnail and corner cracks up to a maximum of 15 cracks per sample. Tension clad and unclad specimens weakened by 50 μm deep scribes developed a unique elongated fracture front only for a sharp notch root radii of 5 μm. In presence of notches with 25 μm and 50 μm root radii in tension samples, elongated crack fronts showed arrays of parallel coalescence steps, proving that the fracture front was made up of several cracks coalesced together. Under bending loading, the transition between multiple crack and elongated fracture fronts occurred in presence on scribes as deep as 100 μm. If the scribe root was completely embedded into the clad layer the number of multiple nucleation sites along notch root was approximately the same as in the corresponding unclad sample but no nucleation from inclusions or machining defects was observed.

Early crack growth seemed to be strongly influenced by the material microstructure despite different notch geometry, cladding and load conditions. The transition between stage I and stage II growth was regulated by the crack tip plastic zone rather than by notch plastic zone. In fact, despite different scribe geometries, microstructure sensitive crack propagation appeared to develop in a zone 180-235 μm and 240-285 μm deep from the sample surface respectively under tensile and bending load. Propagation into the clad layer was characterised by different features than the one in the aluminium substrate, in particular because it coincided with the early microstructure sensitive growth stage. Cracks growth through cladding of small thumbnail cracks was characterised by a geometric structure composed by regular facets, typical of crystallographic stage I along parallel crystallographic planes. In case of large thumbnail or through sample width cracks, growth into cladding generally resulted in a structure insensitive amorphous fracture surface. Scribe geometry appeared to affect the crack propagation and thus the crack shape evolution more by regulating the number of nucleation points along their root than by the local stress raising effect along the notch root.

Short crack growth rate was measured by striation counting on selected tension and bending scribed samples. Striations were observed only in correspondence of the stage II crack growth development. Growth rate in tension specimens seemed to be an exponential function of the crack depth, which was independent of the scribe root radius. The only effect of cladding and notch depth was to modify the sample net ligament length and the consequent finite thickness influence exerted on the crack. All the experimental crack growth data, despite different scribe geometry and cladding, were correlated by the sample thickness fraction parameter. Under bending load, growth rates seemed to be approximated by a third degree polynomial function of crack depth. Scribe geometry had the same effect on short crack growth rate under bending and tensile load, but the sample thickness fraction parameter was not able to unify growth rates in different scribed samples as accurately as for tensile loading. For small values of sample thickness fraction, cracks propagated at comparable rates under tensile and bending loads. As soon as cracks became bigger, bending growth rate turned out to be slower than the tension one.

References chapter 4

[1] ESDU data sheet E.07.01. Endurance of aluminium alloys (unclad) (in bending). March 1993.

[2] Bolingbroke, R. K. and King, J. E. A comparison of long and short fatigue crack growth in high strength aluminium alloy. *The behaviour of short fatigue cracks*, EGF Pub. 1 (Edited by K. J. Miller and E. R. de los Rios) 1986, Mechanical Engineering Publications, London, pp. 101-114.

[3] Rodopoulos, C. A., Choi, J.-H., de los Rios, E. R. and Yates, J. R. Stress ratio and the fatigue damage map-Part II: The 2024-T351 aluminium alloy. *International Journal of Fatigue*, Vol. 26, 2004, pp. 747-752.

[4] Irving, P. E., Hopper, B. and Scott, A. J. Investigation of the effect of machined scratches on fatigue life of clad 2024-T351. Canfield University Report for Airbus ABH1, Dec 2005.

[5] *AMS Handbook Volume 12 Fractography,* 9th ed. United States: ASM International. Handbook Committee, 1987.

[6] Xue, Y., El Kadiri, H., Horstemeyer, M. F., Jordon, J. B. and Weiland, H. Micromechanisms of multistage fatigue crack growth in a high-strength aluminum alloy. *Acta Materialia*, Vol. 55, 2007, pp. 1975-1984.

[7] Merati, A. A study of nucleation and fatigue behaviour of an aerospace aluminum alloy 2024-T3. *International Journal of Fatigue*, Vol. 27, 2005, pp. 33-44.

Chapter 5
Finite element analysis of stress and strain fields at scribe roots

This chapter describes the stress analysis of the scribed samples using 2D finite element models, neglecting the material microstructure variability and modelling aluminium as an isotropic continuum. Stress calculations were performed under tension and bending loads.

Stress concentration factors (K_t) as well as all the elastic stress and strain tensor components were calculated at the gauge sections of all samples. Subsequently static elastic-plastic analyses were performed to investigate distributions of stress, plastic strain, and plastic zone size and shape at different notch roots. Elastic-plastic mechanical properties of 2024-T351 aluminium alloy substrate and cladding were included into the model and the plastic behaviour was investigated under a single monotonic loading ramp from zero to a maxim load. The effect of local material plasticity could be examined comparing pure elastic and elastic-plastic stress analysis results. Finally the cyclic mechanical behaviour at scribe roots under tension and bending fatigue loads was analysed. Cyclic material stress strain curves were implemented into the finite element solver and fatigue cycles simulated to model static and reverse plastic zone evolution together with the development of local residual stresses. How crack nucleation and propagation alter local mechanical conditions at scribe roots was not investigated.

5.1 Finite element model setup

The commercial software Abaqus, version 6.8, was adopted as finite element equation solver and to carry out pre- and post-processing, that is respectively finite element model development and result visualisation [1]. A complete description of the finite element numerical technique is not reported in this chapter and readers can refer to specialised textbooks as [2,3]. A total of 150 finite element analyses covering all depths and root radii of clad and unclad, bend and tension samples were performed. Under particular circumstances tri-axial stress and strain fields, characterising a mechanical component, can be reduced to a two-dimensional plane stress or strain problems where it is sufficient to resolve mechanical equations on a single component section to characterise the whole sample mechanical behaviour [4,5]. Necessary conditions to correctly apply the two-dimensional approximation are that mechanical components show a direction, such as every cross sections perpendicular to it exhibit equal geometry and are equally loaded. Moreover external loads must be contained within the cross section plane [5].

Such conditions were strictly fulfilled in scribed rectangular bend specimens, where bending external stresses were constant across the specimen width and parallel to the longitudinal cross section plane (see chapter 3). In contrast the variation of cross section

geometry across sample width, generated by the dogbone shape of tension samples, seemed to invalidate the two-dimensional approximation for these specimens. However because of the large continuous radius between dogbone sample ends, the specimen gauge region, extended 3-4 cm above and below the scribe line, could be with good approximation assumed to have a rectangular shape (see chapter 3). Furthermore the internal stress acting on the boundaries of such gauge region, due to the low stress concentration of the dogbone filled radius, was similar to that uniform typical of pure tension loading. The mechanical problem of stress calculation around the scribe root in dogbone tension specimen was therefore equivalent to that of a rectangular specimen, with the size of the gauge region and subjected to pure tension. Owing to that mechanical equivalence two-dimensional approximation was correctly applied to tension sample as well. Additionally, because of the large width, scribed samples were modelled to experience plane strain conditions where the strain components perpendicular to cross section plane (x-y in Fig. 5.1), that is ε_z, γ_{xz}, and γ_{yz}, vanish.

Obviously plane strain assumption was representative only of the internal sample region as the boundary conditions at free edges generated a gradual transition to plane stress condition (σ_z, τ_{xz}, τ_{yz}=0). However, since such transition affected just a small portion of the scribe line, it was neglected. It is worth noticing that plane strain assumptions are fulfilled only in the vicinity of the notch root since nothing prevents transversal deformation in other sample regions.

Because of the large number of 2D models required, a systematic procedure was developed to speed up the finite element model generation. Models and meshes were created to update automatically when the scribe geometry was modified. Therefore, once the mesh parameters were set by the preliminary mesh sensitivity analyses, all the input files of the finite element solver, modelling any kind of scribe geometry, could be quickly produced from just two models one for clad and the other for unclad samples. It was sufficient to change notch geometry parameters in clad and unclad models that the new mesh was automatically generated, following pre-set constrains, by the Abaqus graphic software without any additional user action. By modifying material properties, loading conditions, element type and analysis outputs directly on input files, different mechanical analyses (elastic, monotonic elastic-plastic and cyclic elastic-plastic) of tension and bending specimens could be performed [1].

Fig. 5.1 a) shows the finite element model developed for two-dimensional analyses, displaying model geometry, boundary conditions and loads for pure tension and bending calculations. Particulars of the geometry partitions in clad and unclad scribed samples, created to facilitate model meshing and make possible mesh automatic update [1], are shown respectively in Fig. 5.1 b) and c). Longitudinal cross sections of tension and bending samples were modelled as deformable two-dimensional planar model parts assuming an unitary thickness [1]. To reduce the number of calculated finite element degrees of freedom and decrease analysis computational cost, only a portion of samples longitudinal cross section was modelled (see Fig. 5.1 a)).

In fact the stress and strain field changes, caused by a geometry change, are felt strongly near the notch itself but they decade up to vanish as the distance from the notch increases. There will be a distance from the scribe mark, called decay distance, where

the notch effect disappears and the stress field will be equivalent to that of an unnotched section subjected to pure tension or bending. Such distance is function of the notch geometry and generally ranges from 5 to 10 times the notch depth [5]. It was sufficient to model a cross section region larger than the decay distance to correctly characterise the scribe mark stress raising effect on the surrounding material. Moreover that ensured that the stress exerted by the external material portion on the modelled section part had the same distribution found in uniform unscribed clad and unclad specimen sections under elastic pure tension and bending load.

Actually such condition was strictly fulfilled, consistently with the Saint-Venant principle [4,5], far enough from the fatigue machine loading application regions, that is the gripped part of tension samples and the roller contact area in bending specimens. However samples were designed to show nearly pure tension and bending stress distribution at gauge areas, and thus Saint-Venant principle conditions were automatically satisfied as long as the modelled section part was contained inside sample gauge regions. It was decided to model only a rectangular portion of sample cross section, surrounding the scribe mark as wide as the entire sample thickness and 4 mm high (Fig. 5.1 a)).

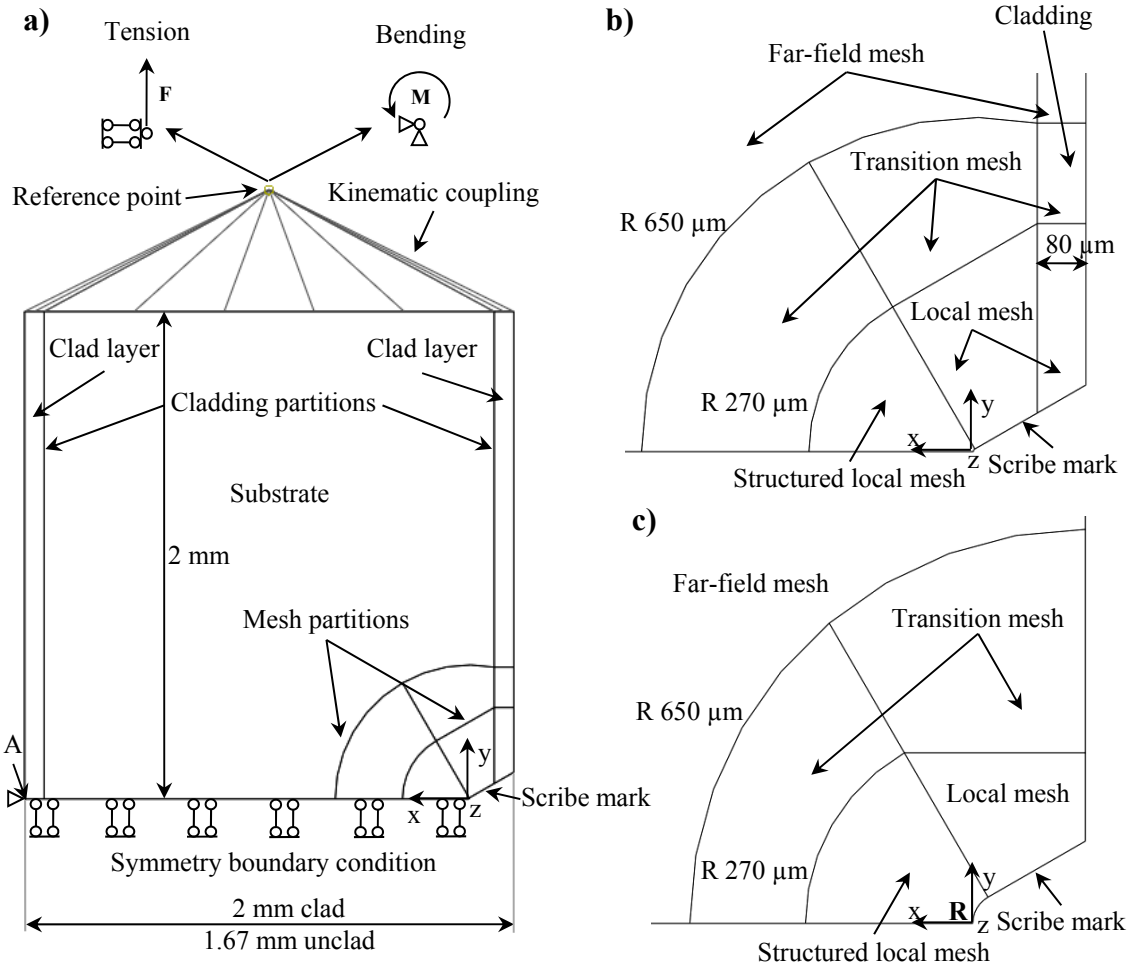

Fig. 5.1: Finite element model geometry (a) and mesh partition magnifications of 185-5 clad (b) and 185-25 unclad (c) scribed samples

The decay distance of 2 mm in the sample longitudinal direction, was selected on the basis of preliminary model set up analyses showing that a distance more than 10 times the deepest notch depth (185 μm) ensured stress distributions equal to those of unscribed tension and bending samples for all the scribes investigated.

Taking advantage of problem mechanical symmetry just half of the rectangular section portion was modelled (see Fig. 5.1 a)). A sample thickness of 2 mm and 1.67 mm was adopted respectively for clad and unclad sections, while the model height of 2 mm, selected to ensure the notch effect decay, was the same in both clad and unclad geometries. Scribe marks were modelled as rounded V shaped notches with a fixed open angle of θ=60° and variable root radius and notch depth values. Obviously because of the problem symmetry just half notch was modelled (Fig. 5.1). Longitudinal geometric partitions, one per side, were introduced in clad models, as shown in Fig. 5.1 a), to allow the assignment of different materials into the same model [1]. Clad layer was assumed 80 μm thick. For sake of simplicity, it was decided to model the boundary between clad layer and substrate as a single line assuming the transition region was infinitesimally small. A jump in mechanical properties was thus allowed at the cladding-substrate boundary.

Clad and substrate materials were modelled associating different material properties to solid homogeneous sections of unitary thickness which were assigned to different models partitions [1]. Boundary conditions of planar symmetry respect to *x*-*z* plane were applied to clad and unclad models along the notch bisector (see Fig. 5.1 a)). Displacement along *y* direction and rotation around *z*-axis were the nodal degrees of freedom constrained on the symmetry plane. Therefore symmetry constraint was depicted in Fig. 5.1 a) as a double pendulum allowing only the nodal displacement on *x* direction. In order to prevent rigid movements and make the mechanical system statically determinate (isostatic) the displacement along the *x*-axis of the model corner A was constrained (Fig. 5.1 a)). That ensured reversibility of the finite element stiffness matrix and consequently the solution of the mechanical problem [2].

Tension and bending external loads, corresponding to maximum loads exerted by fatigue machines during testing were applied to clad and unclad models during monotonic elastic and elastic-plastic analyses. In the case of cyclic elastic-plastic calculations a portion of the entire constant amplitude fatigue load history was modelled to study cyclic plasticity evolution. A particular strategy was required to correctly apply the external load. Although the decay distance of 2 mm ensured the same stress distributions remote from the notch as those of unscribed tension and bending samples, the presence of cladding in clad models made such distributions difficult to predict. In unclad models the external tension and bending stress profiles could be rapidly calculated using Saint-Venant principle. The presence of two materials with different mechanical properties produces a discontinuity of the stress fields in clad models where the clad layer plasticises (chapter 3). This does not occur in case of pure elastic analysis, as explained in the following section. Using laminate theory, imposing the displacement congruence at the substrate-cladding interface, discontinuous external stresses could be analytically calculated, following the same procedure used in the strain gauge measurements prediction model, described in section 3.2. The imposed uniform and butterfly shaped longitudinal strain distributions across the model thickness for tensile

and bending loads, allowed the calculation of longitudinal stress apart from a multiplicative constant that could be determined by equilibrating the external applied force or moment. In that way tension and bending external stress distributions in clad samples corresponding to a maximum nominal equivalent stress of σ_{nom}^{max}=200 MPa could be analytically computed (chapter 3).

However the introduction of irregular stress fronts inside the finite element model requires the use of external subroutines [1] and therefore it was decided to make the model calculate the external stress field internally. The tension and bending displacement fields across sample thickness, corresponding to the external tensile force and bending moment, had to be imposed like in the laminate theory. That could be obtained introducing kinematic coupling [1]. An additional node, named reference point was created above the sample model (see Fig. 5.1 a)). Rigid displacement of such reference point was correlated to the displacements of the model upper boundary nodes by mean of kinematic coupling, represented by lines in Fig. 5.1 a). Kinematic coupling correlation constrained only the model node displacements along *y*-direction to be equal to the *y* component of the reference point rigid displacement. Therefore tension and bending displacement field could be obtained simply applying a vertical translation or a rigid rotation to the reference point. Such translation and rotation must have the magnitude produced by the external tensile force and bending moment applied by fatigue machines. That condition was readily fulfilled applying the external force *F* and the bending moment *M* per unit of width to the reference point (Fig. 5.1 a)). *F* and *M* were calculated using eq. (5.1) and eq. (5.2) where σ^{tens}_{nom}=$\sigma^{bend}_{nom\ max}$=200 MPa and *t* was the different sample thickness (2 mm for clad and 1.67 for unclad specimens).

$$F = \sigma_{nom}^{tens} t \tag{5.1}$$

$$M = \frac{\sigma_{nom\ \max}^{bend} t^2}{6} \tag{5.2}$$

Different constraints were applied to the reference point under tension and bending loadings (see Fig. 5.1 a)). To make the system statically determinate the only reference point degree of freedom of vertical displacement and rotation had to be allowed respectively in tension and bending models. Therefore a double pendulum was applied to reference points under tensile load while an hinge was used in case of pure bending. Reference points and kinematic couplings were introduced in all the developed finite element models to standardise the input files even though they were not necessary for unclad sections.

Additional partitions were created around scribe marks in both clad and unclad models to facilitate mesh definition and its automatic update with scribe geometry changes (Fig. 5.1). A fine well structured local mesh is required at the notch root to correctly calculate stress and strain. Away from the scribe root a coarser conventional mesh can be used. Between these two, an intermediate zone with a transition mesh was used. A partition with the shape of a circular crown sector 60° wide was generated ahead of notch root in both clad and unclad models (see Fig. 5.1 b) and c)). Such partition accommodated a local structured very fine mesh necessary for a proper stress and strain gradient characterisation. The circular crown sector centre was made coincided with the notch root radius so that any notch depth variation simply caused a partition translation without any shape alteration.

An external sector radius of 270 μm was chosen since preliminary analyses demonstrated that structured fine mesh region with a radius bigger than 5 times the largest investigated scribe radius (50 μm) ensured a correct stress gradient characterisation. The external radius was kept constant and notch root radius variations therefore produced changes in partition size. A local fine mesh, although not structured, was applied at the scribe flank where dedicated partitions were produced. For the unclad model a partition with an horizontal upper edge was designed (Fig. 5.1 c)) while for scribed clad model the partition upper edge was parallel to the scribe flank (Fig. 5.1 b). Such differentiation was useful to reduce element distortion in case of clad models. Around the local mesh regions two or three transition mesh partitions were defined. A circular arc with a radius of 650 μm was used as boundary inside the substrate in unclad and clad models. The arc centre was coincident with the notch root radius one. Defining a rule that regulates the element number or size along every partition edge it was possible to obtain an automatic mesh update, simply modifying the scribe geometry. Model generation time was thus considerably reduced since just two geometrical models, one for clad and one for unclad samples were sufficient to generate the input files of all the analyses [1].

Once geometrical partitions had been defined, the number and size of mesh elements were selected on the basis of elastic mesh sensitivity analyses. The (σ_{22}) stress at the notch root (R in Fig. 5.1 c)) was chosen as the control parameter for mesh refinement. First a number of elements was assigned to each partition edge in models with 185 μm deep 5 μm root radius notch. This was the notch, with the steepest stress gradient and fixed the minimum degree of mesh refinement required. The ratio of different partition edges and the bias ratio among elements on the same edge were selected to minimise mesh distortion. Mesh distortion was controlled using Abaqus verify mesh tool [1]. Only quadrilateral elements with an aspect ratio not bigger than 4 were used to maximise stress calculation accuracy. Plane strain quadrilateral 8-node, second-order elements with reduced integration (named CPE8R in Abaqus [1]) were adopted for mesh sensitivity analyses. As soon as a mesh, respecting all the imposed distortion control requirements, was found for both clad and unclad scribed models, the number of elements in local mesh partitions was increased maintaining fixed the element size ratio in the whole section region edge. Transition mesh element size ratio was modified only if local mesh refining caused element distortion in that area. Vertical elastic stress (σ_{22}) at the notch root deepest point in clad and unclad models under tension and bending load was recorded and plotted against the number of elements.

Meshes whose further refinement, produced an accuracy increment of the calculated σ_{22} stress smaller than 0.1% were chosen for K_t calculation. Further mesh sensitivity analyses were performed on selected models containing different notches to verify if the meshes, set for 185 μm deep, 5 μm root radius scribes had the same sensitivity limit of 0.1%. Far-field and local mesh parameters were kept constant, while mesh sensitivity was investigated. Mesh parameters selected for the sharpest scribes were well within 0.1% of sensitivity limit for other notch configuration and therefore they were applied for all the finite element calculation carried out.

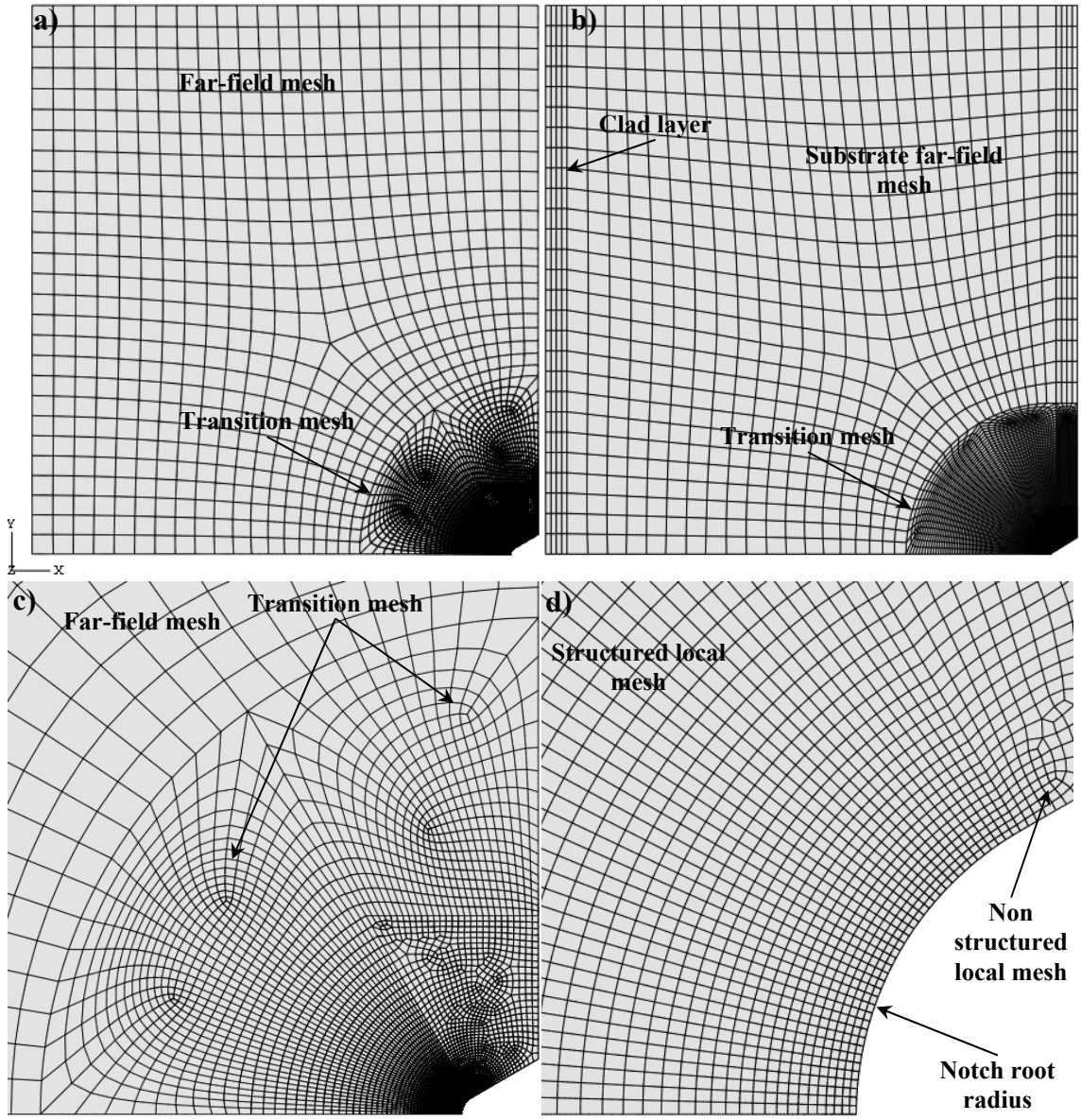

Fig. 5.2: Finite element mesh in 25 µm root radius, 100 µm deep scribe unclad model (a) and in 5 µm root radius, 100 µm deep scribe clad model (b); transition mesh particular (c) and notch root structured mesh (d) in 25 µm root radius, 100 µm deep scribe unclad model

Fig. 5.2 a) and b) show and example of mesh geometry in unclad and clad models. Transition and notch root meshes are displayed in Fig. 5.2 c) and d). Far-field elements in material substrate were nearly 75 µm in size with a slight reduction approaching the circular transition mesh boundary (see Fig. 5.2 a)). In clad models the cladding thickness was occupied by four elements. (Fig. 5.2 b)). Transition mesh consisting of quadrilateral elements was created using the medial axis mesh generation algorithm [1]. The local partition in front of notch root, with the shape of a circular crown sector was generated introducing 40 elements with equal size along the notch root arc and 160 elements along the partition radius. Elements size in the radial direction was progressively reduced approaching the notch root using a bias ratio of 80 (ratio between the size of the biggest element on the smallest one). The smallest element at the scribe root had a size of 0.106 µm. Local mesh close to the scribe flanks was made up of quadrilateral elements too but the advancing front algorithm produced a more irregular

mesh as shown in Fig. 5.2 c) and d). Meshes contained a maximum of 15682 and 23484 elements respectively in unclad and clad models.

5.2 Elastic stress analysis

Table 5.1 shows the elastic properties, that is the Young modulus E, expressed in MPa, and Poisson ratio v, used in finite element calculations for substrate and cladding material. Substrate mechanical properties were experimentally measured by tensile tests on samples machined from the same batch of material of the fatigue specimens [6] (see section 3.1.1). Elastic properties of pure aluminium (Al 1080), forming cladding, were supplied by Alcoa [7] (see section 3.2).

Table 5.1: Aluminium elastic properties [6,7]

Material	E [MPa]	v
Al 2024-T351 (substrate)	72000	0.33
Al 1080 (cladding)	72000	0.33

Clad and unclad sample models differed only in their thickness when pure elastic behaviour was considered. As a thickness variation from 1.67 mm in unclad sample models to 2 mm in clad ones implied a maximum deviation of 2% in the elastic stress fields around equal notches it was decided to use a single value of thickness for both clad and unclad models. Finite element elastic stress analyses were carried out on models having an average thickness between the clad and unclad sample values of 1.84 mm. In that way clad and unclad elastic models were completely equivalent and only 30 analyses were sufficient to characterised elastic stress field of the 15 different notch geometries (5 depth values by 3 root radii) under tension and bending loads.

Scribed sample elastic stress and strain fields were calculated under pure tensile and bending external loads corresponding respectively to a uniform stress (σ^{tens}_{nom}) and a maximum superficial stress ($\sigma^{bend}_{nom\ max}$) of 200 MPa. However that was just a convention as linear elastic internal mechanical variables are linear function of external loads. Two dimensional continuum plane strain quadrilateral 8-node second-order elements with reduced integration (named CPE8R in Abaqus [1]) were adopted for elastic analyses. Second order elements were selected because the presence of additional nodes in the middle of element edges ensured the accurate prediction of steep stress gradients near stress concentrators. To prevent element shear looking caused by excessive distortion or bending stress gradients reduced integration formulation was chosen [1]. The loss of stress accuracy caused by the element integration points reduction was compensated by the very fine mesh around notch roots. In two dimensional elastic problems, with constant body forces, compatibility equations, written in term of stress components, are the same for plane stress and plane strain [5]. Hence in-plane stress fields are the coincident in those two formulations provided that geometry boundary conditions and external load are the same. For that reason only elastic plane strain analyses were performed.

5.2.1 Elastic analysis results

5.2.1.1 Local stress fields and deformation

Local elastic stress and strain fields were analysed in the neighbourhood of 15 different rounded V-shaped notches, examining finite element contour plots under tensile and bending loads. Fig. 5.3 shows the distribution of two stress components calculated at the root of a 50 µm deep notch with 25 µm root radius under tensile load (σ^{tens}=200 MPa). Taking advantage of model symmetry just half of the stress field is represented.

Fig. 5.3 a) and b) show the von Mises stress (σ_{eq}) and the longitudinal stress (σ_{22}) at the notch root respectively. Maximum value of von Mises stress was obtained at the deepest point of the notch root laying on the scribe bisector (see Fig. 5.3 a)). Away from the notch root, equivalent stress gradually decreased down to a constant value that corresponded to that found in unscribed models with plane strain conditions. However the stress decreasing rate depended on the different directions chosen to move away from the notch root, as pointed out by the iso-stress line shapes in Fig. 5.3 a). Close to the notch root, iso-stress lines, delimiting contour stress intervals, showed a nearly circular shape. As the stress decreased, going away from the notch root, iso-stress lines started to grow more along a direction, 65° tilted from the notch bisector, assuming a shape similar to a fish tail.

Longitudinal stress (σ_{22}), Fig. 5.3 b), had a distribution similar to the von Mises stress contour because the major contribution to the equivalent stress magnitude came from the longitudinal stress distribution where local values were generally several times bigger than those of the other stress components. As in the case of von Mises stress, the steepest gradients were observed on the notch bisector.

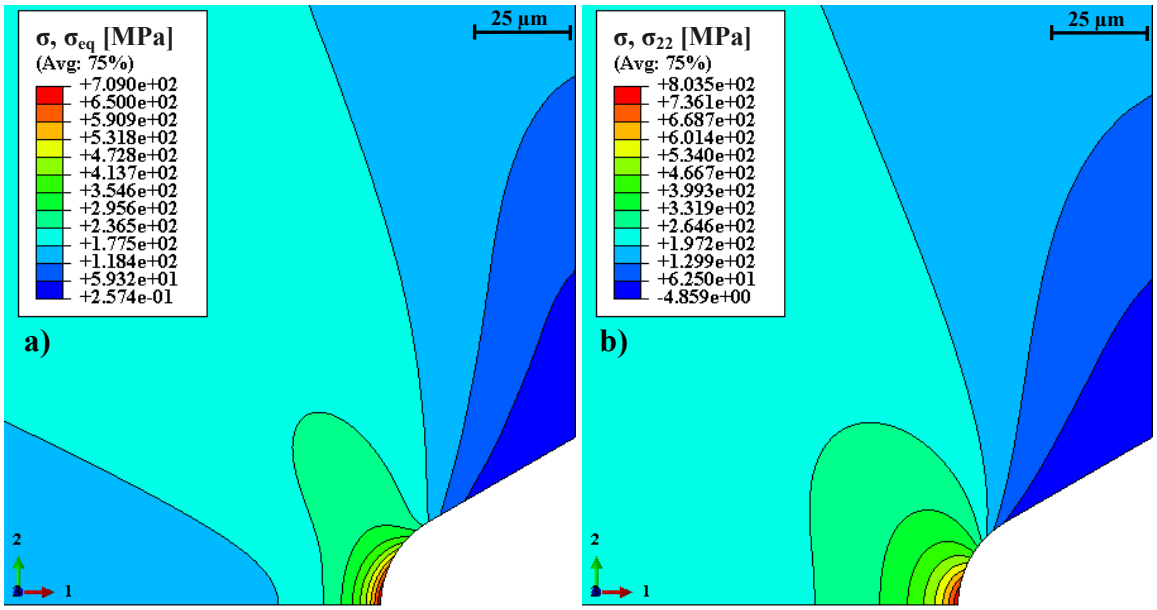

Fig. 5.3: Elastic stress contours at the root of 50 µm deep 25 µm root radius notch under tensile load: von Mises equivalent stress σ_{eq} (a); longitudinal stress σ_{22} (b)

The effect of notch geometry on local elastic stress field was analysed, comparing the maximum values of every stress component.

Table 5.2 lists all the non-dimensional calculated elastic stress maxima, including the equivalent von Mises stress, for different notch geometries under tensile and bending loads. Stress values were normalised dividing tension and bending results respectively by the nominal tensile external stress and by the maximum nominal bending external stress ($\sigma^{tens}_{nom}=\sigma^{bend}_{nom\ \ max}=\sigma_{nom}$=200 MPa). According to such definition, non-dimensional longitudinal maximum stress ($\sigma_{22}^{max}/\sigma_{nom}$) coincided with the gross elastic stress concentration factor (K_t).

The same nomenclature used for scribed fatigue samples was adopted for finite element models. Notch aspect ratio values (ρ/d), are shown as well in

Table 5.2. Maximum values of different stress components were found at nearly the same locations on the notch root. No differences were observed between locations of corresponding maximum values of stresses around the same notch geometry under bending and tensile loads. Actually while σ_{22}, σ_{33} and σ_{eq} anyhow reached their maximum values on the notch root along the bisector despite different scribe geometries, σ_{11} and τ_{12} maximum locations were slightly affected by the notch geometry. Locations along the notch root edge of lateral (σ_{11}) and shear stress (τ_{12}) maximum values seemed to be mainly a function of the notch aspect ratio (ρ/d). However maximum stress position ranges among all the analysed notch geometries were restrained. The angle between the notch bisector and the radial direction where maximum stress points were located on the notch root edge, ranged from 50° to 45° and from 33.5° to 30° respectively for σ_{11} and τ_{12}, when notch aspect ratio changed from ρ/d=0.027 to ρ/d=0.5.

In case of bigger aspect ratios, notch flanks were gradually reduced and rounded V-shaped notches turned into circular ones. Notch shape changes, together with the closeness of the sample free surface, caused bigger variations in the location of stress maximum points. Lateral (σ_{11}) and shear (τ_{12}) maximum stress location angles dropped down respectively to 40.5° and 28.5° for ρ/d=1 and to 35° and 25.5° for ρ/d=2. Longitudinal stress (σ_{22}) maximum values were between 2.7 and 6.2 times larger than the other stress components for every analysed notch geometry under tensile and bending loads (see

Table 5.2). All the other stress components (σ_{11}, τ_{12} and σ_{33}) showed comparable maximum values for given notch geometry and loading conditions. Elastic equivalent von Mises stress (σ_{eq}) maxima were slightly lower than the corresponding longitudinal stress ones (

Table 5.2). The same constant ratio between σ_{eq} and σ_{22} maximum values was obtained in every analysed notch geometry (eq. (5.3)) and more generally in every rounded symmetrical notch machined on samples made of the same material. In case of aluminium such ratio was $\sigma_{eq}^{max}/\sigma_{22}^{max}$ =0.88.

$$\sigma_{eq}^{\max} = \sigma_{22}^{\max}\sqrt{1+\nu^2-\nu} \tag{5.3}$$

Notch geometry lightly affected the ratios between the main longitudinal stress maximum values and those of the other stress components. Notch aspect ratio regulated such maximum values ratios (

Table 5.2). The biggest ratios were observed in case of 25 µm deep, 50 µm root radius notches. The ratio between σ_{22} and σ_{33} maximum values was constant and equal to the inverse of the Poisson ratio, despite different notch geometries and load conditions. The effect of introducing a bending stress gradient in the external stress, was to slightly reduce all the stress maxima for a given notch geometry. Stress maxima in bending ranged from 85% to 100% of the corresponding values in tension (see

Table 5.2). The deeper the notch and the smaller its root radius, the larger were the maximum stress components under both tension and bending.

Table 5.2: Maximum non-dimensional calculated elastic stress components for different scribe geometries under tensile and bending loads

Notch	d [µm]	ρ [µm]	θ [deg]	Aspect ratio ρ/d	Maximum non-dimensional elastic stress components				
					$K_t = \frac{\sigma_{22}^{max}}{\sigma_{nom}}$	$\frac{\sigma_{11}^{max}}{\sigma_{nom}}$	$\frac{\tau_{12}^{max}}{\sigma_{nom}}$	$\frac{\sigma_{33}^{max}}{\sigma_{nom}}$	$\frac{\sigma_{eq}^{max}}{\sigma_{nom}}$
T-25-5	25	5	60	0.200	5.88	1.78	2.06	1.94	5.19
T-50-5	50	5	60	0.100	8.07	2.62	2.91	2.66	7.12
T-100-5	100	5	60	0.050	11.27	3.82	4.13	3.72	9.95
T-150-5	150	5	60	0.033	13.95	4.80	5.15	4.60	12.32
T-185-5	185	5	60	0.027	15.70	5.44	5.81	5.18	13.86
T-25-25	25	25	60	1.000	3.07	0.65	0.94	1.01	2.71
T-50-25	50	25	60	0.500	4.02	1.03	1.32	1.33	3.55
T-100-25	100	25	60	0.250	5.44	1.59	1.88	1.80	4.80
T-150-25	150	25	60	0.167	6.64	2.06	2.34	2.19	5.86
T-185-25	185	25	60	0.135	7.44	2.35	2.65	2.45	6.56
T-25-50	25	50	60	2.000	2.43	0.39	0.67	0.80	2.14
T-50-50	50	50	60	1.000	3.09	0.65	0.94	1.02	2.72
T-100-50	100	50	60	0.500	4.08	1.05	1.34	1.35	3.60
T-150-50	150	50	60	0.333	4.93	1.38	1.67	1.63	4.35
T-185-50	185	50	60	0.270	5.49	1.59	1.89	1.81	4.85
B-25-5	25	5	60	0.200	5.77	1.75	2.02	1.91	5.10
B-50-5	50	5	60	0.100	7.76	2.54	2.81	2.56	6.86
B-100-5	100	5	60	0.050	10.42	3.56	3.83	3.44	9.20
B-150-5	150	5	60	0.033	12.34	4.28	4.57	4.07	10.90
B-185-5	185	5	60	0.027	13.44	4.70	5.00	4.43	11.86
B-25-25	25	25	60	1.000	3.01	0.64	0.92	0.99	2.65
B-50-25	50	25	60	0.500	3.86	1.00	1.27	1.27	3.40
B-100-25	100	25	60	0.250	5.01	1.50	1.74	1.65	4.42
B-150-25	150	25	60	0.167	5.84	1.86	2.08	1.93	5.15
B-185-25	185	25	60	0.135	6.32	2.06	2.28	2.09	5.58
B-25-50	25	50	60	2.000	2.38	0.39	0.66	0.78	2.10
B-50-50	50	50	60	1.000	2.96	0.64	0.91	0.98	2.61
B-100-50	100	50	60	0.500	3.74	0.99	1.24	1.24	3.30
B-150-50	150	50	60	0.333	4.31	1.26	1.49	1.42	3.81
B-185-50	185	50	60	0.270	4.64	1.41	1.63	1.53	4.10

Despite different sizes, notches, having the same aspect ratio, showed almost equal maximum stress components. Non-dimensional stress maxima were determined by notch shape rather than its size. Since the open angle was constant, notch shape could be

quantified using the non-dimensional aspect ratio parameter (ρ/d). Small values of ρ/d indicated sharp notches and vice versa. Actually notch size played a small role in determining maximum stress, (see

Table 5.2). In tension the deeper the notch for a given aspect ratio the larger the non-dimensional maximum stresses. In bending the opposite was true, deeper notches showing slightly smaller maximum values in every stress components. That was a consequence of the far field stress reduction along the model thickness produced by the bending gradient.

Fig. 5.4 a) and b) show non-dimensional maximum in-plane stresses plotted against the notch aspect ratio for tensile and bending cases. Stress maxima for various notch geometries lie on the same curves, proving that elastic stress concentrations, mainly depend on notch aspect ratio. Small misalignments were caused by the weak finite thickness influence due to different ratios between notch depth and model thickness (d/t). Maximum stresses seemed to be power functions of the notch aspect ratio since they followed almost linear trends in bi-logarithmic plots (Fig. 5.4). The larger the notch aspect ratio, the smaller the magnitude of different maximum stresses. Bending results exhibited a behaviour close to that of tension data but shifted to slightly smaller values (see Fig. 5.4).

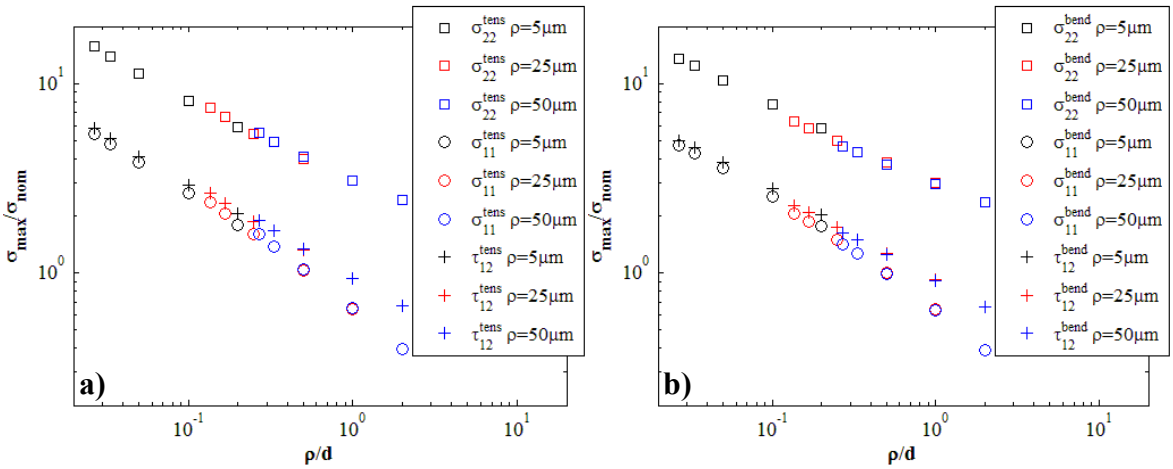

Fig. 5.4: Maximum calculated in-plane non-dimensional stress components against notch aspect ratio under tensile (a) and bending load (b)

As explained above, σ_{22} stress maxima were bigger than those of the other in-plane components. Lateral (σ_{11}) and shear stress (τ_{12}) showed comparable maximum values for a given notch geometry. However their values differed slightly at large notch aspect ratios. Obviously trends, similar to those of σ_{22}, were observed for transverse (σ_{33}) and von Mises (σ_{eq}) stress maxima.

5.2.1.2 Distribution of principal stress on crack plane

The way, in which notch depth and root radius influenced local elastic stress fields, was investigated comparing maximum principal stress distributions on the bisector of selected notches under tensile and bending load. The notch bisector coincided with model symmetry plane (Fig. 5.1 a)). There due to symmetry conditions, the in-plane shear stress (τ_{12}) vanished, making the reference frame axes, principal stress directions (Fig. 5.1 a)). The maximum principal stress hence corresponded to the longitudinal

stress component (σ_{22}). The notch bisector moreover coincided with the plane where fatigue cracks, nucleated and grew. Therefore the maximum principal stress (σ_{22}) acting on it, was the stress component responsible for crack opening and propagation.

For sake of clarity, just the stress analysis results of 9 notch configurations, obtained combining three different depths (25 μm, 100 μm and 185 μm) with the three analysed root radii (5 μm, 25 μm and 50 μm) were compared. Fig. 5.5 shows normalised longitudinal stress distributions calculated on the bisector of the 9 different notches under tensile load. Stress values were plotted against normalised distance from the notch root. Stresses and distances from the notch root were normalised with respect to different stress quantities and geometrical parameters according to particular distribution properties and analogies to point out. Stress distributions were plotted in semi-logarithmic scale in order to make more visible their trends in the proximity of the notch root where stress variations were stronger (see Fig. 5.5). Various notch depths were identified by different curve colours while the root radii by different types of curve. Notch aspect ratio values were reported in the legends of Fig. 5.5 as well.

Fig. 5.5 a) shows σ_{22} distributions on the bisector of the 9 notches normalised with respect to the nominal stress. Stress values were plotted against the distance from the notch root expressed as fraction of the sample thickness (x/t). It is worth noticing that, due to the model thickness fixed value, curves of notches with different depths showed different lengths (see Fig. 5.5 a)). All the σ_{22} distributions along the model symmetry plane, calculated under tensile load, showed a characteristic sigmoid shape when plotted with semi-logarithmic scale. Away from the notch in the far field region, longitudinal stresses exhibited steady values close to the corresponding nominal net stresses, σ_{nom}^{net}, (Fig. 5.5 a)). Approaching the notch, the stress raising effect became dominant and longitudinal stresses progressively increased until they reached constant values near the notch roots. The plateaus formed close to the notch root were a consequence of the semi-logarithmic scale. In fact σ_{22} normalised stress distributions took the values of the corresponding stress concentration factors at the notch root, that is at x/t=0. Since a reference axis with a logarithmic scale tends to zero at minus infinitum, distributions turned out to be stretched in the close neighbourhood of the notch, forming plateaus. On such plateaus non-dimensional stresses asymptotically assumed the value of the corresponding notch stress concentration factor.

The extension of region at the notch root affected by the σ_{22} distribution plateau seemed to be regulated by the notch root radius (see Fig. 5.5 a)). Notches with the same root radius and different depths showed plateau regions with the same lengths. Plateaus of stress curves of 5 μm root radius notches were barely visible in Fig. 5.5 a). The larger the root radius, the bigger the plateaus at the notch root. Actually that was an evidence of the fact that root radius controlled the notch root stress gradients. In fact the smaller was the root radius the steeper was the stress gradient at the notch root. Therefore, when σ_{22} distribution was stretched along the abscissa axis by the semi-logarithmic scale, curves with steeper gradients became nearly flat at smaller distances from the notch root, showing shorted plateaus in Fig. 5.5 a). The normalised coordinates, at which plateau regions began, gave indication of how rapidly stress distributions approached stress concentration factor values at the notch root.

Stress concentration factors and consequently normalised stress magnitudes on the plateau regions close to the notch root were mainly a decreasing function of the notch aspect ratio (see section 5.2.1.1). High stresses corresponded to small aspect ratio values. Therefore for a given notch depth the smaller was the root radius the larger were the notch root stresses and in case of fixed root radius, the deeper was the notch the higher was the σ_{22} distribution near the notch root (see Fig. 5.5 a)). 100 μm deep, 25 μm root radius and 185 μm deep, 50 μm root radius notches showed very close stress values on their distribution plateaus near the notch root since they had nearly the same aspect ratio (respectively ρ/d=0.25 and ρ/d=0.27). However due to different notch depths and root radii such distributions exhibited diverse plateau lengths and decreasing trends towards the respective far field stress values.

Both root radius and notch depth played a role in defining longitudinal stress distribution magnitudes and trends from the notch root to the far field region (Fig. 5.5 a)). Root radius seemed to affect local σ_{22} distribution only in the notch root neighbourhood. In fact at a specific distance from the root, stress curves of notches showing equal depths but different root radii, overlapped following almost the same trend. The normalised coordinates, where stress distributions of notches with different root radius merged, depended on the common notch depth value. The deeper were the notches the larger was the merging point distance from the notch root (Fig. 5.5 a)). Close to the notch root, stress distribution corresponding to notches with smaller root radii showed higher stresses at given coordinates than those of blunter notches characterised by larger radii. In its region of influence near the notch, root radius appeared to regulate not only the plateau length and the stress magnitude but even the decreasing rate which σ_{22} distribution approached the far field stress with. Equally deep notches with smaller root radii exhibited steeper stress gradients at given coordinates, inside notch root radius influence area (Fig. 5.5 a)).

Moreover notches with the same root radius value showed similar distribution trends up to the curve merging point. Close to the notch root such distributions resulted stretched toward higher or lower stresses according to different notch depth values. A notch depth increasing caused a distribution stretch toward higher stress values (Fig. 5.5 a)). Therefore stress gradients and consequently the distribution general trends of notches with equal root radius were slightly affected by notch depth close to the root. The deeper was the notch, the steeper were the stress gradients at any given coordinate (Fig. 5.5 a)). Despite the distortion caused by different notch depths, stress distribution of notches showing the same root radius preserved similar trends, emphasised the role of round radius in defining stress trends in the notch root neighbourhood.

Outside the region where root radius controlled the σ_{22} trend, notch depth became the main geometrical parameter regulating the stress distribution. In fact since curves of equally deep notches overlapped showing the same trend, only the notch depth determined stress magnitude and distribution up to the far field region (Fig. 5.5 a)). However curves superposition was not perfect indicating a residual, but negligible root radius influence even in that area. In the zone controlled by the only notch depth, σ_{22} distributions changed concavity to gradually settle down to constant stress values away from the notch (see Fig. 5.5 a)).

In the far field region, where the notch stress raising effect ceased, longitudinal stresses showed uniform values close to those of the respective nominal net stresses (σ_{nom}^{net}). Nominal net stress values depended on the model net ligament widths. Thus, although all the distributions in Fig. 5.5 a) seemed to merge reaching the same constant values far from the notch root, nominal net stresses of differently deep notches were slightly different and their stresses settled down to different values.

Notch depth regulated the stress magnitude in the curve overlapping region and how quickly the distribution approached the far field constant values. Like close to the notch root the deeper were the notches, the more the distributions were shifted towards higher stresses. At a given coordinate, curves of deeper notches showed higher vertical stresses than those of shallower scratches. Moreover notch depth defined the distance from the root at which any stress distribution reached its far field uniform value (see Fig. 5.5 a)). Far field constant stress value was reached at longer distance from the root in case of deeper notches. Therefore the extension of the material portion in front of the notch affected by stress raising effect was determined by the only notch depth. The deeper was the notch the larger was stress distribution portion affected by notch local stress raising. Notch depth also regulated the stress decreasing rates of longitudinal stress distributions in the curve overlapping region. At a given distance from the notch root curves of deeper notches exhibited steeper gradients, decreasing faster, than those of shallower ones (Fig. 5.5 a)).

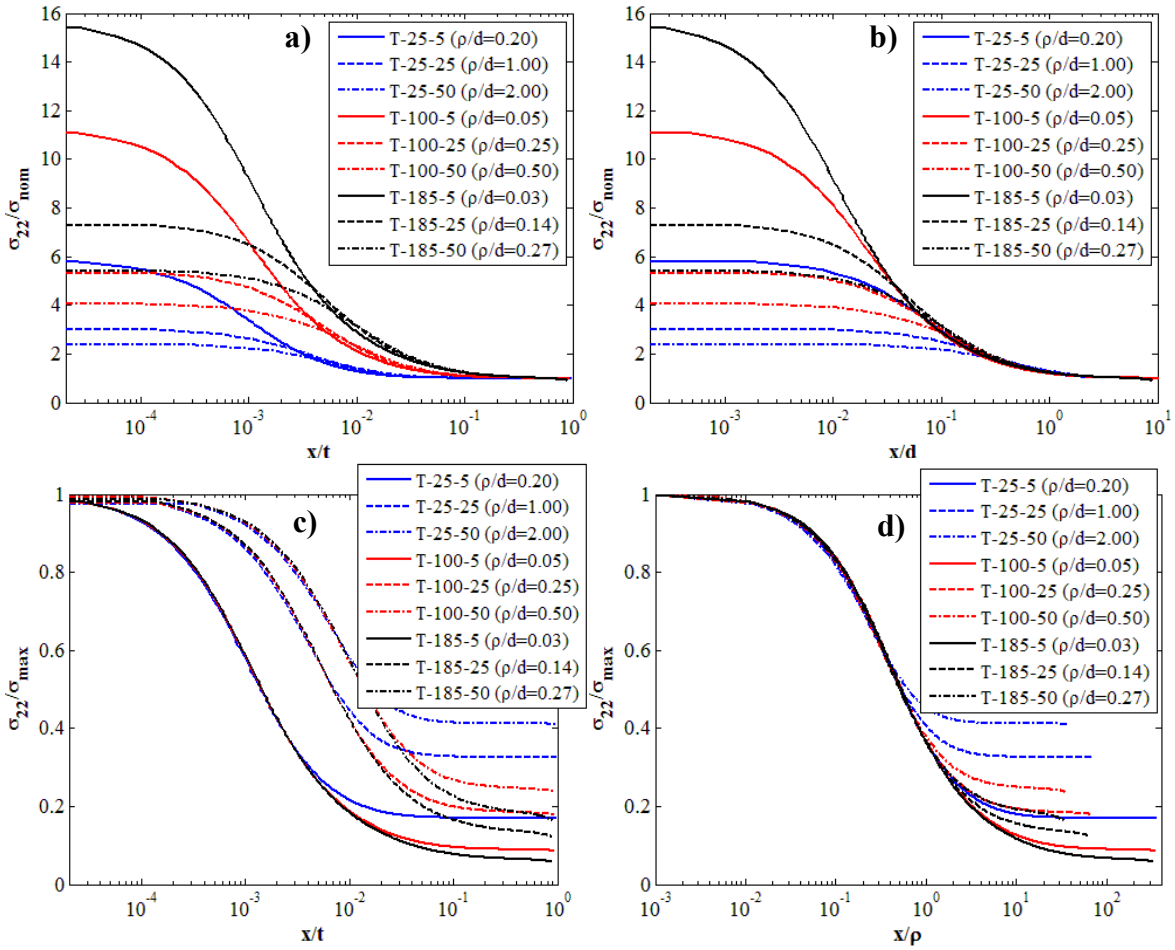

Fig. 5.5: Notch geometry effect on non-dimensional maximum principal stress distribution along the crack plane under tensile load. Stresses normalised by nominal stress plotted against distance from the notch root normalised with respect to model thickness (a) and notch depth (b); maximum principal stresses normalised by their maximum values versus distance from the notch root normalised with respect to model thickness (c) and notch root radius (d)

To better characterise the effect of notch depth on the final part of σ_{22} distributions, an alternative normalisation was adopted for x coordinates. Fig. 5.5 b) shows longitudinal stress curves of the 9 notches plotted against distance from the notch root normalised with respect to d. When drawn versus the non dimensional coordinate x/d, all the stress distributions followed nearly the same trend away from the notch root, as their final parts overlapped (see Fig. 5.5 b)). That proved that outside the region controlled by the root radius the distance from the notch root at which vertical stress assumed a given magnitude was linearly proportional to the notch depth. Stress distribution final parts were simply proportionally stretched along the abscissa axis according to notch depth values. Actually such proportionality could be observed all across the far field region, where distribution becomes uniform, only in case of semi-infinite models. In fact in notched models with the same thickness, different net ligament width alters far field stress values producing a loose of proportionality in that region. Therefore stress distributions proportionality with respect to notch depth and consequent curves overlapping could take place just in a material portion between that affected by the notch root and the far field zone. For the σ_{22} distributions plotted in Fig. 5.5 b) far field stress differences were minimal and stress curves could be with good approximation considered proportional to d even in the far field region. Like in Fig. 5.5 a), further little curve mismatches were caused by the residual root radius influence on longitudinal stress far from the notch root.

Stress distributions seemed to part from the common trend according to the notch aspect ratio when they approached the notch root. The larger was ρ/d, the bigger was the x/d coordinate at which a stress curve diverged from those still overlapped (Fig. 5.5 b)). Thus the extension of the σ_{22} distribution final portion, regulated by the only notch depth, depended on the notch aspect ratio, that is on the root radius value. In the limit case of sharp V-shaped notches (ρ=0) the entire longitudinal stress distributions will be determined just by the notch depth and curves overlapped along the whole notch bisector. In other words, as can be observed in Fig. 5.5 a) as well, the extension of the stress region ahead of the notch directly affected by the root radius, was an increasing function of the radius size. The size of the model region affected by the local elastic stress raising effect resulted proportional to notch depth. In fact, despite different notch geometries, all notch stress fields extended as far as about 3 times d from the notch root. (Fig. 5.5 b)).

Stresses were strongly dependent on root radius close to the notch root and almost independent of ρ further away. Such point could be emphasised if distributions were plotted using a different stress normalisation. Fig. 5.5 c) shows the usual 9 σ_{22} distributions normalised with respect to their maximum stress values, reached at the notch root. Stresses were plotted against the distance from the notch root normalised by the model thickness t. Distributions of notches having the same root radius overlapped almost perfectly near the notch root (see Fig. 5.5 c)). Such superposition demonstrated how normalised stress trends were only determined by the root radius in the neighbourhood of the notch root. In fact, when normalised with respect to maximum

stress values, longitudinal stress gradients at a given distance from the notch root inside the overlapping region were unambiguously defined by the root radius.

The only effect of different notch depths in that region was altering the local stress magnitude, as already observed in Fig. 5.5 a). Stress distributions near the root of notches with the same root radius and various notch depths differed only in a multiplicative constant (Fig. 5.5 a)). Such constants were the corresponding maximum stress values that are proportional to the stress concentration factors. Therefore notch depth effect on stress magnitudes in the neighbourhood of the notch root was analogous to that on the stress concentration values (see Fig. 5.5 a)). Stress curves of notches with the same root radius were thus simply stretched along the ordinate axis according to different notch depths. So stress gradients at given distance from the root of notches with equal root radius and various depths differed, merely because they were multiplied by different constants (Fig. 5.5 a)). When such effect was cancelled by the normalisation, distributions of notches having the same root radius overlapped near the notch root as their normalised stress gradients, defined by ρ, coincided at any x/t coordinate.

All the stress curves showed a sigmoid trend approaching the uniform far field stress away from the notch (see Fig. 5.5 c)). Normalised far field stress values increased according to the notch aspect ratios. That was a consequence of the normalisation, since close far field stresses, reached by the distributions of different notches (Fig. 5.5 a)) were divided by the corresponding maximum longitudinal stresses, related to ρ/d by a decreasing function. An additional effect of the normalised far field stress dependence on notch aspect ratio was determining the curve overlapping region. For a given root radius, the shallower was the notch the shorter was the distance from the root at which stress distributions diverged from the almost linear trend showed in their superposition region (Fig. 5.5 c)). In fact stress curves of shallower notches, characterised by larger ρ/d values, had to reach higher far field stress leaving before the linear common trend.

For a fixed depth value, the stress magnitudes at which distributions started to diverge from the corresponding common linear trends were regulated by the root radius (Fig. 5.5 c)). Curves of notches with larger root radii diverged at higher stresses than those of sharper notches with smaller ρ. In conclusion the extension of central portion, where distributions showed a common linear trend, was regulated by the notch aspect ratio as well.

It is worth noticing that stress curves of equally deep notches showed similar trends as soon as they left the overlapping region controlled by the root radius. Actually such similitude could be observed all across the areas where those distributions overlapped in Fig. 5.5 a). In fact in those regions stress curves of equally deep notches, once normalised in Fig. 5.5 c), differed only by a constant, that is the normalising factor σ_{max}, resulting therefore similar. Distributions approached the notch root, showing different rates according to different root radius values (see Fig. 5.5 c)). Like in Fig. 5.5 a), overlapped stress curves of notches with smaller root radii exhibited steeper normalised gradients at a given x/t coordinate close to the root radius. Therefore in Fig. 5.5 c) such distributions were shifted leftward compared with those of blunter notches with larger root radii.

However curves of notches with different root radii, showed similar trends in their superposition regions. If fact when the distance from the notch root x was normalised with respect to the root radius all the stress distributions overlapped in the notch neighbourhood (see Fig. 5.5 d)). Fig. 5.5 d) shows the 9 stress distributions normalised with respect to their maximum values and plotted against the normalised coordinates x/ρ. The superposition of all the stress curves in Fig. 5.5 d) indicated that, near the notch root, σ_{22} distributions, normalised by the maximum stress values, were proportional to the root radius. For any given normalised stress inside the curve superposition regions in Fig. 5.5 c) corresponding x/t coordinates of different notches were in direct proportion to different root radii. Therefore, in the notch root neighbourhood, normalised distributions in Fig. 5.5 c) turned out to be simply stretched along the abscissa axis according to the root radius value. Moreover normalised stress gradients near the notch root, not only were regulated by the root radius, but any specific gradient magnitude was obtained at distances from the root that were in direct proportion to ρ (see Fig. 5.5 d)).

Longitudinal stresses divided by σ_{22}^{max} were univocally defined in the neighbourhood of the notch root despite different notch depth and root radius values when plotted against the normalised distance from the notch root (x/ρ). Therefore close to the notch root the σ_{22} distribution on the bisector of any rounded V-shaped notch with an open angle of θ=60° could be obtained from Fig. 5.5 d) simply knowing maximum stress and the root radius. That is valid as long as the distance from the notch root remains included into the curve overlapping region of Fig. 5.5 d). In such area maximum stress, that is stress concentration factor K_t, and the root radius were the only parameters characterising different stress distributions. The stress concentration factor controlled local stress magnitudes while the notch root radius defined local normalised stress gradients. Close to the notch root both notch depth and root radius regulated stress magnitudes as K_t values depended on the notch aspect ratio (see Fig. 5.4 a)). Obviously even the model finite thickness, represented by the non-dimensional parameter d/t, altering the stress concentration factor, made a small contribution towards the stress magnitude characterisation.

Away from the notch root the root radius influence almost vanished and both stress magnitudes and gradients were regulated just by the notch depth (Fig. 5.5 b)). Approaching the far field region finite thickness effect on stress distribution became significant as well. Every stress distribution showed a sigmoid shape with plateaus at its ends formed tending to one at minus infinitum and reaching uniform stress in the far field region (see Fig. 5.5 d)). Between those plateaus an almost linear portion characterised by an uniform gradient could be found. As observed in Fig. 5.5 c) as well, stress curves abandoned their linear trend, diverging from the common superposition region near the notch root, according to their notch aspect ratios (Fig. 5.5 d)). The larger was ρ/d, the higher was the normalised far field stress reached by the distribution. Consequently the linear trend in the curve superposition region was left at smaller normalised distance from the notch root (x/ρ). The σ_{22} distribution portion near the notch root univocally defined by K_t and ρ was therefore regulated by the notch aspect ratio. That was a consequence of normalising σ_{22} with respect to the maximum stress. Doing so normalised far field stress turned out to be close to the inverse of the stress

concentration factor ($1/K_t$) whose value depended on the notch aspect ratio. Normalised far field stress equal to $1/K_t$ can be obtained only in case of semi-infinite models. It is worth noticing that, because of the x coordinates normalisation with respect to notch root radius, stress curves covered different lengths on the horizontal axis in Fig. 5.5 d).

5.2.1.3 Notch size effect on principal stress

The effects of different notch size on stress fields on the notch symmetry plane were investigated. Fig. 5.6 a) and b) show the three principal stresses (σ_{11}, σ_{22} and σ_{33}) on this plane for selected notch geometries with the same aspect ratio under tension and bending load. Along the notch bisector, shear stress was zero because of symmetry conditions and thus normal stresses became principal stresses. A clear notch size effect was evident. Stresses ahead of the root of two notches with the same aspect ratio but one twice than the other in depth, showed different trends under both tensile and bending load (see Fig. 5.6 a) and b). Maximum principal stresses (σ_{22}), calculated under tensile load, reached approximately the same maximum values at the notch root (Fig. 5.6 a)), defining the K_t value for the notch. Moving away from the notch root σ_{22} stresses steeply decreased to approach a constant value.

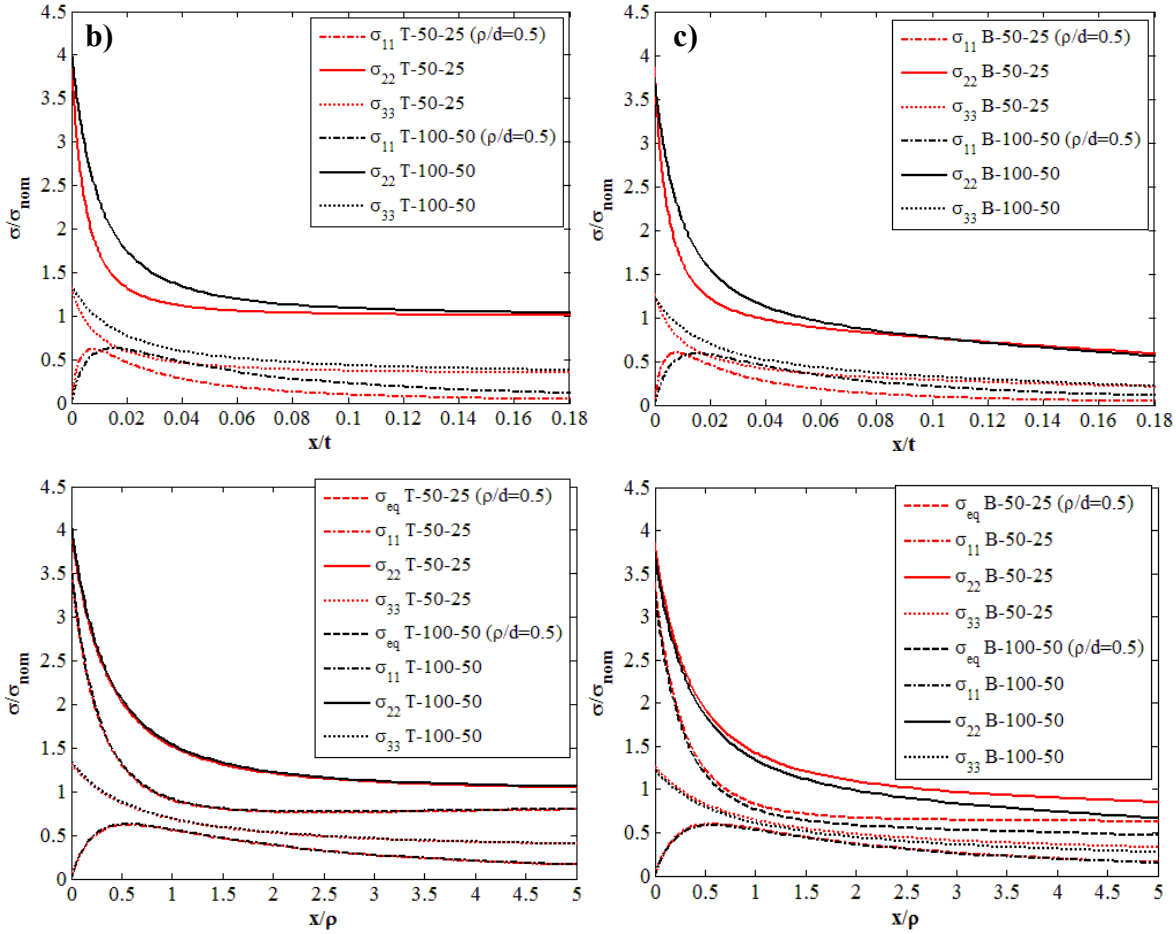

Fig. 5.6: Notch size effect on non-dimensional principal stress distributions along model symmetry plane. Non dimensional stresses plotted against distance from the notch root normalised with

respect to model thickness (*x/t*) under tensile (a) and bending load (b) and with respect to notch root radius (*x/ρ*) under tensile (c) and bending load (d)

The bigger notch showed a smaller stress gradient ahead of the notch (see Fig. 5.6 a)). Therefore, at a given distance from the notch root, the σ_{22} distribution calculated ahead of 100 μm deep notch with 50 μm root radius took higher values than in case of 50 μm deep, 25 μm root radius notch. The bigger the notch the more gentle the stress gradient. Away from the notch, the σ_{22} stress became equal to the nominal net stress (σ_{nom}^{net}). Because of different notch depths nominal net stresses away from the notches were theoretically different. However their difference was of few percent and could be neglected. Because of the different gradients, the σ_{22} stress approached a constant value at x/t=0.15 and x/t=0.30 for 50 μm deep, 25 μm root radius and 100 μm deep, 50 μm root radius notches. The size of the region of enhanced stress was linearly proportional to the notch size.

The lateral stress (σ_{11}) at the notch root, was zero for all notch sizes ad loadings as consequence of notch free edge boundary conditions (see Fig. 5.6). Moving away from the notch σ_{11} increased to a maximum and subsequently decreased to zero. The σ_{11} stress maximum of the 50 μm deep, 25 μm root radius notch was at a closer distance from the notch root than the 100 μm deep, 50 μm root radius one (Fig. 5.6 a)). Stress maxima were located at a distance from the notch root which was proportional to notch size (see Fig. 5.6 a)). The stress maxima of the two notches were almost the same. Hence as in case of the maximum stresses at the notch root (see section 5.2.1.1), relative maximum values were regulated by the notch aspect ratio.

Transverse stress, σ_{33}, distributions showed similar trends to those of the σ_{22} stresses (see Fig. 5.6 a)). As before σ_{33} stresses of the bigger 100 μm deep, 50 μm root radius notch were greater than the smaller one (Fig. 5.6 a)) although they had the same maximum value at the notch root (see section 5.2.1.1). Transverse stress distributions became asymptotic at the same location as σ_{22} stresses, that is respectively x/t=0.15 and x/t=0.30.

Principal stresses at notches under bending showed distributions along the notch bisector similar to those observed ahead of the same notches under tension (see Fig. 5.6 b)). The stress maxima were slightly smaller than the corresponding ones in tension, however their location was the same. Close to the notch root, stress distributions in tension and bending showed nearly identical stress gradients at given locations. Thus the same notch size effect found in tension was observed under bending, with steeper stress gradient close to the root in case of smaller notches. After starting from the same maxima, σ_{22} and σ_{33} stresses in the 100 μm deep, 50 μm root radius notch were greater than those of the 50 μm deep, 25 μm root radius notch (Fig. 5.6 b)). Far from the notch root the similarity between tension and bending disappeared. Approaching the far-field region regulated by the external stress, σ_{22} distributions assumed the trend, characterised by a constant stress gradient, typical of unnotched bending samples.

Stress maxima of notches with equal aspect ratio were found at distances from the notch root proportional to the notch size. Fig. 5.6 c) and d) show alternative plots of the same principal stress distributions along the bisector of the 50 μm deep, 25 μm root radius and 100 μm deep, 50 μm root radius notches under tension and bending. Stress

values were plotted against distances from the notch root, normalised with respect to the notch root radius (x/ρ). Equivalent von Mises stress distributions are also plotted. Once the notch size is included in the definition of non-dimensional coordinates (x/ρ), stress distributions under tensile of notches, with the same ρ/d (equal shape), overlapped almost perfectly (see Fig. 5.6 c)). Therefore the only effect of notch size was scaling proportionally the stress spatial distributions. As explained in the previous section, this is a consequence of the mechanical similitude of elastic stresses. The stress variations produced by different d/t values were imperceptible since stress curves of the two notches seemed to be precisely superimposed (Fig. 5.6 c)).

That did not occurred in case of bending loading (see Fig. 5.6 d)). In fact stress distributions of the two notches, apart from that of σ_{11}, overlapped only in the close neighbourhood of the notch root (Fig. 5.6 d)). For $x/\rho \geq 0.5$ corresponding stress curves of 50 µm deep, 25 µm root radius and 100 µm deep, 50 µm root radius notches diverged assuming different constant gradients. That was caused by the different finite thickness effect of the two notched model, made more evident by the gradient of the bending external stress. Superposition of the stress distributions would have been obtained along the entire model symmetry plane if the two notched samples had the same d/t values. Lateral stresses, σ_{11}, approaching zero in the far field region, were less affected by different d/t values and curves superposition could be observed, as in tension, for all the net ligament length (Fig. 5.6 d)).

5.3 Elastic-plastic monotonic deformation

The elastic-plastic behaviour of substrate and clad materials was modelled using classical metal plasticity constitutive equation implemented in Abaqus [1]. That is the conventional time-independent inelastic constitutive equation based on metal incremental plasticity theory where the mechanical strain increment is decomposed into an elastic and an unrecoverable plastic part [8-10]. Incremental plasticity theory requires the definition of:

- an *yielding criterion* represented by the yield surface which is a generalisation of the uniaxial yield stress to the multiaxial stress state and determines when plastic deformations occur in the material;
- a *flow rule* which characterised the plastic deformation behaviour relating the plastic strains to the respective stress components;
- an *hardening rule* defining how the yield surface and or the plastic flow evolve as plastic deformations take place [8].

Table 5.3: Aluminium elastic-plastic properties [6,7]

Material	E [MPa]	ν	σ_{el} [MPa]	$\sigma_{0.2}$ [MPa]
Al 2024-T351 (substrate)	72000	0.33	350.4	360.0
Al 1080 ε_0=2% (cladding)	72000	0.33	130.0	132.3

Table 5.3 shows the elastic properties, that is the Young's modulus E and Poisson ratio ν, together with the elastic limit, σ_{el} and the yield strength $\sigma_{0.2}$ used in elastic-plastic finite element calculations for substrate and cladding material. The elastic limit was the stress value defining the upper limit of the pure elastic deformation regime in

the material stress-strain curve. It was obtained from the material curve as the stress corresponding to a permanent plastic deformation of 0.01%. The conventional definition as the stress corresponding to a permanent plastic deformation of 0.2% was adopted for the yield strength.

Substrate mechanical properties were experimentally measured by tensile tests on 2024-T351 aluminium alloy samples machined from the same batch of material of the fatigue specimens [6] (see section 3.1.1). The tensile tests were performed along the long transverse direction of the material. Cladding was assumed to be made of pure aluminium with a purity of 80%, Al 1080, pre-stretched with a permanent strain ε_0=2% (see section 3.2). The mechanical properties and stress-strain curve (Fig. 3.10) of the 1080 pre-stretched aluminium alloy were supplied by Alcoa [7]. As explained above, elastic response of cladding and substrate coincided but their plastic behaviours substantially differ both in term of yield strength values and stress-strain curve (Fig. 3.10). Stress-strain data, representing the material hardening behaviour, are necessary to define the constitutive model of metal plasticity. Hardening data of clad and substrate materials were introduced inside the elastic-plastic analysis input files in a tabular form. Arrays of true Cauchy stress values and the corresponding logarithmic plastic strains had to be defined to characterise the hardening behaviour described by the material stress-strain curve [1]. The first data pair had to correspond with the onset of plasticity, that is the plastic strain value had to be zero in the first pair. True stress and plastic strain data were extracted from the stress-strain curves of clad and substrate materials in Fig 3.10 starting from their respective elastic limits and using a total strain step of 0.005.

Elastic-plastic stress and strain fields were calculated for the 15 different notch geometries in clad and unclad samples under tensile and bending load. A total of 60 monotonic elastic-plastic analyses were therefore performed. Elastic-plastic stress and strain components were calculated in clad and unclad models under pure tensile and bending loads corresponding to a nominal tensile stress (σ^{tens}_{nom}) and a maximum nominal bending superficial stress ($\sigma^{bend}_{nom\ max}$) of 200 MPa.

Two dimensional continuum plane strain quadrilateral 4-node elements with full integration (named CPE4 in Abaqus [1]) were used to model both the clad layer and the sample substrate in pure tension and bending analyses. Fully integrated first order elements were chosen as they do not suffer from volumetric locking under plastic deformation due to the use of a constant volume strain in these elements [1]. Therefore the incompressible hypothesis of plastic deformation, that adds kinematic constrains at the element integration points, can be automatically satisfied. To compensate for the loss of model accuracy, caused by the reduction of nodes in first order elements compared to elastic analyses, full integration formulation was chosen. Shear looking was found not to affect the solution accuracy of scribed samples elastic-plastic models under tensile and bending, justifying the use of fully integrated first order element. Only elastic-plastic plane strain analyses representative of the stress state in the bulk of the scribed samples were performed, neglecting therefore the small plane stress region at the sample edges.

5.3.1 Elastic-plastic analysis results

5.3.1.1 Elastic-plastic stress fields and deformations

For sake of brevity only unclad samples results are described in the following section. The main objective of this section is, in fact, to rationalise how the scribe geometry influence the elastic-plastic response of the material in proximity of the notch root. Fig. 5.7 shows the two dimensional distributions of two plane strain stress components calculated under tensile load at the root of a 50 µm deep, 25 µm root radius notch in the unclad sample. The stress magnitude range of the whole distribution was divided into 12 equal intervals, represented by different colours, from red to blue as the stress value decreased. Contour colours and respective stress interval limits are listed in figure legends. All the stress components were expressed in MPa and their values were extrapolated and averaged at nodes, common to two or more elements using a threshold of 75% [1].

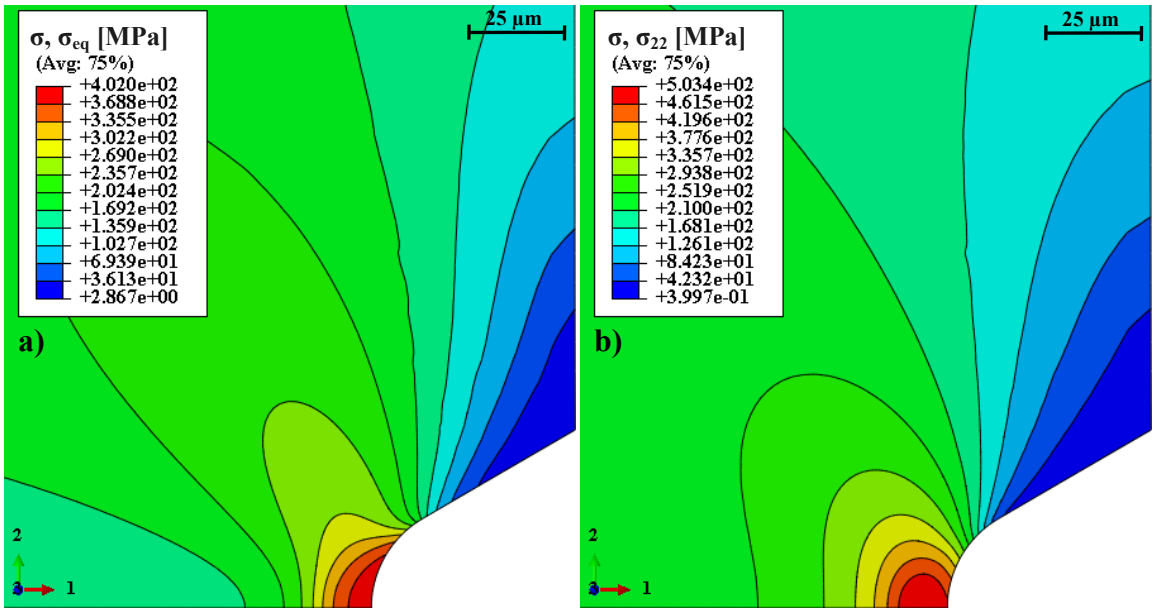

Fig. 5.7: Elastic plastic finite element contours at the root of 50 µm deep 25 µm root radius notch under tensile load: von Mises equivalent stress σ_{eq} (a); longitudinal stress σ_{22} (b)

Fig. 5.7 a) and b) show the elastic-plastic distributions of the equivalent von Mises stress (σ_{eq}) and the longitudinal stress (σ_{22}) at the root of an unclad 50 µm deep, 25 µm root radius notch under tensile load. The von Mises stress contour provides an indication of the material region where plasticity occurred. According to the yielding criterion, substantial plastic deformations take place when the local von Mises stress reaches the material yield strength ($\sigma_{0.2}$=360 MPa). The material thus yielded just in a small semicircular region at the notch root where all the irreversible plastic deformations were located (Fig. 5.7 a)). Elastic-plastic von Mises stress contour showed a morphology of the iso-stress lines similar to that observed for of pure elastic solution (Fig. 5.3 a)). As for pure elastic material response, the maximum value of the von Mises stress was obtained at the notch root in correspondence with the notch bisector (Fig. 5.7

a)). However, consistently with the hardening behaviour described by the material stress-strain curve, the maximum value of the elastic-plastic von Mises stress was restricted to σ_{eq}^{max}=402 MPa being considerably smaller than that obtained in the elastic analysis (see Fig. 5.7 a) and Fig. 5.3 a)). The development of a plastic zone at the scribe root produced a reduction of the equivalent stress gradient along the notch bisector compared to the pure elastic solution (Fig. 5.7 a) and Fig. 5.3 a)).

Fig. 5.8 a) shows the plastic zone developed under monotonic tensile load at the root of an unclad 50 µm deep, 25 µm root radius notch. The plastic zone is identified by the coloured region in Fig. 5.8 a) representing the contour of the equivalent plastic strain, ε^{pl}_{eq} [8]. According to the definition of the yield strength the material was assumed to plasticise when the local equivalent plastic strain was $\varepsilon^{pl}_{eq}\geq$0.2%. Thus setting $2\cdot10^{-3}$ as lower limit of the ε^{pl}_{eq} contour scale the monotonic plastic zone could be identified as a coloured region inside the equivalent plastic strain contour (Fig. 5.8 a)). Outside the plastic zone, that is in the white region of Fig. 5.8 a), inelastic irreversible deformations could take place but, as the equivalent plastic strain was ε^{pl}_{eq}<0.2%, the global mechanical response of the material was considered to be elastic. Inside the notch root plastic zone different colour bands represent regions characterised by same interval of equivalent plastic strain and therefore by the same amount of material hardening. The bigger the equivalent plastic strain the larger the material hardening. The plastic zone at the notch root showed a regular thumbnail shape with a nearly circular internal boundary (Fig. 5.8 a)). The homothetic pattern of the ε^{pl}_{eq} iso-strain lines inside the plastic region showed a regular and uniform material hardening reduction from the notch root to the plastic zone boundary. A maximum equivalent plastic strain of 0.79% was reached at the notch root (Fig. 5.8 a)).

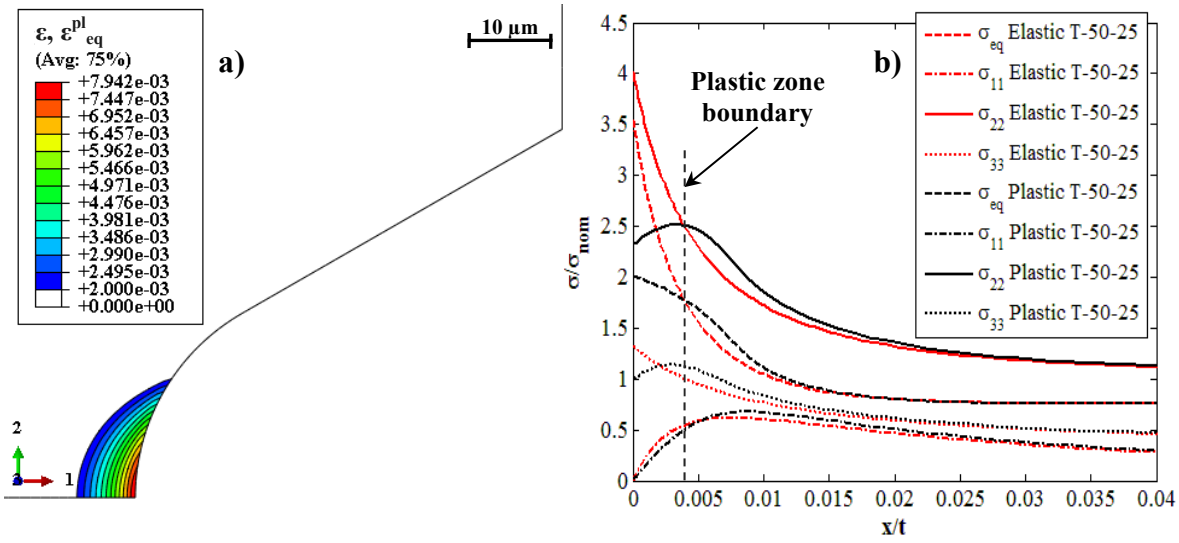

Fig. 5.8: Plastic zone at the root of 50 µm deep 25 µm root radius notch under tensile load a) and elastic plastic stress redistribution

Fig. 5.8 b) shows a comparison between pure elastic and elastic-plastic stress component distributions along the bisector of the 50 µm deep, 25 µm root radius notch under tensile load in the unclad sample. Stress components normalised with respect to the nominal tensile stress of 200 Mpa were plotted against the distance from the notch root, *x*, normalised by the sample thickness, *t*. The position on the plastic zone boundary

is indicated as well in Fig. 5.8 b). Comparing elastic-plastic stress distributions with the corresponding elastic ones allows a quantification of the stress redistribution caused by onset of material plasticity. The occurrence of plastic deformations produced a substantial reduction of the σ_{22} and σ_{eq} inside the plastic zone compared to the elastic stress distributions. Elastic and elastic-plastic distributions of longitudinal and von Mises stress seemed to reach the same magnitude in correspondence with the edge of the plastic zone (Fig. 5.8 b)). Such point was located not far from the maximum of the elastic-plastic σ_{22} distribution. Outside the plastic zone the elastic stresses of σ_{22} elastic-plastic distribution were higher than those of the corresponding pure elastic solutions. As for equilibrium condition the distribution integral along the model symmetry plane was the same for both elastic and elastic-plastic constitutive equations, the stress reduction in the plastic zone implied an increase of the stress magnitude beyond the plastic zone for elastic-plastic σ_{22} distributions. Such phenomenon is known as elastic-plastic stress redistribution. At a distance of nearly $0.025t$ from the notch root elastic and elastic-plastic σ_{22} distributions overlapped indicating the limit of the region affected by the elastic-plastic stress redistribution (Fig. 5.8 b)). All the other elastic-plastic stress components were subjected to the stress redistribution showing behaviours similar to σ_{22} distribution (Fig. 5.8 b)).

Analogous remarks could be make also for stress and strain contours under bending load and thus bending model results are not reported in this section.

5.3.1.2 Notch geometry effects on material plastic behaviour

Only unclad samples were considered to rationalise how different scribes alter the local elastic-plastic stress and strain fields and the resulting plastic zone. The effect of the notch geometry on the monotonic elastic-plastic mechanical response of samples was initially investigated analysing the stress and strain components at the notch root. Fig. 5.9 a) and b) show the longitudinal and the von Mises elastic-plastic stresses at the root of different notches respectively under tensile and bending loads. Stress values normalised with respect to the nominal stress, σ_{nom}=200 MPa, are plotted against the notch aspect ratio, ρ/d in a bi-logarithmic scale. Coloured markers are used to show data of notches with different root radii (Fig. 5.9 a) and b)). Elastic-plastic σ_{22} and σ_{eq} stresses at the root of different scribes under tensile load laid on the same lines when plotted against the notch aspect ratio (Fig. 5.9 a)). As for elastic solutions, the aspect ratio, was able to correlate the elastic-plastic stresses at scribe roots. Tensile σ_{22} and σ_{eq} stresses at the scribe root seemed to be a power function of the ρ/d. The higher the notch aspect ratio, the smaller the values of the normalised longitudinal and von Mises stresses (Fig. 5.9 a)). Under tensile load elastic-plastic σ_{eq} stresses showed the same power trend as σ_{22} but shifted toward smaller stress values.

Small misalignments of the stresses from the linear trend were caused by the effect of the sample finite thickness (Fig. 5.9 a)). Samples weakened by notches with various depths showed different finite thickness parameters d/t, which, like in elastic analyses, slightly affected the stress magnitude at the notch root. Such misalignments were more evident in case of the deepest scribes where the sample finite thickness was more emphasised. Notches having the same aspect ratio but different in size showed almost the same elastic-plastic σ_{22} and σ_{eq} values at their roots (Fig. 5.9 a)). Once again the

small differences in stress magnitude were caused by the different finite thickness effect. Scribes under bending load showed the same behaviour as under pure tension but the σ_{22} and σ_{eq} values reached at the notch roots were slightly lower (Fig. 5.9 b)). Moreover the misalignments from the linear trend were larger than in tension because of the bigger sample finite thickness effect typical of bending loading (Fig. 5.9 b)).

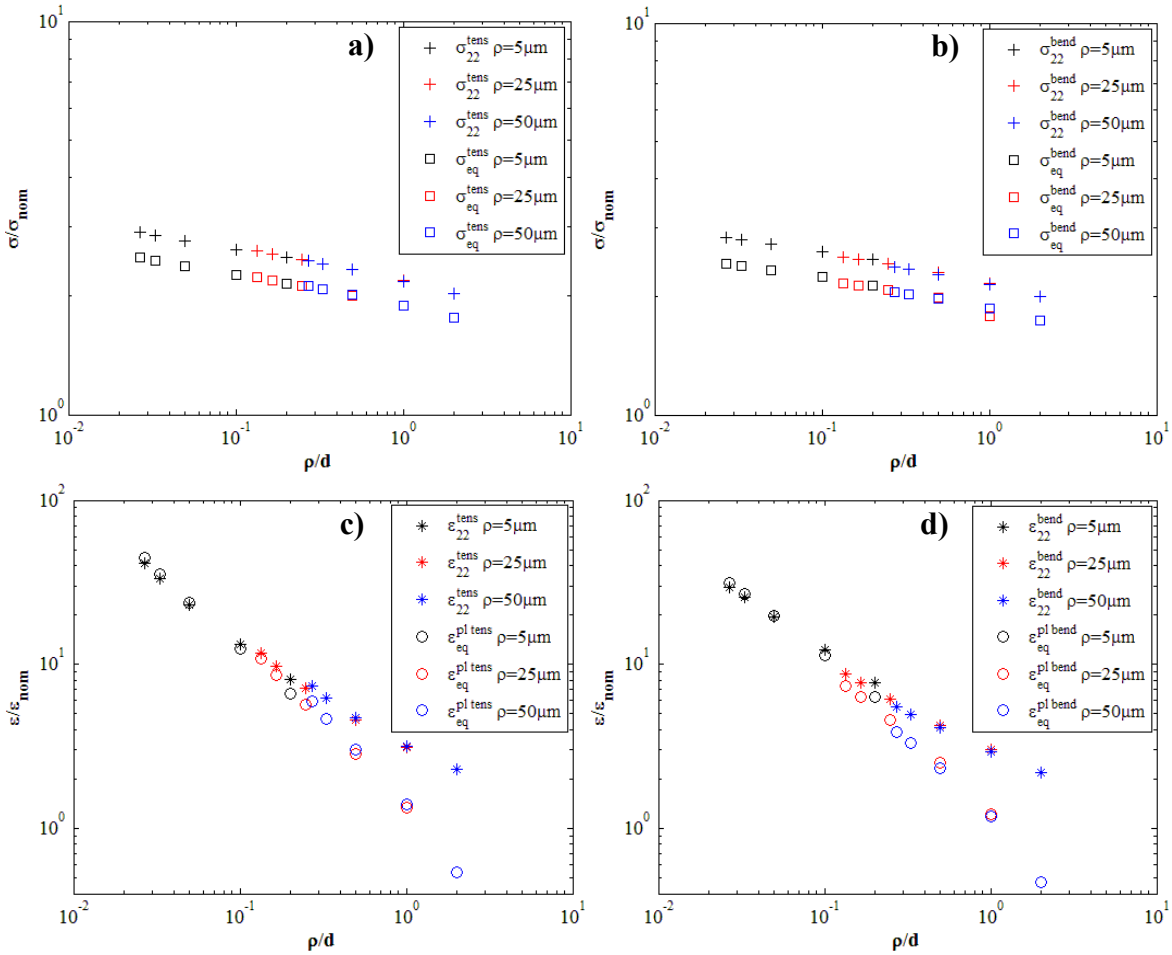

Fig. 5.9: Notch geometry effect on elastic-plastic stresses and strains at the notch root. Normalised longitudinal (σ_{22}) and von Mises stress (σ_{eq}) plotted against notch aspect ratio ρ/d under tensile (a) and bending (b) loads. Normalised longitudinal (ε_{22}) and equivalent plastic strain (ε^{pl}_{eq}) plotted against notch aspect ratio ρ/d under tensile (c) and bending (d) loads

Fig. 5.9 c) and d) show the elastic-plastic longitudinal and the equivalent plastic strains at the root of different scribes under tensile and bending loadings. Strains were normalised with respect to the nominal strain, ε_{nom}, that is the elastic strain corresponding to nominal stress of 200 Mpa, and plotted in bi-logarithmic scale against the notch aspect ratio, ρ/d. As for the stress components, the notch aspect ratio was able to correlated the strain values at the roots of different scribes, making the ε_{22} and ε^{pl}_{eq} data under tensile and bending loads lie on the same curves (Fig. 5.9 c) and d)). Whereas the equivalent plastic strains seemed to be a power function of ρ/d, forming a straight line, the longitudinal strains followed a lightly concave trend. For sharp notches with $\rho/d \leq 0.1$, ε_{22} and ε^{pl}_{eq} at the root of a given scribe showed close values under both tensile and bending loading (Fig. 5.9 c) and d)). Differences between longitudinal and equivalent plastic strains become evident for shallow scribes where the bigger the notch

aspect ratio, the larger the gap between the strain values. The lack on homogeneity in model finite thickness parameters *d/t* also affect the elastic-plastic strains at the scribe roots producing small data misalignments (Fig. 5.9 c) and d)). Changing the loading conditions from pure tension to bending only shifted ε_{22} and ε^{pl}_{eq} to slightly smaller values and emphasised the sample finite thickness effect increasing the data misalignments (Fig. 5.9 c) and d)).

To conclude either the elastic or the elastic-plastic mechanical parameters at the scribe root can be assumed with good approximation to be characterised only by the notch shape expressed by the aspect ratio *ρ/d*.

As notch geometry regulated the local elastic-plastic stress and strain fields, it also affected the size and shape of the plastic zone developed at the scribe root. Fig. 5.10 shows the plastic zone at the root of different notches in unclad samples under tensile load. The monotonic plastic zone shapes of selected notches with 5 μm and 50 μm root radii and depths ranging from 50 μm to 185 μm were compared in Fig. 5.10. Taking advantage from the model symmetry, just half of the plastic zone boundaries was displayed. Plastic zones developed at the root 5 μm root radius notches are sketched in the upper half of Fig. 5.10.

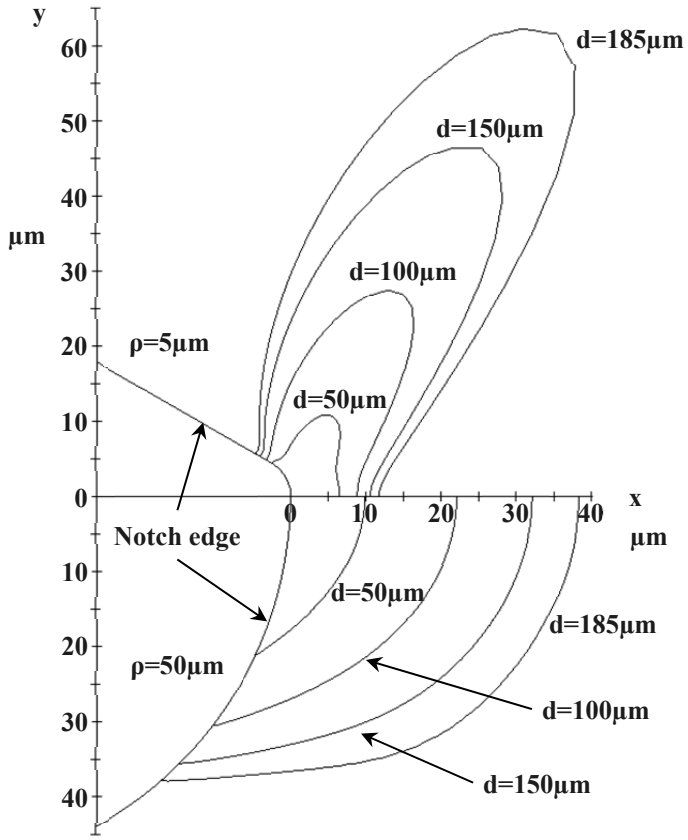

Fig. 5.10: Notch root plastic zones according to different notch geometries in unclad samples under tensile load

5 μm root radius notches developed monotonic plastic zones at their roots having a shape similar to a fish tail with lobes grown in the direction forming a 60° angle with the notch bisector. On the contrary 50 μm root radius notches showed plastic zones with nearly semi-elliptical thumbnail shapes (Fig. 5.10). Increasing the scribe depth for a given root radius enlarged the plastic zone but whereas the plastic zone of 5 μm root radius notches grown mainly along the direction 60° tilted from the model symmetry plane, for 50 μm root radius scribes it expanded almost uniformly (Fig. 5.10).

Despite their different shapes, plastic zones of 5 μm and 50 μm root radius notches seemed to be two diverse stages of plastic zone evolution from the same elastic-plastic stress field. This statement is confirmed by the morphology of the σ_{eq} iso-stress lines in Fig. 5.7 a) which, moving away from the notch root, changed from nearly a circular to a lobed shape. Decreasing the notch aspect ratio, the plastic zone gradually evolved from a semi-elliptical shape for $\rho/d \geq 0.2$ to a lobed one for sharp scribes with $\rho/d < 0.1$. The plastic zone of 50 μm deep, 5 μm root radius notches ($\rho/d = 0.1$) represented an evidence of such transition showing an elliptical boundary with a lobe grown in its middle part (Fig. 5.10). Plastic zones of all the notches showed similar shape under both bending and tensile loading. Therefore plastic zones developed at the root of scribes under bending load are not reported in this section.

Fig. 5.11 a) shows the length of the monotonic plastic zone, measured along the bisector of different notches in unclad samples under tensile and bending loads. The plastic zone length l_{pl} was plotted against the scribe aspect ratio. Increasing the notch deep and the root radius caused an increase in both tensile and bending plastic zone length (Fig. 5.11 a)). For a given root radius value the l_{pl} seemed to be nearly a power function of the notch aspect ratio as markers laid on straight lines for tensile and bending loadings (Fig. 5.11 a)). Notches with the same aspect ratio, that is same shape, showed different plastic zone lengths according to their size. The bigger the notch, the longer the notch bisector portion affected by plastic deformations. l_{pl} was found to be regulated by the notch shape defined by ρ/d and by the notch size. Notches under bending load developed plastic zones with lengths shorter than under tension. The differences in length between tensile and bending plastic zones grew according to the notch depth and root radius (Fig. 5.11 a)). It is worth noticing that no l_{pl} value was showed in Fig. 5.11 a) for the 25 μm deep, 50 μm root radius notch as the stress field in the neighbourhood of this notch remained elastic and no plastic zone was developed at its root.

When the plastic zone size was normalised with respect to a notch size parameter like the root radius ρ all the data of different notches laid on the same curve respectively for both tensile and bending loads (see Fig. 5.11 b)). The notch root aspect ratio was therefore able to correlate the normalised plastic zone lengths of different scribes. The length of the plastic zone measured along the bisector of notches with the same ρ/d was proportional to the notch size. Such behaviour proved that the mechanical similitude exists also for elastic-plastic stress and strain fields in proximity of the notch root. Small deviations of the l_{pl}/ρ values from the common trend were caused by the different sample finite thickness effect expressed by different values of d/t (Fig. 5.11 b)). The finite thickness effect was larger under bending than under tensile loading.

Fig. 5.11 c) and d) show respectively the area of the scribe root plastic zone, A_{pl}, and the same area normalised with respect to the square of the notch root radius, A_{pl}/ρ^2, as a function of the notch aspect ratio in unclad tension and bending samples. The monotonic plastic zone area varied according to the notch depth and root radius in tensile and bending specimens with a trend analogous to that showed by the plastic zone length (Fig. 5.11 c)). Plastic zone areas at the root of different notches, when normalised by ρ^2, were correlated by the notch aspect ratio making all the tension and bending data lay on single trend lines (Fig. 5.11 d)). For a given notch geometry, A_{pl} turned out to be nearly a quadratic function of the scribe size. Also the A_{pl}/ρ^2 values were slightly affected by the different amount of sample finite thickness. It was possible to assume with good approximation that the notch aspect ratio, related to the elastic stress concentration factor, and the notch size defined the area and length of the monotonic plastic zone at the root of scribes. That statement is consistent with the existence of a similitude of the local notch elastic-plastic mechanical response which is regulated by the only notch geometry.

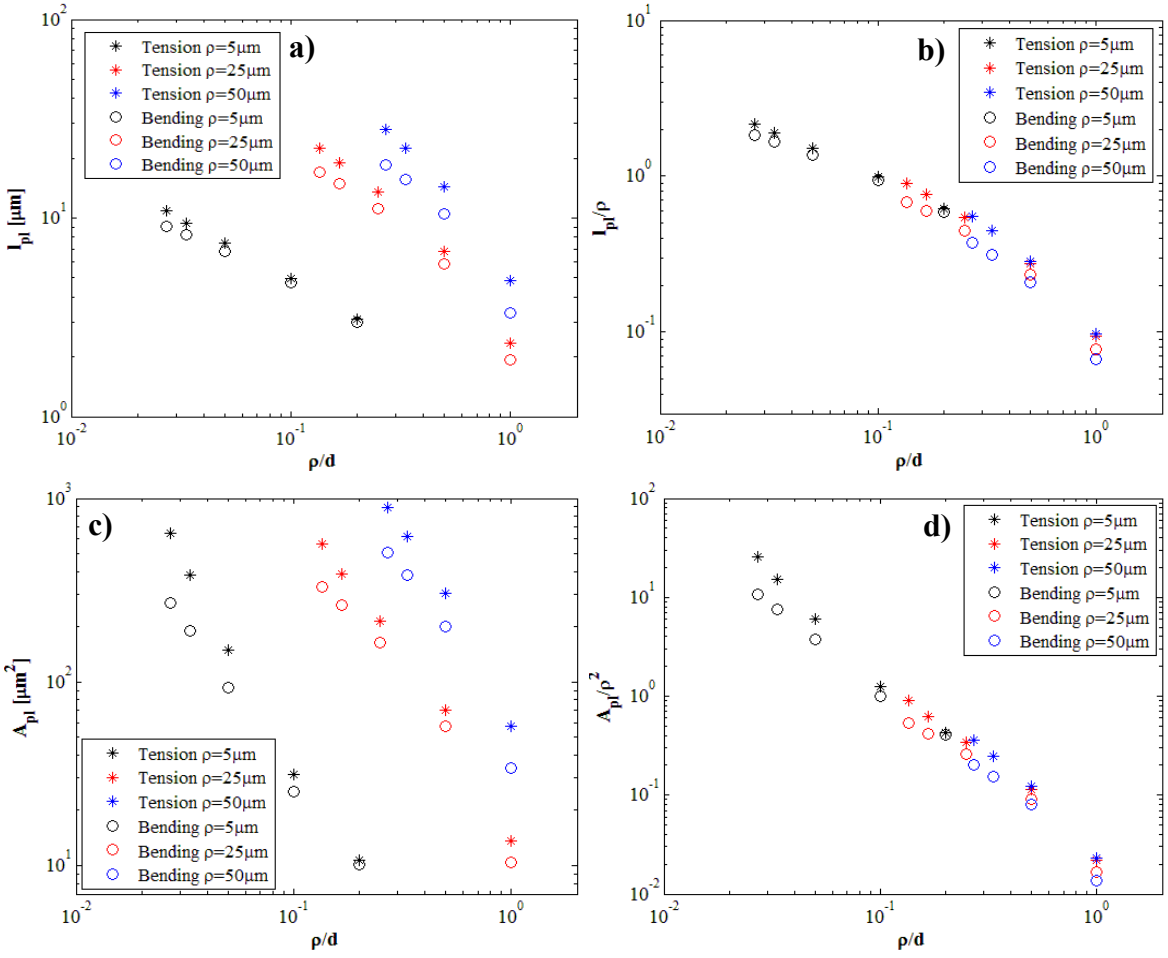

Fig. 5.11: Plastic zone length along the notch bisector and area according to different scribe geometries. Absolute plastic zone length (a) and normalised with respect to ρ (b) plotted against the notch aspect ratio. Absolute plastic zone area (c) and normalised with respect to ρ^2 (d) plotted against the notch aspect ratio

Fig. 5.12 and Fig. 5.13 show the effect of the notch geometry on the elastic-plastic stress and strain distributions along the notch bisector of notches in unclad tension

samples. As scribe geometry affected the elastic-plastic distributions in a similar way under tensile and bending loading, bending stress and strain plots are not described in this section. Fig. 5.12 a) shows the equivalent von Mises stress, normalised by the material yield strength, $\sigma_{0.2}$, along the bisector of selected notches under tensile load. The distance from the notch root, x, was normalised with respect to the sample thickness t. All the stress distributions showed a sigmoid trend with the maximum value reached at the notch root (Fig. 5.12 a)). The normalised von Mises stress, $\sigma_{eq}/\sigma_{0.2}<1$ along the whole bisector of the 25 μm deep, 50 μm root radius notch indicated that no relevant plastic deformations occurred at the root of such scribe. The stress distribution was thus pure elastic. No trend differences were observed between pure elastic and elastic-plastic distributions as what differed was just the stress magnitude (Fig. 5.12 a)).

Since the maximum value of σ_{eq} was regulated by the notch aspect ratio, close to the notch root von Mises stress distributions were shifted upward according to the decrease of ρ/d. The stress gradients in the proximity of the notch root and therefore the length of the region affected by high von Mises stresses depended on the notch root radius. The smaller the root radius, the steeper the stress gradients and the shorter the notch bisector portion affected by high stresses (Fig. 5.12 a)). Like for pure elastic analyses an increase in the scribe depth seemed just to stretch the curves toward higher stresses in the region affected by the notch stress raising effect. Moving away from the notch root σ_{eq} distributions rapidly decreased reaching a local minimum to rise again in the far field region (Fig. 5.12 a)). At sufficient distance from the scribe root distributions of equally deep notches merged together. The merging point location depended on the scribe depth. The deeper the scribe the farther the merging point from the notch root (Fig. 5.12 a)).

Fig. 5.12 b) shows the equivalent plastic strain along the bisector of selected notches plotted against the normalised distance from the notch root (x/t). ε^{pl}_{eq} distributions showed a sigmoid trend with the maximum value at the notch root. Far from the scribe stress raising effect all the strain curves approached zero as no plastic deformations occurred in that sample region (Fig. 5.12 b)). As already explained the maximum value of the equivalent plastic strain at the notch root was regulated by the notch aspect ratio. Analogously to the behaviour observed for σ_{eq}, an increase in the notch root radius reduced the equivalent plastic strain gradients in proximity of the notch enlarging the material region subjected to the highest strains. ε^{pl}_{eq} distributions were stretched toward higher strain values according to the notch depth (Fig. 5.12 b)). The length of the samples region near the notch root affected by positive plastic strains depended on the scribe depth and root radius. The deeper the scribe and the bigger its root radius, the longer the positive portion of the ε^{pl}_{eq} distribution (Fig. 5.12 b)). The strain curve of the 25 μm deep, 50 μm root radius notch, despite its pure elastic behaviour, showed slightly positive equivalent plastic strains close to the scribe root (Fig. 5.12 b)). However since $\varepsilon^{pl}_{eq}<0.2\%$ the plastic deformation was too small to consider the material behaviour as plastic at the scribe root.

Fig. 5.12 c) shows the longitudinal strain, ε_{22}, distributions along the bisector of selected notches plotted against the distance from the notch root, x, normalised by the sample thickness. In Fig. 5.12 d) the same distributions are drawn but the strains were normalised with respect to the their maximum values, $\varepsilon_{max,}$ and the distance from the

notch root by the root radius (x/ρ). ε_{22} distributions showed similar trends to the corresponding equivalent plastic strain curves, but different strain magnitudes (Fig. 5.12 c)). In the far field region not affected by the notch strain raising effect, all the curve assumed an uniform values corresponding to the net nominal strain under tensile load. Net nominal tensile strains of different notches had very close values as all the ε_{22} curved seemed to merge (Fig. 5.12 c)).

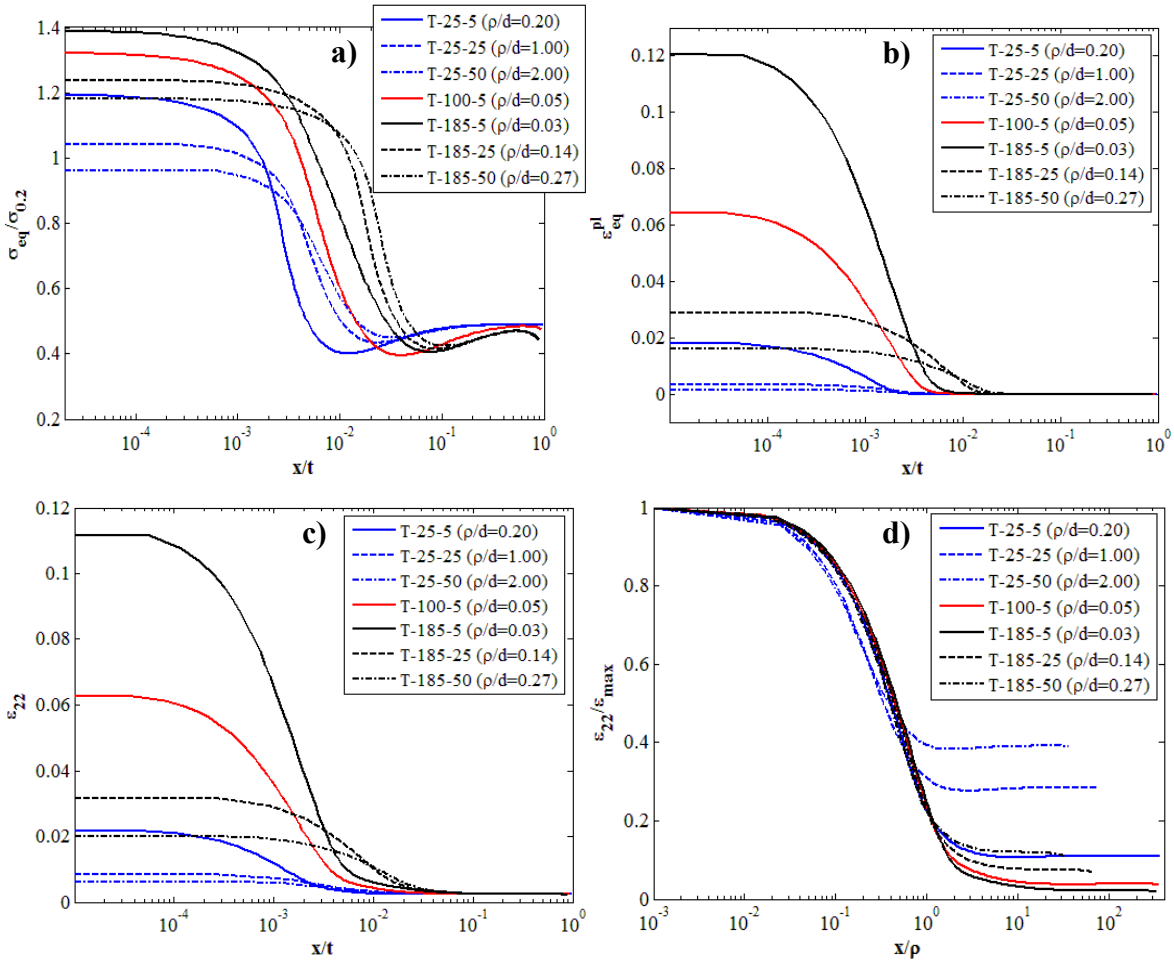

Fig. 5.12: Notch geometry effect on non-dimensional stress and strain distributions along the crack plane under tensile load. Von Mises equivalent stress normalised by the yield strength (a) and equivalent plastic strain (b) plotted against distance from the notch root normalised with respect to model thickness; absolute longitudinal strains and ε_{22} normalised by their maximum values versus distance from the notch root normalised with respect to model thickness (c) and notch root radius (d)

When the longitudinal strains were normalised with respect to their maximum values reached at the notch root (ε_{max}), and plotted against x/ρ the distributions of different scribes approximately overlapped in proximity of the notch (see Fig. 5.12 d)). Moving away from the notch root normalised ε_{22} distributions left the common overlapping region approaching their far field values according to the notch aspect ratio. The bigger the scribe ρ/d, the shorted the normalised distance from the notch root x/ρ at which the superposition area was left (Fig. 5.12 d)). As the elastic longitudinal stress and strain along the notch bisectors, also the elastic-plastic ε_{22} distributions near the scribes could be approximately assumed to be only defined by ρ and ε_{max}. Since the maximum

longitudinal strain was regulated by the notch aspect ratio (Fig. 5.9 c)), the elastic-plastic local strain raising effect of the notch was characterised by the scribe shape and size, expressed by ρ. The former determined the strain magnitude, the latter defined the distribution gradients.

Fig. 5.13 shows the scribe geometry effect on the non-dimensional maximum principal stress distribution along the notch bisector under tensile load. Due to the model symmetry, on the notch bisector the longitudinal stress, σ_{22}, coincided with the maximum principal stress. The stress magnitude and the distance from the notch root were normalised with respect to different parameters appropriately select to point out particular distribution properties.

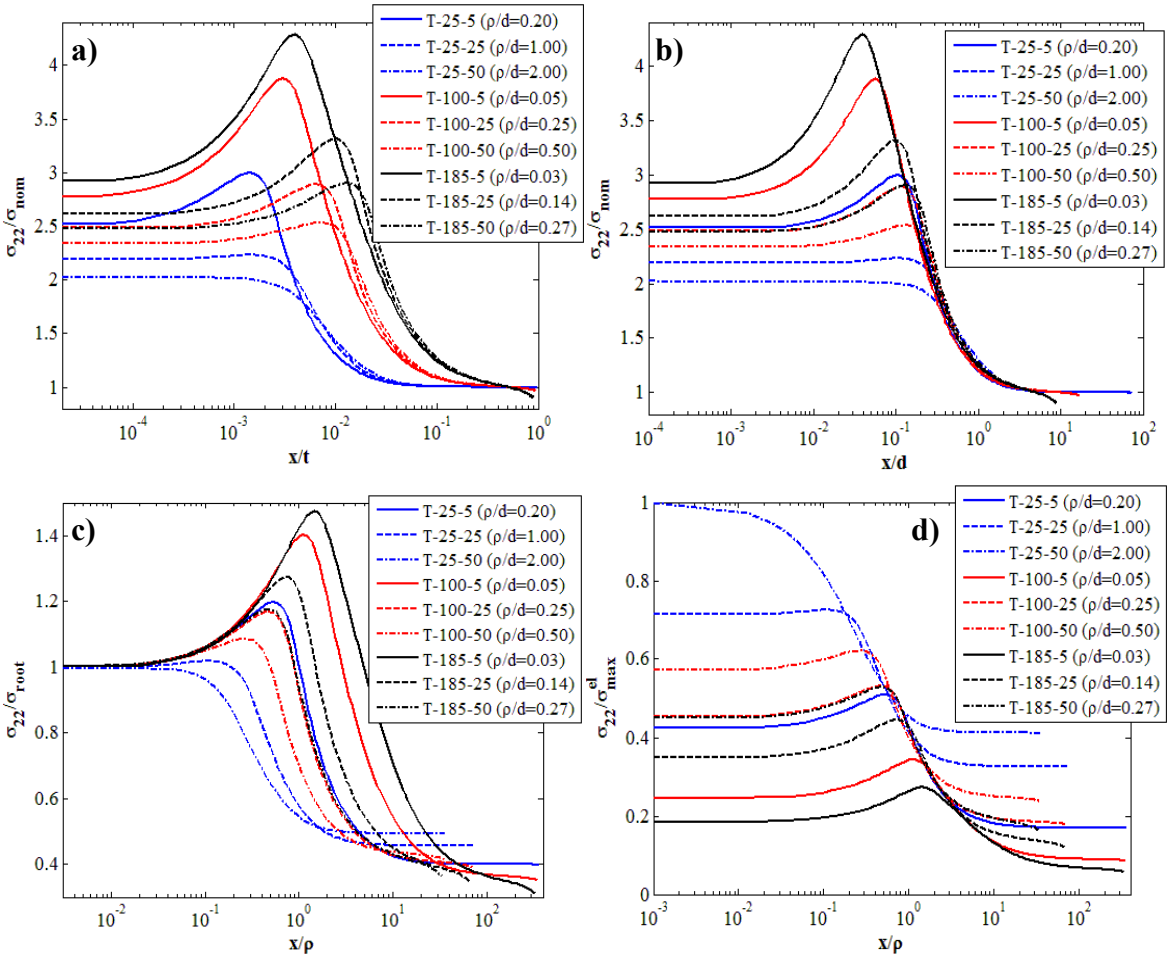

Fig. 5.13: Notch geometry effect on non-dimensional maximum principal stress distribution along the crack plane under tensile load. σ_{22} normalised by nominal stress plotted against distance from the notch root normalised with respect to model thickness (a) and notch depth (b); maximum principal stresses normalised by their values at the notch root (c) and by the maximum stress of the corresponding pure elastic distribution (d) versus distance from the notch root normalised with respect to the notch root radius

Fig. 5.13 a) shows the σ_{22} distributions of selected notches normalised by the nominal tensile stress, σ_{nom}, plotted against x/t. Elastic-plastic σ_{22} curves showed a maximum in proximity of the notch root. The magnitude of the stress maxima was regulated by the notch aspect ratio, being larger for notches with smaller ρ/d. The σ_{22}

maximum was reached at the notch root for 25 μm deep, 50 μm root radius notch as such distribution was purely elastic. Notch geometry determined also the location of the longitudinal stress maximum. The deeper the notch and the larger the root radius the farther from the scribe the location of the maximum σ_{22} value. Away from the notch root the stress distributions steeply decreased from their maxima to a far field nearly uniform stress (Fig. 5.13 a)). Longitudinal stresses of equally deep notches showed nearly the same trends far from the notch root. In fact after they reached their maximum values, σ_{22} distributions of notches with the same depth, almost overlapped following a common tendency line (Fig. 5.13 a)). The normalised coordinate x/t at which the curve overlapping occurred seemed to be proportional to the notch depth. As for elastic maximum principal stresses, the notch root radius seemed to mainly affect the elastic-plastic σ_{22} distributions only in the neighbourhood of the notch root (Fig. 5.13 a)).

When the σ_{22}/σ_{nom} values are plotted against the coordinates from the notch root normalised with respect to the notch depth x/d the dependency of the maximum stress on the notch aspect ratio became more evident (see Fig. 5.13 b)). Moreover at a distance from the notch root of almost $0.3d$ all the σ_{22} curves merged together proving that from that point the σ_{22} trend along the scribe bisector is approximately characterised only by the notch depth (Fig. 5.13 b)). For a coordinate $x>0.3d$ the σ_{22} stress gradient was proportional to the notch depth. The development of plasticity at the notch root and the consequent stress redistribution did not substantially alter the extension of the notch stress raising effect. In fact, as for the elastic distributions elastic-plastic, σ_{22} stresses were affected by the presence of the notch up to nearly $3d$ from the scribe root (Fig. 5.13 b)).

Fig. 5.13 c) shows the same longitudinal stresses along the notch bisector normalised by their respective values at the notch root, σ_{root}, as a function of the coordinate x normalised by the scribe root radius x/ρ. Close to the notch root, stress distributions of different notches showed the same behaviour as they overlapped (Fig. 5.13 c)). Normalised elastic-plastic σ_{22} curves left the common overlapping region before reaching their maximum values according to the notch aspect ratio. The shaper the scribe the farther from the root the common trend was abandoned (Fig. 5.13 c)). Longitudinal stresses of different notches decreased from their maxima to the far field stress in a similar way showing almost the same stress gradients (Fig. 5.13 c)). Contrarily to the case of purely elastic distributions, the σ_{22} value at the notch root, $\sigma_{root,}$ and the root radius, ρ were not able to univocally characterise the elastic-plastic maximum principal stresses in the whole local region affected by the notch stress raising effect. Different σ_{22} distributions were correlated in a unique trend just close to the notch root inside the plastic zone (Fig. 5.13 c)). In fact the boundary of the monotonic plastic zone generally corresponded along the notch bisector with the location of the maximum longitudinal stress. According to the mechanical similitude elastic-plastic stress distributions in the neighbourhood of the scribe are still univocally defined by the notch shape and size but the non linearity introduced by the elastic-plastic constitutive equations makes impossible their characterisation only by means of $\sigma_{root,}$ and ρ.

Fig. 5.13 d) shows the same elastic-plastic σ_{22} distributions normalised with respect to the maximum value of the corresponding σ_{22} elastic stress at the notch root, σ^{el}_{max}, and

plotted against x/ρ. As the mechanical response of samples weakened by the 25 µm deep, 50 µm root radius notch remained elastic, the normalised σ_{22} curve of this notch started from an unitary stress magnitude at the scribe root (Fig. 5.13 d)). The presence of a pure elastic stress curve allowed to investigate the influence of the elastic-plastic stress redistribution as any σ_{22} elastic distribution showed the same trend in proximity of the notch root when normalised by σ^{el}_{max}, and plotted against x/ρ (see Fig. 5.5 d)). Normalised σ_{22} stresses assumed different value at the scribe root according to the notch aspect ratio. The smaller the aspect ratio, ρ/d, the lower the normalised stress at the root (Fig. 5.5 d)). In correspondence with the locations of their maximum values the σ_{22} distributions seemed to follow the trend with a uniform gradient typical of elastic stress curves to then deviate from its approaching different far-field stresses (Fig. 5.5 d)). Except for small deviations produced by the stress redistribution, elastic-plastic σ_{22} distribution showed, outside the notch root plastic zone, the same trend as elastic ones. Elastic-plastic stress redistribution shifted the elastic portion of the elastic-plastic normalised σ_{22} curve toward larger values of x/ρ making the notch behaved as it was slightly deeper. Such behaviour can be clearly observed in Fig. 5.14 where elastic and elastic-plastic normalised σ_{22} distributions along the bisector of 185 µm deep, 5 µm root radius notch under tensile load are plotted.

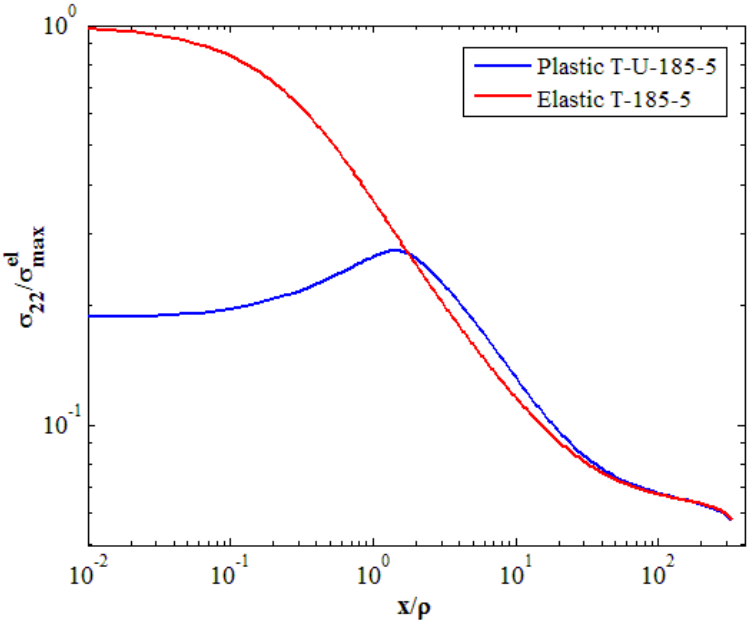

Fig. 5.14: Elastic-plastic stress redistribution effect on the maximum principal stress distribution along the notch bisector. σ_{22} normalised by the maximum elastic stress versus distance from the notch root normalised with respect to the notch root radius

5.3.1.3 Notch size effect in plastic analysis

The notch size effect on the local elastic-plastic material response was investigated comparing the finite element results of notches with the same shape, that is the same aspect ratio, but different size. As the notch size affected tensile and bending stress and strain fields in a similar way only results relative to tensile samples are discussed in this section. Fig. 5.15 shows the principal stress distributions along the bisector of the 50 µm deep, 25 µm root radius and the 100 µm deep, 50 µm root radius notches in unclad

tension samples. Such notches had the same aspect ratio ρ/d=0.5 but one was double in size than the other. Due to the model symmetry and the plane strain assumption maximum principal stresses coincided with the elastic-plastic normal stress components along the notch bisector.

In Fig. 5.15 a) principal stresses normalised by the tensile nominal stress, σ_{nom}, are plotted against the non dimensional distance from the notch root normalised by the sample thickness (x/t). Corresponding principal stress distributions of the two notches showed the same values at the notch root and equal maxima. However the coordinates x/t at which the distributions reached their maximum value were higher for the larger notch (Fig. 5.15 a)). More generally the corresponding stress curves of the two notches had similar trends with those of the bigger 100 µm deep, 50 µm root radius scribe stretched towards higher x/t coordinates. In fact the distance from the root at which a given principal stress value was reached along the notch bisector depended on the notch size. The larger the notch, the longer the distance x from the notch root (Fig. 5.15 a)).

When the coordinate x was normalised with respect to a parameter taking into account the notch size like the root radius, ρ, the corresponding principal stress distributions of the notches merged together (see Fig. 5.15 b)). Small differences in the stress values, making the corresponding curves of the two notches not perfectly overlapped, were caused by the diverse sample finite thickness effect (Fig. 5.15 b)). In fact the lack of proportionality between the net ligament lengths of the two notched samples slightly influence the principal stress magnitude producing small distributions misalignments. The overlapping of the corresponding stress curves proved that for notches with the same aspect ratio the distance from the root at which a given stress magnitudes was obtained was linearly proportional to the notch size (Fig. 5.15 b)). The scribe shape, defined by ρ/d, determined the trend of the elastic-plastic stress distribution while the notch size proportionally stretched such distribution along the abscissa axis.

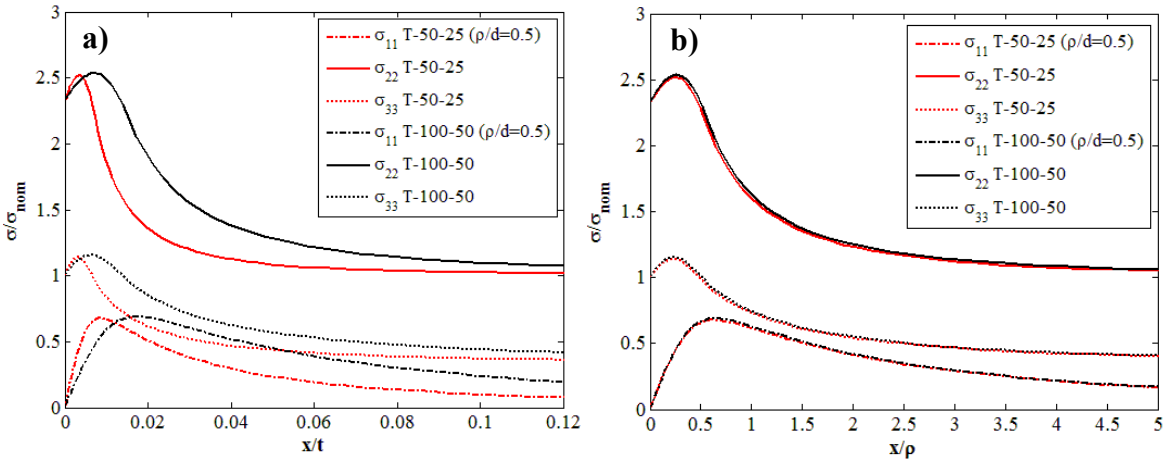

Fig. 5.15: Notch size effect on non-dimensional principal stress distributions along the notch bisector under tensile load. Principal stresses normalised by the nominal stress plotted against distance from the notch root normalised with respect to model thickness, *x/t*, (a) and with respect to notch root radius, *x/ρ*, (b)

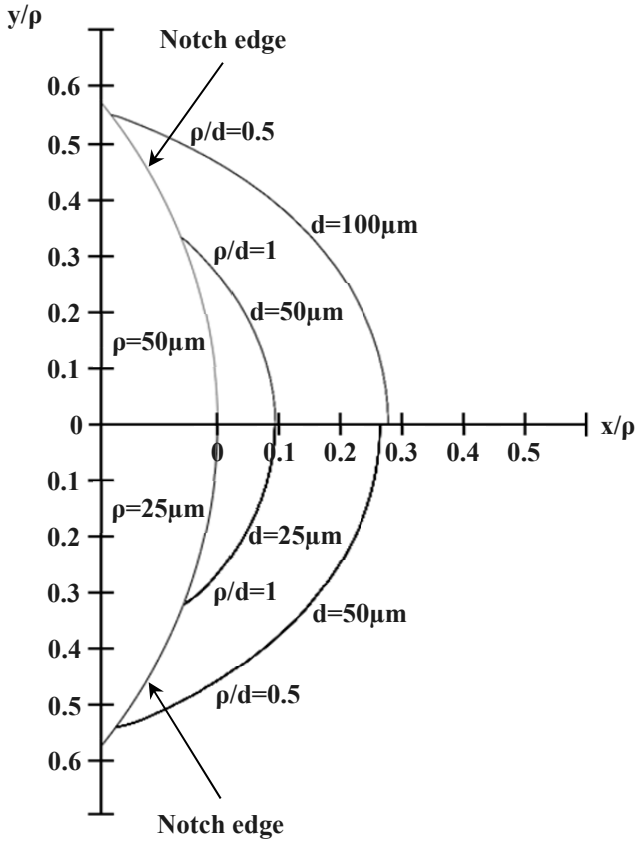

Fig. 5.16: Notch size effect on root plastic zone in unclad specimens

Fig. 5.16 shows the notch size effect on the monotonic plastic zone in unclad samples under tensile loading. The boundaries of plastic zones developed at the root of notches having the same aspect ratio but different size were drawn in Fig. 5.16 normalising the planar coordinates by the root radius. The plastic zones of notches having two aspect ratios (ρ/d=0.5 and ρ/d=1) and two root radii one double the other (ρ=25 μm and ρ=50 μm) were selected and plotted in Fig. 5.16. As long as the planar coordinates were normalised with respect to the root radius, notches with the same aspect ratio showed developed equal plastic zones at their roots (Fig. 5.16). Once again small differences in the normalised plastic zone size and shape of notches with the same ρ/d, were caused by the diverse finite thickness ratio, d/t, resulting from the different notch size (Fig. 5.16). The effect of the dissimilar sample finite thickness was more marked for bigger scribes. As for the elastic-plastic local stress and strain fields in the neighbourhood on scribes, the monotonic plastic zone shape was univocally determined by the notch aspect ratio, whereas its size, according to the mechanical similitude, was proportional to the scribe size.

5.4 Notch root plasticity: cyclic behaviour

Elastic-plastic cyclic finite element analyses were performed to investigate the mechanical response of notched samples under repeated fatigue cyclic load. Due to the lack of cyclic mechanical curves and properties for the Al 1080 pure aluminium forming the cladding, cyclic finite element calculations were carried out only on unclad

scribed samples under tensile and bending loadings. Cyclic elastic-plastic stress and strain fields were calculated for the 15 different notch geometries in tension and bending specimens for a total of 30 analyses. Cyclic finite element analyses are actually elastic-plastic calculations under loading conditions that repetitively varies in time. Therefore the finite element type and the options set for the monotonic elastic-plastic calculations (see section 5.3) were maintained also for cyclic analyses.

The elastic-plastic cyclic behaviour of the Al 2024-T351 aluminium alloy was modelled, using the classical metal plasticity model. The same hypotheses and assumption used in the monotonic elastic-plastic analyses, were applied to the cyclic calculations. The yielding criterion and the flow rule chosen to simulate the monotonic plastic behaviour were selected also for the cyclic analyses. Only the hardening rule was modified to accurately characterise the material cyclic mechanical response. The combined non linear kinematic plus isotropic hardening rule was selected to model the material hardening behaviour after the initial yielding [1]. Such hardening model allows both a translation and an homothetic expansion of the yielding surface in the stress space according to the variation of the equivalent plastic strain, ε^{pl}_{eq}, during the fatigue cycle [8,9]. The non linear kinematic part of the hardening rule ensures the prediction of behaviours typical of material cyclic response such as the Bauschinger effect, the ratchetting and the mean stress relaxation, whereas the isotropic portion allowed the characterisation of the cyclic hardening or softening [8].

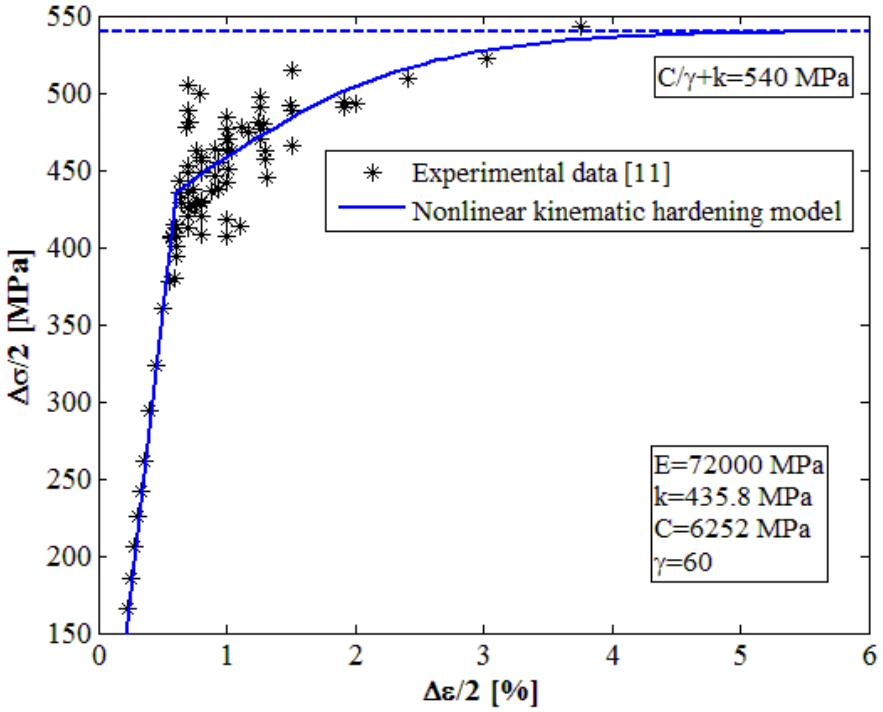

Fig. 5.17: Non linear kinematic hardening model experimental setup

The parameters of the combined non linear kinematic plus isotropic hardening were set on experimental material cyclic stress-strain curve, following the procedure described in [8]. Experimental cyclic curve of the Al 2024-T351 aluminium alloy were obtained from the ESDU data sheets [11]. Fig. 5.17 shows the comparison between the Al 2024-T351 cyclic experimental data and the non linear kinematic hardening model.

The peaks of the stable hysteresis loops, forming the experimental material cyclic stress-strain curve, were plotted in Fig. 5.17 and the hardening model parameters were calculated to fit those experimental data. As the cyclic stress-strain curve is obtained from the stable hysteresis loops reached after the occurrence of the material cyclic hardening of softening, the experimental data were used to set mainly the non linear kinematic part of the hardening model [8]. A cyclic yield stress, k, of 435.8 MPa was measured from the material cyclic stress-strain curve [11]. Then the kinematic hardening exponent γ and coefficient C were set on the basis of least square method to fit the experimental data and to reach an asymptotic stress of 540 MPa (Fig. 5.17).

Since the isotropic part of the hardening model is responsible for the prediction of the material cyclic hardening, its parameters were related to the expansion of the yielding surface during the fatigue cycle. The maximum expansion of the yielding surface radius, Q_∞, was assumed to be equal to the difference between the cyclic yield strength, k, and the monotonic one, $\sigma_{0.2}$. An isotropic hardening exponent, b=4 was chosen for the Al 2024-T351 aluminium alloy in agreement with the work of Khan et al. [12]. Table 5.4 lists all the values of the elastic and cyclic plastic parameters selected for the combined non linear plus isotropic hardening model.

Table 5.4: Aluminium elastic-plastic parameters for combined non-linear kinematic and isotropic hardening model [11,12]

Material	Elasticity		Cyclic plasticity				
	E [MPa]	ν	$\sigma_{0.2}$ [MPa]	Q_∞ [MPa]	b	C [MPa]	γ
Al 2024-T351	72000	0.33	360.0	75.8	4	6252	60

Tensile axial forces and bending moments, applied on the sample models, were initially increased in a linear ramp from zero to their maximum values corresponding to a nominal tensile stress and a nominal bending superficial stress of 200 MPa. The external loads were then linearly decreased to 10% of their maximum values and raised again in a ramp to their maxima simulating a fatigue loading cycle with nominal maximum stress σ_{nom}^{max}=200 MPa and a stress ratio R=0.1. The external loading variation was modelled using the amplitude load module available in Abaqus [1]. Axial forces and bending moments were cycled with triangular loading curve until the sample cyclic mechanical response became stable. Scribed sample were assumed to reach a stable cyclic response as soon as the stress-strain curve measured at the notch root showed a stable hysteresis loop. 10 to 25 cycles were required for the samples, according to different notches, to reach a stable cyclic behaviour. Each loading reversal, which was assumed to occur in 0.1 sec, was divided into 10 increments. Outputs were recorded at every load increment having stress, strain and displacement components any 0.01 sec. Like in the monotonic elastic-plastic analyses, mechanical quantities were calculated at each increments using the Newton's iterative method for non linear problems.

5.4.1 Cyclic analysis results

The elastic-plastic cyclic mechanical response of unclad scribed tension and bending samples was investigated analysing the evolution of the stress and strain components in

the neighbourhood of different notches during the loading cycles. The development at the notch root of a stable cyclic plastic zone where the plastic deformations are contained after the reaching of a stable cyclic material response was assessed as well. Monotonic and cyclic elastic-plastic stress and strain components and plastic zones were compared pointing out the influence of previous plastic deformation history on the material mechanical behaviour.

5.4.1.1 Local cyclic behaviour at the notch root

Fig. 5.18 a) shows the cyclic longitudinal stress-strain curve, that is the evolution of σ_{22} according to the variation of ε_{22} under cyclic loading, calculated at the root of 185 μm deep 5 μm root radius notch under tensile load.

After the first linear trend, indicating a purely elastic response, the material locally yielded and the longitudinal stress-strain curve showed a post yielding behaviour characterised by a monotonic hardening (Fig. 5.18 a)). With the load reversal, σ_{22} and ε_{22} at the notch root linearly decreased according to the elastic unload until the material yielded under compressive load. The material yielded at a stress magnitude in compression lower than in tension showing a typical Bauschinger effect [8] (Fig. 5.18 a)). During the material plastic deformations under compressive load the longitudinal stress and strain gradually decreased following the cyclic hardening rule. As soon as the external load raised again, the stress-strain curve showed a linear elastic loading and a hardening behaviour, after the occurrence of the material local yielding. The hardening took place under tensile load until the first fatigue cycle was completed. The material yielded during the loading part of the fist fatigue cycle in correspondence of a σ_{22}=257.1 MPa, slightly larger in magnitude than the yielding value during the unloading portion, σ_{22}=-224.0 MPa (Fig. 5.18 a)).

Fatigue cycle after cycle the hysteresis loops of the longitudinal stress-strain curve at the notch root progressively shifted towards larger ε_{22} values showing the so called ratchetting effect [8] until, after 10 cycles, a stable hysteresis loop configuration was reached. Under cyclic loading the loops of the stress-strain curve gradually relaxed their mean stress, cycling between σ_{22}^{max}=605.8 MPa and σ_{22}^{min}=-605.8 MPa in their stable configuration (Fig. 5.18 a)). The mean stress relaxation was consistent with the material local cyclic response that occurred at the notch root almost in strain-control conditions The cyclic condition of strain-control were produced by the constrain exerted on the deformations of the local plastic zone by the larger surrounding elastic material [8]. The gradual shifting of the peaks of the hysteresis loop towards higher σ_{22} magnitudes and the resulting increase in the loop area under loading cycles were consequence of the material cyclic hardening. When the cyclic hardening effect ended the stabilised cyclic stress-strain response defined by the stable hysteresis loop was reached (Fig. 5.18 a)).

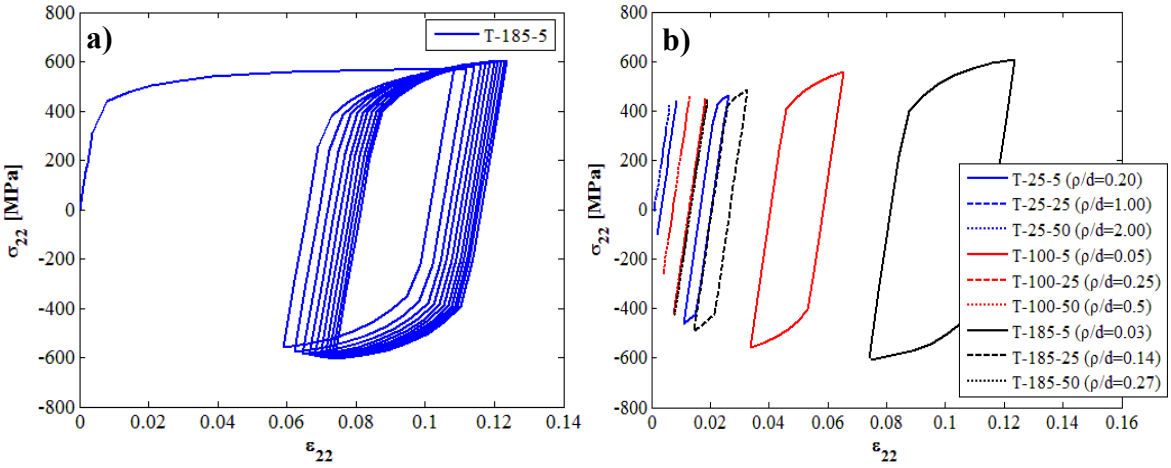

Fig. 5.18: Cyclic longitudinal stress-strain curve computed at the root of the 185 µm deep 5 µm root radius notch in an unclad tension sample (a); stabilised longitudinal stress-strain cycles at the notch root under fatigue loading for different notched unclad tension samples (b)

Fig. 5.18 b) shows the comparison of the stabilised cycles of the longitudinal stress-strain curves at the roots of selected notches under fatigue tensile loading. No plastic deformations were observed in stabilised σ_{22}-ε_{22} cycles of notches with ρ/d>0.2 as they collapsed into straight lines distinctive of a purely elastic response (Fig. 5.18 b)). Stabilised stress-strain cycles were shifted towards higher ε_{22} values according to the notch aspect ratio. The smaller ρ/d the larger the mean strain of the longitudinal stress-strain cycle at the notch root (Fig. 5.18 b)). As the notch aspect ratio was decreased, stabilised cycles progressively reached lower minimum σ_{22} stresses reducing their mean stresses. Scribed samples with ρ/d≤0.2, where stable plastic deformations occurred at the notch root, showed stable hysteresis loops with zero mean stresses consistently with the mean stress relaxation effect (Fig. 5.18 b)). Stress and strain ranges of the stabilised σ_{22}-ε_{22} cycles also increased with the reduction of the notch aspect ratio, enlarging the loop area of sharp notches with ρ/d≤0.2. The area enclosed by the loop represents the local plastic energy dissipated at the notch root at every loading cycle [8]. Therefore the sharper the notch the more energy was dissipated at its root by the plastic deformation in any cycle.

Fig. 5.19 a) and b) show respectively the effect of the notch geometry on the longitudinal stress range, $\Delta\sigma_{22}$, and the equivalent plastic strain range, $\Delta\varepsilon^{pl}_{eq}$, of the stabilised elastic-plastic cyclic response at the notch root under tensile and bending loadings. Stabilised $\Delta\sigma_{22}$ values normalised with respect to the nominal stress range $\Delta\sigma_{nom}$=180 MPa are plotted against the notch aspect ratio for tension and bending samples in Fig. 5.19 a). Coloured markers are used to show data of notches with different root radii. As for monotonic elastic-plastic and purely elastic analyses, the notch aspect ratio was capable of correlating all the stabilised $\Delta\sigma_{22}$ at the root of different notches on a unique trend line in both tensile and bending samples. The sharper the notch, the higher the value of the stabilised $\Delta\sigma_{22}$ reached at its root under cyclic loadings. Notches with the same aspect ratio, but different size showed nearly the same stabilised cyclic stress range at their roots (Fig. 5.19 a)). The lack of mechanical similitude in the samples finite thickness was responsible for the small differences between the stress ranges of notches with equal ρ/d and for the light misalignments of

data. Stabilised longitudinal stress range showed the same trend in tension and bending samples but bending $\Delta\sigma_{22}$ values were slightly smaller than tension ones (Fig. 5.19 a)). Tension and bending $\Delta\sigma_{22}$ stresses, when plotted against the notch aspect ratio, followed a nearly bi-linear trend with a change of slope in correspondence with ρ/d=0.2. Such change in slope was produced by the occurrence of stable cyclic plastic deformations at the root of notches with $\rho/d \leq 0.2$ under both tensile and bending cyclic loads (see Fig. 5.18 b)).

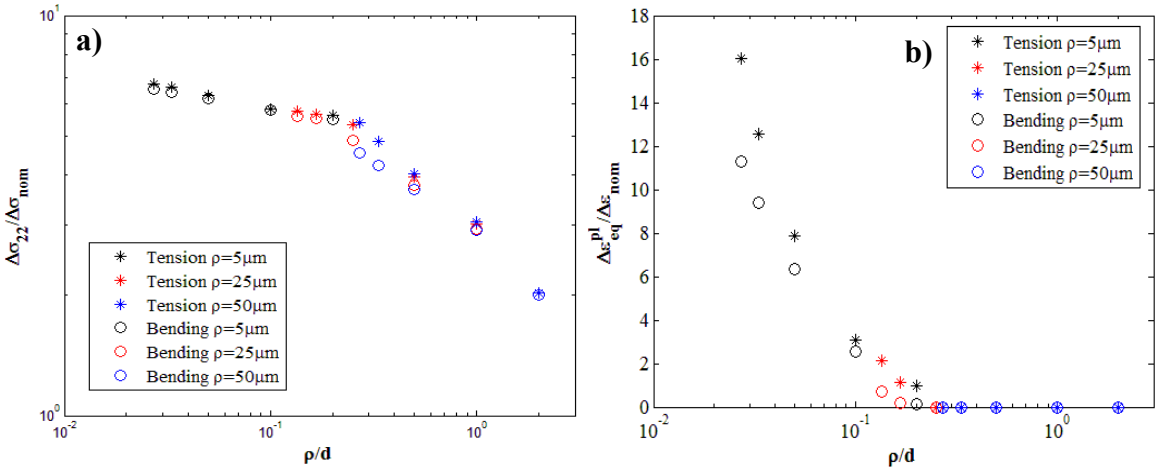

Fig. 5.19: Normalised longitudinal stress range, $\Delta\sigma_{22}$, (a) and equivalent plastic strain range, $\Delta\varepsilon^{pl}_{eq}$, (b) of the stabilised cyclic response at the notch root plotted against the notch aspect ratio ρ/d in tension and bending samples

Fig. 5.19 b) shows the $\Delta\varepsilon^{pl}_{eq}$, of the stabilised elastic-plastic cyclic response at the notch root normalised by the nominal strain range, $\Delta\varepsilon_{nom}=\Delta\sigma_{nom}/E$, and plotted against the notch aspect ratio for tension and bending samples. Blunt notches with an aspect ratio ρ/d>0.2 showed $\Delta\varepsilon^{pl}_{eq}$ values equal to zero under both tension and bending cyclic loading as no further plastic deformations took place at their root when the stable mechanical response was reached. For notches sharper than ρ/d=0.2 the smaller the notch aspect ratio the higher the normalised $\Delta\varepsilon^{pl}_{eq}$ in tension and bending samples. Once again equivalent plastic strain ranges at the root of different scribes were correlated on a unique trend line for tension and bending loading by the notch aspect ratio (Fig. 5.19 b)). Bending samples showed the same trend as tension ones but shifted down to lower $\Delta\varepsilon^{pl}_{eq}$ values. Under tensile load the same notch dissipated more energy at every loading cycle, due to the occurrence of local stable plasticity at its root, than under bending load. The different finite thickness effects was responsible for small data deviations from the common trend (Fig. 5.19 b)).

Fig. 5.20 a) and b) show the comparison between elastic-plastic monotonic and cyclic longitudinal stress and strain at the root of different notches under tensile load. Monotonic σ_{22} and stabilised cyclic $\Delta\sigma_{22}$ at the notch root were normalised by their respective nominal value, σ_{nom} and $\Delta\sigma_{nom}$ and plotted against the notch aspect ratio (Fig. 5.20 a)). Notches showed higher normalised stresses at their roots under the cyclic tensile loading, equivalent to a nominal maximum stress σ_{nom}^{max}=200 MPa with a stress ratio R=0.1, than under the monotonic tensile load, corresponding to a nominal stress σ_{nom}=200 MPa. That behaviour was a consequence of the cyclic hardening occurred

during the plastic deformations at the notch root before the stabilised cyclic response was reached. Only the 25 µm deep 50 µm root radius notch (ρ/d=2) showed the same normalised value of monotonic and cyclic longitudinal stress as no static yielding took place at its root (Fig. 5.20 a)). For notches with $\rho/d \leq 0.2$, where stable plastic deformation occurred at every loading cycle, normalised cyclic data showed a linear trend with the same slope as that of monotonic ones. Cyclic normalised $\Delta\sigma_{22}$ at the root of these notches were nearly 2.3 times the corresponding monotonic stresses (Fig. 5.20 a)). For notches blunted than ρ/d=0.2 the gap between cyclic and monotonic stresses was progressively reduced, as the notch aspect ratio increased, up to it vanished for the 25 µm deep 50 µm root radius scribe (Fig. 5.20 a)).

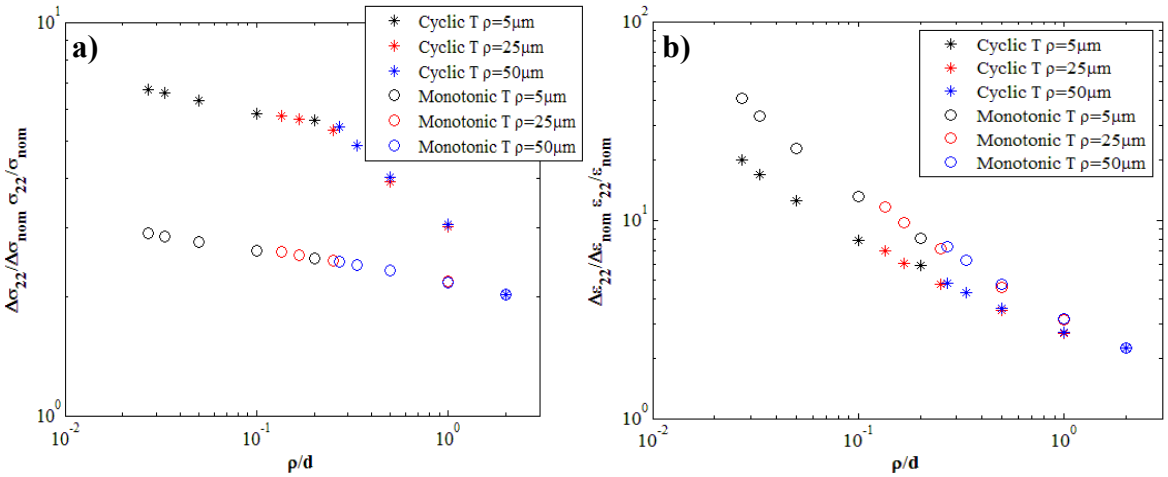

Fig. 5.20: Normalised monotonic elastic-plastic σ_{22} and cyclic elastic-plastic stabilised $\Delta\sigma_{22}$ (a) and normalised monotonic elastic-plastic ε_{22} and cyclic elastic-plastic stable $\Delta\varepsilon_{22}$ (b) at the root of different notches under tensile load plotted against ρ/d

Fig. 5.20 b) shows the elastic-plastic monotonic ε_{22} and stabilised cyclic $\Delta\varepsilon_{22}$ at the roots of notched tension samples normalised by σ_{nom} and $\Delta\sigma_{nom}$ and plotted against ρ/d. Unlike the behaviour observed for the longitudinal stresses, cyclic normalised $\Delta\varepsilon_{22}$ at the notch roots were smaller than the corresponding monotonic ε_{22} values (Fig. 5.20 b)). 185 µm deep 5 µm root radius, notches (ρ/d=0.03) showed at their root a normalised longitudinal strain under monotonic tensile load nearly twice the $\Delta\varepsilon_{22}$ value reached after the stabilisation of the mechanical response under cyclic tension. Due to its purely elastic behaviour the 25 µm deep 50 µm root radius, notches (ρ/d=2) reached at the root the same normalised strain under both monotonic and cyclic loads (Fig. 5.20 b)). Like the monotonic strain data, cyclic stabilised $\Delta\varepsilon_{22}$ values of different notches were correlated by the ρ/d on a unique trend line where small misalignments were produced by the effect of the different sample finite thickness.

Despite the occurrence or not of stable plastic deformations, stress and strain ranges at the scribe root obtained after the mechanical response stabilisation under cyclic tensile and bending loadings were uniquely defined by the scribe shape expressed by the notch aspect ratio.

5.4.1.2 Cyclic plastic zone

The effect of the notch geometry on the development of a stable cyclic plastic zone was investigated comparing the size and shape of stabilised plastic zone at the root of different notches under tensile and bending cyclic loading. Fig. 5.21 a) shows the cyclic plastic zone developed at the root of different notches under tensile load. The cyclic plastic zone was defined as the material region that contains plastic deformations occurring ad every loading cycle after the stabilisation of the cyclic mechanical response.

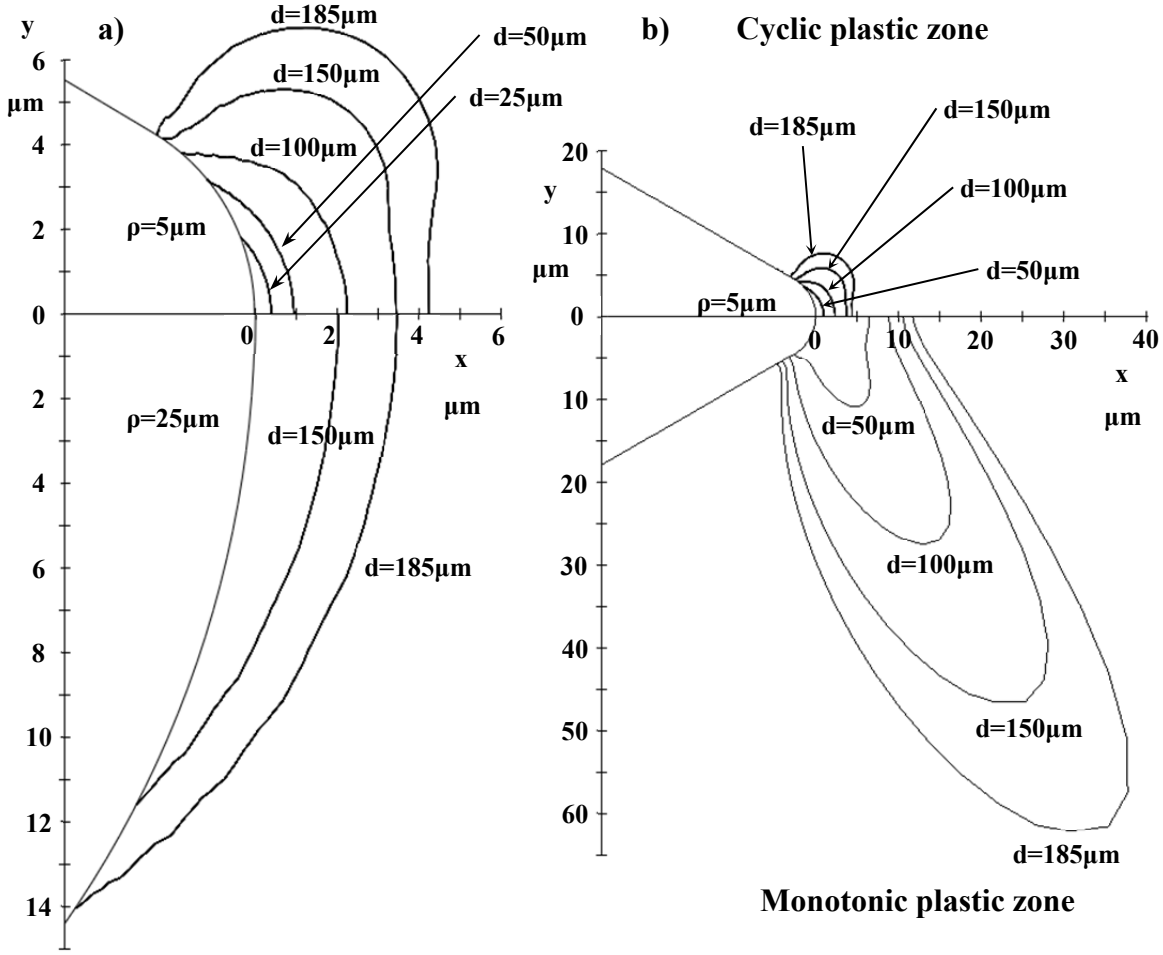

Fig. 5.21: Notch root cyclic plastic zone according to different notch geometries in unclad samples under tensile load (a) and comparison between cyclic and monotonic plastic zones of 5 µm root radius notches (b)

Stable cyclic plastic zones developed only at the root of notches with $\rho/d<0.2$ that means only for all the 5 µm root radius scribes and for 185 µm and 150 µm deep, 25 µm root radius notches. All the cyclic plastic zones calculated under cyclic tensile loading were showed in Fig. 5.21 a). Taking advantage from the model symmetry only half of the plastic zone boundaries was drawn. According to the behaviour observed for the monotonic plastic zones, cyclic plastic zone enlarged as the notch depth increased. Cyclic plastic zone of equally deep notches with 5 µm 25 µm root radii showed nearly the same area but different shapes (Fig. 5.21 a)). The 25 µm root radius scribes

developed at their roots stable cyclic plastic zones with a semi-elliptical thumbnail shape. 5 μm root radius notches showed thumbnail cyclic plastic zones just for depths $d \leq 100$ μm whereas in scribes deeper than 100 μm plastic deformations preferentially took place along the direction forming an angle of 66° with the notch bisector. The anisotropy of cyclic plastic deformation behaviour gave rise to a progressive stretch of plastic zones along that preferential direction, according to the notch depth. As the notch depth increased from 100 μm to 185 μm cyclic plastic zone gradually assumed a bean-like lobed shape (Fig. 5.21 a)). Like for the monotonic plastic zones at the scribe roots, also the shape of stabilised cyclic plastic zones was exclusively regulated by the notch aspect ratio. Notches with the same aspect ratio showed cyclic plastic zones with the same shape. For $0.03 \leq \rho/d < 0.05$ the cyclic plastic zone at the scribe root assumed a bean-like lobed shape whereas for $0.05 \leq \rho/d \leq 0.20$ the plastic zone shape was semi-elliptical (Fig. 5.21 a)).

Fig. 5.21 b) shows the comparison between cyclic and monotonic plastic zone developed at the root of 5 μm root radius notches with depths ranging from 50 μm to 185 μm. Due to the local loading conditions close to a strain controlled cycle with an high mean strain developed at the notch root (see Fig. 5.18 a)) stabilised cyclic plastic zones were much smaller than the corresponding monotonic ones (Fig. 5.21 b)). Cyclic plastic zones at the notch roots are always contained into the monotonic ones produced at the first loading reversal and they represent the portion of the monotonic plastic zones were stable plastic deformations occur at every loading cycle. The size and shape of the cyclic plastic zones are therefore determined by the plastic deformation history and consequent residual stresses developed inside the monotonic plastic zone. Despite the large difference in size monotonic and cyclic plastic zones seemed to be diverse stages of evolution of the same plastic zone. They appeared to follow the same shape evolution from semi-elliptical thumbnail shapes to lobed fish tale-like ones passing though the intermediate lobed bean-like shape (Fig. 5.21 b)). Monotonic plastic zones similar to the corresponding cyclic ones could be obtained from static finite element analyses by appropriately increasing the material yield strength.

Fig. 5.22 a) and b) show respectively the length of the stabilised plastic zone along the notch bisector, l_{pz}, and the cyclic plastic zone area, A_{pz}, normalised with respect to ρ and the ρ^2 for tension and bending samples. The normalised cyclic plastic zone lengths and areas were plotted against the notch aspect ratio only for the samples which developed a stable cyclic plastic zone at their notch roots under cyclic loadings. When normalised by parameters relating to the notch size, like ρ and the ρ^2, cyclic plastic zone lengths and areas of different scribes were correlated by the notch aspect ratio on a single trend curve for tension and bending samples (Fig. 5.22 a) and b)). Notches with the same shape, that is ρ/d, showed cyclic plastic zones with dimensions proportional to the notch size, defined by ρ. Their plastic zone areas were therefore proportional to the squared of the notch root radius. Such behaviour was consistence with the presence of a mechanical similitude between the local stress and strain fields in the neighbourhood of scribes even under fatigue loads. Normalised l_{pz} and A_{pz} in tension and bending scribed samples seemed to be power functions of the notch aspect ratio as data followed almost a linear trend in bi-logarithmic plots. Normalised lengths and areas of cyclic plastic zones showed nearly the same trend in both tension and bending samples (Fig. 5.22 a) and b)). In opposition to the behaviour observed for monotonic plastic zone, where the

differences between tension and bending values were small, tension cyclic plastic zone lengths were between 1.33 and 2.34 times larger than the corresponding bending ones. On the other side, A_{pz} were between 1.98 and 2.79 times bigger under cyclic tension than under cyclic bending (Fig. 5.22 a) and b)). The larger differences between tension and bending stabilised plastic zone size in comparison with those of monotonic ones were caused by the different residual stresses developed inside the monotonic plastic zone during tensile and bending cyclic loadings.

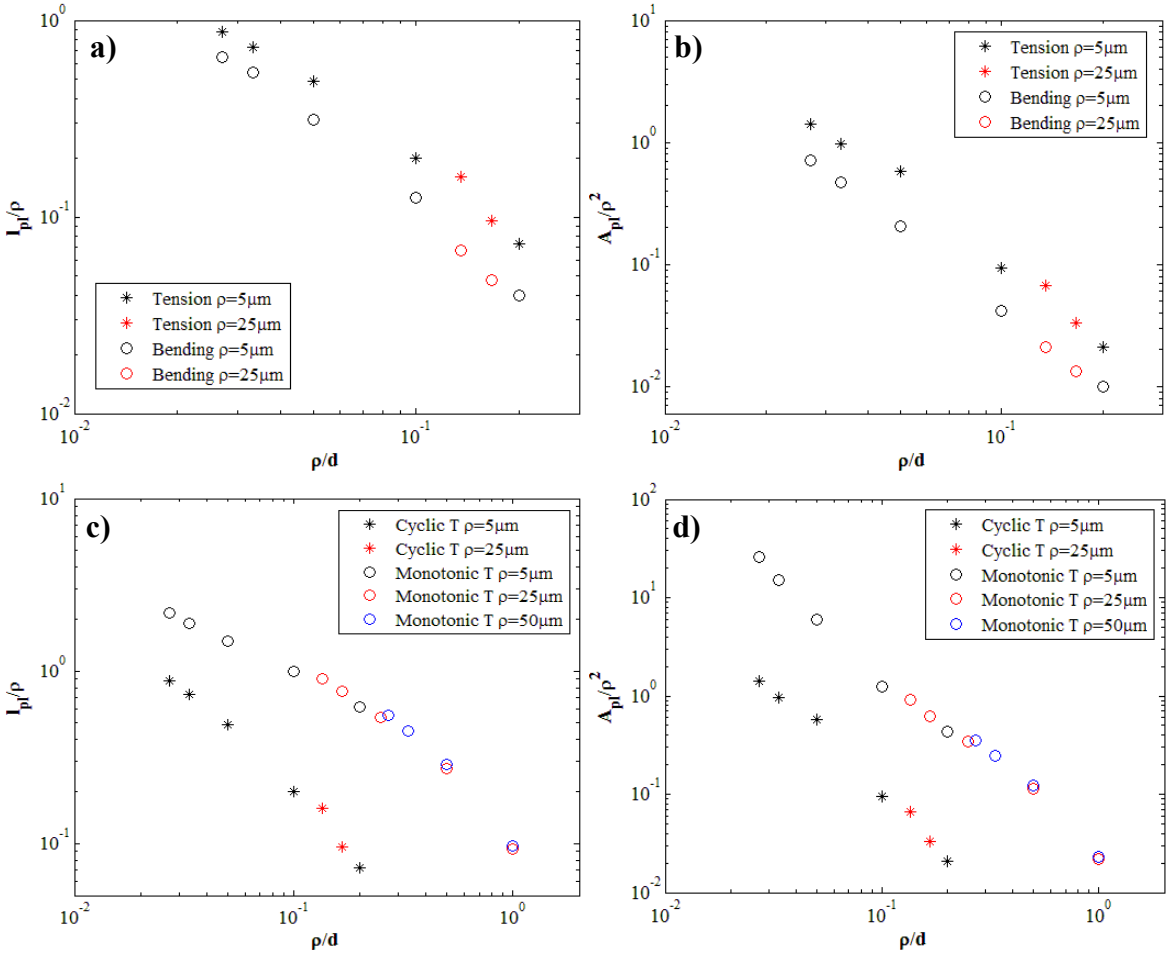

Fig. 5.22: Stabilised cyclic plastic zone length along the notch bisector normalised by ρ (a) and cyclic plastic zone area normalised by ρ^2 (b) of different scribes under tensile and bending load. Comparison between monotonic and cyclic normalised plastic zone lengths (c) and normalised plastic zone areas (d) in scribed tension samples

Fig. 5.22 c) and d) show the comparison between monotonic and cyclic normalised plastic zone lengths measured along the notch bisector and areas in notched tension samples. Monotonic plastic zone lengths were between 2.49 and 8.49 times larger than those of the stabilised cyclic plastic zones developed at the same notch root (Fig. 5.22 c)). Whereas the cyclic plastic zone areas were 18.41-20.34 times smaller than the corresponding monotonic ones (Fig. 5.22 d)). Monotonic and cyclic A_{pz} values followed linear trends with the same slope whereas the trends of plastic zone lengths calculated in monotonic and cyclic analyses seemed to differ (Fig. 5.22 c) and d)).

Due to the condition of local mechanic similitude the shape of the stabilised plastic zone developed at the scribe root was uniquely defined by the scribe shape described by ρ/d. That was proved by the correlation of normalised cyclic plastic zone lengths and areas of different scribes by means of the notch aspect ratio. Like in case of monotonic elastic-plastic analysis, notches with the same ρ/d but different size will show similar cyclic plastic zones, that is plastic zones with the same shape and dimensions proportion to the notch size. Obviously that holds true only for samples weakened by scribes sharper than ρ/d=0.2 where continuous plastic deformations occurred at the notch root in every fatigue cycle.

5.4.1.3 Cyclic stress distribution on the crack path

Cyclic elastic-plastic stress and strain distributions along the bisector of different notches were investigated to rationalise the effect of the cyclic plastic deformation history at the notch root and of the consequent residual stress and strain fields on the nucleation and early propagation of fatigue cracks from scribes. In fact, although the cyclic stress and strain distributions will be altered by the presence of a propagating crack, its driving force will be related to the local cyclic stress and strain fields produced by the notch. According to the assumptions of several notch fatigue life prediction methods (see chapter 2), the distributions of the cyclic maximum principal stress and strain along the plane of future crack propagation were chosen to describe the local mechanical conditions in proximity of the notch root under cyclic loadings. As cyclic elastic-plastic distributions along the notch bisector showed similar properties under tensile and bending fatigue loads, only cyclic tension stress and strain distributions are described in this section.

Fig. 5.23 a) shows the comparison between monotonic and cyclic elastic-plastic longitudinal stress distributions along the bisector of selected notches in unclad tension samples. Monotonic stresses, σ_{22}, and cyclic stress ranges $\Delta\sigma_{22}$ were normalised with respect to their respective nominal values, σ_{nom} and $\Delta\sigma_{nom}$, and plotted against the distance from the notch root, x normalised by the samples thickness t. Three notches showing three different cyclic responses were compared in Fig. 5.23 a): the 185 µm deep 5 µm root radius notch, which produced at its root a stabilised cyclic plastic zone; the 100 µm deep 50 µm root radius scribe, which showed an elastic stabilised cyclic response forming only a monotonic plastic zone and the 25 µm deep 50 µm root radius notch whose mechanical response remained elastic without any plastic deformation. Due to the purely elastic nature of its mechanical behaviour the 25 µm deep 50 µm root radius notch showed identical normalised monotonic and cyclic stress distributions (Fig. 5.23 a)).

Cyclic $\Delta\sigma_{22}$ stress ranges of notches, that developed a stable cyclic plastic zone, had trend similar to that of monotonic σ_{22} stresses. Both normalised cyclic and monotonic stresses of the 185 µm deep 5 µm root radius notch increased, moving away from the notch root, reaching their maximum values close to the boundary of the respective plastic zone (Fig. 5.23 a)). Outside the cyclic and monotonic plastic zone normalised stresses, become elastic, decreased approaching one in far field region. In proximity of the notch root, cyclic normalised $\Delta\sigma_{22}$ were nearly 2.3 times higher than the monotonic σ_{22} inside the respective plastic zones. A sharp variation of the stress gradient was

observed in the normalised $\Delta\sigma_{22}$ distribution at the cyclic plastic zone boundary (Fig. 5.23 a)). In correspondence with the monotonic plastic zone boundary the 185 μm deep 5 μm root radius notch cyclic distribution assumed nearly the same values as the monotonic one (Fig. 5.23 a)). However due to the larger amount of elastic-plastic stress redistribution caused by the bigger plastic zone, the pure elastic part of the σ_{22} monotonic curve was slightly above the cyclic one approaching the far field stress with a gentler gradient.

The cyclic $\Delta\sigma_{22}$ curve along the bisector of the 100 μm deep 50 μm root radius notch, which showed an elastic stabilised cyclic response assumed the classical sigmoid shape peculiar of elastic distributions (Fig. 5.23 a)). Also in this case the cyclic distribution reached higher normalises stresses close to the notch root than the monotonic one. Cyclic stresses were almost twice the monotonic ones. The σ_{22} curve showed the classical trend of elastic-plastic monotonic distributions increasing from the notch root to its maximum value near the monotonic plastic zone boundary to then decreased approaching the far field stress (Fig. 5.23 a)). As in case of a stabilised plastic cyclic response at the notch root, also for the 100 μm deep 50 μm root radius notch outside the monotonic plastic zone the normalised σ_{22} stresses were slightly higher than the cyclic $\Delta\sigma_{22}$ stress ranges (Fig. 5.23 a)). Such behaviour was caused by the higher elastic-plastic redistribution of the monotonic longitudinal stress.

Fig. 5.23 b) shows the comparison between the cyclic and monotonic elastic-plastic longitudinal strain distributions along the bisector of the same three selected scribes. Cyclic strain ranges and monotonic strains, normalised by their respective nominal values, $\Delta\varepsilon_{nom}$ and ε_{nom}, were plotted against the non dimensional distance from the notch root, x/t, in Fig. 5.23 b). Cyclic and monotonic strain distributions along the notch bisector showed similar sigmoid trends reaching their maxima at the scribe root and progressively decreasing to a common uniform value far from the notch (Fig. 5.23 b)). The cyclic and monotonic normalised strain curves of 25 μm deep 50 μm root radius notch coincided as no plastic deformations occurred at its root under both monotonic and cyclic tensile loadings.

As soon as the material yielded at the notch root, monotonic normalised ε_{22} were higher than the cyclic normalised $\Delta\varepsilon_{22}$ in proximity of the same notch. The differences between normalised ε_{22} and $\Delta\varepsilon_{22}$ were larger for notched samples showing a stable elastic-plastic cyclic response than for those having a purely elastic cyclic behaviour (Fig. 5.23 b)). The monotonic maximum strain at the root of the 185 μm deep, 5 μm root radius notch was 2.1 times higher than maximum $\Delta\varepsilon_{22}$ value, whereas the ratio between monotonic and cyclic maximum strains was only 1.3 for the 100 μm deep, 50 μm root radius scribe. The occurrence of plastic deformations at the notch root under fatigue loadings before the reaching of the stabilised cyclic mechanical response caused an increase of the cyclic stress and a decrease of the cyclic strain in proximity of the notch compared to the monotonic values (Fig. 5.23 a) and b)).

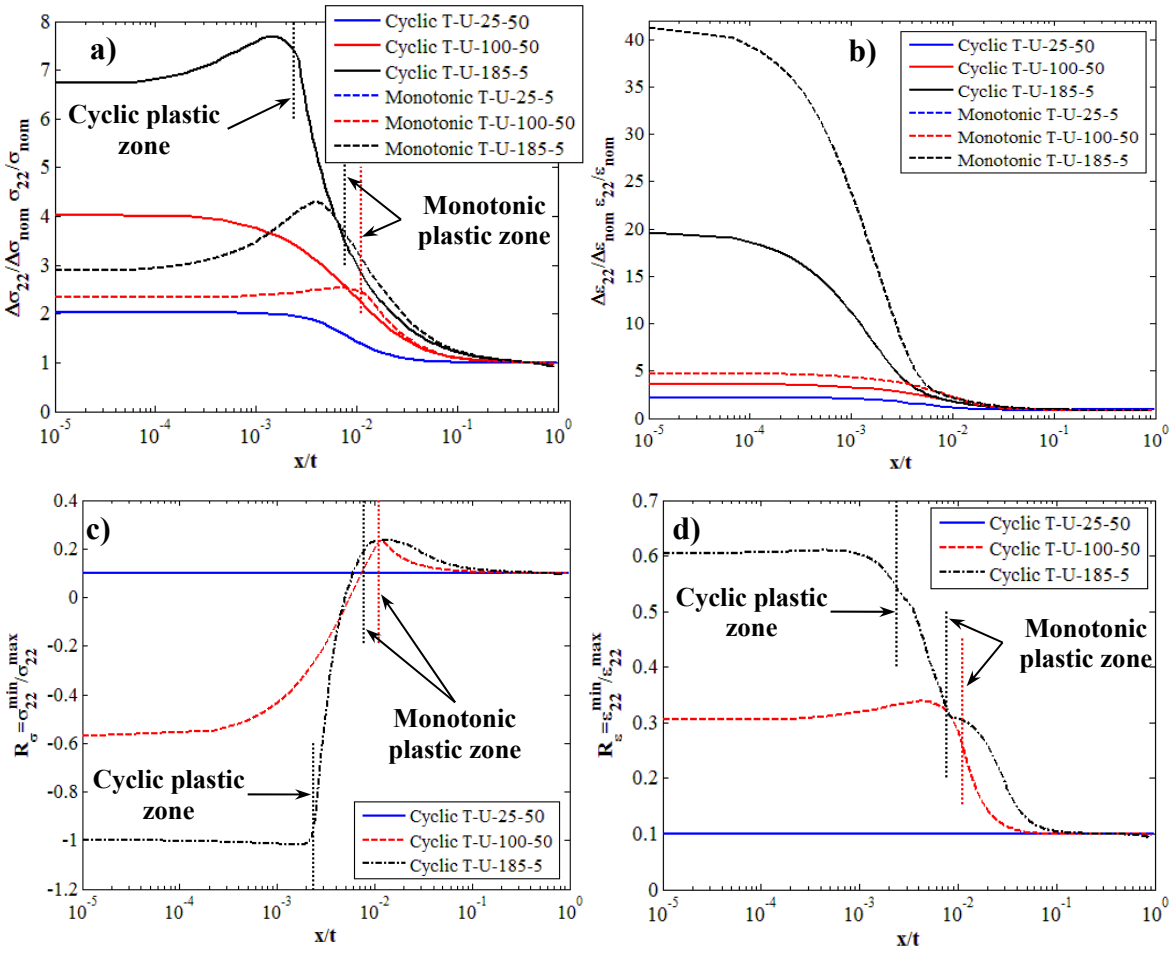

Fig. 5.23: Comparison between cyclic and monotonic longitudinal stresses (a) and strains (b) along the bisector of selected notches normalised by their nominal values and plotted against the non dimensional distance from the notch root *x/t*. Local cyclic longitudinal stress (c) and strain (d) ratios along the bisector of selected notches as function of *x/t*

Fig. 5.23 c) and d) show the local cyclic longitudinal stress and strain ratio along the bisector of the same three notches in tension samples as a function of the distance from the notch root normalised by t. Stress and strain ratios, R_σ and R_ε, were defined as the ratios between the local minimum and maximum σ_{22} and ε_{22} values assumed during the loading cycle after the material response stabilisation. Due to its purely elastic behaviour the 25 µm deep 50 µm root radius notch showed R_σ and R_ε equal to the nominal cyclic load ratio R=0.1 at any distance from the notch root (Fig. 5.23 c) and d)).

For notches showing a stabilised elastic-plastic cyclic response, like the 185 µm deep 5 µm root radius scribe, a uniform stress ratio of R_σ=-1 was reached inside the cyclic plastic zone (Fig. 5.23 c)). Such behaviour was consistent with the mean stress relaxation effect produced by the nearly local cyclic strain controlled conditions developed inside the cyclic stabilised plastic zone. Outside the cyclic plastic zone the stress ratio steeply increased along the bisector of the 185 µm deep 5 µm root radius notch reaching a maximum value of R_σ=0.23 just beyond the monotonic plastic zone boundary (Fig. 5.23 c)). Outside the monotonic plastic zone, where no plastic deformations occurred under cyclic loading, R_σ gradually decreased approaching the

nominal value of the cyclic load ratio R=0.1 (Fig. 5.23 c)). The variations of the stress ratio from the nominal condition of R=0.1 outside the cyclic plastic zone were caused by the residual stresses generated by previous the plastic deformations. Therefore the R_σ curve provided information on the residual stress distribution along the notch bisector. The region between the cyclic and the monotonic plastic zone boundaries, where the material behaved elastically after the cyclic response stabilisation was mainly affected by compressive plastic-induced residual stresses, reducing the cycle mean stress. In opposition the tensile plastic-induced residual stresses, indicating by a stress ratio R_σ>0.1 developed during fatigue loading outside the monotonic plastic zone (Fig. 5.23 c)).

For the 100 μm deep, 50 μm root radius, scribe, which showed a stabilised elastic cyclic response, a stress ratio R_σ=-0.57 was reached at the notch root (Fig. 5.23 c)). The stress ratio distribution gradually increased, moving away from the notch root to assume the maximum value of R_σ=0.23 at the boundary of the monotonic plastic zone. The stress ratio distribution reached the same maximum value as that of the 185 μm deep, 5 μm root radius, notch, however due to the lack of a cyclic plastic zone, it showed gentler gradients inside the monotonic plastic zone (Fig. 5.23 c)). Outside the monotonic plastic zone the stress ratio curve along the bisector of the 100 μm deep, 50 μm root radius scribe, changed rapidly its slope approaching the value of the cyclic load ratio R=0.1 far from the notch root. The far field value of R_σ=0.1 was reached at smaller x/t normalised distance than for the notches developing a stabilised cyclic plastic zone at their roots (Fig. 5.23 c)). After the material cyclic response stabilisation, the monotonic plastic zone of scribes, showing a cyclic elastic behaviour like the 100 μm deep, 50 μm root radius, notch was subjected to compressive plastic-induced residual stresses while the elastic surrounding material was affected by tensile residual stresses.

The three different types of scribes showed longitudinal strain ratios $R_\varepsilon \geq 0.1$ at every normalised distance x/t from the notch root (Fig. 5.23 d)). Such behaviour was consistent with the occurrence of plastic deformations in proximity of the notch root during the first loading cyclic reversal (see Fig. 5.18). Obviously no material yielding took place at the root of the 25 μm deep 50 μm root radius notch and its strain ratio distribution was constantly equal to 0.1. Strain ratios along the bisector of the 185 μm deep, 5 μm root radius, notch were higher than those of the 100 μm deep, 50 μm root radius, scribe (Fig. 5.23 d)). R_ε inside the stabilised cyclic plastic zone at the root of the 185 μm deep, 5 μm root radius, notch were nearly uniform, assuming the value of R_ε=0.6, until they gradually decreased approaching the plastic zone boundary. Outside the cyclic plastic zone, the strain ratio steeply decreased up to the monotonic plastic zone boundary where the distribution slope was suddenly reduced showing a gradient discontinuity. Beyond the monotonic plastic zone the strain ratio kept decreasing up to it reached the nominal R=0.1 far from the notch root. The 100 μm deep, 50 μm root radius, notch, characterised by a cyclic elastic behaviour after the material mechanical response stabilisation, showed a nearly uniform strain ratio around 0.3 inside the monotonic plastic zone (Fig. 5.23 d)). Approaching the boundary of the monotonic plastic zone strain ratio distribution rapidly decreased reaching the far field value of R_ε=0.1. No discontinuity were observed in the distribution gradient crossing the monotonic plastic zone boundary.

References chapter 5

[1] Abaqus analysis user's manual version 6.8. Dassault Systèmes, 2008.

[2] O. C. Zienkiewicz and R. L. Taylor. *The finite element method. Volume 1: the basis*, 5th ed. Boston: Butterworth-Heinemann, 2000.

[3] O. C. Zienkiewicz and R. L. Taylor. *The finite element method. Volume 2: solid and structural mechanics*, 5th ed. Boston: Butterworth-Heinemann, 2000.

[4] I. S. Sokolnikoff. *Mathematical theory of elasticity*, 2nd ed. New York: McGraw-Hill, 1956.

[5] S. P. Timoshenko and J. N. Goodier. *Theory of elasticity*, 3rd ed. Singapore: McGraw-Hill, 1970.

[6] Khan, M. K. *Scribe marks at fuselage joins-Determination of residual stress and effect of fatigue loading using nanoindentation and synchrotron X-ray diffraction*. PhD thesis, Open University, UK, 2009.

[7] Alcoa private communication to Airbus, April 2007.

[8] Jean Lemaitre and Jean-Louis Chaboche. *Mechanics of solid materials*, 1st ed. UK: Cambridge University Press, 1994.

[9] Chaboche, J. L. Time-independent constitutive theories for cyclic plasticity. *International Journal of plasticity*, Vol. 2, 1986, pp. 149-188.

[10] Chaboche, J. L. Constitutive equations for cyclic plasticity and cyclic viscoplasticity. *International Journal of plasticity*, Vol. 5, 1989, pp. 247-302.

[11] ESDU data sheet F.603 Cyclic mechanical properties of aluminium alloys. April 2007.

[12] Khan, S., Vyshnevskyy, J. and Mosler, J. Low cycle lifetime assessment of Al2024 alloy. *International Journal of Fatigue*, Vol. 32, 2010, pp. 1270-1277.

Chapter 6
Discussion of experimental and numerical results

Experimental test data, fractographic observations, and finite element numerical results are discussed in this chapter in an attempt to rationalise the fatigue behaviour of scribed samples and the mechanisms involved in the development of cracks from small mechanical notches. The detrimental effect of scribes on fatigue lives of mechanical components was examined and experimental results were compared with data from other investigations on scratches. Attention was drawn to the correlation between scribe geometry and fatigue life of clad and unclad scribed samples, assessing the local stress and strain raising effect produced by the notch under tensile and bending loading. Differences between the fatigue behaviour of regular diamond tool machined notches and irregular scribes, detected in service on fuselage joints, were analysed as well.

The process of crack development from scribe roots under cyclic loadings was subsequently discussed. The whole damage evolution from the nucleation of cracks to the final instable failure was reconstructed in fatigue samples on the basis of fractographic observations. Particular emphasis was placed on the microstructural scale of the scribe mark problem, which makes the fatigue behaviour of samples containing tens of microns deep scribes substantially different from that of conventional notched components, weakened by notches the size of several millimetres. How the local stress and strain fields at the scribe root affected crack nucleation, regulating the number of nucleation sites and consequently the fracture front shape, it was subsequently discussed. Short crack propagation was divided into the early crack propagation stage, where the crack growth mechanism was strongly influenced by the material microstructure and by the notch stress raising effect, and the stage II growth, where striations were observed. The scribe geometry effect on the crack diving force and the possible coalescence of multiple cracks in the early stage of propagation were investigated and striation counting results discussed. A fatigue initiation life was defined considering the fatigue cycles spent by the main crack to nucleate and fully develop the stage II propagation characterised by striations. Initiation life was, therefore, calculated subtracting from the total fatigue life up to the sample failure, the life obtained integrating the experimental growth rates.

6.1 Fatigue life of scratched components

The detrimental effect of superficial damages, like scribes, on the fatigue life of 2024-T351 aluminium components is discussed in the following section, analysing the experimental fatigue test results described in chapter 4. How the scribe geometry, cladding and loading condition affected the fatigue performances of scribed samples it was rationalised, relating the local notch stress field to the total life required to completely break fatigue specimens. During the calculation of the local stresses produced by the scribe marks, no residual stresses and plasticity induced by the scribing procedure were considered, assuming therefore the diamond tool notch machining as a pure metal cutting process. Such hypothesis was confirmed by the residual stress

measurements performed by Khan [1] at the Open University. The issue of the influence of machining-induced residual stresses on the fatigue behaviour of scribed components is discussed in detail in section 6.1.5.

6.1.1 Fatigue life comparison with other scratch investigations

In this section fatigue lives of scribed samples, obtained during this PhD fatigue test campaign, were compared to analogous data available in literature on the effect of scratches on aluminium components. Fig. 6.1 shows the total fatigue life, up to the specimen complete failure, of scribed clad tension specimens as function of scribe depth and root radius. Fatigue test results, obtained by Nader [2] during his investigation on the fatigue effect of scratches on 2024-T3 clad aluminium sheets, are shown as well for comparison (Fig. 6.1). Rounded V-shaped scratches, with a constant included angle of 90° and a root radius of 83 μm, were machined by Nader on the sample surface using an high speed steel tool mounted on an end mill [2]. Despite the different scribing tool, Nader was able to obtain scribes with a regular cross section similar to those machined with the aid of diamond tools. Scratches, ranging from 40 μm to 225 μm in depth, were introduced on a single sample surface across the whole gauge length. All the fatigue lives shown in Fig. 6.1 were obtained on clad samples tested under constant amplitude fatigue tensile load at a maximum stress of σ_{max}=200 MPa and a stress ratio R=0.1. To allow the direct comparison of experimental data gathered with samples of two different thicknesses (1 mm thick specimens for Nader's investigation [2] and 2 mm thick for this test campaign), the fatigue lives of scribed samples, $N^{tot}{}_{n}$, were normalised with respect of those of the corresponding unscribed specimens, $N^{tot}{}_{un}$ (Fig. 6.1). In this way it was also possible to characterise and isolate the fatigue life reduction effect caused by the scribe. The unscribed sample total life, $N^{tot}{}_{un}$, was calculated as the average of the unscribed sample fatigue lives plus those of specimens insensitive to scratches (chapter 4). The clad layer boundaries of the two kind of clad samples, 1 mm thick 2024-T3 and 2 mm thick 2024-T351 aluminium specimens, are displayed as well in Fig. 6.1.

2024-T351 aluminium alloy clad and unclad sheets were found to be very sensitive to superficial scratches, as scribes negatively affect the fatigue life of samples under tensile and bending loads (chapter 4) causing up to 97.8% of life reduction (Fig. 6.1). The notch sensitivity increased as the scribe became deeper and sharper. The deeper the notch and the smaller the root radius the shorter the total fatigue life (Fig. 6.1). These findings were consistent with the results of other investigations on the fatigue effect of scratches [2-9], where mechanically machined scratches were observed to remarkably reduce the fatigue performances of aluminium alloys and steels. However components were found to be very sensitive only to regular mechanically machined scribes produced by pure metal cutting [2-9]. In fact, as described in section 6.1.5, when the scribing procedure involves material plastic deformation and consequent induced residual stresses, the material scribe sensitivity drastically drops. 2024-T351 clad samples seemed insensitive to scratches as small as 25 μm deep with root radius equal or bigger than 50 μm, although the sensitive to the other 25 μm deep scribes was very small (Fig. 6.1).

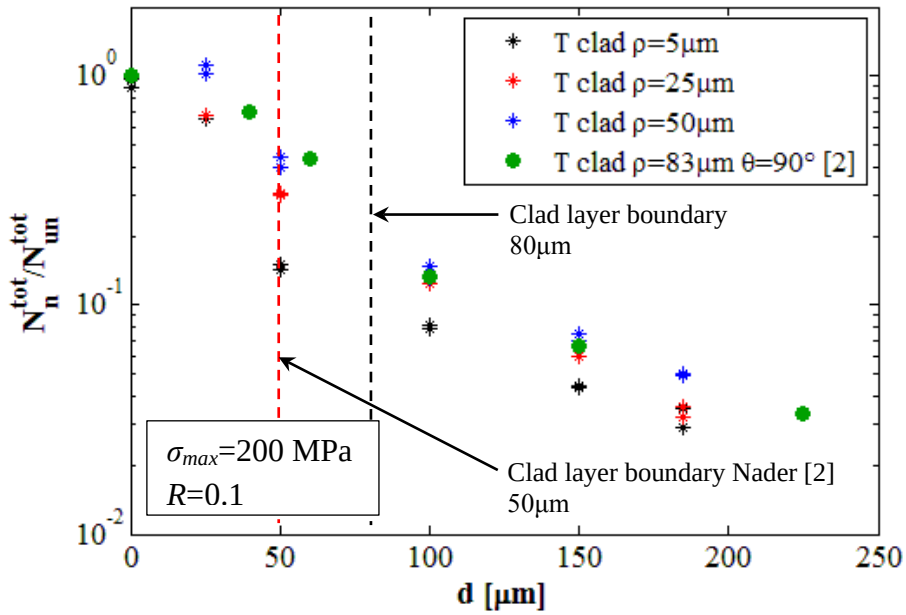

Fig. 6.1: Scribe geometry effect on total fatigue life up to sample complete failure in clad tension specimens

Despite the different material, notch geometry and scribing procedure Nader's experimental results [2] seemed to follow a trend analogous to that of the total fatigue lives of scribed clad tension samples (Fig. 6.1). Actually, although they have different monotonic mechanical properties, 2024-T3 and 2024-T351 aluminium alloys show similar fatigue behaviour both in term of S-N curves and fatigue crack growth rates [10]. That allowed a direct comparison of the scribe effect in these two alloys. As far as the different scribe included angle, θ, is concerned, this is a trivial difference as numerical and analytical investigations on the elastic stress filed in the neighbourhood of rounded V-notches [11-13] proved the effective equivalence of stress and strain of V-notches with $0° \leq \theta \leq 90°$. Such equivalence is likely to be maintained under cyclic plasticity since the similar fatigue behaviour of the 2024-T3 and 2024-T351 aluminium alloys.

The only real difference between Nader's results and those of scribed clad samples thus consists of the scribing procedure. No detailed information was available on the procedure used by Nader [2] to scribe his samples except that he used an high speed steel tool. This kind of tool generally is not able to generate scribes with regular cross section by pure material cutting as the diamond tool, introducing on the sample machining-induced plasticity and residual stresses [14,15]. The two sets of data showed in Fig. 6.1 could therefore not seem comparable, being representative of ideal scribes, obtained cutting the material, and of in-service like scratches, characterised by a large amount of scribing induced plasticity. However, considering the very well-defined cross section, without any sign of material piling up, of the Nader's scribes [2], and the trend of the fatigue test data, it is reasonable to assume the scribes generated by Nader as machined by pure material cutting and thus ideal scribes. In conclusion Fig. 6.1 shows the fatigue lives of aluminium clad samples weakened by ideal superficial scratches, where the only effect of scribes is modifying the local stress field acting as stress raisers.

For scratches shallower than 100 μm Nader's samples showed, according to their larger root radius of 83 μm, normalised total lives longer than those of the clad tension specimens of this investigation (Fig. 6.1). Conversely for scribes as deep as or deeper than 100 μm Nader's results laid between the data of scratches with 25 μm and 50 μm root radii (Fig. 6.1). Such anomalous behaviour could be the result of inaccurate measurements of the scribe root radius or the scribe depth more than being related to a particular fatigue mechanism. In fact no specific procedures were used by Nader [2] to measure the scratch root radius. Cladding seemed not to alter the scribe sensitivity of 2024 aluminium clad samples since, despite different scribe root radii, all the fatigue data in Fig. 6.1 did not change trend in correspondence to the corresponding clad layer boundary. Scratches inside the clad layer had a detrimental effect on fatigue life consistent to that observed for scratches with their root embedded into the substrate for both Nader's and clad tension samples. As described in detailed in the following sections, the explanation of such behaviour could be found in the occurrence of the same crack nucleation and early propagation mechanisms at the notch root in both cladding and substrate (chapter 4). To conclude total fatigue lives of scribed clad samples tested under tensile load were found to be really consistent with those obtained by Nader [2].

Another investigation on the effect of ideal scribes, machined cutting the material rather than ploughing and plastically deforming it, on the fatigue life of 2024-T351 aluminium alloy sheets is the one performed by Morency [16]. The sample geometry, the fatigue test loading and the scribing procedure used by Morency [16] were identical to those adopted in this fatigue investigation. In fact, Morency machined scribes on the surface of clad and unclad fatigue samples using a diamond tipped tool [16]. The scribing procedure produced rounded V-shaped notches along the sample gauge section with an included angle of 60° and a root radius of 5 μm. Clad and unclad dogbone samples containing nominal 50 μm, 100 μm and 200 μm deep scribes were fatigued under constant amplitude tensile loading at a maximum stress of 200 MPa and a stress ratio R=0.1 [16]. Fig. 6.2 shows the comparison between the total fatigue lives of scribed tension samples and Morency's results. All fatigue tests were performed considering as failure criterion the sample complete failure. The total fatigue life was therefore measured up to the complete breaking of the sample. Total fatigue lives of clad and unclad samples, normalised with respect to the corresponding lives of unscribed specimens, $N^{tot}{}_{n}/N^{tot}{}_{un}$ were plotted respectively in Fig. 6.2 a) and b) as function of different scribe geometries. As above the unscribed sample lives were calculated including into the average also the lives of those specimens insensitive to scribes. Runout samples, which had their tests stopped as no failure was observed after a defined number of cycles, were indicated by arrows in Fig. 6.2.

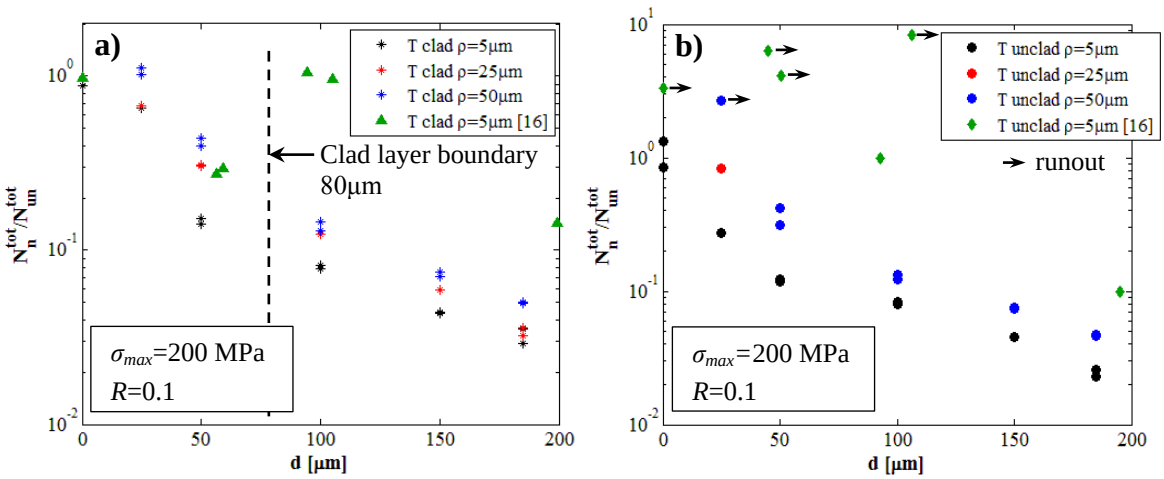

Fig. 6.2: Comparison between fatigue test and Morency's results [16] of clad a) and unclad b) tension samples

Also Morency [16] found that scribes negatively affected the fatigue life of both clad and unclad specimens, up to 90% of reduction in case of 200 μm deep scribed unclad samples. However his experimental data showed trends completely different from those of the clad and unclad samples of this PhD test campaign (Fig. 6.2). As far as clad tension specimens are concerned, only scribes with their roots into the cladding or deeply embedded into the substrate developed cracks leading to sample failure (Fig. 6.2 a)). 100 μm deep scribes, which terminated near the clad layer/substrate interface, did not affect the fatigue life of clad samples as specimens failed because of cracks nucleated from other locations than the scribe root [15]. Even those coupons sensitive to scratches, which failed at the scribe root, showed fatigue lives, longer than the 5 μm root radius scribed samples tested in this campaign (Fig. 6.2 a)). For instance, Morency's clad specimens, weakened by scribes with a nominal depth of 50 μm and a root radius of 5 μm, exhibited fatigue lives comparable to those of the 50 μm deep, 25 μm root radius scribed samples of this investigation (Fig. 6.2 a)). Morency's 200 μm deep scratches showed fatigue lives as long as those of 50 μm deep, 5 μm root radius scribes.

Analogous discrepancies were observed in unclad tension samples where only Morency's scribes deeper than 200 μm were able to nucleate cracks which caused failure (Fig. 6.2 b)). Unclad samples, weakened by shallower scratches, failed from locations remote from the scribe root or they were runout [16]. On the other hand the unclad scribed samples tested in this investigation showed a trend similar to that of clad specimens, increasing the notch sensitivity as the scribe became deeper and sharper (Fig. 6.2 b)). Moreover unclad samples seemed insensitive to scratches as deep as 25 μm with a root radius equal or bigger than 25 μm. Also the unclad specimens proved to be more sensitive to scribes machined during this test campaign than to those produced by Morency, despite the same scribing procedure [16]. In fact the Morency's nominal 200 μm deep scribe reached a total fatigue life slightly shorter than that of 50 μm deep, 5 μm root radius scribed samples (Fig. 6.2 b)). In conclusion, in spite of the same material, sample geometry and preparation and scribing procedure, Morency's results were not consisted with the ones obtained during this PhD.

The reason of such different behaviour has to be ascribed to the diamond tipped tool used by Morency [16]. In fact optical observations of such diamond tool revealed damages on its tip. The damaged diamond tool was not capable of correctly cutting the aluminium surface ploughing a portion of material. The produced scribes were, therefore, characterised by high levels of machining-induced residual stresses and plastic deformations, pointed out by the material piling up at the scratch flanks [16]. Khan [1], investigating the residual stresses and the material conditions around scribes, machined by this damaged tool, found severe tensile residual stress fields and work hardening around their roots in comparison with scribes machined by undamaged diamond tools. The magnitude and the extent of residual stress fields of damaged tool scratches were twice those of undamaged tool scribes [1]. The work hardening in the neighbourhood of the scribes root indicated the occurrence of plastic deformations during the scribing procedure. Due to the diamond tool damage, Morency's scribes were not ideal scribes produced by pure material cutting but like in-service scratches characterised by machining-induced plasticity and residual stresses. That can explain the different fatigue lives between Morency's scribed specimens and those tested in this test campaign. Clad and unclad 2024-T351 aluminium samples have proved to be less sensitive to like in-service scratches than to ideal scribes [17-19]. That can explain the different fatigue lives between Morency's scribed specimens and those tested in this test campaign. The work hardened material around the roots of like in-service scribes is likely to delay the crack nucleation or retard the early propagation of cracks initiated from the scribe root. In fact Morency [16] showed the presence of cracks at the scribe root also for samples where the failure occurred away from the scratch. Machining-induced residual stresses could also retard the crack nucleation and growth but they should be compressive more than tensile stresses [1]. The different behaviour of ideal and like in-service scribes is discussed in detail in section 6.1.5. No fatigue data were available in literature on clad and unclad 2024-T351 aluminium samples, weakened by ideal scribes and tested under bending load. Therefore fatigue tests results of 4 point bending samples were not discussed in this section.

6.1.2 Finite element stress analysis validation

The scribe mark effect on the total fatigue life of aluminium components as well as on crack nucleation and propagation will be analysed on the basis of the local stress and strain fields at the scribe root. Moreover, according to conventional prediction methodologies (see section 2.3.1), fatigue lives of notched components are estimated considering the elastic stress field in the notch neighbourhood. A validation of finite element stress results, is thus required to assess the accuracy of the calculated stress fields in different scribed samples. The finite element analysis validation was performed comparing the numerical results of this investigation to stress analyses of rounded V-notch found in literature. Due to difficulties in finding literature works about monotonic and cyclic elastic-plastic stress analyses of V-notches, using the same constitutive equations as the finite element models described in chapter 5, only the elastic stress analyses were validated.

The elastic stress concentration factors, calculated by finite element analyses for scribes under tensile load were compared with the analytical K_t values proposed by Nowell et al. [13]. They used a boundary element method, based on the discrete

dislocation density approach, to calculate the elastic stress distribution ahead of an arbitrary rounded V-notch in a semi-infinite plate under tensile load [13]. V-notches were defined by their depth, d, root radius, ρ, and included angle, θ [13]. Consistently with the results described in section 5.2.1.1, Nowell et al. [13] found that the elastic K_t of rounded V-notches could be characterised just by the notch aspect ratio, ρ/d, and included angle θ. Table 6.1 shows the comparison between finite element and Nowell's stress concentration factors calculated under tensile load for selected rounded V-notches with an included angle of θ=60° and different aspect ratios. Only the scribe geometries, which Nowell's analytical K_t values were available for [13], were listed in Table 6.1. Percentage errors, e, between the stress concentration factors obtained from finite element analyses and those calculated by Nowell et al. [13] were listed in the last column of Table 6.1.

Table 6.1: Finite element stress concentration factor validation against Nowell et al. [13] results

Notch	ρ/d	θ [deg]	K_t		e [%]
			FEM	Nowell [13]	
T-100-5	0.050	60°	11.272	10.569	6.65
T-50-5	0.100	60°	8.066	7.979	1.09
T-25-5	0.200	60°	5.885	5.875	0.17
T-50-25	0.500	60°	4.017	3.987	0.75
T-100-50	0.500	60°	4.082	3.987	2.38
T-25-25	1.000	60°	3.070	3.058	0.39
T-50-50	1.000	60°	3.085	3.058	0.88

Finite element elastic K_t computed at the root of different scribes showed a good correlation with the analytical values calculated by Nowell et al. [13] (Table 6.1). Except for a maximum difference of 6.65%, obtained for the sharpest notch (T-100-5), all the other finite element results showed errors from the corresponding Nowell's analytical K_t solutions smaller than 3% (Table 6.1). The maximum result discrepancy, showed by the 100 μm deep, 5 μm root radius notch, could be ascribed to the effect of the scribed sample finite thickness. In fact, as Nowell's analytical elastic stress sulutions were calculated for semi-infinite plates [13], they did not take into account the influence of the sample finite thickness. If scribes were shallower than 50 μm, the sample finite thickness effect on stress concentration factors was negligible and numerical and analytical results showed excellent agreements with e<1.1% (Table 6.1). In case of 100 μm deep scribes the sample finite thickness produced a rise of the finite element stress concentration factors compared to the analytical ones and a consequent increase of the percentage differences. The maximum percentage errors, e, were, in fact, obtained for scribes as deep as 100 μm (Table 6.1). The sharper the notch the higher the effect of the sample finite thickness and the larger the discrepancy between finite element and Nowell's stress concentration factors. The higher stress raising effect of sharp notches enhances the difference between the nominal net stress acting on the net ligament of a finite sample and that of a semi-infinite plate, increasing the value of the percentage error (Table 6.1). Evidences of the sample finite thickness effect on K_t values can be found analysing scribes with the same aspect ratio but differ size. While for a given ρ/d Nowell's stress concentration factor was independent of the notch size, finite element

results, which considered the sample finite thickness influence, showed slightly higher K_t values for larger scribes (Table 6.1). That caused, in case of equally sharp scribes, an increase of the percentage error according to the notch size (Table 6.1). To conclude, apart from the sample finite thickness effect, correctly characterised by the finite element elastic stress analyses, the stress concentration factors computed in this investigation were consistent with the analytical ones calculated by Nowell et al. [13]. Due to the lack of analytical expressions, stress concentration factors of scribes under bending load were not validated in this section.

Finite element elastic stress distributions of scribed samples were additionally compared with the analytical stress solutions developed by Filippi et al. [12]. Approximate analytical expressions of elastic stress distributions in the root neighbourhood of rounded V-shaped notches were obtained by Filippi et al. [12], using the Muskhelishvili method [20] based on complex potential functions. Filippi et al. improved the accuracy of previous analytical stress expressions, suggested by Lazzarin and Tovo [11], introducing an additional term inside the complex potential stress functions [12]. The developed stress solutions were valid only for rounded V-notches with infinite depth in infinite plates under general mode I and mode II loading conditions. However they proved to accurately predict stress distributions near the notch root also in case of finite width plates under tensile load [12].

Finite element elastic stress fields of scribed samples were validated, comparing the maximum principal stress, that is the longitudinal stress $\sigma_{22,}$ distributions along different notch bisectors with the corresponding analytical stresses developed by Filippi et al. [12]. The analytical longitudinal stress distribution along the bisector of a generic rounded V-notch under mode I loading conditions was expressed as follows [12]:

$$\sigma_{22} = \frac{\sigma_{22}^{\max}}{4(q-1)+q\omega_1}\left[4(q-1)\left(\frac{q}{q-1}\frac{x}{\rho}+1\right)^{\lambda_1-1} + q\omega_1\left(\frac{q}{q-1}\frac{x}{\rho}+1\right)^{\mu_1-1}\right] \qquad (6.1)$$

where σ_{22}^{max} is the maximum longitudinal stress reached at the notch root, and x/ρ is the distance from the notch root, measured along the scribe bisector, normalised with respect to the root radius. The factors q, ω_1 as well as the exponent λ_1 and μ_1 depend only on the notch included angle θ [12]. The subscript 1 of the parameters in eq. (6.1) indicates that such factors are related to mode I loadings. Values of the analytical parameters, specialised for notches with an open angle of θ=60°, are listed in Table 6.2.

Table 6.2: Characteristic parameters defining the longitudinal stress component along the bisector of rounded V-notch with θ=60° under mode I loads [12]

θ [deg]	q	λ_1	μ_1	ω_1
60°	1.6667	0.5122	-0.4057	1.5519

The shape of the stress distribution in eq. (6.1), relating the σ_{22} values to the corresponding non-dimensional coordinate x/ρ, is therefore univocally defined by the notch included angle and σ_{22}^{max}, that is the stress concentration factor. For a fixed value of the included angle, analytical σ_{22} distributions of different rounded V-notches differ

only for the multiplicative factor, represented by σ_{22}^{max}, if plotted against the non-dimensional distance from the notch root, x/ρ (see eq. (6.1)). Therefore, when specialised for scribe marks showing the same open angle of 60°, analytical distributions are regulated only by the maximum stress value at the notch root, and by the root radius. Normalising the longitudinal stress with respect to its maximum value (σ_{22}^{max}), a unique analytical relation, linking the normalised stress to the non-dimension distance from the notch root x/ρ, can be obtained for a given value of θ. For that reason it was convenient to compare analytical and numerical stress distributions of different notches, plotting the σ_{22} stresses normalised by the corresponding maximum values against the distance from the root normalised with respect to the root radius values. Doing so analytical stress distributions of different notches with the same open angle are represented by a unique curve, described by eq. (6.1).

Fig. 6.3 shows the graphical comparison between analytical and numerical stress distributions along the bisector of different notches under pure tension load. Only the numerical distributions of 9 selected notch configurations, obtained, combining three different depths (25 μm, 100 μm and 185 μm) with the three root radius values (5 μm, 25 μm and 50 μm) were plotted in Fig. 6.3. Longitudinal stress distributions, normalised with respect to their corresponding maximum values were plotted against the non-dimensional distance from the notch root x/ρ. Numerical stress distributions of different notches were almost coincident to the analytical non-dimensional stress solution developed by Filippi et al. [12] in proximity of the notch root (Fig. 6.3). As soon as the numerical distributions went out from the respective notch stress concentration regions, approaching different net stress values, they progressively diverged from the trend predicted by eq. (6.1). In fact at sufficient distance from the notch root, that is for large value of the non-dimensional coordinate x/ρ, eq. (6.1) tends to zero, while numerical distributions settle down to constant values close to the corresponding nominal net stresses.

This divergence is a consequence of the fact that Filippi's analytical stress solutions were calculated for semi-infinite notches in infinite plates [12]. Such particular geometry allows to accurately characterise the notch stress field using only the first terms of the asymptotic solution expansion series [12]. As just the first terms of the asymptotic solution expansion series were considered, eq. (6.1) results valid only in the highly stressed area near the root where those terms are dominant. The length of the overlapping area between analytical and numerical σ_{22} distributions varied according to the notch geometry (Fig. 6.3). The deeper the notch and the smaller the root radius the larger the normalised distance from the notch root (x/ρ) at which analytical stresses started to diverge from numerical results (Fig. 6.3). The largest overlapping region was obtained for 185 μm deep 5 μm root radius notches. Numerical elastic maximum principal stress distributions along the bisector of different scribes showed and excellent agreement with the analytical stress solution developed by Filippi et al. [12], confirming the accuracy of the finite element analyses described in chapter 5. Moreover also the finite element σ_{22} elastic stress contours in the neighbourhood of different scribe roots were consistent with those calculated by Nowell et al. [13] using the discrete dislocation density method.

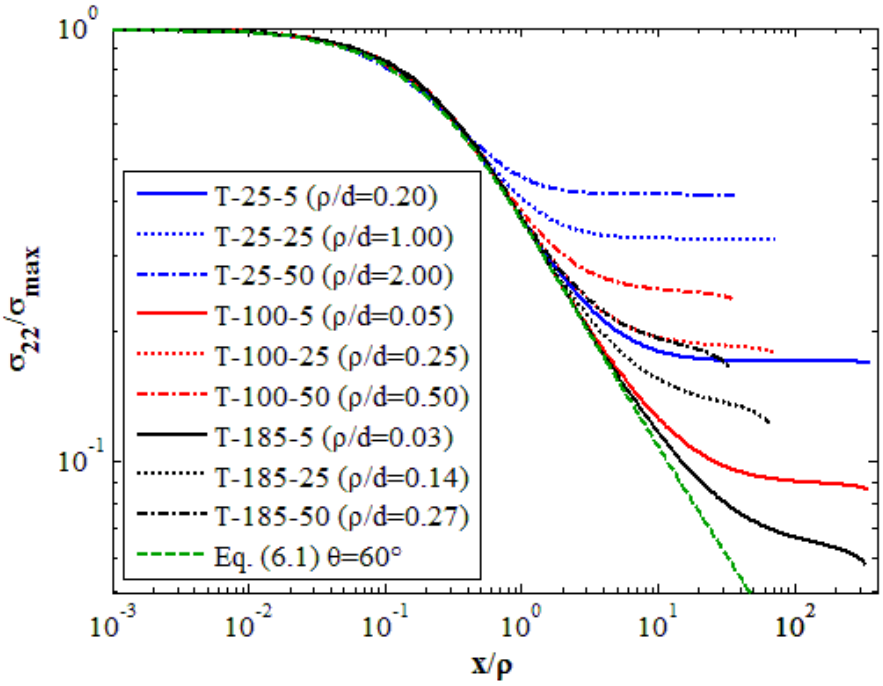

Fig. 6.3: Comparison of the finite element non-dimensional σ_{22} distributions on the bisector of different V-notches under tensile load with analytical results of Filippi et al. [12]

6.1.3 Scribe geometry effect on total fatigue life

The fatigue life reduction, caused by the introduction of superficial mechanically machined scribes in 2024-T351 aluminium alloy sheets, is discussed in this section. As scribes were machined by material cutting, minimising the amount of machining-induced plasticity and residual stresses, only the effect of the notch geometry could be investigated by the fatigue test result analysis. How the notch depth and root radius affected the fatigue performances of scribed samples it was discussed, correlating the local stress and strain fields at the scribe root with the measured total fatigue lives. Moreover traditional and recently developed notch fatigue life prediction methodologies were applied to the fatigue test results to assess their capability in evaluating the fatigue life of scribed components.

One of the simplest ways to characterise the influence of a notch on the local surrounding stress field and evaluate therefore its sharpness, is to calculate the notch stress concentration factor, K_t. Such non-dimensional parameter describes the stress raising effect of a notch in term of the value reached by the elastic stress at its root [21]. No information is thus available on the local material plastic behaviour and the stress distribution in the neighbourhood of the notch under cyclic loading if K_t is used to characterised its stress raising effect. Fig. 6.4 a) and b) show respectively the experimental total fatigue lives of clad and unclad scribed samples under tensile and bending load as function of the scribe stress concentration factors. All samples were tested under constant amplitude fatigue loading at a maximum stress of σ_{max}=200 MPa and a stress ratio R=0.1. Runout specimens, which did not failed after a selected number of cycles (see chapter 4), are indicated by arrows in Fig. 6.4.

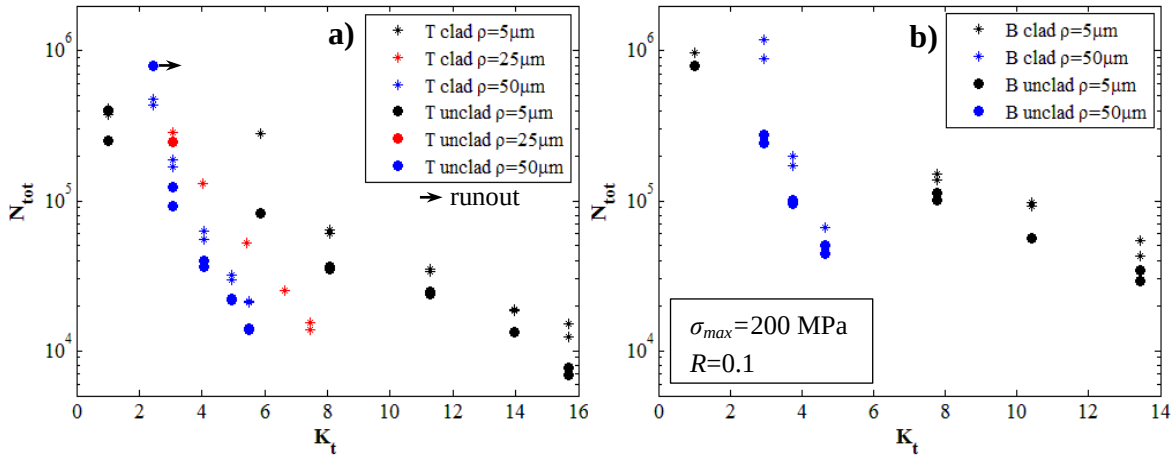

Fig. 6.4: Total fatigue life of tension a) and bending b) scribed samples plotted against notch elastic stress concentration factor

For a given value of the notch root radius, the total fatigue life of scribed tension and bending samples was reduced according to K_t (Fig. 6.4). The higher the stress concentration factor, that is the sharper the notch, the smaller the total fatigue life of scribed samples. Analogous trends were observed for clad and unclad samples, showing that the only effect of cladding was to increase scribed sample fatigue lives (Fig. 6.4). It is worth mentioning that scribes with equal geometry showed the same K_t values in unclad and clad samples, as the elastic properties of pure aluminium and 2024-T351 aluminium alloy coincided (chapter 5). How the clad layer and the loading condition affected the fatigue behaviour of scribed samples it is discussed in the following section. As explained in chapter 5, the elastic stress concentration factor of scribes was mainly regulated just by the notch aspect ratio ρ/d. Therefore for a given root radius, the deeper the notch the smaller its aspect ratio and consequently the higher the elastic K_t. For a fixed value of the scribe root radius, increasing the scribe depth was equivalent to increase the scribe stress concentration factor. In fact fatigue lives of scribes with the same root radius, when potted against K_t (Fig. 6.4), showed similar trends to the data in Fig. 4.1 and Fig. 4.2 where lives are plotted against the scribe depth d. Notches with smaller root radii were characterised by higher stress concentration factors but not by larger fatigue life reductions (Fig. 6.4). Scribes showing the same or very close stress concentration factors, like the 185 μm, 50 μm root radius and the 25 μm, 5 μm root radius scribes under tensile load (Fig. 6.4 a)), exhibited different fatigue lives according to the notch root radius. The larger the root radius the shorter the total fatigue life (Fig. 6.4 a)).

Total fatigue lives of scribed samples showed the same trend when plotted against stress concentration factors, despite different loading conditions and the presence of cladding (Fig. 6.4). Cladding and bending load seemed to shift sample fatigue lives to higher number of cycles compared to the corresponding unclad and tension scribed specimens. In fact if total fatigue lives of scribed samples were normalised with respect to the corresponding lives of unscribed specimens, $N^{tot}{}_n/N^{tot}{}_{un}$, as in Fig. 6.5, all data relevant to scribes with equal root radius in clad, unclad, tension and bending samples appeared to lay on the same curve. The only exception was the 25 μm deep, 5 μm root radius scribe, which showed a different life reduction for clad and unclad samples (Fig.

6.5). Such anomalous behaviour could be caused by the different mechanical properties of the soft pure aluminium clad layer where the scribe was embedded (see section 6.1.4). Also the 25 μm deep, 50 μm root radius scribe showed different fatigue lives in clad and unclad samples since the latter was a runout specimen (Fig. 6.5). However, despite the diverse fatigue lives, the notch effect on the fatigue behaviour was the same since both clad and unclad samples were insensitive to this kind of scribe. The graph of Fig. 6.5 proved that the detrimental effect of scribes on fatigue life of 2024-T351 aluminium alloy samples, regulated by the notch geometry, was independent of the loading condition and the presence of clad layer. In fact scribes with the same geometry caused equal fatigue life reductions in clad and unclad samples and under both tensile and bending loads (Fig. 6.5).

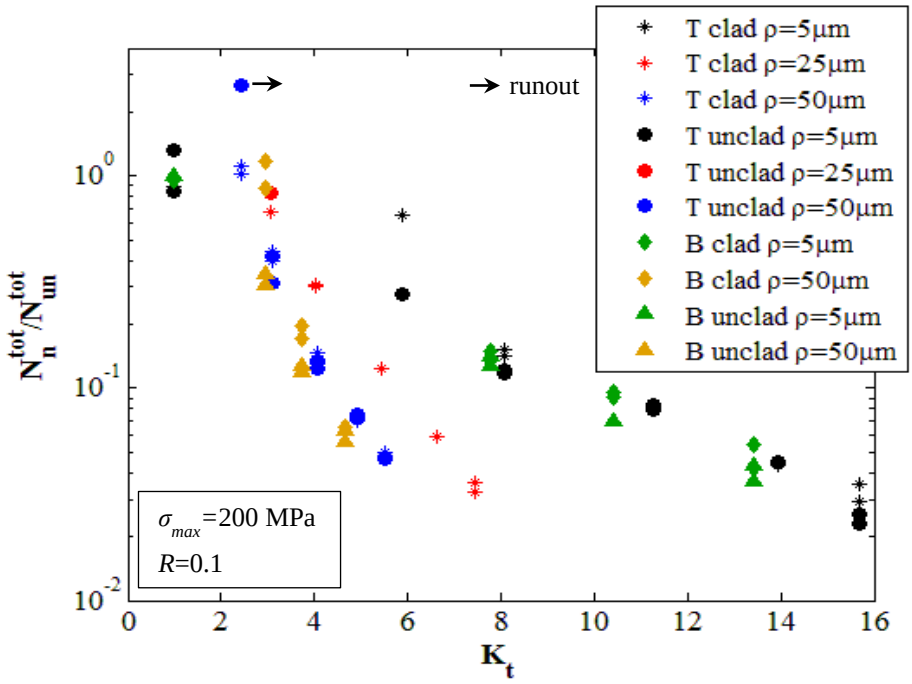

Fig. 6.5: Scribe geometry effect on total fatigue life for different loading and material conditions

Clad and unclad 2024-T351 aluminium alloy samples, fatigued under tensile load, were insensitive to scribes with $K_t \leq 2.43$, as specimens scribed by such notches showed lives comparable to those of unscribed ones (Fig. 6.5). Under bending load the scribe sensitivity threshold was shifted towards slightly sharper notches, since bending samples resulted insensitive to scribes with $K_t \leq 2.96$. In theory any kind of notch should reduce the fatigue life of a structural component. In fact, even if extremely small, a stress concentrator produces an increase of the local stress and strain fields enlarging the strain energy available for crack nucleation compared to that existing in a defect-free pristine component [10,22]. However commercial alloys are not defect-free and they contain several geometrical discontinuities like voids and inclusion particles [23-26]. Such defects act as notches under cyclic loading, raising the local stress and strain fields and promoting the crack nucleation. Unscribed clad and unclad samples were observed to fail under tensile and bending loads as a consequence of cracks nucleated from quite large inclusion clusters, located close to the sample surface (section 4.2.3.1). Those inclusion clusters were likely to affect the fatigue life of 2024-T351 aluminium alloy sheets as the 25 μm deep scribes, which samples were insensitive to. Actually the size

of the crack-nucleating inclusions (23-60 μm) was of the same order of magnitude as the depth of undamaging scribes. Since the fatigue life reduction effect of the inclusion clusters and the undamaging notches was the same, scribed samples showed fatigue lives comparable to those of unscribed specimens. It is worth noticing that a wide variety of scribe geometries ranging from blunt (K_t=2.43) to very sharp notches (K_t=15.70) was analysed during this fatigue test campaign (Fig. 6.5). Due to the wide range of examined notch sharpness, scribed sample fatigue lives covered a large region from medium-cycle to low-cycle fatigue regime (Fig. 6.4).

Graphs in Fig. 6.4 and Fig. 6.5 show that, since the elastic stress concentration factor is not able to correlate fatigue lives of different scribed samples on a unique curve, it cannot be used as single fatigue prediction parameter for scratched components. The inability of the elastic K_t to entirely define the stress raiser effect on fatigue strength was known since the first pioneering investigations on notch fatigue [27,28]. A notch sensitivity factor, q, depending on the stress raiser size [27,28], was in fact introduced to characterise the experimental evidence that notches caused less concentration effect under fatigue load than predicted by elastic analysis, such that $K_f \leq K_t$ (chapter 2). The stress concentration factor is able to define the fatigue strength of notched components only for large blunt notches where the notch sensitivity is fully developed and K_f tends to the value of the theoretical K_t [27,28].

Atzori et al. [29-32] evaluated the notch size effect on the material fatigue strength, bridging the gap between notch sensitivity and defect sensitivity. For a given notch shape, that is for a fixed K_t, they plotted the fatigue limit of notched components against the notch depth, rationalising the influence of the stress raiser size [29]. Notch sensitivity was fully developed, that is $K_f=K_t$, for stress raisers deeper that the critical notch depth a^* [29]. For this kind of notches defined as blunt, elastic stress gradients are so gentle that a volume of material head of the stress raiser, not only the notch root, can be considered subjected to the peak stress. For that reason the peak stress criterion can be applied to characterise the notched component fatigue strength and only K_t can define the notch sensitivity [29]. If a notch was shallower than a^*, the fatigue notch sensitivity decreased and the peak stress criterion had to be replaced by a stress field criterion, like the notch stress intensity factor threshold [33-38]. Notches, included in the stress field criterion regime, behaved as cracks, showing fatigue limits regulated by threshold values of a stress field parameter, the notch stress intensity factor [30]. In that region, the fatigue limit of notched components only depend on the notch size being, like the crack growth threshold stress, an exponential function of the notch depth. Therefore, the critical notch depth a^* divided the sharp notch regime, where the fatigue limit is defined by a stress field criterion, to the blunt notch one, where the notch sensitivity is the largest and a peak stress criterion has to be applied [30]. When the notch size became smaller than the critical length a_0, defined by the Kitagawa-Takahashi diagram [39], mechanical components turned out to be insensitive to notches, showing fatigue limits equal to those of pristine unnotched ones, K_f=1 [29].

Smith and Miller [40], using an analogous approach, developed a diagram where the fatigue limit was plotted against the notch stress concentration factor. The notch depth was maintained constant and the root radius was varied, changing K_t. A critical stress concentration value, K_t^*, was therefore found which divided the blunt and the sharp

notch regimes characterised respectively by the peak stress and the stress field criterion [40]. The purpose of notch sensitivity factor expressions, derived in conventional fatigue notch factor prediction methods, as those suggested by Neuber [27] and Peterson [28], was to describe the dependence of the notched component fatigue limit on the notch size. However the lack of accurate analytical and numerical methods to calculate the stress field in proximity of the notch allowed only approximate and semi-empirical definitions of q.

The aforementioned approaches are generally valid for notched components at the fatigue limit, while scribe mark fatigue tests were performed in the finite life region, in the medium- low-cycle fatigue regime. Therefore a direct comparison between the critical notch size, a^*, [31] or the critical stress concentration value, K_t^*, [40], which divide the blunt to the sharp notch regimes, and scribe marks geometrical properties cannot be carried out. The development of the notch root plasticity and the occurrence of the fatigue crack growth, characterising the finite life region, would, in fact, invalidate the assumptions at the basis of the described approaches. However, the distinction between blunt and sharp notches could be extended to the finite fatigue life region, considering as blunt notches, those stress raisers where the crack initiation life is regulated by the local elastic-plastic peak stress. In case of sharp notches the initiation life will be defined by a stress field criterion, that is by crack propagation [41].

Due to the scribe mark small size, the local notch stress field can be assumed to influence only the crack nucleation and early propagation leaving nearly unaltered the further crack growth. Therefore the scribe marks effect on sample total fatigue lives will be equal to those on initiation lives. Taking in account that, and noticing that the local elastic-plastic stress can be described by the elastic K_t, as both depend on the scribe aspect ratio (see chapter 5), it is possible to define the scribe mark sharpness just analysing the fatigue results in Fig. 6.4 and Fig. 6.5. It is evident that scribe marks can be considered as sharp notches since the stress concentration factor and thus the peak stress criterion were not able to correlate all fatigue lives in Fig. 6.4 and Fig. 6.5. Scribes with the same K_t, that is the same peak stress, showed different lives according to their size in agreement with the sharp notch behaviour.

Due to the lack of experimental data in the fatigue limit region, the accuracy of conventional notch sensitivity prediction methods [27,28] in evaluating the scribe effect on fatigue life cannot be directly assessed using the scribe mark test results. However, owing to the similarity between their behaviour and that of scribed samples (Fig. 6.1), Nader's fatigue test data [2] were used to investigate 2024 aluminium alloy sensitivity to scribes at the fatigue limit regime. Nader [2] tested scratched samples under constant amplitude fatigue loading at different maximum stresses, obtaining the whole S-N curves of scribed components. Fig. 6.6 shows the S-N curves developed by Nader [2] at a constant stress ratio of R=0.1 for notched samples weakened by V-shaped scribes with an included angle of 90° and a root radius of 83 μm. Different S-N curves were obtained according to various scribe depths ranging from 40 μm to 225 μm (Fig. 6.6). 40 μm and 60 μm deep scribes, completely embedded into the clad layer, had their curve indicated in red. The S-N curve of unnotched samples, is also shown in Fig. 6.6 allowing the evaluation of the sample sensitivity to scribes. Fatigue lives, obtained in this investigation for 185 μm deep, 5 root μm radius scribes in clad and unclad samples at

three different maximum stress values, σ_{max}=100 MPa, 160 MPa and 200 MPa (section 4.1.1), are displayed as well for sake of comparison.

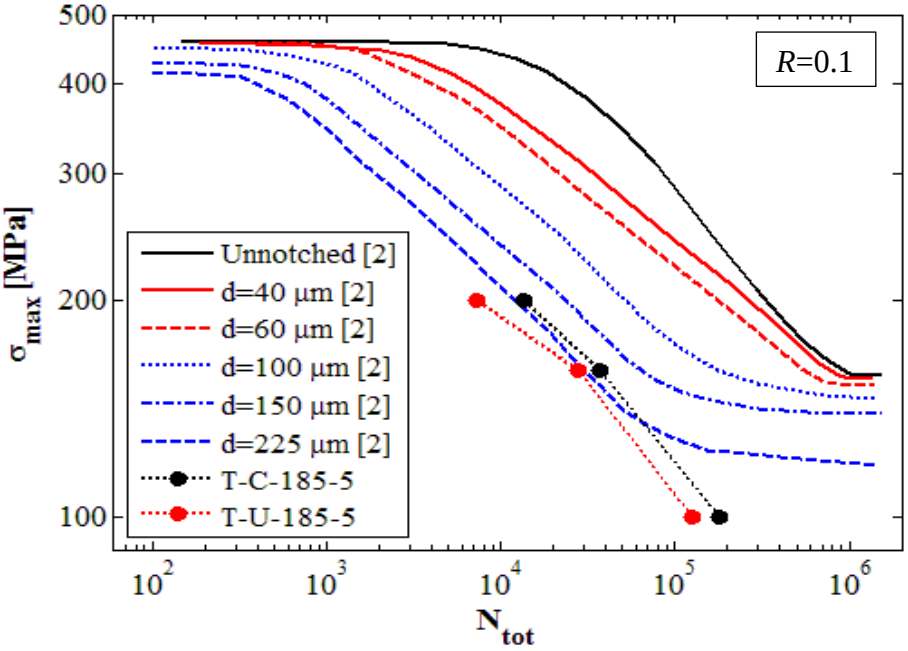

Fig. 6.6: Scribed components S-N curves from Nader [2]

For a given value of the applied maximum stress, the sample fatigue life in the finite life regime was reduced according to the scribe depth (Fig. 6.6). The deeper the scribe, the larger the total fatigue life reduction compared to unnotched specimens. An analogous behaviour could be observed at the endurance limit (Fig. 6.6), defined as the stress corresponding to a total life of 10^6 cycles [2]. The notch sensitivity at the fatigue limit region is discussed below. No information was available on the effect of notch root radius on the shape of scribed samples S-N curve. The presence of scribes seemed to alter the S-N curve slope in the medium-cycle fatigue regime as scribed samples showed curves with gentler gradients than that of unnotched ones (Fig. 6.6). However, regardless of different scribe depths, scribed sample S-N curves showed nearly the same slope in medium-cycle fatigue regime (Fig. 6.6). Only scribes shallower than 80 µm, totally embedded into the clad layer, exhibited S-N with slightly gentler gradients, pointing out a small cladding effect on the scribed component fatigue finite life. Fatigue data of 185 µm deep, 5 root µm radius scribed clad and unclad samples showed slopes comparable with those of Nader's sample S-N curves, confirming once again the similitude between the scratches of reference [2] and the diamond tool machined scribes of this investigation (Fig. 6.6). However, due to the smaller root radius, diamond tool scribes seemed to have smaller endurance limits than Nader's scratches.

With the aid of the experimental data of Fig. 6.6, scribe fatigue effect and material notch sensitivity at the endurance limit can be discussed. As first thing, according to Atzori et al. [31,32], the critical stress concentration factor and notch dimensions, dividing the sharp to the blunt notch regime and defining the defect sensitivity, were derived. Atzori et al. [31,32], including the effect of the notch included angle and the component finite size, extended the definition of the critical notch size a_0 and a^* to V-

shaped notches in engineering components. They developed the following expressions for the two critical notch dimensions a_D^V and a_N^V, which respectively divided the notch insensitivity to the sharp notch region and the sharp to the blunt notch regime:

$$a_D^V = \frac{a_0^V}{\alpha_\gamma^{\frac{1}{\gamma}}} \quad a_N^V = \frac{K_t^{\frac{1}{\gamma}} a_0^V}{\alpha_\gamma^{\frac{1}{\gamma}}} \tag{6.2}$$

The exponent γ took into account the different degree of singularity of V-notches and α_γ was a non-dimensional coefficient depending on the notch open angle, loading type and component geometry [31]. The length a_0^V was the extension of the Kitagawa-Takahashi critical length a_0 [39] to sharp V-notches and it was related to a_0 by the following equation:

$$a_0^V = \alpha_{0\gamma} a_0 \tag{6.3}$$

where $\alpha_{0\gamma}$ was a non-dimensional coefficient depending only on the notch opening angle [31]. Finally, the characteristic stress concentration factor, K_t^*, which ideally separates sharp and blunt notch behaviours could be derived as function of the V-notch size, a, and the critical length a_0^V [31]:

$$K_t^* = \left(\frac{\alpha_\gamma^{\frac{1}{\gamma}} a + a_0^V}{a_0^V} \right)^\gamma \tag{6.4}$$

Using eq. (6.2) to eq. (6.4) and the critical stress concentration factor, K_t^*, could be calculated for rounded V-notch scribes in 2024-T531 aluminium alloy samples according to different notch depth. The geometric coefficients α_γ calculated by Chen [42] for single edge sharp V-notches with different depths under tensile load, and the value of a_0=172 μm derived by Atzori et al. [31] for 2024-T351 aluminium alloy on the basis of Du Quesnay's results [43], were used for the calculation. The critical length a_0 was derived from fatigue tests performed under a stress ratio of R=0 [43], however it was considered a good estimation of the a_0 value for R=0.1. All the other coefficients were obtained from reference [31]. Table 6.3 lists the critical stress concentration factor, K_t^*, calculated for the rounded V-shaped scribes analysed in this research and in Nader's work [2]. The scribe depth was selected as notch size parameter, a, (eq. (6.4)), therefore it was kept constant while the notch root radius was varied to find K_t^* [31]. A critical stress concentration factor, corresponding to a particular root radius, was calculated for each selected scribe depth (Table 6.3). The critical K_t^* dividing sharp and blunt notch regimes, was mainly influenced by the scribe depth, and slightly by the included angle (Table 6.3). The deeper the scribe the larger the critical stress concentration factor. All diamond tool scribes and Nader's ones showed stress concentration factors well above the corresponding critical values K_t^* (Table 6.3). Therefore all the analysed scribes can be considered as sharp notches where the fatigue limit condition is regulated by the growth threshold of cracks nucleated at the notch root [40]. In other words sharp notches behave as crack and their fatigue limit can be estimated on the basis of fracture mechanics or any other stress field criterion [31]. Scribes fatigue limit condition cannot be predicted using a peak stress criterion, that is by the only elastic stress concentration factor.

Table 6.3: Critical stress concentration factor of different scribes under tensile load

Scribe geometry				K_t		K_t^*
d [µm]	ρ_{min} [µm]	ρ_{max} [µm]	θ [deg]	ρ_{min}	ρ_{max}	eq. (6.4)
25	5	50	60°	5.885	2.428	1.093
50	5	50	60°	8.066	3.085	1.180
100	5	50	60°	11.272	4.082	1.344
150	5	50	60°	13.952	4.931	1.504
185	5	50	60°	15.702	5.495	1.615
40	-	83	90°	-	2.448	1.129
60	-	83	90°	-	2.775	1.189
100	-	83	90°	-	3.294	1.304
150	-	83	90°	-	3.812	1.446
225	-	83	90°	-	4.446	1.669

Several semi-empirical methods were proposed to evaluate the notch effect on component fatigue limit by means of parameters like the fatigue-notch factor, K_f and concepts as notch sensitivity (section 2.3.1). The suggested K_f equations were attempts to predict the variation of notch sensitivity from blunt notch regime, $K_f=K_t$, to region of notch insensitivity, $K_f=1$, according to different notch geometry. The capability of the traditional notch sensitivity equations proposed by Neuber [27] and Peterson [28] to accurately predict the fatigue limit of scribed samples was evaluated using Nader's S-N curves [2], shown in Fig. 6.6. Experimental fatigue-notch factors of different scribes were compared with the analytical expressions of eq. (6.5) and eq. (6.6) respectively suggested by Neuber [27] and Peterson [28].

$$K_f = 1 + \frac{K_t - 1}{1 + \sqrt{\frac{c_n}{\rho}}} \tag{6.5}$$

$$K_f = 1 + \frac{K_t - 1}{1 + \frac{c_p}{\rho}} \tag{6.6}$$

Notch geometry is defined in eq. (6.5) and eq. (6.6) by means of the stress concentration factor, K_t, and the root radius, ρ. The material constants, c_n and c_p, were specialised for the 2024-T3 aluminium alloy, choosing the values of c_n=271 µm and c_p=635 µm proposed respectively in reference [44] and [28]. The more recent fatigue notch factor expression suggested by Atzori et al. [31] was also validated against Nader's fatigue results. Atzori et al. [31] developed the following K_f equation for rounded V-notches:

$$K_f = \frac{K_t}{\left[1 + \left(\frac{K_t^{1/\gamma} a_0^V}{\alpha_\gamma^{1/\gamma} d + a_0^V}\right)^{1/\gamma}\right]^{\gamma^2}} \tag{6.7}$$

where the notch shape was defined by the elastic stress concentration factor and the notch size by the depth, d. The material and geometrical parameters, γ, a_0^V and α_γ were already defined above. For the calculation of a_0^V, according to eq. (6.3), a value of the

Kitagawa-Takahashi critical length of a_0=172 μm was chosen [31]. Table 6.4 shows the comparison between the experimental fatigue notch factor, K_f, obtained by Nader [2] for rounded V-shaped scribes with different depths, and the analytical expressions proposed by Neuber [27], Peterson [28] and Atzori [31]. Percentage errors from the experimental K_f are listed as well in Table 6.4 for every analytical prediction method.

Table 6.4: Comparison between analytical fatigue notch factor predictions and Nader's experimental results [2]

Scratch geometry				K_t	Test [2]	Neuber [27]		Peterson [28]		Atzori [31]	
d [μm]	ρ [μm]	θ [deg]	ρ/d		K_f	K_f	e [%]	K_f	e [%]	K_f	e [%]
40	83	90°	2.075	2.448	1.015	1.516	-49.35	1.167	-15.03	1.123	-10.65
60	83	90°	1.383	2.775	1.037	1.632	-57.41	1.205	-16.24	1.185	-14.29
100	83	90°	0.830	3.294	1.076	1.817	-68.88	1.265	-17.58	1.301	-20.91
150	83	90°	0.553	3.812	1.135	2.002	-76.36	1.325	-16.78	1.443	-27.18
225	83	90°	0.369	4.446	1.326	2.228	-68.00	1.398	-5.50	1.666	-25.69

Scribes showed increased values of the experimental fatigue notch factor according to the notch depth. The deeper the notch, the larger the notch sensitivity causing an increase in the K_f value (Table 6.4). However the overall notch sensitivity of 2024-T3 aluminium alloy samples to scribes at the fatigue limit was really low as fatigue notch factors ranged from K_f=1.015 to K_f=1.326 for scribe depths between 40 μm and 225 μm (Table 6.4). Samples were practically insensitive to scribes shallower than 60 μm, with their roots embedded into cladding. Analytical prediction methods were not able to correctly characterise the fatigue limit reduction caused by scribes from 40 μm to 225 μm deep. In fact, all the analytical formulae overestimated the fatigue notch factors compared to experimental results (Table 6.4). Prediction methods provided conservative K_f estimations, but they were too conservative to be used into an analytical methodology to assess the effect of scribe marks on fuselage joints. Neuber's formula [27] appeared to be the most inaccurate, showing percentage errors from -49% to -76% (Table 6.4). Despite its analogy with the Neuber's notch sensitivity expression, Peterson's K_f equation [28] gave the closest estimations with an average error of about -15%. Even Aztori's expression (eq. (6.7)), where the transition from blunt to sharp notch regime and from sharp notch to insensitive region according to the notch size, was accurately considered, was not able to predict fatigue results with an accuracy higher than 10-30% (Table 6.4).

The lack of prediction accuracy for Neuber's and Peterson's traditional analytical notch sensitivity equations could be ascribed to the small size of scribe marks, while for Atzori's formula an erroneous selection of the material critical length could explain the large estimation errors. Fig. 6.7 shows the comparison between experimental fatigue endurance limits of scribed samples and analytical predictions as function of the scribe depth. Notched component fatigue limits were normalised with respect to that of unnotched samples, obtaining $1/K_f$ on the ordinate axis (Fig. 6.7).

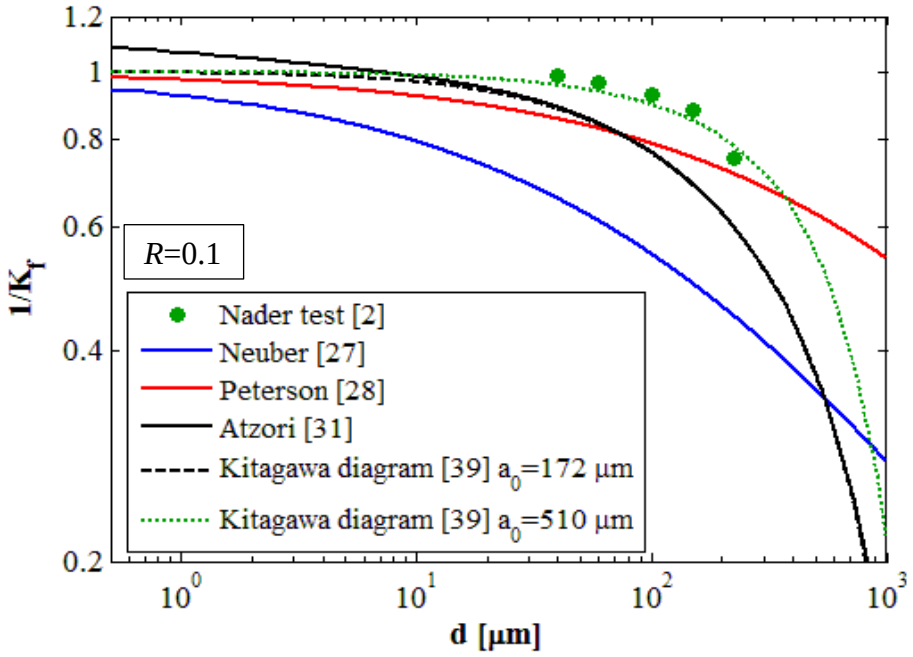

Fig. 6.7: Comparison between experimental fatigue limits of scribed tension samples and analytical predictions

The scarce accuracy in predicting the fatigue limit of scribed components, derived from the inability of traditional equations to correctly describe the notch sensitivity for notches the size of the critical length a_0 [44]. Neuber's and Peterson's equations predict a notch sensitivity factor, q, which is a function of the notch size expressed by the notch root radius, ρ (eq. (6.5) and eq. (6.6)). For a fixed value of the notch root radius, like in this case, the notch sensitivity remains constant and K_f varies according to different scribe depth, due to the variation of the elastic K_t. When the notch depth is reduced to zero, the stress concentration factor tends to 1 as well as K_f (Fig. 6.7), predicting a material insensitivity to very small stress raisers. On the other hand, Atzori et al. [30] showed that below the critical depth, a^*, notches behaved as cracks regardless of their root radius value. Notch sensitivity became equivalent to defect sensitivity and the endurance limit of notched components could be predicted using the Kitagawa-Takahashi diagram [30]. Therefore for depths comparable to the critical length a_0, materials become almost insensitivity to notches. To correctly predict the notch sensitivity in this notch size range, prediction methods should reproduce the trend of the Kitagawa-Takahashi diagram according to the notch depth variation. As shown in Fig. 6.7, Neuber's and Peterson's equations were not able to follow the Kitagawa diagram trend, overestimating K_f for scribed components. Atzori's K_f expression [31] was explicitly derived with the aim of describing the whole transition from notch to defect sensitivity. In fact it could correctly reproduce the trend of the Kitagawa diagram specialised for V-notches with an included angle of θ=90° (Fig. 6.7). However even Atzori's equation was found to overestimate experimental fatigue notch factors with an average error of about e=-20% (Fig. 6.7). Such behaviour was likely to be caused by the selection of an inaccurate value of the critical length a_0 for the 2024-T3 aluminium alloy clad samples tested by Nader [2]. If a critical length of a_0=510 µm, instead of a_0=271 µm, was used, the Kitagawa-Takahashi diagram, and consequently Atzori's equation were able to correctly predict the experimental K_f values (Fig. 6.7). The effect of the

scribe root radius, ρ=83 μm, comparable in size with notch depths could also make experimental data slightly diverge from the Kitagawa-Takahashi diagram [31].

In medium- low-cycle fatigue regimes, where, due to the high stress level, local notch plastic deformations become relevant, strain-based methods, like the local strain approach, are traditionally applied to determine the total fatigue life of notched components (chapter 2). According to the local strain approach, a macroscopic crack was assumed to develop at the notch root after the same number of fatigue cycles as in a smooth sample under a strain amplitude equal to that reached at the notch root [45-47]. Therefore the fatigue life of notched components was related to the local elastic-plastic strain at the notch root. Due to its local nature, the local strain approach will be more accurate in case of blunt notches, where the portion of material at the notch root affected by the stress raising effect is large and a peak stress criterion can characterise the notched component fatigue life. However, as shown in Table 6.3, scribes tested during this investigation because of their small size, were far from being considered blunt notches.

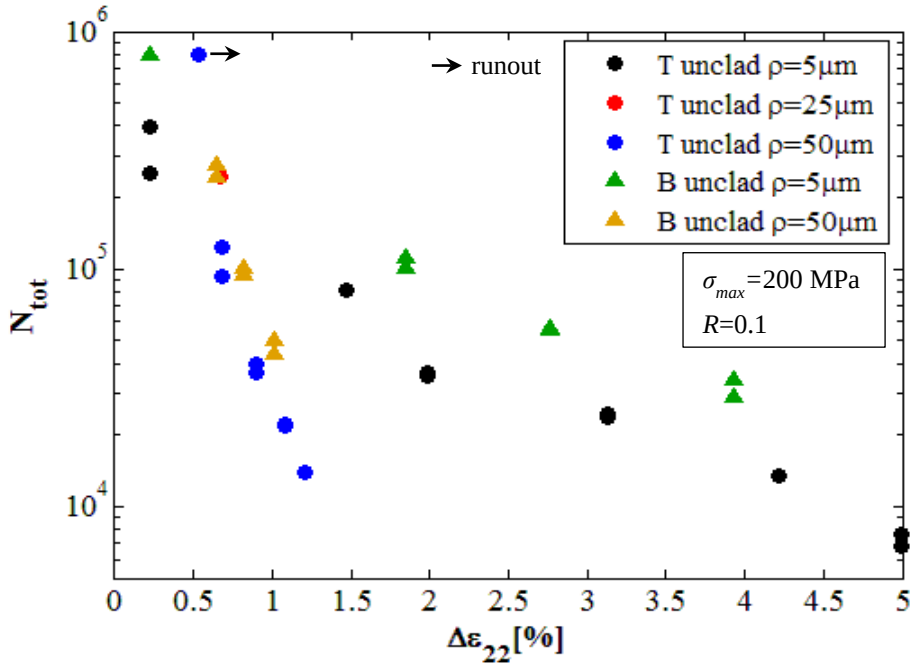

Fig. 6.8: Total fatigue life of scribed unclad samples as function of the cyclic strain range at the notch root, $\Delta\varepsilon$

Fig. 6.8 shows the total fatigue lives of scribed unclad samples, under tension and bending loads plotted against the cyclic longitudinal strain range at the scribe root, $\Delta\varepsilon_{22}$, calculated by finite element analysis (chapter 5). Scribed tension and bending samples exhibited different total fatigue lives according to the cyclic elastic-plastic longitudinal strain range. The larger $\Delta\varepsilon_{22}$ at the scribe root, the shorter the total fatigue life (Fig. 6.8). However fatigue lives of scribes with different root radii seemed to follow different trends, showing that the elastic-plastic cyclic strain range at the notch root is not able to correlate all the experimental data on a unique curve (Fig. 6.8). Therefore the local strain approach or any other fatigue prediction method, based on local elastic-plastic stress and strain components at the notch root, cannot accurately estimate the scribe

effect on fatigue life. Notches with the same aspect ratio but different size, like the 25 μm deep, 25 μm root radius and the 50 μm deep, 50 μm root radius scribes, showed dissimilar total fatigue lives (Fig. 6.8). However, as local cyclic elastic-plastic stress and strain components at the notch root depend only on the scribe aspect ratio (see Fig. 5.20), they reached the same $\Delta\varepsilon_{22}$ at their roots. The local strain approach, which considers only the strain value at the scribe root and does not take into account the influence of the notch size, would therefore incorrectly predict the same fatigue life for scribes with the same ρ/d and different size. Any approach to predict the fatigue behaviour of scribed components should characterise the notch size influence on the local stress distribution and consequently on the component fatigue life.

The capability of the local strain approach to predict fatigue lives of scribed components was assessed on the basis of experimental fatigue test results. Experimental lives of scribed unclad samples under tensile load were compared with those calculated using the local strain approach. Analytical fatigue lives were obtained introducing the elastic-plastic cyclic strain range, computed at the scribe root by finite element analyses, into the following strain-life relation:

$$\Delta\varepsilon = 2\left(\frac{\sigma'_f - \sigma_m}{E}\left(2N_f\right)^b + \varepsilon'_f\left(2N_f\right)^c\right) \tag{6.8}$$

Eq. (6.8) is the Coffin-Manson strain-life uniaxial equation modified to incorporate the effect of the fatigue cycle mean stress, σ_m [10]. A mean stress of σ_m=110 MPa was used for fatigue life calculation, while the strain-life coefficients, σ'_f, ε'_f, and exponents, b, c, of the 2024-T351 aluminium alloy were taken from reference [10]. The values of the selected coefficients are listed in Table 6.5.

Table 6.5: Cyclic strain-life equation coefficients [10]

Material	E [MPa]	σ'_f [MPa]	ε'_f	b	c
Al 2024-T351	72000	1103	0.22	-0.124	-0.59

Fig. 6.9 shows the comparison between experimental fatigue lives of scribed unclad samples under tensile load and local strain approach analytical predictions. Experimental and calculated total fatigue lives of different scribes are listed in Table 6.6 as well. For each different scribed sample Table 6.6 reports an average of the measured experimental fatigue life, the local strain approach prediction and its percentage error from experimental data.

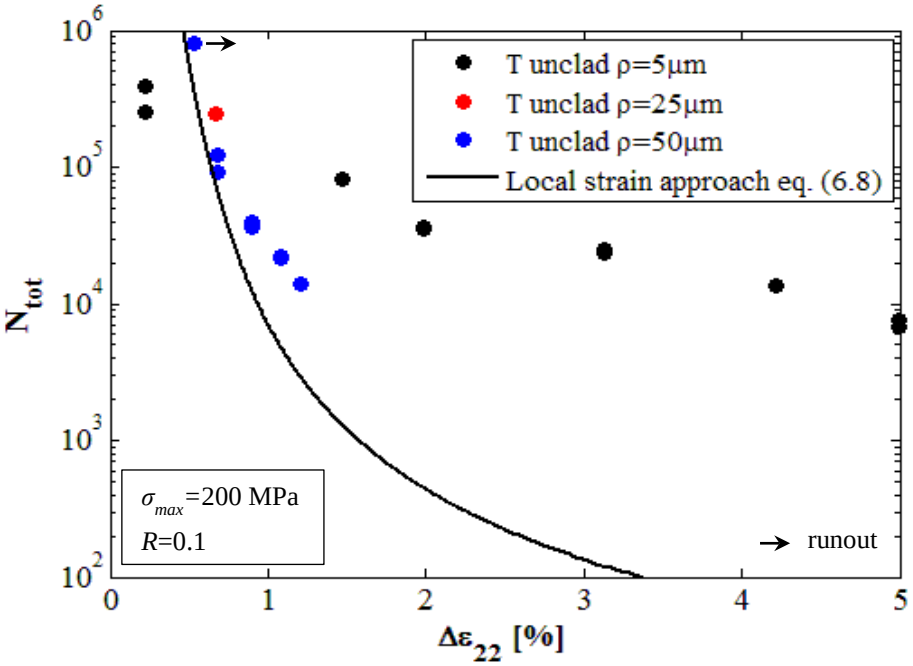

Fig. 6.9: Comparison between experimental fatigue lives of scribed unclad tension samples and local strain approach prediction

Table 6.6: Analytical total fatigue lives of scribed tension sample calculated using the local strain approach

Sample	Scribe geometry			Experimental fatigue life [cycle]	Local strain approach eq. (6.8)	
	d [μm]	*ρ* [μm]	*θ* [deg]		*N*	*e* [%]
T-U-25-5	25	5	60°	81914	1289	98.43
T-U-50-5	50	5	60°	35774	447	98.75
T-U-100-5	100	5	60°	24172	121	99.50
T-U-150-5	150	5	60°	13399	57	99.57
T-U-185-5	185	5	60°	7230	39	99.46
T-U-25-25	25	25	60°	246478	66057	73.20
T-U-25-50	25	50	60°	797159 (runout)	376095	52.82
T-U-50-50	50	50	60°	108471	66057	39.10
T-U-100-50	100	50	60°	38203	12433	67.46
T-U-150-50	150	50	60°	22053	4782	78.32
T-U-185-50	185	50	60°	13920	2937	78.90

As already stated, the local strain approach was not able to correctly predict the total fatigue life of scribed samples (Fig. 6.9). Also the life of unscribed samples was not properly characterised, as it was largely overestimated by eq. (6.8). Such behaviour could be caused by the different geometry of the samples used in this investigation, compared to those used to derive the strain-life relation [45-47]. However, even if the strain-life curve parameters were changed to correctly predict the life of unnotched samples or to fit data of scribes with a fixed root radius, the model could not anyway

correlate results of notches with different root radii (Fig. 6.9). The strain-file analytical expression seemed to show a trend similar to that of samples weakened by 50 μm root radius scribes, estimating their lives with improved accuracy (Fig. 6.9). However as the scribe depth increased the curve diverged from the experimental data and the prediction error became larger (Table 6.6). Eq. (6.8) underestimated the fatigue lives of all the scribed samples, calculating a number of cycles, which decreased as the cyclic strain range at the notch root increased (Table 6.6). For 5 μm root radius scribes, fatigue lives from 39 to 1289 cycles were estimated, producing errors of 98-99% from the experimental data (Table 6.6). The prediction accuracy was slightly improved in case of 25 μm and 50 μm root radius notches reducing the error to a range of 39-79% (Table 6.6). The local strain approach was too inaccurate to be used to assess the residual fatigue live of scribed component and in particular of scribed fuselage joints.

The causes of the substantial underestimation of fatigue lives of scribed samples by the local strain approach have to be ascribed to the scribe small size. Such approach is generally used to predict the crack initiation life at the root of conventional engineering notches the size of few millimetres [45-47]. In fact, due to the assumptions at the basis of its formulation, the local strain approach can correctly estimate the number of cycles required to nucleate a crack few millimetres long under the local raised stress produced by a notch. If the fatigue life to propagate a crack nucleated at the notch root is negligible, compared to that spent for the initiation and the early propagation of such crack inside the notch stress concentration region, the local strain approach can be used to characterise the total fatigue life of components. That condition is commonly satisfied for components comparable in size to the samples used to obtain the strain-life curves [10] and weakened by blunt notches, showing a wide stress concentration region at their roots. Scribed samples nucleated cracks as deep as those developed inside the strain-life curve specimens. However due to their small size, scribes affected with their stress raising effect a region no larger than 4% of the sample net ligament thickness (see Fig. 5.12 c)). For that reason, considering the entire sample ligament subjected to the local strain range reached at the scribe root, it could lead to a substantial underestimation of the total fatigue life, as the crack propagation outside the notch stress concentration region is neglected. Therefore the prediction error of the local strain approach will be bigger the shorter is the portion of the total fatigue life spent to initiate a crack the size of the stress concentration region [45-47].

For sharp notches, like the 5 μm root radius scribes, where the majority of the fatigue life was spent to propagate cracks outside the sample region affected by the scribe stress raising effect, the local strain approach was completely inaccurate (Fig. 6.9 and Table 6.6). Only for blunt 50 μm deep, 50 μm root radius scribes the initiation life was long enough to ensure a prediction accuracy of nearly 40% (Table 6.6). Scribes with the same aspect ratio showed stress concentration regions proportional to the notch size (Fig. 5.15). For such scribes, despite the different extension of the stress raising zone, the local strain approach estimates the same fatigue life since the strain range at the scribe root is the same (Table 6.6). However the number of cycle to initiate cracks of dissimilar lengths inside the stress concentration regions cannot be same and the sample total fatigue lives will be different. Thus the local strain approach is not able to characterise the notch size effect on fatigue life, even if the remaining crack propagation life outside the notch stress raising region is negligible (Table 6.6). Any fatigue life

prediction method should take into account the notch size effect to correctly describe the fatigue behaviour of scribed samples.

A local stress field parameter which depends on the notch geometry and includes the effect of the scribe size is the notch root plastic zone. As explained in chapter 5, the extension of both monotonic and cyclic plastic zone ahead of the scribe root is regulated by the notch shape, defined by the aspect ratio, and notch size (Fig. 5.11 and Fig. 5.22). Since also the total fatigue life of scribed samples depended on both notch shape and size (Fig. 6.5), the plastic zone length along the scribe bisector could be a parameter capable of correlating and predicting the scribe geometry effect on component total fatigue life. Moreover fatigue processes are strictly correlated to the material plastic behaviour since a crack cannot nucleate and propagate without the occurrence of the local plastic deformations produced by dislocation motion along slip bands [10]. Even if the cyclic plastic zone is a region of continuous plastic deformations where cracks can nucleate during fatigue cycles the length of the monotonic plastic zone was selected as fatigue life correlation parameter. In fact the occurrence of irreversible deformations inside the monotonic plastic zone produced residual stresses which altered the local stress ratio, *R*, of the subsequent stabilised elastic cyclic stress (Fig. 5.23). Therefore the scribe influence on the local cyclic stress field can be better characterised by the monotonic plastic zone length. Fig. 6.10 shows total fatigue lives of scribed unclad tension and bending samples plotted against the length of the monotonic plastic zone, l_{pl}^{mon}, along the notch bisector.

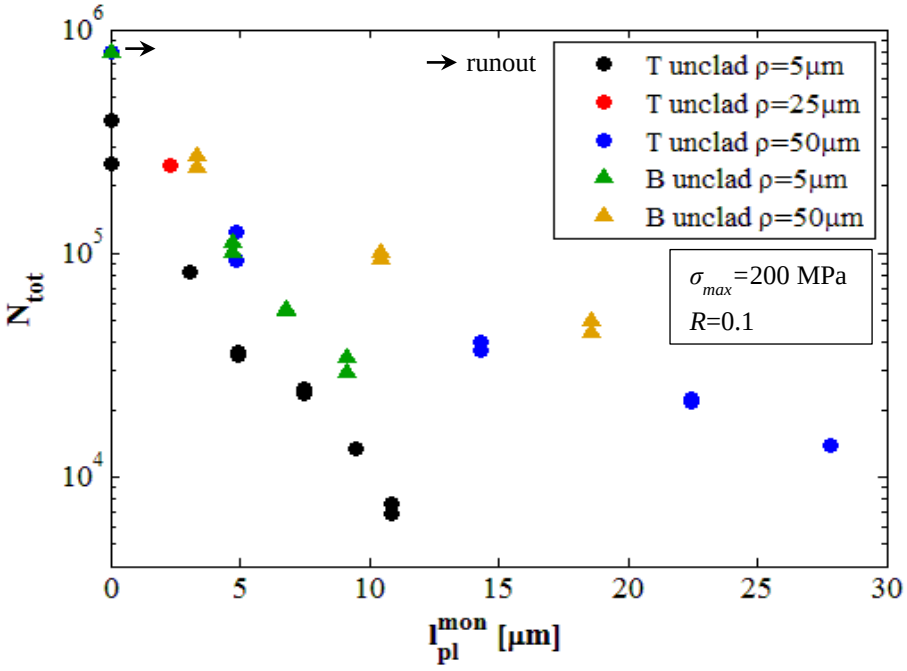

Fig. 6.10: Total fatigue life of scribed unclad samples as function of the monotonic plastic zone length, l_{pl}^{mon}, along the notch bisector

Scribes samples showed different total fatigue lives according to the monotonic plastic zone length along the notch bisector (Fig. 6.10). The larger l_{pl}^{mon} the shorter the total fatigue life. However also the monotonic plastic zone length was not able to correlate fatigue lives of samples, weakened by scribes with different root radii, along a

unique curve respectively for tensile and bending loading (Fig. 6.10). Notches with similar monotonic plastic zone lengths at their roots like the 50 μm deep 5 μm root radius and the 50 μm deep 50 μm root radius scribes showed longer total fatigue lives as the scribe root radius increased (Fig. 6.10). The notch geometry effect on the scribed sample total fatigue life was not entirely characterised by the monotonic plastic zone length along the scribe bisector, l_{pl}^{mon}. Actually the extent of the monotonic plastic zone is related to the magnitude and the length of the scribe stress concentration region. The higher the notch elastic K_t and the larger the notch size, which regulates local stress gradients, the larger the monotonic plastic zone (Fig. 5.11). Therefore l_{pl}^{mon}, as any other local notch mechanical parameter is more related to the fatigue life spent to initiate a crack at the scribe root than to the total fatigue life. Neglecting the crack propagation stage, l_{pl}^{mon} was not able to correlate the fatigue lives of 5 μm and 50 μm root radius scribes, where crack initiation occupied a different fraction of the total life.

A common and promising method to estimate the fatigue strength of notched components is the theory of critical distances [48-51]. Such method was subsequently extended to the medium-cycle fatigue regime by Susmel and Taylor [52,53], allowing the prediction of notched component finite lives. Critical distance theory was applied to scribe fatigue test results to assess its capability to predict fatigue lives of scribed components. In the medium-cycle fatigue regime the theory was reformulated introducing the idea that the material characteristic critical distance L varied according to the component number of cycles to failure [53]. The critical distance was assumed to be a power function of the cycles to failure and such law, supposed to be a material properties, could be obtained for a particular material knowing the S-N curves of a plain and a notched specimen under a given loading condition [53].

Due to the lack of S-N curves of unnotched clad and unclad samples, the alternative method suggested by Yamashita et al. [54,55] to determine the critical distance in a wide range of fatigue lives from low-cycle to high-cycle fatigue life regimes was adopted. Critical distances for the point L_{pm} and the line L_{lm} methods were defined comparing the elastic longitudinal stress range $\Delta\sigma_{22}$ distributions along the bisectors of notches with different root radii, which showed comparable total fatigue lives. Fatigue data of 185 μm deep 5 μm root radius scribes, tested under tensile load at different maximum stress (Table 4.3), were used for the critical distance determination to account for the effect of different nominal stresses. Three pairs of clad and unclad scribed tension samples, showing similar total fatigue lives in different fatigue regimes were selected [55]. Doing so the variability of critical distances L_{pm} and L_{lm} according to the total fatigue life was investigated for clad and unclad samples in a range from 10^4 to $2 \cdot 10^5$ cycles. The elastic $\Delta\sigma_{22}$ distributions along the bisector of notches in samples with similar total lives were used to calculate the critical stress range $\Delta\sigma_0$ as function of the distance from the notch root x, according to the point and the line method [55]. As samples had similar lives, following the assumptions behind the critical distance theory [52,53], they had to show the same critical stress range $\Delta\sigma_0$ in correspondence with the critical distance L. Thus L_{pm} and L_{lm} were defined as the distances from notch root where the stress ranges $\Delta\sigma_0$, calculated respectively with the point and the line methods showed the same values for samples with similar total fatigue lives [55]. Table 6.7 shows the critical distances, calculated using the point and the line methods L_{pm} and L_{lm} for different total fatigue lives in clad and unclad scribed tension samples.

Table 6.7: Critical distance calibration under tensile load

Fatigue life *N*		Compared samples		Critical distance [μm]	
Unclad	**Clad**			**Point method** L_{pm}	**Line method** L_{lm}
124479	178758	T-185-5 (100 MPa)	T-50-50	7.31	37.11
36736	36736	T-185-5 (160 MPa)	T-150-50	7.06	38.71
13660	19920	T-150-5	T-185-50	6.92	38.51
Average				7.10	38.11

Consistently with the results obtained by Yamashita et al. [54,55], who analysed the fatigue strength of titanium specimens weakened by small V-shaped notches in the finite life regime, critical distances L_{pm} and L_{lm} of clad and unclad scribed samples were substantially independent of the total life (Table 6.7). The average values of L_{pm} and L_{lm} were used as fixed critical distances in each fatigue life regime for both clad and unclad samples. It is worth noticing that the elastic longitudinal stress range $\Delta\sigma_{22}$ distributions along the notch bisectors were the same in clad and unclad samples (section 5.2). Therefore, as the pairs of clad and unclad scribed specimens showing similar total life contained the same kind of scribes (Table 6.7), the calculated critical distances were identical in clad and unclad specimens. Critical distance values of L_{pm}=7.10 μm and L_{lm}=38.11 μm were obtained, in contrast with L_{pm}=135.5 μm and L_{lm}=542.0 μm calculated at the fatigue limit by Susmel [51] for 2024-T351 aluminium alloy samples tested under constant amplitude fatigue tensile load at a stress ratio of R=0. The calculated line and point method critical distances seemed to be related to the material grain size along the short transversal direction. In fact L_{lm} was about the length of two grain diameters along the short transversal direction, $2d$=40 μm, while L_{pm} was slightly smaller than $d/2$=10 μm (section 3.1.1).

The critical distance stress ranges $\Delta\sigma_{pm}$ and $\Delta\sigma_{lm}$ of point and line methods, which were respectively the elastic $\Delta\sigma_{22}$ at a distance from the notch root equal to L_{pm} and the average of $\Delta\sigma_{22}$ over a distance L_{lm} from the notch root [48-51], were calculated for each tested tension sample. Critical distance stress ranges were than used to characterise the total fatigue lives of different clad and unclad scribed specimens. Fig. 6.11 a) and b) show respectively the total fatigue lives of unclad and clad scribed tension samples, plotted against the scribe critical stress range, $\Delta\sigma_{lm}$ calculated according to the line method. The fatigue lives of 185 μm deep 5 μm root radius scribes, tested under different maximum stresses and used to calculate the values of the critical distances were plotted as well in Fig. 6.11. Since the point method produced analogous graphs to those in Fig. 6.11, obtained using the line method, it was not discussed in this section. Scatter apart, the critical distance stress range $\Delta\sigma_{lm}$ was able to correlate almost all the total fatigue lives of scribed unclad and clad samples, making test data of different scribes lie on the same curve (Fig. 6.11). Only the 50 μm deep, 5 μm root radius scribes in unclad and unclad samples and the 25 μm deep, 5 μm root radius notches in unclad ones seemed to diverge from the common trend, showing shorter fatigue lives (Fig. 6.11). Total lives of pristine unscribed clad and unclad specimens, which had a critical distance stress range of $\Delta\sigma_{lm}$=180 MPa, did not follow the common trend of scribed

sample data either, giving rise to prediction curves with an asymptote in correspondence to the unnotched specimen life (Fig. 6.11).

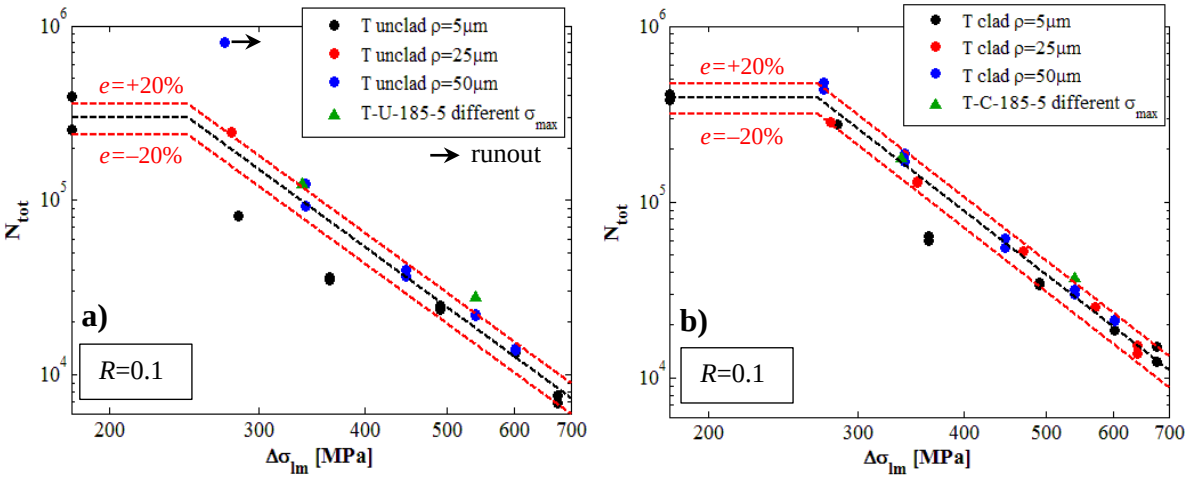

Fig. 6.11: Total fatigue life of scribed unclad a) and clad b) tension samples as function of the line method critical distance stress $\Delta\sigma_{lm}$

The total fatigue life up to failure of scribed clad and unclad samples seemed to be a power function of the critical distance stress range $\Delta\sigma_{lm}$, calculated averaging the elastic principal stress range distribution $\Delta\sigma_{22}$ along the scribe bisector over a distance L_{lm}=38.11 μm from the notch root. Scribed sample total lives could be therefore estimated using the following expression:

$$N_n^{tot} = C\Delta\sigma_{lm}{}^{g} \tag{6.9}$$

where the parameter C and the exponent g were obtained by performing a best fit least square analysis of fatigue test results. Table 6.8 lists the parameters of the critical distance-based fatigue life prediction equation (eq. (6.9)), calculated for unclad and clad scribed samples under constant amplitude tensile load at R=0.1.

Table 6.8: Critical distance equation parameters to predict total fatigue life of scribed tension samples

Material	C	g
Al 2024-T351 unclad	$8.961\cdot10^{13}$	-3.544
Al 2024-T351 clad	$4.539\cdot10^{14}$	-3.730

Analytical life predictions of eq. (6.9) for unclad and clad samples are displayed respectively in Fig. 6.11 a) and b) together with scatter bands corresponding to an error of e=±20%. Almost all the scribed sample experimental data fell inside the error bands, proving that the critical distance theory was able to estimate fatigue lives of unclad and clad scribed specimens with an accuracy of about ±20% (Fig. 6.11 a) and b)). The prediction accuracy of eq. (6.9) was higher for clad samples than for unclad ones, where the larger scatter caused some data to be outside the error bands. However critical distance analytical predictions were conservative for any scribed sample, apart from the unclad 25 μm and 50 μm deep, 5 μm root radius scribed specimens and the clad 25 μm deep, 5 μm root radius scribed samples (Fig. 6.11). The reasons for the deviation of such scribes from the common trend were not entirely understood.

Unclad and clad samples seemed insensitive to scratches as small as 25 μm deep with root radii equal or bigger than respectively 25 μm and 50 μm (Fig. 6.5). For those specimens eq. (6.9) estimated fatigue lives comparable to those of the corresponding pristine unscribed samples (Fig. 6.11). However, despite the same fatigue life corresponding critical stress ranges of pristine and scribed coupons were different. Thus there was a graph region where, for a constant external nominal tensile stress, the scribed sample fatigue life was independent of the critical stress range $\Delta\sigma_{lm}$ and constantly equal to that of pristine samples (Fig. 6.11). Drawing an horizontal line in correspondence with the unscribed sample life, a threshold value of the critical stress range $\Delta\sigma_{lm}$ below which, the material was insensitive to scribes could be obtained for a given external nominal stress (Fig. 6.11). Threshold $\Delta\sigma_{lm}$ values were $\Delta\sigma_{lm}^{th}$=246.99 MPa and $\Delta\sigma_{lm}^{th}$=268.74 MPa respectively for clad and unclad 2024-T351 aluminium alloy samples fatigued under tensile load with σ_{max}=200 MPa and R=0.1. The critical distance model therefore predicted an asymptotic behaviour of the fatigue life when the pristine sample life was reached (Fig. 6.11). However such asymptote could be caused by a miscalculation of the critical stress range for unnotched specimens. Crack nucleation in fact occurred in unscribed specimens at large intermetallic inclusions 25-50 μm in size. It is likely that the elastic stress field in proximity of such inclusions is comparable to that of 25 μm deep scribes with 25 μm and 50 μm root radii, giving rise to similar value of $\Delta\sigma_{lm}$. If the stress raising effect of the inclusions is considered, it is likely that the also the fatigue life of unnotched samples will be predicted by eq. (6.9).

In conclusion the critical distance theory was able to characterise the total fatigue life reduction, produced by the introduction of scribes with different depths and root radii in clad and unclad 2024-T351 aluminium alloy samples. The critical stress range $\Delta\sigma_{lm}$ was therefore capable of describing the effect of elastic stress distributions produced by dissimilar notches on fatigue crack nucleation and propagation. However the critical distance theory assumes the material behaviour as purely elastic, neglecting any kind of stress redistribution produced by the occurrence of plasticity in physical material. For that reason the theory of critical distances can be correctly applied to those notches where small-scale yielding conditions exist, that is where the cyclic plastic zone is small compared to the critical distance L [48-51]. Unclad samples showed cyclic plastic zone lengths along the notch bisector up to 4.36 μm (section 5.4.1.2) which is about 12% of the critical distance L_{lm}. The plastic zone extension could be large enough to invalidate the small-scale yielding conditions. To investigate this problem critical stress ranges $\Delta\sigma_{lm}$ of scribed unclad samples were calculated using the cyclic elastic-plastic $\Delta\sigma_{22}$ distributions and compared to those obtained from pure elastic distributions. Table 6.9 shows the comparison between the critical stress ranges of unclad specimens computed using the elastic and elastic-plastic cyclic longitudinal stress distributions along the scribe bisectors. Percentage difference between elastic and elastic-plastic $\Delta\sigma_{lm}$ are listed as well in Table 6.9. The critical stress ranges calculated using elastic and elastic-plastic cyclic stress distributions were nearly identical, showing a maximum difference of e=0.5% for the 185 μm deep, 5 μm root radius scribes characterised by the largest cyclic plastic zone (section 5.4.1.2). Small-scale yielding conditions were therefore fulfilled in case of scribed samples tested at a maximum tensile test of σ_{max}=200 MPa and elastic $\Delta\sigma_{22}$ distributions could be used to calculate the critical distance stress range $\Delta\sigma_{lm}$. However when the occurrence of the small-scale yielding conditions is not verified the

more realistic elastic-plastic cyclic distributions should be considered to calculated $\Delta\sigma_{lm}$ in the framework of the critical distance theory.

It is worth noticing that generally the critical distance theory, taking into account the local stress at the notch root, is capable of predicting the initiation life of notched components not their total life up to failure [48-51]. The life spent to propagate a crack outside the region affected by the scribe stress concentration did not substantially influence the sample total life reduction caused by scribe introduction. Crack propagation stage is discussed in section 6.2.4. Despite its possible extension to elastic-plastic stress fields, critical distance theory approach remains without physical basis. In fact no physical evidences support the correlation between the notch local maximum principal stress, averaged over a specific length or calculated at a specific distance from the notch root, and fatigue crack initiation and propagation from notches [48-51]. Moreover, even if the calculated critical distances L_{pm} and L_{lm} seemed to be related to the grain size along the crack propagation direction, their values were computed by imposing the equality of critical stress ranges of scribed samples with similar total lives and thus fitting the experimental results. Critical distance theory, despite its success in predicting the fatigue life of notched components nowadays is nothing more than an engineering tool without any physical basis. That is true in particular if the approach is applied in the finite fatigue life regime, where the critical distance is calculated fitting experimental fatigue lives and it loses therefore any relation to the material fatigue limit and crack growth threshold [52,53].

Table 6.9: Analytical critical stress range $\Delta\sigma_{lm}$ of unclad samples calculated at the scribe root using elastic and elastic-plastic stress distributions

Sample	$\Delta\sigma_{lm}$ [MPa]		e [%]
	Elastic	Elastic-plastic	
T-U-25-5	283.42	283.74	0.114
T-U-50-5	363.11	363.09	-0.004
T-U-100-5	491.08	490.50	-0.119
T-U-150-5	601.48	599.48	-0.335
T-U-185-5	674.74	671.36	-0.503
T-U-25-25	278.52	278.35	-0.063
T-U-25-50	273.12	272.86	-0.095
T-U-50-50	340.06	339.58	-0.141
T-U-100-50	447.29	446.54	-0.168
T-U-150-50	540.45	539.35	-0.204
T-U-185-50	602.70	600.80	-0.315

6.1.4 Cladding and loading condition effect on total fatigue life

How the presence of clad pure aluminium layer and the external applied nominal stress gradient of bending load affected the scribed sample fatigue life, it is discussed in this section. Clad samples showed total fatigue lives on average 40-50% longer than the corresponding unclad specimens (section 4.1). Even for pristine unscribed specimens cladding seemed to increase the fatigue total life on nearly 43%. This behaviour was

inconsistent with the outcomes of traditional literature researches on fatigue performances of clad aluminium sheets [56,57] where the clad layer was found to have a large detrimental effect on S-N curve of aluminium alloys. In fact early crack nucleation inside cladding was promoted by the plastic shake down of the soft pure aluminium, leading to initiation lives in clad samples of about 40% of those of unclad ones [56,57]. Traditionally fatigue cracks are considered to nucleate inside the soft cladding after few cycles, assuming the fatigue life of clad specimens to be regulated by the time required for a crack to penetrate into the material substrate [57]. A possible crack retardation at the cladding/substrate interface, however, cannot explain the longer life of clad samples as clad specimens showed longer life also for scribes with their root embedded into the substrate. In that kind of coupons, in fact, cracks nucleated at the scribe roots never crossed the cladding/substrate boundary, excepting in their final instable growth. It is likely that the crack retardation at the boundary between clad layer and material substrate contributed towards the extension of clad sample fatigue life, but another physical phenomenon was its main cause.

As the unclad samples tested during this investigation were actually stripped specimens, obtained from previous clad material sheets by chemical milling, they had a thickness of t=1.67 mm against t=2 mm of clad specimens (section 3.1). Therefore for the same external applied nominal stress thicker scribed clad samples, because of their lower net ligament stress, should show longer crack initiation and propagation lives. In case of unnotched specimens just the crack propagation would be longer, but in this case the crack retardation at the cladding/substrate interface could play a role in extending the initiation life. Due to presence of the clad layer with a smaller yield strength than the harder substrate, the stress inside the substrate of clad samples resulted increased of 3% (section 3.2). Such small stress increase, however was irrelevant as fatigue cracks of given depths were observed to propagate slower in clad samples than in unclad ones (section 4.2.4). Cracks growth stage outside the scribe stress concentration region in clad specimens was therefore longer than in unclad ones. Anyway also the process of crack development from scribe roots and early growth in the notch stress concentration region had to be retarded by the presence of clad layer. In an attempt to rationalise the effect of cladding on crack development at the scribe root, notch stress and strain fields inside clad samples are briefly discussed.

The presence of two materials with different mechanical properties, separated by a nearly sharp boundary, markedly influenced the mechanical response of clad samples. The effect of cladding on elastic-plastic finite element results was investigated comparing local monotonic elastic-plastic notch stress and strain fields of clad and unclad scribed samples under tensile loading. Due to the similarity of the cladding influence under tensile and bending loads only elastic-plastic results of tension samples are discussed below.

Fig. 6.12 shows the clad effect on monotonic elastic-plastic longitudinal stress and strain distributions along the bisector of selected notches in tension samples. Clad and unclad samples weakened by 50 μm and 100 μm deep notches with 5 μm and 50 μm root radii were selected and had their stress and strain distributions compared in Fig. 6.12. Fig. 6.12 a) shows the elastic-plastic σ_{22} distributions along the notch bisector in clad and unclad samples normalised with respect to the nominal tensile stress, σ_{nom}=200

MPa and plotted against the normalised distance from the notch root x/ρ. Notches with their roots inside the substrate like the 100 μm deep scribes showed vertical normal stress distributions in clad samples very close to those of the same notches in unclad specimens (Fig. 6.12 a)). The effect of cladding seemed just to shift such distributions down to slightly lower σ_{22} values. The presence of the cladding made notches deeper than the clad layer behave as they were shallower than their real depths. The 100 μm deep, 5 μm root radius scribe showed at the notch root a local σ_{22} value in clad samples higher than in unclad ones (Fig. 6.12 a)). Such anomalous behaviour seemed to be caused by the different finite element discretisation more than being a distribution properties.

Scribes shallower than the clad layer showed completely different σ_{22} distributions in clad and unclad samples (Fig. 6.12 a)). Vertical normal stresses at the notch root in clad samples were between 2.6 and 3 time smaller than the corresponding ones in unclad specimens. Moving away from the notch root in clad samples σ_{22} gradually increased inside the clad layer up to reach the cladding/substrate interface for 50 μm deep, 50 μm root radius scribes (Fig. 6.12 a)). For 50 μm deep, 5 μm root radius notches in clad samples instead the σ_{22} reached a local maximum in the cladding to then decrease up to the clad layer boundary (Fig. 6.12 a)). In correspondence to the cladding/substrate interface vertical normal stresses showed a discontinuity, jumping to higher values in the substrate. In the substrate the σ_{22} stresses along the bisector of notches shallower than the clad layer reached higher values than the corresponding unclad distributions, following almost the stress curves of clad samples containing notches with the same root radius but different depth (Fig. 6.12 a)). In the far field region all the clad distributions merged together approaching a uniform stress in the substrate. Two different uniform σ_{22} stresses were reached far from the notch in the cladding and the substrate causing a far field stress discontinuity (Fig. 6.12 a)).

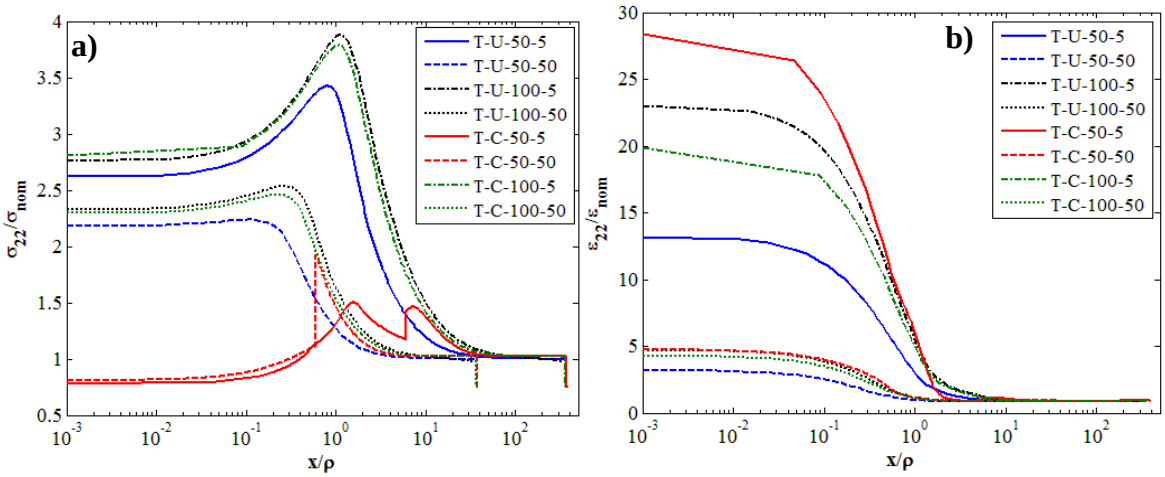

Fig. 6.12: Clad effect on monotonic stress and strain elastic-plastic distributions along the notch bisector under tensile load. Longitudinal stress (a) and strain (b) normalised with respect to their nominal values plotted against distance from the notch root normalised by the notch root radius.

Fig. 6.12 b) shows the elastic-plastic ε_{22} monotonic distributions, normalised by the nominal vertical normal strain (ε_{nom}), in clad and unclad tension samples plotted against the coordinate from the notch root x normalised with respect to the root radius. Vertical

normal strain curves of clad samples did not show any kind of discontinuity as the strains in the cladding and in the substrate must have the same value at the material interface to respect the sample displacement congruence. All the normalised ε_{22} distributions showed the same trend reaching their maximum value at the notch root and decreasing down nearly to one in the far field region, not affected by the notch raising effect (Fig. 6.12 b)). Notches deeper than the clad layer in clad samples showed ε_{22} values slightly lower than the corresponding distributions in unclad specimens. On the contrary ε_{22} distributions of notches with their roots inside the cladding of clad samples reached in proximity of the notch root higher strains than those of the same scribes in unclad samples. Far from the notch root the ε_{22} curves of notches deeper than the clad layer seemed to approach the uniform unitary far field strain faster in clad samples than in unclad ones (Fig. 6.12 b)). The smaller the notch root radius the larger the strain gap between clad and unclad scribed samples for both 50 μm and 100 μm deep scribes (Fig. 6.12 b)).

For scribes deeper than the clad layer the smaller stress and strain distributions in proximity of the notch root, compared to those of the corresponding scribed unclad samples, could be the cause of the longer total fatigue lives of clad specimens. In fact the strain energy available for crack nucleation and the driving force for the early crack growth at the root of a given scribe resulted reduced in case of clad samples. It is worth noticing that an analogous stress and strain reduction occurred at the tip of a crack penetrated into the material substrate, reducing its driving force and thus slowing its growth even outside the notch stress concentration region. When scribes are totally embedded into the clad layer, like 25 μm and 50 μm deep scribes, due to the easy plasticisation of the soft pure aluminium layer, the energy available for crack nucleation and propagation is larger than in the corresponding unclad samples. That promotes an early fatigue crack initiation at the scribe root and in general inside the whole clad layer. Crack nucleation was therefore quite easy inside cladding [58]. In fact several secondary cracks were found to nucleate inside the clad layer of unscribed clad samples (Fig. 4.12 a)). However they became non-propagation cracks once the cladding/substrate interface was reached (section 4.2.3.1). That was thought to be a possible evidence of the difficulty of cracks in overcoming the barrier formed by the cladding/substrate boundary and penetrating into the substrate. For notches entirely embedded into the cladding, where crack nucleation and early growth at the scribe root were accelerated, the time spent by cracks to overcome the cladding/substrate interface is believed to be responsible for the longer total fatigue lives of clad samples compared to unclad ones. Despite the different fatigue life between clad and unclad samples, as already explained, cladding did not alter the life reduction caused by the scribe introduction (Fig. 6.5).

The effect of changing the loading condition from pure tension to 4 point bending was to increase the total fatigue life of scribed components. Bending samples showed fatigue lives on average 3 times longer than the corresponding tensile specimens (section 4.1). Such behaviour was consistent with the experimental evidences of other investigation available in literature [10]. Bending samples showed smaller cyclic plastic zones and lower elastic-plastic stress and strain ranges at the notch root than the corresponding tension specimens (section 5.4.1). The differences in local stress and strain fields in the neighbourhood of the scribe produced a reduction of the energy

available for the fatigue crack nucleation and early propagation under bending load. Therefore the number of fatigue cycles required to initiate a crack and make it propagate through the scribe local stress concentration region will be larger under bending load than under tensile one. However the local notch stress and strain field reductions produced by the external nominal stress gradient of bending load, were small, ranging between 1% and 20% according to the scribe geometry (section 5.4.1). The fatigue crack initiation and early propagation life thus was expected to be just slightly longer for scribed bending samples remaining anyway comparable to that of the corresponding tensile specimens.

What really differentiated the sample fatigue behaviour under tensile and bending loads, making the total life of bending specimens longer than those of tension ones, it was the crack propagation away from the scribe under the far-field stress. For a given crack depth, crack growth rates in the far field stress region were found to be smaller in scribed bending samples than in the corresponding tension ones (section 4.2.4.2). Such slower crack propagation was caused by the far field stress gradient which reduced the driving force at the crack tip, ΔK, available for crack growth under bending loading compared to that under tensile one [59]. The smaller crack driving force at the deepest point of the crack front in bending samples also promoted crack propagation along the direction parallel to the scribe root, further increasing the fatigue growth life (section 4.2.2). The differences in the crack growth far from the scribe local stress concentration region were believed to be the cause of the longer total fatigue life of bending samples compared to tension ones.

As the scribe effect on total fatigue lives of tension and bending samples was nearly the same (Fig. 6.5), the critical distance theory could be capable of estimating the scribed specimen life also under bending load. The lack of enough couples of scribed bending samples with comparable fatigue lives made problematic the calculation of critical distances for different ranges of fatigue cycles under bending load. Therefore the values of L_{lp} and L_{lm} computed for tension samples were also applied to bending specimens. It is worth noticing, that, according to the critical distance theory assumptions, L_{lp} and L_{lm} are supposed to be material properties which also depend on the loading condition [48-51]. Therefore critical distances are expected to change from tension to bending samples. However due to the lack of sufficient experimental data the values of L_{pm}=7.10 μm and L_{lm}=38.11 μm were used for bending samples. According to the point and the line methods, critical distance stress ranges were calculated under bending load from the elastic $\Delta\sigma_{22}$ distributions at the scribe root. The obtained critical stress ranges were then used to correlate total fatigue lives of bending samples. Fig. 6.13 a) and b) show respectively the total fatigue lives of unclad and clad scribed bending samples, as function of the line method critical stress range $\Delta\sigma_{lm}$. Power function trend lines calculated by a least square best fit of the experimental data (section 6.1.3), and the related scatter bands corresponding to an accuracy of e=±20% are displayed as well in Fig. 6.13.

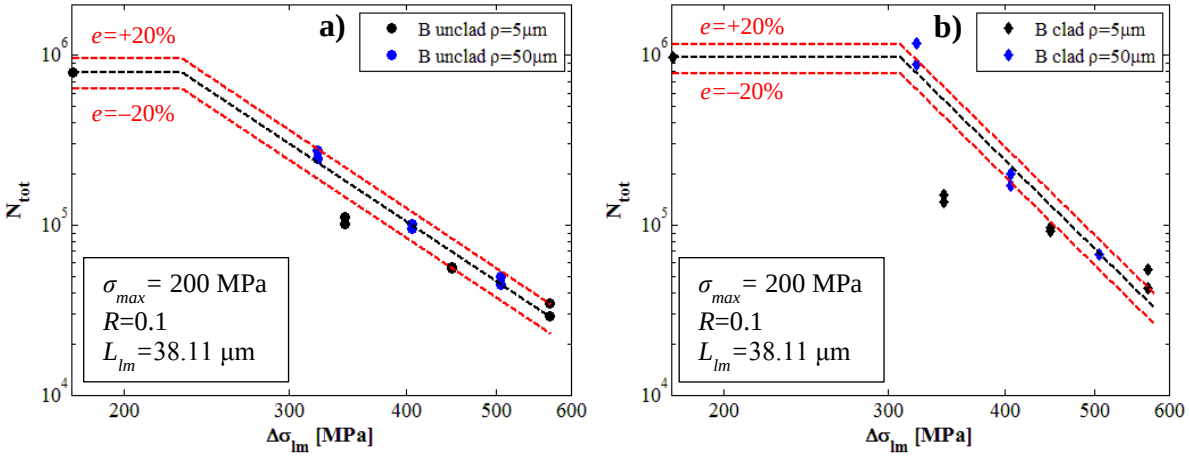

Fig. 6.13: Total fatigue life of scribed unclad a) and clad b) bending samples as function of the line method critical distance stress $\Delta\sigma_{lm}$

Despite the inappropriate value of the critical distance L_{lm}, critical distance theory, applied by means of line method, was able to characterise the fatigue behaviour of unclad scribed bending samples, estimating their fatigue lives with an accuracy of e=±20% (Fig. 6.13 a)). As for tension specimens, only the 50 μm deep, 5 μm root radius scribes diverged from the data common power function trend, showing fatigue lives smaller than the critical distance estimations (Fig. 6.13 a)). Such divergence was due to the fact that, in spite of the fatigue life correlation, data of scribes with 5 μm and 50 μm root radii maintained trends with different slopes (Fig. 6.13). This was especially evident for clad bending samples where fatigue lives of 5 μm and 50 μm root radius scribes showed well-distinct slopes and $\Delta\sigma_{lm}$ was not able to accurately correlate all the experimental data (Fig. 6.13 b)). Several total lives, in fact laid outside the ±20% accuracy band of the critical distance analytical prediction (Fig. 6.13 b)).

The differences in the critical distance estimation accuracy and data correlation between bending clad and unclad samples could be caused by using the same value of L_{lm}=38.11 μm for unclad and clad aluminium alloy. As they are actually two different materials, according to the critical distance theory they should have different values of L_{lm} [48-51]. However that should have held true also for scribed tension samples, where the line method prediction accuracy for clad and unclad specimens was not so dissimilar (Fig. 6.11). The critical distance line method, calculating an averaged elastic stress in proximity of the notch root is more accurate in predicting the number of cycles spent to initiate a crack at the scribe root than the total fatigue life of components. Therefore total lives of notched components can still be accurately estimated using critical distance methods if crack propagation life is a small fraction of the fatigue life up to failure. Bending scribed samples showed longer crack propagation lives compared to the corresponding tension specimens (section 6.2.3). Therefore the critical distance theory should be less accurate for bending samples, where crack propagation life was a larger portion of the total life, than for tension specimens. That is believed to be a possible explanation for the different trends maintained by the fatigue lives of scribed bending samples with 5 μm and 50 μm root radii when plotted against $\Delta\sigma_{lm}$ (Fig. 6.13).

6.1.5 Diamond tool vs. in-service scribes

Diamond tool machined scribes, due to their regular and controllable geometry, were suitable to investigate the effect of scratch geometry on the fatigue life of scribed samples. In fact the scribing procedure ensured the accurate control of scribe depth and root radius, necessary to have the reproducibility of fatigue tests (section 3.1.2). Obviously regular diamond tool scribes were far from being representative of in-service scratches, which can be produced by sealant removal from fuselage joints during maintenance operations. Even if machined and in-service scratches showed similar shapes, the different scribing procedure inevitably altered the material hardening and plasticity at the notch root, affecting fatigue crack nucleation and early propagation from scratches. In fact, whereas diamond tool scribes were machining cutting the material, scrapers or metal knifes, inappropriately used by maintainers to remove sealant, generated scratches mainly ploughing and deforming the material at every tool pass [17-19]. The plastic deformation resulting from the material ploughing modified the local stress field and hardening at the notch root, where fatigue cracks developed.

Some investigations were performed at Cranfield university to analyse the local material and mechanical alterations produced on clad and unclad 2024-T351 aluminium alloy sheets by the introduction of diamond tool and like in-service scribes [17-19]. Such local alterations inevitably affected the capability of scribes to initiate fatigue cracks. Like in-service scribes were introduced by hand or machined with a milling machine using plastic scrapers, Stanley knife blades, manufactured aluminium alloy and high strength steel tools [17-19]. Plastic scrapers, recommended for sealant removal, were not able to damage clad and unclad 2024-T351 aluminium alloy samples, producing scratches on their surfaces [17]. Like in-service scribes showed an increase level of material hardness around their profiles and compressive residual stresses at their roots close to the material yield strength, caused by the ploughing nature of the scribing process [19]. The material hardness and the residual stress magnitude seemed to be independent of the scribe depth [19]. Tools commonly available within the aircraft maintenance environment, since their inability to properly cut materials by shaving removal, introduced scribes on aluminium samples ploughing their surfaces. The surface material was therefore plastically deformed, producing local hardening around the newly formed scribe [19]. Moreover the ploughing nature of the scribing procedure forced a portion of material in the neighbourhood of the scribe root to plastically expand. Such expansion was however prevented by the surrounding elastic material creating a compressive residual stress field at the scribe root. The occurrence of plastic deformation for like in-service scribes was pointed out by the material piling up at the scratch flanks [17-19].

Diamond tool machined scribes did not show any material hardening around their profiles, and negligible levels of tensile residual stresses were measured at their roots [1,19]. Those experimental findings, together with the absence of material piling up at the scribe flanks (Fig. 3.7), confirmed by the scanning confocal measurements performed by Tizard [19], proved the cutting nature of the scribing procedure developed using diamond tipped tools. However if it is damaged, even the diamond tool is not able to properly cut the material, introducing scribes by ploughing the aluminium sample surface. In fact Khan [1], investigating scribes produced by a damaged diamond tool,

found an increase of work hardening at the notch root, but associated with severe tensile residual stress fields. Scribes machined by the damaged diamond tool, as scratches produced by conventional maintenance tools, were characterised by a large amount of plastic deformation, pointed out by the material piling up at the scratch flanks [1]. Plastic deformations were a consequence of the fact that the damaged diamond tool scribed the samples by ploughing the material rather than cutting them. Scribes machined by damaged diamond tools were therefore considered like in-service scribes.

Like in-service scribes were introduced on clad and unclad 2024-T351 aluminium alloy samples, which were subsequently fatigued under constant amplitude tensile load to assess the scratch capability to initiate fatigue cracks [17-19]. For sake of comparison with diamond tool scribes, tensile fatigue tests of like in-service scribed samples were performed testing the specimen geometry used for this PhD research (Fig 3.1) at a maximum stress of σ_{max}=200 MPa and at a stress ratio of R=0.1 [17-19]. Fig. 6.14 shows the total fatigue lives of unclad tension samples, weakened by diamond tool and like in-service scribes, plotted against the scratch elastic stress concentration factors. Fatigue test results of diamond tool scribes were compared to those obtained by Morency [16], testing 5 μm root radius scribes machined by a damaged diamond tool and by Tizard [19], who fatigued samples scribed by an high strength steel tool (Fig. 6.14). Runout samples are indicated by arrows in Fig. 6.14, while open symbols specified specimens which failed at their edge rather than at the scribe root.

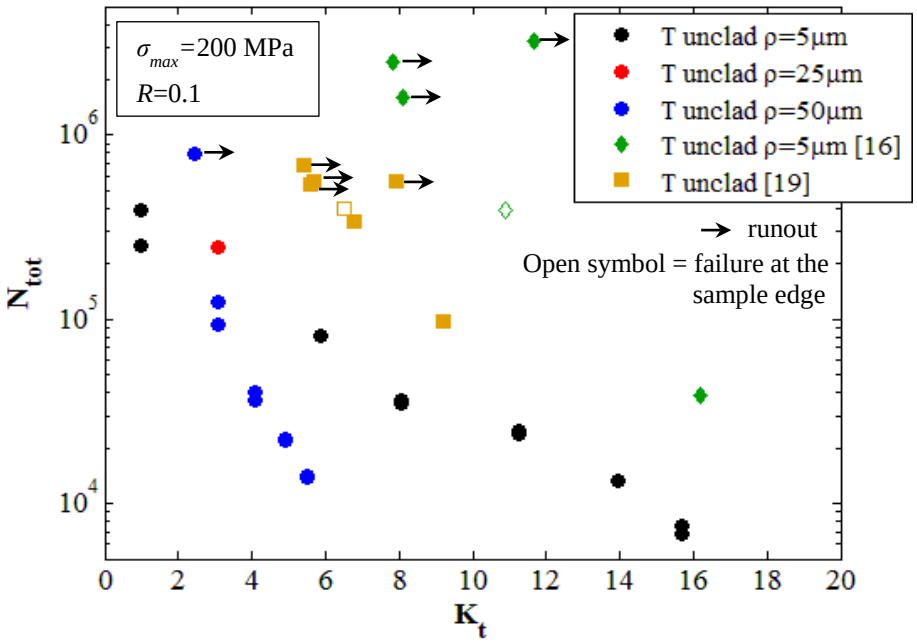

Fig. 6.14: Comparison between the total fatigue life of unclad samples weakened by diamond tool and like in-service scribes

Like in-service scribes were more averse than diamond tool ones to initiate fatigue cracks (Fig. 6.14). For scribes produced by common maintenance tools in fact a stress concentration factor of K_t=6 seemed to exist, below which scratches did not affect the sample fatigue life [19]. No propagating cracks were observed to nucleate at the root of scribes with K_t<6 (Fig. 6.14). Such threshold was shifted up to K_t=11.6 for scribes

machined by the damaged diamond tool [16] (Fig. 6.14). Generally unclad tensile samples, weakened by like in-service scratches, showed longer fatigue lives than those containing diamond tool scribes with the same nominal elastic stress concentration factor K_t (Fig. 6.14). All the like in-service scribes data, among which are included also the scratches machined by the damaged diamond tool, were in fact well above those of undamaged diamond tool scribes. Fig. 6.15 shows the comparison between the fatigue lives of clad tension samples containing diamond tool and like in service scribes. Fatigue lives of diamond tool and like in-service scribed clad samples are plotted as function of the scratch K_t in Fig. 6.15. Fatigue data of like in-service scribes, obtained by Irving et al. [15] using an high speed steel tool, Morency [16] with a damage diamond tool, Walmsley [17] by plastic and aluminium scrapers and Jozelich [18] using aluminium tools and Stanley knifes, were compared with those of diamond tool scribes (Fig. 6.15).

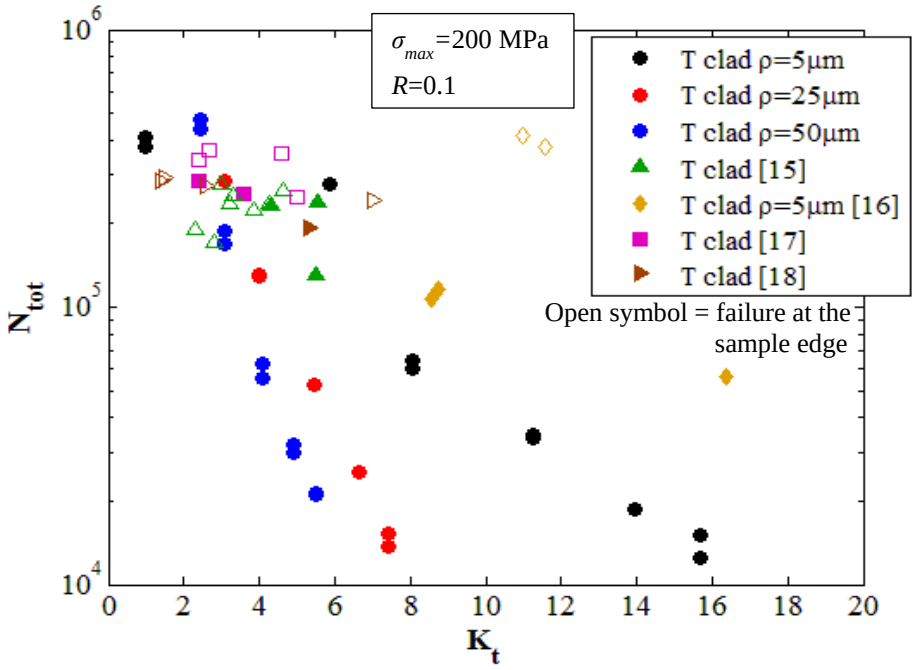

Fig. 6.15: Comparison between the total fatigue life of unclad samples weakened by diamond tool and like in-service scribes

Also in clad specimens, crack initiation at the root of like in-service scratch was more difficult than for diamond tool scribes (Fig. 6.15). Only the scratches, penetrated into the material substrate and with large enough nominal elastic K_t had the probability to initiate fatigue cracks [15,17,18]. Irving et al. [15] and Walmsley [17] found stress concentration threshold values respectively of K_t=4 and K_t=5.5 below which like in-service scratches were not able to nucleate propagating cracks. For scribes machined by the damaged diamond tool, fatigue crack nucleation and propagation from the scribe root was possible even if it was embedded into clad layer, like for nominal 50 μm deep scratches [16]. That was thought to be caused by the sharpness of the 50 μm deep 5 μm root radius damaged diamond tool scribes which showed stress concentration factors around K_t=8.5 (Fig. 6.15). However all the like in-service scribes in clad tension samples were less damaging than diamond tool ones. In fact for a given stress

concentration factor, like in-service scratched samples showed longer total fatigue lives than those weakened by diamond tool scribes (Fig. 6.15).

Generally scratches like, those found on in-service aircraft were less damaging for clad and unclad 2024-T351 aluminium alloy sheets than scribes precisely machined by diamond tools. Clad and unclad tension samples, in fact, showed longer total fatigue lives, when they were damaged by like in-service scratches rather than by diamond tool ones with the same nominal elastic stress concentration factor K_t (Fig. 6.14 and Fig. 6.15). The increase in material hardness and the compressive residual stresses, caused by the ploughing nature of the scribing process, are believed to be responsible for the improved fatigue performances of like in-service scribed samples [19]. In fact the material hardening and the compressive residual stresses could prevent or retard crack initiation and early propagation at the scribe root making the total lives of like in-service scribed samples longer than those of diamond tool ones [19]. A fatigue life prediction method based on the experimental data of diamond tool scribed samples results therefore conservative when applied to real world scratches found on in-service aircraft.

Another possible difference between reproducible diamond tool scribes produced in laboratory and scratches found on aircraft during maintenance can be their geometry. Generally in-service scratches showed rounded V-shapes (Fig 1.2) but sometimes they can have very irregular profiles (Fig. 4.3 b)). Jozelich [18] studied the geometric characteristics of like in-service scribes. He found that such scratches, contrary to well defined V-shaped scribes machined by diamond tipped tools, had an irregular geometry that cannot be totally defined by the notch depth, root radius and included angle [18]. However the linear elastic stress field in the neighbourhood of irregular real world scribes, calculated by finite element analyses, was found to be mainly characterised by the geometry of local pits and undulations rather than by global geometrical parameters. For that reason the idealisation of the in-service scratch irregular profile as an equivalent U or V-shaped notch provides anyway a good approximation of the local stress field at notch root, with an error no bigger than 8.5% [18].

6.2 Crack development from scribes

Crack nucleation and propagation processes from scribe roots, leading to sample failure under tensile and bending fatigue cycles are discussed in the following section on the basis of the results of fractographic post-failure observations (section 4.2). Facture surface different morphologies and features were related to different stages of crack development in clad and unclad samples. How the scribe geometry, influencing the local cyclic stress and strain fields, regulated crack nucleation and early propagation in proximity of the scratch root, it was investigated, correlating fracture surface characteristics with finite element stress analysis results. The effect of cladding and loading conditions on crack development was discussed as well, considering the fracture front morphology. The peculiarities of the scribe marks problem and in general of considering the effect of scratches on component fatigue behaviour were also highlighted.

6.2.1 Problem scale

Analysing the effect of scribe marks on component fatigue performances it is a particular notch fatigue problem, where the examined stress concentrators are scratches several centimetres long but few tens of microns deep. According to the direction taken into account, the fatigue problem has thus two different scales which place scribe marks, and in general any kind of long superficial scratch or defect, in an intermediate position between conventional engineering notches, several millimetres in size and small defects the size of the material characteristic microstructural lengths [60-62]. Locally crack nucleation and early propagation at the scribe root and at micro-scale defects occur in an analogous way, being regulated by similar microstructural and mechanical phenomena. Due to their small depths in fact, both defects [60-62] and scribes (section 5.4.1) show stress raising regions the size of few grain diameters. The reduced extension of the local notch stress concentration area makes crack nucleation and especially early propagation extremely sensitive to the material microstructure [63-65]. Short crack growth generally occurs along crystallographic planes and microstructural barriers, like grain boundaries, can slow down or even arrest propagating cracks [63-65].

However for long defects as scribes, the notch root is extended across many grains. Since the scribe cross section is nominally constant, stress conditions are almost identical at any location along the scratch length. Therefore, according to the local microstructure variability, several multiple cracks can nucleate simultaneously and interact in the early stage of their propagation (section 4.2.3), reducing the strong microstructural influence. If a long region of possible crack nucleation sites exists, like for scribe marks, the microstructure variability is averaged over many grains and the fatigue crack nucleation process results less affected by the material microstructure [70]. If at a small superficial defect the size of few grain diameters on a component crack nucleation is prevented by an unfavourable grain orientation, it will not affect the fatigue life of such mechanical component. On the other hand along the root of a scribe several centimetres long it is likely that, under the same loading conditions, a favourably oriented grain exists and fatigue cracks can nucleate reducing the component fatigue life. The same concepts can be applied to crack propagation. In fact a long scribe, with uniform local stress conditions at its root, generally promotes the formation of elongated crack fronts, due to the nucleation of multiple cracks and their coalescence during propagation (section 4.2.3). As the tip of an elongated crack also encompasses many grains, the microstructural variability will be averaged reducing the microstructural influence on short crack growth [70]. That does not happen for short cracks nucleated by micro-scale defects which show a strong dependence on the material microstructure, (microstructurally short-crack) (section 2.2.4.1).

Because of the different crack nucleation and propagation behaviours, caused by the length of the scribe root, conventional fatigue strength and life prediction methods for small notches [60-69] cannot be applied to correctly estimate the fatigue life reduction produced by scribes. However, due to the small scribe depth altering the notch sensitivity, also the life prediction methods based on fatigue-notch factor [27,28] and local strain approach (section 6.1.3), commonly used for engineering size notches, are not able to characterise the fatigue behaviour of scribes and scratches.

The small scale of scribes also makes the application of conventional continuum mechanics to calculate local stress and strain fields in the notch neighbourhood questionable. In fact since the problem geometrical dimensions have the same order of magnitude as the microstructural characteristic length, the assumption of medium continuum, homogenous and isotropic, at the basis of the continuum mechanics, breaks down [71]. Every equation, modelling material deformation process inside the frame of continuum mechanics, is valid independently on the integration domain being few microns or meters in size. That is consequence of the hypotheses of continuum and homogeneous medium at the basis of conventional continuum mechanics deformation theories [21,71]. Every material is ideally modelled as composed by a continuum medium, without any voids, showing the same material properties at each location (homogeneous). However a scale effect is intrinsically hidden behind such hypotheses. It is well known that real engineering materials, and in the specific case metals, contain defects, inclusions and microstructural grain textures, introducing local material unhomogeneities. Hence material properties actually depend on the location inside the material, since grain size and orientation, inclusion and defect distributions are themselves random functions of the spatial position. Metallic materials are therefore intrinsically non homogeneous. However as long as the scale of the mechanical problem is orders of magnitude larger than the characteristic microstructural length, the material properties and mechanical response are averaged out over many randomly oriented grains and the assumption of homogeneity can be applied with large accuracy [21,71]. That is the case of conventional stress analysis of notched mechanical components.

There is a length below which homogeneity assumption and continuum mechanics approach loose validity and their applicability results, thus, scale dependent. For scribes comparable in size with the characteristic microstructure length such assumption breaks down and the continuum mechanics characterisation of stress and strain fields can differ substantially from the real conditions, affected by the microstructural inhomogeneity. In fact the global behaviour of a material portion, containing the notch and large enough in comparison with the microstructure size, will be accurately predicted. On the contrary stress and strain gradients ahead of notch root, where fatigue cracks develop and therefore necessary for crack nucleation and growth prediction, extend across few grains and so their continuum mechanics calculation will be inconsistent (section 5.4). Effective local stress and strain fields near the scribe root will be strongly influenced by the local microstructure as the region subjected to the notch stress raising effect is few grain diameters deep. Due to the scribe length and the microstructure inherent heterogeneity, different sections along the scribe root will experience different stress fields. Accurate mechanical characterisations of the scribe mark effect should require, therefore, computationally expensive stochastic models, considering the microstructure variability and based on crystal plasticity [72,73].

However, due to the scribe length, conventional continuum mechanics stress analyses can still characterise the global mechanical behaviour along the entire scribe root, averaging out local microstructural responses. The large number of randomly oriented grains along the scratch length in fact ensures the validity of the material homogeneity assumption, where material properties are the average of the local ones of different grains. During this research, it was decided to characterise such average notch

mechanical behaviour by means of finite element analyses, modelling the aluminium as a continuum homogenous medium (section 5.1). Local real stress conditions, depending on the material microstructure variability, were neglected to have the average knowledge of homogeneous stress fields. Fatigue crack nucleation and early propagation are sensitive to local stress conditions inside single grains, but, since nucleation from multiple sites along scribe roots occurred (section 4.2.3), an average stress and strain field characterisation was thought to be more indicated to describe the scribe effect in fatigue. It is computationally less expensive than crystal plasticity models [72,73], which include different properties for every grain, and it is still able to give indication about the mechanical conditions, where crack nucleation and early propagation took place.

6.2.2 Crack nucleation

The crack nucleation process under cyclic loading at the scribe root of different 2024-T351 aluminium alloy samples is discussed in this section. Scribes reduced specimen fatigue lives by nucleating fatigue cracks at their roots, which under fatigue loading grew up to sample complete failure (section 4.2.3). Fatigue cracks nucleated at the scribe root and grew through the sample thickness in clad and unclad tension and bending scribed specimens. Multiple crack initiation under tensile and bending loads occurred usually from inclusions, defects or weak points along the scribe root (section 4.2). The nucleation mechanism was consist with that observed by Nader [2] for scratches on the surface of clad 2024-T3 aluminium samples. A similar multiple nucleation was also observed Das et al. [74] at the root of scribe marks on longitudinal and circumferential aircraft fuselage joints. The region in front of the scribe root is affected by raised stresses and plastic deformations produced by the notch (see chapter 5.4). It is not surprising therefore that crack nucleation occurred at the scribe root in every scribed sample, since it was the zone of higher available energy, where dislocation motion, responsible for crack formation, was favoured. Stress conditions were nominally the same along the notch root but the local material microstructure varied in grain size and shape, orientation and inclusion and constituent particle distribution. The microstructure variability implied that crack nucleation took place at the most favourable locations along the notch root, where microstructure conditions (grain size, orientation and or inclusion size) were such to promote crack formation [22-26].

The number and density of crack nucleation sites seemed to be determined by the scribe sharpness, increasing for deeper notches with smaller root radii. According to the number of nucleation points, multiple cracks could coalesce during their propagation, forming fracture surfaces with different shapes (section 4.2.2). For scribes deeper than 50 μm in clad and unclad tension samples, the big number of active nucleation points made short cracks coalesce during their early propagation, forming a unique fracture front elongated along the whole sample width (section 4.2.3). Scribes shallower than 50 μm in tension samples showed fracture surfaces made of multiple thumbnail and corner cracks, up to a maximum of 15 cracks per sample. That confirmed the activation of multiple nucleation points at the scribe root (section 4.2.3). Tension clad and unclad specimens, weakened by 50 μm deep scribes, developed a unique elongated fracture front only for notch root radii as sharp as 5 μm. In presence of notches with 25 μm and

50 μm root radii in tension samples, elongated crack fronts showed arrays of parallel coalescence steps (coalesced front), proving that the fracture front was made up of several cracks coalesced together (section 4.2.2). Under bending loading, the transition between multiple crack and elongated fracture fronts occurred in presence on scribes as deep as 100 μm.

Single coalesced crack fronts were produced by the coalescence of several cracks, separately nucleated at notch roots (section 4.2.2). Scribed tension samples, failed developing single coalesced crack fronts on their fracture surfaces, exhibited, therefore, a multitude of nucleation points all along the scribe root. Preferential nucleation sites were voids and defects produced at the notch root, during the scribing procedure, and weak points, likely to be in grains with slip systems favourably oriented for dislocation motion (Fig 4.13 b)). Due to the large number of active sites along the scribe root, some nucleation points resulted inevitably few tens of microns far from each other. Depending on the spacing of nucleation points, cracks could coalesce during their early microstructure sensitive growth or when stage II propagation was already developed. The fracture surface morphology suggested that nucleation of different cracks took place almost simultaneously at various notch root locations. In fact steps were almost evenly spaced, indicating the nearly simultaneous growth of multiple cracks (Fig 4.13 b)). Multiple cracks coalesced during their propagation to form a single front. It was the further growth of such unique fatigue fracture front, made by cracks propagating on parallel plane, that leaded to sample failure.

Tension samples failed by means of single elongated fronts did not show any evidence of multiple cracks nucleation or coalescence along their scribe roots (Fig 4.14). They seemed to generate suddenly a short 2D through sample width crack from the notch root. Obviously the simultaneous nucleation of a through-crack from a scribe root 80 mm long was a circumstance highly improbable to occur. Because of the material microstructural inhomogeneity, definitely at the notch root were favoured spots, where nucleation process was quicker than in other locations. However the spreading of the entire nucleation process along the scribe root was so rapid that no evidences of multiple crack nucleation or coalescence were observed. Even if inclusion particles and machining introduced defects were observed at the scribe root, they appeared to be situated on the crack growth plane rather than being favourite sites for crack nucleation (Fig 4.14). It is likely that a single crack, few microns deep, but running all along the notch root length was produced as result of the nucleation stage. The orientation perpendicular to the scribe line of characteristic arrays of crystallographic lamellae and steps, found at the notch root, indicated a likely homogeneous growth of the entire crack front through the sample thickness. In fact, if multiple surface cracks had developed and grown, the lamellar steps, being parallel to the local crack propagation direction, would have assumed a radial disposition pointing to the nucleation point as in Fig 4.13 a).

If scribe roots were completely embedded into the clad layer, as in the case of 25 and 50 μm deep scribed clad tension samples, no substantial changes of the various nucleation mechanisms, described above for unclad specimens, were observed. Different crack development processes, producing different fatigue surface morphologies, occurred in a similar way into both 2024-T351 aluminium alloy substrate

and soft pure aluminium cladding. The number of multiple nucleation sites along notch roots were approximately the same (Table 4.6), despite the cladding, and depended only on scribe geometry. The only difference for clad samples with scribe roots contained into cladding was that no nucleation from inclusions or machining defects were observed. The only nucleation mechanism available inside the clad layer seemed to be the formation of slip bands by dislocation motion on grain slip systems. That was a consequence of the absence of inclusion intermetallic particles inside the superficial clad layer.

Scribe geometry seemed to regulated the fracture surface morphology of fatigue samples tested in tension and bending loads (section 4.4.2). That was a mere consequence of the scribe stress concentration effect on crack nucleation and early propagation stages. The region in front of the scribe root, where crack nucleation and early propagation took place, was affected by the cyclic stress field and the relative plastic zone produced by the notch. The magnitude of local stresses and strains as well as the extension of the notch affected region are functions of different scribe size and shape (section 5.4). Obviously such local stress and plasticity play a fundamental role in early fatigue crack development, that is therefore regulated by the notch geometry. Fig. 6.16 shows the correlation between the fracture surface morphology and the local cyclic stress a strain condition at the scribe root for unclad tension and bending samples. The longitudinal elastic-plastic stress range, $\Delta\sigma_{22,}$ calculated at the scribe root after the cyclic response stabilisation (section 5.4) is plotted against the corresponding longitudinal strain range, $\Delta\varepsilon_{22}$, for tension and bending samples (Fig. 6.16). A colour code indicates fracture surface morphologies divided into multiple crack fronts (MC), coalesced crack fronts (C) and elongated crack fronts (E) (Fig. 6.16). For those samples showing a fracture front consisting of multiple thumbnail cracks, the crack number is displayed as well in Fig. 6.16.

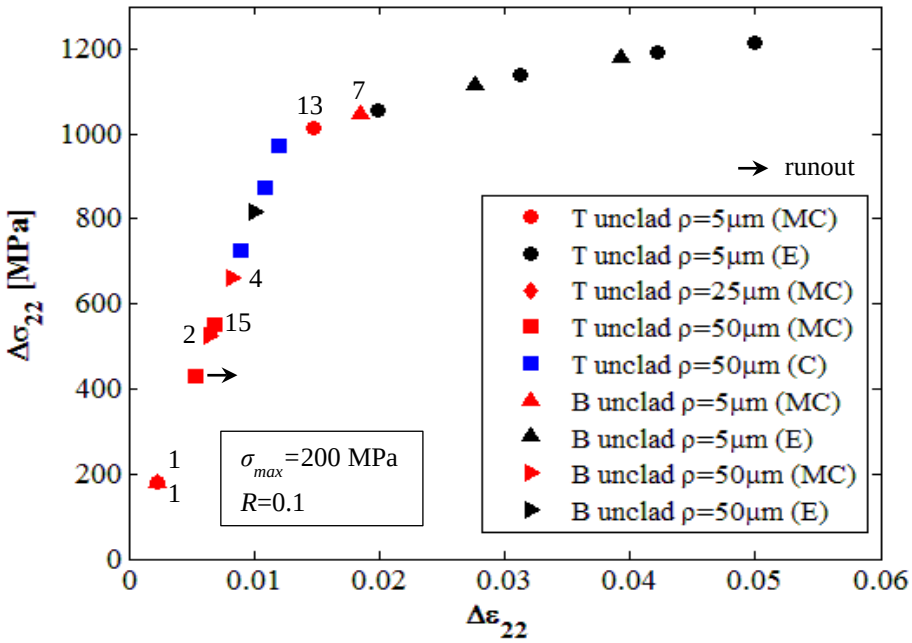

Fig. 6.16: Correlation between notch root local longitudinal stress and stain ranges and the fracture surface morphology for unclad tension and bending samples

Data of tension and bending samples lays on a unique curve when the local longitudinal stress at the scribe root is plotted versus the longitudinal strain range (Fig. 6.16). Such curve is related to the cyclic stress-strain curve of the material (section 5.4). The fracture front morphology seemed to be regulated by local longitudinal stress and strain magnitude at the scribe root (Fig. 6.16). If the local strain range $\Delta\varepsilon_{22}$>1.85%, tension and bending samples failed showing an elongated fracture front (Fig. 6.16). At this strain range level the material showed a local cyclic plastic response and a stable cyclic plastic zone developed at the scribe root (section 5.4.1.1), as also indicated by the non-linear portion of the data trend curve in Fig. 6.16. On the hand when the elastic-plastic strain range at the scribe root $\Delta\varepsilon_{22}$<0.89%, the material cyclic response was purely elastic and a fracture front composed by multiple thumbnail cracks was observed for tension and bending unclad specimens (Fig. 6.16). In the transition region 0.89%≤$\Delta\varepsilon_{22}$≤1.85%, where the material began to develop an inelastic cyclic response at the scribe root, tension and bending samples showed elongated, coalesced, or multiple crack fracture fronts, depending on scribe depth and loading condition (Fig. 6.16).

Local elastic-plastic $\Delta\sigma_{22}$ and $\Delta\varepsilon_{22}$ at the scribe root are function of the scribe aspect ratio and consequently of the notch elastic stress concentration factor (Fig. 5.20). The sharper the scribe, the larger K_t, and the higher the elastic-plastic longitudinal stress and strain ranges at the notch root. The magnitude of $\Delta\sigma_{22}$ and $\Delta\varepsilon_{22}$ is related to the elastic-plastic mechanical work done at the scribe root at any fatigue reversal, giving an indication of the energy available for crack nucleation during cyclic load. Therefore, a correlation exists between the energy available to form a new crack at the scribe root and the notch shape, expressed by the elastic K_t. Both of these parameters can define the fracture morphology of tension and bending scribed samples. Fig. 6.17 shows the correlation between the scribe stress concentration factor, the longitudinal elastic-plastic mechanical work done at the scribe root, and the sample fracture morphology for unclad tension and bending samples. The elastic-plastic work, w_{22}, performed by the longitudinal stress, σ_{22}, on the longitudinal strain, ε_{22}, at the scribe root during every reversal, after the material cyclic stabilisation, is plotted against the scribe elastic stress concentration factor for tension and bending samples (Fig. 6.17). The longitudinal internal plastic work was calculated as follows:

$$w_{22} = \int_{\varepsilon_{22}^{in}}^{\varepsilon_{22}^{fin}} \sigma_{22}\varepsilon_{22} d\varepsilon_{22}\Big|_{root} \tag{6.10}$$

where ε_{22}^{in} and ε_{22}^{fin} are respectively the scribe root longitudinal strain at the beginning and at the end of every stable cyclic reversal. Since the elastic plastic longitudinal work was calculated in a singular point, that is at the scribe root, it is a mechanical work density, measured in MPa [21]. Different sample fracture surface morphologies are characterised by different colours in Fig. 6.17. The longitudinal elastic-plastic work, w_{22}, representing the amount of irreversible energy available to dislocation motion at the scribe root, was regulated by the scratch stress concentration factor, increasing as K_t increased (Fig. 6.17). As for the elastic-plastic local values of $\Delta\sigma_{22}$ and $\Delta\varepsilon_{22}$, tension and bending samples showed different fracture surface morphologies, according to different amount of longitudinal plastic work, w_{22}. As explained above, the longitudinal plastic work is related to the notch sharpness, that is to K_t (Fig. 6.17). The scribe elastic stress concentration factor, easier to calculate than the elastic-plastic stress and strain ranges, can therefore be used to define the fracture morphology. If K_t>7.76 tension and bending

samples fractured, developing an elongated fracture front, while for K_t<4.08 a fracture front consisting of several multiple cracks was observed (Fig. 6.17). For intermediate ranges of scribe stress concentration factors, 4.08≤K_t≤7.76, specimens showed mainly coalesced crack fronts, even if multiple cracks and elongated fronts could develop, depending on scribe geometry and loading condition (Fig. 6.17).

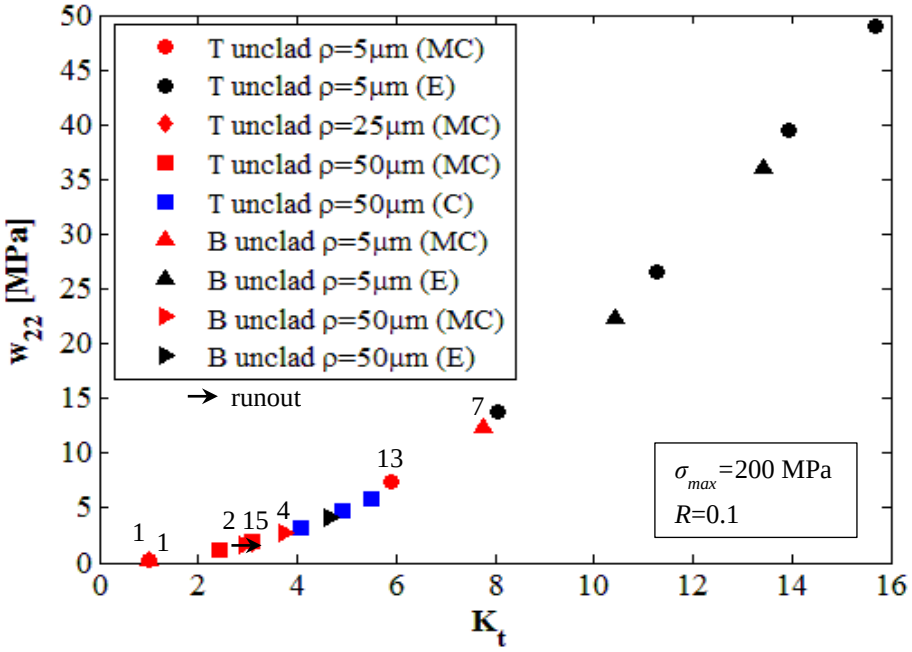

Fig. 6.17: Correlation between notch root local longitudinal elastic-plastic work density, w_{22}, elastic, K_t, and the morphology for unclad tension and bending samples

To conclude the notch stress concentration factor seemed to regulate local elastic-plastic stress and strain ranges, defining the fracture front morphology of scribed tension and bending samples. That was a consequence of the control exerted by local stress and strain conditions on the number of activated crack nucleation sites at the scribe root. If the stress and strain acting on the nucleation site increases, as in the case of sharp notches, the number of potential nucleation points will be larger (Table 4.6). In fact raising the stress and strain, the available amount of force, driving dislocations motion, increases, activating additional slip systems in grains less favourably oriented, or from smaller inclusion particles [22]. Thus crack nucleation process can occur in a larger number of spots at the scribe root. In energetic terms, crack nucleation is regulated by the balance between available dislocation motion driving energy, proportional to the local stress, and a motion resistance energy, characterised by local microstructural conditions [22]. The bigger the stress and strain at the scribe root, the larger the probabilistic distribution of microstructural conditions able to initiate a crack, and the number of nucleation points increases [10].

For shallow and blunt scribes with K_t<4.08, corresponding to $\Delta\varepsilon_{22}$<0.89% at their roots, like in 25 μm deep 25 μm root radius scribed tension samples, the local available mechanical energy was such to activate few nucleation points. Crack nucleation therefore occurred only inside grains favourably oriented or from inclusions and defects offering weak resistance to dislocations motion. Cracks grew from those sparse sites,

scattered along the scribe root, generating fracture fronts made by multiple superficial flaws. If the notch was sharp enough, $4.08 \leq K_t \leq 7.76$, to reach elastic-plastic longitudinal strain ranges, $0.89\% \leq \Delta\varepsilon_{22} \leq 1.85\%$ at its root, the resistance to dislocations motion was overcame on several slip systems. Therefore, as in the case of 185 µm deep 50 µm root radius scribed tension samples, a large number of nucleation points was observed. The linear distribution of activated sites along the scribe root was so dense that initiation points were few tens, sometimes hundreds, of microns close to each other. The multiple nucleated cracks, thus, could coalesce in the early stage of their propagation to form a single elongated fracture front, where coalescence steps were clearly visible (Fig. 4.13 b)). A coalesced fracture front or a front, consisting of a large number of superficial cracks was therefore observed on such sample fracture surfaces. Once the scribe was very sharp, $K_t > 7.76$ to produce $\Delta\varepsilon_{22} > 1.85\%$ at its root, as in the case of 185 µm deep 5 µm root radius scribed tension samples, the local energy was high enough to activate dislocations motion in almost every grain along the notch root. In a short time a crack few microns deep but lengthened along the entire scribe length appeared at the notch root (Fig. 4.9 a)). The nucleation process was so spread on different grains that no signs of crack coalescence, even at micrometric scale level, were found. The further growth of such 2D through sample width crack produced an elongated fracture front.

6.2.3 Short crack early propagation

The early stage of crack grow process, when newly developed cracks were subjected to the local high stress produced by the scribe stress concentration effect, is discussed in this section. Multiple nucleated cracks grew away from the scribe root under fatigue loading, until the main crack developed unstable growth, breaking the sample. If nucleation points were close enough, cracks could coalesce during propagation to form a bigger surface flaw. No information was available on when cracks developed at different nucleation sites. It is not known if all the cracks nucleated at the same time along a scribe and the main crack became larger during its growth, or if secondary cracks initiated after the main flaw initiation as consequence of the stress increase produced by the net gauge section reduction. Nucleated cracks began to grow as small surface flaws in the region affected by the notch stress field. Even if the characteristic facets of stage I growth were absent on the fracture surfaces (Fig 4.13 a) and Fig. 4.14), early growth stage of multiple cracks, seemed to occur along crystallographic planes (section 4.2.3.2). It is worth mentioning that conventional stage I growth is normally not observed in presence of high stress as at the root of a notch [75].

In fact fracture surfaces, produced by early crack growth, showed arrays of parallel lamellar features which formed micro cliffs perpendicular to the local growth direction. Such lamellae converged toward the nucleation point facilitating its identification and showed smooth surfaces without any sign of striations on them (section 4.2.3.2). They appeared to be sensitive to the material microstructure, changing orientation and planar slope at grain boundaries (Fig 4.13 a) and Fig. 4.14). Therefore a kind of stage I like growth with different orientation in every grain should have taken place. Similar lamellar features were found on the aluminium fracture surfaces, analysed in [26,76]. They seemed to be produced by crystallographic propagation through grains showing a twist angle between their favoured slip systems. In fact the crack growth plane twist across grain boundaries was accommodated by a propagation into the next grain

characterised by a regular switching onto different planes of the same slip system, leaving steps on the fracture surface [76]. Such crystallographic crack growth on several parallel slip planes was a way to reduce the effective twist angle between final crack faces in two neighbouring grains. The occurrence of steps was controlled by the slip system twist angle: the larger the twist angle, the larger the size of those steps [76]. Cross-slip into other slip planes inside the same grain, promoted by shear stress, seemed to be the mechanism responsible for the formation of the side faces of steps (micro cliffs). The planar faces of the lamellae were smooth, because produced by growth on favoured slip planes, and obviously showed different tilt angles at the grain boundaries (Fig 4.13 a) and Fig. 4.14)).

The surface of small thumbnail cracks, growing through cladding, was characterised by a geometric structure composed by regular facets (see Fig 4.16 a)). Such features, typical of crystallographic stage I crack growth, were very similar to those distinguishing the structure sensitive crack growth through the clad layer found in reference [15]. It was evident that cracks propagated in cleavage-like stage I along parallel crystallographic planes, joined by steps, inside the same grain [75]. Growth plane orientation changed at grain boundaries. As soon as the crack get closer to the substrate the geometric structure was replaced by the ‘feathery’ corrugated features typical of crystallographic stage I growth in 2024-T351 aluminium alloy (Fig 4.16 a)). The change of features was likely produced by the diffusion of precipitation particles into the clad layer near the clad-substrate boundary. The absence of precipitate particles into cladding made easier dislocation motion along crystallographic planes, promoting the formation of a proper facetted stage I surface, compared to that observed in the substrate [75]. When the precipitate density was high enough, ‘feathery’ corrugated fracture surface began to develop (Fig 4.16 a)). In some cases the cleavage-like stage I growth features were observed across the entire clad depth. Crack growth in the substrate was made recognisable (Fig 4.16 a)) by the development of lamellar features arrays like those found on the fracture surface of unclad samples (Fig 4.13).

In case of large thumbnail or through sample width cracks, growth into cladding generally resulted in a different fracture surface morphology (Fig 4.16 b)). It was much more amorphous than the growth through the substrate, which showed a more regular surface with crystallographic lamellae and steps. Crack propagation into cladding seemed to be structure insensitive, being perpendicular to the loading direction (section 4.2.3.3). No sighs of crystallographic facets, as in the case of the growth surfaces of small thumbnail cracks, were found. Propagation returned microstructure sensitive once the crack grew into the substrate. A similar clad layer fracture surface was found in reference [15]. What were the processes producing different clad fracture surface appearances, and why crystallographic facetted were likely to occur on the surface of small thumbnail cracks, it is not entirely understood yet. A possible explanation for such different behaviours could be imputed to different constrains along crack fronts. If the front of a newly formed crack ranged over many grains, as in the case of through sample width or elongated thumbnail cracks, growth planar constrain on the whole crack front produced an amorphous structure-insensitive surface. In fact growth congruence across differently oriented grains prevented the formation of crystallographic propagation on different planes in favour of an amorphous but uniform and globally flat surface, where multiple slip systems were activated. On the other hand,

if the crack front ranged over few grains, congruence constrains was not fully developed and crystallographic stage I growth could take place. The same clad fracture surface appearance was found in both bending and tensile samples.

If scribes were machined in unclad samples or they were deeper than clad layer thickness in clad specimens, cracks grew into the 2024-T351 aluminium alloy. No differences were observed in the morphology of fracture surfaces produced by cracks growing in unclad samples or in the material substrate of clad specimens (section 4.2.3.2). Fracture surfaces of unclad samples showed, close to the scribe root, a facetted aspect with arrays of lamellae and steps parallel to the local crack growth direction (Fig 4.17). Lamellar step surfaces were smooth with no signs of striations. Crack growth from scribe roots inside 2024-T351 aluminium alloy was therefore crystallographic (stage I-like), showing a strong microstructure sensitivity. Cracks nucleated from scribe marks exhibited microstructure sensitive early propagation, as in the case of naturally initiated cracks in unscribed samples (section 4.2.3.1). The only difference seemed to be the absence of 'feathery' corrugated features, observed only on unscribed sample fracture surfaces. Stage I like growth was observed in every region along the notch root, where cracks developed. Early crack growth seemed to be strongly influenced by the material microstructure despite different notch geometry, cladding and load condition.

However those parameters played a role on crack growth transition to transgranular stage II propagation. Scribe geometry, loading condition, and cladding regulated the depth of the fracture surface region at the notch root occupied by the microstructure sensitivity growth (microstructural short crack region). The deeper the scratch the shallower the region influenced by crystallographic propagation. 185 μm deep scribed tension samples showed transitions to transgranular growth nearly 50 μm far from the notch root (Fig. 4.19 a)), while for 50 μm deep scribes, transition took place, when cracks had grown about 100-130 μm through the sample thickness (section 4.2.3.3). Actually if the transition depth was measured starting from the sample free surface, growth shift to transgranular stage II seemed to occur at similar distances from the sample surface, under the same load conditions. In fact microstructure sensitive crack propagation appeared to develop on tension samples in a zone 180-235 μm deep from the sample surface despite different scribe geometries. Bending test samples had an increased depth of stage I growth which reached up to 240-285 μm (Fig. 4.19 b)). The transition between stage I and stage II growth seemed to be regulated by the crack tip plastic zone rather than by the notch plastic zone.

Early crack growth at the scribe root occurred inside the cyclic plastic zone and under the local stress field, produced by the stress raising effect of the notch (section 5.4). As notch geometry affects the local cyclic elastic-plastic longitudinal stress and strain distributions acting on the crack path (section 5.4.1.3), it will inevitably influence also the early stage of the short crack propagation. Scribe depth and root radius regulated the shape and the magnitude of the $\Delta\sigma_{22}$ and $\Delta\varepsilon_{22}$ elastic-plastic distributions along the notch bisector, defining the extension of the stress concentration region (Fig. 5.23). The notch stress raising effect affected a portion of the crack plane at the scribe root between 1% and 10% of the sample thickness, according to the scribe geometry (section 5.4.1.3). Moreover, the occurrence of notch root plasticity during the cyclic loading process, also caused the variation of local stress and strain ratios, R_σ and R_ε,

along the notch bisector (Fig. 5.23). However, because of the stress redistribution, produced by the formation of new free surfaces during crack nucleation and propagation [59], the length of the crack growth portion ahead of the scribe root influenced by the local notch stress field generally differs from the extent of the stress concentration region.

Finite element crack growth analyses were thus performed to investigate the effect of local scribe stress field on early crack propagation. The linear elastic stress intensity factor of cracks, propagating from the scribe root under tensile load, was calculated as function of the crack length in scribed samples. Cracks were assumed to grow along the notch bisector as 2D through-width flaws. Therefore just two dimensional plane strain finite element analyses were performed. An initial crack length of a_0=0.4 μm was introduced ahead of the scribe root. Then the nodes at the crack tip were progressively open, using the function disbound available in Abaqus [77], to simulate the crack propagation along the notch bisector under static tensile load. The *J*-integral around the crack tip was computed at every crack increment and the corresponding stress intensity factor derived [77]. Geometry factors, β, at the root of different scribes were calculated according to the crack length and compared to those of single edge cracks [78]. Fig. 6.18 shows the β geometry factors of through-width cracks propagating from the root of selected scribes under tensile load. For sake of comparison, β factors of edge cracks growing from the edge of unnotched specimens are showed as well in Fig. 6.18. To underline the crack driving force reduction, produced in this case only by the notch root radius, ρ, and also by the included angle for θ>90° [11-13], β factors were calculated measuring the crack depth, *a*, from the sample edge. However the β factor distributions were plotted against the distance from the respective scribe root, *x*. The crack depth, *a*, and the coordinate, *x*, were thus linked by the following relation:

$$a = d + x \tag{6.11}$$

As the origin of the coordinate system was placed on the scribe root and the crack depth was measured from the sample edge, different reference curves of the edge crack β factors are plotted, according to the scribe depth, *d* (Fig. 6.18). In fact for a given value of the coordinate *x*, the edge crack depth, and consequently the value of its β factor will change as the scribe depth, that is the position of the reference frame, varies (eq. (6.11)).

Close to the scribe root, due to the notch non-zero root radius, β factors of cracks growing from scribes were smaller than the corresponding values for edge cracks (Fig. 6.18). In fact the root radius alters the local σ_{22} stress at the scribe root, which reaches a finite value, reducing the available crack driving force [11-13]. The β factors near the scribe root were regulated only by the notch root radius, increasing as ρ approached zero (Fig. 6.18). Scribe depth seemed to increase the difference between β factors in proximity of the notch root and the corresponding edge crack values (Fig. 6.18). Moving away from the scribe root β factors of scribed sample cracks tent to merge the curves of edge cracks. The distance from the scribe root, *x* where cracks growing from scribes showed the same β factors of edge cracks and thus behaved as edge cracks with $a=d+x$, depended on the notch geometry. The smaller the notch root radius the smaller the distance from the scribe root where edge and notch crack curves merged (Fig. 6.18). Also the scribe depth affected the merging distance, which increased according to the value of *d* (Fig. 6.18). Such distance represents the size of the crack growth region affected by the local notch stress field. Scratches influenced early crack propagation up

to a distance from the notch root ranging from nearly x=10 μm, for 50 μm deep, 5 μm root radius scribes, to x=50 μm, in case of 185 μm deep, 50 μm root radius scribes (Fig. 6.18).

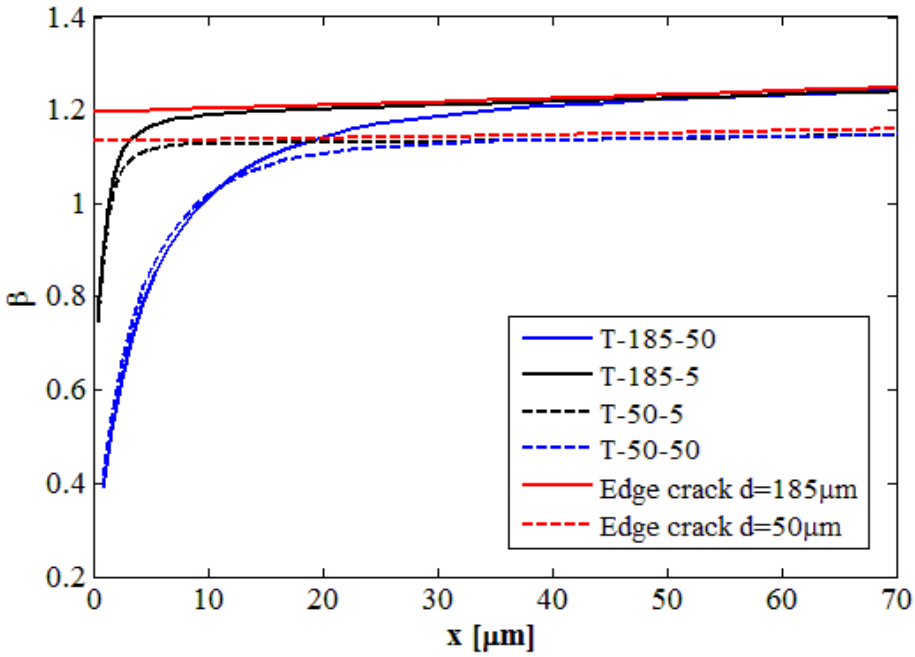

Fig. 6.18: Scribe geometry effect on geometry factor, *β*, of cracks emanating from scribe roots under tensile load

The β factor distributions in Fig. 6.18 also give an indication of the error committed, inside the frame of the linear elastic fracture mechanics, considering scribe marks as cracks. As expected, such error is bigger the larger the notch root radius and the deeper the scribe (Fig. 6.18). Scribed sample β factors were calculated performing linear elastic analyses, therefore they did not consider the short crack behaviour or the effect of local scribe root plasticity on crack propagation. Moreover a simple 2D through-width crack was assumed neglecting any kind of interactions or coalescences between multiple growing cracks. Nevertheless the performed analysis gave an indication of the crack grow region affect by the local scribe field. As different scribes affected early crack growth up to a maximum distance from their root of about x=50 μm, their influence was exerted only on the microstructure sensitive stage I-like crack propagation. When cracks developed the transgranular stage II growth, where striations were visible, the notch effect was already exhausted. That explains why striation counting data, measured at the root of different scribes, showed the same trend (Fig 4.28).

6.2.4 Crack propagation

Short crack growth rates measured by striation counting on tension and bending scribed samples are discussed and elaborated in this section. Striations were observed only in correspondence of the stage II crack growth development. Crack growth rate in tension specimens was found to be an exponential function of crack depth, which was independent of the scribe root radius (section 4.2.4.1). The effect of cladding and notch depth was to modify the sample net ligament length and the consequent finite thickness

influence exerted on cracks. In fact all crack growth data, despite different scribe geometry and cladding, were correlated by the sample thickness fraction parameter (section 4.2.4.1). Scribe geometry therefore did not influence crack growth data except for changing the sample net ligament length. That was due to the fact that scribe geometry affected early crack growth up to a maximum distance of x=50 μm from the notch root, while fatigue striations were clearly visible just 50-100 μm from the scribe root (section 6.2.3). The scribe geometry effect on short crack growth rate was identical under bending and tensile load. However the sample thickness fraction parameter was not able to unify growth rates of different scribed bending samples as accurately as under tensile loading (section 4.2.4.1). Such behaviour could be caused by the different fracture front of 50 μm deep 5 μm radius scribed bending samples, which showed a multiple crack front against the elongated ones, developed by the other measured specimens (Fig. 4.27). Under bending load, growth rates seemed to be approximated by a third degree polynomial function of crack depth. For small values of sample thickness fraction, cracks propagated at comparable rates under tensile and bending loads (Fig. 4.28). As soon as cracks became bigger, bending growth rate turned out to be slower than the tension one (Fig. 4.28). Moreover for cracks approaching the sample edge the development of a plastic hinge additionally reduced the growth rate under bending load (section 4.2.4.1).

Striations were clearly visible only when transgranular stage II growth developed, that is just 50-100 μm and 100-190 μm from the scribe root respectively under tensile and bending loads (section 4.2.3.3). The smallest measured growth rate was $3 \cdot 10^{-8}$ m/cycle, and the largest $8 \cdot 10^{-7}$ m/cycle (Fig 4.28). Elastic stress intensity factor ranges, ΔK, corresponding to measured crack lengths, were calculated for tension and bending samples, to compare the experimental growth rates of short cracks with the material Paris's curve. Only the main crack of each sample was considered, neglecting the propagation of multiple secondary cracks and their mutual interaction with the main crack, which led to specimen failure. Cracks were modelled as through-thickness, corner quarter-elliptic or surface semi-elliptical flaws, with shapes and geometrical characteristics listed in Table 4.6. Crack shape was assumed to remain constant during the whole propagation. As the scribe geometry was found to influence the crack growth up to a maximum of 50 μm from the scribe root, an initial crack length of a_{in}=50 μm was assumed for the calculation of stress intensity factor ranges. Doing so, cracks developed from scribe roots could be considered as conventional through thickness, corner quarter-elliptic or surface semi-elliptical, including the notch depth in the crack length (Table 4.6). The elastic stress intensity factor ranges could be therefore calculated from standard linear elastic fracture mechanics solutions [78,79]. The initial crack length a_{in}=50 μm was considered to be the initiation crack length, as no growth rate data were available for cracks shorter than 50 μm. The initiation life was therefore defined as the number of fatigue cycles required to nucleate a crack at the scribe root and propagate it up to a length of 50 μm from the notch root. Final critical crack length values, measured during post-failure fractographic investigations and listed in Table 4.6, were used for the ΔK calculation. Fig. 6.19 shows the experimental crack growth rate of scribed samples as a function of linear elastic stress intensity factor range, ΔK, together with the 2024-T351 aluminium alloy long crack curve, R=0.1, taken from [80] for the long transversal direction.

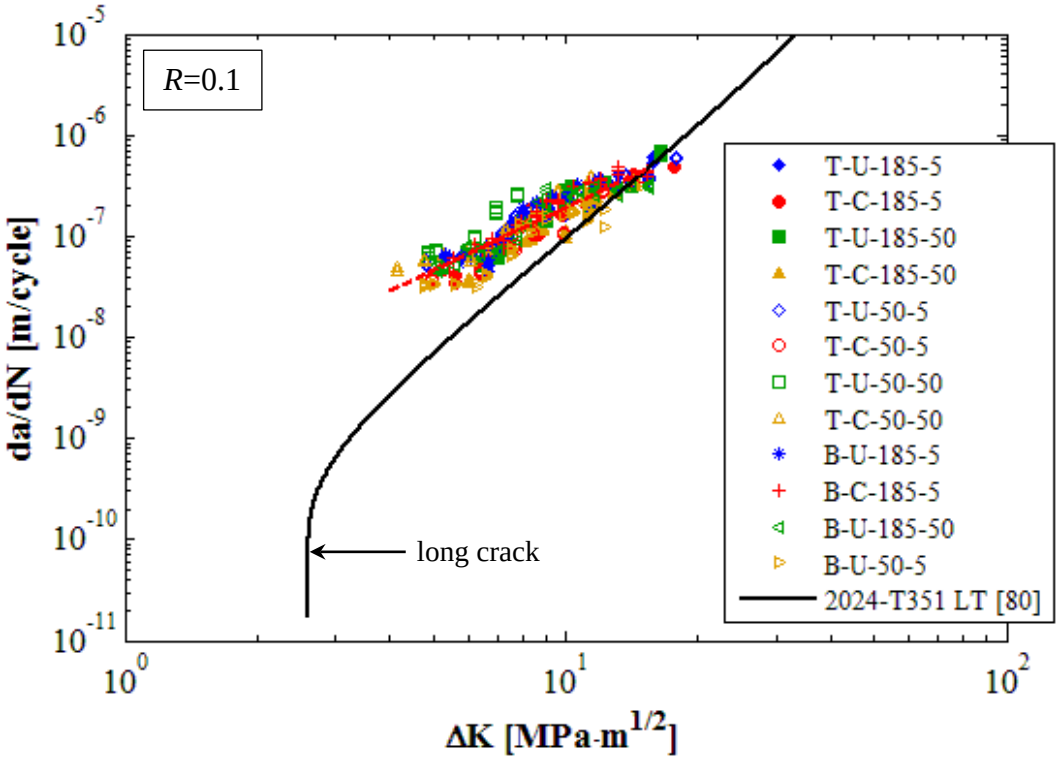

Fig. 6.19: Crack growth rates in different scribed samples

All data showed non-conservative short crack behaviour, with cracks growing faster than long crack growth rates for the same ΔK value (Fig. 6.19). The measured data met the long crack data just when crack length is approaching the final critical value for fast fracture (Fig. 6.19). Crack growth rates of different notches under tension and bending loads were correlated on a unique common trend line using standard linear elastic ΔK solutions for quarter-elliptical, semi-elliptical and through thickness cracks (Fig. 6.19). Such behaviour confirmed that the influence of the local notch stress concentration on short crack growth was limited to cracks shallower than 50 μm deep from the notch root. On the contrary Nader [2] and Talia [81], observed that growth rates of cracks, nucleated by machined scratches in 2024-T3 clad and unclad samples, increased as the scratch depth increased. However their cracks propagated along the notch root instead of moving away from it. Cracks were subjected to the local notch enhanced stress field for all their growth period. It is not surprising therefore that notch depth, which determined the local notch stress field, affected crack growth rates at any crack length. The growth rate of short cracks developed from scribes under tension and bending loads seemed to be a power function of the linear elastic stress intensity factor range but with different slope than the long crack curve (Fig. 6.19). It is worth noticing however that the long crack growth rate curve was measured on the material long transversal direction, while short cracks propagated along the sample short transversal one. Despite this discrepancy, scribed sample cracks seemed to show the typical short crack behaviour for all their propagation stage (Fig. 6.19).

Fig. 6.20 shows the comparison between crack growth rates measured by striation counting on scribed tension and bending 2024-T351 aluminium alloy samples and other short crack propagation data available in literature [82,83]. Scribe samples data were

compared to the growth rate curve, obtained by Newman et al. [82] for short cracks growing from circular holes in 2024-T3 aluminium alloy under constant amplitude fatigue loading with R=0. The propagation curve, suggested by the ESDU data sheets [83] for short cracks in unnotched 2024-T3 aluminium alloy samples, fatigued under constant amplitude loading at R=0, was displayed as well in Fig. 6.20.

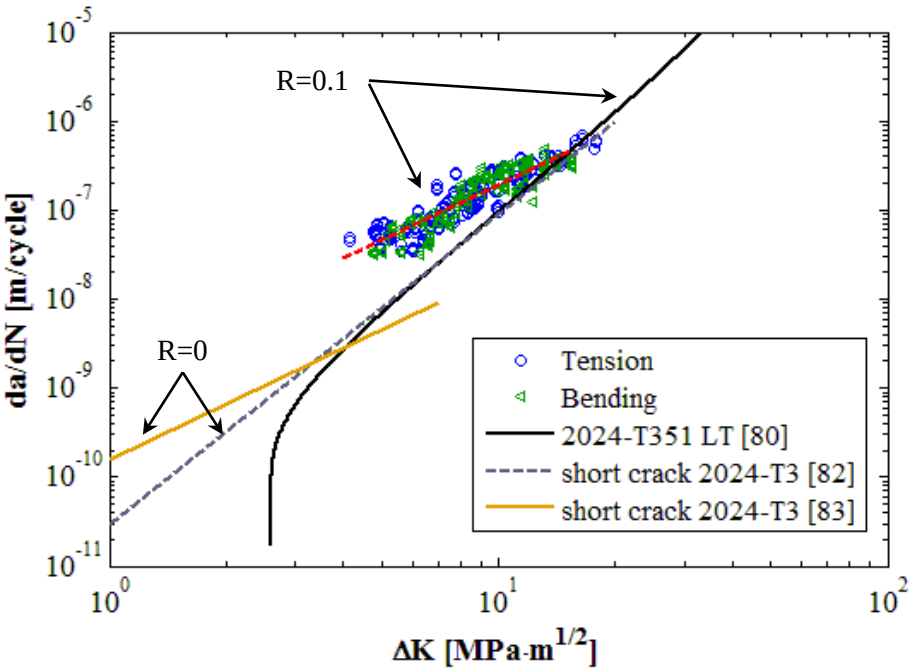

Fig. 6.20: Comparison between short crack propagation rates measured in scribed samples and other short crack propagation data

Both short crack curves from references [82,83] were obtained near the long crack threshold (Fig. 6.20). On the other hand short cracks of scribed samples showed higher growth rates ranging from $3 \cdot 10^{-8}$ m/cycle to $8 \cdot 10^{-7}$ m/cycle. For a given value of the stress intensity factor range, scribed sample short cracks grew faster than those analysed in references [82,83]. Such different growth rate was thought to be mainly caused by the presence of scribes, which, activating several nucleation sites along their roots, promoted the development of elongated through-width crack fronts or multiple elliptical cracks. Those cracks grow faster than isolated thumbnail short cracks in aluminium components. For constant amplitude fatigue loading with a positive stress ratio, Newman et al. [82] found short crack growth rates, above the long crack threshold, equal or smaller than the long crack ones at the same nominal stress intensity factors (Fig. 6.20). The same behaviour was observed for the ESDU data [83], but not for growth rates of short cracks in scribed samples under tensile and bending loads. However the scribed samples and the ESDU short crack data [83] showed trends with similar slopes (Fig. 6.20).

The capability of conventional stress intensity factor analytical corrections, used to correlate short and long crack growth data [84-86], of characterising the growth rate of short crack in scribed samples was investigated. Analysing the prediction accuracy of different short crack analytical corrections, the physical mechanisms at the basis of the short crack behaviour of cracks nucleated from scribe roots could be identified. Fig.

6.21 shows the comparison between experimental crack growth rates measured in scribed samples and the effective crack growth curve suggested by Newman et al. [84] for 2024-T3 aluminium alloy to predict short crack behaviour by means of fatigue crack closure models. The effective growth curve was obtained under a constant amplitude loading with a stress ratio of R=0.7 [84]. Fig. 6.21 also shows the short crack growth curves calculated using El Haddad's crack length correction [85] and the plastic zone correction suggested by Dugdale [86]. Both analytical curves were obtained, considering a two-dimensional edge crack growing from an initial length of a_{in}=50 μm to a final length of a_{fin}=700 μm. A value of the critical crack length of a_0=71.79 μm was used for El Haddad's crack length correction. Such value was calculated using the following equation:

$$a_0 = \frac{1}{\pi}\left(\frac{\Delta K_{th}}{\Delta \sigma_e}\right)^2 \tag{6.12}$$

assuming a crack growth threshold of ΔK_{th}=2.58 MPa·m$^{1/2}$, according to reference [80], and the fatigue limit value of $\Delta \sigma_e$=172 MPa suggested by Atzori et al. [31].

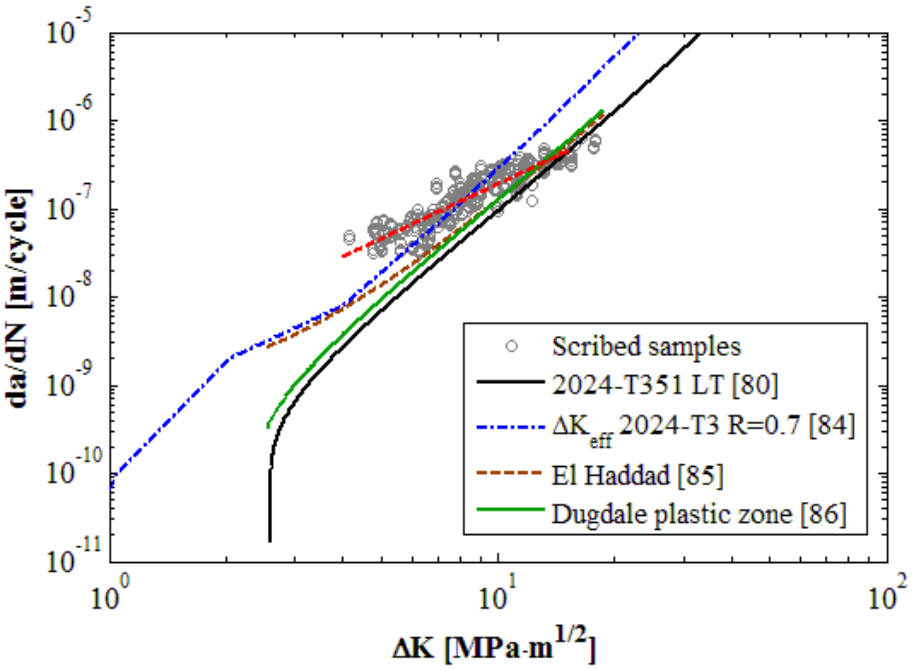

Fig. 6.21: Comparison between experimental short crack growth rate and short crack analytical corrections

None of the investigated analytical short crack ΔK corrections was able to correctly characterise the short crack behaviour of cracks nucleated from scribe marks (Fig. 6.21). For stress intensity factors ranges ΔK<8.13 MPa·m$^{1/2}$, scribed sample short cracks showed growth rates higher than those predicted by the ΔK_{eff} curve (Fig. 6.21). That is inconsistent with the linear elastic plastic-induced crack closure model [84,87], where short cracks showed faster propagation rates due to the absence or partial development of crack closure. Therefore the effective crack growth curve, derived in absence of crack closure, should represent an upper limit for growth rates [84,87]. However such limit can be crossed if crack tip small-scale yielding conditions are violated. In fact in

this case a cyclic plastic zone correction is required for the effective stress intensity range to take into account the influence of the large plastic zone on short crack propagation [88]. For cracks growing in tension and bending scribed samples small-scale yielding conditions should be fulfilled according to reference [88], as the ratio between the applied stress range $\Delta\sigma$ and two times the cyclic yield strength $2\sigma_{0.2}^{cyc}$ was $\Delta\sigma/(2\sigma_{0.2}^{cyc})<0.3$. That was also confirmed by the trend of the crack growth curve related to Dugdale's plastic zone correction [86] (Fig. 6.21). In fact, due to the small-scale yielding conditions at the crack tip, such curve was slightly translated toward higher growth rates compared to the long crack one, failing to characterise the short crack behaviour of cracks propagating from scribes (Fig. 6.21). Even the crack growth curve containing El Haddad's crack length correction [85] was not able to correctly predict the short crack behaviour of cracks growing in tension and bending scribed samples, underestimating their growth rates (Fig. 6.21). Obviously the prediction accuracy could be improved, changing the value of the critical crack length a_0. Good accuracy was obtained for a critical crack length of a_0=271 μm but such a_0 value was not anymore related to the material fatigue and crack propagation properties, being a mere fitting parameter. To conclude no one of the conventional approaches to correlate short and long crack data was able to characterise growth rates of cracks propagating from scribes under tensile and bending loads in 2024-T351 aluminium alloy sheet samples. Therefore it is not known yet which are the main mechanisms behind the short crack behaviour in scribed samples. A prediction model should probably consider the development of crack closure, the introduction of a crack length correction and the small effect of the crack tip plastic zone combined together, to accurately estimate the growth rate of short cracks in scribed samples.

6.2.5 Fatigue initiation and propagation life

By using crack growth data, total fatigue lives were divided into numbers of cycles, necessary to nucleate a fatigue crack 50 μm deep from micro-scale notches, and cycles to propagate it up to complete specimen failure. Because of the lack of information on early crack propagation at crack depths $a<50$ μm, the nucleation period was defined as the number of cycles required to form a short crack and propagate it through the sample thickness up to a depth of 50 μm from the notch root. Beyond $a=50$ μm, striations were visible on fracture surfaces and crack growth could be measured. Knowing crack shapes and critical crack lengths from the post failure fractographic investigation, ΔK values could be calculated for different crack depths and propagation lives evaluated by integrating the curve in Fig. 6.19. All data in Fig. 6.19 were fitted by the same best fit curve which was used for crack growth rate integration.

Fig. 6.18 a) shows the propagation lives, calculated in this way, for all the notches in tension samples. Propagation life decreased with increasing notch depth. Propagation life was a small fraction of total life for all the tested samples, up to a maximum value of 34%. This was for the most severe 185 μm 5 μm root radius unclad notched specimen. As previously noted, crack growth rate was insensitive to notch geometry and K_t, but ΔK was calculated including notch depth in the crack length definition, and the initial ΔK increased with increasing notch depth, remaining life being reduced. Changes in crack shape were influenced by K_t and they modified calculated ΔK values and the propagation life still further. Evidence of this effect was the influence of notch root

radius observed in Fig. 6.18 a). Root radius played a role just for notches shallower than 100 µm because that was the boundary for the appearance of several thumbnail cracks instead of a single elongated one.

Nucleation life (life to generate a 50 µm deep crack) was obtained by subtracting propagation life from the total life. A plot of percentages of total life to achieve a 50 µm crack is shown in Fig. 6.18 b) and it shows that, although propagation life reduces with increasing notch depth, the fraction of life occupied by crack growth is increasing up to a maximum of around 60% for the deepest notch of 185 µm and 5 µm root radius. Larger root radii of 50 µm had between 88% to over 95% of their life occupied by crack growth life to 50 µm depth.

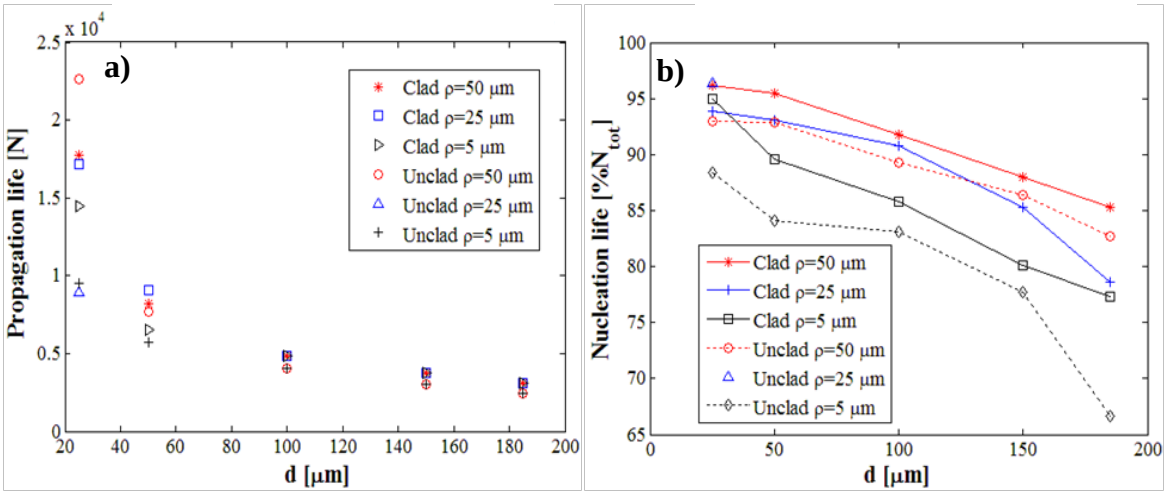

Fig. 6.22: Crack propagation life for different notch geometries in clad and unclad tension samples plotted against notch depth *d* (a). Percentage of life occupied by initiation and growth up to 50 µm crack depth plotted against notch depth *d* (b)

As crack growth up to 50 µm length was always the largest fraction of life in tension samples (between 66 and 90%), notch effect in this region dominated the entire life. That is in contrast with the short crack propagation at the root of circular holes in 2024-T3 aluminium alloy observed by Newman et al. [82] where 80 to 90% of the total fatigue life was spent to grow cracks from the length of 20 µm up to the breakthrough. The different notch size with respect to the crack length seemed to caused such behaviour discrepancy. Fig. 6.19 shows the cycles to achieve 50 µm deep crack (defined nucleation life) plotted against K_t for 5, 25 and 50 µm notch roots, in clad and unclad samples. As expected, 50 µm radius notches had significantly smaller lives with data points falling on entirely different curves for clad and unclad samples. Samples with root radii of 25 and 5 µm fell on different curves with progressively increased lives. Notch geometry influenced the extension of the notch stress concentration region and so the fatigue nucleation behaviour (section 5.4). The sharper the scribe, the higher the elastic-plastic stress and strain ranges acting on the stress concentration region (section 5.4). Moreover for a given notch shape, that is for a given aspect ratio ρ/d, the bigger the scribe size the larger the local region at the notch root influenced by the stress raising effect (section 5.4). As crack nucleation and growth up to 50 µm length occur under different stress ranges according to notch shape and size, the nucleation life at the scribe root was regulated by the scribe geometry, being shorter as the notch became sharper and larger in size (Fig. 6.19).

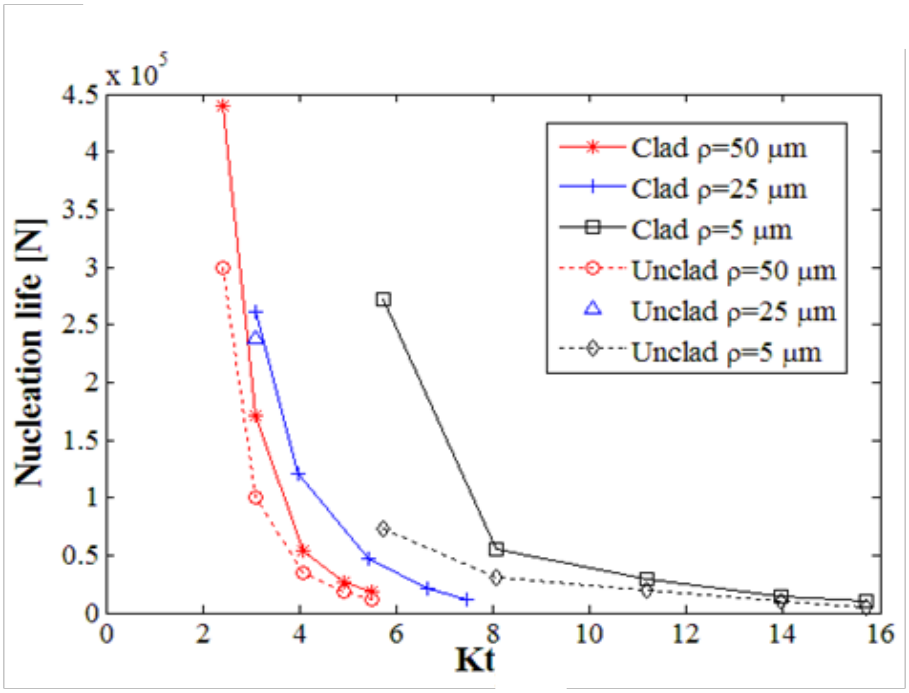

Fig. 6.23: Fatigue nucleation life to produce a 50 µm deep crack plotted against K_t for clad and unclad samples with different notch root radii

References chapter 6

[1] Khan, M. K. *Scribe marks at fuselage joins-Determination of residual stress and effect of fatigue loading using nanoindentation and synchrotron X-ray diffraction*. PhD thesis, Open University, UK, 2009.

[2] Nader, N. A. *The effect of scratches on fatigue life and fatigue crack growth of Al 2024-T3 clad*. PhD thesis, Wichita State University, 1993.

[3] Talia, M. and Talia, J. E. The effects of scratches and shot peening on the high cycle fatigue crack growth of aluminium alloy 2024-T3. In: *High Cycle Fatigue of Structural Materials*, Indianapolis Indiana USA, 14-18 Sept 1997, pp. 409-426.

[4] Inchekel, A. and Talia, J. E. Effect of scratches on the fatigue behaviour of an Al-Li alloy. *Fatigue & Fracture of Engineering Materials & Structures*, Vol. 17, No. 5, 1994, pp. 501-507.

[5] Everett, R. A. Jr., Newman J. C. Jr. and Phillips, E. P. The effect of Machining-like scratch on the fatigue life of 4340 steel. *Journal of the American Helicopter Society*, Vol. 47, No. 3, 2002, pp. 151-155.

[6] Suhr, R. W. The effect of surface finish on high cycle fatigue of a low alloy steel. *The behaviour of short fatigue cracks*, EGF Pub. 1 (Edited by K. J. Miller and E. R. de los Rios) 1986, Mechanical Engineering Publications, London, pp.68-86.

[7] Nowell, D., Dini, D. and Duò, P. Stress analysis of V-notches with and without cracks with application to foreign object damage. *Journal of Strain Analysis for Engineering Design*, Vol. 38, No. 5, 2003, pp. 429-441.

[8] Oakley, S. Y. and Nowell, D. Prediction of the combined high- and low-cycle fatigue performance of gas turbine blades after foreign object damage. *International Journal of Fatigue*, Vol. 29, 2007, pp. 69-80.

[9] Das, G., Kosai, M. and Miller, M. Development of a method for damage tolerance analysis for scribe marks adjacent to fuselage longitudinal and circumferential splices. In: *International Committee on Aeronautical Fatigue (ICAF) meeting*, Napoli, Italy, 14-18 May 2007.

[10] Suresh, S. *Fatigue of materials*, 2nd ed. New York: Cambridge University Press, 2004.

[11] Lazzarin, P. and Tovo, R. A unified approach to the evaluation of lineal elastic stress fields in the neighbourhood of cracks and notches. *International Journal of Fracture*, Vol. 78, 1996, pp. 3-19.

[12] Filippi, S., Lazzarin, P. and Tovo, R. Developments of some explicit formulas useful to describe elastic stress field ahead of notches in plates. *International Journal of Solids and Structures*, Vol. 39, 2002, pp. 4543-4565.

[13] Nowell, D., Dini, D. and Duò, P. Stress analysis of V-notches with and without cracks with application to foreign object damage. *Journal of Strain Analysis for Engineering Design*, Vol. 38, No. 5, 2003, pp. 429-441.

[14] Kyle, C. *Investigation of the transformation of defects in aircraft structures into cracks*. M Sc thesis, Cranfield University, 2005.

[15] Irving, P. E., Hopper, B. and Scott, A. J. Investigation of the effect of machined scratches on fatigue life of clad 2024-T351. Canfield University Report for Airbus ABH1, Dec 2005.

[16] Morency, R. *Fatigue crack initiation and growth from scratches in 2024 T-351 aluminium*. M Sc thesis, Cranfield University, 2006.

[17] Walmsley, S. W. *Fatigue potential of tool scratches on clad 2024-T351 aluminium alloy*. M Sc thesis, Cranfield University, 2007.

[18] Jozelich, A. M. *Investigation of the transformation of defects into fatigue cracks*. M Sc thesis, Cranfield University, 2009.

[19] Tizard, D. G. I *The influence of plasticity and residual stress in the fatigue performance of real world scribes in fuselage materials*. M Sc thesis, Cranfield University, 2010.

[20] Muskhelishvili, N. I. *Some basic problem of the theory of elasticity*, 4th ed. Groningen, Netherlands: Noordhoof Leyden, 1954.

[21] S. P. Timoshenko and J. N. Goodier. *Theory of elasticity*, 3rd ed. Singapore: McGraw-Hill, 1970.

[22] Schijve, J. The practical and theoretical significance of small cracks. An evaluation. In: *Fatigue 84*, University of Birmingham, UK, 1984, pp. 751-771.

[23] Laz, P. J. and Hillberry, B. M. Fatigue life prediction from inclusion initiated cracks. *International Journal of Fatigue*, Vol. 20, No. 4, 1998, pp. 263-270.

[24] Foth, J., Marissen, R., Nowach, H. and Lütjering, G. Fatigue crack initiation and microcrack propagation in notched and unnotched aluminium 2024-T3 specimens. In: *Fatigue 84*, University of Birmingham, UK, 1984, pp. 791-801.

[25] Blom, A. F., Hedlund, A., Zhao, W., Fathulla, A., Weiss, B. and Stickler, R. Short fatigue crack growth behaviour in Al 2024 and Al 7475. *The behaviour of short fatigue cracks*, EGF Pub. 1 (Edited by K. J. Miller and E. R. de los Rios) 1986, Mechanical Engineering Publications, London, pp. 37-66.

[26] Merati, A. A study of nucleation and fatigue behaviour of an aerospace aluminum alloy 2024-T3. *International Journal of Fatigue*, Vol. 27, 2005, pp. 33-44.

[27] Neuber, H. *Theory of notch stresses: principle for exact stress calculation* ed. Ann Arbor, MI: Edwards, 1946.

[28] Peterson, R. E. Notch sensitivity. In: *Meal fatigue*, edited by Sines, G. and Waisman J. L. New York: MacGraw-Hill, 1959, pp. 293-306.

[29] Atzori, B. and Lazzarin, P. Notch sensitivity and defect sensitivity under fatigue loading: two sides of the same medal. *International Journal of Fracture*, Vol. 107, 2000, pp. L3-L8.

[30] Atzori, B., Lazzarin, P. and Meneghetti, G. Fracture mechanics and notch sensitivity. *Fatigue & Fracture of Engineering Materials & Structures*, Vol. 26, 2003, pp. 257-267.

[31] Atzori, B., Lazzarin, P. and Meneghetti, G. A unified treatment of the mode I fatigue limit of components containing notches or defects. *International Journal of Fracture*, Vol. 133, 2005, pp. 61-87.

[32] Atzori, B., Lazzarin, P. and Meneghetti, G. Estimation of fatigue limits of sharply notched components. In: *Proceedings of FATIGUE 2006*, Atlanta, USA, 2006.

[33] Boukharouba, T., Tamine, T., Niu, L., Chehimi, C. and Pluvinage, G. The use of notch stress intensity factor as a fatigue crack initiation parameter. *Engineering Fracture Mechanics*, Vol. 50, No. 3, 1995, pp. 503-512.

[34] Lazzarin, P. and Tovo, R. A notch intensity factor approach to the stress analysis of welds. *Fatigue & Fracture of Engineering Materials & Structures*, Vol. 21, 1998, pp. 1089-1103.

[35] Atzori, B., Lazzarin, P. and Tovo, R. From a local stress approach to fracture mechanics: a comprehensive evaluation of the fatigue strength of welded joints. *Engineering Fracture Mechanics*, Vol. 22, No. 5, 1999, pp. 369-382.

[36] Atzori, B., Lazzarin, P. and Tovo, R. Stress field parameters to predict the fatigue strength of notched components. *Journal of Strain Analysis for Engineering Design*, Vol. 34, No. 6, 1999, pp. 437-453.

[37] Lazzarin, P. and Livieri, P. Notch stress intensity factors and fatigue strength of aluminium and steel welded joints. *International Journal of Fatigue*, Vol. 23, 2001, pp. 225-232.

[38] Lazzarin, P., Lassen, T. and Livieri, P. A notch stress intensity approach applied to fatigue life predictions of welded joints with different local toe geometry. *Fatigue & Fracture of Engineering Materials & Structures*, Vol. 26, 2003, pp. 49-58.

[39] Kitagawa, H. and Takahashi, S. Applicability of fracture mechanics to very small cracks or the cracks in the early stage. In: *Proceedings of Second International Conference on Mechanical Behavior of Materials*, pp. 627-631, Metals park: American Society for metals, 1976.

[40] Smith, R. A. and Miller, K. J. Prediction of fatigue regimes in notched components. *International Journal of Mechanical Science*, Vol. 20, 1978, pp. 201-206.

[41] Verreman, Y. and Limodin, N. Fatigue notch factor and short crack propagation. *Engineering Fracture Mechanics*, Vol. 75, 2008, pp. 1320-1335.

[42] Chen, D. Stress intensity factor for V-notched strip under tension or in-plane bending. *International Journal of Fracture*, Vol. 70, 1995, pp. 81-97.

[43] Du Quesnay, D. L., Yu, M. T. and Topper, T. H. An analysis of the notch size effect on the fatigue limit. *Journal of Testing and Evaluation*, Vol. 4, 1988, pp. 375-385.

[44] Ciavarella, M. and Meneghetti, G. On fatigue limit in the presence of notches: classical vs. Recent unified formulations. *International Journal of Fatigue*, Vol. 26, 2004, pp. 289-298.

[45] Manson, S. S. and Hirschberg, M. H. Low cycle fatigue of notched specimens by consideration of crack initiation and propagation. NASA Technical Note D-3146, 1967.

[46] Dowling, N. E. Combined use of strain-based fatigue methodology and notched member test data. In: *Proceedings of 2005 USAF Structural Integrity Program (ASIP) Conference*, Memphis, USA, 2005.

[47] Troshchenko, V. T. Fatigue of metals under nonuniform stressed state. Part 1. Stresses state assessment methods and results of investigation. *Strength of Materials*, Vol. 42, No. 2, 2010, pp. 129-143

[48] Taylor, D. The theory of critical distances. *A new perspective in fracture mechanics* ed. Amsterdam: Elsevier, 2007.

[49] Taylor, D. The theory of critical distances. *Engineering Fracture Mechanics*, Vol. 75, 2008, pp. 1696-1705.

[50] Taylor, D. Analysis of fatigue failures in components using the theory of critical distances. *Engineering Failure Analysis*, Vol. 12, 2005 pp. 906-914.

[51] Susmel, L. The theory of critical distances: a review of its applications in fatigue. *Engineering Fracture Mechanics*, Vol. 75, 2008, pp. 1706-1724.

[52] Susmel, L and Taylor, D. On the use of the theory of critical distances to estimate fatigue strength of notched components in the medium-cycle fatigue regime. In: *Proceedings of FATIGUE 2006*, Atlanta, USA, 2006.

[53] Susmel, L and Taylor, D. A novel formulation of the theory of critical distances to estimate lifetime of notched components in the medium-cycle fatigue regime. *Fatigue & Fracture of Engineering Materials & Structures*, Vol. 30, 2007, pp. 567-581.

[54] Yamashita, Y., Ueda, Y., Kuroki, H., and Shinozaki, M. Fatigue life prediction of small notched Ti-6Al-4V specimens using critical distance. *International Committee on Aeronautical Fatigue (ICAF) symposium*, Rotterdam, Netherland, 27-29 May 2009.

[55] Yamashita, Y., Ueda, Y., Kuroki, H., and Shinozaki, M. Fatigue life prediction of small notched Ti-6Al-4V specimens using critical distance. *Engineering Fracture Mechanics*, Vol. 77, 2010, pp. 1439-1453.

[56] Edwards, P. R. and Earl, M. G. A comparative study of the fatigue performance of notched specimens of clad and unclad aluminium alloy, with and without pre-stress. Royal Aircraft Establishment TR 75148, Dec 1975.

[57] Schijve, J., Jacobs, F. A. and Tromp, P. J. The significance of cladding for fatigue of aluminium alloys in aircraft structures. NLR TR 76065 U, 1976.

[58] Merati, A. A study of nucleation and fatigue behaviour of an aerospace aluminum alloy 2024-T3. *International Journal of Fatigue*, Vol. 27, 2005, pp. 33-44.

[59] Anderson, T. L. *Fracture mechanics fundamentals and applications*, 3rd ed. New York: CRC Press, Taylor & Francis Group, 2005.

[60] Murakami, Y. and Endo, M. Quantitative evaluation of fatigue strength of metal containing various small defects or cracks. *Engineering Fracture Mechanics*, Vol. 17, No. 1, 1983, pp. 1-15.

[61] Murakami, Y. and Endo, M. Effect of small defects on fatigue strength of metals. *International Journal of Fatigue*, Vol. 2, No. 1, 1980, pp. 23-30.

[62] Murakami, Y. and Endo, M. Effects of hardness and crack geometries on ΔK_{th} of small cracks emanating from small defects. *The behaviour of short fatigue cracks*, EGF Pub. 1 (Edited by K. J. Miller and E. R. de los Rios) 1986, Mechanical Engineering Publications, London, pp. 275-293.

[63] Vallellano, C., Navarro, A. and Domínguez, J. Fatigue crack growth threshold conditions at notches. Part I: theory. *Fatigue & Fracture of Engineering Materials & Structures*, Vol. 23, 2000, pp. 113-121.

[64] Vallellano, C., Navarro, A and Domínguez, J. Fatigue crack growth threshold conditions at notches. Part II: generalization and application to experimental results. *Fatigue & Fracture of Engineering Materials & Structures*, Vol. 23, 2000, pp. 123-128.

[65] Vallellano, C., Mariscal, M. R., Navarro, A. and Domínguez, J. A Micromechanical approach to fatigue in small notches. *Fatigue & Fracture of Engineering Materials & Structures*, Vol. 28, 2005, pp. 1035-1045.

[66] Lukas, P. and Klesnil, M. Fatigue limit of notched bodies. *Material Science & Engineering*, Vol. 34, 1978, pp. 61-66.

[67] Lukas, P., Kunz, L., Weiss, B. and Stickler, R. Notch size effects in fatigue. *Fatigue & Fracture of Engineering Materials & Structures*, Vol. 12, 1989, pp. 175-186.

[68] Lukas, P., Kunz, L., Weiss, B. and Stickler, R. Non-Damaging notches in fatigue. *Fatigue & Fracture of Engineering Materials & Structures*, Vol. 9, No. 3, 1986, pp. 195-204.

[69] DuQuesnay, D. L., Topper, T. H. and Yu, M. T. The effect of notch radius on the fatigue notch factor and the propagation of short cracks. *The behaviour of short fatigue cracks*, EGF Pub. 1 (Edited by K. J. Miller and E. R. de los Rios) 1986, Mechanical Engineering Publications, London, pp. 323-335.

[70] Taylor, D. Fatigue short cracks: the limitations of fracture mechanics. *The behaviour of short fatigue cracks*, EGF Pub. 1 (Edited by K. J. Miller and E. R. de los Rios) 1986, Mechanical Engineering Publications, London, pp. 479-490.

[71] I. S. Sokolnikoff. *Mathematical theory of elasticity*, 2nd ed. New York: McGraw-Hill, 1956.

[72] Potirniche, G. P., Daniewicz, S. R. and Newman J. C. Jr. Simulating small crack growth behaviour using crystal plasticity theory and finite element analysis. *Fatigue & Fracture of Engineering Materials & Structures*, Vol. 27, No. 1, 2004, pp. 59-71.

[73] Hill, R. Generalised constitutive relations for increment deformation of metals crystals by multislip. *Journal of the Mechanics and Physics of Solids*, Vol. 14, 1966, pp. 95-102.

[74] Das, G., Kosai, M. and Miller, M. Development of a method for damage tolerance analysis for scribe marks adjacent to fuselage longitudinal and

circumferential splices. In: *International Committee on Aeronautical Fatigue (ICAF) meeting*, Napoli, Italy, 14-18 May 2007.

[75] *AMS Handbook Volume 12 Fractography*, 9th ed. United States: ASM International. Handbook Committee, 1987.

[76] Zhai, T., Jiang, X. P., Li, J. X., Garratt, M. D. and Bray, G. H. The grain Boundary geometry for optimum resistance to growth of short fatigue cracks in high strength Al-alloys. *International Journal of Fatigue*, Vol. 27, 2005, pp. 1202-1209.

[77] Abaqus analysis user's manual version 6.8. Dassault Systèmes, 2008.

[78] Rooke, D. P. and Cartwright D. J. *Compendium of Stress Intensity Factors*, London: Her Majesty's Stationery Office, 1974.

[79] Newman, J. C. Jr. and Raju, I. S. Stress-intensity factor equations for cracks in three-dimensional finite bodies subjected to tension and bending loads. NASA Technical Memorandum 85793, Apr 1984.

[80] Afgrow database

[81] Talia, M. and Talia, J. E. Crack propagation modeling for surface generated scratches in Al 2024-T3 clad alloy. *Journal of the Mechanical Behavior of Materials*, Vol. 8, No. 2, 1997, pp. 117-139.

[82] Newman, J. C. Jr., Edwards, P. R. et al. Short-crack growth behaviour in aluminium alloy-An AGARD cooperative test programme. AGARD report 732, 1988.

[83] ESDU data sheet F.92030 Fatigue propagation behaviour of short cracks in aluminium alloys.

[84] Newman, J. C. Jr., Phillips, E. P. and Swain, M. H. Fatigue-life prediction methodology using small crack theory. NASA Technical Memorandum 1103079, (1997).

[85] El Haddad, M. H., Dowling, N. E., Topper, T. H. and Smith, K. N. Fatigue crack propagation of short crack. *Journal of Engineering Materials and Technology*, Vol. 101, No. 1, 1979, pp. 42-46.

[86] Dugdale, D. S. Yielding in steel sheets containing slits. *Journal of Mechanics and Physics of Solids*, Vol. 8, 1960, pp. 100-104.

[87] Newman, J. C. Jr., Phillips, E. P. and Everett, R. A. Jr. Fatigue analyses under constant- and variable-amplitude loading using small-crack theory. NASA Technical Memorandum 209329, (1999).

[88] Newman, J. C. Jr. A review of modelling small-crack behavior and fatigue-life predictions for aluminium alloys. *Fatigue & Fracture of Engineering Materials & Structures*, Vol. 17, No. 4, 1994, pp. 429-439.

Chapter 7
Conclusion and recommendations

7.1 Conclusion

- A procedure to machine accurate and reproducible notches as deep as few tens of microns has been developed, using diamond tipped tools. Despite the different geometry and scribing process between the regular diamond tool cut scribes and the irregular ploughed in-service scribe marks, found on aircraft fuselage joints during maintenance inspections, fatigue life predictions of real world in-service scratches based on experimental data of diamond tool scribed samples are conservative.

- Clad and unclad 2024-T351 sheet samples containing diamond cut scribes, with depths ranging from 25 to 185 μm and root radii from 5 to 50 μm, were fatigued under tensile and bending constant amplitude fatigue loading at σ_{max}=200 MPa and R=0.1. Fatigue test results show that every samples, but the unclad 25 μm deep 50 μm root radius scribed specimen, failed from the scratch. Scribes with elastic stress concentration factors $K_t \geq 2.43$ initiated fatigue cracks, which fractured the sample under tensile load. Scratches on clad and unclad samples of 2024-T351 aluminium alloy negatively affected the fatigue life under tension load up to 97.8% of life reduction. Clad samples showed nearly 50% increased fatigue life compared to unclad specimens with the same scribe geometry. Every scribe initiated fatigue cracks, which fractured samples under bending load, apart from the 50 μm deep 50 μm root radius scratch in clad samples. Scribes with $K_t \geq 2.96$ were able to initiated fatigue cracks under bending load which fractured the sample. Scribed samples, fatigued under pure bending load, showed the same trend as under tension, but produced lives on average 3 times longer than corresponding tension specimens.

- Multiple crack initiation occurred at scribe roots usually from inclusions, defects or weak points along the root. The number and density of crack nucleation sites appeared to be determined by the scribe sharpness, increasing for notches with larger stress concentrations. If $K_t > 7.76$, corresponding to an elastic-plastic longitudinal strain range at the scribe root $\Delta\varepsilon_{22} > 1.85\%$, multiple short cracks coalesced, during their early propagation, forming a unique crack elongated along the whole sample width. Such crack, growing through the samples thickness, was difficult to detect. Notches with $K_t < 4.08$, reaching $\Delta\varepsilon_{22} < 0.89\%$ at their roots, generated fracture surfaces, made of multiple thumbnail and corner cracks up to a maximum of 15 cracks per sample. For an intermediate elastic-plastic longitudinal strain range of $0.89\% \leq \Delta\varepsilon_{22} \leq 1.85\%$, obtained for $4.08 \leq K_t \leq 7.76$, tension and bending samples showed elongated or multiple crack fracture fronts depending on scribe depth and loading conditions. Early crack growth seemed to be strongly influenced by the material microstructure, despite different notch geometry, cladding and load conditions. The transition between

stage I and stage II growth seemed to be regulated by the crack tip plastic zone rather than by the notch plastic zone. Different scribes affected the early crack growth up to a maximum distance from their roots of about x=50 μm, influencing only the microstructure sensitive stage I-like crack propagation.

- Fatigue striations were clearly visible just 50-60 μm from the scribe root and such limit was considered the nucleation crack length. Crack growth rate was measured performing striation counting on fracture surfaces. Scribe geometry did not affect the fatigue growth rate, but the propagation life of cracks deeper than 50-100 μm was influenced. Growth rate in tension specimens seemed to be an exponential function of crack depth, which was independent of scribe root radius. Under bending load, growth rates appeared to be approximated by a third degree polynomial function of crack depth. For small crack lengths, cracks propagated at comparable rates under tensile and bending loads. As soon as cracks became bigger, bending growth rate turned out to be slower than the tension one. Cracks nucleated from scribe marks showed the typical short crack behaviour, growing faster than long cracks with the same linear elastic stress intensity factor. Due to the presence of long scribes, which promoted the development of elongated through-width crack fronts or multiple elliptical cracks, by activating several nucleation sites, short cracks grew faster in scribed samples than in other aluminium specimens. Growth rates of cracks propagating from scribes under tensile and bending loads were not characterised by plastic-induced crack closure, plastic zone correction or crack length correction short crack growth models. Between 66% and 90% of total fatigue life was spent growing cracks, under tensile load, from the notch root up to a length of 50 μm. Failure crack depths were approximately 1 mm; the entire life being occupied by short crack growth.

- Elastic-plastic stress and strain components at the notch root under monotonic and cyclic loadings were defined only by the scribe shape, that is related to the elastic stress concentration factor K_t. However monotonic and cyclic elastic-plastic stress and strain fields in the neighbourhood of scribes, as well as monotonic and cyclic plastic zones, were characterised by the notch shape and size. According to the occurrence of mechanical similitude conditions, scribes with the same shape but different size showed similar plastic zones and stress and strain distributions. A stabilised cyclic plastic zone was developed just at the root of scribes with a ratio between the root radius and depth $\rho/d \leq 0.2$. Cyclic plastic zones with an area up to A_{pl}=35.2 μm^2 were developed at the scribe root under fatigue tensile load. Small-scale yielding conditions existed at the scribe root. That makes possible the application of fatigue life prediction methods based on purely elastic stress distributions, like the theory of critical distances. No correlations were observed between the occurrence of a stabilised cyclic plastic zone and the sample nucleation life, defined as the number of cycles to obtain an initial crack, 50 μm deep from the notch root.

- K_t could characterise fracture morphology, the occurrence of cyclic plastic zone, plastic zone shape and stress trend but a dimension parameter is required to predict fatigue life. Traditional fatigue life prediction methods, based on the

notch sensitivity factor, are not able to correctly characterise the effect of scratches, few tens of microns deep, on the fatigue life of 2024-T351 aluminium alloy components. Due to the small scribe size, also the tradition local strain approach was not able to correctly predict the life reduction caused by scribes, underestimating total fatigue lives of scribed samples. The critical distance theory was capable of characterising the total fatigue life reduction produced by the introduction of scribes, by relating the fatigue live to a critical stress range $\Delta\sigma_{lm}$. The critical stress range was able to describe the effect of elastic stress distributions produced by dissimilar notches on the nucleation and propagation of fatigue cracks, considering also the effect of the variation of fatigue load nominal applied stress. The calculated critical distances seemed to be related to the material grain structure along the crack growth direction. A threshold value of the critical stress range $\Delta\sigma_{lm}$ below which, the material was insensitive to scribes for a given external nominal stress, could be obtained. Threshold $\Delta\sigma_{lm}$ values were $\Delta\sigma_{lm}^{th}$=246.99 MPa and $\Delta\sigma_{lm}^{th}$=268.74 MPa respectively for clad and unclad 2024-T351 aluminium alloy samples, fatigued under a tensile load with σ_{max}=200 MPa and R=0.1. Critical distance theory, despite its success in predicting the fatigue life of scribed components, cannot rationalise the process behind the transformation of superficial defects, like a scribes, into fatigue cracks, as it is nothing more than an engineering tool without any physical basis.

7.2 Recommendations for further research

- Irregular scratches with several local pits, similar to in-service scribe marks found on aircraft fuselage joints during maintenance inspections, could be analysed, comparing their effect on fatigue life of aluminium samples with that of regular rounded V-shaped scribes. If irregular real world scribes were produced cutting the material, like those machined with diamond tools, the influence of scratch geometry could be separately analysed. The geometrical effect of real world scribes in fact could be isolated from that of residual stresses and material hardening caused by the material ploughing during sealant removal. The effect of other geometrical parameters such the scratch length on sample fatigue life could also be analysed.
- Proper S-N curves of samples weakened by different scribes could be obtained, testing samples at different maximum stress under constant amplitude fatigue loading. The effect of varying the stress ratio could also be investigated.
- A methodology to measure the growth rate of cracks propagating from the scribe root inside the bulk of samples could be developed, to investigate short crack propagation from its early stage. By means of travelling optical microscope, on-line crack length measurements could be performed on lateral surfaces of samples with small width. However changing the sample width, crack loading constrain conditions were changed too, as on the sample surface, plane stress conditions instead of plane strain occurred. Interruptive fatigue tests, where samples are stopped at given numbers of cycles and statically fracture to measure the fatigue crack length on the fracture surface, could be performed. The effect of local notch stress field on early short crack growth could be assessed, comparing experimental results.

- The effect of combined tension plus bending load condition at the scribe location in fuselage joints could be assessed, performing a fatigue test campaign using scribed coupons, representative of longitudinal and circumferential joints. The effect of sealant and rivets on the coupon stiffness and consequently on local stress conditions at the scribe site could be evaluated as well.
- A damage tolerance approach for fatigue life estimation based on short fatigue crack growth prediction could be developed, as soon as crack growth data for the entire crack development from nucleation to sample final failure are available. Such approach could be based on a numerical simulation of crack propagation using a finite element code. In that case the effect of the local notch stress field on the crack opening displacement or closure could be readily evaluated.